

## FLUIDS ENGINEERING DIVISION

Editor  
**J. KATZ (2005)**

Assistant to the Editor  
**L. MURPHY (2005)**

Associate Editors  
**M. J. ANDREWS (2006)**  
**S. BALACHANDAR (2005)**  
**A. BESHOK (2008)**  
**K. S. BREUER (2006)**  
**G. L. CHAHINE (2006)**  
**S. GÖGINENI (2006)**  
**A. GOTTO (2007)**  
**F. F. GRINSTEIN (2006)**  
**T. J. HEINDEL (2007)**  
**H. JOHARI (2006)**  
**J. LEE (2006)**  
**Y. T. LEE (2007)**  
**J. A. LIBURDY (2007)**  
**P. LIGRANI (2008)**  
**T. J. O'HERN (2008)**  
**H. PIOMELLI (2007)**  
**S. ROY (2007)**  
**D. SIGINER (2005)**  
**K. D. SQUIRES (2005)**  
**Y. TSUJIMOTO (2006)**  
**S. P. VANKA (2007)**

**PUBLICATIONS DIRECTORATE**  
Chair, **A. G. ERDMAN**

**OFFICERS OF THE ASME**  
President, **H. ARMEN**  
Executive Director, **V. R. CARTER**  
Treasurer, **T. D. PESTORIUS**

**PUBLISHING STAFF**  
Managing Director, Engineering  
**T. G. LOUGHLIN**  
Director, Technical Publishing  
**P. DI VIETRO**  
Production Coordinator  
**A. HEWITT**  
Production Assistant  
**M. ANDINO**

## TECHNICAL PAPERS

- 405 **Mass Flow Rate Controlled Fully Developed Laminar Pulsating Pipe Flows**  
S. Ray, B. Ünsal, F. Durst, Ö. Ertunc, and O. A. Bayoumi
- 419 **Laminar Flow Across a Bank of Low Aspect Ratio Micro Pin Fins**  
Ali Koşar, Chandan Mishra, and Yoav Peles
- 431 **Two-Dimensional Pipe Model for Laminar Flow**  
M. C. P. Brunelli
- 438 **Controlling Turbulence in a Rearward-Facing Step Combustor Using Countercurrent Shear**  
David J. Forliti and Paul J. Strykowski
- 449 **Boundary-Layer Transition Affected by Surface Roughness and Free-Stream Turbulence**  
S. K. Roberts and M. I. Yaras
- 458 **Unsteady Numerical Simulations of Turbulence and Coherent Structures in Axial Flow Near a Narrow Gap**  
D. Chang and S. Tavoularis
- 467 **Three-Dimensional Numerical Simulation and Performance Study of an Industrial Helical Static Mixer**  
Ramin K. Rahmani, Theo G. Keith, and Anahita Ayasoufi
- 484 **Influence of Bulk Fluid Velocity on the Efficiency of Electrohydrodynamic Pumping**  
Vishal Singhal and Suresh V. Garimella
- 495 **Flow Study in the Impeller-Diffuser Interface of a Vaned Centrifugal Fan**  
Sofiane Khelladi, Smaïne Koudri, Farid Bakir, and Robert Rey
- 503 **On the Physics of Flow Separation Along a Low Pressure Turbine Blade Under Unsteady Flow Conditions**  
Meinhard T. Schobeiri, Burak Öztürk, and David E. Ashpis
- 514 **Experimental and Numerical Investigation on the Effects of the Seeding Properties on LDA Measurements**  
Angelo Algieri, Sergio Bova, and Carmine De Bartolo
- 523 **Growth of Binary Alloyed Semiconductor Crystals by the Vertical Bridgman-Stockbarger Process with a Strong Magnetic Field**  
Stephen J. LaPointe, Nancy Ma, and D. W. Mueller, Jr.
- 529 **Behavior of Short Lateral Dead Ends on Pipeline Transients: A Lumped Parameter Model and an Analytical Solution**  
Xiao-Jian Wang, Martin F. Lambert, and Angus R. Simpson
- 536 **The Effects of Polymer Solution Preparation and Injection on Drag Reduction**  
R. Sun Chee Fore, J. Szwalek, and A. I. Sirviente
- 550 **Optimum Bifurcating-Tube Tree for Gas Transport**  
Tianshu Liu
- 554 **New Physically Based Approach of Mass Conservation Correction in Level Set Formulation for Incompressible Two-Phase Flows**  
Snehamooy Majumder and Suman Chakraborty
- 564 **Population Balance Modeling of Turbulent Mixing for Miscible Fluids**  
Giridhar Madras and Benjamin J. McCoy

(Contents continued on inside back cover)

This journal is printed on acid-free paper, which exceeds the ANSI Z39.48-1992 specification for permanence of paper and library materials. ©™  
♻️ 85% recycled content, including 10% post-consumer fibers.

Transactions of the ASME Journal of Fluids Engineering (ISSN 0098-2202) is published bimonthly (Jan., Mar., May, July, Sept., Nov.) by The American Society of Mechanical Engineers, Three Park Avenue, New York, NY 10016. Periodicals postage paid at New York, NY and additional mailing offices.

POSTMASTER: Send address changes to Transactions of the ASME, Journal of Fluids Engineering, c/o THE AMERICAN SOCIETY OF MECHANICAL ENGINEERS, 22 Law Drive, Box 2300, Fairfield, NJ 07007-2300.

CHANGES OF ADDRESS must be received at Society headquarters seven weeks before they are to be effective. Please send old label and new address.

STATEMENT from By-Laws. The Society shall not be responsible for statements or opinions advanced in papers or printed in its publications (B7.1, Par. 3).

COPYRIGHT © 2005 by the American Society of Mechanical Engineers. Authorization to photocopy material for internal or personal use under those circumstances not falling within the fair use provisions of the Copyright Act, contact the Copyright Clearance Center (CCC), 222 Rosewood Drive, Danvers, MA 01923, tel: 978-750-8400, www.copyright.com. Request for special permission or bulk copying should be addressed to Reprints/Permission Department, Canadian Goods & Services Tax Registration #126148048.

- 572 Unstructured Grid Based Reynolds-Averaged Navier-Stokes Method for Liquid Tank Sloshing  
Shin Hyung Rhee
- 583 Influence of Wall Proximity on the Lift and Drag of a Particle in an Oscillatory Flow  
Paul F. Fischer, Gary K. Leaf, and Juan M. Restrepo
- 595 Slot Jet Impinging On A Concave Curved Wall  
Virginie Gilard and Laurent-Emmanuel Brizzi
- 604 Statistical Approach for Estimating Intervals of Certification or Biases of Facilities or Measurement Systems Including Uncertainties  
F. Stern, A. Olivieri, J. Shao, J. Longo, and T. Ratcliffe

## TECHNICAL BRIEFS

- 611 Energy Separation in Steady Separated Wake Flow  
B. W. van Oudheusden
- 615 Comparison of Exact and Sommerfeld Solution for the Pressure of a Journal Bearing  
Yan Qu, Dohyung Kim, and Ronald L. Panton
- 619 Numerical Investigation of Baffle-Plate Effect on Hood-Capture Flow  
Ming-Jyh Chern and Jang-Xing Lee
- 624 Analysis for Slip Flow Over a Single Free Disk With Heat Transfer  
Aytac Arikoglu and Ibrahim Ozkol

The ASME Journal of Fluids Engineering is abstracted and indexed in the following:

*Applied Science & Technology Index, Chemical Abstracts, Chemical Engineering and Biotechnology Abstracts (Electronic equivalent of Process and Chemical Engineering), Civil Engineering Abstracts, Computer & Information Systems Abstracts, Corrosion Abstracts, Current Contents, Ei EncompassLit, Electronics & Communications Abstracts, Engineered Materials Abstracts, Engineering Index, Environmental Engineering Abstracts, Environmental Science and Pollution Management, Excerpta Medica, Fluidex, Index to Scientific Reviews, INSPEC, International Building Services Abstracts, Mechanical & Transportation Engineering Abstracts, Mechanical Engineering Abstracts, METADEX (The electronic equivalent of Metals Abstracts and Alloys Index), Petroleum Abstracts, Process and Chemical Engineering, Referativnyi Zhurnal, Science Citation Index, SciSearch (The electronic equivalent of Science Citation Index), Shock and Vibration Digest, Solid State and Superconductivity Abstracts, Theoretical Chemical Engineering*

S. Ray<sup>1</sup>

B. Ünsal

e-mail: buensal@lstm.uni-erlangen.de

F. Durst

Ö. Ertunc

O. A. Bayoumi

Institute of Fluid Mechanics (LSTM),  
Friedrich-Alexander-Universität Erlangen-  
Nürnberg, Cauerstr. 4, D-91058 Erlangen,  
Germany

# Mass Flow Rate Controlled Fully Developed Laminar Pulsating Pipe Flows

*Pressure gradient driven, laminar, fully developed pulsating pipe flows have been extensively studied by various researchers and the data for the resultant flow field are available in a number of publications. The present paper, however, concentrates on related flows that are mass flow driven, i.e., the flows where the mass flow rate is prescribed as  $\dot{m} = \dot{m}_M + \dot{m}_A f_m(t)$  and  $f_m(t)$  is periodically varying in time. Sinusoidal and triangular mass flow rate pulsations in time are analytically considered in detail. Results of experimental investigations are presented and are complemented by data deduced from corresponding analytical and numerical studies. Overall, the results provide a clear insight into mass flow rate driven, laminar, fully developed pulsating pipe flow. To the best of the authors' knowledge, flows of this kind have not been studied before experimentally, analytically and numerically. [DOI: 10.1115/1.1906265]*

## 1 Introduction and Aim of Work

The basic theory of incompressible, internal, laminar flows is well developed and the state of knowledge up to the middle of the 20th century is well documented in books by Howarth [1] and Moore [2]. However, much progress has been made since then. Most recently, time-dependent, periodic pipe and channel flows have received increasing attention from the fluid mechanics community. In the review by Gündoğdu and Carpinlioglu [3], literature surveyed, shows that nearly all theoretical treatments of time-dependent pulsating flows are pressure gradient driven, i.e., the flow is pulsating owing to an imposed pressure gradient of the following form:

$$\frac{dP}{dx} = \left(\frac{dP}{dx}\right)_M + \left(\frac{dP}{dx}\right)_A \sin(2\pi ft) \quad (1)$$

where the time-varying part is described by a single-frequency harmonic oscillation,  $f$ , and the amplitude of an axial pressure gradient,  $(dP/dx)_A$ . The resultant flows are usually referred to as pulsating flows when the time-averaged pressure gradient  $(dP/dx)_M \neq 0$  and as oscillating flows when  $(dP/dx)_M = 0$ . Lambossy [4] was the first to derive an analytical solution for this type of flow. A few years later, Uchida [5] presented the general analytical solution for arbitrary, time-varying, axial pressure gradient driven, laminar pulsating flows through pipes. A brief summary of this solution is presented in the Appendix for the sake of completeness. The axial pressure gradient in such cases is considered as a general wave form, which may be represented by a Fourier series

$$\frac{dP}{dx} = \left(\frac{dP}{dx}\right)_0 + \sum_{n=1}^{\infty} \left(\frac{dP}{dx}\right)_{C_n} \cos(2\pi nft) + \sum_{n=1}^{\infty} \left(\frac{dP}{dx}\right)_{S_n} \sin(2\pi nft), \quad (2)$$

where  $(dP/dx)_0$  has the same meaning as  $(dP/dx)_M$  in Eq. (1) and the oscillating part of the longitudinal pressure gradient is expressed as a composition of basic harmonic functions, with am-

plitudes  $(dP/dx)_{C_n}$  and  $(dP/dx)_{S_n}$ . Each of the wave forms has a frequency corresponding to integer multiples of the basic frequency  $f$ . Utilizing the linear property of the governing differential equation for an incompressible fluid, describing the flow, Uchida [5] applied the solution for a single frequency to each of the terms in the Fourier series. In this manner, he obtained the general solution for periodically pulsating, laminar, fully developed pipe flows by a summation over all the individual solutions. It is obvious that the solution of Lambossy [4] is a special case of this general solution and can easily be derived from the solution of Uchida [5].

Recently, Majdalani and Chibli [6] extended the work of Uchida [5] for channel flows, which was otherwise not available in the literature. Hence analytical treatments of the pressure gradient driven, pulsating, laminar, fully developed pipe flows involving incompressible fluids are well established and extension of the work for channel flows is also available.

Many experimental studies have also been conducted with flow facilities in which the pressure gradient, in the form of Eq. (1), was generated and (or) controlled by flow interrupters, by reciprocating pistons, by rotary valves, etc. Among these, the studies of Denison et al. [7], Muto and Nakane [8], and Shemer and Wygnanski [9] are examples of comprehensive investigations. These results are also well supported by the analytical solutions of Lambossy [4] and Uchida [5]. More recently, Durst et al. [10] combined the solution of Lambossy [4] and instantaneous local density approximation-velocity measurements at the center of a pipe to carry out instantaneous volume flow rate measurements for different pulsating flows. It is important to note that pulsations, having wave forms other than sinusoidal, for example, triangular pulsations with time, have not yet been investigated, probably because of the experimental difficulties associated with accurate and reproducible generation of the desired pressure gradient.

A careful study of the literature on pulsating pipe flows suggests that equally good knowledge does not exist for periodically pulsating, fully developed, laminar pipe flows generated by a controlled, time-dependent mass flow rate. More recently Das and Arakeri [11] presented analytical solutions of resulting pressure gradient and velocity distribution for a prescribed, time varying volume flow rate through a pipe. The flow was assumed to be laminar and fully developed. They presented examples of starting flows with trapezoidal variation in the volume flow rate with time and sinusoidally oscillating flows that are either impulsively blocked or starting from the rest. Very recently, a similar study on

<sup>1</sup>On leave from the Department of Mechanical Engineering, Jadavpur University Kolkata 700 032, India.

Contributed by the Fluids Engineering Division for publication in the JOURNAL OF FLUIDS ENGINEERING. Manuscript received by the Fluids Engineering Division February 18, 2004; revised manuscript received March 6, 2005. Associate Editor: S. Balachandar.

pulsating channel flow for arbitrary volume flow rate variation was presented by Muntges and Majdalani [12]. However, none of these studies are well supported by simultaneous experimental validations. This is probably due to the fact that no reliable experimental data could be produced earlier owing to the difficulties associated with generation of accurate and reproducible volume flow rate variation with time.

For a periodic flow, the general variation of the mass flow rate through a pipe may be considered as

$$\dot{m} = \dot{m}_M + \dot{m}_A f_m(t), \quad (3)$$

where  $\dot{m}_M$  is the cycle-averaged mass flow rate and  $\dot{m}_A$  is the corresponding amplitude of pulsation. The function  $f_m(t)$  is a periodic function in time and has a period  $t_p$ , such that  $f_m(t+t_p) = f_m(t)$ . To the best of the authors' knowledge, there does not exist either an analytical solution for the resultant time-varying flow field and the corresponding pressure gradient variation or an experimental flow facility that generates accurate time-dependent mass flow rates. This finding initiated the authors' work on time-dependent, laminar, mass flow rate controlled, pulsating flow through pipes, which is summarized in this paper.

During this work, a mass flow rate control system was developed that permits one to produce any arbitrary time variation of  $\dot{m}(t)$ . The developed system is described shortly in Sec. 2 together with the flow facility and the appropriate measuring equipment. For detailed description, one may refer to the paper by Durst et al. [13]. The whole setup was employed to study experimentally laminar, fully developed, pulsating pipe flows.

It is obvious from the previous discussions that when the axial pressure gradient is given in the form of a Fourier series, the velocity field and, hence, the mass flow rate for a laminar, pulsating flow through a pipe can be obtained analytically. In the present case, however, the mass flow rate through a pipe is prescribed. This gives rise to an "inverse" problem, where the resultant pressure gradient that occurs in the governing equation is not a priori known. Based on the initial solutions of Uchida [5], an analytical solution is derived for the resultant time-varying velocity field and the corresponding pressure variations for a given mass flow rate variation,  $\dot{m}(t)$ . The general form of the mass flow rate can be described by a Fourier series

$$\dot{m} = \dot{m}_0 + \sum_{n=1}^{\infty} \dot{m}_{C_n} \cos(2\pi nft) + \sum_{n=1}^{\infty} \dot{m}_{S_n} \sin(2\pi nft) \quad (4)$$

where  $\dot{m}_0 = \dot{m}_M$  in Eq. (3). Moreover, the solution suggests that the time-varying mass flow rate and the time-varying pressure gradient can be written as functions of each other and knowledge of one of these two is sufficient for the determination of all other unknowns of the flow. The details of the analytical solution are presented in Sec. 3. In this section, sinusoidally and triangularly pulsating mass flow rate variations are treated as examples and the final results are presented. The analytical results are also compared in the same section with the corresponding experimental data. Some other types of pulsating flows, having higher degrees of discontinuities than the triangular pulsation, are treated numerically as well. In general, these pulsations cannot be accurately represented by an appropriate Fourier series of the type shown in Eq. (4) and one must apply Lanczos' sigma factor to avoid the Gibbs Phenomenon. The comparisons of the analytical solution with applied sigma factor, numerical solution, and experimental results are also presented in this section for power-type mass flow rate pulsations.

Finally, with the aid of experimental, analytical, and numerical tools, various physical aspects of the mass flow rate controlled, laminar, pulsating flows of incompressible fluids through pipes are considered in detail. Section 4 presents conclusions and an outlook towards future research in this field.

## 2 Experimental Investigations

**2.1 Experimental Setup and Measuring Equipment.** In order to carry out the experimental investigations on mass flow rate controlled pulsating flows, a mass flow rate control system was developed. The basic design concepts of the system and its essential parts were presented by Durst et al. [13]. Some verification experiments were also presented in this article in order to demonstrate the outstanding properties of the mass flow control unit. The developed mass flow controller allowed to generate any kind of preset time-dependent mass flow rate variations with very high cycle to cycle repeatability and accuracy in the range of 0–217.8 g min<sup>-1</sup>. The overall accuracy of the mass flow rate controller was found to be within  $\pm 1\%$ .

An experimental setup employing the developed mass flow rate control system was set up in the authors' laboratory for time-dependent, laminar mass flow driven pipe flow investigations. A schematic diagram of the setup is given in Fig. 1. For the authors' experiments, the mass flow rate control system was supplied with pressurized air of 5 bar. An externally produced signal from the computer was used to supply the time-dependent mass flow rate signal to the mass flow control unit. The signal can be, in principle, any function of time and can be freely chosen via the computer software employed. After the mass flow control unit, the flow was conditioned with wire screens and a flow straightener. A 2 m  $\times$  14-mm-diam Perspex pipe was added after the flow conditioner for the present investigations. For the present experimental setup, under steady flow conditions, the flow remained laminar up to Re=6000. However, to be on the safer side, in the present investigations the maximum Reynolds number was maintained below 4650 for all the experimental runs. Furthermore, in order to ensure the laminar state of flow in the pipe, the centerline velocity was monitored at the end of the pipe with a DISA 55 M01 constant-temperature hot-wire anemometer.

Static pressure measurements were performed with ten pressure transducers distributed along the length of the pipe. The operating range of the pressure sensors was 20 mbar and the transducers were temperature compensated. The natural frequency of these transducers was around 1 kHz, which allowed tracking of fast pressure changes resulting due to pulsating flows. All the measurements were digitized simultaneously by the computer through a 16 bit 333 kHz data acquisition card and measurements were synchronized with input signals of the mass flow rate controller, which were produced by a 12 bit 200 kHz data acquisition card. During postprocessing of the data, the statistical information and the time-based information (frequency, amplitude, etc.) were extracted and other analyses, such as digital filtering and fast Fourier transforms, were conducted as and when required.

As mentioned earlier, the mass flow rate variations with time were generated using the mass flow rate controller by supplying the corresponding electrical signal (0–10 V) to its analog port. In the present experiments, the mass flow rates were not directly measured, but, they were taken from the given input signals. The entire mass flow rate control unit, which produces highly accurate mass flow rates (within  $\pm 1\%$ ), was previously calibrated and the details were provided by Durst et al. [13].

**2.2 Experimental Investigations.** In order to study the behavior of mass flow rate controlled pulsating flows through pipes, experiments were carried out in which sinusoidal and triangular mass flow rate pulsations were applied for various flow frequencies  $f$ . The resulting axial pressure gradients were measured at a location 1.75 m away from the pipe entrance such that the flow may be considered to be fully developed at this position (this location corresponds to 125 D). For sinusoidal pulsations, three-dimensional mass flow rate amplitudes ( $\dot{m}_A^*$ ), namely, 0.95, 0.72 and 0.61, were chosen, where,  $\dot{m}_A^*$  is the ratio of the amplitude of time-varying part of the mass flow rate ( $\dot{m}_A$ ) to the cycle-averaged mass flow rate ( $\dot{m}_M$ ). For each of these cases, the frequency of

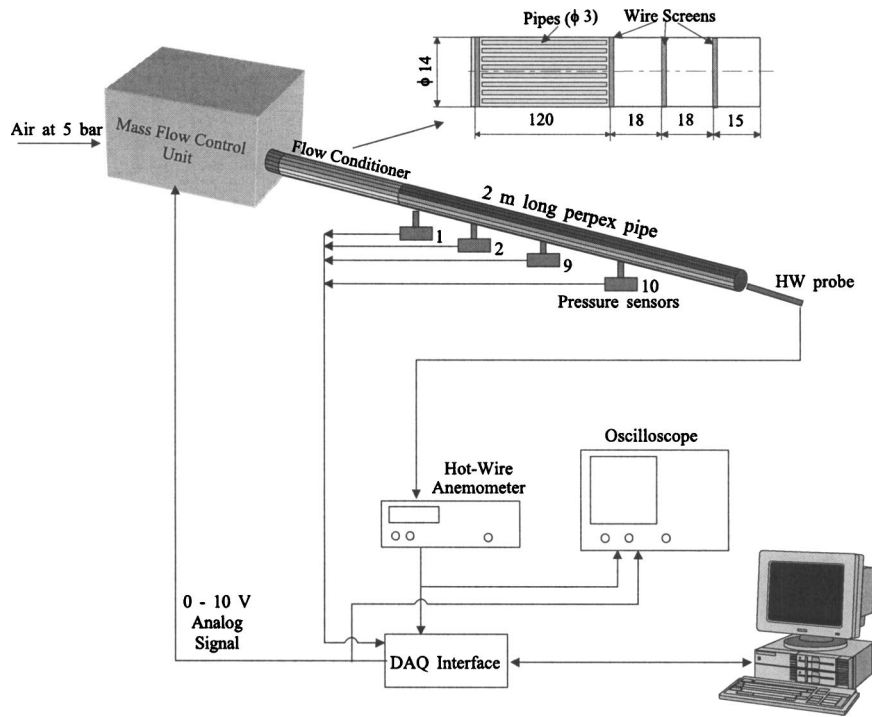


Fig. 1 Schematic diagram of the experimental setup

pulsation was varied over a wide range,  $f=0.001-22.5$  Hz. Triangular pulsations, on the other hand, were applied only for  $m_A^* = 0.95$  and the frequency range was varied from 0.001 to 20 Hz.

Acquired pressure signals were analyzed through Fourier transformation and the corresponding phase and amplitude information was obtained from the first harmonic, which is satisfactory for sinusoidal pulsations. In the case of triangular pulsations, owing to deviations of the shape of the signal, which will be considered

later, digital filtering was first applied in order to remove the noise, before applying fast-Fourier transform to obtain amplitude and phase information. For all cases, the mean (time-averaged) value of the pressure signals was calculated by considering more than 50 periods.

2.2.1 *Flow With Sinusoidal Pulsations.* In Fig. 2 examples of applied sinusoidal mass flow pulsations and measured axial pres-

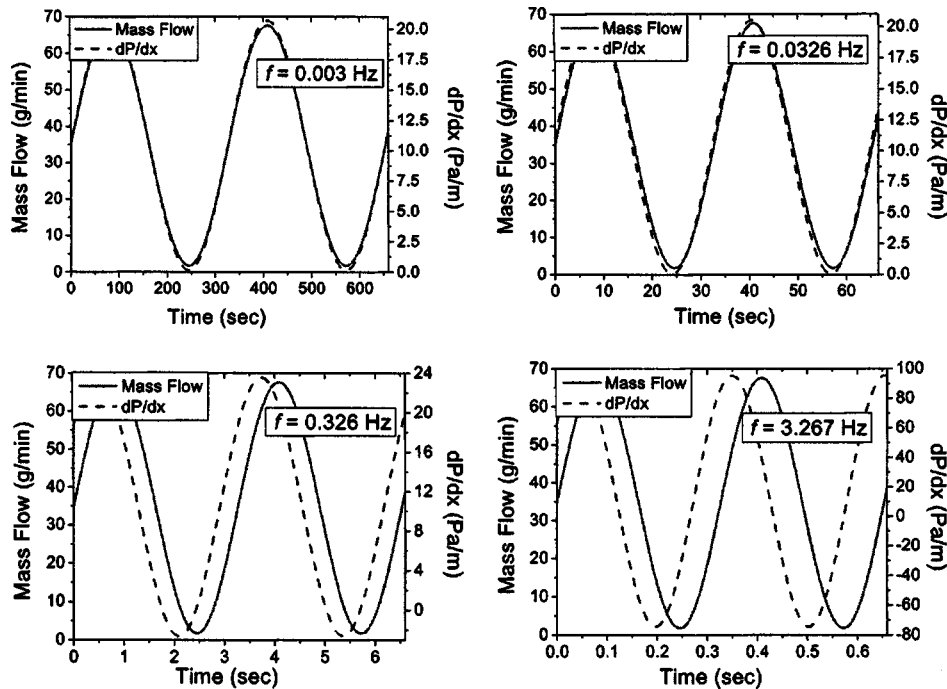


Fig. 2 Applied sinusoidal mass flow rate and measured pressure gradients for  $m_A^* = 0.9473$ , for different pulsation frequencies

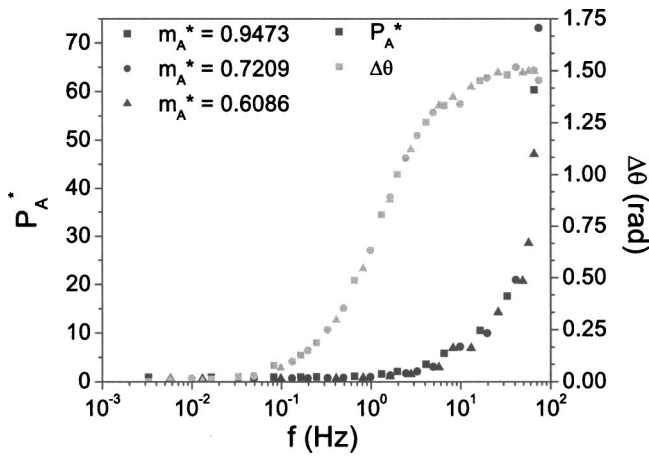


Fig. 3 Variation of  $\Delta\theta$  and  $\hat{P}_A^*$  with  $f$  and  $\hat{m}_A^*$  for sinusoidal pulsations

sure gradients are presented. The mass flow rate amplitude and mean mass flow rates were kept constant and the pulsation frequency was increased logarithmically from 0.003 to 3.267 Hz. Since these are raw experimental data, the results are presented in the form of dimensional quantities. It is clear from Fig. 2 that, as expected, with increase in pulsation frequency, the amplitude of axial pressure gradient also increases. The phase difference between the two signals is virtually nonexistent at very low frequencies ( $f=0.0033$  and  $0.0326$  Hz), whereas it increases with further increase in pulsation frequency.

Figure 3 shows the variation in the phase difference,  $\Delta\theta$  in radians, between the applied mass flow rate pulsation and the resultant axial pressure gradient with the pulsation frequency. The figure also shows the variation of dimensionless pressure drop amplitude,  $\hat{P}_A^*$ , with the pulsation frequency,  $f$ , for different mass flow rate amplitudes,  $\hat{m}_A^*$ . It can be observed from the figure that

the variation of  $\hat{m}_A^*$  has no effect on the phase difference and hence it can be concluded that the only parameter on which the phase difference depends is the pulsation frequency. The phase difference does not exist up to  $f=0.02$  Hz. It then appears and increases with increase in flow frequency, and after  $f=10$  Hz, the phase difference reaches a constant value of around  $\pi/2$ . It also appears from Fig. 3 that the dimensionless amplitude ratio,  $\hat{P}_A^*$ , is independent of  $\hat{m}_A^*$ . However, as will be shortly evident during the analytical treatment of the problem, this is not true. This false appearance may be attributed solely to the very high scale of  $\hat{P}_A^*$ , which varies from  $\hat{P}_A^* \approx \hat{m}_A^*$  (for very low frequency) to  $\hat{P}_A^* \approx 75$  (for  $f \approx 30$ ). The figure, however, reveals certain other important characteristics of flow. For very low pulsation frequencies, the value of  $\hat{P}_A^*$  remains nearly constant and then increases gradually up to  $f=10$  Hz. With further increase in  $f$ ,  $\hat{P}_A^*$  shows a very rapid increase.

**2.2.2 Flow With Triangular Pulsations.** Examples of applied triangular mass flow pulsations and measured axial pressure gradients are provided in Fig. 4 for  $\hat{m}_A^*=0.9473$  and the pulsation frequency is increased logarithmically from 0.0033 to 3.267 Hz. It is clear from the pressure gradient wave forms that, particularly for higher pulsation frequencies, there occurs a sudden jump in the axial pressure gradient, where a discontinuity exists in the mass flow rate variation. For very low values of  $f$ , the resultant axial pressure gradient also appears to be triangular. However, the shape of the pressure gradient changes with increase in  $f$  and when  $f=0.326$  and  $3.267$  Hz the resulting pressure gradients are distinctly different from the applied mass flow rate pulsation, characterized by sudden changes, where the accelerating (or decelerating) flow changes suddenly to decelerating (or accelerating) flow. The magnitude of this sudden change also increases with increase in pulsation frequency. It may be recognized that with increase in pulsation frequency, the acceleration (or deceleration) and, hence, the rate of change of acceleration (or deceleration) near the point of discontinuity in mass flow rate pulsation also

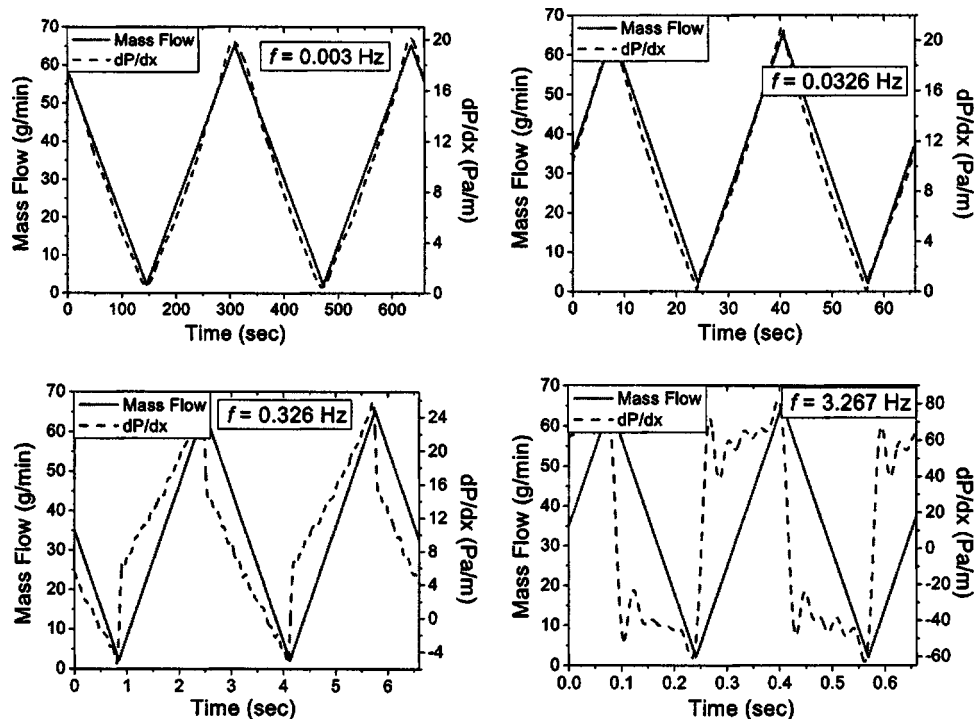


Fig. 4 Applied triangular mass flow pulsations and measured pressure drop wave forms for different pulsation frequencies

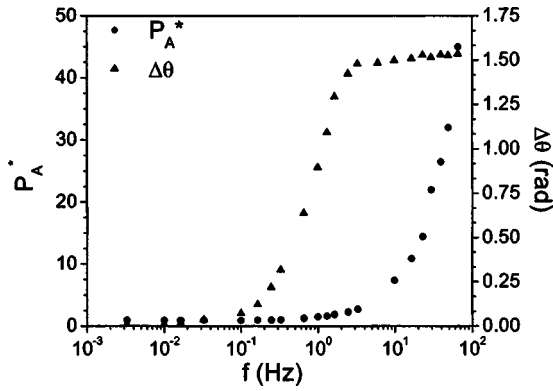


Fig. 5 Variation of  $\Delta\theta$  and  $\hat{P}_A^*$  with  $f$  for triangular pulsations

increase. To generate such flows, the resultant axial pressure gradient also changes rapidly and this rate of change increases with increase in frequency. This is clearly demonstrated in the Fig. 4. The presence of higher harmonics is also evident for  $f=3.267$ . This is due to the fact that the mass flow variation can no longer be represented as a perfect triangular wave, since the time constant of the equipment is 125 Hz. These effects and the probable cause will be discussed further during the presentation of analytical results in the next section.

Figure 5 shows the variation of the phase difference between the mass flow and the axial pressure gradient along with the variation in  $\hat{P}_A^*$  with  $f$ .  $\hat{P}_A^*$  shows a similar behavior, as observed for the case of sinusoidal pulsations. However, as is evident from Fig. 5, triangular pulsations resulted in a higher values of  $\Delta\theta$  compared to those obtained for sinusoidal pulsations. As a result, it attains the asymptotic value of  $\pi/2$  at a much lower frequency. This behavior may be attributed to the presence of sharp discontinuity in the pressure gradient.<sup>3</sup>

### 3 Analytical Investigations

The analytical solution for pressure gradient driven, axisymmetric, laminar, fully developed, pulsating pipe flows is presented in the Appendix A. The solution clearly shows that, if the pressure gradient is known as a function of time and is expressed in the form of a Fourier series, the solution for other important quantities, such as, the velocity and the mass flow rate, can be easily obtained by analytical treatment of the governing equation. It is evident from proper scaling considerations, introduced in the Appendix, that the analytical solutions for all important quantities may be expressed in terms of their steady and oscillating parts, where the normalized oscillating parts are functions of only dimensionless frequency. Hence, pressure driven pulsating pipe flows cannot only be treated analytically, but the results may also be presented in a very general form that provides a good insight into the physics of the flow. However, as explained in the previous section, under the present experimental conditions, the mass flow rate through the tube, rather than the pressure gradient, is controlled. As a result, the pressure gradient is not known a priori and hence it is necessary to solve the “inverse” of the problem treated in the Appendix A. These derivations are presented in this section.

#### 3.1 Treatment of General Mass Flow Rate Pulsation.

Based on the considerations in the Appendix A, it is shown that the following relationship holds between the time-varying axial pressure gradient and the resulting mass flow rate:

<sup>3</sup>According to the present definition, when, after the sudden increase (or decrease) in the axial pressure gradient, the resultant value reaches the mean of the overall waveform,  $\Delta\theta$  is equal to  $\pi/2$ .

$$\dot{m}^* = \frac{\dot{m}}{\dot{m}_A} = 1 - \sum_{n=1}^{\infty} \frac{4\hat{P}_{en}^* i^n}{\pi n F} \left[ 1 + \frac{2i^{1/2} J_1[(2\pi n F)^{1/2} i^{3/2}]}{(2\pi n F)^{1/2} J_0[(2\pi n F)^{1/2} i^{3/2}]} \right] \exp(2\pi n F \tau i) \quad (5)$$

This equation holds for the normalized mass flow rate pulsations that result from a normalized pulsating pressure field and vice versa, i.e.,  $\hat{P}_{en}^*$  is also given by the above equation if  $\dot{m}^*$  is prescribed. Hence the entire analysis provided in the Appendix A for pressure gradient driven flow can be adopted for mass flow rate driven pulsating pipe flows with only minor modifications. At this point, let us consider only the sine terms in the expression for the pressure gradient, as given in Eq. (A3). This is done for simplicity, however, without losing the generality of the analysis.<sup>4</sup> Under this condition, the  $n$ th amplitude of the sine wave is given by  $\hat{P}_{en}^* = -i\hat{P}_{sn}^*$ . It is also obvious from Eq. (A9) that the mass flow rate contains two distinct parts, where the steady part, in the dimensionless form, is given by unity and the  $n$ th oscillating component is given by

$$\dot{m}_{os,n}^* = -\frac{4\hat{P}_{sn}^*}{\pi n F} \left[ 1 + \frac{2i^{1/2} J_1[(2\pi n F)^{1/2} i^{3/2}]}{(2\pi n F)^{1/2} J_0[(2\pi n F)^{1/2} i^{3/2}]} \right] \exp(2\pi n F \tau i) \quad (6)$$

It may also be identified from the above equation that a complex variable,  $\psi_n$ , may be defined, which is solely a function of  $n$ th frequency,  $nF$ . Therefore,  $\psi_n(nF)$  is written as

$$\psi_n(nF) = -\frac{4}{\pi n F} \left[ 1 + \frac{2i^{1/2} J_1[(2\pi n F)^{1/2} i^{3/2}]}{(2\pi n F)^{1/2} J_0[(2\pi n F)^{1/2} i^{3/2}]} \right] \quad (7)$$

Splitting the complex variable,  $\psi_n$ , into real and imaginary parts, one obtains

$$\psi_n(nF) = \Re(\psi_n) + i\Im(\psi_n) \quad (8)$$

where  $\Re(\psi_n)$  is the real part and  $\Im(\psi_n)$  is the imaginary part of  $\psi_n(nF)$ , respectively. Substituting the expression for  $\psi_n(nF)$  from Eq. (8) and expanding the exponential term, Eq. (6) may be written as

$$\dot{m}_{os,n}^* = \hat{P}_{sn}^* [\Re(\psi_n) + i\Im(\psi_n)] [\cos(2\pi n F \tau) + i \sin(2\pi n F \tau)] \quad (9)$$

The real part of the above equation is obtained as

$$\dot{m}_{os,n}^* = \hat{P}_{sn}^* [\Re(\psi_n) \cos(2\pi n F \tau) - \Im(\psi_n) \sin(2\pi n F \tau)] \quad (10)$$

which may also be written in the form of a sine function as

$$\dot{m}_{os,n}^* = \hat{P}_{sn}^* |\psi_n| \sin \left[ 2\pi n F \tau - \tan^{-1} \left\{ \frac{\Re(\psi_n)}{\Im(\psi_n)} \right\} \right] \quad (11)$$

The complete expression for the mass flow rate through the pipe for a pressure driven flow may, therefore, be written as

$$\dot{m}^* = 1 + \sum_{n=1}^{\infty} \hat{P}_{sn}^* |\psi_n| \sin \left[ 2\pi n F \tau - \tan^{-1} \left\{ \frac{\Re(\psi_n)}{\Im(\psi_n)} \right\} \right] \quad (12)$$

It is easily recognized from the above expression that each of the oscillating components of the mass flow rate is expressed in terms

<sup>4</sup>It may be recognized that the pressure gradient in Eq. (A3) may also be expressed as

$$-\frac{1}{\rho} \left( \frac{dP}{dx} \right) = \hat{P}_0 \left[ 1 + \sum_{n=1}^{\infty} \{ (\hat{P}_{cn}^*)^2 + (\hat{P}_{sn}^*)^2 \}^{1/2} \sin \{ 2\pi n F \tau + \tan^{-1} \{ \hat{P}_{cn}^* / \hat{P}_{sn}^* \} \right]$$

which is clearly a sine series, with a modified magnitude (the absolute value of the complex variable,  $\hat{P}_{en}^*$ ) and a corresponding phase. Thus, the foregoing analysis may also be applied for the general situation as well with minor modification in the expression for pressure gradient.

of a sine function. The series also contains a distinct amplitude and a phase lag corresponding to each of the frequencies. Let us now consider the mass flow rate controlled flows, where the time-varying pulsating mass flow rate is given generally in the form of a Fourier series<sup>5</sup>

$$\dot{m}^* = 1 + \sum_{n=1}^{\infty} \dot{m}_n^* \sin(2\pi n F \tau) \quad (13)$$

Now, it would be essential to compare Eq. (12), which is the solution for mass flow rate for pressure-driven flows, with the prescribed mass flow rate for the mass flow rate controlled flow in Eq. (13). For the sake of comparison, it is better to rewrite Eq. (12) in the following form:

$$\dot{m}^* = 1 + \sum_{n=1}^{\infty} \dot{m}_n^* \sin(2\pi n F \tau - \Delta\theta_{m,n}) \quad (14)$$

where  $\dot{m}_n^*$  and  $\Delta\theta_{m,n}$  are, respectively, the normalized amplitude and the phase lag of the  $n$ th wave of the mass flow rate oscillation and are given as follows:<sup>6</sup>

$$\dot{m}_n^* = \hat{P}_{sn}^* |\psi_n| \quad (15)$$

$$\Delta\theta_{m,n} = \tan^{-1} \left\{ \frac{\Re(\psi_n)}{\Im(\psi_n)} \right\} \quad (16)$$

It is obvious from Eq. (15) that a dimensionless amplitude ratio of the mass flow rate for the  $n$ th signal can be defined as  $\phi_{m,n} = \dot{m}_n^* / \hat{P}_{sn}^* = |\psi_n|$ . It is also important to note that both the amplitude ratio and the phase lag are only functions of the  $n$ th frequency,  $nF$ . For a prescribed mass flow rate problem, however, all the amplitudes,  $\dot{m}_n^*$ , are known for each of the frequencies. Hence, Eq. (15) can be used to obtain the values of the required pressure gradient amplitudes,  $\hat{P}_{sn}^*$ , since  $|\psi_n|$  depends only on the given frequency,  $nF$  [see Eq. (7) for further clarification]. Similarly, the required phase difference of the pressure gradient, which would generate the given mass flow rate distribution, can also be obtained from Eq. (16). Therefore, the complete form of the normalized resultant pressure gradient pulsation is given as

$$\left( -\frac{1}{\rho} \frac{dP}{dx} \right)^* = \left( -\frac{1}{\rho} \frac{dP}{dx} \right) / \hat{P}_0 = 1 + \sum_{n=1}^{\infty} \hat{P}_{sn}^* \sin(2\pi n F \tau + \Delta\theta_{m,n}) \quad (17)$$

It may be observed that in order to obtain the complete pressure gradient, one would also require the value of the steady part (mean) of the pressure gradient pulsation,  $\hat{P}_0$  (which is also equal to  $\hat{P}_M$ ). This may be obtained from the knowledge of the cycle-averaged mass flow rate,  $\dot{m}_M$ . The mean cycle-averaged axial velocity through the cross section of the tube,  $U_{av}$ , can be written in terms of both  $\dot{m}_M$  and  $\hat{P}_M$  as (see Appendix A for details)

$$U_{av} = \frac{\dot{m}_M}{\rho \pi R^2} = \frac{\hat{P}_M R^2}{8\nu} \quad (18)$$

From the above equation,  $\hat{P}_M$  is obtained as

$$\hat{P}_M = \frac{8\mu\dot{m}_M}{\rho^2 \pi R^4} \quad (19)$$

<sup>5</sup>In Eq. (13),  $\dot{m}_n^*$  is the prescribed dimensionless amplitude of the  $n$ th frequency of the mass flow rate oscillation. It will be further clarified when the analysis for triangular pulsating mass flow rate controlled flow will be described.

<sup>6</sup>It is important to note that Eq. (14) is the solution of the pressure gradient driven flows. In this equation,  $\dot{m}_n^*$  and  $\Delta\theta_{m,n}$  are obtained using Eqs. (15) and Eq. (16).

**3.2 Treatments of Flows With Sinusoidal Pulsation.** Before presenting the details of complicated mass flow rate pulsations, let us first consider the simple case of a sinusoidal pulsation, which is given by

$$\dot{m}^* = \frac{\dot{m}}{\dot{m}_M} = 1 + \dot{m}_A^* \sin(2\pi f t) = 1 + \dot{m}_A^* \sin(2\pi F \tau) \quad (20)$$

The above equation shows that the flow is characterized by a single frequency and, hence, one can easily obtain the amplitude ratio,  $\phi_m = |\psi_n|$ , and the phase lag,  $\Delta\theta_m$ , for the mass flow rate from Eqs. (15) and Eq. (16), respectively. The corresponding function,  $\psi(F)$ , is obtained from Eq. (7) by putting  $n=1$ . The required mean pressure gradient is obtained from Eq. (19). Therefore, the normalized pressure gradient, that would generate the given mass flow rate through the tube, may now be written as

$$-\frac{1}{\rho} \left( \frac{dP}{dx} \right) = \hat{P}_0 [1 + \hat{P}_s^* \sin(2\pi F \tau + \Delta\theta_m)] \quad (21)$$

where the amplitude of pressure gradient pulsation,  $\hat{P}_s^* = \dot{m}_A^* / \phi_m$ , is obtained in a straightforward manner.

The analytical solutions of the axial pressure gradients for sinusoidally pulsating flows are compared with the corresponding experimental results in Fig. 6 for  $F=0.01, 0.1, 1$ , and  $10$ . For the sake of comparison, in this figure the experimental results for pressure drop are also presented in the form of dimensionless quantities. It is obvious that the general agreement is extremely good. The figure also shows the applied mass flow rate as a function of dimensionless time. It is clear that for very low frequencies ( $f=0.01$  and  $0.1$ ), the magnitude of the dimensionless axial pressure gradient,  $(dP/dx)_A^*$ , is almost equal to the dimensionless amplitude of the prescribed mass flow rate,  $\dot{m}_A^*$ . The phase difference is also almost nonexistent at these low frequencies. Both the phase difference and  $(dP/dx)_A^*$ , however, increase with the increase in frequency of pulsation.

It is also obvious from the analytical treatment of the inverse problem that the amplitude ratio, defined as  $\dot{m}_A^* / (dP/dx)_A^*$ , and also the phase difference are only functions of the pulsation frequency,  $F$ . The comparison of the analytical solution and the experimental data for the amplitude ratio and the phase difference, as presented in Fig. 7, not only shows excellent agreement between the two, but also reveals this fact.

**3.3 Treatments of Flows With Triangular Pulsation.** It is evident from the previous discussion that the inverse problem can be easily solved when a simple sinusoidal pulsation in the mass flow rate is considered. Let us now consider a more complex case of a triangular pulsation. A typical triangular pulsation can be expressed in the form of a Fourier series as follows:

$$\dot{m}^* = 1 + \frac{8\dot{m}_A^*}{\pi^2} \sum_{n=1,3,5,\dots}^{\infty} \frac{(-1)^{(n-1)/2}}{n^2} \sin(2\pi n F \tau) \quad (22)$$

Let us now consider the  $n$ th term in the above series, that describes the oscillating part of the mass flow rate. This is given as

$$\dot{m}_{os,n}^* = \frac{8(-1)^{(n-1)/2} \dot{m}_A^*}{\pi^2 n^2} \sin(2\pi n F \tau) \quad (23)$$

Therefore, it can be immediately identified that for the  $n$ th sinusoidal signal, the amplitude and the frequency are given as

$$\dot{m}_n^* = \frac{8(-1)^{(n-1)/2} \dot{m}_A^*}{\pi^2 n^2} \quad (24)$$

$$F_n = nF \quad (25)$$

One should therefore construct the  $n$ th pressure signal which would generate the corresponding mass flow rate as described by Eqs. (23)–(25). As was performed earlier for sinusoidal pulsation,



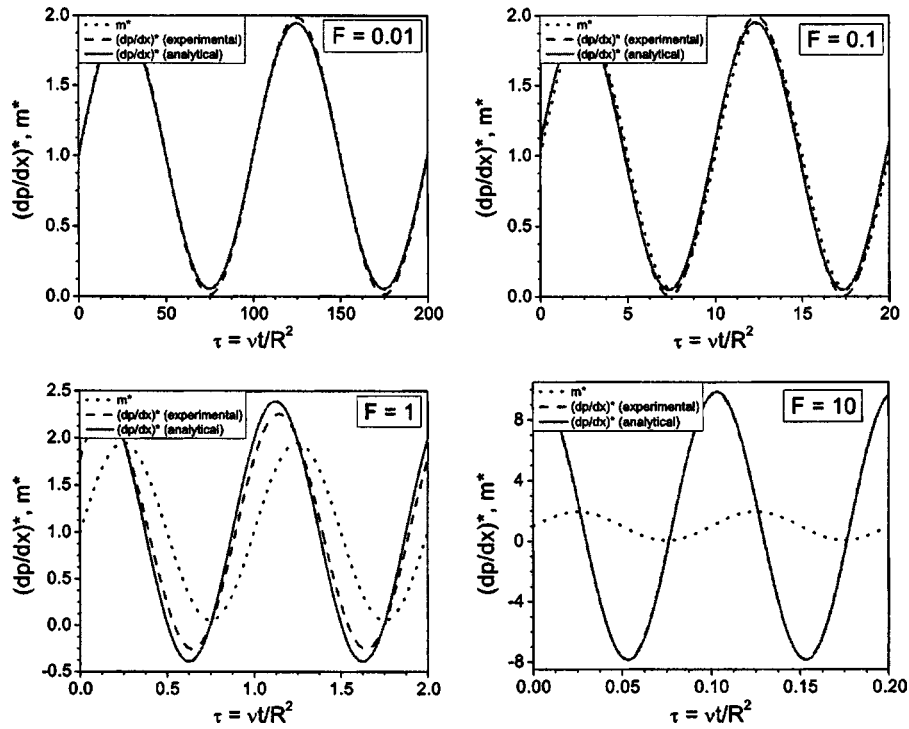


Fig. 6 Comparison of experimental and analytical pressure gradients for sinusoidal mass flow rate pulsations for  $F=0.01, 0.1, 1$  and  $10$

the amplitude ratios,  $\phi_{m,n}$ , and the phase lags,  $\Delta\theta_{m,n}$ , are obtained for each of the frequencies,  $nF$ , using Eqs. (15) and (16), respectively. Therefore, the complete normalized pressure gradient that would generate the given triangular mass flow rate pulsation is obtained as

$$-\frac{1}{\rho} \left( \frac{dP}{dx} \right) = \hat{P}_0 \left[ + \sum_{n=1,3,5,\dots}^{\infty} \hat{P}_{sn}^* \sin(2\pi nF\tau + \Delta\theta_{m,n}) \right] \quad (26)$$

where the amplitude of pressure gradient pulsation for the  $n$ th wave is given as  $\hat{P}_{sn}^* = \hat{m}_n^* / \phi_{m,n}$ .

In Fig. 8, the analytical solutions of the axial pressure gradients for the case of triangular pulsations are compared with the corresponding experimental results for  $F=0.01, 0.1, 1$ , and  $10$ . It also shows the applied mass flow rate as a function of dimensionless time. It is observed that the general agreement is extremely good for lower frequencies. However, the agreement is moderate for

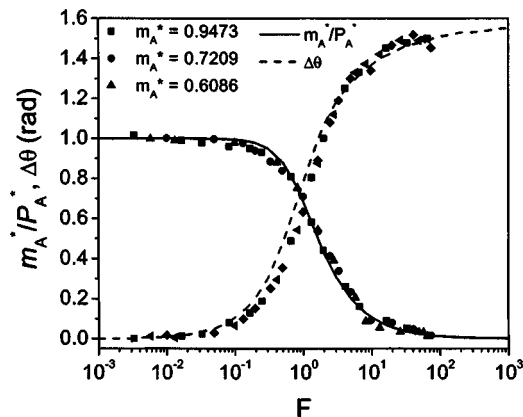


Fig. 7 Variation of  $\Delta\theta$  and  $\hat{P}_A^*$  with  $F$  and  $\hat{m}_A^*$  for sinusoidal pulsations

higher frequencies. Particularly at a very high frequency ( $F=10$ ), the presence of higher harmonics in the experimental results is different in appearance from the analytical solutions, which also show the presence of higher harmonics, particularly prominent near the discontinuity. This issue is addressed below. From Fig. 8, it is also clear that for very low frequencies ( $F=0.01$  and  $0.1$ ), the magnitude of the dimensionless axial pressure gradient,  $(dP/dx)_A^*$ , is almost equal to the dimensionless amplitude of the prescribed mass flow rate,  $\hat{m}_A^*$ . The phase difference is also almost nonexistent at these low frequencies. Both the phase difference and  $(dP/dx)_A^*$ , however, increase with increase in frequency of pulsation.

Figure 9 shows the variations of the analytically obtained and experimentally observed phase difference and amplitude ratio [defined in a manner similar to that for sinusoidal pulsation,  $\hat{m}_A^* / (dP/dx)_A^*$ ] with the dimensionless frequency of pulsation. It is clear that here also, the general agreement between the analytical and experimental results is extremely good. Figure 9 also shows that the phase difference, which is small (almost nonexistent) for lower frequencies, increases sharply for moderate values of  $F$  and reaches its asymptotic value of  $\pi/2$  at a much lower frequency as compared to the case of sinusoidal pulsations (see Fig. 7 for comparison).

Let us now focus on the presence of the higher harmonics in the experimental results for  $F=10$  and its associated discrepancy with the analytical results. In order to explain this apparent disagreement the power spectrum of the axial pressure gradient data is analyzed in Fig. 10. It clearly shows that for all cases, a strong secondary frequency is generated at around  $f=33$  Hz. The question that remains to be answered is, therefore, from where does this frequency appear? It may be postulated that this frequency appears from the experimental system and its associated instrumentation. The system as a whole, therefore, has a cutoff frequency of 33 Hz and all the signals, beyond this frequency are essentially of no importance. In the analytical study, when the mass flow rate is expressed in terms of a Fourier series, a certain number of terms is considered (which is usually very high). The

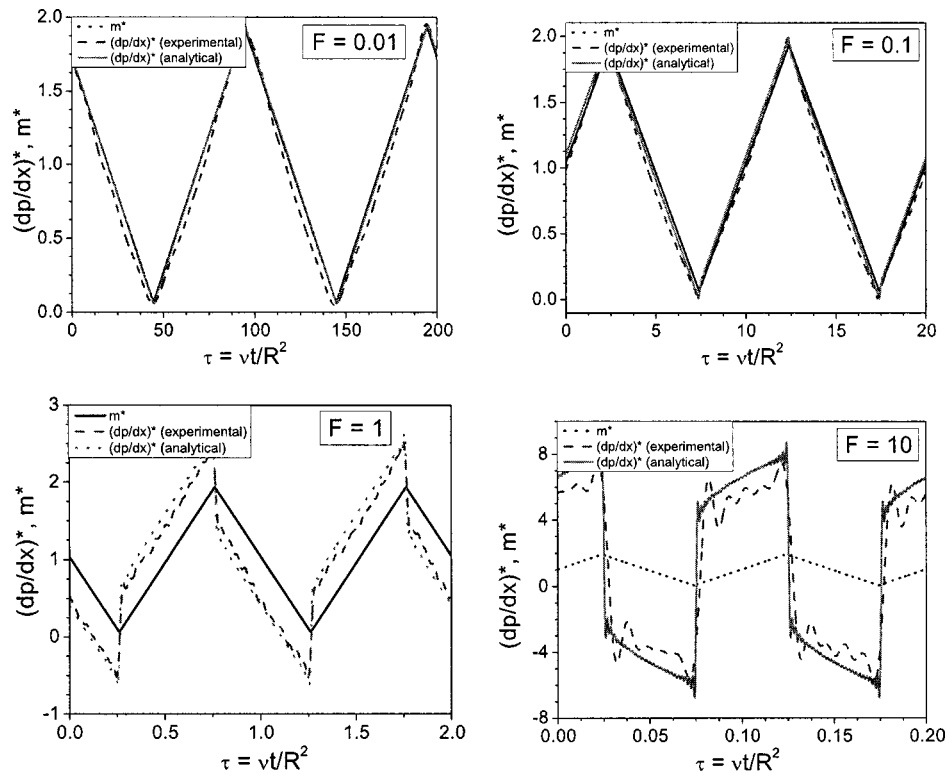


Fig. 8 Applied triangular mass flow pulsations and comparison of experimental and analytical pressure gradient wave forms for  $F=0.01, 0.1, 1$  and  $10$

apparent discrepancy may be attributed to this fact. In order to demonstrate this, the analytical results are presented in Fig. 11 for  $F=10$ , using up to 40 terms (corresponding to  $f \approx 125$  Hz) and ten terms (corresponding to  $f \approx 33$  Hz). It is obvious that when the cutoff frequency for the analytical solution is restricted to its appropriate value, the result also shows the presence of similar higher harmonics, as observed in the experiments. It is also important to note that when the mass flow rate data are generated by considering smaller number of terms in the Fourier series, some amount of error is automatically introduced. In the experiments a similar error is also present because of the time constant of the mass flow rate control system and the associated instrumentation.

**3.4 Identification of Different Flow Regimes.** From Figs. 7 and 9 for sinusoidal and triangular pulsations, different flow regimes for pulsating flows may be identified for sinusoidal and triangular pulsations, respectively. Earlier, Ohmi and Iguchi [14]

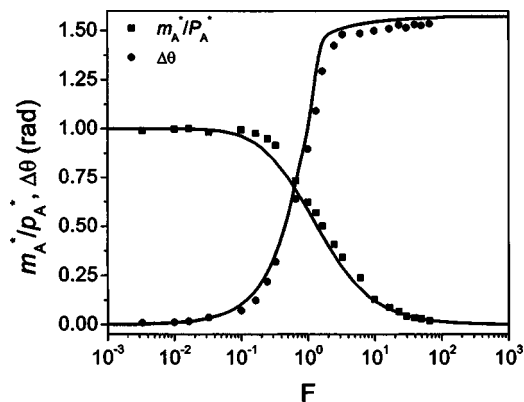


Fig. 9 Variation of  $\Delta\theta$  and  $\hat{P}_A$  with  $F$  for triangular pulsations

made similar classifications for sinusoidally pulsating flows based on the phase difference data. They termed the flow regime “quasi-steady” when the value of  $\dot{m}_A^*/(dP/dx)_A^* \leq 0.95$ , which corresponds to a dimensionless frequency of pulsation  $F \leq 0.277$ . Similarly, the regime is termed “inertia dominated,” when  $F \geq 124$ . The regime between these two is termed “intermediate.” However, it may be noted here that these definitions, although being conceptually true, are not unique and depend strongly on the parameter and the criterion chosen to identify such regimes. From Fig. 7, it is observed that if the same definitions for different flow regimes are adopted in the present study, almost the same values of limiting pulsation frequencies are obtained. However, these values would be substantially modified if the phase difference is chosen as the parameter for such definitions. Similar observations are made for the case of triangular pulsations, presented in Fig. 9, hence, the comments are also similar. As such, there is no need for further precise definition of these regimes, as long as the entire variation is available.

**3.5 Pulsations With Discontinuities.** In the case of power or sawtooth pulsations, the discontinuity in mass flow rate is more severe than that for triangular pulsation. The results for flows with power pulsation for  $F=0.1$  and  $10$  are presented in Fig. 12, where the figures at the top show the complete variation and those at the bottom show the zoomed view near the discontinuity in mass flow rate. It is obvious that the sudden decrease (or increase) in pressure gradient near the discontinuity is more than that observed earlier for triangular pulsation. The overall agreement in the observed pressure gradients, obtained with different methods, is excellent at lower frequencies (for example,  $F=0.1$ ). However, the zoomed views show that even at lower frequencies, the analytical solution produces an oscillatory pressure gradient near the discontinuity, which is nonphysical in nature. It may be noted that for such pulsations with strong discontinuities, the Fourier series produces an exact (or desired) oscillatory mass flow rate, since it cannot handle such a strong discontinuity and this is known as

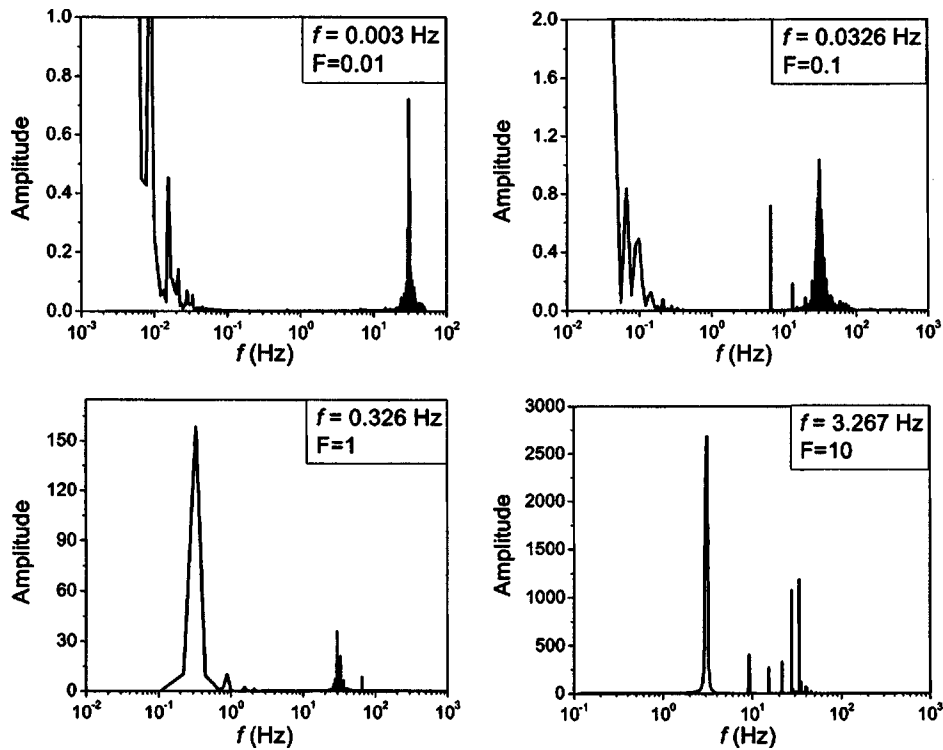


Fig. 10 Power spectrum of pressure wave forms for  $F=0.01, 0.1, 1$  and  $10$  triangular mass flow rate pulsations

Gibb's phenomenon. In the numerical method (see Appendix B), however, the discontinuity is handled by setting a very small value of  $\delta t$ , above which, the mass flow rate is allowed to change. This may be regarded as one of the techniques to avoid discontinuity. Figure 12 shows (particularly the zoomed view) that with numerical treatment, the generated pressure field appears to be smooth. When the pulsation frequency is very high (for example,  $F=10$ ), the analytical solution produces severe oscillations in the pressure gradient (they are also high in magnitude) and, hence, they are not shown. On the other hand, the nonphysical oscillations in analytical solution can be removed by the application of Lanczos' Sigma factor (see Hamming [15] for details) which is defined as

$$f(\theta) = \frac{1}{2}a_0 + \sum_{n=1,3,5,\dots}^{k-1} \text{sinc}\left(\frac{2n}{k}\right) [a_n \cos(n\theta) + b_n \sin(n\theta)] \quad (27)$$

where the sinc term is the sigma factor.

In Fig. 13 a comparison is provided between the analytical solution with applied sigma factor and the numerical solution. It is clear from the figure that by the application of sigma factor, analytical solution gives smooth pressure field as good as the numerical one.

#### 4 Conclusions

In the present paper, various issues of laminar, fully developed, mass flow rate controlled, pulsating pipe flows have been considered experimentally, analytically, and numerically. The review of the literature shows that although much effort has been put into solving pressure gradient driven pulsating pipe flows, to the best of the authors' knowledge, little effort has been put into the study of mass flow rate controlled flows. In this paper, results were

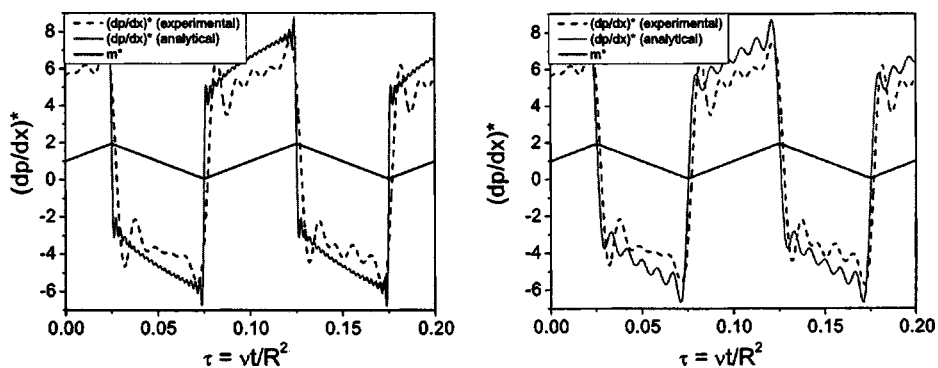


Fig. 11 Effect of number of terms used in Fourier series in analytic solution of triangular mass flow rate pulsations for  $F=10$  (left one with 40 terms corresponding to 125 Hz, right one with ten terms corresponding to 33 Hz)

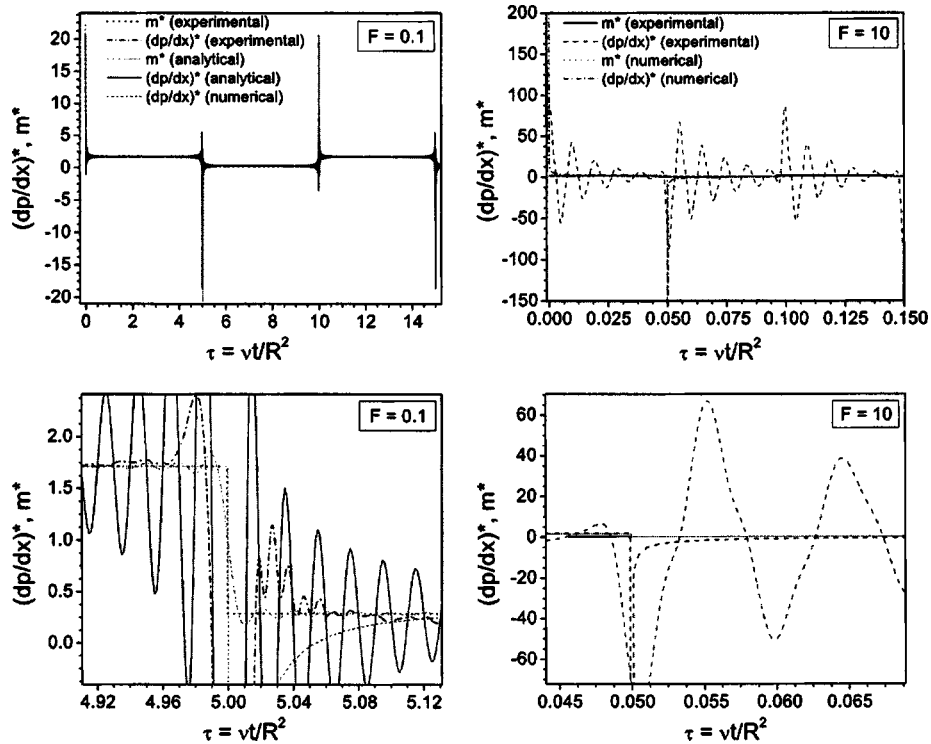


Fig. 12 Results for flows with power pulsation for  $F=0.1$  and  $10$  (top: the complete variation, bottom: zoomed view near the discontinuity)

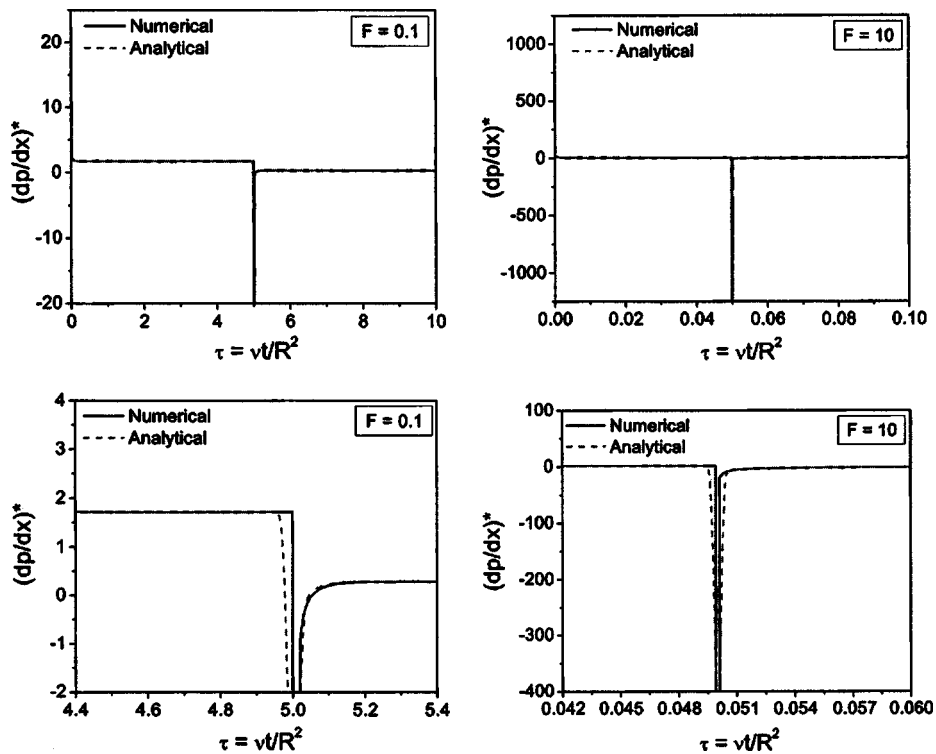


Fig. 13 Comparison of analytical solution with applied  $\sigma$  factor and numerical solution for flows with power pulsation for  $F=0.1$  and  $10$  (top: the complete variation, bottom: zoomed view near the discontinuity)

generated for sinusoidal, triangular, and power-type pulsations. The major conclusions may be summarized as follows:

- The results for sinusoidal pulsation show that the amplitude ratio, defined as  $\hat{m}_A^*/(dP/dx)_A$ , and the phase difference between the mass flow rate and the pressure gradient depend solely on the dimensionless frequency  $F$ . Hence this forms the most important basis for analytical solutions of other types of pulsations. Both of these data were verified with experiments and the results were found to be in excellent agreement.
- The analytical solution for other types of pulsations, where the mass flow rate can be expressed in terms of a Fourier series, can be obtained from the knowledge of sinusoidal pulsation. In these situations, the amplitude ratio and the phase difference for each of the frequencies (where the  $n$ th frequency is given by  $nF$ ) are obtained separately. The required pressure gradient can then be generated by superposing the results for each of the frequencies that construct the mass flow rate signal. The results generated from this analytical treatment have been successfully used for the solution of triangular pulsations. The results obtained for lower frequencies are in excellent agreement with the experimental data. However, for higher frequencies, both analytical and experimental results show oscillations, particularly near the point of discontinuity.
- For flows with a higher order of discontinuity, such as power pulsations, the analytical solution produces a very high degree of nonphysical oscillations, particularly near the discontinuity. This is due to the poor definition of Fourier series for such pulsations and it is shown that these oscillations can be removed by the application of Lanczos' sigma factor.

Finally, the present study has shown that the employed mass flow rate control system permits time variations of pulsating flows to be chosen that have mass flow rate controlled properties regarding their time variations. The instrument provides an excellent basis for detailed experimental investigations of time-varying internal flows. Through well controlled time variations of the mass flow rate, experimental investigations can be carried out and their results can also be compared with data from analytical and numerical studies. In this way, extensive investigations into pulsating internal flows are feasible and should be carried out in the future.

## Acknowledgments

Dr. Subhashis Ray thanks the authorities of Jadavpur University for granting leave to carry out this research work. He also thanks the Alexander von Humboldt Foundation for financing his research stay at the Institute of Fluid Mechanics (LSTM-Erlangen), Friedrich Alexander Universität, Erlangen-Nürnberg, Germany.

## Appendix A: Analytical Treatments of Pressure Driven, Axisymmetric, Laminar, Fully Developed, Pulsating Pipe Flow

The analytical solution for axisymmetric, laminar, fully developed, pulsating pipe flows, driven by an arbitrary time varying pressure gradient, is available in the literature; see, for example, Lambossy [4], Uchida [5] for details. The derivations in this Appendix represent a repetition, but contain some extensions to the existing analysis.

The governing momentum equation in the cylindrical coordinates for axisymmetric, laminar, fully developed (no transverse flow), pulsating pipe flow is

$$\frac{1}{\rho} \frac{\partial U}{\partial t} = -\frac{dP}{dx} + \frac{\mu}{r} \frac{\partial}{\partial r} \left( r \frac{\partial U}{\partial r} \right) \quad (A1)$$

Since in the present paper the emphasis is placed on a general-type of pulsating pipe flow, the driving pressure gradient is considered in the following form:

$$\frac{dP}{dx} = \left( \frac{dP}{dx} \right)_M + \left( \frac{dP}{dx} \right)_A f(t) \quad (A2)$$

This has a periodicity  $t_p$  and hence,  $f(t+t_p)=f(t)$ . In order to treat all possible functions of  $f(t)$ , it is the best to express the axial pressure gradient in the form of a Fourier series

$$\begin{aligned} -\frac{1}{\rho} \left( \frac{dP}{dx} \right) &= \hat{P}_0 + \sum_{n=1}^{\infty} \hat{P}_{cn} \cos(2\pi nft) + \sum_{n=1}^{\infty} \hat{P}_{sn} \sin(2\pi nft) \\ &= \hat{P}_0 \left[ 1 + \sum_{n=1}^{\infty} \hat{P}_{cn}^* \cos(2\pi nF\tau) + \sum_{n=1}^{\infty} \hat{P}_{sn}^* \sin(2\pi nF\tau) \right] \\ &= \hat{P}_0 \left[ 1 + \sum_{n=1}^{\infty} \hat{P}_{cn}^* \exp(2\pi nF\tau i) \right] \end{aligned} \quad (A3)$$

where  $\hat{P}_{c,sn}^* = \hat{P}_{c,sn} / \hat{P}_0$  is the dimensionless amplitude of the pressure gradient pulsation and  $f$  is the overall frequency of pulsation.  $F (=R^2 f / \nu)$  and  $\tau (=vt/R^2)$  are the dimensionless (characteristic) frequency and time for the flow problem, respectively.  $\hat{P}_0$  is equal to  $\hat{P}_M$ , the time-averaged axial pressure gradient.  $\hat{P}_{en}^*$  is the complex form of the pressure gradient, given in the following form:

$$\hat{P}_{en}^* = \hat{P}_{cn}^* - i\hat{P}_{sn}^* \quad (A4)$$

The equality in Eq. (A3) for the last part of the equation holds only for the real part of the right-hand side. The same equation clearly shows that the pressure gradient consists of two parts. First is the steady part (the mean pressure gradient), characterized by  $\hat{P}_0$ , or,  $\hat{P}_M$  (in the dimensionless form, unity), and the second is the oscillating part, characterized by the amplitude of the pressure gradient pulsation,  $\hat{P}_{c,sn}$  (in the complex and dimensionless form,  $\hat{P}_{en}^*$ ) and frequency of oscillation  $f$  (in the dimensionless form,  $F$ ).

With the above Fourier series for the driving pressure gradient, the solution for velocity is sought in the following form:

$$\begin{aligned} U &= U_0 + \sum_{n=1}^{\infty} U_{cn} \cos(2\pi nF\tau) + \sum_{n=1}^{\infty} U_{sn} \sin(2\pi nF\tau) \\ &= U_0 + \sum_{n=1}^{\infty} U_{en} \exp(2\pi nF\tau i) \end{aligned} \quad (A5)$$

The boundary conditions for this problem are given by (i) at  $r=0$ ,  $U$  is finite or  $\partial U / \partial r=0$ , and (ii) at  $r=R$ ,  $U=0$ . Substituting  $U$  from Eq. (A5) in the momentum Eq. (A1) and using these boundary conditions, the analytical solution for velocity distribution as a function of radius and time can be obtained as

$$\begin{aligned} U^* &= \frac{U}{U_{av}} = 2(1-r^{*2}) - \sum_{n=1}^{\infty} \frac{4\hat{P}_{en}^*}{\pi nF} \left[ 1 \right. \\ &\quad \left. - \frac{J_0[(2\pi nF)^{1/2} i^{3/2} r^*]}{J_0[(2\pi nF)^{1/2} i^{3/2}]} \right] \exp(2\pi nF\tau i) \end{aligned} \quad (A6)$$

where  $U^*$  is the dimensionless axial velocity and  $U_{av}$  is the average velocity of the fluid through the tube corresponding to the steady part of the pressure gradient and is given by,  $U_{av} = \hat{P}_0 R^2 / 8\nu$ . This result may be obtained by solving the steady, laminar, fully developed flow through pipes.

The mass flow rate through the cross section of the tube as a function of time is obtained by integrating the velocity solution in the following manner:

$$\dot{m} = 2\pi\rho \int_0^R rU dr = 2\pi\rho U_{av} R^2 \int_0^1 r^* U^* dr^* = 2\dot{m}_M \int_0^1 r^* U^* dr^* \quad (A7)$$

Using Eq. (A6), the mass flow rate through the tube is expressed as

$$\dot{m}^* = \frac{\dot{m}}{\dot{m}_M} = 1 - \sum_{n=1}^{\infty} \frac{4\hat{P}_{en}^* i}{\pi n F} \left[ 1 + \frac{2i^{1/2} J_1[(2\pi n F)^{1/2} i^{3/2}]}{(2\pi n F)^{1/2} J_0[(2\pi n F)^{1/2} i^{3/2}]} \right] \exp(2\pi n F \tau) \quad (A8)$$

where  $\dot{m}^*$  is the dimensionless mass flow rate,  $\dot{m}_M$  is the steady part of the mass flow rate through the tube due to  $U_{av}$  and is given as  $\dot{m}_M = \rho\pi R^2 U_{av}$ . Equation (A8) may also be written in a more convenient form

$$\dot{m}^* = 1 - \sum_{n=1}^{\infty} \dot{m}_{os,n}^* \quad (A9)$$

where,  $\dot{m}_{os,n}^*$  is the  $n$ th oscillating part of the mass flow rate pulsation. It may be noted that  $\dot{m}_{os,n}^*$  is directly proportional to the  $n$ th amplitude of complex pressure gradient,  $\hat{P}_{en}^*$ . Therefore, the ratio,  $\dot{m}_{os,n}^*/\hat{P}_{en}^*$ , depends only on the  $n$ th frequency of pulsation,  $nF$ .

It is interesting to note that both the velocity and the mass flow rate are expressed in terms of dimensionless variables. Moreover, the dimensionless mass flow rate is expressed in such a fashion that its steady part is expressed as unity. One may also rewrite Eq. (A3) by normalizing the pressure gradient with  $\hat{P}_0$  and may express the steady part of the pressure gradient also as unity. Most of the previous authors, for example, Lambossy [4], Uchida [5], Majdalani and Chibli [6], however, chose different ways to express these quantities. It may not be out of context to emphasize here that if the scales are properly chosen, all the results (such as velocity, mass flow rate, etc.) can be expressed in a very simple manner as presented in this Appendix. The advantage of proper scaling is further clarified in Sec. 3, while extending the analytical solution for mass flow rate driven pulsating pipe flows.

The analytical solution, presented here also clearly brings out the various dimensionless parameters, which affect the laminar, fully developed, pulsating fluid flow through pipes. This knowledge is utilized in Appendix B, which deals with the numerical solution of such problems.

## Appendix B: Numerical Investigation

Under the present experimental conditions, as explained in Sec. 2, the mass flow rate, rather than the axial pressure gradient, is controlled. The analytical solution for the pressure gradient controlled flows (see Appendix A) clearly shows that if the pressure gradient is known, the velocity profile and, hence, all other important quantities can be easily obtained. In Sec. 3, it was also shown that for mass flow rate controlled flows, where the pressure gradient is not known a priori, the inverse problem can be solved analytically and the required axial pressure gradient can still be obtained if the mass flow rate is expressed in the form of a Fourier series. However, when this time-dependent, mass flow rate controlled, pulsating flow is complex<sup>7</sup> and contains strong discontinuities, the analytical solution seems to be too difficult and less accurate and, hence, the numerical solution is essential. Although

<sup>7</sup>For example, consider power wave or sawtooth wave type pulsations, where a Fourier series cannot express the pulsation with reasonable accuracy without application of Lanczos' Sigma factor.

the solution of the inverse problem is the primary objective of this paper, we would first present the forward problem, where the pressure gradient is considered to be a known function of time. The reason will soon be apparent.

**B.1 Solution for Pressure Gradient Controlled Flow.** The governing equation for such flow is given by Eq. (A1) and the boundary conditions are discussed in the Appendix A. This type of flow is characterized by a known pressure gradient as a function of time, which consists of two parts—a steady part and an oscillating part. A typical example is given in Eq. (A3). However, it is obvious that the oscillating part could be complex in nature, particularly when the controlled mass flow rate through the tube is complex, as may be observed in Sec. 3.

In order to cast the governing equation in the dimensionless form, the nondimensional variables must be defined. The dimensionless radius, time, velocity and frequency are already defined in the Appendix A. The reference pressure gradient is defined on the basis of the expression for the average velocity as shown in Eq. (18)

$$\left( -\frac{1}{\rho} \frac{dP}{dx} \right)_{ref} = \frac{\nu U_{av}}{R^2} = \frac{\hat{P}_0}{8} \quad (B1)$$

Therefore, the dimensionless pressure gradient is expressed as<sup>8</sup>

$$\left( -\frac{1}{\rho} \frac{dP}{dx} \right)^* = 8 \left[ 1 + \sum_{n=1}^{\infty} \hat{P}_{sn}^* \sin(2\pi n F \tau) \right] \quad (B2)$$

The terms in the square brackets can be recognized as the normalized pressure gradient with respect to the steady part of the pressure gradient pulsation. With the help of the various dimensionless variables, the nondimensional governing equation may be written as

$$\frac{\partial U}{\partial \tau} = \left( -\frac{1}{\rho} \frac{dP}{dx} \right)^* + \frac{1}{r^*} \frac{\partial}{\partial r^*} \left( r^* \frac{\partial U}{\partial r^*} \right) \quad (B3)$$

It is important to note that, owing to the proper choice of scaling, the dimensionless governing equation does not contain any dimensionless number. In the above equation, the nondimensional pressure gradient could be, in principle, any periodic function of time. The above equation can now be discretized by using a non-uniform mesh and control volume approach. For the time derivative, implicit treatment was used as it is known to be unconditionally stable. At the centerline, zero velocity gradient was prescribed via a one-sided first-order differencing, and at the wall the velocity was set to zero by suitably adjusting the coefficients of the discretized equation. The resulting discretized equations for any time step exhibit a tri-diagonal-matrix structure and they were solved using the Thomas algorithm (see Patankar [16] for details). From the velocity solution of the discretized equations, the mass flow rate was obtained by numerically integrating the velocity profile as

$$\dot{m}^* = \frac{\dot{m}}{\dot{m}_A} = 2 \int_0^1 U r^* dr^* \quad (B4)$$

From the above presentation, it is obvious that for a laminar, fully developed, pulsating flow through a pipe, if the pressure gradient is known as a function of time, the governing equation can be numerically integrated to obtain the solution for velocity and the mass flow rate. This solution will be utilized to obtain the velocity and the pressure gradient for the inverse problem.

<sup>8</sup>If the pressure gradient is expressed in the form of a Fourier series, which is also not essential for the numerical solution. Also note that this definition is different (by a factor of 8) from the definition given in Eq. (17).

**B.2 Solution for Mass Flow Rate Controlled Flow.** For the mass flow rate controlled problem, the mass flow rate through the tube is expressed in a general form as

$$\dot{m} = \dot{m}_M + \dot{m}_A f_m(t) \quad (\text{B5})$$

The above equation may also be written in the dimensionless form as

$$\dot{m}^* = \frac{\dot{m}}{\dot{m}_M} = 1 + \dot{m}_A^* f_m(\tau) \quad (\text{B6})$$

Some examples of these types of mass flow rates were shown in Secs. 2 and 3. The analysis in the previous subsection clearly shows that if the pressure gradient is known, all other quantities can be obtained by numerical integration. Since for mass flow rate controlled flows the pressure gradient is not known a priori, in order to start the solution, a guessed value for the pressure gradient is required. The first guessed value for dimensionless pressure gradient was taken as 8, corresponding to the steady part of the mass flow rate variation. However, since the guessed pressure gradient is incorrect, the obtained mass flow rate would also be incorrect. Therefore, mathematically, one may write,

$$\dot{m}^* \left[ \left( -\frac{1}{\rho} \frac{dP}{dx} \right)_g^* \right] \neq \dot{m}^* \quad (\text{B7})$$

where the subscript “g” indicates the guessed value and  $\dot{m}^*$  on the right-hand side is given by Eq. (B6). Let  $h$ , which would be a function of time, be the correction required to the guessed pressure gradient. Thus, one may write

$$\dot{m}^* \left[ \left( -\frac{1}{\rho} \frac{dP}{dx} \right)_g^* + h(\tau) \right] = \dot{m}^* \quad (\text{B8})$$

Expanding the above equation by a Taylor series and retaining only up to the first-order terms, the following equation is obtained:

$$\dot{m}^* \left[ \left( -\frac{1}{\rho} \frac{dP}{dx} \right)_g^* \right] + h(\tau) \frac{\partial \dot{m}^*}{\partial \left[ -1/\rho \cdot (dP/dx)_g^* \right]} = \dot{m}^* \quad (\text{B9})$$

Therefore, the correction,  $h(\tau)$ , is obtained as

$$h(\tau) = \frac{\dot{m}^* - \dot{m}^* \left[ -1/\rho \cdot (dP/dx)_g^* \right]}{\dot{m}^* \partial \left[ -1/\rho \cdot (dP/dx)_g^* \right]} \quad (\text{B10})$$

where the denominator on the right-hand side implies the rate of change of mass flow rate with respect to the change in guessed pressure gradient. This term was numerically evaluated from the basic definition of the partial derivative as follows:

$$\frac{\partial \dot{m}^*}{\partial \left[ -1/\rho \cdot (dP/dx)_g^* \right]} = \frac{\dot{m}^* \left[ -1/\rho \cdot (dP/dx)_g^* + \epsilon \right] - \dot{m}^* \left[ -1/\rho \cdot (dP/dx)_g^* \right]}{\epsilon} \quad (\text{B11})$$

where,  $\epsilon$  is a preassigned small number (in the present problem,  $\epsilon = 10^{-7}$ ). After obtaining  $h(\tau)$  from Eq. (B10), the new pressure gradient was obtained by under relaxation as follows:

$$\left( -\frac{1}{\rho} \frac{dP}{dx} \right)_{\text{new}}^* = \left( -\frac{1}{\rho} \frac{dP}{dx} \right)_g^* + \alpha h(\tau) \quad (\text{B12})$$

The iterative process was continued until convergence. The convergence was checked on the basis of the absolute value of the numerator on the right-hand side of Eq. (B10). In the present problem, this was set as,  $10^{-5}$ .

## Nomenclature

- $a$  = constant  
 $D$  = pipe diameter (m)

- $f$  = frequency (Hz)  
 $h$  = function of time  
 $\dot{m}$  = mass flow rate (kg/s)  
 $n$  = integer number  
 $P$  = pressure (Pa)  
 $R$  = pipe radius (m)  
 $r$  = radial location (m)  
 $t$  = time (s)  
 $U$  = velocity (m/s)  
 $x$  = axial coordinate (m)

## Subscripts

- $0$  = averaged quantity  
 $A$  = amplitude  
 $\text{av}$  = time averaged mean  
 $C$  = cosine term of Fourier series  
 $g$  = guessed value  
 $M$  = time averaged mean  
 $n$  =  $n$ th term of Fourier series  
 $\text{os}$  = oscillating component  
 $p$  = period  
 $S$  = sine term of Fourier series  
 $w$  = wall

## Superscripts

- $*$  = dimensionless quantity  
 $\wedge$  = pressure gradient

## Greek Letters

- $\epsilon$  = initialization value  
 $\mu$  = dynamic viscosity  
 $\nu$  = kinematic viscosity  
 $\theta$  = phase (rad)  
 $\rho$  = density (kg/m<sup>3</sup>)  
 $\tau$  = shear stress

## Dimensionless Numbers

- $F$  =  $(R^2 f) / \nu$  dimensionless frequency  
 $P_A^*$  =  $(dP/dx)_A / (dP/dx)_M$  dimensionless pressure amplitude ( $= \hat{P}_A^*$ )  
 $\dot{m}_A^*$  =  $\dot{m}_A / \dot{m}_M$  dimensionless mass flow rate amplitude  
 $\dot{m}^*$  =  $\dot{m} / \dot{m}_M$  dimensionless mass flow rate  
 $\text{Re}$  =  $(U_M D) / \nu$  Reynolds number  
 $r^*$  =  $r / R$  dimensionless radial location  
 $\tau$  =  $(\nu t) / R^2$  dimensionless time  
 $U^*$  =  $U / U_M$  dimensionless velocity

## References

- [1] Howarth, L., 1956, *Modern Developments in Fluid Dynamics: High Speed Flows*, Clarendon, Oxford, Vols. I and II.
- [2] Moore, F. K., 1964, *Theory of Laminar Flows*, Princeton University Press, Princeton, NJ.
- [3] Gündoğdu, M. Y., and Carpinlioğlu, M. Ö., 1999, “Present State of the Art on Pulsatile Flow Theory (Part I: Laminar Flow Regime),” *JSME Int. J., Ser. B*, **42**(3), pp. 384–397.
- [4] Lambossy, P., 1952, “Oscillations Forcees d’un Liquide Incompressible et Visqueux Dans un Tube Rigide et Horizontal. Calcul de la Force Frottement,” *Helv. Phys. Acta*, **25**, pp. 371–386.
- [5] Uchida, S., 1956, “The Pulsating Viscous Flow Superposed on the Steady Laminar Motion of Incompressible Fluid in a Circular pipe,” *J. Appl. Math. Phys. (ZAMP)*, **7**, pp. 403–422.
- [6] Majdalani, J., and Chibli, H. A., 2002, “Pulsatory Channel Flows with Arbitrary Pressure Gradients,” 3rd AIAA Theoretical Fluid Mechanics Meeting, 2981.
- [7] Dension, E. B., Stevenson, W. H., and Fox, R. W., 1971, “Pulsating Laminar Flow Measurements with a Directly Sensitive Laser Velocimeter,” *AIChE J.*, **17**, pp. 781–787.
- [8] Muto, T., and Nakane, K., 1980, “Unsteady Flow in Circular Tube (Velocity Distribution of Pulsating Flow),” *Bull. JSME*, **23**(186), pp. 1990–1996.
- [9] Shemer, L. B., and Wygnanski, E. K., 1985, “On the Impedance of the Pipe in Laminar and Turbulent Pulsating Flows,” *Exp. Fluids*, **3**, pp. 185–189.
- [10] Durst, F., Ismailov, M., and Trimis, D., 1996, “Measurement of Instantaneous

- Flow Rates in Periodically Operating Injection Systems," *Exp. Fluids*, **20**, pp. 178–188.
- [11] Das, D., and Arakeri, J. H., 2000, "Unsteady Laminar Duct Flow with a Given Volume Flow Rate Variation." *Trans. ASME, J. Appl. Mech.*, **67**, pp. 274–281.
- [12] Muntges, D. E., and Majdalani, J., 2002, "Pulsatory Channel Flow for an Arbitrary Volumetric Flow Rate," 3rd AIAA Theoretical Fluid Mechanics Meeting, 2856.
- [13] Durst, F., Heim, U., Ünsal, B., and Kullik, G., 2003, "Mass Flow Rate Control System for Time-Dependent Laminar and Turbulent Flow Investigations," *Meas. Sci. Technol.*, **20**, pp. 893–902.
- [14] Ohmi, M., and Iguchi, M., 1981, "Flow Pattern and Frictional Losses in Pulsating Pipe Flow. Part 6: Frictional Losses in a Laminar Flow," *Bull. JSME*, **24**(196), pp. 1756–1767.
- [15] Hamming, R. W., 1986, "Lanczos'  $\sigma$  Factors and the  $\sigma$  Factors in the General Case 32.6 and 32.7," in *Numerical Methods for Scientists and Engineers*, Dover, New York, pp. 534–536.
- [16] Patankar, S. V., 1980, *Numerical Heat Transfer and Fluid Flow*, Hemisphere, Washington D.C.



# Laminar Flow Across a Bank of Low Aspect Ratio Micro Pin Fins

Ali Koşar

Chandan Mishra

Yoav Peles<sup>1</sup>

Department of Mechanical, Aerospace and Nuclear Engineering, Rensselaer Polytechnic Institute, Troy, NY 12180

*Pressure drops and friction factors associated with the forced flow of de-ionized water over staggered and in-line circular/diamond shaped micro pin-fin bundles 100  $\mu\text{m}$  long with hydraulic diameter of 50 and 100  $\mu\text{m}$  have been experimentally investigated over Reynolds number ranging from 5 to 128. Pin fins were arranged according to two different horizontal and vertical pitch ratios (1.5 and 5). The applicability of conventional scale correlations to evaluate micro flow tests results has been assessed. It is shown that the available large-scale correlations do not adequately predict the pressure drop obtained at the micro scale. A modified correlation, based on the experimental results obtained using micro scale devices, has been proposed. The refined correlation accounts for fin density and the endwall effects encountered in micro scale configurations. [DOI: 10.1115/1.1900139]*

## Introduction

Recent advances in microfabrication technology have resulted in a surge in Micro-Electro-Mechanical Systems (MEMS) research for various heat and mass transfer applications. In the last half decade, forced flow over a bank of pin fins (tubular or non-tubular) in MEMS devices has received increasing attention for applications such as micro chemical reactors [1], micro rockets [2,3], and micro biological systems [4]. Fluid flow over a bank of pins results in a characteristic pressure drop, which is often used as a criterion to optimally design heat transfers systems like heat exchangers [5]. A literature survey reveals numerous instances of experimental and numerical studies aspiring to estimate the pressure drop for fluid flow over pin fin-tube bundles using various geometrical fin configurations in conventional scale systems. It is therefore tempting to use scaled down versions of conventional models to predict hydrodynamic properties arising out of fluid flow across a bank of micro pin fins. However, various studies on fluid flow in MEMS devices have shown unexpected phenomena and deviations from established large scale results. Additional difficulties are encountered while attempting to adopt conventional scale correlations to model micro devices since micro fins in cross flow tend to be shorter (aspect ratio smaller than  $\sim 8$ ) than the recommended height for ideal tube bundles in large scale systems [6], primarily because as size diminishes heat transfer coefficient surges, which results in lower fin efficiencies and thus shorter pin fins are desired. Moreover limited data is available for laminar flow of intermediate size tubes ( $8 > H/D > 1/2$ ) at the conventional scale, and large deviations (up to 50%) have been observed between various empirical pressure drop correlations in conventional scale studies.

Over the past century, numerous studies have investigated various aspects of flow across conventional sized tube bundles. Pressure drop data for water and air in circular, rectangular, and oval tubes collected primarily through experimental studies have been employed to develop friction factor correlations for laminar, transitional, and turbulent flows. The developed correlations have been widely used to ameliorate the design of large scale systems. Gaddis and Gnielski [6] proposed general correlations for laminar, turbulent, and transition regions for long tubes ( $H/D > 8$ ) using data obtained from previous experimental studies of pressure drop. The correlations included the effects of fluid temperature,

number of rows of tubes, and tube geometrical configurations. Sparrow and Grannis [7] studied air flow across staggered forward-facing vertex diamond-shaped pin fins (45 deg and 90 deg) over Reynolds numbers based on the fin hydraulic diameter ranging from 20 to 2200 and noticed high friction factors in the 45 deg arrangement for low Reynolds number ( $Re < 100$ ). At higher Reynolds numbers, the inertial effects dominate and the friction factor increased for the 90 deg arrays. The authors employed the experimental data to propose friction factor correlations for a variety of geometrical configurations. Chyu et al. [8] studied heat transfer and pressure drop characteristics for circular, cubic, and diamond fin arrays in a narrow channel for both in-line and staggered arrangements, and they concluded that cube arrays are the best arrangement for heat exchangers because of their enhanced heat transfer characteristics and moderate pressure losses. Ruth [9] compared the performance of lenticular with circular cross section tube banks in cross flow and reported a 20% increase in the ratio between the Stanton number and the friction coefficient for the lenticular pins for  $2 \times 10^4 < Re < 5 \times 10^4$ . The increase has been attributed to the lower accelerations and pressure gradients of the lenticular configuration, which results in reduced separation and drag. Şara [10] studied the effect of tip clearance ratio and inter-fin distance on pressure drop in flow across square cross-section pin fins in a staggered arrangement for Reynolds numbers ranging from  $1 \times 10^4$  to  $3.4 \times 10^4$  and observed that a decrease in the clearance ratio results in a decrease in the friction factor. Correlations involving the prediction of the friction factor have been presented in this article.

Flows over intermediate size pin fin banks are commonly used in turbine cooling systems to increase the internal heat transfer characteristics. The pin height-to-diameter ratios of typical heat sink used for such applications are between 1/2 and 4 [11]. Damerow et al. [12] measured pressure drops in channels with arrays of pin fins having  $H/D$  from 2 to 4 with various pin spacing geometries and found no  $H/D$  effect on the friction factor. A similar trend has been reported by Metzger et al. [13], who also obtained friction factors data, which agreed well with the long tube correlations proposed by Jacob [14]. Armstrong and Winstanley [15] compared the experimental data obtained by Peng [16], Metzger et al. [13], Damerow et al. [12], and Jacob [14]. The correlation proposed by Metzger et al. [13] provided the best fit for the data (within  $\pm 15\%$ ), while Damerow's [12] correlation did not match the experimental results. Although Jacob's [14] correlation was originally developed for long fins, it predicted the experimental data fairly well. An interesting result that might explain the similar pressure drop trends for long and intermediate size tubes was obtained by Sparrow et al. [17], who studied the

<sup>1</sup>Corresponding author. Telephone: 518-276-2886; Fax: 518-276-2623; E-mail: pelesy@rpi.edu

Contributed by the Fluids Engineering Division for publication in the JOURNAL OF FLUIDS ENGINEERING. Manuscript received: July 29, 2004. Final manuscript received: February 19, 2005. Associate Editor: M. Volkan Otugen.

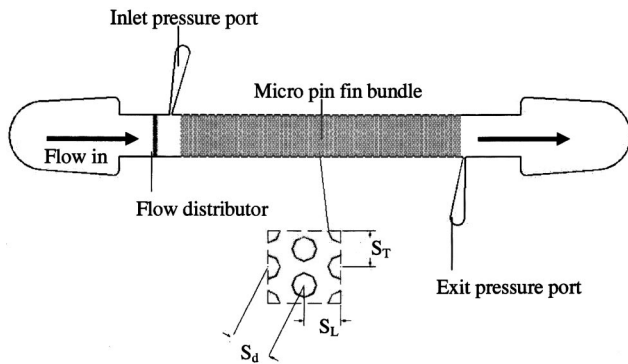


Fig. 1 CAD model of pin fin array

endwall effect of cross flow over a cylinder attached to a wall for Reynolds numbers ranging from 3500 to 23,000. Wall-cylinder interaction was found to be confined to within one diameter from the wall, and the interaction height was Reynolds number dependent. Low Reynolds number flows result in thicker interaction heights than high Reynolds number flow. Since the correlations cited above were developed based on transitional and turbulent flow data, no apparent dependency on  $H/D$  was found. However, Short et al. [5,18] showed that the friction factors over intermediate size tubes are strongly dependent on the height-to-diameter ratio for laminar flows but not for turbulent flows.

The aforementioned studies provide valuable insight into the pressure drop characteristics of fluid flow across a bank of pin fins at the conventional scale. It is not clear if the correlations and prediction tools developed for conventional scale systems are applicable to micro devices. Moreover, scaling studies have not been conducted to validate these correlations in the micro scale. In addition, the data on friction factor for intermediate size cylinders (and noncylindrical pin fins) at the conventional scale is limited and primarily available for transitional and turbulent flows ( $Re > 1000$ ). Therefore, there is a strong need for conducting experimental studies on the pressure drop in cross flows over various micro pin fin bundles to either validate the correlations available from conventional scale studies or dispute their utility at the micro scale. The present study investigates pressure drops due to flow of water over staggered and in-line micro pin fin bundles. Micro scale results are compared with the existing large scale data and the conventional scale correlations are assessed in terms of their ability to predict pressure drop characteristics in micro flows. Finally, a modified correlation, which includes endwall effects, is proposed for flows over micro pin fin bundles.

## Device Fabrication and Experimental Procedure

**MEMS Device Design.** The microchannels employed in the present study are fabricated using techniques adapted from semiconductor manufacturing. The process flow is very flexible and allows the creation of different fin geometries (circular, square, diamond, etc.) inside the microchannel. Positioning of the pin arrays in both staggered and in-line arrangements is achieved by simply incorporating these features into the masks. The fins are arranged inside a  $1500 \mu\text{m}$  wide microchannel of depth  $100 \mu\text{m}$  as shown in the CAD model in Fig. 1.

A double side polished,  $n$ -type  $\langle 100 \rangle$  single crystal silicon wafer is processed on both sides to create a microfluidic device, which consists of a microchannel embedded with an array of fins. Pressure tapings are created at appropriate places on the device (Fig. 1). At first, the top side and bottom side masks are designed and fabricated. A  $1 \mu\text{m}$  thick thermal oxide is deposited on both sides of the silicon wafer to protect the bare wafer surface. The top side mask pattern is transferred onto the silicon wafer through a photolithography step. The resist pattern on the wafer protects areas,

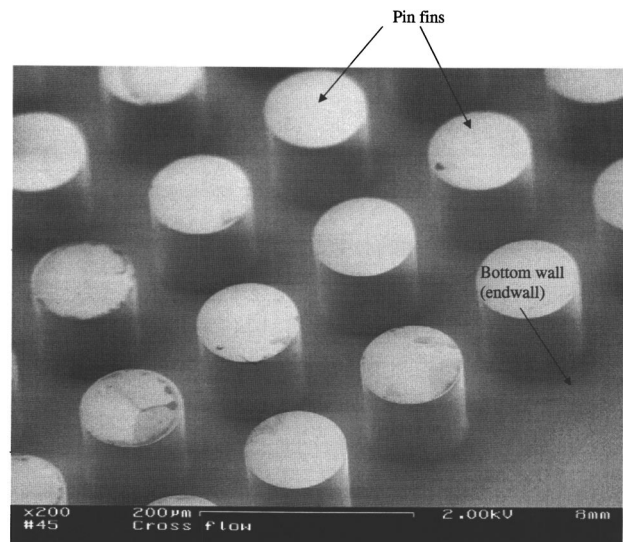


Fig. 2 SEM image of pin fins bundle

which are not to be etched during the DRIE (deep reactive ion etching) process. A subsequent RIE (reactive ion etching) process is used to remove oxide in places not protected by the resist. The wafer is then etched in a DRIE process and silicon is removed up to a depth of  $100 \mu\text{m}$  forming the microchannel containing pin fin bundles along with the pressure ports and the inlet and exit ports of the device. The DRIE process forms deep vertical trenches on the silicon wafer with a characteristic scalloped sidewall possessing a peak-to-peak roughness of  $\sim 0.3 \mu\text{m}$ . Once top side processing is completed, the resist is stripped and the wafer is flipped for bottom side processing. The wafer is again taken through a photolithography, RIE step but the bottom mask is employed instead and the mask pattern is transferred on to the other side of the wafer. Finally, a DRIE process is used to etch the silicon and create openings for the inlet, the exit, and the pressure ports. Subsequent wet bench processing removes all oxide and resist on the wafer. The completed silicon wafer is anodically bonded to a 1 mm thick Pyrex wafer to seal the microchannels. The processed stack is finally diced to separate the devices from the parent wafers and prepare them for packaging and interfacing with the experimental setup. An SEM image of the actual device is shown in Fig. 2 and a CAD model is presented in Fig. 1 displaying the fin bundles and the pressure ports on the device.

**Experimental Setup Design.** The experimental setup is classified into three major subsystems: (a) The test section, (b) the flow subsystem, and (c) the instrumentation and data acquisition subsystem. A detailed layout of the experimental setup is provided in Fig. 3.

The test section consists of microchannels and an opposite packaging module to facilitate the transit of fluids through the micro device and to allow pressure measurements at different locations via the ports in the device. The packaging module consists of three components: (a) A transparent top plate, (b) a bottom plate with alignment pins, and (c) an adapter plate.

The bottom plate houses a number of o-rings for fluidic sealing while the alignment pins are provided to facilitate the easy positioning of microchannels. The adapter plate compensates for any die-saw errors and the transparent polycarbonate top plate allows flow visualization during test runs. The silicon device is compressed against the gaskets (o-rings) by the top and the bottom plate to forge the fluidic seals. This setup ensures hermetic sealing and offers access to the fluidic connections (inlet, outlet, and pressure ports) of the micro device through the bottom block.

The flow subsystem includes an inlet and an exit pressure

## Experimental Setup

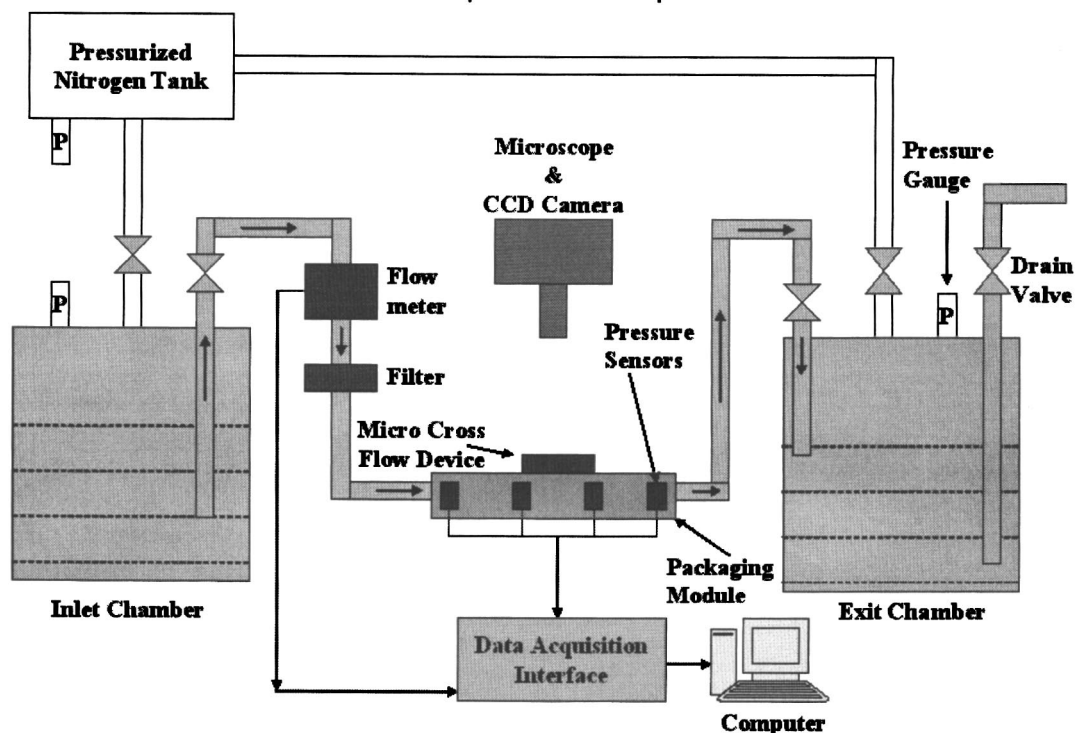


Fig. 3 Experimental setup

chamber capable of withstanding pressures up to 190 Psi and all plumbing to and from the test section. The fluidic connections to the test section from the pressurized tanks are established through appropriate stainless steel fittings. A pressure difference between the inlet and the exit chambers causes a flow through the microchannel. The inlet chamber is pressurized with filtered dry nitrogen and filtered de-ionized water is the working fluid in all experiments. The de-ionized water is delivered through a calibrated flow meter and a  $0.2 \mu\text{m}$  filter is introduced before the test rig to deplete the fluid and avoid any clogging of the microfluidic device. Air is removed from the flow circuit by a Welch vacuum pump before any de-ionized water is introduced into the microchannel.

The instrumentation and data acquisition subsystem consists of a few precision pressure transducers, which are mounted on the bottom plate of the packaging through appropriate fittings. Pressure data is obtained at various locations in the microchannel through the pressure ports created inside the microfluidic device (Fig. 1). The pressure sensors deliver data to a PC based LABVIEW® data acquisition subsystem, which collects and stores the data for further analysis. The working liquid is not recirculated in any of the experiments and is collected in the exit chamber.

**Experimental Procedure.** The flow rate is induced by the pressure difference between the inlet and exit chambers and it can also be controlled by a fine adjustment ball valve located upstream of the test section (Fig. 3). Experiments are conducted over a wide range of inlet pressures and pressure gauges are used to monitor the pressure inside the inlet chambers. All experiments are performed at room temperature ( $22^\circ\text{C}$ ) and no heat is supplied to the devices, maintaining adiabatic conditions. The exit chamber is kept at atmospheric pressure throughout the experiments and the de-ionized water temperature is continuously monitored. The inlet chamber pressure is increased in a controlled manner and pressure and flow rate data are collected from various pressure and flow sensors through the LABVIEW® interface and stored for further

analysis. The pressure drop caused by the flow over a bank of pin fins is detected by the pressure transducers for the desired flowrate and data is collected only after reaching steady state conditions.

## Data Reduction and Uncertainty Analysis

**Data Reduction.** Friction factor  $f$  is obtained from the following expression:

$$f_{\text{exp}} = \frac{(P_{\text{in}} - P_{\text{exit}})2\rho_F}{N_{\text{row}}G^2} \quad (1)$$

where the mass flux ( $G$ ) is calculated based on the minimum cross-sectional flow area using the expression

$$G = \frac{Q \rho_F}{A_{\text{min}}} \quad (2)$$

The Reynolds number and the minimum cross-sectional flow area are usually calculated using two different approaches depending on the pin height-to-diameter ratio. For arrays with long fins ( $H/D > 8$ ), referred in this paper as “tube bundle” fins, the pressure drop (and heat transfer) is dominated by the fin while the endwall effects are secondary [19]. In this approach, the length scale for calculating the Reynolds number is simply the fin hydraulic diameter. Very short fins ( $H/D < 1/2$ ) are commonly used in compact heat exchangers, where the characteristic pressure drop is severely influenced by the top and bottom walls. These fin configurations are referred as “compact heat exchanger” fins in this paper. This approach utilizes the hydraulic diameter of the heat exchanger for calculating the Reynolds number.

The Reynolds number and  $A_{\text{min}}$  for the “tube bundle” approach for in-line and staggered fin configuration are expressed as follows:

**Table 1** Uncertainties in variables used in uncertainty analysis (friction factor)

Uncertainty	Error (%)
Flow rate, $Q$ (for each reading)	1
Experimental inlet and exit pressure	0.25
Tube hydraulic diameter, $D$	1
Channel width, $w$	1
Channel height, $H$	0.67
Density of the fluid, $\rho_F$	0.5
$G$	3.8
$f$	7.2

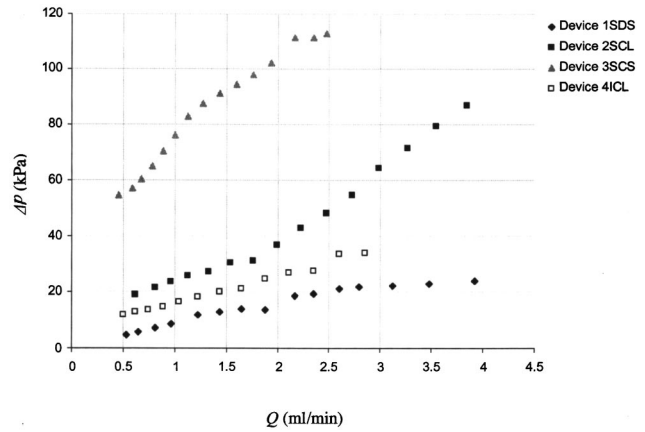


**Fig. 4** Pressure drop vs flow rate for device 1SDS through 4SCL

$$Re = \frac{G D}{\mu} \quad (3)$$

for in-line configuration

$$A_{min} = \frac{S_T - D}{S_T} w H \quad (4)$$

for staggered configuration

$$A_{min} = \frac{S_T - D}{S_T} w H \text{ for } \frac{S_T + D}{2} < S_d \quad (5)$$

$$A_{min} = \frac{2(S_d - D)}{S_T} w H \text{ for } \frac{S_T + D}{2} > S_d \quad (6)$$

The Reynolds number for the “compact heat exchanger” approach is given by:

$$Re_d = \frac{G d_h}{\mu} \quad (7)$$

where

$$d_h = \frac{4 A_{min} L}{A} \quad (8)$$

and

$$A = \pi D H N_t + 2 \left( w L - \frac{\pi D^2}{4} N_t \right) \quad (9)$$

For in-line tube configuration:

$$A_{min} = N H (S_T - D) \quad (10)$$

For staggered tube configuration:

$$A_{min} = \left( \left( \frac{w}{S_T} - 1 \right) c + (S_T - D) \right) H \quad (11)$$

where

$$c = \begin{cases} S_T - D & \text{if } S_T - D < S_d - D \\ S_d - D & \text{if } S_d - D < S_T - D \end{cases}$$

The friction factor for the entire fin pin configuration is obtained from Eq. (1). The comparison of the experimental data with existing correlations is done through the mean absolute error (MAE), which is defined as:

$$MAE = \frac{1}{M} \sum_{i=1}^M \frac{|f_{exp} - f_{pred}|}{f_{pred}} \times 100\% \quad (12)$$

**Uncertainty Analysis.** The uncertainties of the measured values are given in Table 1 and are derived from the manufacturer’s specification sheet while the uncertainties of the derived parameters are obtained using the propagation of uncertainty method developed by Kline and McClintock [20].

## Results and Discussion

**Pressure Drop.** Four devices, listed in Table 2, are tested in this study, for which the pressure drops between the inlet and exit are shown in Fig. 4. The geometrical configurations of the selected four devices provide a measure (although limited in extent) of pin arrangement (staggered and in-line), aspect ratio, and pin shape. As expected, the pressure drop is higher for the denser

**Table 2** Devices dimensions

Device	$S_T/D$	$S_L/D$	$H/D$	$D$ (μm)	clearance (μm)
1SDS (Staggered, Diamond, 45°, of Small fin hydraulic diameter)	5	5	2	50	0
2SCL (Staggered, Circular, of Large fin hydraulic diameter)	1.5	1.5	1	100	0
3SCS (Staggered, Circular, of Small fin hydraulic diameter)	1.5	1.5	2	50	0
4ICL (In-line, Circular, of Large fin hydraulic diameter)	1.5	1.5	1	100	0

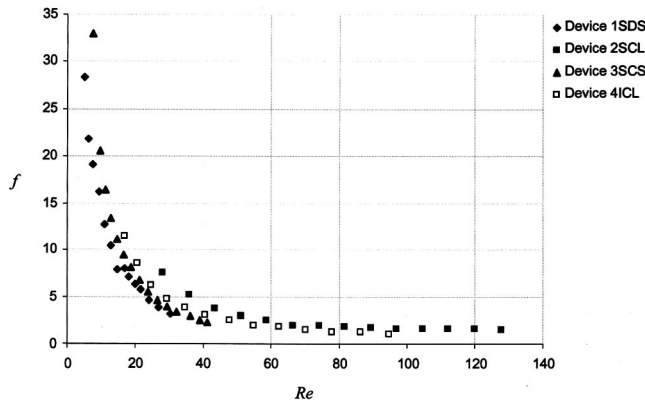


Fig. 5 Friction factors for “tube bundle” approach

configurations. Because of its smaller diameter, the Reynolds number based on the fin hydraulic diameter corresponding to the same flow rate is smaller for device 3SCS (Staggered, Circular, of Small fin hydraulic diameter) than for device 2SCL (Staggered, Circular, of Large fin hydraulic diameter). Consequently, the friction factor is higher and the pressure drop required to maintain the same flow rate is higher for device 3SCS. Due to the cylinder-wake interaction with increasing flow rate device 2SCL has increasing slope after a certain  $Q$ , while devices 3SCS and 1SDS have decreasing slopes. As expected the flow resistance of device 4ICL (In-line, Circular, of Large fin hydraulic diameter) is smaller than the staggered arrangements with the same fin diameter (device 2SCL). At high pitch-to-diameter ratio, the flow resistance drops (device 1SDS).

**Trends in Experimental Friction Factor.** Friction factors vs. Reynolds number profiles are given in Figs. 5 and 6 for “tube bundle” and “compact heat exchanger” approaches. The general trends of the experimental results are consistent with the effects of tube arrangement, and pitch ratio on friction factor for “tube bundle” approach in conventional scale.

Although the tube density of device 2SCL and 3SCS are the same, the friction factor is much larger for device 2SCL. For example using the “tube bundle” approach at  $Re=28.0$  the friction factor for device 2SCL is  $f=7.495$ , while at  $Re=29.30$  the friction factor for device 3SCS is  $f=3.915$ . Using the “compact heat exchanger” approach at  $Re=25.25$  the friction factor for device 2SCL is  $f=2.891$ , while at  $Re=25.35$  the friction factor for device 3SCS is  $f=2.507$ . The discrepancies between the friction factors are attributed to the differences in the height-to-diameter of the

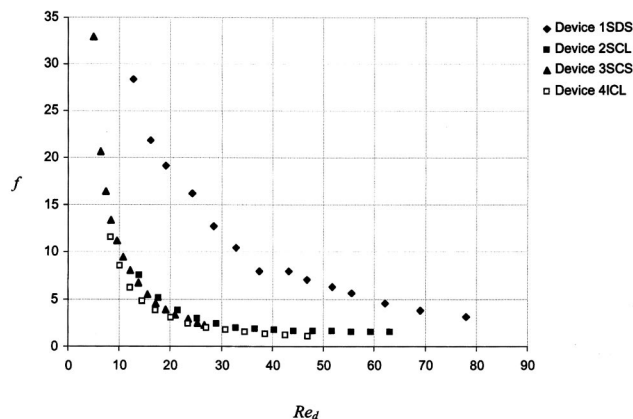


Fig. 6 Friction factors for “compact heat exchanger” approach

two devices ( $H/D=1$  for device 2SCL, and  $H/D=2$  for device 3SCS). This, to some extent, contradicts most previous studies [12,13,16] which have found that  $H/D$  had no effect on the friction factor. However, Short et al. [5] have reported that the friction factor is dependent on  $H/D$  for laminar flows and this compares favorably with the current data. As discussed by Sparrow et al. [17] wall-fin interactions are confined to within one diameter of the wall for Reynolds number larger than 3500, and tend to diminish at higher Reynolds numbers. At lower Reynolds number, the wall boundary layer thickness extends a few tube diameters from the wall and can strongly affect the hydrodynamic field (and, therefore, the pressure drop) throughout the entire fin height. Note that to some respect the aspect ratio effect should have been accounted for by the use of the Reynolds number based on the “compact heat exchanger” approach. Indeed, for a given Reynolds number, the ratios between the friction factors of the two devices reduced. However, there are still considerable discrepancies between the values of the friction factors of the two devices.

Flow through staggered configuration is more tortuous than flow over an in-line arrangement, and as a result, larger friction factors are expected for staggered configuration. However, at low Reynolds numbers the ratio between the friction factor of similar tube diameters and pitch-to-diameter ratio are larger than for larger Reynolds numbers. As seen in Figs. 5 and 6, at Reynolds numbers below 40 the friction factors for device 2SCL are about 1.6 times larger than for device 4ICL, while at higher Reynolds number the ratio between the friction factors approaches unity. A similar trend was obtained by Short et al. [5] thereby emphasizing the fact that as  $Re$  increases, the effects of the arrangement (in-line versus staggered) on friction factor diminishes.

The friction factors of devices 1SDS and 3SCS are approximately equal for a range of Reynolds numbers although the density of device 1SDS having diamond shaped fins is about five times less than device 3SCS with circular fins for the “tube bundle” approach, whereas they are greater for the “compact heat exchanger” approach. This signifies the importance of the pin’s shape. It can be inferred that diamond shaped fins result in considerably larger friction factors compared to circular fins, which is consistent with the finding of Chyu et al. [8]. This is because the sharp pointed regions of diamond shaped fins produce increased form drag on the pins, which results in larger friction factors.

**Comparison Between Experimental and Conventional Friction Factor.** A large number of correlations developed for long and short tubes are used to evaluate the friction factors. In the present study, ten long tube correlations and four intermediate size tube correlations are included, which are summarized in Table 3. Among the ten long tube correlations, four are specified as applicable only for laminar flow (1,4,6,11), four only for turbulent flow (2,3,5,7), and the remaining are either for all ranges, transition range, or some combination of two or more flow regimes. The experimental friction factors together with the calculated ones obtained from these correlations are presented in Tables 4 and 5. The mean absolute errors are presented in Tables 6 and 7. The correlation that results with the overall lowest MAE value is Sparrow and Grannis [7] correlation with an average MAE of 31.9% using the “tube bundle” approach. Although Sparrow and Grannis [7] correlation was obtained for air and recommended for diamond shaped tubes, it represents the data well particularly for the staggered arrangements. This might be since it was originally developed for Reynolds numbers similar to the current study and was based on tests from dense fin arrangements. It is also not surprising that the correlation provided the best prediction for the data of device 1SDS, which has relatively long ( $H/D=2$ ) diamond shaped fin pins. Excluding the diamond shape configuration (device 1SDS) Gunter and Shaw [21] and the HEDH [22] correlations predicted the experimental data quite well. Gunther and Shaw [21] correlation predicted the friction factor for device 2SCL, 3SCS, and 4ICL with MAEs of 22.5%, 22.0%, and 17.1%, respectively, while for device 1SDS it underpredicted the data by

**Table 3 Correlations for the friction factor and their mean absolute errors; Conventional scale friction factor correlations**

Correlation	Referenc e	Fluid	Reynolds number	H/D	Configuration	Friction factor
1	Chilton and Generaux [24]	Air	Laminar region	Long tubes	Circular staggered	$f = \frac{106}{Re}$
2	Chilton and Generaux [24]	Air	Turbulent region	Long tubes	Circular Staggered inline	$f = \frac{C_c}{Re^{0.2}}$ $C_c = 3$ for in line tube configuration $C_c = 1.32$ for staggered tube configuration
3	Jacob [14]	Air	Turbulent region	Long tubes	Circular Staggered inline	For in-line configuration: $f = \frac{1}{Re^{0.15}} \left( 0.176 + \frac{0.32(S_T/D)}{\left(\frac{S_T}{D} - 1\right)^{0.43+(1.13D/S_T)}} \right)$ For staggered configuration: $f = \frac{1}{Re^{0.16}} \left( 1 + \frac{0.47}{\left(\frac{S_T}{D} - 1\right)^{1.08}} \right)$
4	Gunther and Shaw [21]	Air	Laminar region	Long tubes	Circular In-line Staggered	$f = \frac{180}{Re} \left( \frac{4 S_T S_L}{\pi D^2} - 1 \right)^{0.4} \left( \frac{D b_G}{S_T} \right)^{0.6}$ $b_G = \frac{S_L}{D}$ for in line tube configuration $b_G = \frac{S_d}{D}$ for staggered tube configuration
5	Gunther and Shaw [21]	Air	Turbulent region	Long tubes	Circular In-line Staggered	$f = \frac{1.92}{Re^{0.145}} \left( \frac{4 S_T S_L}{\pi D^2} - 1 \right)^{0.4} \left( \frac{D b_G}{S_T} \right)^{0.6}$ $b_G$ is defined in the previous row
6	Bergelin et al. [25]	Mobile oil	Laminar region	Long tubes	Circular In-line Staggered	$f = \frac{280}{Re} \left( \frac{1}{a_b} \right)^{1.6}$ $a_b = \frac{S_T}{D}$ for in line tube configuration and for staggered configuration with $\frac{S_L}{D} \geq \sqrt{2 \frac{S_T}{D} + 1}$ $a_b = \frac{S_d}{D}$ for staggered tube configuration for staggered configuration with $\frac{S_L}{D} \leq \sqrt{2 \frac{S_T}{D} + 1}$
7	Damerow [12]	Air	Turbulent regime	Short tubes $2 < H/D$ $< 4$	Airfoils	$f = [8.24(S_T/D)^{-1.1}] Re_D^{-0.16}$
8	Kast [26]	Air	Laminar and turbulent regime	Long tubes	Circular In-line Staggered	$f = \frac{128}{Re} + \frac{4}{Re^{0.16}}$

81.6%. Using the HEDH [22] correlation the MAE's for device 2SCL, 3SCS, and 4ICL are 17.4%, 25.8%, and 21.9%, respectively, whereas for device 1SDS the MAE is 99.5%. The higher friction factors values for the diamond shape pins are in accordance with conventional scale findings (Chyu et al. [8]).

Comparison between the results for device 1SDS and device 2SCL with Sparrow and Grannis correlation [7] reveals another important aspect of endwall effects [endwall effects account for the interaction between the pin fins and the base, on which they

reside (top and bottom walls)]. If endwall effects are neglected, the correlation should have resulted in higher friction factors for device 2SCL than the experimental data, since the pin fins in device 2SCL are circular and the correlation was developed for diamond shape pin fins. On the other hand, the correlation should have underpredicted the experiments results for device 1SDS since the pins are diamond shaped and the only discrepancy between the data used for correlation 12 and the current data (other than the scale) is endwall effects. However, the opposite occurs.

Table 3 (Continued.)

correlation	Reference	Fluid	Reynolds number	H/D	Configuration	Friction factor															
9	Metzger et al. [13]	Air	1000-100000	Short tubes $H/D=1$	Rectangular Staggered Short tubes $H/D=1, P_T=2.5, P_L=1-5$	For $1000 < Re < 10000$ $f = 1.268 Re^{-0.132}$ For $10000 < Re < 100000$ $f = 7.04 Re^{-0.318}$															
10	HEDH [22]	All fluids	All $Re$	Long tubes	Circular Both in-line and staggered	$f = 4b \left( \frac{1.33}{S_T/D} \right)^b (Re)^{b_2}$ $b = \frac{b_3}{1 + 0.14(Re)^{b_4}}$															
11	Gaddis and Gnielski [6]	All fluids	Laminar regime	Long tubes	Circular Both in-line and staggered	$f = \frac{280\pi \left( \left( \frac{S_L}{D} \right)^{0.5} - 0.6 \right)^2 + 0.75}{Re \left( 4 \frac{S_L S_T}{D^2} - \pi \right) c^{1.4}}$ where $c = \frac{S_T}{D}$ for in line arrangement and a staggered arrangement with $\frac{S_L}{D} \geq \frac{1}{2} \sqrt{2 \frac{S_T}{D} + 1}$ $c = \frac{S_L}{D}$ for in line arrangement and a staggered arrangement with $\frac{S_L}{D} < \frac{1}{2} \sqrt{2 \frac{S_T}{D} + 1}$															
12	Sparrow and Grannis [7]	Air	20-2200	Long tubes	Diamond 45° deg vertex 90° deg vertex $P_T=1.15-2$ $P_L=1-2$ staggered	For $P_L=0.866P_T$ $f = \frac{127}{Re} + 0.90 \quad P_T < 135$ $f = \frac{88}{Re} + 0.70 \quad P_T \geq 135$ For $P_L=P_T$ $f = \frac{155}{Re} + 0.82 \quad P_T < 135$ $f = \frac{98}{Re} + 0.72 \quad P_T \geq 135$															
13	Moores and Joshi [23]	Water	200-10000	Short Tubes $0.5 < H/D < 1$ .	Circular Staggered 1 $P_T=1.3-1.36$ $P_L=1.13-1.18$	$f = 4\alpha_0 \left( \frac{H}{D} \right)^{\alpha_1} \left( \frac{cl+H}{H} \right)^{\alpha_2} Re^{\alpha_3}$ <table border="1"> <thead> <tr> <th></th> <th><math>10^2 &lt; Re &lt; 10^3</math></th> <th><math>10^3 &lt; Re &lt; 10^4</math></th> </tr> </thead> <tbody> <tr> <td><math>\alpha_0</math></td> <td>4.76</td> <td>3.2</td> </tr> <tr> <td><math>\alpha_1</math></td> <td>-0.742</td> <td>-0.138</td> </tr> <tr> <td><math>\alpha_2</math></td> <td>0.505</td> <td>-0.183</td> </tr> <tr> <td><math>\alpha_3</math></td> <td>-0.502</td> <td>-0.42</td> </tr> </tbody> </table>		$10^2 < Re < 10^3$	$10^3 < Re < 10^4$	$\alpha_0$	4.76	3.2	$\alpha_1$	-0.742	-0.138	$\alpha_2$	0.505	-0.183	$\alpha_3$	-0.502	-0.42
	$10^2 < Re < 10^3$	$10^3 < Re < 10^4$																			
$\alpha_0$	4.76	3.2																			
$\alpha_1$	-0.742	-0.138																			
$\alpha_2$	0.505	-0.183																			
$\alpha_3$	-0.502	-0.42																			
14	Short et al. [5]	Air	175-4500	Short Tubes $1.9 < H/D < 7.5$	Circular Staggered $S_T=1.3-1.36$ $S_L=2.0-6.4$	$f = 140.4 \left( \frac{S_L}{D} \right)^{-1.3} \left( \frac{S_T}{D} \right)^{-0.78} \left( \frac{H}{D} \right)^{-0.55} Re^{-0.65}$ for $Re < 1000$ $f = 0.884 \left( \frac{S_L}{D} \right)^{-1.4} \left( \frac{S_T}{D} \right)^{-0.54} \left( \frac{H}{D} \right)^{0.656} Re^{-0.08}$ for $Re \geq 1000$															

The correlation underpredicted the experiment results for device 2SCL, and overpredicted results for device 1SDS. This suggests that endwall effects are significant for  $H/D=1$ , but much less important for  $H/D=2$ , and a shift from pressure drop dominated by endwall effects to pressure drop dominated by pin fin effects occurs at some value between  $1 < H/D < 2$ . The endwall effects are also apparent when comparing device 2SCL and 2SCS with Gunther and Shaw [21] correlation. At Reynolds number above  $\sim 25$  the correlation overpredicted the experimental results for the relatively long pin fins of device 3SCS, while for device 2SCL the correlation underpredicted the results even at  $Re=127.7$ .

Moores and Joshi [23] poorly predicted the experimental data correlation. This is not surprising since their laminar region data also correlated poorly with their own correlation. Moreover, larger transverse and longitudinal pitches were used in their study, which

are beyond the recommended range for this correlation. From all the various studies considered here only Short et al. [5] addressed endwall effects on intermediate size pins. Therefore, it was expected that correlation 14 would agree well with the experimental results. However, the correlation did not predict the experimental data well even for the circular pins staggered array (for device 2SCL and 3SCS, the MAE's are 71.3% and 34.7%, respectively), and the prediction of the in-line array is much above the experimental data (for device 4ICL the MAE's is 99.1%).

The existing correlations best fit the data obtained from device 3SCS ( $H/D=2$ ). This might further support the hypothesis that endwall effects are significant in the low Reynolds number range of the current experiments, especially when comparing the results obtained for device 2SCL ( $H/D=1$ ). Since all correlations (except

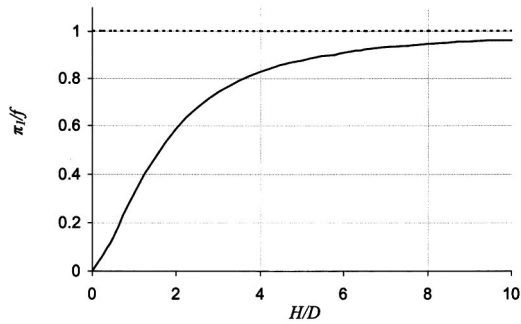


Fig. 7  $\pi_1$  to the total friction factor  $f$  [Eq. (13)] ratio versus  $H/D$  ratio at  $Re=40$

correlations 13 and 14), assume long fins (including the one that was developed for the short fins) it is expected that their prediction capabilities will deteriorate for smaller  $H/D$ , where endwall effects become significant. However, for device 1SDS all correlations, except Sparrow and Grannis [7] generated much lower friction factors than experiments. This is somewhat surprising since device 1SDS has  $H/D$  similar to device 2SCL. Moreover it has been tested at higher Reynolds numbers (in comparison to the other devices) and endwall effects should have diminished. However, as discussed in previous sections conventional scale studies strongly suggest that friction factor across diamond shape pins are larger than circular pins.

Using the “compact heat exchanger” approach did not seem to improve the prediction results. Although three correlations (Gaddis and Gnielski [6], Chilton and Generaux [24], Bergelin et al. [25]) provided better predictions under the “compact heat exchanger” approach, the predictions of the other correlations in Tables 6 and 7 were poorer. Bergelin et al. [25] provided the best prediction with an average MAE of 41.7%. Chilton and Generaux [24] produced the largest improvement with the “compact heat exchanger” approach compared to the “tube bundle” approach (from an MAE of 68.4% to an MAE of 44.8%). Since it was recommended only for the laminar regime, the effects of the change in the approach were more pronounced and these effects played an improving role in the prediction of experiment data, for devices 2SCL, 3SCS, and 4ICL (MAEs are 28.0%, 35.6%, and 15.3%, respectively). It is difficult to draw a conclusion regarding the approach, which provides best overall approximation, since the average MAEs for all correlations are relatively large for both approaches.

In conclusion, the comparison of the test results with existing correlations provided relatively large discrepancies, and only the correlation presented by Short et al. [5] attempted to capture all the important physical parameters that derive the pressure drop across intermediate size fin pin banks at low Reynolds numbers. In the following section, the development of a more general correlation that will especially account for endwall effects is detailed.

**Development of a New Correlation for Friction Factor.** Based on the experimental results a friction factor correlation for flow across fin pin array was developed which accounts for endwall effect and fin density. The correlation has the following form:

$$f = \pi_1 + \pi_2 \quad (13)$$

where

$$\pi_1 = \frac{C_3}{Re^{k_1}} \left( \frac{H/D}{H/D+1} \right)^{k_2} \left( \frac{S_T S_L}{A_C} \right)^{k_3} \quad \text{and};$$

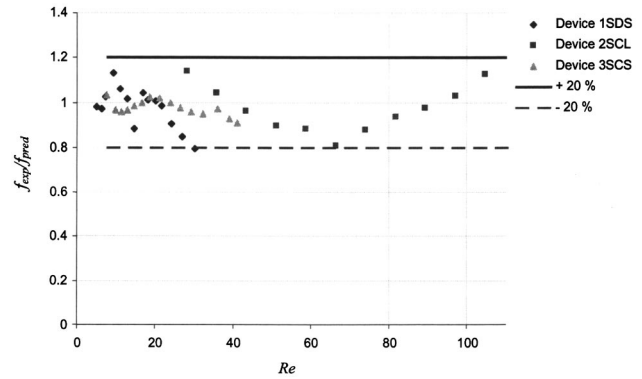


Fig. 8 Comparison between measured and calculated friction factors [Eq. (13)] for staggered configurations

$$\pi_2 = \frac{C_4}{Re_d^{k_5}} \left( \frac{1}{1+H/D} \right)^{k_4} \left( \frac{S_T S_L}{A_C} \right)^{k_6}$$

$C_3$ ,  $C_4$ ,  $k_1$ ,  $k_2$ ,  $k_3$ ,  $k_4$ , and  $k_5$  are constants, which minimize the prediction error of the experimental data. Using the least-square method similar to the procedure presented by Mathews [27], the values of these constants, which best fit the experimental data, are found and are listed in Table 8.

The first ( $\pi_1$ ) and second ( $\pi_2$ ) terms on the right hand side of Eq. (13) have a similar form to Gunther and Shaw [21] correlation and account for the friction on the fin and on the top and bottom walls, respectively. This hybrid approach to the representation of the friction factor acknowledges that neither  $Re$  nor  $Re_d$  alone can fully capture the physical parameters that govern friction factors at intermediate tube sizes. At large tube aspect ratio  $\pi_2$  vanishes (the term powered by  $k_4$  diminishes), and the pressure drops are mainly due to friction exerted on the pins. As the pins become shorter,  $\pi_1$  diminishes (the term powered by  $k_2$  diminishes), and the friction losses on the top and bottom walls, which are accounted by  $\pi_2$ , gradually dominate. This trend is demonstrated in Fig. 7 for device 3SCS at  $Re=40$ . For  $H/D=1$ ,  $\pi_1$  is much smaller than  $\pi_2$ . As  $H/D$  becomes larger, the ratio between  $\pi_1$  and the total friction factor approaches unity. For  $H/D > 5$ ,  $\pi_1$  accounts for  $\sim 90\%$  of the friction factor.

The correlation with the constant values of Table 8 predicted all friction factor data of the staggered arrangements with a MAE of 7.3%, while for in-line arrangement, the MAE is 2.7%. Table 9 lists all MAE's of Eq. (13). A comparison between the experimental data and the calculated friction factors obtained from Eq. (13) is given in Figs. 8 and 9, and as can be seen, almost all the data

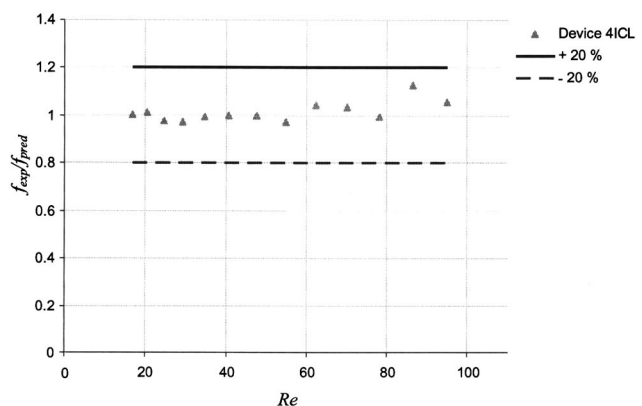


Fig. 9 Comparison between measured and calculated friction factors [Eq. (13)] for in-line configuration







**Table 7 MAE's (%) of the correlations for each device using the "compact heat exchanger" approach**

Device	Gaddis and Gnielski [6]	Sparrow and Grannis [17]	Moore and Joshi [23]	Kast [26]	Gunther and Shaw [21]	Chilton and Genereaux [24]	Bergelin et al. [25]	Short et al. [5]	HEDH [22]
1SDS	99.3	48.4	29.4	70.4	92.9	98.9	99.8	96.2	98.0
2SCL	16.1	104.4	51.6	187.0	56.8	28.0	11.5	169.0	53.7
3SCS	22.9	63.2	49.1	107.9	44.1	35.6	22.0	44.6	36.6
4ICL	49.5	151.5	72.6	240.5	105.6	15.3	34.4	210.8	94.1
Overall	46.5	90.3	50.3	149.1	73.8	44.8	41.7	127.2	69.6

ingly very few correlations are available for such pin fin configurations and flow regime. The correlations, which are applicable, provided large deviations from experimental results. At this point it is not clear whether this discrepancy is due to the limited data obtained in conventional scale, which is applicable to micro scale configuration and flow conditions or whether the differences arise from inherent scale effects.

- (3) Pin fin height to diameter ratio has a significant effect on the friction factor. The device with lower  $H/D$  ratio produces higher friction factors at the same tubes densities and Reynolds number. The  $H/D$  ratio effect reduces with increasing Reynolds number. A similar trend was observed by Short et al. [5].
- (4) A new correlation accounting for the fin density and end-wall effects has been developed for in-line circular, staggered circular, and staggered diamond shaped pin fin arrangements. The proposed correlation predicted the experimental data with MAEs of 2.7%, 7.4%, and 7.2% for in-line circular, staggered circular, and staggered diamond shaped pin fins arrangements, respectively. For large  $H/D$  ratios ( $H/D > 8$ ), the correlation converges to a long tube type correlation while small  $H/D$  ratios transform it to short tube correlations.
- (5) Staggered tube configuration results in higher friction factors than the in-line configuration. This trend has also been observed in conventional scale studies. The difference between the friction factors obtained from different arrangements diminishes with the increase in the Reynolds number.
- (6) The diamond shaped tubes produce higher friction factors when compared with the circular tubes. This is consistent with the results obtained by Chyu et al. [8] in their conventional scale experiments.

**Table 8 Constant values for Eq. (13) that best fits experimental results**

	staggered arrangement (circular fin pins)	staggered arrangement (diamond shaped fin pins)	in-line arrangement
$C_3$	1739	1126	7259
$C_4$	345	6.6	54
$k_1$	1.7	1.1	1.7
$k_2$	1.1	1.5	1.9
$k_3$	-0.3	-0.4	-0.4
$k_4$	2.0	1.7	2.0
$k_5$	1.0	0.7	0.7
$k_6$	-0.3	-1.0	-0.7

**Nomenclature**

- $A$  = total area,  $m^2$
- $A_c$  = cross section area of a single tube,  $m^2$
- $a_B$  = constant
- $b, b_1, b_2, b_3, b_4, b_G$  = constants
- $c, C, C_3, C_4, C_c$  = constants
- $d_h$  = hydraulic diameter of compact heat exchanger, m
- $D$  = tube hydraulic diameter diameter, m
- $f$  = friction factor
- $G$  = mass flux based on minimum flow area,  $kg/m^2s$
- $H$  = fin height, m
- $k_1, k_2, k_3, k_4, k_5$  = constants
- $L$  = channel length, m
- $m$  = exponent in Blasius type friction factor
- $M$  = number of data points
- MAE = mean absolute error
- $N$  = number of fins per column
- $n$  = constant
- $N_{row}$  = number of tubes per row
- $N_t$  = number of total tubes
- $\Delta p$  = pressure drop, kPa
- $p_{exit}$  = exit pressure, kPa
- $p_{in}$  = inlet pressure, kPa
- $S_d$  = diagonal pitch, m
- $S_L$  = longitudinal pitch, m
- $S_T$  = transverse pitch, m
- $Q$  = volumetric flowrate,  $m^3/s$
- Re = Reynolds number based on the pin fin hydraulic diameter,  $GD/\mu$
- $Re_d$  = Reynolds number based on the hydraulic diameter of the channel,  $Gd_h/\mu$
- $w$  = channel thickness, m

**Greek**

- $\alpha_0, \alpha_1, \alpha_2, \alpha_3$  = constants
- $\mu$  = viscosity,  $kg/ms$
- $\rho$  = density,  $m^3/s$
- $\pi_1$  = first term of the right hand side in Eq. (13)

**Table 9 MAE's of the new correlation for each device**

Device	MAE (%)
1SDS	7.2
2SCL	11.5
3SCS	3.5
4ICL	2.7

$\pi_2$  = second term of the right hand side in Eq. (13)

## Subscripts

av = average  
exp = experimental  
 $f$  = frictional  
 $F$  = fluid  
min = minimum  
pred = predicted

## References

- [1] Losey M. W., Jackman J., Firebaugh S. L., and Schmidt M. A., Jensen K., 2002, "Design and fabrication of microfluidic devices for multiphase mixing and reaction," *J. Microelectromech. Syst.*, **11**(6), pp. 709–717.
- [2] Hitt, D. L., Zakrzewski, C. M., and Thomas, M. A., 2001, "MEMS-based Satellite Micropropulsion via Catalyzed Hydrogen Peroxide Decomposition," *Smart Mater. Struct.*, **10**, pp. 1163–1175.
- [3] London, A., Development and Testing of a Microfabricated Bipropellant Rocket Engine, 2000, Ph.D. thesis, Massachusetts Institute of Technology, Boston, MA.
- [4] Christel, L. A., Petersen K., McMillan W., and Northrup M. A., 1999, "Rapid, Automated Nucleic Acid Probe Assays using Silicon Microstructures for Nucleic Acid Concentration," *J. Biomech. Eng.*, **121**, pp. 22–27.
- [5] Short, Jr., B. E., Raad P. E., and Price D. C., 2002, "Performance of Pin Fin Cast Aluminum Coldwalls, Part. 1: Friction Factor Correlations," *J. Thermophys. Heat Transfer*, **16**(3), pp. 389–396.
- [6] Gaddis, E. S. and Gniewski, V., 1985, "Pressure Drop in Horizontal Cross Flow across Tube Bundles," *Int. Chem. Eng.*, **25**(1), pp. 1–15.
- [7] Sparrow, E. M. and Grannis, V. B., 1991, "Pressure Drop Characteristics of Heat Exchangers Consisting of Arrays of Diamond- Shaped Pin Fins," *Int. J. Heat Mass Transfer*, **34**(3), pp. 589–600.
- [8] Chyu, M. K., Hsing, Y. C., and Natarajan, V., 1998, "Convective Heat Transfer of Cubic Fin Arrays in a Narrow Channel," *J. Heat Transfer*, **120**, pp. 362–367.
- [9] Ruth, E. K., 1983, "Experiments on a Cross Flow Heat Exchanger With Tubes of Lenticular Shape," *J. Heat Transfer*, **105**, pp. 571–575.
- [10] Şara, O. N., 2003, "Performance Analysis of Rectangular Ducts With Staggered Square Pin Fins," *Energy Convers. Manage.*, **44**, pp. 1787–1803.
- [11] Lau, S. C., Kim, Y. S., and Han, J. C., 1985, "Effects of Fin Configuration and Entrance Length on Local Endwall Heat/Mass Transfer in a Pin Fin Channel," ASME Paper No.81-WA/HT-6.
- [12] Damerow, W. P., Murtaugh, J. C., and Burgraf, F., 1972, "Experimental and Analytical Investigation of the Coolant Flow Characteristics in Cooled Turbine Airfoils," NASA, CR-120883.
- [13] Metzger, D. E., Fan, Z. N., and Shepard, W. B., 1982b, "Pressure Loss and Heat Transfer Through Multiple Rows of Short Pin Fins," *Journal of Heat Transfer*, Vol. 3, edited by U. Grigull et al., Hemisphere, Washington, pp. 137–142.
- [14] Jacob, M., 1938, "Discussion-Heat Transfer and Flow Resistance in Cross Flow of Gases Over Tube Banks," *Mech. Eng. (Am. Soc. Mech. Eng.)*, **60**, pp. 381–392.
- [15] Armstrong, J. and Winstanley, D., 1988, "A Review of Staggered Array Pin Fin Heat Transfer for Turbine Cooling Applications," *ASME J. Turbomach.*, **110**, pp. 94–103.
- [16] Peng, Y., 1984, "Heat Transfer and Friction Loss Characteristics of Pin Fin Cooling Configurations," *ASME J. Eng. Gas Turbines Power*, **106**, pp. 246–251.
- [17] Sparrow, E. M. and Kang, S. S., 1985, "Longitudinally-finned Cross Flow Tube Banks and their Heat Transfer and Pressure Drop Characteristics," *Int. J. Heat Mass Transfer*, **28**(2), pp. 339–350.
- [18] Short, Jr., B. E., Price D. C., and Raad P. E., 2004, "Design of Cast Pin Fin Coldwalls for Air-Cooled Electronic Systems," *J. Electron. Packag.*, **126**, pp. 67–73.
- [19] Zukauskas, A. A., 1972, "Heat Transfer From Tubes in Cross Flow," *Advances in Heat Transfer*, Vol. 8, Academic, New York, pp. 93–160.
- [20] Kline, S. and McClintock, F. A., 1953, "Describing Uncertainties in Single-Sample Experiments," *Mech. Eng. (Am. Soc. Mech. Eng.)*, **75**(1), pp. 3–8.
- [21] Gunter, A. Y. and Shaw, W. A., 1945, "A General Correlation of Friction Factors for Various Types of Surfaces in Cross Flow," *Mech. Eng. (Am. Soc. Mech. Eng.)*, **67**, pp. 643–660.
- [22] Taborek, J., 1983, "Shell-and-Tube Heat Exchangers: Single phase Flow," *Handbook of Heat Exchanger Design*, Hemisphere, New York, Chap. 3.3.
- [23] Moores, K. A. and Joshi, Y. K., 2003, "Effect of Tip Clearance on the Thermal and Hydrodynamic Performance of a Shrouded Pin Fin Array," *J. Heat Transfer*, **125**, pp. 999–1006.
- [24] Chilton, T. H. and Generaux, R. P., 1933, "Pressure Drop Across Tube Banks," *Trans. Am. Inst. Chem. Eng.*, **29**, pp. 161–173.
- [25] Bergelin, O. P., Colburn, A. P., and Hull, H. L., 1950, "Heat Transfer and Pressure Drop during Viscous Flow across Unbaffled Tube Banks," *Engineering Experimental Station, Bulletin No.2*, University of Delaware, Newark, DE.
- [26] Kast, W., 1974, *Druckverlust bei der Strömung quer zu Rohrbündeln (Pressure Drop in Cross Flow across Tube Bundles)*, VDI-Wärmeatlas, Section Ld, 2nd ed.
- [27] Mathews, J. H., 1992, *Numerical Methods for Mathematics, Science, and Engineering*, Prentice Hall, New Jersey, pp. 258–280.

# Two-Dimensional Pipe Model for Laminar Flow

M. C. P. Brunelli

e-mail: marco.brunelli@siemens.com  
Siemens VDO Automotive AG, Siemensstrasse  
12, D-93055 Regensburg, Germany

*The one-dimensional Zielke model of the energy loss in laminar pipe flow is exact but gives no information about the velocity profile. Here a two-dimensional pipe model is presented which gives the two-dimensional velocity profile in the time domain for an unstationary pipe flow of a compressible fluid that follows an equation of state. The continuity and the motion equations are projected over two sets of functions accounting for the radial and the axial dependence. A set of ordinary differential equations for the time-dependent coefficients is obtained, which is numerically integrated according to the boundary conditions at the pipe ends needed in practical applications. The model reproduces the experimental results of a water hammer and the analytical transfer functions over a wide range of frequencies. [DOI: 10.1115/1.1905645]*

## 1 Introduction

The modeling of the laminar unstationary energy loss of a fluid in a pipe has great relevance for its technological applications, and is a well known and understood problem. The special symmetry of the problem makes it possible to simplify the full Navier–Stokes equations by considering the pressure and the component of the velocity perpendicular to the pipe cross section as the only representative dynamic variables of the fluid motion. The three-dimensional problem—which is reduced to a two-dimensional problem where the independent spatial variables are the position along the pipe axis and the distance from the pipe center—can be further simplified since the radial dependence is fictitious. Performing the Laplace transform of the equations of motion, it can be shown that the shape of the velocity profile in the pipe is not free, but can be given an analytical expression in the Laplace domain even for transients in terms of Bessel functions of the first kind modulated by the transform of the pressure gradient [1]. Moreover, Zielke showed that the shear stress at the wall is a function of the instantaneous mean velocity and of the weighted past velocity changes [2], and he could write a set of one-dimensional equations involving only the pressure and the mean velocity. The one-dimensional equations of the Zielke model are accurate, since they reproduce the experimental results of a water hammer where frequency dependent friction causes distortion of the traveling wave; and they are easy to implement in a simulation program, since the information of the velocity profile is implicitly contained in the expression of the fluid friction experienced by the mean velocity. The only problem, however, is represented by the computational cost of the calculation of the weighted past velocity changes, which tends to increase unbounded for longer simulation times. Suzuki et al. [3] overcame this problem and developed a method which significantly reduces the computational cost of the calculation of the frequency dependent friction and gives the same results as the Zielke model.

The shape of the velocity profile, which is implicitly contained in the Zielke model, is known in the Laplace domain but it is generally unknown in the time domain. Only if the boundary conditions of the pressure and of the mean velocity at the pipe ends are set to sinusoidal functions is it possible to have an expression of the velocity shape also in the time domain. The goal of this work is to numerically solve in the time domain the full two-dimensional equations of motion for a compressible fluid that follows an equation of state. Two sets of complete orthogonal func-

tions, one in the axial and the other in the radial direction, are the basis over which the pressure and the velocity field are expanded. From the equations of continuity and of motion, a set of first-order ordinary differential equations are obtained for the time-dependent coefficients of the expansion, which can be numerically integrated, taking into account the boundary conditions by introducing Lagrange multipliers. The method has been tested on the experimental results of the water hammer presented in the Zielke article, and on the calculation of transfer functions.

## 2 Basic Equations

Here the basic differential equations for the laminar motion of a fluid in a pipe following D'Souza and Oldenburger are reported [1]. The pressure and the velocity field of a fluid in a pipe with nonelastic walls can be described using cylinder coordinates  $x$ ,  $r$ ,  $\theta$ . The coordinate  $x$  gives the position in the pipe's axial direction,  $r$  is the distance from the pipe center, and  $\theta$  counts the circumferential angle around the pipe axis. Due to the rotational symmetry of the pipe, the pressure and the velocity are assumed to be independent of  $\theta$ . The velocity field describing the laminar motion of the fluid then has two components: One  $v$  along the axial direction, and the other  $u$  lying in the pipe cross section. Since it can be shown that the value of  $u$  is always much less than  $v$ , the pressure  $P$  can be assumed to be a function of  $x$  only. With these assumptions the equations of motion and of continuity are

$$\rho \frac{\partial v}{\partial t} + \frac{\partial P}{\partial x} - \rho \nu \left( \frac{\partial^2 v}{\partial r^2} + \frac{1}{r} \frac{\partial v}{\partial r} \right) = 0 \quad (1)$$

$$\frac{1}{K} \frac{\partial P}{\partial t} + \frac{\partial v}{\partial x} + \frac{\partial u}{\partial r} + \frac{u}{r} = 0 \quad (2)$$

where  $\nu$  is the kinematic fluid viscosity, which is assumed to be constant for a fluid at constant temperature, and  $K$  is the fluid bulk modulus given by the equation of state for liquids

$$\frac{d\rho}{\rho} = \frac{dp}{K}$$

Integrating Eqs. (1) and (2) over the pipe cross section the dependence on  $u$  disappears

$$\rho \frac{\partial V}{\partial t} + \frac{\partial P}{\partial x} - \tau(x) = 0 \quad (3)$$

Contributed by the Fluids Engineering Division for publication in the JOURNAL OF FLUIDS ENGINEERING. Manuscript received by The Fluids Engineering Division November 19, 2004; final manuscript received: March 16, 2005. Associate Editor: Subrata Roy.

$$\frac{1}{K} \frac{\partial P}{\partial t} + \frac{\partial V}{\partial x} = 0 \quad (4)$$

and the velocity component  $v$  is substituted by its mean value  $V = V(x, t)$

$$V = \frac{1}{\pi R^2} \int_0^R 2\pi r v \, dr. \quad (5)$$

Equation (3), which still contains a trace of the velocity profile in the shear stress  $\tau$  at the wall

$$\tau(x) = \frac{2\rho\nu}{R} \left. \frac{\partial v}{\partial r} \right|_{r=R}$$

turns out to be fully one-dimensional since Zielke [2] showed that  $\tau$  can be expressed as a weight of the past velocity changes

$$\tau = \frac{4\rho\nu}{R} V(t) + \frac{2\rho\nu}{R} \int_0^t \frac{\partial V}{\partial t}(u) W(t-u) du \quad (6)$$

where  $W$  is a function which can be represented as a series.

The only reason that it is possible to end up with a set of one-dimensional equations from the full two-dimensional equations [Eqs. (1) and (2)], is that the shape of the velocity profile solution of Eq. (1) is not free, but it is given a form which can be easily computed by performing the Laplace transform of the equation of motion. Following Zielke, the Laplace transform of Eq. (1) is

$$\frac{d^2 \bar{v}}{dr^2} + \frac{1}{r} \frac{d\bar{v}}{dr} - \frac{s}{\nu} \bar{v} = \frac{1}{\nu} \bar{F} \quad (7)$$

where

$$\bar{v}(x, r, s) = \int_0^\infty v(x, r, t) e^{-st} dt$$

$$\bar{F}(x, s) = \int_0^\infty \frac{1}{\rho} \frac{\partial P}{\partial x} e^{-st} dt.$$

The velocity field  $v$  solution of Eq. (1) must satisfy two boundary conditions, one imposed by physics, which prescribes zero fluid velocity at the pipe walls

$$v(x, R, t) = 0 \quad (8)$$

and the other which guarantees the existence of the time derivative of the velocity profile at the center of the pipe

$$\left. \frac{\partial v}{\partial r}(x, r, t) \right|_{r=0} = 0. \quad (9)$$

From the general solution of Eq. (7)

$$\bar{v}(x, r, s) = C_1 J_0 \left( i \sqrt{\frac{s}{\nu}} r \right) + C_2 N_0 \left( i \sqrt{\frac{s}{\nu}} r \right) - \frac{\bar{F}}{s} \quad (10)$$

where  $J_0$  and  $N_0$  are, respectively, the Bessel functions of first and second kind and of order zero, the solutions that fulfill the boundary conditions Eqs. (8) and (9) are found by imposing

$$C_2 = 0$$

$$C_1 = \frac{\bar{F}}{s} / J_0 \left( i \sqrt{\frac{s}{\nu}} R \right)$$

and read

$$\bar{v}(x, r, s) = \frac{\bar{F}}{s} \left[ \frac{J_0 \left( i \sqrt{\frac{s}{\nu}} r \right)}{J_0 \left( i \sqrt{\frac{s}{\nu}} R \right)} - 1 \right] \quad (11)$$

Since the shape of velocity profile overall in the pipe is given by Eq. (11), it is not possible to prescribe a general shape of the velocity profile at one of the pipe ends, where only the value of the mean velocity can be imposed, whose Laplace transform  $\bar{V}$  is

$$\bar{V} = \frac{\bar{F}}{s} \left[ \frac{2J_1 \left( i \sqrt{\frac{s}{\nu}} R \right)}{i \sqrt{\frac{s}{\nu}} R J_0 \left( i \sqrt{\frac{s}{\nu}} R \right)} - 1 \right]. \quad (12)$$

In order to get a numerical solution to Eqs. (1) and (2) we expand the velocity profile and the pressure over two independent basis of functions, one for the length and one for the radius. For the length coordinate we use the Chebyshev polynomials  $T_n$ , which are a complete set of orthogonal functions in the domain  $[-1, 1]$  with respect to the weight function  $(1-x^2)^{-1/2}$ . For the radial coordinate we choose in the set of the Jacobi polynomials those polynomials  $Z_n$ , which are a complete set of orthogonal functions in the domain  $[0, 1]$  with respect to the weight function  $x$  (see Appendixes A and B).

The equations of continuity and of motion mapped on the orthogonality domain of the  $T_n$  and  $Z_n$  polynomials with the change of variables

$$\xi = r/R \quad \xi \in [0, 1] \quad [0, R] \rightarrow [0, 1]$$

$$\epsilon = 2x/L - 1 \quad \epsilon \in [-1, 1] \quad [0, L] \rightarrow [-1, 1]$$

read

$$\frac{\partial \hat{v}}{\partial t} + \frac{2}{L\rho} \frac{\partial \hat{P}}{\partial \epsilon} - \frac{\nu}{R^2} \left( \frac{\partial^2 \hat{v}}{\partial \xi^2} + \frac{1}{\xi} \frac{\partial \hat{v}}{\partial \xi} \right) = 0 \quad (13)$$

$$\frac{1}{K} \frac{\partial \hat{P}}{\partial t} + \frac{2}{L} \frac{\partial \hat{V}}{\partial \epsilon} = 0 \quad (14)$$

where  $\hat{v}$ ,  $\hat{V}$ , and  $\hat{P}$  are functions of the variables  $\epsilon$ ,  $\xi$ , and of time  $t$ .

The expansion of the function  $\hat{v}$  and  $\hat{P}$  in series of Jacobi and Chebyshev polynomials is

$$\begin{aligned} \hat{v} &= v_{k,m}(t) Z_k(\xi) T_m(\epsilon) \\ \hat{P} &= p_m(t) T_m(\epsilon) \end{aligned} \quad k, m = 0, 1, \dots \quad (15)$$

where the convention of summation over repeated indices is assumed. Since the definition of the mean velocity  $\hat{V}$  contains the scalar product of the polynomial  $Z_k$  with the polynomial of order zero, the expansion of  $\hat{V}$  contains only the elements  $v_{0,m}$

$$\hat{V} = 2 \int_0^1 \hat{v} \xi \, d\xi = 2 v_{k,m} T_m \int_0^1 Z_k Z_0 \xi \, d\xi = v_{0,m} T_m.$$

Inserting the expansion of the pressure and of the velocity in the equation of motion and continuity Eqs. (13) and (14) we obtain

$$\dot{v}_{k,m} Z_k T_m + \frac{2}{L\rho} \frac{\partial T_m}{\partial \epsilon} p_m - \frac{\nu}{R^2} \left[ \frac{\partial^2 Z_k}{\partial \xi^2} + \frac{1}{\xi} \frac{\partial Z_k}{\partial \xi} \right] T_m v_{k,m} = 0 \quad (16)$$

$$\frac{1}{K} \dot{p}_m T_m + \frac{2}{L} \frac{\partial T_m}{\partial \epsilon} v_{0,m} = 0 \quad (17)$$

and, under the hypothesis that the pressure fluctuations are not large enough to account for a change in the bulk modulus  $K$ , we can project Eqs. (16) and (17) over the Jacobi and Chebyshev polynomials of order  $i$  and  $j$ , respectively, so as to obtain the equations of motion for the single  $v_{i,j}$  and  $p_j$  components

$$\begin{aligned} \frac{1}{K}\dot{p}_j + \frac{2}{L}A_{j,k}v_{0,k} &= 0 \\ \dot{v}_{0,j} + \frac{2}{L\rho}A_{j,i}p_i - \frac{2\nu}{R^2}B_{0,k}v_{k,j} &= 0 \\ \dot{v}_{i,j} - \frac{2\nu}{R^2}B_{i,k}v_{k,j} &= 0 \quad i = 1, \dots \end{aligned} \quad (18)$$

The matrix elements  $A_{i,k}$  involve the scalar product of the derivatives of the Chebyshev polynomial  $T_k$  with the polynomial  $T_i$  and they have a simple expression

$$A_{i,k} = \frac{1}{\epsilon_i} \int_{-1}^1 \frac{\partial T_k}{\partial \xi} T_i \frac{d\xi}{\sqrt{1-\xi^2}} = \frac{\pi}{\epsilon_i} \begin{cases} 0 & k \leq i \\ 0 & i-k \text{ even} \\ k & i-k \text{ odd} \end{cases} \quad (19)$$

where

$$\epsilon_i = \begin{cases} \pi & i = 0 \\ \frac{\pi}{2} & i = 1. \end{cases}$$

The matrix elements  $B_{i,k}$  have a more complicated expression

$$B_{i,k} = (i+1) \int_0^1 \left[ \frac{\partial^2 Z_k}{\partial \xi^2} + \frac{1}{\xi} \frac{\partial Z_k}{\partial \xi} \right] Z_i \xi d\xi \quad (20)$$

and they can be numerically computed.

In the derivation of Eq. (18) the norm of the Chebyshev and Jacobi polynomials has been used (see Appendixes A and B).

In Eq. (18) we can clearly recognize the underlying structure of a one-dimensional model. If we had no viscosity, or if we would assume a given velocity profile, only the components of the pressure and of the mean velocity would be involved in the dynamics, resulting in a fully one-dimensional model. With the viscosity, the two dimensional nature of the velocity field affects the dynamics of the mean velocity and of the pressure through the term

$$\tau_j = \frac{2\nu}{R^2} B_{0,k} v_{k,j} \quad (21)$$

which is the  $j$  component of the expansion of the wall shear stress over the Chebyshev polynomials, and it depends on the full two-dimensional velocity profile.

### 3 Boundary Conditions

As stated before, the velocity field must satisfy the two boundary conditions, Eqs. (8) and (9), which can be realized by imposing a constraint on the coefficients of the expansion of the pressure and of the velocity.

The velocity is zero at the pipe wall if the following equation holds

$$v_{k,m}(t)Z_k(1)T_m(\epsilon) = 0$$

which is equivalent to

$$\sum_k v_{k,m} = 0, \quad (22)$$

since  $Z_k(1)=1$ .

The velocity profile attains a maximum or a minimum at the pipe center if

$$\frac{\partial Z_k}{\partial \xi} \Big|_{\xi=0} v_{k,m} = \delta_k v_{k,m} = 0 \quad (23)$$

where the derivative  $\delta_k$  of  $Z_k$  at zero can be analytically computed [see Eq. (B3)].

During the dynamics, the constraints Eqs. (22) and (23) can be fulfilled by introducing two Lagrange multipliers  $\lambda_m$  and  $\nu_m$ , which correct the time derivative  $\mu_{k,m}$  of the velocity components from Eq. (18)

$$\dot{v}_{k,m} = \mu_{k,m} + \lambda_m + \delta_k \nu_m \quad k = 1, \dots \quad (24)$$

The multipliers  $\lambda_m$  and  $\nu_m$  can be easily found by inserting Eq. (24) into the time derivative of the constraints Eqs. (22) and (23).

It must be noted that the Lagrange multipliers  $\lambda_m$  and  $\delta_k$  do not correct the components  $v_{0,m}$  of mean velocity. In fact, the mean velocity and the pressure, which are really the only two independent variables of the fluid motion, determine the energy of the fluid in the pipe, whose energy is dissipated only through pipe friction. Correcting the value of the mean velocity would result in a dynamic with an artificial contribution to pipe energy, eventually causing unpredictable dynamic instabilities. The idea here is to do exactly what is done in the Laplace domain: Given a distribution of the mean velocity through the coefficient  $v_{0,m}$ , the shape of the velocity profile is sought which fulfills the boundary conditions but does not change the value of  $v_{0,m}$ .

Two additional boundary conditions must be imposed on the solutions of Eqs. (13) and (14). In practical applications the mean velocity  $V$  and the pressure  $P$  are prescribed at the pipe ends by the interaction with other hydraulic components of the system. A pipe can be considered as a four-terminal network, where the mean velocities  $V_a, V_b$ , and the pressures  $P_a, P_b$  at the open ends are inputs or outputs of the pipe model. Stenning and Shearer [4] demonstrated that it is impossible through external means to prescribe the value of the mean velocity and of the pressure independently at the same end. Therefore, only two of the four variables  $V_a, V_b, P_a, P_b$  which are not at the same end can be independent and can be considered as inputs to the model, the other two are the outputs.

Thus, in practical applications a pipe model must be able to deal with three kinds of boundary conditions.

- Pressure–Velocity boundary condition

In the pressure–velocity boundary condition, a pressure  $P_-(t)$  is prescribed at the left end of the pipe, and a mean velocity  $V_+(t)$  is imposed at the right end. Since  $T_m(-1) = (-1)^m$  and  $T_m(1)=1$ , during the dynamics the pressure components and the velocity components must satisfy the following constraint

$$\begin{aligned} \sum_m v_{0,m} &= V_+(t) \\ (-1)^m p_m &= P_-(t). \end{aligned} \quad (25)$$

The time derivative  $\mu_m$  and  $\gamma_m$  of the mean velocity and pressure components from Eq. (18) can be corrected by two Lagrange multipliers  $\lambda$  and  $\nu$

$$\begin{aligned} \dot{v}_{0,m} &= \mu_m + \lambda \\ \dot{p}_m &= \gamma_m + \nu(-1)^m \end{aligned} \quad (26)$$

which can be easily found by inserting Eq. (26) into the time derivative of Eq. (25).

- Pressure–Pressure boundary condition

In the pressure–pressure boundary condition the value of the pressure  $P_-(t)$  at the left and at the right end  $P_+(t)$  are prescribed, resulting in the following condition for the pressure components

$$\begin{aligned} \sum_m p_m &= P_+(t) \\ (-1)^m p_m &= P_-(t) \end{aligned} \quad (27)$$

The time derivative  $\gamma_m$  of the pressure components from Eq. (18) can be corrected by two Lagrange multipliers  $\lambda$  and  $\nu$

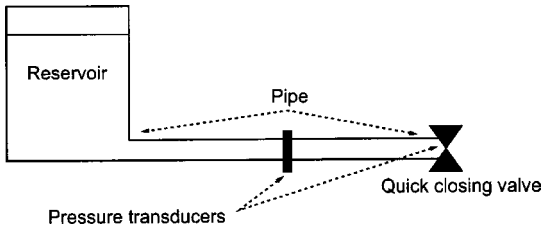


Fig. 1 Setup of the water hammer experiment as in the article of Zielke [2]

$$\dot{p}_m = \gamma_m + \lambda + \nu(-1)^m \quad (28)$$

which can be easily found, once again, by inserting Eq. (28) into the time derivative of Eq. (27).

- Velocity–Velocity boundary condition

In the velocity–velocity boundary conditions the mean velocity is prescribed at both ends, where it must be equal, respectively, to  $V_-(t)$  and  $V_+(t)$ . The constraint on the velocity components in this case is identically realized as for the case pressure–pressure boundary condition.

#### 4 Validation of the Model

**4.1 Comparison With the Zielke Model.** In his original paper Zielke presented a comparison of the numerical results from his model with measurements of a water hammer in a pipe of length  $L=36$  m and diameter  $D=25.4$  mm, connected upstream to a reservoir kept at constant pressure, and downstream to a fast-closing valve (see Fig. 1). When the valve closes, the pressure is measured at the downstream end and at the midpoint of the tube. In order to enhance the dissipation effect due to the two-dimensional nature of the damping, a fluid was chosen with a viscosity of about  $\nu=39$  cS, almost forty times the viscosity of water. The comparison of the numerical results from the Zielke model is presented in the original article [2] and it is very accurate.

In order to test the pipe model presented in this article the water hammer in the Zielke article has been simulated using a fourth-order Runge–Kutta integrator, and an expansion of the Chebyshev and Jacobi polynomials from Eq. (15), respectively, up to the order  $m=0, 1, \dots, 15$  and  $k=0, 1, \dots, 20$ .

When the valve is open, the velocity in the pipe  $\hat{v}_0(\epsilon, \xi, t)$  is not time and position dependent, and has the usual parabolic form

$$\hat{v}_0(\epsilon, \xi, t) = V_0(Z_0(\xi) - 4/5Z_1(\xi) - 1/5Z_2(\xi))$$

resulting in a constant mean fluid velocity  $V_0$ . The closing phase of the valve has been modeled by decreasing the value of the mean velocity at one pipe end to zero.

We present in Fig. 2 the downstream pressure fluctuation  $\Delta P$  around the mean value in units of  $\rho V_0 c$ , where  $c$  is the sound velocity in the fluid. A comparison is made with numerical results from the two-dimensional pipe model, represented by the solid curve, with the original measurements reported in the Zielke article, illustrated by the dotted curve. The agreement between the simulation and the measurements is satisfactory. In Fig. 3, the velocity profile is represented in three dimensions over the pipe length and the pipe cross section at  $t=14c/L$ . The pressure reservoir is located at the beginning of the line ( $x=0$  in Fig. 3), and the valve at the end ( $x=1$ ). The number of expansion of the Jacobi polynomials has been set to  $k=0, 1, \dots, 20$ , as this value reproduces the transfer function very well (see next section).

**4.2 Calculation of the Transfer Functions.** One of the methods which can be used to theoretically verify the validity of a pipe model is the calculation of a transfer function. The underlying idea of the transfer function is quite simple. The boundary condi-

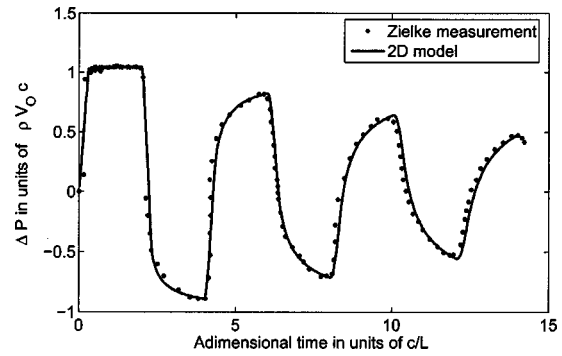


Fig. 2 Pressure at the pipe downstream end. The Chebyshev and Jacobi polynomials have been expanded, respectively, up to the order  $m=0, 1, \dots, 15$  and  $k=0, 1, \dots, 20$ .

tions at the pipe ends are set to sinusoidal functions of frequency  $\omega$ , and, since the system is linear, at equilibrium the pressure and the velocity in the pipe oscillate around an equilibrium value with the frequency of the external excitation. The amplitude of the fluctuations is a function of the frequency itself, the so-called transfer function, and it can be calculated analytically at any position in the pipe. The calculation is simplified if one considers only the pipe ends, where the amplitudes of the oscillations of the mean velocity and of the pressure  $V_a$  and  $P_a$  at the beginning of the line ( $x=0$ ), and at the end  $V_b$   $P_b$  ( $x=L$ ), are linked by a four-pole equation [1]

$$\begin{aligned} V_b &= V_a \cos\left(\frac{s\beta L}{c}\right) - P_a \frac{1}{\beta c \rho} \sin\left(\frac{s\beta L}{c}\right) \\ P_b &= V_a \beta c \rho \sin\left(\frac{s\beta L}{c}\right) + P_a \cos\left(\frac{s\beta L}{c}\right) \\ s &= i\omega \end{aligned} \quad (29)$$

where  $c=(K/\rho)^{1/2}$  is the speed of sound in the fluid and  $\beta$  is given by

$$\frac{1}{\beta^2} = \frac{2}{iR(s/\nu)^{1/2}} \frac{J_1[iR(s/\nu)^{1/2}]}{J_0[iR(s/\nu)^{1/2}]} - 1.$$

As pointed out, only three boundary conditions are of practical importance, and therefore, we only consider three transfer functions. All the calculations have been performed for the pipe and fluid properties of the measurements of the Zielke experiment, and the Chebyshev and Jacobi polynomials have been expanded to the order  $m=0, 1, \dots, 15$  and  $k=0, 1, \dots, 20$ , respectively. The transfer function has been calculated up to the frequency where discrepancies with the analytical transfer function have been observed.

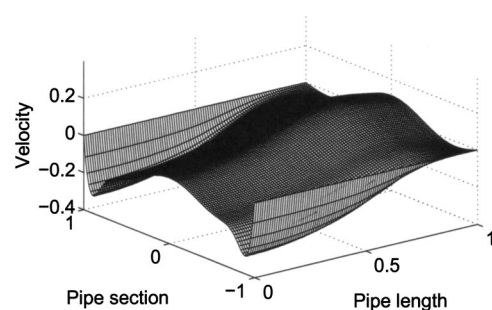


Fig. 3 Velocity profile over the pipe length and pipe cross section at  $t=14c/L$ . The units in the figure are:  $1/L$  for the pipe length,  $1/R$  for the pipe section, and  $1/V_0$  for the velocity.



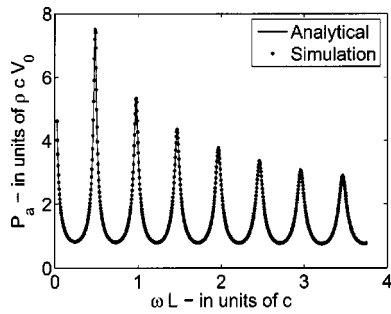


Fig. 4 Transfer function  $P_a$  for a pipe with velocity–velocity boundary condition

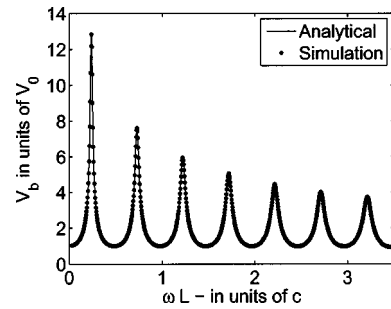


Fig. 7 Transfer function  $V_b$  for a pipe with pressure–velocity boundary condition

- Velocity–velocity transfer function

Here we consider a pipe with velocity–velocity boundary conditions. The velocity  $V_a$  at one pipe end is zero and the other  $V_b$  oscillates with a frequency  $\omega$  and with an amplitude  $V_0$ . We show in Figs. 4 and 5, the comparison of the pressure oscillations  $P_a$  and  $P_b$  at the pipe ends with the analytical transfer function.

- Pressure–velocity transfer function

The transfer function with pressure–velocity boundary conditions has been calculated imposing a zero velocity  $V_a$  at one pipe end and a pressure  $P_b$  at the other end oscillating with a frequency  $\omega$  and with an amplitude  $P_0$ . The comparison of the pressure oscillations  $P_a$  and of the velocity  $V_b$  at the pipe ends with the analytical transfer function is presented in Figs. 6 and 7. The dotted curve represents the analytical transfer function, and the solid the computed transfer function.

- Pressure–pressure transfer function

For the calculation of the transfer function with pressure–pressure boundary conditions, the pressure  $P_a$  at one pipe end is kept constant and the other  $P_b$  oscillates with a fre-

quency  $\omega$  and with an amplitude  $P_0$ . In Figs. 8 and 9 the comparison of the velocity oscillations  $V_a$  and  $V_b$  at the pipe ends with the analytical transfer function is presented.

The number of Jacobi polynomials needed to correctly reproduce the pipe damping over the frequency range of interest depends qualitatively on the dissipation number  $D_n$

$$D_n = \frac{\nu L}{cR^2}.$$

The formulation of a general rule giving the least number of Jacobi polynomials needed to attain the right damping for a given  $D_n$  deserves a numerical analysis which is outside the scope of this article. In Fig. 10, an example illustrates the influence of the number of Jacobi polynomials for the pressure–velocity transfer function, in particular for the oscillation of the pressure  $P_a$  at the pipe end where there is no volume flow. The analysis is restricted only to the first three eigenfrequencies. For  $k=0, 1, \dots, 10$ , the damping of the first frequency is still close to the correct one, but the higher frequencies undergo a higher damping than the analytical one. When  $k=0, 1, \dots, 5$ , the damping of all eigenfrequencies

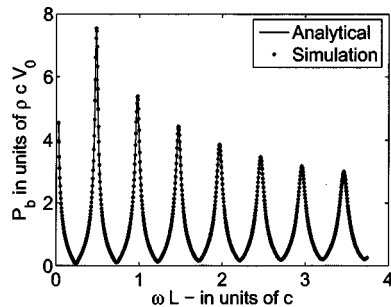


Fig. 5 Transfer function  $P_b$  for a pipe with velocity–velocity boundary condition

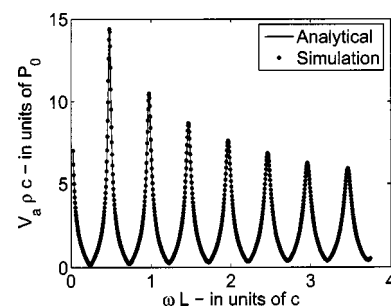


Fig. 8 Transfer function  $V_a$  for a pipe with pressure–pressure boundary condition

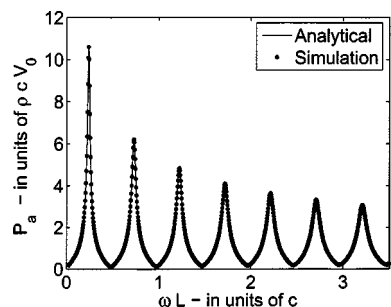


Fig. 6 Transfer function  $P_a$  for a pipe with pressure–velocity boundary condition

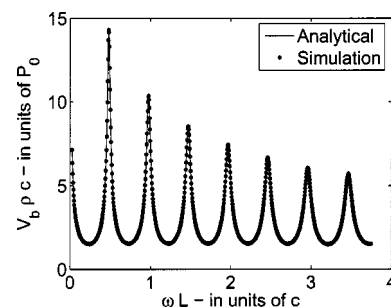
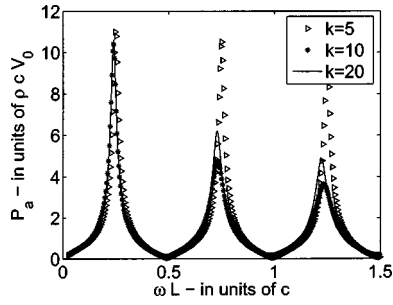


Fig. 9 Transfer function  $V_b$  for a pipe with pressure–pressure boundary condition



**Fig. 10** Transfer function  $P_a$  for a pipe with pressure–velocity boundary condition for three different expansion orders of the Jacobi polynomials

becomes too small. In this case, the number of Jacobi polynomials is not enough to resolve the gradient of the velocity at the wall.

## 5 Conclusions

A model is presented which gives the two-dimensional velocity profile in the time domain for an unstationary pipe flow. The model has been tested on the experimental results of a water hammer presented in the original Zielke article. The agreement of the simulation with the experiment is satisfactory. For a proper choice of the number of the Jacobi polynomials used in the expansion of the pressure and of the velocity field, the simulated transfer functions reproduce the analytical transfer functions over a wide range of frequencies.

## Appendix A: The Chebyshev Polynomials

The Chebyshev polynomial  $T_n$  of order  $n$  is defined in terms of trigonometric functions

$$T_n(x) = \cos(n \arccos(x))$$

and the Chebyshev polynomials form a complete orthogonal set of functions in the interval  $[-1, 1]$  with respect to the weighting function  $1/(1-x^2)^{1/2}$ . The scalar product of the two polynomials  $T_n$  and  $T_m$  is defined as

$$\langle T_m, T_n \rangle = \int_{-1}^1 T_m(x) T_n(x) \frac{dx}{\sqrt{1-x^2}} = \begin{cases} 0 & m \neq n \\ \pi & m = n = 0 \\ \pi/2 & m = n = 1, 2, 3, \dots \end{cases} \quad (\text{A1})$$

## Appendix B: The Jacobi Polynomials

The Jacobi polynomials  $P_n^{(\alpha, \beta)}(x)$  form a complete orthogonal set of functions in the interval  $[-1, 1]$  with respect to the weighting function  $(1-x)^\alpha(1+x)^\beta$  if  $\alpha > -1$  and  $\beta > -1$  (see Ref. [5], p. 775). The scalar product of the two polynomials  $P_m^{(\alpha, \beta)}(x)$  and  $P_n^{(\alpha, \beta)}(x)$  is defined as (see Ref. [5], p. 774)

$$\langle P_m^{(\alpha, \beta)}, P_n^{(\alpha, \beta)} \rangle = \int_{-1}^1 P_m^{(\alpha, \beta)}(x) P_n^{(\alpha, \beta)}(x) (1-x)^\alpha (1+x)^\beta dx = \begin{cases} 0 & m \neq n \\ \frac{2^{\alpha+\beta+1}}{2n+\alpha+\beta+1} \frac{\Gamma(n+\alpha+1)\Gamma(n+\beta+1)}{n!\Gamma(n+\alpha+\beta+1)} & m = n \end{cases} \quad (\text{B1})$$

From the Jacobi polynomials it is possible to build the set of polynomials  $Z_n(x)$

$$Z_n(x) = P_n^{(0,1)}(2x-1)$$

which are orthogonal in the interval  $[0, 1]$  with respect to the weighting function  $x$ . From Eq. (B1) the scalar product of two polynomials  $Z_m$  and  $Z_n$  is

$$\langle Z_m, Z_n \rangle = \int_0^1 Z_m(x) Z_n(x) x dx = \begin{cases} 0 & m \neq n \\ 1/(2m+2) & m = n. \end{cases} \quad (\text{B2})$$

The derivative  $\delta_k$  of  $Z_n(x)$  in  $x=0$  can be derived, after some algebra, from the following equations (see Ref. [5], pp. 777, 774, 783)

$$P_n^{(0,1)}(-1) = (-1)^n P_n^{(1,0)}(1)$$

$$P_n^{(1,0)}(1) = n + 1$$

$$(2n+1) \dot{P}_n^{(0,1)}(-1) = n^2 P_n^{(0,1)}(-1) + n(n+1) P_{n-1}^{(0,1)}(-1)$$

and reads

$$\delta_k = \left. \frac{\partial Z_k}{\partial \xi} \right|_{\xi=0} = \frac{(-1)^{k+1}}{4} k(k+1)(k+2). \quad (\text{B3})$$

## Appendix C: Calculation of $A_{i,k}$

The Chebyshev polynomials  $T_n(x)$  satisfy the two following equations (see Ref. [5], p. 782)

$$(1-x^2) \dot{T}_n = -n x T_n + n T_{n-1}$$

$$2T_n T_m = T_{n+m} + T_{n-m} \quad n \geq m$$

which are needed for the calculation of  $A_{i,k}$ .

The first equation can be written as

$$\frac{1}{2}(T_0 - T_2) \dot{T}_n = -n T_1 T_n + n T_{n-1}$$

and combining it with the second equation gives

$$(T_0 - T_2) \dot{T}_n = n(T_{n-1} - T_{n+1}) \quad n \geq 1.$$

Multiplying by  $T_m$  and performing some algebra, we end up with the following expression

$$T_{m+2} \dot{T}_n + T_{m-2} \dot{T}_n - 2T_m \dot{T}_n = 2n(-T_{n-1} T_m + T_{n+1} T_m)$$

from which we obtain a recurrence relation for the elements of  $A$

$$A_{q+4,n} + A_{q,n} - 2A_{q+2,n} = -\frac{2n}{\epsilon_q} (\langle T_{n-1}, T_{q+2} \rangle - \langle T_{n+1}, T_{q+2} \rangle)$$

where

$$\epsilon_q = \begin{cases} \pi & q = 0 \\ \frac{\pi}{2} & q = 1. \end{cases}$$

The elements  $A_{m,n}$  are zero if  $m \geq n$ , since the derivative of the polynomial of degree  $n$  cannot have any component on the polynomials of higher order. Therefore, we readily know the following elements

$$q = n - 1 \quad A_{n-1,n} = n\pi/\epsilon_{n-1}$$

$$q = n - 2 \quad A_{n-2,n} = 0$$

$$q = n - 3 \quad A_{n-3,n} = n\pi/\epsilon_{n-3}$$

$$q = n - 4 \quad A_{n-4,n} = 0$$

and since if  $q < n - 4$

$$A_{q+4,n} + A_{q,n} - 2A_{q+2,n} = 0$$

it follows immediately that

$$A_{i,k} = \frac{\pi}{\epsilon_i} \begin{cases} 0 & k \leq i \\ 0 & i - k \text{ even} \\ k & i - k \text{ odd.} \end{cases}$$

## References

- [1] D'Souza, A. F. and Oldenburger, R., 1964, "Dynamic Response of Fluid Lines," *J. Basic Eng.*, **86**, 589–598.
- [2] Zielke, W., 1968, "Frequency-Dependent Friction in Transient Pipe Flow," *J. Basic Eng.*, **90**, 109–115.
- [3] Suzuki, K., Taketomi, T., and Sato, S., 1991, "Improving Zielke's Method of Simulating Frequency Dependent Friction in Laminar Liquid Pipe Flow," *J. Fluids Eng.*, **113**, 569–573.
- [4] *Fluid power control*, edited by J. S. Blackburn and G. Reethof, (Wiley, New York, 1960), p. 85.
- [5] Abramowitz, I., and Stegun, M., 1972, *Handbook of Mathematical Functions with Formulas, Graphs, and Mathematical Tables*, Dover, New York.

# Controlling Turbulence in a Rearward-Facing Step Combustor Using Countercurrent Shear

David J. Forliti<sup>1</sup>  
e-mail: dforliti@buffalo.edu

Paul J. Strykowski

Mechanical Engineering Department  
University of Minnesota,  
111 Church St. SE  
Minneapolis, MN 55455

*The present work describes the application of countercurrent shear flow control to the nonreacting flow in a novel step combustor. The countercurrent shear control employs a suction based approach, which induces counterflow through a gap at the sudden expansion plane. Peak turbulent fluctuation levels, cross-stream averaged turbulent kinetic energy, and cross-stream momentum diffusion increased with applied suction. The control downstream of the step operates via two mechanisms: enhanced global recirculation and near field control of the separated shear layer. The use of counterflow also enhances three dimensionality, a feature that is expected to be beneficial under burning conditions. [DOI: 10.1115/1.1899170]*

## 1 Introduction

The objective of the present work was to study the control of the isothermal turbulent flow within a rearward-facing step combustor using countercurrent shear. The work was motivated by an interest in exploiting the features of countercurrent shear in a combustion device. The step geometry is relevant to dump combustors found in rocket and missile propulsion systems and has similar features to bluff-body stabilized flames found in jet engine afterburners. The nonreacting study was done to examine the effects of counterflow on the turbulent velocity and length scales without the added complexity of heat release. Although no combustion is occurring in the present work, the results will be analyzed in the context of understanding how turbulent combustion may benefit from the countercurrent shear flow environment. Pitz and Daily [1] and Gabruk and Roe [2] showed that the presence of heat release does impact the flowfield in the combustor, but the qualitative features of the flow are similar in both reacting and nonreacting scenarios. Present studies [3] are ongoing for the step combustor with counterflow control in the reacting flow situation, and it appears that burning rates are augmented in a manner consistent with expectations based on the cold flow measurements. Additionally, the cold flow experiments are relevant to the fundamental understanding of flow control in a sudden expansion.

Why use counterflow in a turbulent combustor? Previous studies of counterflow applied to free jets and shear layers suggest that dramatic effects can be realized with modest levels of counterflow [4]. Counterflow has been shown to produce high turbulence levels and large turbulent structures, features that can be exploited in a turbulent combustor to generate highly convoluted flames [5,6]. Thus it is expected that the proper implementation of counterflow in a turbulent combustor would create intense burning rates, facilitating the design of compact and lightweight systems. In addition to the increase in turbulent energy and length scales, counterflow has been shown to produce highly three-dimensional structures [7], a feature that should also enhance combustion.

Counterflow control has been applied successfully for shear layers [8] and free jets [4,9], two flows that are predominantly unconfined. Flows which are confined will have different dynamics, and may be more susceptible to global stagnation problems as the reattaching flow contains a stagnation point. The stagnation

flow observed by Humphrey and Li [10] was not effective at promoting turbulent mixing, possibly due to the lack of nominally parallel flow. Hence it was expected that confinement may have a detrimental effect on enhancing turbulence with counterflow control.

**1.1 Rearward-Facing Step Flow.** There has been a vast amount of research done on the rearward-facing step. Studies have often focused on static pressure distributions, turbulence characteristics, and shear layer reattachment [11–17]. Much of this work was motivated by the drag characteristics of the separated boundary layer. Other investigations were of dump combustors under isothermal flow conditions to document the base flow.

The turbulence levels typically found in rearward-facing step geometries are high when compared to the shear layer formed between a jet and ambient fluid, commonly referred to as the single-stream shear layer. Studies often find turbulence levels on the order of 15–17% percent of the primary stream velocity for the single-stream shear layer (e.g., Mehta [18]). Peak turbulence levels for the rearward-facing step/sudden expansion geometry range from 15% to 25% of the velocity upstream of the expansion plane, with dependence on the step geometry, boundary layer state, and operating conditions [11,19,20]. A thorough review of the experimental findings of the rearward-facing step flows can be found in Eaton and Johnston [21]. Clearly this flow is complicated in that there are a number of important parameters, both geometrical and operational. Eaton and Johnston conclude that the region near the dump plane behaves very similar to a free shear layer.

Pitz and Daily [1] addressed the difference between the rearward-facing step flows and free shear layers. It was conjectured that the increased spreading rate they observed for the separated shear layer in the step geometry was due to the fact that there was reverse flow generated in the separation region. Thus the appropriate shear layer for comparison is not a single-stream shear layer, but a counterflowing shear layer. In the present study, suction will be used to augment the natural recirculation caused by separation and reattachment in order to control the turbulence produced downstream of the step.

**1.2 Flow Control.** Many different flow control strategies have been applied to the rearward-facing step flow. A natural extension of using acoustic forcing, which has been found to be successful in altering mixing in free jets [22], has been used in the rearward-facing step geometry [23,24]. Other methods have been employed using vibrating trailing edges [25] and transversely oscillating airfoils located in the separated flow region [26]. These techniques tend to produce strong spanwise coherent structures that enhance mixing and accelerate reattachment. The spanwise

<sup>1</sup>Current address: Department of Mechanical and Aerospace Engineering, State University of New York at Buffalo, Buffalo, NY.

Contribution by the Fluids Engineering Division for publication in the JOURNAL OF FLUIDS ENGINEERING. Manuscript received by the Fluids Engineering Division February 24, 2004; revised manuscript received November 24, 2004. Associate Editor: Sivaram Gogenini.

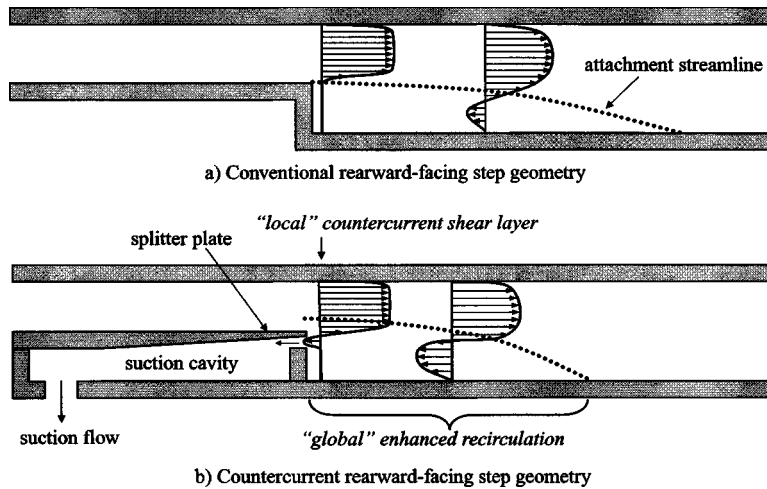


Fig. 1 Conventional and countercurrent rearward-facing step geometries

coherent structures may be detrimental in the combustion application as they can strengthen (or induce) thermo-acoustic instabilities which are driven by coherent structures [27]. To alleviate spanwise coherence, additional measures such as streamwise vortex generators can be used to encourage the formation of flow three dimensionality [28]. In this regard, countercurrent flow has potential benefits over other approaches as it tends to be a broadband amplifier, thus increasing mixing without strong spanwise coherence [4].

**1.3 Countercurrent Shear Control.** Huerre and Monkewitz [29] conducted a linear stability analysis of the hyperbolic tangent velocity profile for a shear layer with arbitrary velocity ratio, and found that a transition from convective to absolute instability occurred when the reverse velocity had a magnitude larger than approximately 13.5% of the forward velocity. In spatially developing flows this stability transition can lead to self-excitation [7]. This result gives motivation for the study of countercurrent shear layers that does not suffer from the stagnation flow observed by Humphrey and Li [10].

An experiment using a round jet with annular counterflow was conducted by Strykowski and Wilcoxon [4]. The counterflow was induced using a suction based system. Significant enhancement of mixing was observed for the jet with counterflow, which was supported by the increased turbulence levels and reduced potential core lengths. Strong levels of counterflow essentially set up a global oscillation, which is expected to occur when a significant spatial region of the flow becomes absolutely unstable [29]. Counterflow was found to be a robust control technique, as its effect on the flow was found to be independent of the state of the boundary layer at the exit of the nozzle.

The effect of counterflow on the organization of the jet shear layer structures has been addressed by Strykowski and Niccum [7,30]. It has been found from flow visualization that the turbulent structures are much more disorganized in the presence of counterflow. The presence of streamwise vorticity was also observed, which plays an important role in the breakdown of organized structures into three-dimensional turbulence.

The long term goal of the present research program is to investigate the benefits of using countercurrent shear for the control of combustion. A rearward-facing step has been chosen as a promising combustor design, which has been modified to include counterflow driven by a suction system. The rearward-facing step geometry has been the subject of previous studies on combustion performance and stability [1,31]. This will be helpful in evaluating the performance of counterflow compared to other control strategies.

## 2 Facility and Experimental Methods

This section will describe the experimental facility and the measurement techniques used to study the control of the rearward-facing step flow. A description of the detailed flow configuration as well as the important geometrical parameters for the countercurrent rearward-facing step will also be discussed. The complicated features expected for the rearward-facing step including reverse flow and large local turbulence intensities has led to the use of particle image velocimetry in the present study. The approach used for generating counterflow is suction based, which has been found to be more successful [4,9] than counterflow, which is driven by interacting momentum streams [10,32].

The conventional and countercurrent step geometries are shown in Figs. 1(a) and 1(b), respectively. For the conventional step flow, there is a streamwise region downstream of the step having natural counterflow caused by separation and reattachment. The region near the dump plane behaves similar to a single-stream shear layer, since the recirculation zone is relatively stagnant in this region [21]. Farther downstream, towards the middle region of the recirculation bubble, the reverse velocities approach a maximum, and the velocity profile gradually approaches the no-slip condition at the lower wall. The velocity profile is wall bounded in this region, and flow behavior is expected to differ from a free shear layer. The attachment streamline shows the global extent of the recirculation bubble, but it is worth repeating that the upstream region of this flow is expected to be similar to a free shear layer [21].

The suction driven countercurrent step design used a vacuum source to lower the pressure in the suction cavity, causing flow to pass from the test section into the cavity. One can expect that the use of suction will cause a movement of the attachment point in the upstream direction. Note that the attachment streamline for the countercurrent step geometry originates in the primary stream while it is anchored to the trailing edge for the conventional step. The suction flow creates a "local" region near the dump plane that is expected to behave like a countercurrent shear layer. Reverse velocities are large in this region due to the proximity and narrow height (relative to the step height) of the suction gap. The wall bounded region is again representative of a recirculation bubble, although the strength of the reverse flow is expected to be larger with suction.

With reference to the combustion application, the suction flow represents an energy loss. The present work employs a relatively large suction flow up to approximately 10% of the primary flow. Preliminary burning experiments [3] show that lower suction mass flow rates (~6%) have a significant impact on the burning rates,

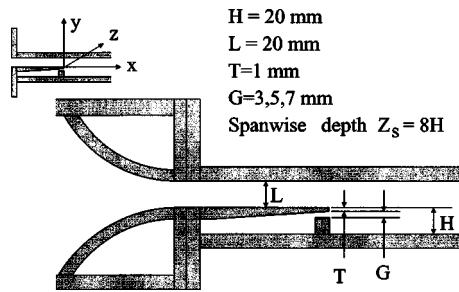


**Fig. 2 Counter-current rearward-facing step geometry parameters**

on the order of a 100% increase with potential for further improvement upon optimization of the combustor geometry. Although for the current approach the suction flow is a penalty to the system, one could conceive of designs where the combustion gases are recombined with the remaining combustor flow at some downstream location.

The test section in the vicinity of the expansion plane is shown in Fig. 2. There are a number of important length scales for the counter-current step geometry.  $L$  is the height of the channel upstream of the expansion plane, and was fixed at 20 mm.  $H$  is the height of the step, which was also fixed for this study at 20 mm. The suction gap  $G$  plays an important role, as the reverse velocity in the vicinity of the dump plane will scale with this dimension for a fixed suction mass flow. In a practical sense, it is desirable to minimize the suction mass flow rate because it requires more work input.

The spanwise dimension  $Z_s$  of the rearward-facing step is an important parameter, as shown by the work of Berbee and Ellzey [19]. In the present study,  $Z_s/H$  was equal to 8, a value representative of other rearward-facing step/dump combustors studied in the literature. The streamwise length of the test section from the step to the outlet was  $20H$ . Studies on reward-facing step flows [12,15,21] show that attachment lengths should be expected to be approximately 6–8 $H$  for high Reynolds number operating conditions, which is shorter than the streamwise length of the test section, guaranteeing shear layer attachment within the test section itself. In order to conduct particle image velocimetry (PIV), optical access is required. The lower plate of the test section is inset with a large silica window as were the sidewalls allowing for both side and spanwise plane PIV measurements to be made.

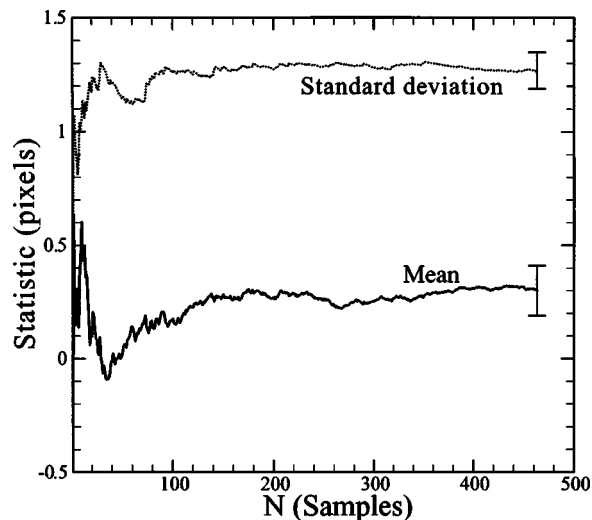


**Fig. 3 The effect of sample size on the convergence of first and second order velocity statistics**

The primary flow was driven by a Fuji model VFC804A-7W 10 hp ring compressor. A fraction of the total mass flow through the pump was diverted to a throttled bleed-off line allowing for control of the primary flow rate. The flow rate was metered through the measurement of the pressure drop across a fine mesh screen located upstream of the combustor.

To accommodate the PIV measurements, tracer particles were added to the flow. Compressed air was passed through a Laskin nozzle filled with olive oil, producing droplets predominantly in the submicron range [33]. The air seeded with olive oil droplets exited the Laskin nozzle and was mixed with the primary flow.

The droplet laden air was piped to the facility, consisting of a diffuser, flow conditioning section, nozzle, and rearward-facing step test section. The diffuser converts the cross section from a circular shape to the rectangular shape with dimensions of 160 × 120 mm. The flow conditioning consists of a perforated plate, followed by a short section of honeycomb, and two fine mesh screens. The nozzle is constructed from sectors of a large radius pipe, and has an area ratio of 6:1. Pitot probe surveys showed that this setup produced a uniform top-hat velocity distribution across the area of the nozzle exit (see Forliti [34] for additional details). The exit of the test section is connected to a large diameter pipe which exhausts to the outside environment.

The counterflow was induced using a suction based system implementing an air ejector. The ejector system was connected to the facility using seven hoses fastened to the suction cavity through evenly spaced spanwise ports. The suction hoses were manifolded together, and the flow passed through a Venturi meter to measure the suction mass flow rate. The suction flow eventually entered the ejector where it was mixed with the compressed air being used as the ejector primary flow. The combined flow was then ducted to the atmosphere.

The laser and camera were controlled by a TSI Model 610032 synchronizer, with input from a personal computer through TSI Insight software version 2.0. The laser is a Continuum Surelite II-10, which is capable of laser pulses of 200 mJ with a pulse duration of approximately 9 ns. The laser power and time separation between the two laser pulses was software controlled. A TSI Model 630046 charge coupled device camera allows for cross-correlation mode PIV, which is advantageous over autocorrelation mode in that there is no directional ambiguity and the signal-to-noise ratios are larger. An earlier study by Forliti, Strykowski, and Debatin [35] suggests that for this system, the Gaussian curve-fit algorithm is the most accurate approach for determining the displacement measurements to good subpixel accuracy. The interrogation region in the digital image domain was 32 × 32 pixels, and the image was spatially sampled with 50% overlapping interrogation regions.

The PIV diagnostic was used for the present work to study the flow in a two-dimensional plane in both the side and spanwise planes. The laser was positioned below the rearward-facing step assembly, with the laser beam aligned parallel to the test section streamwise axis. Light sheet forming optics mount onto an optical support downstream of the laser output aperture. The light sheet optics consisted of a cylindrical and spherical lens of focal lengths –50 and 1000 mm, respectively.

For the side view PIV experiments, the light sheet was positioned along the midspan plane of the test section. Because of the highly inhomogeneous nature of the step flow, a large spatial domain must be studied with PIV in order to examine how the suction based counterflow impacts the global flowfield. The study of the global flowfield was done using three different streamwise camera locations that were patched together. The camera was mounted on a rail, allowing for movement of the camera along an axis parallel to the facility streamwise axis.

Spanwise PIV measurements were also taken to explore the effects of counterflow on the turbulence in the spanwise plane. For these measurements, the test section assembly was rotated 90 deg

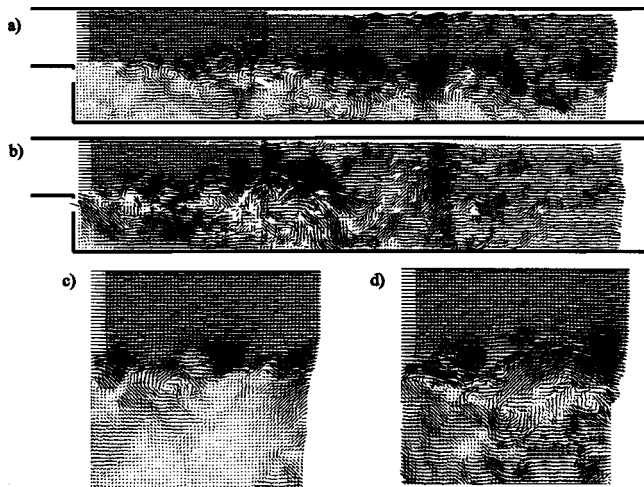


**Fig. 5 Global and high-resolution instantaneous velocity-vector fields for (a), (c) the base line case and (b), (d) the 10.7% suction mass flow case**

about the streamwise axis, such that the light sheet was coincident with the spanwise plane containing the splitter plate trailing edge.

Mean and turbulent flow statistics were computed from ensembles of PIV realizations. Figure 3 presents the convergence trend for displacements measured with PIV for a point in the highly turbulent region of the recirculation bubble. Both the mean and standard deviation of the streamwise displacement converge for a sample set size of approximately 500 measurements. Error bars presented in Fig. 3 represent the precision error of the measurement. Instantaneous velocity measurements have bias errors on the order of 2% of the inlet velocity. The bias error estimates include peak locking and window bias errors as described in Forliti et al. [35]. A minimum of 500 velocity fields were used to compute the statistics, resulting in precision errors in the mean and fluctuating velocities of nominally 2% of the inlet velocity (see Forliti [34] for a complete uncertainty analysis).

### 3 Results and Discussion

The specific objectives of the experiments were to obtain performance measures of the controlled rearward-facing step flow, determine the important control parameters, and explore sensitivity of the flow control to minor changes in geometry. The study was divided into a series of data sets, each one having unique motivations. The first series of tests were conducted to establish the effects of applying suction on the rearward-facing step flowfield for a fixed geometry. A subsequent study was undertaken to explore the effects of suction gap height  $G/H$ . Spanwise measurements were also taken to establish the effect of suction on the turbulence intensities in the spanwise plane.

The initial conditions at the expansion plane play an important role in the flow development downstream of the step. In general, the initial conditions are characterized by cross-stream profiles of the mean  $\bar{U}$  and rms fluctuating  $\sqrt{u'^2} = u'_{rms}$  velocities. For the present work, the internal surfaces of the plenum and test section are rough and the boundary layers are expected to be turbulent. The cross-stream profiles of the mean velocity  $\bar{U}$  and velocity fluctuation  $u'_{rms}$  slightly upstream of the splitter plate trailing edge are shown in Fig. 4. The characteristic velocity  $\bar{U}_0$  is the maximum value in the mean velocity profile. The mean velocity has a top-hat shape with thin boundary layers. The rms of the velocity fluctuation near the channel walls suggests the boundary layers are turbulent or experiencing transition. The velocity in the center core of the flow is approximately 12.5 m/s, which was held constant for all experiments. The fluctuation level within the potential

core was less than 1% of the potential core mean velocity. Although the global features of the rearward-facing step flow are strongly affected by the initial conditions, the counterflow control in free jets has been shown to produce results that are nominally independent of initial conditions [4].

**3.1 Effects of Suction.** The basic effects of suction driven counterflow on the flowfield were studied using a fixed test section geometry with a suction gap  $G/H$  equal to 0.25. The Reynolds number  $Re_H$  was 13 600. The base line study at zero suction mass flow was achieved by removing the suction hoses from the facility and sealing the taps.

Figure 5 shows instantaneous velocity-vector fields for the zero and maximum suction mass flow (10.7%) cases. Figures 5(a) and 5(b) show instantaneous flowfields over the entire measurement domain for these two cases. The data are actually divided into three overlapping streamwise segments that were taken at different times, but are presented together to give a qualitative view of the effect of suction. The case without suction shown in Fig. 5(a) illustrates that the high velocity stream persists for a large streamwise distance. The flow is seen to be diffusing although a lower velocity region near the lower wall is maintained over the entire measurement domain. The case with high suction in Fig. 5(b) shows enhanced mixing between the high-speed stream and the recirculation region. The primary flow interacts with the lower wall much earlier and the flow in the downstream region is becoming increasingly homogeneous in the cross-stream direction.

Figures 5(c) and 5(d) show high-resolution measurements of the velocity field in the vicinity of the sudden expansion for the zero and high-suction mass flow levels. The zero suction case shows the presence of nominally stagnant flow in the recirculation region. Although some turbulent structure is present, the velocity difference available for turbulent energy production is limited in this region. In contrast, the case with high suction shown in Fig. 5(d) shows a relatively strong reverse flow and increased presence of vortex structures. The presence of a larger domain containing velocity gradients will enhance flame wrinkling processes during reacting flow operation.

Ensemble measurements using PIV allow for the exploration of the effect of suction on the mean and turbulent characteristics. Figures 6(a)–6(c) show the streamlines for the mean velocity fields for three different suction mass flow levels. These streamlines were calculated using the streamline function of the Tecplot® software package, thus are not stream function contours. The streamlines are calculated through trajectories which are parallel

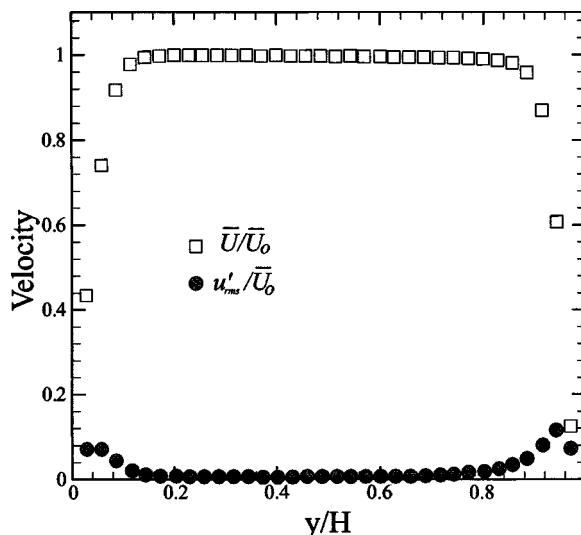


**Fig. 4 Test section initial conditions upstream of expansion plane**

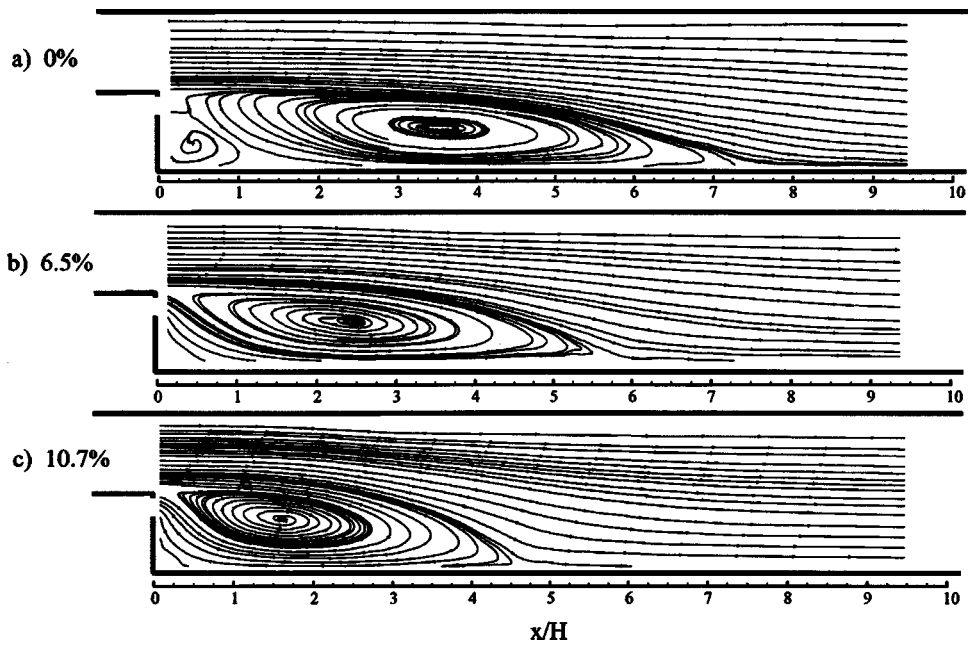


Fig. 6 Streamlines for the mean velocity fields for the countercurrent step flow at various suction mass flow levels

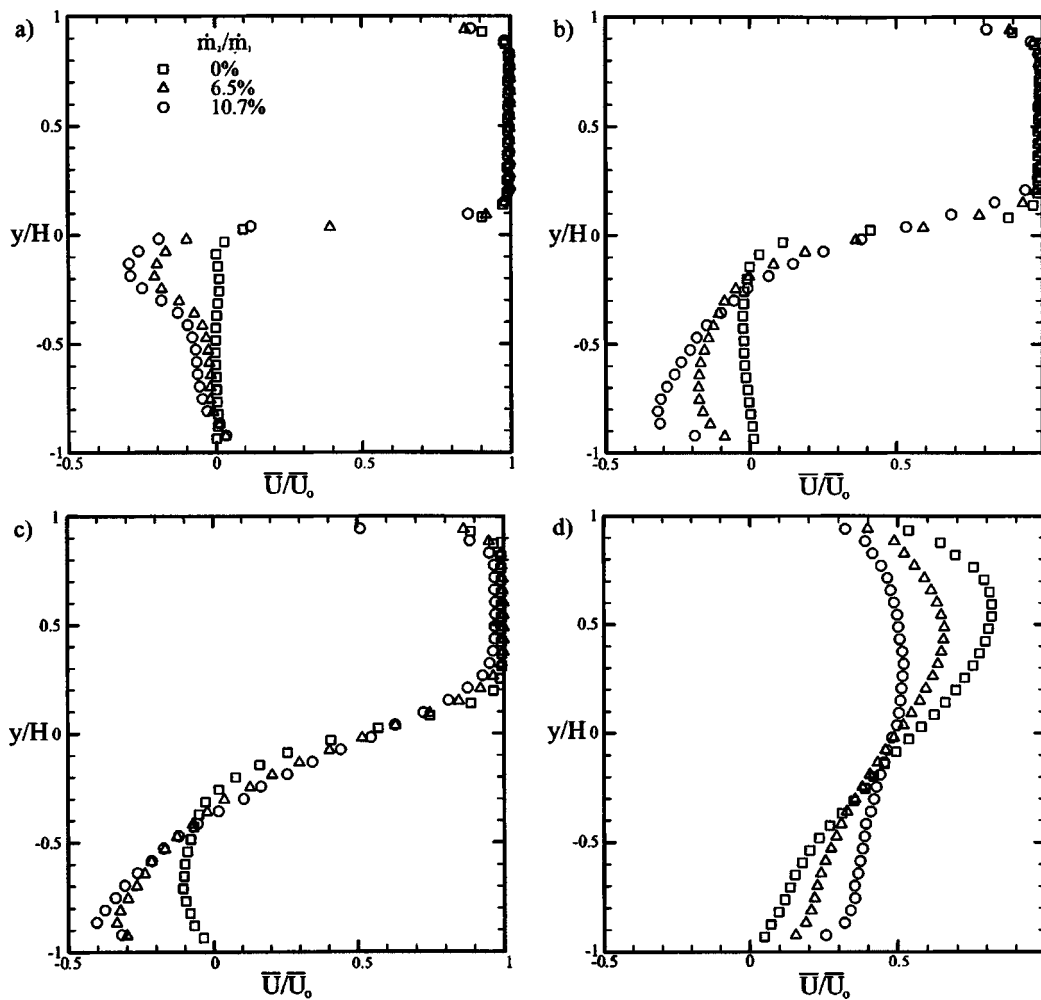
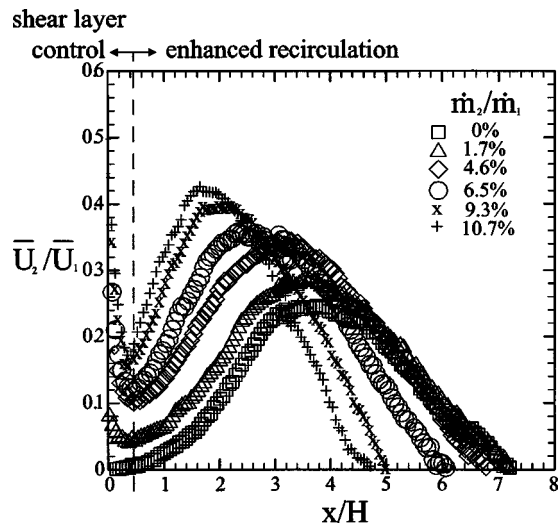


Fig. 7 Mean streamwise velocity profiles for a variety of suction mass flows at (a)  $x/H=0.1$ , (b)  $x/H=1.0$ , (c)  $x/H=2.0$ , and (d)  $x/H=8.0$





**Fig. 8 Streamwise velocity ratio distributions for the counter-current step flow at various suction mass flow levels**

to the local velocity vectors. Because the data have nonzero error, recirculation regions do not have closing streamlines, but slightly spiral inwards or outwards. Nonetheless, the streamlines are useful in understanding the basic features of the mean flowfield.

Figure 6(a) shows the streamlines for the base line case (no suction). As can be seen, there is a large recirculation bubble which is present over most of the streamwise domain of study. The stagnation streamline begins at the trailing edge and impacts the wall at approximately  $x/H$  of 7.2, in general agreement with Adams and Johnston [12]; the stagnation streamline is the streamline that separates the primary flow and recirculation region. There is a secondary recirculation region near the trailing edge which also has been observed by other researchers in rearward-facing step flows [36]. Downstream of the reattachment point, the primary flow streamlines are nearly parallel across the entire cross section as the flow begins to approach a turbulent channel flow.

The most noticeable change in the streamline patterns with increasing suction level is the reduction in the streamwise extent of the recirculation bubble. This trend is indeed predictable and has been shown to occur with other control strategies in rearward-facing step geometries [24–26]. Because of the confined nature of the present flow, the suction mass flow will originate in the primary stream. This is different than the free jet configuration studied by Strykowski and Wilcoxon [4] where the suction flow originated from ambient air. This is an important difference, since the confined case by definition must have an internal stagnation region, having features similar to the global saddle-point flow observed by Humphrey and Li [10].

Cross-stream profiles of the mean streamwise velocity for various levels of suction are shown in Figs. 7(a)–7(d) for four different streamwise locations. The profiles at  $x/H=0.1$  shown in Fig. 7(a) illustrate the effect of suction near the dump plane. The case without suction shows a nominally stagnant fluid below the high-speed primary stream. The application of suction shows an increase in reverse flow over a narrow thickness that represents flow accelerating towards the suction gap. The suction causes an increase in the velocity difference available for production of turbulence. The location of the suction gap high on the expansion plane near the trailing edge is important in creating a local counter-current shear layer.

The velocity profiles shown in Figs. 7(b) and 7(c) show that suction increases the reverse velocity magnitude in the upstream portion of the recirculation bubble. At these locations the peak reverse velocity is located near the wall. The effect of control at this location is more representative of enhanced recirculation; suc-

tion tends to increase the strength of the naturally occurring recirculation bubble. The relative roles of the counter-current shear layer and the enhanced recirculation were explored through suction gap changes and will be addressed later.

The final cross-stream profiles shown in Fig. 7(d) indicate the influence of suction on the flow downstream of the attachment location. The case with zero suction shows a strong nonuniformity in the velocity profile suggesting momentum mixing is incomplete. The velocity becomes increasingly uniform as suction is increased, an indication of enhanced mixing in the upstream region. For engineering applications, uniformity in velocity and temperature distributions across the exit of the combustor directly impact performance and efficiency.

From the standpoint of stability theory of shear layers, separation bubbles, or any nominally parallel flow, the velocity ratio  $\bar{U}_2/\bar{U}_1$  is an important parameter. For each  $x/H$  location, the velocity ratio can be calculated where  $\bar{U}_1$  and  $\bar{U}_2$  are the local maximum and minimum streamwise velocity values along the  $y/H$  axis. For the present flows, the velocity ratio is a strong function of the streamwise coordinate  $x/H$ ; the streamwise velocity ratio distributions for various suction levels are shown on Fig. 8. An error propagation calculation suggests the velocity ratios are accurate to  $\pm 0.03$  [34]. The base line case has a velocity ratio of zero near the trailing edge, then increases with downstream distance, reaches a peak magnitude of 0.22 at  $x/H \sim 3.6$ , then decreases with downstream distance, until attachment.

As previously described, the application of suction alters the size and strength of the recirculation region. As seen in Fig. 8, the peak velocity ratio for the recirculation bubble ( $x/H > 0.5$ ) increases with suction and moves upstream. The peak bubble reverse velocity nearly doubles for the highest suction level. Because the bubble location is far downstream compared to the size of the sink source (i.e., the suction gap height  $G$ ), it is expected that the recirculation strength is predominantly determined by the suction mass flow rate. In other words, it is expected that modest changes in the suction gap will have a minimal impact on the recirculation region structure for a fixed suction mass flow rate. This is not the case for the unconfined suction configurations that do not contain a recirculation bubble (i.e., attachment), that are governed predominantly by the velocity ratio [4,37].

The initial region of the domain ranging from  $x/H$  of 0–0.5 shows that the use of suction increases the velocity ratio considerably in this range; this is the region that behaves similar to a free shear layer. This is an important region of the flow, because the mean velocity gradients are large and the potential for turbulent energy production is greater than for regions further downstream. If the shear layer dynamics near the trailing edge play a role in the overall flow development, it is expected that the control in this region is sensitive to velocity ratio and not suction mass flow rate. Again, this reinforces the concept that the suction flow causes changes in the flow through two mechanisms: enhanced recirculation that is predominantly a function of mass flow ratio  $\dot{m}_2/\dot{m}_1$ , and local shear layer control near the trailing edge dominated by velocity ratio ( $-\bar{U}_2/\bar{U}_1$ ) effects near the trailing edge. These two regions of influence are shown in Fig. 8. Because the shear layer and recirculation zones are expected to have different dependencies, choices in suction gap  $G$  and suction mass flow rate  $\dot{m}_2/\dot{m}_1$  allow for separate control of these two mechanisms.

The analysis of the mean flow was insightful in understanding how suction impacts the flowfield. In order to evaluate the performance of counter-current shear flow control in a rearward-facing step flow in the context of a combustion device, turbulence quantities must be used because they directly impact combustor performance [6]. Cross-stream profiles of streamwise turbulent fluctuations  $u'_{rms}/\bar{U}_0$  are presented in Fig. 9 for a variety of streamwise locations. It is observed that the peak turbulence level increases at the three upstream locations. The farthest downstream profiles show similar levels in the recirculation region; the de-

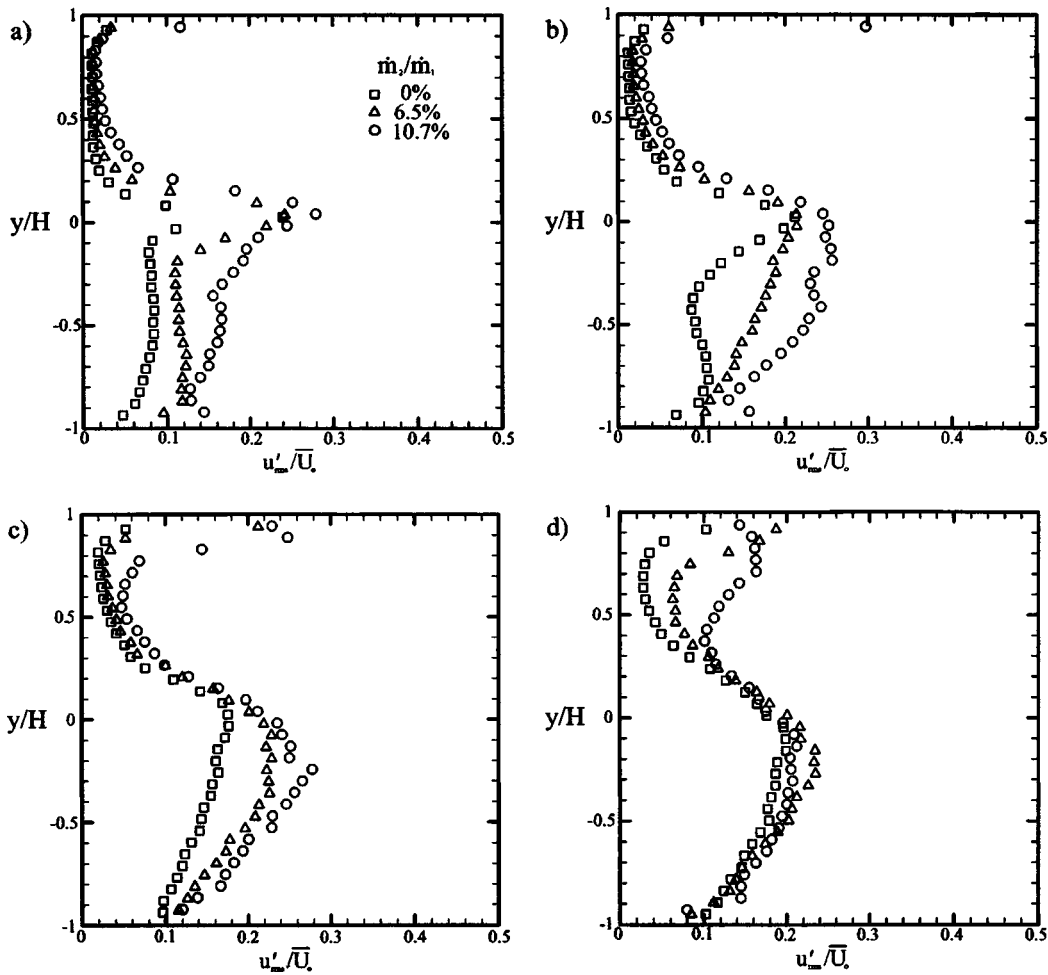


Fig. 9 Rms streamwise velocity fluctuation profiles for a variety of suction mass flows at (a)  $x/H = 1.0$ , (b)  $x/H = 2.0$ , (c)  $x/H = 3.0$ , and (d)  $x/H = 5.0$

layed production of turbulence for the base line case has nearly caught up to the maximum suction case that has already reached peak levels and has begun to decay. Not only are the peak turbulence levels increased with suction but higher turbulence levels are distributed over a larger cross-stream distance, a feature that will be beneficial for combustion since higher turbulence levels distributed over a larger volume will have enhanced flame wrinkling potential [6].

Because of the importance of the spatial distribution of energetic turbulence which exists across the test section, in the context of combustion control, the cross-stream averaged turbulent kinetic energy has been calculated, normalized by the cross-stream averaged mean kinetic energy into the test section

$$\frac{1}{A\bar{U}_0^2} \int_A \overline{u'^2 + v'^2} dA \cong \frac{1}{\bar{U}_0^2} \frac{\sum_{y/H=-1}^1 \overline{(u'^2 + v'^2)}}{n_{y/H}} \quad (1)$$

where  $A$  is the cross sectional area and  $n_{y/H}$  is equal to the number of measurement nodes in the vertical direction across the entire cross section. This mean turbulent energy is a function of  $x/H$ , and is presented in Fig. 10. As the suction mass flow is increased, the maximum cross-stream averaged turbulent energy increases monotonically. The suction generates high levels of turbulent energy in a shorter streamwise distance from the dump plane. The peak turbulent energy for the high suction case is approximately 70% higher than the peak for the base line case. The peak also moves upstream with increasing suction, a trend that was also

seen in the velocity ratio distributions of Fig. 8. It is interesting to note that the peak turbulent energy is generally one or two step heights  $H$  downstream of the peak velocity ratio in the recirculation zone at all suction mass flow levels. This is evidence that the recirculation zone plays an important role in generating turbulence.

The turbulent energy near the downstream end of the measurement domain is approximately the same for all suction levels. This suggests that the cases with suction undergo higher levels of dissipation of turbulent kinetic energy into thermal energy, which is expected since the fluctuation levels are very high in the upstream region. For all cases, the downstream flow is approaching the turbulent channel flow, with the suction cases being further developed as seen from the uniform mean velocity profiles in the downstream region [see Fig. 7(d)].

In order to explore the mechanism behind the flow control achieved with suction, length scale measurements were made as a function of streamwise coordinate. The integral length scale is a measure of the large scales present in the flow. Often the integral length scale is calculated through an integration of the spatial correlation function along the streamwise coordinate. For the present work, the interest is focused on the cross-stream dimension of the turbulent structures, therefore a vertical integration was used to quantify the integral length scale. For each  $x/H$  location, the integral scale was calculated using the numerical approximation to the integration

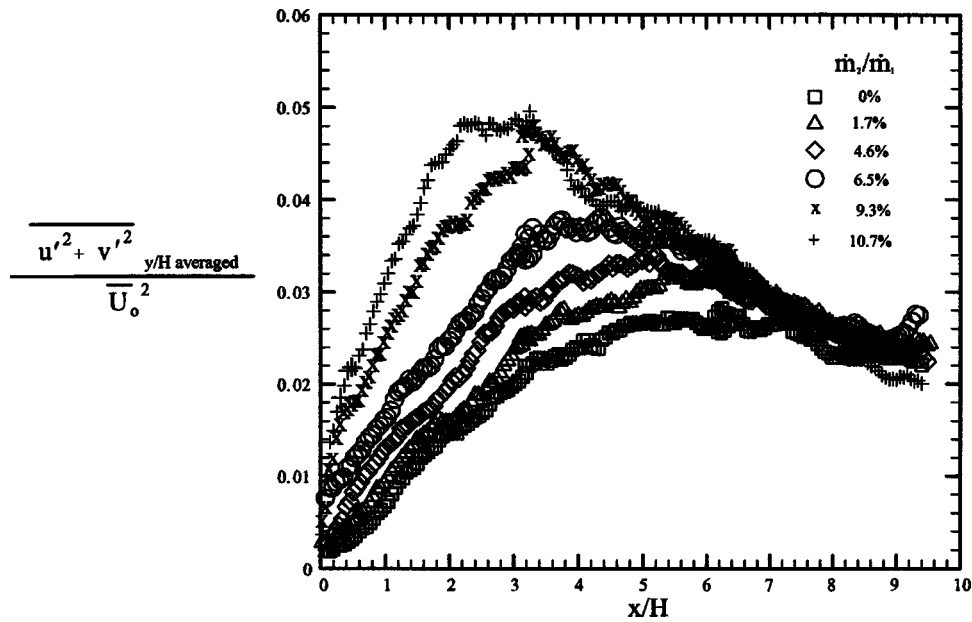


Fig. 10 Cross-stream averaged turbulent energy distributions for the countercurrent step flow at various suction mass flow levels

$$\ell_0(x_0) = \int_{y=-H}^{y=+H} R_{11}(x_0, y_0 + y; x_0, y_0) dy \quad (2)$$

with the vertical reference point  $y_0/H$  coincident with the point of maximum turbulence level for each  $x/H$  location;  $R_{11}(x, y, x_0, y_0)$  is the spatial correlation function using the streamwise velocity fluctuations.

The integral length scale distributions for the base line and the maximum suction cases are shown in Fig. 11. Error propagation shows the uncertainty in the integral length scale calculations is  $\pm 0.04 H$  [34]. As can be seen, the rate of growth of large structures in the upstream region is much larger for the high suction case. Farther downstream, the growth of the structures is impeded by the walls, as the growing shear layer begins to interact and attach to the lower wall. The lines shown on the figure are a linear fit to the data located in the upstream near field region, which has a nearly linear growth trend. The near field growth rate of structures is approximately 70% greater for the high suction case, and persists approximately halfway to the reattachment point. Thus the downstream half of the recirculation bubble is a region where confinement effects begin to impact the growth of turbulent structures. Even in the wall affected region, where the rate of growth of the structures is nominally the same for the two cases, the high counterflow case maintains larger structure over the entire measurement domain.

The ability to generate larger length scales in conjunction with higher turbulence levels is relevant to combustion. Larger scales will enhance flame wrinkling processes resulting in increased volumetric heat release rates. The seminal work of Abdel-Gayed, Bradley, and Lawes [6] indicates the interaction between turbulent burning velocities, turbulence level ( $u'/S_L$ , where  $S_L$  is the laminar flame speed), and turbulent Reynolds number. In the absence of quenching, it is clear that an increase in the integral scale and turbulence level will result in an increase in turbulent burning velocities. Near the quenching boundary, increases in turbulence level may lead to local or global quenching that can actually reduce the burning rates or lead to blowout. Increasing the length scale is beneficial in both minimizing quenching and increasing turbulent burning velocities [6,38].

The quenching observed for highly turbulent burning conditions is attributed to strain rate effects on the internal flame struc-

ture [5]. Although the strain rate effects are often attributed to the smallest turbulent scales, recent evidence suggests that the scales most relevant for quenching have a length scale on the order of the flame thickness [39]. The present study (under nonreacting conditions) was able to resolve scales of this size with PIV, and it was found that the strain rates were nominally constant with or without counterflow control [34]. Hence the turbulence levels and length scales increase in a manner such that the strain rates of the important scales are nominally constant. This should allow for increasing the turbulent flame wrinkling without the detrimental effect of high strain rates.

**3.2 Effects of Suction Gap Height.** The geometry of the suction gap will play a role in the dynamics of the controlled rearward-facing step flow. As described earlier, the use of suction tends to have two effects: enhanced shear layer growth near the trailing edge caused by local intense counterflow, and global enhancement of the naturally occurring recirculation region. It is expected that for small changes in the suction gap, the recircula-

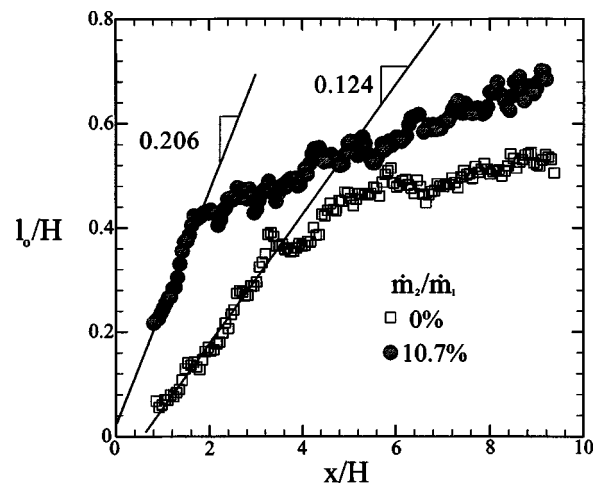


Fig. 11 Cross-stream integral length scales for the 0% and 10.7% suction mass flow cases

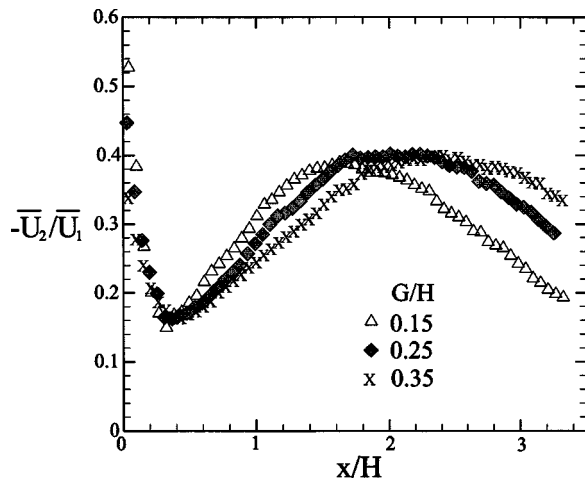


Fig. 12 Streamwise velocity ratio distributions for gap heights  $G/H$  of 0.15, 0.25, and 0.35 for 9.3% suction mass flow

tion should be generally controlled by the suction mass flow, since it is responding to a sink located sufficiently far upstream. Thus we would predict that the recirculation region will depend very weakly on the suction gap  $G$ . If these two mechanisms are in fact governed as hypothesized, then the selection of the gap height  $G$  and the suction mass flow should allow for some control of the relative roles of the near field separated countercurrent shear layer and the global recirculation region.

A series of tests was conducted to study the effect of the velocity ratio near the trailing edge on the global flowfield. The results of two new gap heights will be presented,  $G/H$  of 0.15 and 0.35, with the previously presented tests having a  $G/H$  of 0.25. Only the upstream camera location ( $0 < x/H < 3.3$ ) was used for this study, as the focus was on the effects of suction over a range including the trailing edge and upstream portion of the recirculation bubble.

In order to study the effect of the various gap heights on the mean and turbulent field, the velocity ratio and cross-stream averaged turbulent energy is plotted as a function of the streamwise coordinate  $x/H$ , as was done previously for the base line gap. Figure 12 shows the streamwise velocity ratio distribution for all three gaps for a 9.3% suction mass flow. The main effect of changing the suction gap is a change in the velocity ratio near the trailing edge, as can be seen in the figure for  $x/H < 0.2$ . The recirculation bubble appears to move slightly upstream with de-

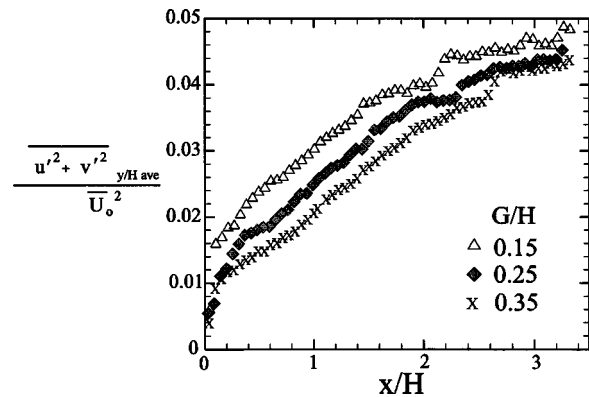


Fig. 13 Cross-stream averaged turbulent kinetic energy distributions for gap heights  $G/H$  of 0.15, 0.25, and 0.35 for 9.3% suction mass flow

creasing suction gap. It is expected that the shear layer growth rate near the trailing edge will be larger for the smaller gaps, because the velocity ratio ( $-\bar{U}_2/\bar{U}_1$ ) is higher. The increased near field growth rate will result in a thickened shear layer in the downstream region, even though the growth rate in the downstream region may be nominally the same for all gaps. The slightly thickened shear layer will have a tendency to attach to the wall earlier, which is likely to be responsible for the slight upstream movement of the recirculation zone. The velocity difference across the bubble can be seen to be independent of the suction gap height  $G$ .

The cross-stream averaged turbulent kinetic energy is shown for the three gaps for a 9.3% suction mass flow in Fig. 13. There appears to be an increase in the turbulent energy with decreasing gap dimension. Thus at this suction mass flow rate, there is a benefit for using a small gap, which appears to be caused by the sensitivity of the near field separated shear layer to changes in the local velocity ratio. It is seen that the turbulence levels in the downstream region shown in Fig. 13 (i.e., for  $x/H \geq 3$ ) are comparable to one another, where the global recirculation is likely to govern the flow development. Although there is an increase in turbulence level in the upstream region with the smaller gap, the gain is moderate near in the downstream region, hence it is suggested that the primary mechanism for turbulent energy production in this region is the enhanced recirculation.

**3.3 Spanwise PIV Measurements.** The importance of spanwise coherence, as well as understanding how counterflow affects

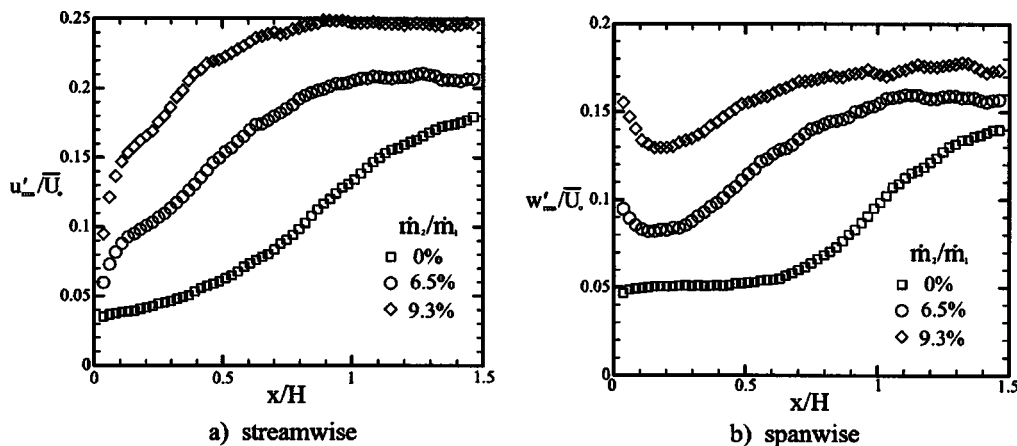


Fig. 14 Spanwise averaged (a) streamwise and (b) spanwise velocity fluctuation levels for 0%, 6.5% and 9.3% suction mass flows

the development of three-dimensional turbulence, gives motivation for using PIV in the spanwise plane. For these experiments, the test section was rotated 90 deg, and positioned such that the light sheet was parallel and coincident with the trailing edge plane. The image capture region was just downstream of the trailing edge, and centered on the midspan with a spanwise range  $Z/H$  of  $-0.75$ – $0.75$ .

Turbulent initial conditions probably play an important role in the observed lack of coherence in the structures downstream of the step. The mere presence of the suction gap may also play a role in effecting the spanwise coherence, since there is the allowance for unsteady flow to enter and exit the suction cavity. Although there was no strong spanwise coherence found under the isothermal flow conditions studied here, the turbulent statistics in the spanwise plane give insight into the three dimensionality of the turbulence.

The spanwise uniformity of the turbulent statistics allows for averaging along the spanwise length to get smooth profiles of normalized streamwise and spanwise rms velocity fluctuations, which are shown in Fig. 14. The shapes of the turbulence profiles suggest that counterflow essentially moves the development of the turbulence upstream towards the trailing edge. The overall levels achieved downstream also increase with increasing suction. This is in agreement with results presented earlier indicating that the effect of suction is essentially an acceleration of the flow development in the upstream direction, as well as an increase in the production of turbulent energy. The spanwise velocity fluctuations are important, because they represent the ability for the counterflow to manipulate the spanwise coherent structure, which will exist under low frequency forcing, such as thermo-acoustic instability in reacting flow applications.

#### 4 Conclusions

The implementation of countercurrent shear control to the rearward-facing step flow was used to understand the role of counterflow control in a confined separated flow. The effect of counterflow is dramatic on both the mean and turbulent flow statistics. The peak turbulence levels increase with suction, but more importantly, the high turbulence levels are distributed over a much larger volume within the test section.

The experiments indicate that the use of suction based counterflow has essentially two separate mechanisms for achieving shear flow control. (1) Counterflow has an effect of augmenting the natural reverse flow, caused by the sudden expansion of the step. Augmentation of the recirculation was indicated by both an increase in the strength of the reverse flow, as well as a movement of the strong recirculation zone upstream, where the mean velocity gradients are higher and turbulent production is enhanced [34]. This modified recirculation is predominantly a function of the suction mass flow rate. (2) The second mechanism employed using the counterflow is the modification of the shear layer near the expansion plane. The suction causes the development of a countercurrent shear layer near the separation point. The increased shear near the trailing edge causes an increase in the turbulence production. Various configurations that were explored showed that both the modified recirculation and the near field shear layer play important roles in the mechanics of the flowfield downstream of the step, although enhanced recirculation appears to be the dominant mechanism that generates the overall peak turbulence levels and large length scales.

The measurements in the spanwise plane showed that stronger three-dimensional turbulence is generated with counterflow, causing the disruption of the spanwise coherence that plays a role in the thermo-acoustic instability mechanism during reacting flow. It is unclear whether the enhanced three dimensionality is caused by a feedback loop through the convection of turbulence upstream by the suction mass flow, or the enhanced instability of the velocity profile which contains counterflow. While no effort was made in the present study to identify the presence of global flow instabili-

ties, no noticeable stability transitions were observed over the range of conditions examined. The fact that high levels of counterflow are observed in the base line step geometry suggests that the flow may already be experiencing globally unstable behavior. This is a vital question which will require additional study.

The ability for the countercurrent shear flow control to work so universally in a confined geometry is surprising, since other studies [10] have shown that it is difficult to establish confined countercurrent shear layers that are not dominated by a global stagnation flow.

#### Acknowledgments

The authors would like to thank the generous support of the Office of Naval Research under Contract No. N00014-01-1-0644 as well as the guidance they have received from technical monitor Dr. Gabriel D. Roy.

#### References

- [1] Pitz, R. W. and Daily, J. W., 1983, "Combustion in a Turbulent Mixing Layer Formed at a Rearward-Facing Step," *AIAA J.*, **21**(11), pp. 1565–1570.
- [2] Gabruk, R. S., and Roe, L. A., 1994, "Velocity Characteristics of Reacting and Nonreacting Flows in a Dump Combustor," *J. Propul. Power*, **10**(2), pp. 148–154.
- [3] Forliti, D. J., Behrens, A. A., and Strykowski, P. J., 2003, "Combustion Control in a Dump Combustor Using Countercurrent Shear," *Proc. International Colloquium on Combustion and Noise Control*, G. Roy, ed. August 12–15, Cranfield, England, pp. 140–146.
- [4] Strykowski, P. J., and Wilcoxon, R. K., 1993, "Mixing Enhancement Due to Global Oscillations in Jets With Annular Counterflow," *AIAA J.*, **31**(3), pp. 564–570.
- [5] Smith, K. O., and Gouldin, F. C., 1979, "Turbulence Effects on Flame Speed and Flame Structure," *AIAA J.*, **17**(11), pp. 1243–1250.
- [6] Abdel-Gayed, R. G., Bradley, D., and Lawes, M., 1987, "Turbulent Burning Velocities: A General Correlation in Terms of Straining Rates," *Proc. R. Soc. London, Ser. A*, **414**, pp. 389–413.
- [7] Strykowski, P. J., and Niccum, D. L., 1991, "The Stability of Countercurrent Shear Layers in Circular Jets," *J. Fluid Mech.*, **227**, pp. 309–343.
- [8] Tang, B. A., 2002, "Experimental Investigation of Planar Countercurrent Turbulent Shear Layers," Masters thesis, University of Minnesota, Minneapolis, MN.
- [9] Strykowski, P. J., Krothapalli, A., and Jendoubi, S., 1996, "The Effect of Counterflow on the Development of Compressible Shear Layers," *J. Fluid Mech.*, **308**, pp. 63–96.
- [10] Humphrey, J. A. C., and Li, S., 1981, "Tilting, Stretching, Pairing, and Collapse of Vortex Structures in Confined Countercurrent Flow," *J. Fluids Eng.*, **103**(3), pp. 466–470.
- [11] Adams, E. W., and Johnston, J. P., 1988a, "Effects of the Separating Shear Layer on the Reattachment Flow Structure Part 1: Pressure and Turbulence Quantities," *Exp. Fluids* **6**(6), pp. 400–408.
- [12] Adams, E. W., and Johnston, J. P., 1988b, "Effects of the Separating Shear Layer on the Reattachment Flow Structure Part 2: Reattachment Length and Wall Shear Stress," *Exp. Fluids* **6**(7), pp. 493–499.
- [13] Driver, D. M., and Seegmiller, H. L., 1985, "Features of a Reattaching Turbulent Shear Layer in Divergent Channel Flow," *AIAA J.*, **23**(2), pp. 163–171.
- [14] Sinha, S. N., Gupta, A. K., and Oberai, M. M., 1982, "Laminar Separating Flow Over Backsteps and Cavities Part 2: Cavities," *AIAA J.*, **20**(3), pp. 370–375.
- [15] Ra, S. H., and Chang, P. K., 1990, "Effects of Pressure Gradients on Reattaching Flow Downstream of a Rearward-Facing Step," *J. Aircr.*, **27**(1), pp. 93–95.
- [16] Spazzini, P. G., Iuso, G., Onorato, M., Zurlò, N., and Di Cicca, G. M., 2001, "Unsteady Behavior of Back-Facing Step Flow," *Exp. Fluids* **30**(5), pp. 551–561.
- [17] Ahmed, S. A., and Abidogun, K. B., 1998, "Measurements of Turbulence Statistics and Energy Budgets in a Model Combustor," *Energy* **23**(9), pp. 741–752.
- [18] Mehta, R. D., 1991, "Effect of Velocity Ratio on Plane Mixing Layer Development: Influence of the Splitter Plate Wake," *Exp. Fluids* **10**(4), pp. 194–204.
- [19] Berbee, J. G., and Ellzey, J. L., 1989, "Effect of Aspect Ratio on the Flow Over a Rearward-Facing Step," *Exp. Fluids*, **7**(7), pp. 447–452.
- [20] Stevenson, W. H., Thompson, H. D., and Craig, R. R., 1984, "Laser Velocimeter Measurements in Highly Turbulent Recirculating Flows," *J. Fluids Eng.*, **106**(2), pp. 173–180.
- [21] Eaton, J. K., and Johnston, J. P., 1981, "A Review of Research on Subsonic Turbulent Flow Reattachment," *AIAA J.*, **19**(9), pp. 1093–1100.
- [22] Crow, S. C., and Champagne, F. H., 1971, "Orderly Structure in Jet Turbulence," *J. Fluid Mech.* **48**, pp. 547–591.
- [23] Bhattacharjee, S., Scheelke, B., and Trout, T. R., 1986, "Modification of Vortex Interactions in a Reattaching Separated Flow," *AIAA J.*, **24**(4), pp. 623–629.
- [24] Chun, K. B., and Sung, H. J., 1996, "Control of Turbulent Separated Flow

- Over a Backward-Facing Step by Local Forcing,” *Exp. Fluids* **21**(6), pp. 417–426.
- [25] Roos, F. W., and Kegelmann, J. T., 1986, “Control of Coherent Structures in Reattaching Laminar and Turbulent Shear Layers,” *AIAA J.*, **24**(12), pp. 1956–1963.
- [26] Lai, J. C. S., Yue, J., and Platzer, M. F., 2002, “Control of Backward-Facing Step Flow Using a Flapping Foil,” *Exp. Fluids* **32**(1), pp. 44–54.
- [27] Schadow, K. C., and Gutmark, E., 1992, “Combustion Instability Related to Vortex Shedding in Dump Combustors and their Passive Control,” *Prog. Energy Combust. Sci.*, **18**(2), pp. 117–132.
- [28] McManus, K. R., 1990, “The Effects of Controlling Vortex Formation on the Performance of a Dump Combustor,” Topical Report No. T-262, Mechanical Engineering Department, Stanford University, Stanford, CA.
- [29] Huerre, P., and Monkewitz, P. A., 1985, “Absolute and Convective Instabilities in Free Shear Layers,” *J. Fluid Mech.*, **159**, pp. 151–168.
- [30] Strykowski, P. J., and Niccum, D. L., 1992, “The Influence of Velocity and Density Ratio on the Dynamics of Spatially Developing Mixing Layers,” *Phys. Fluids A*, **4**(4), pp. 770–781.
- [31] McManus, K. R., Vandsburger, U., and Bowman, C. T., 1990, “Combustor Performance Enhancement Through Direction Shear Layer Excitation,” *Combust. Flame*, **82**(1), pp. 75–92.
- [32] Forliti, D. J., and Strykowski, P. J., 2000, “Examining the Application of Counterflow in Dump Combustors,” *Proc. of 13th ONR Propulsion Meeting*, Minneapolis, MN, pp. 57–62.
- [33] Gerbig, F. T., and Keady, P. B., 1985, “Size Distributions of Test Aerosols From a Laskin Nozzle,” *Microcontamination*, **3**(7), pp. 56–61.
- [34] Forliti, D. J., 2001, “Controlling Dump Combustor Flows Using Countercur-rent Shear,” Ph.D. thesis, University of Minnesota, Minneapolis, MN.
- [35] Forliti, D. J., Strykowski, P. J., and Debatin, K., 2000, “Bias and Precision Errors of Digital Particle Image Velocimetry,” *Exp. Fluids*, **28**, pp. 436–447.
- [36] So, R. M. C., and Ahmed, S. A., 1989, “Characteristics of Dump Combustor Flows,” *Int. J. Heat Fluid Flow*, **10**(1), pp. 66–74.
- [37] Wilcoxon, R. K., 1996, “Mixing Enhancement in an Axisymmetric Jet With Annular Counterflow,” Ph.D. thesis, University of Minnesota, Minneapolis, MN.
- [38] Peters, N., 1999, “The Turbulent Burning Velocity for Large-scale and Small-scale Turbulence,” *J. Fluid Mech.*, **384**, pp. 107–132.
- [39] Poinot, T., Veynante, D., and Candel, S., 1991, “Quenching Processes and Premixed Turbulent Combustion Diagrams,” *J. Fluid Mech.*, **228**, pp. 561–606.

# Boundary-Layer Transition Affected by Surface Roughness and Free-Stream Turbulence

**S. K. Roberts**

e-mail: skrobert@connect.carleton.ca

**M. I. Yaras**

e-mail: metin\_yaras@carleton.ca

Carleton University, Department of Mechanical and Aerospace Engineering, 3135 Mackenzie Bldg., 1125 Colonel By Dr., Ottawa, Ontario, Canada K1S 5B6

*This paper presents experimental results documenting the effects of surface roughness and free-stream turbulence on boundary-layer transition. The experiments were conducted on a flat surface, upon which a pressure distribution similar to those prevailing on the suction side of low-pressure turbine blades was imposed. The test matrix consists of five variations in the roughness conditions, at each of three free-stream turbulence intensities (approximately 0.5%, 2.5%, and 4.5%), and two flow Reynolds numbers of 350,000 and 470,000. The ranges of these parameters considered in the study, which are typical of low-pressure turbines, resulted in both attached-flow and separation-bubble transition. The focus of the paper is on separation-bubble transition, but the few attached-flow test cases that occurred under high roughness and free-stream turbulence conditions are also presented for completeness of the test matrix. Based on the experimental results, the effects of surface roughness on the location of transition onset and the rate of transition are quantified, and the sensitivity of these effects to free-stream turbulence is established. The Tollmien–Schlichting instability mechanism is shown to be responsible for transition in each of the test cases presented. The root-mean-square height of the surface roughness elements, their planform size and spacing, and the skewness (bias towards depression or protrusion roughness) of the roughness distribution are shown to be relevant to quantifying the effects of roughness on the transition process. [DOI: 10.1115/1.1906266]*

## Introduction

Surface imperfections that gradually develop on the blades of gas-turbine engines can result in substantial reductions in stage aerodynamic efficiency, and in thermal damage to the blades due to changes in the surface heat transfer rates. On turbine blades, the source of surface imperfections is typically hydrocarbon deposits and/or pitting and spalling damage caused by the impact of small particles. Bons et al. [1] compiled extensive measurements of roughness statistics for a wide range of in-service gas-turbine blades.

One important mechanism by which surface roughness affects the aerodynamic characteristics and thermal loads of turbine blades is through alteration of the boundary-layer transition process. In gas turbines, the prediction of transition is further complicated by the nonuniform distribution of surface roughness on the blade surfaces, as documented by Bons et al. [1] and Taylor [2]. These studies have noted significant variations in surface roughness in both the streamwise and spanwise directions, with the largest roughness heights typically occurring near the leading edges of blades. It is well known that the natural transition process, for which the growth of Tollmien–Schlichting (TS) waves is a precursor, is bypassed in the presence of sufficiently large levels of surface roughness. In such instances, transition inception typically occurs shortly downstream of the beginning of the rough surface, and the rate of transition tends to be notably higher than that encountered in natural transition (e.g., Kerho and Bragg [3], Gibbings et al. [4–6]). According to the database compiled by Bons et al. [1], in the midspan/midchord region of the suction side of in-service low-pressure turbine blades, the root-mean-square (rms) roughness height varies between approximately 2 and 9  $\mu\text{m}$ . For the range of flow Reynolds numbers and streamwise pressure gradients typical of these blades, this level of surface

roughness tends to be insufficient to cause bypass transition. It is, however, expected that the disturbances created by the roughness elements would tend to accelerate the natural transition process. This may occur through earlier transition inception, a higher rate of transition, or possibly a combination of both.

Many published studies have examined the effects of isolated surface disturbances on the transition process (e.g., Würz et al. [7], Kachanov [8], and Lang et al. [9]). These studies have documented increased receptivity of the boundary layer to disturbances in the presence of surface roughness, and increased amplification rates of TS waves. These trends were noted to be applicable to attached- [7,8] as well as separated-flow transition [9]. However, these studies do not reproduce the conditions of nonuniform streamwise pressure gradients, elevated free-stream turbulence and periodic unsteadiness that are typical in turbomachinery blade passages. Thus, while such studies offer considerable insight into the flow physics of boundary-layer transition over rough surfaces, they are not of direct use to designers of turbomachinery. Several studies (e.g., Kerho and Bragg [3], Cummings and Bragg [10]) have examined the effects of large scale leading-edge roughness on boundary-layer transition over aircraft airfoils. However, the intent of such studies was to simulate the effects of leading-edge icing on aircraft wings, and the tested roughness patterns make them less applicable to turbomachinery applications.

Based on the measured roughness distributions documented in the studies of Bons et al. [1] and Taylor [2], Pinson and Wang [11] examined the effects of streamwise variation in roughness conditions in order to better simulate the roughness patterns typical of gas-turbine blades. They concluded that the abrupt change in roughness height between the leading edge and the remainder of the surface is more influential on attached-flow transition than the downstream roughness level. The combined influence of surface roughness and free-stream turbulence has been studied recently by Wang and Rice [12]. This study demonstrated that the process of attached-flow boundary-layer transition remains sensitive to surface roughness at elevated levels of free-stream turbulence.

The effects of streamwise pressure gradient, free-stream turbulence, periodic-unsteady free-stream velocity, and the interactions

Contributed by the Fluids Engineering Division for publication in the JOURNAL OF FLUIDS ENGINEERING. Manuscript received by the Fluids Engineering Division July 27, 2004; revised manuscript received February 21, 2005. Associate Editor: M. Volkan Otugen.

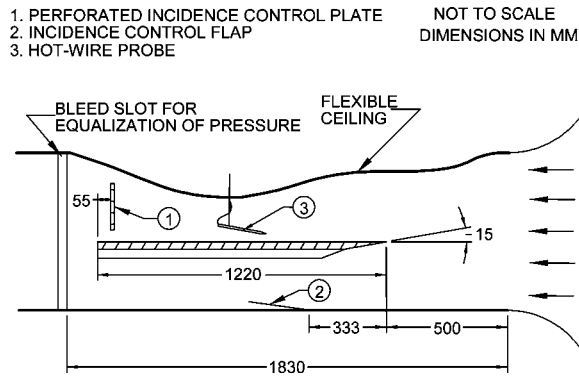


Fig. 1 Schematic of the wind tunnel test section

between these parameters as they affect transition on turbomachinery blades are reasonably well understood, as is evident by the large number of studies dedicated to this subject (e.g., [13–24]). Such studies have formed the basis for models that predict transition in attached flows (Abu-Ghannam and Shaw [16], Johnson [17,25], Narasimha [26], Solomon et al. [27]), and in separation bubbles (e.g., Yaras [22], Hatman and Wang [28], Horton [29]). However, to the authors' knowledge, no models are yet available in the open literature that account for the effects of surface roughness on boundary-layer transition. The current study has been undertaken to supplement the limited data available on attached-flow transition affected by surface roughness, and to establish the effect of surface roughness on separated-flow transition. The study covers a range of distributed roughness and free-stream turbulence levels. These parameters and the streamwise pressure distribution have been chosen to be typical of those present on low-pressure turbine blades of in-service gas-turbine engines.

### Experimental Setup

The experiments are performed in a closed-circuit wind tunnel on a flat test surface upon which streamwise pressure gradients are imposed using a contoured wall forming the ceiling of the test section (Fig. 1). In the context of boundary-layer transition studies, the use of such a testing arrangement is well established (e.g., [24,30,31]). The boundary layer developing over the 1220-mm-long test surface is measured using a hot-wire anemometer with a single tungsten sensor of 5  $\mu\text{m}$  diameter and 1.3 mm length. The flow field, from the leading edge to the reattached turbulent boundary layer, is resolved by 20 cross-stream traverses. The number of measurement locations across the boundary layer varies between 25 near the test plate leading edge and about 80 just downstream of the transition zone. The streamwise spacing of boundary layer traverses is chosen as 25 mm near and inside the separation bubble, and 50 mm elsewhere. In the test cases where a separation bubble is present, flow separation occurs approximately 500 mm downstream of the leading edge, and the distance between the time-averaged separation and reattachment locations varies between 50 and 125 mm. Thus, the separation bubbles in the current study are resolved by 2–5 cross-stream traverses. In addition to the cross-stream traverses, the boundary layer is traversed in the streamwise direction in 2.0 mm increments, at a distance of 1.25 mm from the test surface, providing streamwise intermittency distributions and growth rates of instabilities with high resolution.

Control of the level of free-stream turbulence in the test section is achieved by placing a perforated plate in the flow path at the inlet to the test section. Each of the plates, made of 3.175-mm-thick aluminum, is designed to cover the entire cross section of the flow path, and the openings in the plate consist of nonstaggered, square holes. Based on single-sensor hot-wire

Table 1 Turbulence-generating grid specifications

	No plate installed	Perforated Plate No.	
		1	2
Square hole size (mm)	-	12.7	25.4
Hole spacing (mm)	-	15.9	31.8
Open-area ratio	-	0.64	0.64
Range of $Tu_{ref}$ (%)	0.4–0.9	2.2–2.6	3.4–4.8
Range of $TF$ (%)	0.6–2.0	5.3–6.5	8.4–11.9

traverses 10 mm upstream of the test plate leading edge, extending from the level of the test plate to the ceiling of the test section, these turbulence-generator locations have been found to be adequate to produce uniform mean-flow and turbulence distributions at the leading edge of the test surface. The specifics of the perforated plates are summarized in Table 1, along with the ranges of turbulence intensity and Taylor's [32] turbulence factor measured 10 mm upstream of the leading edge. This turbulence factor ( $TF = Tu_{ref}(L/\lambda_s)^{0.2}$ ) is the parameter preferred by the authors for developing transition models, since it contains information about the integral length scale ( $\lambda_s$ ) as well as the intensity of free-stream turbulence.

The analog output of the hot-wire anemometer is sampled at 8 kHz over 20 measurement cycles, with each containing 8192 samples. The signal is low-pass filtered with a cutoff frequency of 3.8 kHz prior to digitization.

**Test Surfaces.** The smoothest surface ( $k_{rms}=0.7 \mu\text{m}$ ) of the present study is a 25-mm-thick CHART-MIC-6 aluminum plate used in earlier phases of this research project [e.g., [22,23]], with an elliptic leading edge of 15.9 and 3.2 mm axis dimensions. The remaining test plates were constructed by bonding materials of desired roughness patterns onto a 25.4-mm-thick medium density fiber board. These roughness layers (see Fig. 2) consist of countertop laminate ( $k_{rms}=31 \mu\text{m}$ ), tar paper ( $k_{rms}=53 \mu\text{m}$ ), fine asphalt shingle ( $k_{rms}=107 \mu\text{m}$ ), and coarse asphalt shingle ( $k_{rms}=185 \mu\text{m}$ ) surfaces. The leading edge of these rough-surface test plates consists of a 50.8-mm-long aluminum section with a smooth surface, mounted onto the test plates such that its top surface is aligned with the peaks of the roughness elements. The tip geometry of this leading-edge attachment is elliptic with the same major and minor axis dimensions as for the smooth test plate.

The roughness geometries were measured through laser triangulation scans. The statistical roughness parameters deemed to have the strongest influence on the flow are summarized in Table

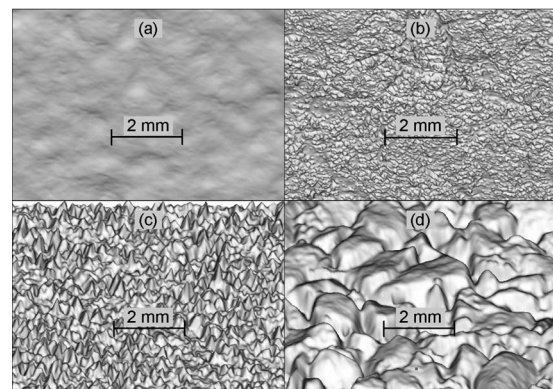


Fig. 2 Topography of the rough surfaces—(a)  $k_{rms}=31 \mu\text{m}$ ; (b)  $k_{rms}=53 \mu\text{m}$ ; (c)  $k_{rms}=107 \mu\text{m}$ ; (d)  $k_{rms}=185 \mu\text{m}$



**Table 2 Surface roughness parameters**

Surface	Laminate	Tar Paper	Fine Shingle	Coarse Shingle
Scan Area (mm <sup>2</sup> )	10 × 10	8 × 8	8 × 8	12 × 12
Δx (μm)	40	20	25	40
k <sub>rms</sub> (μm ±7%)	31	53	107	185
W (mm ±0.1)	2.72	0.49	0.54	1.61
S <sub>sk</sub>	0.42	0.42	-0.05	-0.60

2. The height of the roughness elements is quantified by the root-mean-square (rms) of the roughness height distribution, computed as

$$k_{rms} = \sqrt{\frac{1}{N} \sum_{i=1}^N (y_i - \mu)^2} \quad (1)$$

where  $\mu = \sum y_i / N$  is the mean surface elevation and  $N$  is the number of samples included in the surface scan.

The average spacing of roughness elements is quantified by

$$W = \frac{2N\Delta x}{n} \quad (2)$$

where  $\Delta x$  is the scanning resolution, and  $n$  is the number of times the roughness distribution crosses the mean surface elevation.

The effects of protrusions and depressions on the boundary layer development are expected to be different. The tendency of the roughness pattern toward protrusions or depressions is identified by the skewness of the roughness height distribution

$$S_{sk} = \frac{1}{k_{rms}^3 N} \sum_{i=1}^N (y_i - \mu)^3 \quad (3)$$

For positive values of  $S_{sk}$ , the peaks of the roughness elements lie on average further from the mean elevation compared to the depths of the indentations, and negative values indicate the inverse.

The chosen range of roughness conditions is consistent with the roughness patterns typically observed on low-pressure turbine blades of in-service gas-turbine engines. This is based on comparison with the values of  $k_{rms}$  documented by Bons et al. [1] ranging between 2.4 and 8.8 μm for the midspan/midchord region of such turbine blades. Assuming that typical chord lengths for low-pressure turbines ranging between 3 and 15 cm are equivalent to the length of the test surface in the current study, the range of  $k_{rms}/c$  between  $25 \times 10^{-6}$  and  $250 \times 10^{-6}$  based on the measurements of Bons et al. [1] compares favorably to the present values of  $k_{rms}/L$  ranging from  $25 \times 10^{-6}$  to  $150 \times 10^{-6}$ . The corresponding range of skewness measured by Bons et al. is  $-0.11 < S_{sk} < +0.72$ , and the range of spacing is estimated from their data to be  $40 < W/k_{rms} < 150$ . These also compare reasonably well with the ranges of the present study of  $-0.6 < S_{sk} < +0.42$ , and  $9 < W/k_{rms} < 90$ .

**Test Matrix.** Each roughness configuration was tested for three levels of free-stream turbulence intensity, which were about 0.5%, 2.5%, and 4.5% (Table 1). All measurements were performed for flow Reynolds numbers of 350,000 and 470,000, based on the plate length of  $L=1.22$  m and reference velocity values of about 4.5 and 6.0 m/s (measured at  $x=25$  mm,  $y=25$  mm). During the experiments, the flow Reynolds number was kept constant to within ±5%.

The pressure distribution imposed upon the test surface is similar to the suction-surface pressure distributions of typical turbine blades. Variations in the flow Reynolds number and surface roughness are expected to cause changes in the growth rate of the boundary layer on the test surface. For the same geometric setting,

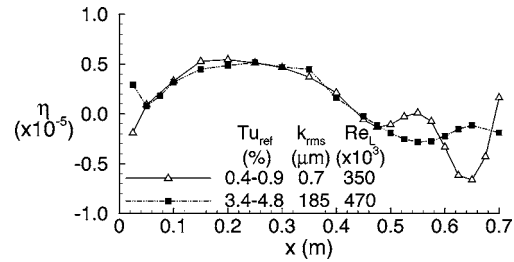


**Fig. 3 Streamwise distribution of the free-stream acceleration parameter**

this would affect the effective free-stream flow area and its streamwise variation in the test section, hence yield variations in the pressure distribution imposed upon the test-surface boundary layer. The extent of these variations is found to be small, as is evident from the trends in the acceleration parameter ( $\eta = (\nu/U_e^2) dU_e/dx$ ) up to about  $x=0.4$  m, shown in Fig. 3.

**Intermittency Distributions.** Streamwise and cross-stream intermittency distributions were determined by conditional sampling of the digitized velocity time traces obtained with the single-wire probe, using the algorithm described by Volino et al. [33]. In this algorithm, the first and second temporal derivatives of the fluctuating streamwise velocity ( $u'$ ) are computed. If either derivative exceeds a preset threshold value, the flow is declared to be turbulent at that instant, and the flow state parameter,  $\beta$ , is set to 1. If both derivatives are below their respective thresholds, the flow is declared to be nonturbulent, and  $\beta$  is set to zero. The resulting distribution of  $\beta$  is then low-pass filtered to reduce the number of artificial dropouts, and verified visually against the velocity traces.

**Wavelet Analysis.** To overcome certain limitations of Fourier analysis, the wavelet transform is used in a growing number of studies of intermittent flow phenomena (e.g., Schoefer et al. [34], Volino [35]). Summarizing briefly, wavelet analysis consists of the convolution of an input signal with a test function, or wavelet, which is chosen such that it approximates the input signal over a short duration. The convolution is repeated for different durations, or frequencies, of this test function, to produce a matrix of coefficients representing the level of correlation between the input signal and the wavelet at different frequencies and instances in time. These coefficients can then be selectively averaged in time to obtain a frequency spectrum of the signal during a particular event, or series of events.

In the present study, the input signals of the analysis are time traces of the hot-wire signal, and the test function is the Marr, or “Mexican hat,” wavelet. The wavelet transform is computed at 60 discrete frequencies, ranging from 4 Hz to 4 kHz, equally spaced on a logarithmic scale. The wavelet coefficients are averaged based on the temporal distribution of the flow state parameter,  $\beta$ , allowing the frequency content of the turbulent and nonturbulent phases of an intermittent signal to be examined separately. Hence, frequencies that may dominate during events of short duration, such as the passage of turbulent spots, are not concealed or attenuated by the time averaging inherent in the Fourier transform.

## Results and Discussion

**Streamwise Variation of Integral Boundary-Layer Parameters.** Streamwise distributions of boundary-layer displacement thickness ( $\delta^*$ ) and shape factor ( $H$ ) are presented in Figs. 4 and 5, respectively. In measurements over rough surfaces, an effective location for  $y=0$  needs to be established for use in the computation of  $\delta^*$  and  $H$ . For the present study,  $y=0$  is taken as the mean surface elevation,  $\mu$ , averaged over the test surface area. This choice is based on the qualitative argument that flow regions below this effective  $y=0$  location are likely to be of very low

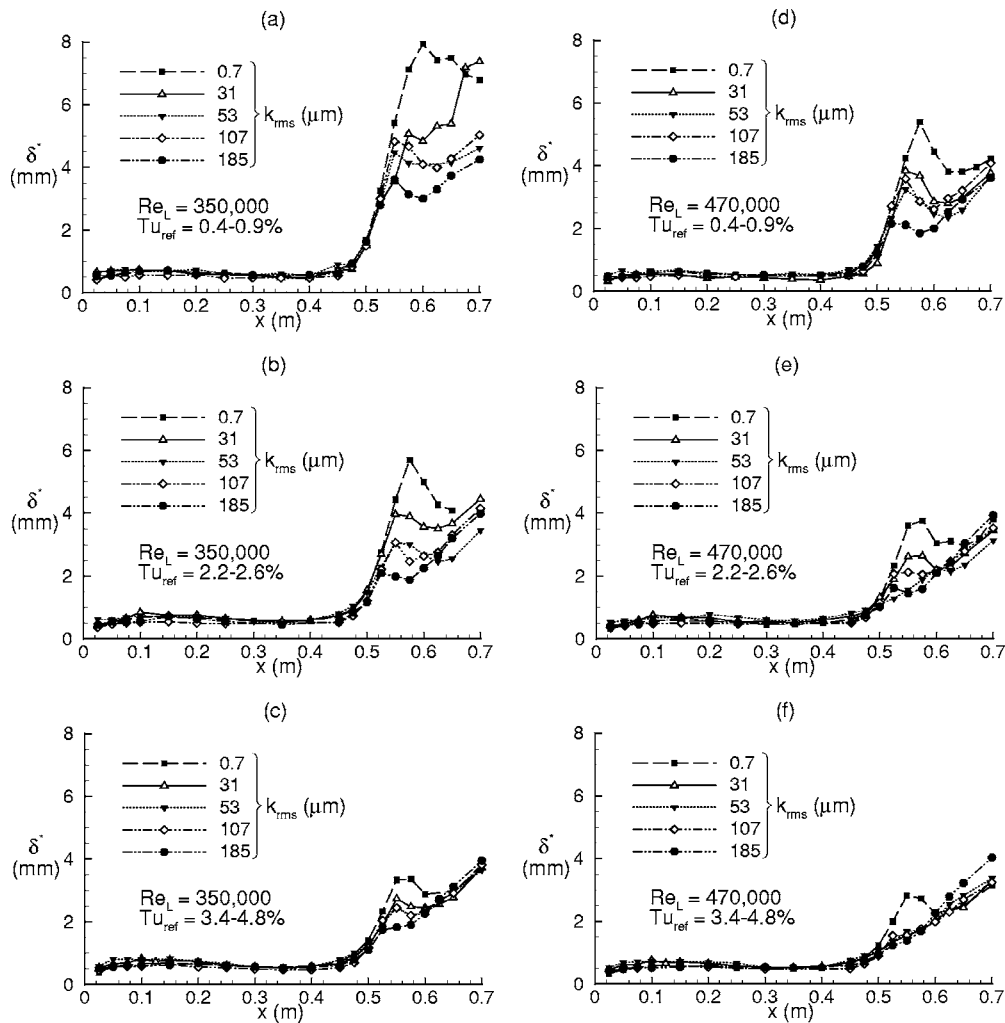


**Fig. 4 Distributions of boundary-layer displacement thickness. (a–c):  $Re_L=350,000$ ; (d–f):  $Re_L=470,000$**

momentum, hence are unlikely to participate significantly in the dynamics of the boundary layer. The uncertainty in the position of the hot-wire sensor at the beginning of each boundary-layer traverse with respect to the peaks of the roughness elements is  $\pm 0.15$  mm. The resulting uncertainty in the displacement thickness is thus conservatively estimated to be  $\pm 0.15$  mm. Uncertainty in probe positioning has a lesser effect on the calculation of momentum thickness ( $\pm 0.05$  mm) than on  $\delta^*$ . With the present values of  $\delta^*$  and  $\theta$  in the laminar boundary layer of approximately 0.5 and 0.25 mm, respectively, the resulting uncertainty in the shape factor is  $\pm 0.2$ . As the boundary layer thickness increases with streamwise distance, the relative uncertainties in  $\delta^*$  and  $\theta$  are diminished. The shape factors at the location of separation, and in the turbulent boundary layer, are considered accurate within  $\pm 0.1$  and  $\pm 0.05$ , respectively.

In the laminar boundary layer, from  $x=0$  to approximately  $x=0.5$  m, the distributions of  $\delta^*$  and  $H$  are seen to be substantially unaffected by the flow Reynolds number and surface roughness, within the noted uncertainties of  $\delta^*$  and  $H$ . Thus, the observed variations in the transition onset and completion locations are direct results of changes in the transition process as the flow Reynolds number, surface roughness and free-stream turbulence intensity are varied.

The rapid growth and subsequent decrease in  $\delta^*$  and  $H$  seen between about  $x=0.5$  m and  $x=0.6$  m in many of the test cases is indicative of the presence of a separation bubble. This trend is

most prominent in the distributions of  $H$  in Fig. 5. The peaks in these integral parameters near  $x=0.55$  m coincide with the locations of maximum separation-bubble thickness, with the magnitudes of these peaks giving an indication of the relative thickness of the bubble.

Through examination of the velocity profiles in the region of the separation bubble, the bubble thickness has been observed to reduce with increasing surface roughness. This trend is reflected in the peak values of the integral parameters in Figs. 4 and 5. In the case of the lowest turbulence level ( $Tu_{ref}=0.4-0.9\%$ ), the effect of an increase in the rms roughness height from 0.7 to 185  $\mu\text{m}$ , or roughly 20% of the boundary layer displacement thickness at separation, on the size of the separation bubble is seen to be similar to that of an increase in free-stream turbulence intensity from about 0.5–4.8% over the smooth plate. Surface roughness and free-stream turbulence are therefore equally important to the transition process for ranges of these parameters typical of low-pressure turbine blades.

The trends for  $Tu_{ref}=2.2-2.6\%$  in Figs. 4(e) and 5(e) suggest the presence of a small separation bubble for  $k_{rms}=185 \mu\text{m}$  and  $k_{rms}=107 \mu\text{m}$ , but not for  $k_{rms}=53 \mu\text{m}$ . The average spacing of the roughness elements is very similar for the surfaces with  $k_{rms}=107 \mu\text{m}$  ( $W=0.54$  mm) and  $k_{rms}=53 \mu\text{m}$  ( $W=0.49$  mm), while there is a bias towards protrusions for the latter surface as is evident from the value of the skewness parameter ( $S_{sk}=+0.42$  for

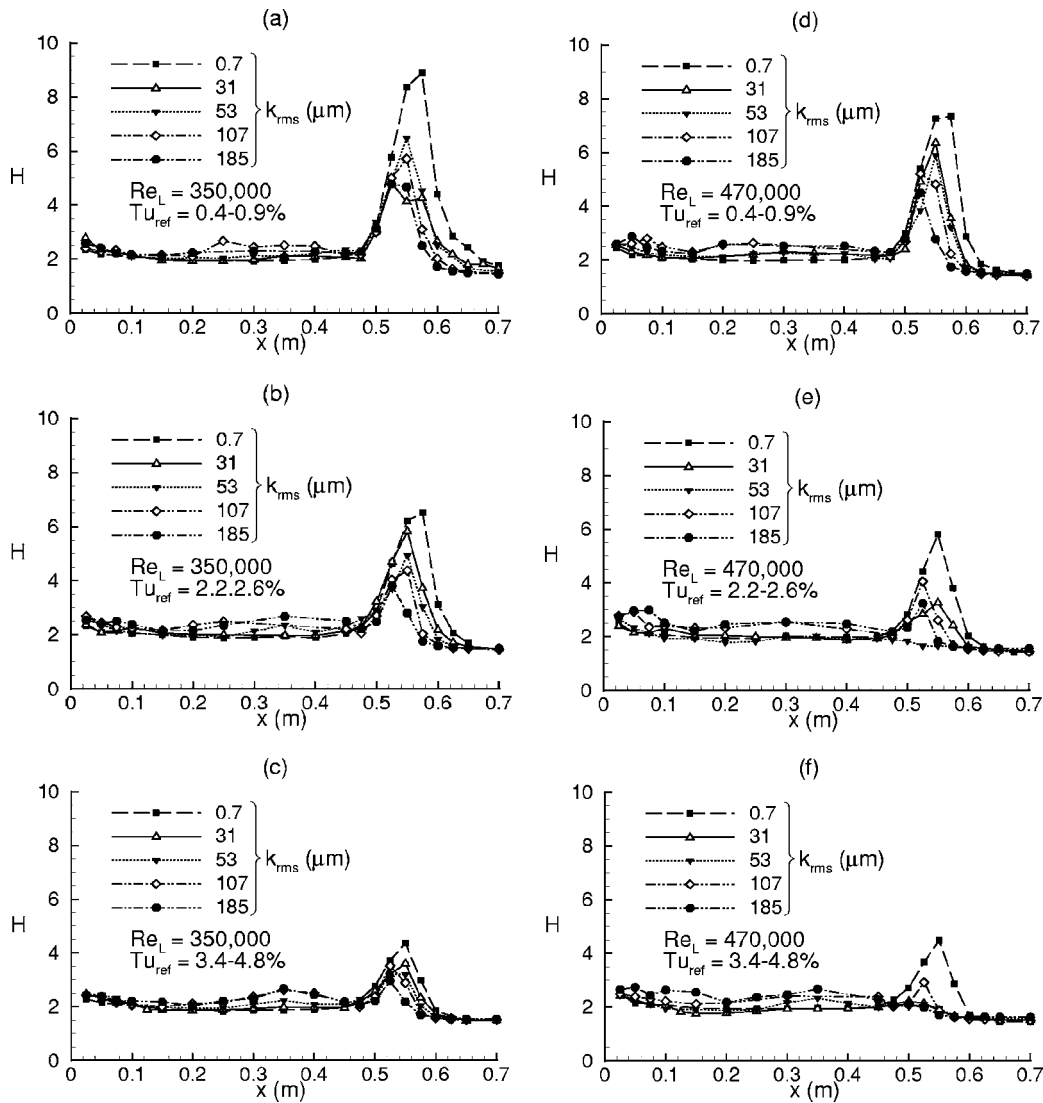


Fig. 5 Distributions of boundary-layer shape factor. (a–c):  $Re_L=350,000$ ; (d–f):  $Re_L=470,000$

$k_{rms}=53 \mu\text{m}$ , compared to  $-0.05$  for  $k_{rms}=107 \mu\text{m}$ ). Thus, surface roughness with a bias towards protrusions and a rms height of  $53 \mu\text{m}$  appears to have been more effective in suppressing the separation bubble than a rms roughness height of  $107 \mu\text{m}$  with a very small bias towards depressions.

**Transition Inception.** The location of transition inception,  $x_{ts}$ , identified as the first streamwise position at which turbulent spots are clearly identifiable by visual inspection of the velocity signals, is presented for  $Re_L=350,000$  and  $Re_L=470,000$  in Tables 3 and 4, respectively. In the test cases with a separation bubble, this location falls into the range where the boundary layer was traversed with high resolution in the streamwise direction, hence is

resolved within  $\pm 4 \text{ mm}$  in most cases. In instances of elevated free-stream turbulence and surface roughness, distinguishing turbulent spots from velocity fluctuations caused by the perturbations of free-stream turbulence eddies and roughness elements becomes more difficult, hence the uncertainty in  $x_{ts}$  is judged to be closer to  $\pm 6 \text{ mm}$ . In the test cases where the flow remains attached, the uncertainty in  $x_{ts}$  is dictated by the streamwise spacing of the measurements ( $25\text{--}50 \text{ mm}$ ).

At the lowest free-stream turbulence level, transition inception is noted to occur further upstream on each of the rough surfaces, compared to the smooth surface. However, within the uncertainty in  $x_{ts}$ , the transition inception locations are substantially the same

Table 3 Streamwise location of transition inception (mm)  $Re_L=350,000$

$k_{rms} \setminus Tu_{ref}$	0.4-0.9%	2.2-2.6%	3.4-4.8%
0.7 $\mu\text{m}$	567	569	537
31 $\mu\text{m}$	559	551	529
53 $\mu\text{m}$	561	541	523
107 $\mu\text{m}$	545	539	521*
185 $\mu\text{m}$	537	529	499*

\* test case with attached-flow transition

Table 4 Streamwise location of transition inception (mm)  $Re_L=470,000$

$k_{rms} \setminus Tu_{ref}$	0.4-0.9%	2.2-2.6%	3.4-4.8%
0.7 $\mu\text{m}$	567	558	539
31 $\mu\text{m}$	555	545	450*
53 $\mu\text{m}$	555	450*	450*
107 $\mu\text{m}$	535	525*	509*
185 $\mu\text{m}$	521	505*	450*

\* test case with attached-flow transition

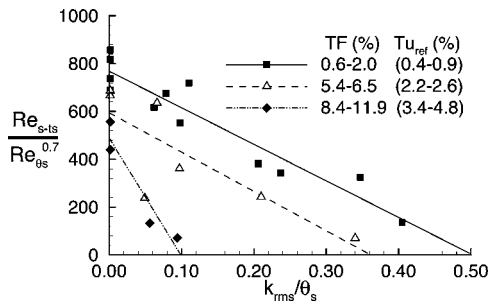


**Fig. 6 Sensitivity of the transition inception location in separation bubbles to surface roughness and free-stream turbulence**

for the surfaces with  $k_{rms}=31 \mu\text{m}$  and  $k_{rms}=53 \mu\text{m}$  at both  $\text{Re}_L=350,000$  ( $x_{ts}=559 \text{ mm}$  for  $k_{rms}=31 \mu\text{m}$  versus  $561 \text{ mm}$  for  $k_{rms}=53 \mu\text{m}$ ) and  $\text{Re}_L=470,000$  ( $x_{ts}=555 \text{ mm}$  for both surfaces). This similarity in the value of  $x_{ts}$  despite the difference of approximately 70% in the rms roughness height suggests that some aspect of the roughness geometry other than  $k_{rms}$  is also influencing the transition process. Evidence of this is also present in the streamwise distributions of the boundary layer shape factor  $H$  given in Figs. 5(a) and 5(d). The relative magnitudes of the peaks in  $H$  for the two surfaces in question are inconsistent with the remaining surfaces if they are characterized based on  $k_{rms}$  alone. The roughness geometries of the two surfaces in question differ most notably in the average spacing of the roughness elements, which are much larger for the surface with  $k_{rms}=31 \mu\text{m}$  ( $W=2.72 \text{ mm}$ ) than for the surface with  $k_{rms}=53 \mu\text{m}$  ( $W=0.49 \text{ mm}$ ). It appears that the larger spacing of the roughness elements of the  $k_{rms}=31 \mu\text{m}$  surface are more effective at initiating the transition process than the more densely packed elements of the  $k_{rms}=53 \mu\text{m}$  surface. This is not particularly surprising, since with increased density of the roughness elements, the wake region and effective frontal area of each element are reduced. Of course, this trend would eventually reverse as the density of roughness elements is reduced further, since in the limit a smooth surface condition would be reached.

The tabulated data also demonstrate that the transition inception location in the separation bubble remains sensitive to surface roughness as the free-stream turbulence intensity is increased. This observation is consistent for all turbulence and roughness levels tested, as illustrated in Fig. 6. From the trends in this figure, the sensitivity of the transition inception location to roughness height is noted to be essentially constant up to the intermediate turbulence level of  $Tu_{ref}=2.2\text{--}2.6\%$ , but this sensitivity is notably increased for  $Tu_{ref}=3.4\text{--}4.8\%$ . This trend is intuitive, since with increased free-stream turbulence, the transition inception location moves upstream in the separated shear layer, and therefore closer to the surface. Thus, with high free-stream turbulence, the separated shear layer is expected to respond more readily to changes in the surface conditions.

In the attached-flow-transition cases, because of their limited number and the coarser resolution of the location of transition inception, the variation of  $x_{ts}$  with surface roughness and free-stream turbulence cannot be identified with the same precision and generality as for the separation-bubble cases. Nonetheless, transition inception is noted to occur further upstream for the  $k_{rms}=53 \mu\text{m}$  surface ( $x_{ts}=450 \text{ mm}$ ), compared to the  $k_{rms}=107 \mu\text{m}$  and  $k_{rms}=185 \mu\text{m}$  surfaces at  $Tu_{ref}=2.2\text{--}2.6\%$ ,  $\text{Re}_L=470,000$ , ( $x_{ts}=525$  and  $505 \text{ mm}$ ) and also compared to the  $k_{rms}=107 \mu\text{m}$  surface at  $Tu_{ref}=3.4\text{--}4.8\%$ ,  $\text{Re}_L=470,000$  ( $x_{ts}=509 \text{ mm}$ ). This result is consistent with the observations in some of the other test cases with separation bubbles involving these

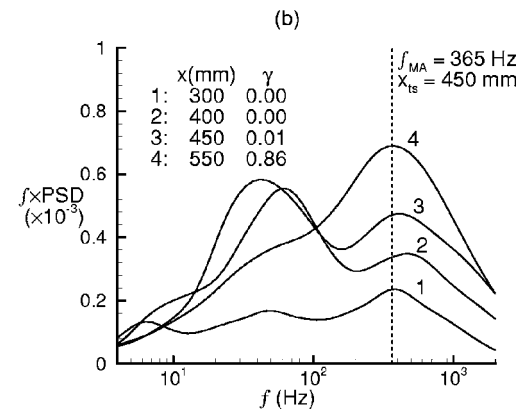
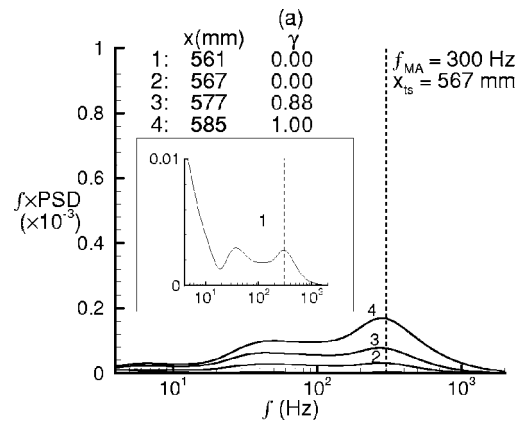


**Fig. 7 Wavelet-averaged power spectra of  $u'/U_{ref}$ . (a)  $Tu_{ref}=0.4\%$ ;  $k_{rms}=0.7 \mu\text{m}$ ;  $\text{Re}_L=470,000$ . (b)  $Tu_{ref}=4.5\%$ ;  $k_{rms}=185 \mu\text{m}$ ;  $\text{Re}_L=470,000$**

surfaces, as was discussed in the previous section, and provides further support for the relevance of the skewness of the roughness distribution to transition onset.

**Spectral Analysis.** The noted trends in the location of transition inception are the result of surface roughness and free-stream turbulence affecting the initial amplitude and/or streamwise rate of growth of the instability waves in the boundary layer. Wavelet-averaged power spectra of  $u'/U_{ref}$  in the laminar boundary layer and at various streamwise locations within the transition region, are shown in Fig. 7 for one low disturbance case ( $Tu_{ref}=0.4\%$  and  $k_{rms}=0.7 \mu\text{m}$ ) in which the transition takes place in a separation bubble, and one case with high disturbance levels ( $Tu_{ref}=4.5\%$  and  $k_{rms}=185 \mu\text{m}$ ) with attached-flow transition. In the transitional boundary layer, the wavelet spectra are averaged during the times at which turbulent spots are present in the flow. Distinct peaks are observed in the spectra of both test cases. In the case of elevated free-stream turbulence and surface roughness, the peak in the  $u'/U_{ref}$  spectrum is clearly visible in the laminar boundary layer well upstream of the transition inception location [labeled “1” in Fig. 7(b)]. This peak is much fainter, however, in the case with low free-stream turbulence and surface roughness; it is only visible shortly prior to transition inception [inset in Fig. 7(a)], and is typically not observed in the attached laminar boundary layer. In both test cases, the velocity fluctuations near these frequencies increase in amplitude in the transition region (labeled “2” and “3”) through to transition completion (labeled “4”).

While it may be suggested that the peaks in these spectra for the separation-bubble case are caused by periodic ejection of fluid from the bubble, the fact that they have also been observed in each of the attached-flow transition test cases at similar frequencies suggests that they more likely represent pretransitional Tollmien–Schlichting (TS) instability waves. The frequencies of

the peaks in the spectra shown in Fig. 7 are also in good agreement with the frequency of maximum amplification rate of TS waves as predicted using the correlation of Walker [36] [Eq. (4)], which is based on attached-flow transition data published by Obremski et al. [37], and is shown by a dashed vertical line in Fig. 7.

$$f_{MA} = \frac{3.2U_e^2}{2\pi\nu Re_{\delta^*}^{3/2}} \quad (4)$$

In cases of attached flow, the Reynolds number based on displacement thickness,  $Re_{\delta^*}$ , appearing in Eq. (4) is evaluated at the nearest measurement station upstream of the transition inception location. Since this expression was developed from an analysis of attached boundary layers, in cases of separation-bubble transition,  $Re_{\delta^*}$  is evaluated just prior to the separation point. The agreement between the observed peaks in the wavelet spectra and the predictions of Eq. (4) are similar in cases of attached-flow and separation-bubble transition. In the majority of experiments included in the current study (25 out of the 30 test cases), the agreement is also within the level of scatter noted by Walker while developing this correlation ( $\pm 30\%$ ). This suggests the dominant mechanism leading to transition in the separation bubbles of the current study to be the growth of Tollmien-Schlichting waves, as in attached-flow transition. Additionally, the good agreement between the measured and predicted values of  $f_{MA}$  for  $k_{rms} = 0.7 \mu\text{m}$  and  $k_{rms} = 185 \mu\text{m}$ , combined with the similarity of  $Re_{\delta^*}$  just upstream of separation in these two cases, indicates that  $f_{MA}$  is insensitive to the range of surface roughness considered in this study.

**Transition Length.** Streamwise distributions of intermittency are presented for the separation-bubble and attached-flow test cases in Figs. 8 and 9, respectively. For the separation-bubble test cases, a notable effect of surface roughness on the transition length is not evident in the majority of test cases, within the uncertainty of intermittency values extracted from the velocity-time traces. This suggests that the rate of production of turbulent spots, and their subsequent lateral and streamwise spreading rates, are not affected by surface roughness. The lack of change in the spot propagation characteristics with surface roughness in these test cases is consistent with the portion of the free shear layer in which transition takes place being located above the peaks of the roughness elements.

Comparison of parts (a), (b), and (c) of Fig. 8 reveals an effect of turbulence intensity on the rate of transition in the separation bubble, with increased turbulence levels resulting in a slightly longer transition length. This somewhat counterintuitive trend is consistent with the observed variations in spot production rates with free-stream turbulence in attached boundary layers (e.g., Solomon et al. [27]). It was recently shown by the present authors that the production rate of turbulent spots increases with the boundary layer shape factor at the transition inception location,  $H_{ts}$  [38]. Buffeting of the boundary layer by the free-stream turbulence results in increased momentum exchange near the surface, which is observed as a decrease in the shape factor in the laminar boundary layer [38]. This in turn decreases the turbulent spot production rate. Nonetheless, the variation in transition length with free-stream turbulence observed in the current separation-bubble test cases is too small to be captured within the precision of current prediction models.

As was noted earlier, a very small separation bubble appears to be present in both the  $k_{rms} = 107 \mu\text{m}$  and  $k_{rms} = 185 \mu\text{m}$  test cases shown in Fig. 9(a), although these test cases have been categorized as attached-flow transition in Table 4. It is noted that the transition rate in these two instances is similar to those of the separation-bubble test cases at the same turbulence level and Reynolds number, shown in the bottom half of Fig. 8(b). Thus, while the separation and reattachment locations in these two cases cannot be reliably identified with the present spatial resolution of the

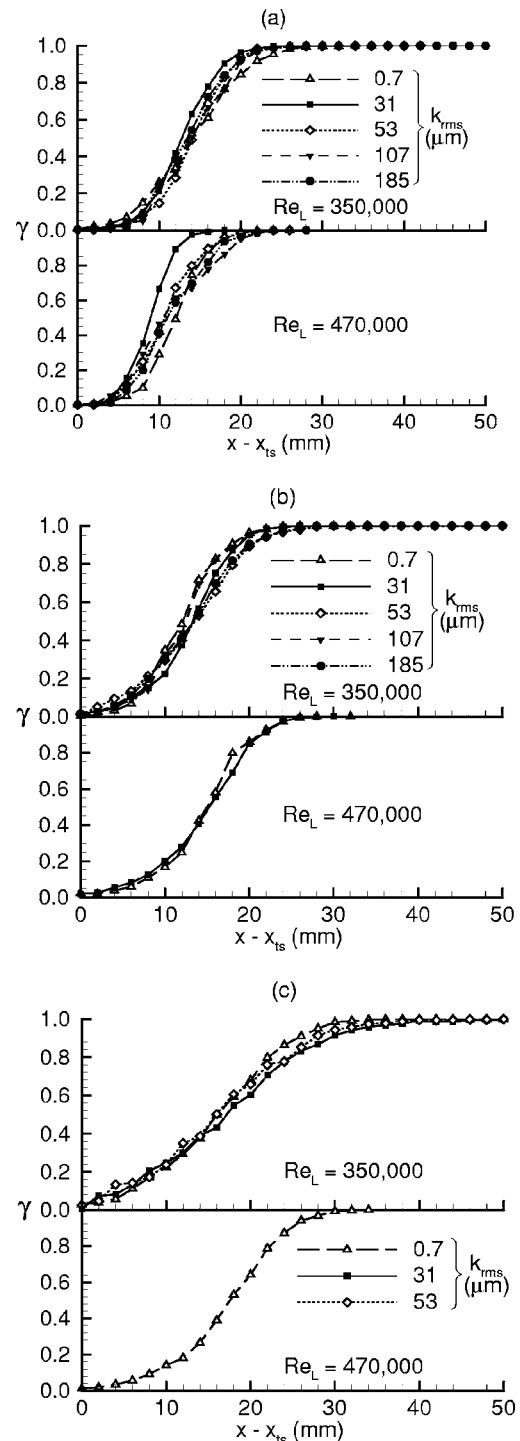


**Fig. 8 Streamwise distributions of intermittency—separation-bubble cases (a)  $Tu_{ref} = 0.4-0.9\%$ ; (b)  $Tu_{ref} = 2.2-2.6\%$ ; (c)  $Tu_{ref} = 3.4-4.8\%$**

measurements, clearly the presence of even a very short and shallow separated region (relative to the local thickness of the boundary layer) is able to affect the transition rate. The different transition rates for the test cases shown in Fig. 9(a) are consistent with the variations in  $H_{ts}$  between these three test cases ( $H_{ts} = 1.9, 4.0,$  and  $2.5$  for the  $k_{rms} = 53, 107,$  and  $185 \mu\text{m}$  surfaces in Fig. 9(a), respectively).

For the attached-flow transition cases in Fig. 9, the rates of transition are observed to be lower for the  $k_{rms} = 31 \mu\text{m}$  and  $k_{rms} = 53 \mu\text{m}$  surfaces than for the surfaces with  $k_{rms} = 107 \mu\text{m}$  and

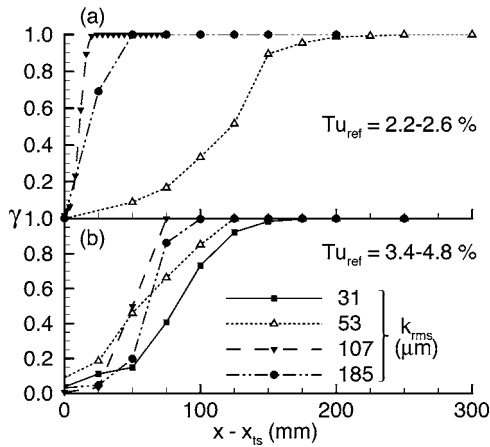


**Fig. 9 Streamwise distributions of intermittency—attached-flow cases ( $Re_L=470,000$ ). (a)  $Tu_{ref}=2.2-2.6\%$ ; (b)  $Tu_{ref}=3.4-4.8\%$**

$k_{rms}=185 \mu\text{m}$ . At the lower turbulence intensity [ $Tu_{ref}=2.2-2.6\%$  in Fig. 9(a)], this is at least partly due to the differences in  $H_{ts}$ , since the locations of transition inception are different for these surfaces. However, the values of  $H_{ts}$  are similar at  $Tu_{ref}=3.4-4.8\%$  for the  $k_{rms}=31 \mu\text{m}$ ,  $k_{rms}=53 \mu\text{m}$ , and  $k_{rms}=185 \mu\text{m}$  surfaces in Fig. 9(b) ( $H_{ts}=2.0$ ,  $2.0$ , and  $2.1$ , respectively). Thus, an increase in rms roughness height from  $53$  to  $185 \mu\text{m}$  appears to affect the rate of spot production, the spot spreading rate, or both. Based on comparisons with the measurements of Chong and Zhong [39], the roughness elements of the surface with  $k_{rms}=185 \mu\text{m}$  are expected to protrude into the regions of the boundary layer that are most active in turbulence production, at least during the earlier phases of the transition process. It is therefore plausible that the roughness elements directly affect the rate of production or the structure of turbulent spots. This hypothesis is supported by the visible differences in the cross-stream intermittency distributions between test cases. This is shown in Fig. 10 for the  $k_{rms}=53 \mu\text{m}$  and  $k_{rms}=185 \mu\text{m}$  surfaces, at two stages in the transition process where the peak intermittencies are similar ( $\gamma_{max} \approx 0.2$ , and  $\gamma_{max} \approx 0.8$ ). A more concentrated cross-stream intermittency profile for the  $k_{rms}=185 \mu\text{m}$  surface is evident, particularly at the earlier stage of transition ( $\gamma_{max} \approx 0.2$ ).

## Conclusions

This paper has documented the results of an experimental study on the effects of uniformly distributed surface roughness on boundary-layer transition under low and elevated free-stream turbulence conditions, for a range of roughness conditions typical of the suction side of low-pressure turbine blades in-service gas turbines. The following are the main findings of the study:

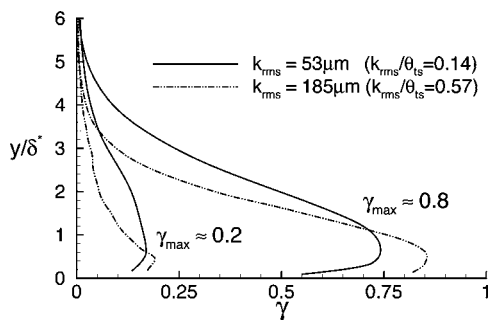


**Fig. 10 Cross-stream distributions of intermittency for  $k_{rms}=53 \mu\text{m}$  and  $k_{rms}=185 \mu\text{m}$  ( $Tu_{ref}=3.4-4.8\%$ ;  $Re_L=470,000$ )**

- For the conditions typical of in-service gas-turbine blades, surface roughness and free-stream turbulence are found to have comparable effects on the location of transition inception in separation bubbles.
- The root-mean-square height of the roughness elements, their spacing, and the skewness (bias towards depression or protrusion roughness) of the roughness distribution are shown to be relevant in quantifying the effects of roughness on the transition process.
- The rate of upstream movement of the transition inception location in the separation bubble with increasing surface roughness is found to be sensitive to the level of free-stream turbulence, for part of the tested turbulence range.
- For most of the range of surface roughness heights considered, the roughness elements remained below the transitioning shear layer of the bubble, resulting in absence of a direct effect of roughness on the rate of transition. Free-stream turbulence is observed to yield a slight decrease in the rate of transition.
- The frequency of maximum amplification rate of Tollmien-Schlichting waves is shown to closely correlate with  $Re_{\delta^*}$  just upstream of the point of separation, and the correlation is found to be the same as that for attached-flow transition, with  $Re_{\delta^*}$  evaluated locally.

## Acknowledgments

The authors gratefully acknowledge the financial support of Pratt & Whitney Canada in this project.

## Nomenclature

- $A$  = surface area
- $f$  = frequency (Hz)
- $H$  = boundary layer shape factor
- $k_{rms}$  = rms roughness height [Eq. (1)]
- $L$  = length of the test plate = 1.220 m
- $N$  = number of surface measurement samples
- $n$  = number of times the roughness distribution crosses the mean elevation ( $\mu$ )
- PSD = power spectral density of  $u'/U_{ref}$
- $Re_L$  = reference Reynolds number based on  $L$  and  $U_{ref}$
- $Re_{s-ts}$  = Reynolds number based on  $(x_{ts}-x_s)$  and  $U_{es}$
- $Re_{\theta}$  = Reynolds number based on  $\theta$  and  $U_e$
- $S_{sk}$  = skewness of the roughness height distribution [Eq. (3)]
- $TF$  = Taylor's turbulence factor =  $Tu_{ref}(L/\lambda_s)^{0.2}$
- $Tu_{ref}$  = reference turbulence intensity (%), measured 10 mm upstream of the test surface leading edge
- $t$  = time (s)
- $U_e$  = local free-stream velocity
- $U_{ref}$  = reference streamwise velocity measured at  $x=25$  mm,  $y=25$  mm,  $z=382$  mm
- $u'$  = streamwise component of fluctuating velocity (m/s)
- $W$  = average spacing of roughness protrusions [Eq. (2)]
- $x, y, z$  = streamwise, normal to the test surface, and spanwise spatial coordinates
- $\beta$  = flow state parameter
- $\delta^*$  = boundary layer displacement thickness
- $\Delta x$  = surface scan lateral resolution
- $\gamma$  = boundary layer intermittency
- $\eta$  = acceleration parameter =  $(\nu/Ue^2)dU_e/dx$
- $\lambda_s$  = integral length scale of free-stream turbulence

$\mu$  = mean elevation of the roughness distribution  
 $\theta$  = boundary layer momentum thickness  
 $\nu$  = kinematic viscosity

### Subscripts

MA = maximum amplification rate of TS waves  
s = separation  
ts = start of transition

### References

- [1] Bons, J. P., McClain, S. T., Taylor, R. P., and Rivir, R. B., 2001, "The Many Faces of Turbine Surface Roughness," *J. Turbomach.*, **123**, pp. 739–748.
- [2] Taylor, R. P., 1990, "Surface Roughness Measurements on Gas Turbine Blades," *J. Turbomach.*, **112**, pp. 175–180.
- [3] Kerho, M. F., and Bragg, M. B., 1997, "Airfoil Boundary-Layer Development and Transition with Large Leading-Edge Roughness," *AIAA J.*, **35**, pp. 75–84.
- [4] Gibbings, J. C., Goksel, O. T., and Hall, D. J., 1986, "The Influence of Roughness Trips Upon Boundary-Layer Transition—Part 1 Characteristics of Wire Trips," *Aeronaut. J.*, **90**, pp. 289–301.
- [5] Gibbings, J. C., Goksel, O. T., and Hall, D. J., 1986, "The Influence of Roughness Trips Upon Boundary-Layer Transition—Part 2 Characteristics of Single Spherical Trips," *Aeronaut. J.*, **90**, pp. 357–67.
- [6] Gibbings, J. C., Goksel, O. T., and Hall, D. J., 1986, "The Influence of Roughness Trips Upon Boundary-Layer Transition—Part 3 Characteristics of Rows of Spherical Transition Strips," *Aeronaut. J.*, **90**, pp. 393–398.
- [7] Würz, W., Herr, S., Wörner, A., Rist, U., Wagner, S., and Kachanov, Y. S., 2003, "Three-Dimensional Acoustic-Roughness Receptivity of a Boundary Layer on an Airfoil: Experiment and Direct Numerical Simulations," *J. Fluid Mech.*, **478**, pp. 135–63.
- [8] Kachanov, Y. S., 2000, "Three-Dimensional Receptivity of Boundary Layers," *Eur. J. Mech. B/Fluids*, **19**, pp. 723–44.
- [9] Lang, M., Rist, U., and Wagner, S., 2004, "Investigations on Controlled Transition Development in a Laminar Separation Bubble by Means of LDA and PIV," *Exp. Fluids*, **36**, pp. 43–52.
- [10] Cummings, M. J., and Bragg, M. B., 1996, "Boundary-Layer Transition Due to Isolated Three-Dimensional Roughness on Airfoil Leading Edge," *AIAA J.*, **34**, pp. 1949–52.
- [11] Pinson, M. W., and Wang, T., 1997, "Effects of Leading-Edge Roughness on Fluid Flow and Heat Transfer in the Transitional Boundary Layer Over a Flat Plate," *Int. J. Heat Mass Transfer*, **40**, pp. 2813–23.
- [12] Wang, T., and Rice, M. C., 2003, "Effect of Elevated Free-Stream Turbulence on Transitional Heat Transfer over Dual-Scaled Rough Surfaces," *GT-2003-38835, Proc. ASME Turbo Expo*, Atlanta, GA.
- [13] Mayle, R. E., 1991, "The Role of Laminar-Turbulent Transition in Gas Turbine Engines," *J. Turbomach.*, **113**, pp. 509–537.
- [14] Gostelow, J. P., and Walker, G. J., 1991, "Similarity Behavior in Transitional Boundary Layers Over a Range of Adverse Pressure Gradients and Turbulence Levels," *J. Turbomach.*, **113**, pp. 617–625.
- [15] Hall, D. J., and Gibbings, J. G., 1972, "Influence of Stream Turbulence and Pressure Gradient Upon Boundary Layer Transition," *J. Mech. Eng. Sci.*, **14**, pp. 134–146.
- [16] Abu-Ghannam, B. J., and Shaw, R., 1980, "Natural Transition of Boundary Layers—The Effects of Turbulence, Pressure Gradient, and Flow History," *J. Mech. Eng. Sci.*, **22**, pp. 213–228.
- [17] Johnson, M. W., 1994, "A Bypass Transition Model for Boundary Layers," *J. Turbomach.*, **116**, pp. 759–764.
- [18] Schobeiri, M. T., and Radke, R. E., 1994, "Effects of Periodic-Unsteady Wake Flow and Pressure Gradient on Boundary Layer Transition along the Concave Surface of a Curved Plate," *94-GT-327, Proc. ASME Turbo Expo*, The Hague, NL.
- [19] Addison, J. S., and Hodson, H. P., 1990, "Unsteady Transition in an Axial-Flow Turbine: Part 1—Measurements on the Turbine Rotor," *J. Turbomach.*, **112**, pp. 206–214.
- [20] Dong, Y., and Cumpsty, N. A., 1990, "Compressor Blade Boundary Layers: Part 2—Measurements With Incident Wakes," *J. Turbomach.*, **112**, pp. 231–240.
- [21] Sharma, O. P., Renaud, E., Butler, T. L., Milsaps, K. Jr., Dring, R. P., and Joslyn, H. D., 1988, "Rotor-Stator Interaction in Multi-Stage Axial-Flow Turbines," *AIAA-88-3013*.
- [22] Yaras, M. I., 2002, "Measurements of the Effects of Freestream Turbulence on Separation-Bubble Transition," *GT-2002-30232, Proc. ASME Turbo Expo*, Amsterdam, NL.
- [23] Roberts, S. K., and Yaras, M. I., 2003, "Measurements and Prediction of Free-Stream Turbulence Effects on Attached-Flow Boundary-layer Transition," *GT-2003-38261, Proc. ASME Turbo Expo*, Atlanta, GA.
- [24] Volino, R. J., and Simon, T. W., 1997, "Boundary Layer Transition Under High Free-Stream Turbulence and Strong Acceleration Conditions: Part 1—Mean Flow Results," *J. Heat Transfer*, **119**, p. 420.
- [25] Johnson, M. W., 1998, "Turbulent Spot Characteristics in Boundary Layers Subjected to Streamwise Pressure Gradient," *ASME-98-GT-124, Proc. ASME Turbo Expo*, Stockholm, Sweden.
- [26] Narasimha, R., 1985, "The Laminar-Turbulent Transition Zone in the Boundary Layer," *Prog. Aerosp. Sci.*, **22**, pp. 29–80.
- [27] Solomon, W. G., Walker, G. J., and Gostelow, J. P., 1996, "Transition Length Prediction for Flows With Rapidly Changing Pressure Gradients," *J. Turbomach.*, **118**, pp. 744–751.
- [28] Hatman, A., and Wang, T., 1999, "A Prediction Model for Separated-Flow Transition," *J. Turbomach.*, **121**, pp. 594–602.
- [29] Horton, H. P., 1968, "A Semi-Empirical Theory for the Growth and Bursting of Laminar Separation Bubbles," *ARC CP-1073*.
- [30] Lou, W., and Hourmouziadis, J., 2000, "Separation Bubbles Under Steady and Periodic-Unsteady Main Flow Conditions," *2000-GT-0270, Proc. ASME Turbo Expo*, Munich, Germany.
- [31] Volino, R. J., and Hultgren, L. S., 2000, "Measurements in Separated and Transitional Boundary-Layers Under Low Pressure Turbine Airfoil Conditions," *J. Turbomach.*, **123**, pp. 189–197.
- [32] Taylor, G. I., 1938, "Some Recent Developments in the Study of Turbulence," *Proc. Fifth Int. Cong. Appl. Mech.*
- [33] Volino, R. J., Schultz, M. P., and Pratt, C. M., 2001, "Conditional Sampling in a Transitional Boundary-Layer Under High Free-Stream Turbulence Conditions," *J. Fluids Eng.*, **125**, pp. 28–37.
- [34] Schobeiri, M. T., Read, K., and Lewalle, J., 1995, "Effect of Unsteady Wake Passing Frequency on Boundary Layer Transition, Experimental Investigation and Wavelet Analysis," *J. Fluids Eng.*, **125**, pp. 251–266.
- [35] Volino, R. J., 2002, "An Investigation of the Scales in Transitional Boundary Layers Under High Free-Stream Turbulence Conditions," *GT-2002-30233, Proc. ASME Turbo Expo*, Amsterdam, NL.
- [36] Walker, G. J., 1989, "Transitional Flow on Axial Compressor Blading," *AIAA J.*, **27**, pp. 595–602.
- [37] Obremski, H. J., Morkovin, M. V., and Landahl, M., 1969, "A Portfolio of Stability Characteristics of Incompressible Boundary Layers," *AGARDograph* 134.
- [38] Roberts, S. K., and Yaras, M. I., 2005, "Modeling Transition in Separated and Attached Boundary Layers," *ASME J. Turbomach.*, **127**, pp. 402–411.
- [39] Chong, T. P., and Zhong, S., 2003, "On the Three-Dimensional Structure of Turbulent Spots," *GT-2003-38435, Proc. ASME Turbo Expo*, Atlanta, GA.

# Unsteady Numerical Simulations of Turbulence and Coherent Structures in Axial Flow Near a Narrow Gap

D. Chang  
Doctoral Student

S. Tavoularis<sup>1</sup>  
Professor  
e-mail: tav@eng.uottawa.ca

Department of Mechanical Engineering,  
University of Ottawa,  
Ottawa, Ontario K1N 6N5, Canada

*Axial flow in a rectangular channel containing a cylindrical rod has been simulated numerically by solving the unsteady Reynolds-averaged Navier–Stokes equations with a Reynolds stress model. The time- and phase-averaged mean velocity and turbulent stresses are in fair agreement with previous experimental results in a similar configuration. The study further documents the formation of quasi-periodic coherent structures in the form of vortex pairs and the important role that they play in transporting fluid across the gap region. [DOI: 10.1115/1.1900140]*

## 1 Introduction

Axial flows in complex channels with narrow gap regions can be found in a wide variety of industrial, biological, and environmental systems. Common examples are rod bundle flows in nuclear reactors, annular flows in heat exchangers, blood flows in arteries containing catheters or stents, and inundated river flows in channels composed of a deep main channel and shallow flood plains. The turbulence characteristics in such flows are very different from those in pipe flows and cannot be predicted by conventional turbulence models, such as gradient transport models. Of particular interest to the present research is the phenomenon of strong momentum, heat and mass transfer across narrow gaps formed between fuel-containing rods or between such a rod and the surrounding pressure tube in nuclear reactor cores. It has been long established that flow in the gap region is dominated by quasi-periodic, large-scale, flow pulsations across the gap [1]. The origin of these pulsations has generated considerable debate among researchers. Early speculations attributing them to secondary flows generated by Reynolds stress anisotropy were contradicted by direct measurements [2–7]. It is now accepted that the flow pulsations near the gap regions are associated with coherent structures.

Among the documented effects of cross-gap flow pulsations is a reduction in the azimuthal variation of both the skin friction coefficient and the heat transfer coefficient on the rod surface [6,7]. Moreover, flow pulsations generate large axial and azimuthal turbulence intensities as well as large turbulent shear stress in the gap region [5,7–12]. The characteristic frequency of these pulsations was found to depend on the gap size and the Reynolds number [8,9,13–16]. The most detailed relevant experimental studies are by Guellouz and Tavoularis (GT) [12], hereafter to be referred to as GT, who identified the formation of large-scale coherent structures in the gap region between a cylindrical rod and the wall of a rectangular channel using conditional sampling and phase averaging. GT concluded that the coherent structures formed a street of pairs of counter-rotating vortices with axes alternating on either side of the gap.

Most previous numerical simulations of turbulent flows in rod-bundle-like geometries have utilized conventional turbulence models and have presented their results as time-averaged statistics. Such simulations have generally shown a very limited agree-

ment with experiments and have relied on empirical adjustments for their improvement, as, for example, the use of nonisotropic eddy viscosities whose values were adjusted to experimental ones. Early attempts to simulate rod bundle flows include the work of Meyder [17], who employed an anisotropic eddy diffusivity, and the work of Seale [18], who also examined the effect of secondary flows. Even relatively recent simulations have generally used conventional turbulence models to solve the Reynolds-averaged Navier–Stokes equations (RANS), although some preliminary large eddy simulations (LES) have also been attempted. Wu [19] conducted a numerical simulation of flow in a rod bundle contained in a trapezoidal channel employing an algebraic stress model along with the  $k-\varepsilon$  turbulence model. He found that the predicted variations of the axial mean velocity and the normalized turbulent kinetic energy were in good agreement with measurements by Wu and Trupp [9], but acknowledged the limited capabilities of conventional gradient-type turbulence models. To overcome that limitation, he introduced an anisotropy factor based on the experimental results. Biemüller et al. [20] performed a large eddy simulation of flow in a channel consisting of two rectangular subchannels connected by a narrow passage. Their predictions of turbulence intensities were in qualitative agreement with their experiment and they noted the presence of a pair of counter-rotating vortices rotating in opposite directions, which were compatible with a model proposed by Meyer and Rehme [16]. Lee and Jang [21] performed numerical simulations of rod bundle flows using a nonlinear  $k-\varepsilon$  model and were unable to predict large-scale flow pulsation across the gap, in contrast with the experimental results of Hooper [5].

The present work is focused on the application of the unsteady RANS (URANS) approach to simulate rod-bundle-like flows by capturing coherent structure effects. For simplicity, we use the same idealized geometry as that in the GT experiments. Some preliminary results in the same geometry have been presented by Tavoularis et al. [22] and Chang and Tavoularis [23]. A thorough understanding of these coherent structures and their role in inter-subchannel mixing would be of benefit to safety analyses of nuclear reactors and to the design of future, improved rod bundles. An essential objective of the present simulations is to accurately predict the unsteady evolution of the large-scale structures and to provide a thorough understanding of the influence of coherent structures on flow characteristics in a rod-bundle-like configuration, which may lead to improved modeling of such processes.

<sup>1</sup>Corresponding author.

Contributed by the Fluids Engineering Division for publication in the JOURNAL OF FLUIDS ENGINEERING. Manuscript received by the Fluids Engineering Division November 11, 2004; revised February 3, 2005. Associate Editor: Ugo Piomelli.



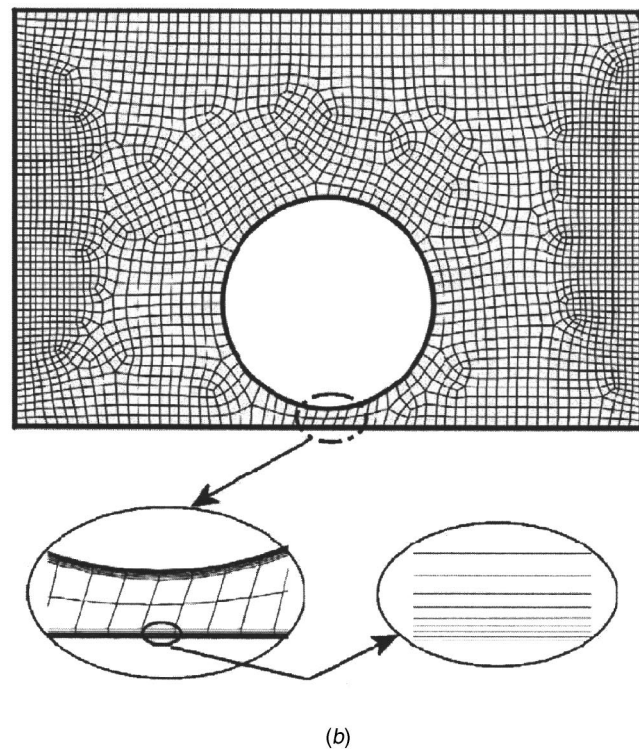
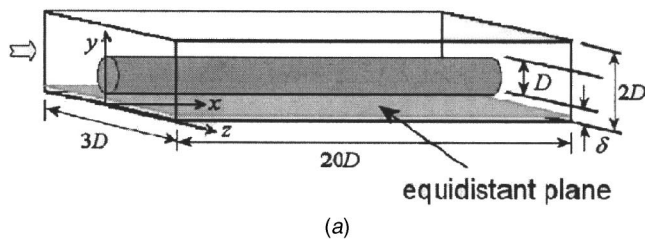


Fig. 1 Sketches of (a) the computational geometry and (b) the computational mesh on the  $y$ - $z$  plane, also showing details in the gap region and near the bottom wall

## 2 Computational Procedures and Conditions

The commercial software package FLUENT, version 6.1.22 based on the finite volume method, has been used for these simulations. Computations were conducted in the SunFire cluster at HPCVL (High Performance Computing Virtual Laboratory, a consortium of four Universities in Eastern Ontario), configured with  $24 \times 1.05$  GHz UltraSPARC-III processors and 96 Gb of RAM memory. The SunGrid Engine in the SunFire cluster was used with 10 nodes.

The computational domain consisted of a rectangular channel containing a rod with a diameter  $D$ , as shown in Fig. 1. The height, width and length of the computational section were, re-

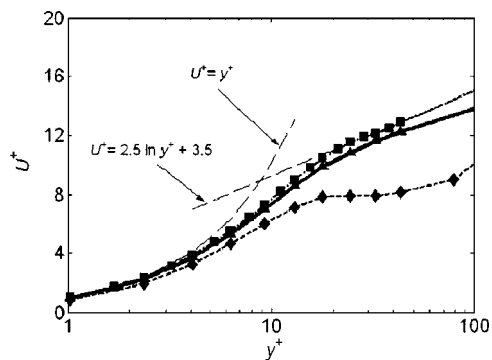


Fig. 2 Variation of the time-averaged streamwise velocity at  $z/D=1$ ,  $x/D=10$ , near the bottom wall (■: case 1; - : case 2, ♦: case 3, ▲: case 4)

spectively,  $2D$ ,  $3D$ , and  $L=20D$ . The gap between the rod wall and the adjacent plane wall was set at  $\delta=0.1D$  and the equidistant plane was defined by  $y=\frac{1}{2}\delta$ .

The computations were carried out using a specified mass flow rate and a periodic boundary condition in the streamwise direction, by which the velocity field on the outlet plane was inserted back on the inlet plane. The use of this periodic boundary condition permitted the attainment of fully developed conditions in a relatively short flow domain, thus reducing the computational requirements. The length of the domain was sufficiently large to permit complete spatial decorrelation of turbulent statistics available from the GT experiments. No-slip conditions were applied at the walls of the rectangular channel and the cylindrical rod, while compressibility and body forces were neglected. The Reynolds number, based on the bulk velocity  $U_b$  and the hydraulic diameter  $D_h=1.59D$ , was 108,000, nearly matching the available experimental value. Hexahedral and quadrilateral elements were used for volume and face grid elements, respectively. To permit application of the periodic boundary condition, the meshes at the inlet and outlet were matched by linking both faces. To resolve the steep velocity gradient in the near wall region without using wall functions, five grid elements were placed in the region with  $y^+ < 10$ , with the first grid element located at  $y^+=1$ . The transverse and spanwise grid spacings were maintained below the roughly estimated Taylor microscale, equal to  $0.0495D$  [22], while the streamwise grid spacing was uniform and equal to 2.5 times the Taylor microscale. Grid independence studies were conducted using  $404 \times 160 \times 160$ ,  $202 \times 80 \times 80$ , and  $101 \times 40 \times 40$  elements (see Table 1, cases 1–3). As an example of the effect of grid choice on our computations, Figure 2 shows computed velocity profiles at a representative location. It can be seen that the velocity variation predicted by the  $202 \times 80 \times 80$  grid was in good agreement with the universal law of the wall within the viscous and logarithmic sublayers and was fairly close to the one predicted by the  $404 \times 160 \times 160$  grid, while the  $101 \times 40 \times 40$  grid predictions displayed significant discrepancies. The  $202 \times 80 \times 80$  element grid was, therefore, adopted for further computations, as the use

Table 1 Cases studied

Case	Grid element size			Number of grid elements	Total number of elements	Time step size
	$x/D$	$y/D$	$z/D$			
1	0.05	0.015	0.02	$404 \times 160 \times 160$	10,217,362	$1.9 \times 10^{-3} T_c$
2	0.1	0.03	0.04	$202 \times 80 \times 80$	1,278,054	$1.9 \times 10^{-3} T_c$
3	0.2	0.06	0.08	$101 \times 40 \times 40$	281,588	$1.9 \times 10^{-3} T_c$
4	0.1	0.03	0.04	$202 \times 80 \times 80$	1,278,054	$1.9 \times 10^{-2} T_c$

of finer grids required excessive computational times. Time step dependence was tested by repeating the computations with two time steps  $\Delta t$ , equal to  $1.9 \times 10^{-2} T_c$  and  $1.9 \times 10^{-3} T_c$ , where  $T_c = L/U_b$  is the average flow turn-over time, namely the average time that it takes for the fluid to pass through the computational domain. As shown in Fig. 2 by a representative example, the time-averaged velocity variations were essentially the same for these two time steps. Both time steps also resolved fairly well the coherent structures over some time, however, the larger time step led to distorted patterns for longer computations [23]. Furthermore, it turned out that computations with the smaller time step were faster than those with the larger one, because the former required far fewer iterations for the solution at each time step to converge. For the larger time step (case 4) the CPU time was about 4 min per time step and the real computing time was 5 h per time step, while for the smaller one (case 2) these times were, respectively, 5.6 s and 12.6 min. This means that flow computation over one turn-over time took 11 days for the larger time step but only 4.6 days for the smaller one. Thus, the smaller time step, equal to  $(1/526)T_c$ , was adopted for the main computations.

For high accuracy, the second-order upwind scheme with a linear reconstruction procedure, similar to that of Barth and Jespersen [24], was chosen for deriving the face values of different variables for space discretization. Those values were used to compute the convective fluxes. The Rhie–Chow scheme [25] was selected to interpolate pressure at the control volume face and to satisfy the mass conservation without pressure oscillations (checkerboarding). The SIMPLEC (Semi-Implicit Pressure Linked Equations - Consistent) algorithm [26] was used for the treatment of pressure-velocity coupling for stability. Time discretization was achieved by a second-order implicit method (second-order backward Euler scheme) [27]. Although implicit methods are not restricted by the CFL (Courant–Friedrichs–Lewy number) limit  $CFL = U_{\max} \Delta t / \Delta x < 1$ , it may be noted that the time step size may affect the accuracy of solutions because of truncation error increase. For the smaller time step case (case 2), CFL was equal to 0.456, which is deemed to be sufficiently low.

Because time-dependent flow patterns cannot be resolved by conventional RANS (Reynolds-averaged Navier–Stokes equations) procedures, we used the URANS (Unsteady Reynolds-averaged Navier–Stokes equations) approach. Unlike RANS, which solve for time-averaged velocities, URANS retain the unsteady terms in the mean momentum equations, although utilizing turbulence models for the turbulent stresses. The time step used is sufficiently fine to resolve time-dependent large-scale motions, but not nearly as fine as that used in direct numerical simulations (DNS), which fully resolve even the finest turbulence motions. Moreover, mesh density requirements of URANS are significantly less stringent than those of both DNS, which require the resolution of the finest turbulence motions (comparable in scale to the Kolmogorov microscale), and LES, which require the resolution of motions with scales within the inertial subrange.

The Reynolds stress model (RSM) was used for the majority of the present simulations. Unlike one- and two-equation models, RSM accounts for the effect of flow history due to terms representing the convection and diffusion of the shear stress tensors [28]. RSM also has modeled terms, which are derived from a combination of theoretical assumptions and empirical results. One of the modeled terms in the RSM is the pressure-strain term, which plays an important role in determining the structure of turbulent flows, re-partitioning turbulent energy among the Reynolds stress components and accounting for flow anisotropy. The linear model for the pressure-strain term [29,30] was chosen, with the values of the constants taken equal to those suggested by Launder [30]. To maintain solution stability, the turbulent diffusion term was modeled using a scalar diffusivity rather than a diffusivity tensor [31]. Due to the highly three-dimensional and unsteady nature of the flow in the gap region, the two-layer model of Chen and Patel [32] was employed to resolve the viscous sublayer,

rather than using a wall function. Consequently, the low Reynolds number version of RSM was used, following the suggestion of Launder and Shima [33].

It was verified that this model was successful in resolving the turbulence anisotropy and the secondary flows near the corners of a rectangular duct. However, to avoid possible divergence, the computations were initiated using the more stable RNG (Renormalization Group)  $k-\varepsilon$  model [34]. These preliminary computations extended over a time equal to  $5.7T_c$ , which was sufficient to allow full development of the flow. The velocity field at the end of the preliminary computations was used as starting condition for the main simulations with the RSM.

The output of URANS/RSM solutions includes time dependent velocity components  $U$ ,  $V$ , and  $W$  and pressure  $P$ , resolved at the time step and grid element size resolutions, as well as time dependent local turbulent stresses, which are solutions of the modeled Reynolds stress equations. In order to compare the results of the present computations with experimental, time-averaged turbulence statistics, one needs to consider both the modeled turbulent stresses and the fluctuations of the resolved velocity. The latter constitute the coherent structure contributions, while the former are noncoherent contributions. Both contributions have to be time-averaged (to be indicated by overbars) over a time interval that is sufficiently long to capture a significant number of coherent structures. For example, the time-averaged, total turbulent kinetic energy per unit mass would be [23]

$$\bar{k} = \bar{k}_{nc} + \bar{k}_{coh} \quad (1)$$

where  $\bar{k}_{nc}$  is the time-averaged local turbulent kinetic energy provided by the solution of the Reynolds stress equations (noncoherent part) and  $\bar{k}_{coh}$  is based on the mean squared instantaneous local “mean” velocity fluctuations (coherent part), as,

$$\bar{k}_{coh} = \frac{1}{2} \{ \overline{(U - \bar{U})^2} + \overline{(V - \bar{V})^2} + \overline{(W - \bar{W})^2} \} \quad (2)$$

Time averaging in the present simulations was over  $3.8T_c$ , which is equal to 2000 time steps, following full development of the flow structure inside the channel. The full development of the flow structure was checked by examining the spanwise velocity fluctuation patterns on the equidistant plane, on which the effects of coherent structures are most apparent [23]. The convergence of the solution was verified by comparing the time averaged local velocity and time averaged kinetic energy across the gap region at different time steps. It was found that the differences between the values of these parameters at 1000 and 1500 time steps were 0.2% and 8.6%, respectively, while the differences between the values of the same parameters at 1500 and 2000 time steps were 0.2% and 0.6%, respectively.

### 3 Coherent Structure Identification

Although there is no consensus on the definition of coherent structures (CS), the following definitions would help one understand the general concept. Hussain [35] referred to CS as “connected turbulent mass with instantaneous phase-correlated vorticity over its spatial extent.” Robinson [36] defined CS as “a three-dimensional region of the flow over which at least one fundamental flow variable exhibits significant correlation with itself or with another variable over a range of space and/or time that is significantly larger than the smallest local scales of the flow.” Jeong and Hussain [37] defined CS as “spatially coherent, temporally evolving vortical structures.” Vortices are among the most common types of coherent structures in turbulent flows, as they tend to persist in the absence of instabilities. Hussain [35] emphasized that coherent vorticity is the primary identifier of coherent structures, which have distinct boundaries and independent territories.

It has been known from experiments employing conditional sampling that coherent structures in turbulent shear flows account for a significant fraction of the turbulent kinetic energy and of the

Reynolds stresses and fluxes. Identification of CS in highly turbulent shear flows is subject to considerable difficulties, as they can be easily confused with noncoherent turbulence and mean vorticity patterns. Such identification can only be based on an unambiguous quantitative criterion. Early criteria were rather intuitive and identified coherent structures as minimum pressure regions, iso-vorticity surfaces or circular streamlines. More recently, two quantitative criteria for coherent structure identification were proposed. They are known as the  $Q$  criterion, proposed by Hunt et al. [38], and the  $\lambda_2$  criterion, proposed by Jeong and Hussain [37]. Both methods are based on analysis of properties of the velocity gradient tensor  $\partial U_i / \partial x_j$ . The present study will focus on the  $Q$  criterion, which has been used more widely than the  $\lambda_2$  criterion, because of its simplicity and applicability. The parameter  $Q$  is defined as

$$Q = -\frac{1}{2} \frac{\partial U_i}{\partial x_j} \frac{\partial U_j}{\partial x_i} = -\frac{1}{2} (S_{ij} S_{ji} + \Omega_{ij} \Omega_{ji}) \quad (3)$$

where the strain rate tensor and rotation rate tensor are, respectively, defined as

$$S_{ij} = \frac{1}{2} \left( \frac{\partial U_i}{\partial x_j} + \frac{\partial U_j}{\partial x_i} \right), \quad \Omega_{ij} = \frac{1}{2} \left( \frac{\partial U_i}{\partial x_j} - \frac{\partial U_j}{\partial x_i} \right) \quad (4)$$

The latter can be expressed in terms of the vorticity vector  $\omega_k$  as

$$\Omega_{ij} = -\frac{1}{2} \varepsilon_{ijk} \omega_k, \quad (5)$$

where  $\varepsilon_{ijk}$  is the Eddington alternating tensor ( $=1$ , if  $i, j, k$  is a cyclic permutation of 1,2,3;  $-1$ , if  $i, j, k$  is a cyclic permutation of 2,1,3; 0, otherwise)

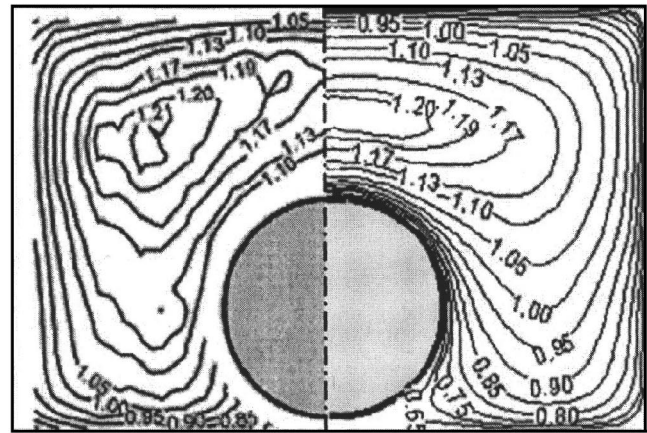
Thus,  $Q$  can be obtained in terms of the vorticity modulus  $\omega$  and the strain modulus  $S = (S_{ij} S_{ij})^{1/2}$  as

$$Q = \frac{1}{4} (\omega^2 - 2S^2) \quad (6)$$

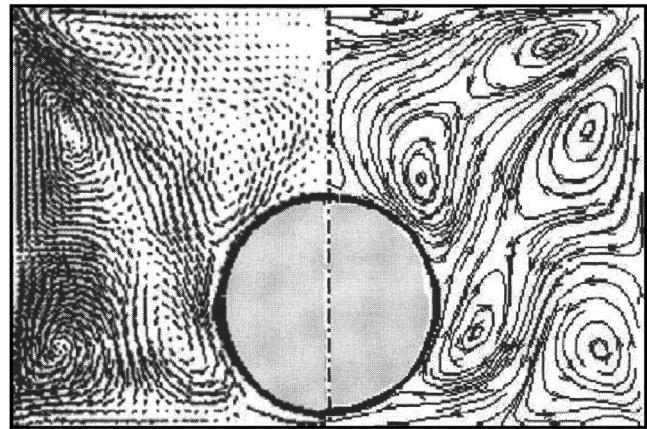
Positive  $Q$  indicates regions where vorticity overcomes strain, thus distinguishing vortical activity from high-strain activity. Unlike iso-vorticity surfaces, which cannot identify CS near a wall where the magnitudes of vorticity and strain are almost the same,  $Q$  can, because it is not influenced by near-wall vorticity. Thus, a criterion for identifying a vortical coherent structure is to determine a surface on which  $Q$  maintains a constant positive value, called the threshold. Experimentation with different values of the threshold led us to use the value  $Q=1.0$  as appropriate for the present coherent structure identification purposes.

## 4 Results and Discussion

The present simulations were partially validated by a comparison with available measurements by GT [12]. Figure 3(a) compares the simulated and experimental time-averaged streamwise velocity variations on a cross plane, while computed time-averaged streamline projections and velocity vectors on the same plane are shown in Fig. 3(b). When comparing the values of the velocity at corresponding locations, it becomes evident that the two "core" regions in which the velocity maintains relatively large values are larger in the experimental case than in the simulations. In other words, the wall regions appear to be somewhat thicker in the simulations than in the experiments. Although the simulations reproduced quite well the bulging of the experimental velocity contours in the gap region and in the corners of a duct, they also presented a notable difference from the experiments in that the predicted maximum velocity was on the symmetry plane above the rod, while in the experiments two maxima were observed in the two open subchannels, half way between the symmetry plane and the side walls. This difference is associated with secondary flows near the corners of the duct, but is not very disconcerting, because the velocity variation in the core region was only of the order of a small percent in both the simulations and the experiments. We have performed a number of additional simulations, not discussed here, showing some sensitivity of the maximum



(a)



(b)

**Fig. 3 (a) Isocontours of the time-averaged dimensionless axial velocity  $\bar{U}/U_b$  in the GT experiments [12] (left) and the present simulations (right) (b) vector plots of the time-averaged velocity component (left) and projected streamlines (right) on a cross-sectional plane in the present simulations**

velocity location on the type of turbulence model used, on the grid size and on the type of boundary condition employed. Furthermore, part of the difference can be attributed to differences in flow development: Unlike the present computations which represent fully developed flow, the experimental results correspond to a flow in which the turbulence structure was still evolving, albeit slowly.

Figure 4 compares the predicted rms turbulent velocity components and the turbulent kinetic energy with the corresponding experimental values, with all values normalized by the bulk velocity. Fairly good qualitative agreement can be observed in all cases, while the quantitative agreement may also be considered as at least fair, in view of the differences in the numerical and experimental conditions and the uncertainties involved in both. The axial rms turbulent velocity reached minimum values in the core region above the rod and maximum values in the gap region. The spanwise rms turbulent velocity had a distribution that was comparable to that of the axial one, while the transverse rms-turbulent velocity was maximum on the sides of the rod. All these trends can be observed both in the experimental and the numerical results. The variations of the three turbulent shear stresses and the corresponding correlation coefficients in the simulations are compared to the experimental ones in Fig. 5. Once more, the qualitative agreement is reasonably good and the corresponding magnitudes of the local stresses are, in most cases, not too far from each

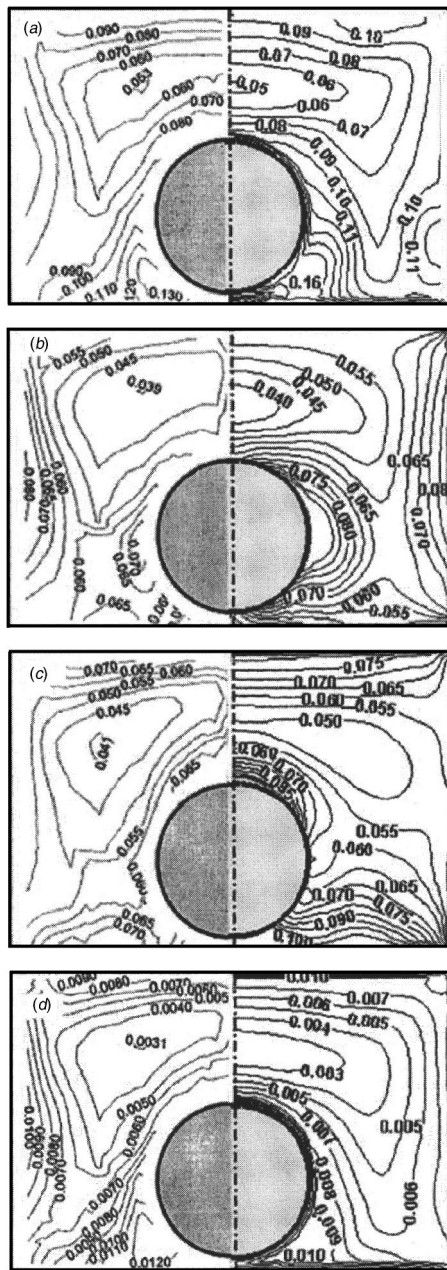


**Fig. 4** Isocontours of time-averaged, nondimensionalized GT measurements [12] (left) and present simulations (right): (a) axial rms velocity fluctuation  $u'/U_b$ ; (b) transverse rms velocity fluctuation  $v'/U_b$ ; (c) spanwise rms velocity fluctuation  $w'/U_b$ ; and (d) turbulent kinetic energy  $\bar{k}/U_b^2$

other, considering the differences in the two sets of conditions and the main objective of the present study, which is to identify the effect of coherent structures. A general observation that can be made by comparing the magnitudes of turbulent stresses with the corresponding local mean velocity gradients is that gradient transport seems to describe approximately the time-averaged turbulence structure in much of the cross section but fails to do so in the core region. In the gap region, the time-averaged mean velocity reaches a minimum and gradient transport would imply that turbulence activity should be minimum there as well. On the contrary, the axial and spanwise turbulent stresses as well as the turbulent kinetic energy reach their maxima in the center of the gap, which are trends observed in both the experimental and the numerical results.

To assess the importance of the coherent components on the turbulent activity, we have plotted, in Fig. 6, the ratios of the coherent and total values of the three normal rms turbulent velocities and the turbulent kinetic energy. This figure clearly demonstrates that the coherent contributions to the streamwise and spanwise components are very significant, and indeed dominant, in the gap region, where they account for up to 70% and 80%, respectively, of the total activity. The coherent contribution to the transverse stress is insignificant in the gap region and takes a maximum value of 20% on the sides of the rod, indicating that the flow pulsations follow the rod contour. About 60% of the total turbulent kinetic energy in the gap region is due to the coherent activity, while such activity is negligible away from the gap.

GT have provided some rough estimates of the contributions of the coherent stresses on the total turbulent activity along the spanwise direction on the equidistant plane. Their results are compared to the present simulations in Fig. 7. Although agreement is not perfect, it may be considered as remarkably good, both qualitatively and, in most cases, quantitatively, considering the differences in flow conditions and the uncertainties of both experiment and simulations. The experimental trends and the orders of magnitude of the different stresses are captured realistically by the simulations. Both experiments and simulations show that the maximum coherent streamwise stress occurs at an intermediate position between the gap and the side wall of the channel, while the maximum coherent spanwise stress occurs on the symmetry plane and the transverse coherent stress is negligible on the entire equidistant plane.

From the above discussion, it is evident that the resolved velocity fields are strongly time-dependent. This time dependence is intimately associated with the convection of large-scale, quasi-periodic, vortical coherent structures, which appear in pairs on either side of the gap between the rod and the channel plane wall. Such structures, captured using the  $Q$  criterion, are shown in Fig. 8. Their appearance is consistent with the heuristic model presented by GT.

To illustrate the influence of the coherent structure location on the instantaneous pressure and velocity fields, Fig. 9 shows isocountours of the instantaneous resolved static pressure and spanwise velocity as well as instantaneous surface streamlines constructed from the velocity vector projections on the equidistant plane using the graphics package Tecplot (Amtec Engineering, Inc.). The main structures coincide with low static pressure regions. This confirms their vortical character, demonstrated by cores with high vorticity and low pressure. The spanwise velocity at the gap alternates in direction with streamwise location and seems to be an excellent indicator of coherent structure passage near the gap, in conformity with experimental observations [12]. The instantaneous streamlines clearly show the presence of pairs of counter-rotating vortices with axes alternating on either side of the gap and transporting fluid far across the gap. The sense of rotation of the vortices is the same as the sense of rotation of coherent structures in mixing layers, if one considers the subchannel core to be the high-speed stream and the gap region to be the low-speed stream. It is also clear that these vortices transport fluid across the gap and deeply into the opposite subchannel. This fact is further illustrated in Fig. 10, which shows surface streamlines on the equidistant plane for both the experimental and the numerical studies. Besides the striking agreement between the two sets of streamlines, one may observe without doubt that the coherent structures are counter-rotating vortices causing large-scale transport of fluid across the gap. The spanwise spacing of the axes of vortices obtained by the numerical study was comparable to that in the experimental study, within the expected uncertainty due to differences in the imposed conditions and cycle-to-cycle variations.

To characterize the coherent structures, we have determined their frequency, streamwise spacing (wavelength) and convection speed. There was substantial variability from one structure to the next and the averages reported below were based on statistical

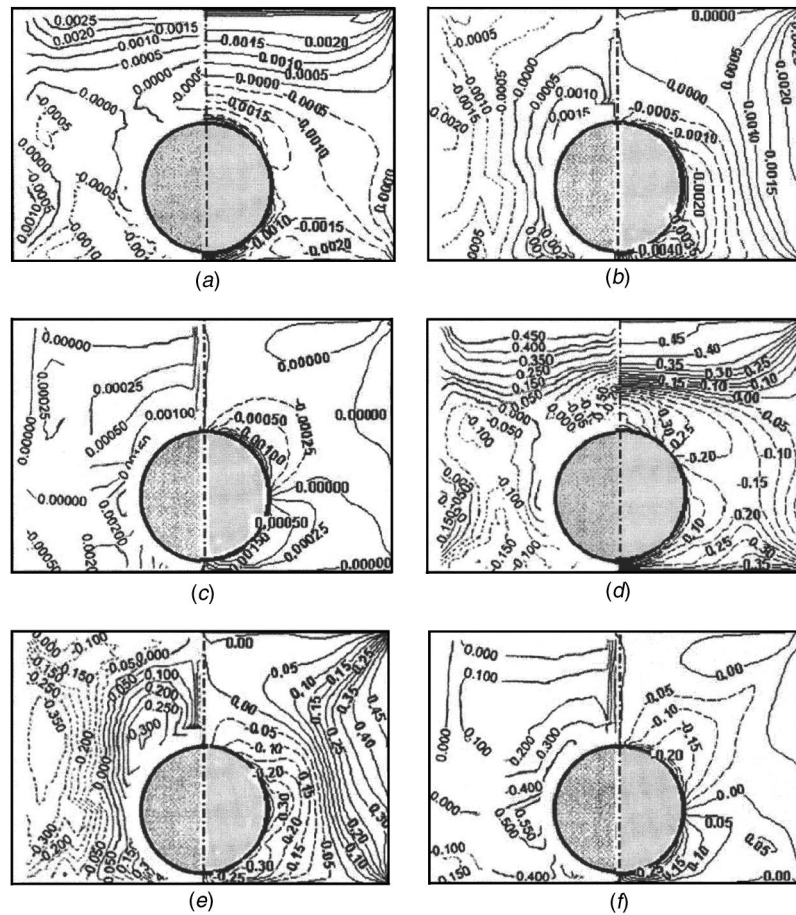


**Fig. 5 Isocontours of time-averaged, nondimensionalized GT measurements [12] (left) and present simulations (right): (a) Transverse turbulent shear stress  $\overline{uv}/U_b^2$ ; and (b) dimensionless spanwise turbulent shear stress  $\overline{uw}/U_b^2$ ; (c) dimensionless axial turbulent shear stress  $\overline{vw}/U_b^2$ ; (d) dimensionless transverse turbulent shear stress coefficient  $\overline{uv}/u'v'$ ; (e) dimensionless spanwise turbulent shear stress coefficient  $\overline{uw}/u'w'$ ; (f) dimensionless axial turbulent shear stress coefficient  $\overline{vw}/v'w'$**

populations which, although quite small, are considered to be sufficient for the present purposes. Figure 11(a) shows representative time histories of the spanwise velocity in the centre of the gap in the experimental and numerical studies. Both time histories show a quasi-periodic character, with a zero average and a nearly constant amplitude of about  $0.17U_b$ , which demonstrates the significant strength of flow pulsations across the gap. The average computed period of the pulsations, based on 9 cycles, was  $0.37T_c$ , with a standard deviation of  $0.09T_c$  and extreme values  $0.54T_c$  and  $0.23T_c$ . The corresponding Strouhal number ( $f$  is the frequency of pulsations) was

$$St = \frac{fD_h}{U_b} = 0.23 \pm 0.06 \quad (7)$$

The Strouhal number computed from the peak frequency of the power spectrum of the simulated velocity, shown in Fig. 11(b) was about 0.27. In view of the relatively large uncertainty of these estimates, the simulation values are deemed to be compatible with the experimentally found value of 0.17 [12]. The dimensionless spacing between pairs of structures, based on four structure pairs, was  $\lambda/D = 4.9 \pm 1.2$ , also compatible with the experimental value of 4.2. Finally, the dimensionless convection speed of the structures, averaged over eight structures and measured from animated sequences of images similar to Fig. 8, was  $U_c/U_b \approx 0.62$ , which is not too far from the experimental value of 0.78. Overall, the above

results show that velocity fluctuations in the gap region are of sufficiently large wavelength and low frequency for local conditions to potentially prevail in wall heating and possible phase change.

## 5 Conclusion

The present simulations have clearly documented the significance of coherent vortical structures in turbulent flow near a rod-wall gap region. The use of the  $Q$  criterion has identified the formation of such coherent structures, with features comparable to those found experimentally [12]. The time-averaged mean velocities and turbulent stresses in the simulations were also in fair agreement with their experimental counterparts. It is, therefore, concluded that the present approach is sufficiently accurate for the conduction of parametric studies of the effects of gap size, geometry and Reynolds number on the variation of flow and heat transfer characteristics in rod bundles.

It is also observed that the coherent components were very significant in the gap region, where they accounted for 60% of the total kinetic energy. The coherent contribution to the transverse stress was much lower than the coherent contributions to the spanwise and streamwise stresses. It is evident that the time dependent velocity fields in the gap region are mainly associated with the convection of large-scale, quasi-periodic, vortical coherent structures, which appear in pairs of counter-rotating vortices with axes

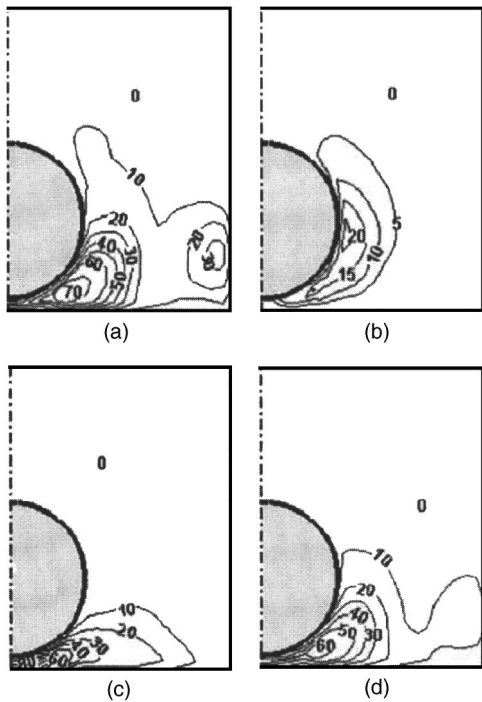


Fig. 6 Predicted isocontours of the percent ratio of the coherent components to the totals: (a) Streamwise rms velocity ratio  $u'_{coh}/u'$ ; (b) transverse rms velocity ratio  $v'_{coh}/v'$ ; (c) spanwise rms velocity ratio  $w'_{coh}/w'$ ; and (d) turbulent kinetic energy ratio  $\bar{k}_{coh}/\bar{k}$

alternating on either side of the gap and transporting fluid far across the gap. Velocity fluctuations in the gap region are of sufficiently large wavelength and low frequency for local conditions to potentially prevail in wall heating and possible phase change.

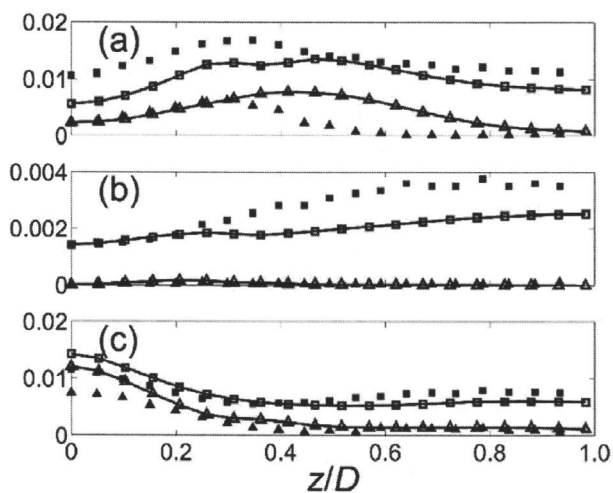


Fig. 7 Comparison of present simulations (open symbols) with experimental results [12] (solid symbols) for total averages ( $\square$ ,  $\blacksquare$ ) and coherent ( $\triangle$ ,  $\blacktriangle$ ) parts on the equidistant plane: (a) Streamwise normal stress; (b) transverse normal stress; (c) spanwise normal stress; the simulation results have been connected by solid lines as an aid to the eye.

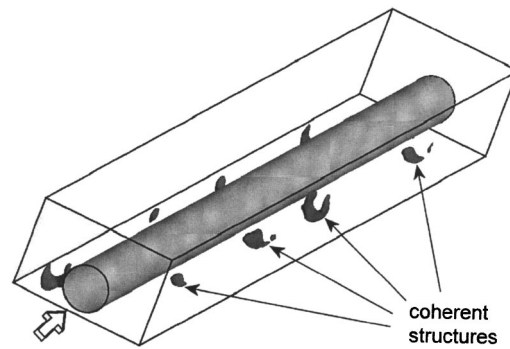


Fig. 8 Coherent structures identified by the  $Q$  criterion; the section shown is  $20 D$  long

### Acknowledgment

Financial support for this project has been provided by the Natural Sciences and Engineering Research Council of Canada.

### Nomenclature

- $D$  = rod diameter
- $D_h$  = hydraulic diameter
- $f$  = frequency of flow pulsations
- $\bar{k}, \bar{k}_{coh}, \bar{k}_{nc}$  = time-averaged total, coherent, and noncoherent parts of turbulent kinetic energy per unit mass, respectively
- $L$  = streamwise length of the duct

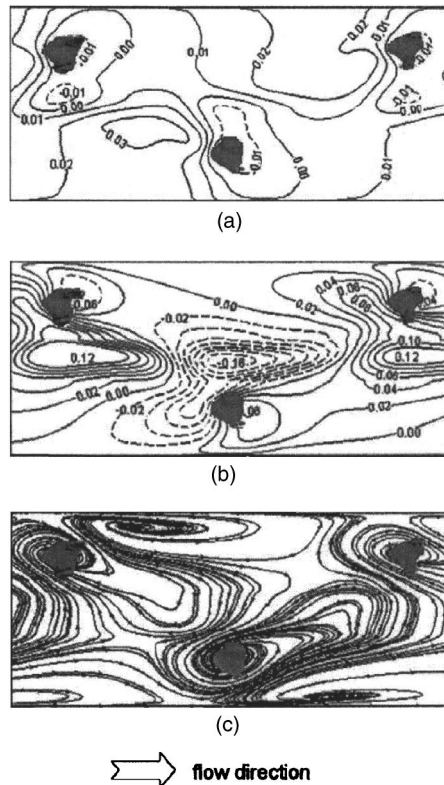
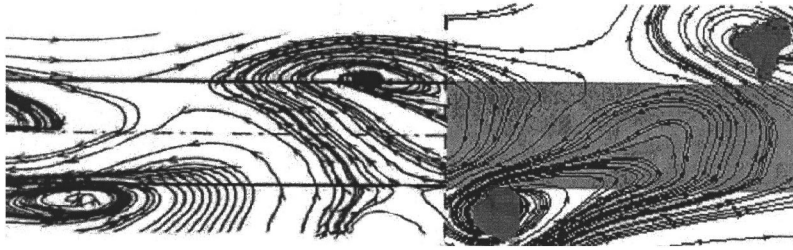


Fig. 9 Predicted isocontours on the equidistant plane of: (a) The dimensionless instantaneous static pressure  $P/(1/2\rho U_b^2)$ ; (b) the dimensionless instantaneous spanwise velocity  $W/U_b$ ; and (c) instantaneous streamlines; coherent structures identified by the  $Q$  criterion are also shown in all plots; all plots are  $7.2 D$  long and  $3 D$  high



**Fig. 10** Experimental (left) and simulated (right) surface streamlines of velocity fields as seen by an observer moving with the average convective speed of the coherent structures

$P$  = pressure  
 $Re$  = Reynolds number,  $\rho U_b D_h / \mu$   
 $S$  = strain modulus  
 $St$  = Strouhal number,  $f D_h / U_b$   
 $S_{ij}$  = strain rate tensor  
 $T_c$  = average flow turn-over time  
 $t$  = time  
 $U, V, W$  = time dependent velocity components  
 $U^+$  = time-averaged velocity nondimensionalized by  $u^*$   
 $U_b$  = bulk velocity  
 $U_c$  = convective velocity of coherent structure  
 $U_i, i=1,2,3$  = velocity vector in Cartesian tensor notation  
 $u^*$  = friction velocity,  $\sqrt{\tau_w / \rho}$   
 $\overline{uw}, \overline{vw}, \overline{vw}$  = time-averaged turbulent shear stresses  
 $x, y, z$  = streamwise, transverse and spanwise coordinates, respectively  
 $x_i, i=1,2,3$  = coordinates in Cartesian tensor notation  
 $y^+$  = dimensionless distance from the wall,  $\rho u^* y / \mu$

#### Greek symbols

$\Delta$  = difference in the values of a quantity at two times or two locations  
 $\delta$  = gap between the rod wall and the adjacent plane wall  
 $\varepsilon_{ijk}$  = Eddington alternating tensor  
 $\lambda$  = spacing between pairs of coherent structures  
 $\mu$  = dynamic viscosity  
 $\rho$  = density

$\tau_w$  = wall shear stress  
 $\Omega_{ij}$  = rotation tensor  
 $\omega$  = vorticity modulus  
 $\omega_k$  = vorticity vector

#### Subscripts

$b$  = bulk quantity  
 $coh$  = coherent component  
 $max$  = maximum value in the channel  
 $nc$  = noncoherent component

#### Superscripts

$+$  = quantity nondimensionalized by wall scales  
 $(\bar{\quad})$  = time-averaged value  
 $(\prime)$  = fluctuation value

#### References

- [1] Rowe, D. S., Johnson, B. M. and Knudsen, J. G., 1974, "Implications Concerning Rod Bundle Crossflow Mixing Based on Measurements of Turbulent Flow Structure," *Int. J. Heat Mass Transfer* **17**, pp. 407–419.
- [2] Trupp, A. C. and Azad, R. S., 1975, "The Structure of Turbulent Flow in Triangular Array Rod Bundles," *Nucl. Eng. Des.* **32**(1), pp. 47–84.
- [3] Carajilescov, P. and Todreas, N. E., 1976, "Experimental and Analytical Study of Axial Turbulent Flows in an Interior Subchannel of a Bare Rod Bundle," *ASME J. Heat Transfer* **98**, pp. 262–268.
- [4] Seale, W. J., 1979, "Turbulent Diffusion of Heat between Connected Flow Passages, Part 1: Outline of Problem and Experimental Investigation," *Nucl. Eng. Des.* **54**, pp. 183–195.
- [5] Hooper, J. D., 1980, "Developed Single Phase Turbulent Flow through a Square-Pitch Rod Cluster," *Nucl. Eng. Des.* **60**, pp. 365–379.
- [6] Hooper, J. D. and Wood, D. H., 1984, "Fully Developed Rod Bundle Flow over a Large Range of Reynolds Number," *Nucl. Eng. Des.* **83**, pp. 31–46.
- [7] Hooper, J. D. and Rehme, K., 1984, "Large-Scale Structural Effects in Developed Turbulent Flow through Closely-Spaced Rod Arrays," *J. Fluid Mech.* **145**, pp. 305–337.
- [8] Rehme, K., 1987, "The Structure of Turbulent Flow through Rod Bundles," *Nucl. Eng. Des.* **99**, pp. 141–154.
- [9] Wu, X. and Trupp, A. C., 1993, "Experimental Study on the Unusual Turbulence Intensity Distributions in Rod-to-Wall Gap Regions," *Exp. Therm. Fluid Sci.* **6**, pp. 360–370.
- [10] Wu, X., 1995, "On the Transport Mechanisms in Simulated Heterogeneous Rod Bundle Subchannels," *Nucl. Eng. Des.* **158**, pp. 125–134.
- [11] Krauss, T. and Meyer, L., 1998, "Experimental Investigation of Turbulent Transport of Momentum and Energy in a Heated Rod Bundle," *Nucl. Eng. Des.* **180**, pp. 185–206.
- [12] Guellouz, M. S. and Tavoularis, S., 2000, "The Structure of Turbulent Flow in a Rectangular Channel Containing a Cylindrical rod - Part 1: Reynolds-Averaged Measurements," *Exp. Therm. Fluid Sci.* **23**, pp. 59–73; , 2000, "-Part 2: Phase-Averaged Measurements," *Exp. Therm. Fluid Sci.* **23**, pp. 75–91.
- [13] Möller, S. V., 1991, "On Phenomena of Turbulent Flow through Rod Bundles," *Exp. Therm. Fluid Sci.* **4**, pp. 25–35.
- [14] Möller, S. V., 1992, "Single-Phase Turbulent Mixing in Rod Bundles," *Exp. Therm. Fluid Sci.* **5**, pp. 26–33.
- [15] Rehme, K., 1992, "The Structure of Turbulence in Rod Bundles and the Implications on Natural Mixing between the Subchannels," *Int. J. Heat Mass Transfer* **35**(2), pp. 567–581.
- [16] Meyer, L. and Rehme, K., 1994, "Large-Scale Turbulence Phenomena in Compound Rectangular Channels," *Exp. Therm. Fluid Sci.* **8**, pp. 286–304.
- [17] Meyer, R., 1975, "Turbulent Velocity and Temperature Distribution in the Central Subchannel of Rod Bundles," *Nucl. Eng. Des.* **35**, pp. 181–189.
- [18] Seale, W. J., 1982, "Measurements and Predictions of Fully Developed Turbulent Flow in a Simulated Rod Bundle," *J. Fluid Mech.* **123**, pp. 399–423.

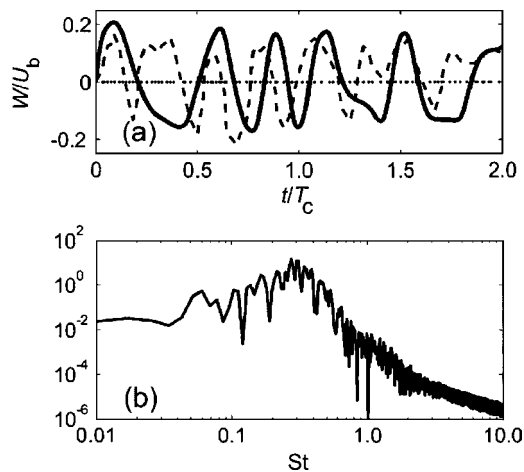


**Fig. 11** (a) Representative time histories of the spanwise velocity in the centre of the gap: present simulations (—) and experimental results (---); (b) the power spectrum, in arbitrary logarithmic scale, of the time history of the simulated spanwise velocity in the center of the gap

- [19] Wu, X., 1994, "Numerical Study on the Turbulence Structures in Closely Spaced Rod Bundle Subchannels," *Numer. Heat Transfer, Part A* **25**, pp. 649–670.
- [20] Biemüller, M., Meyer, L. and Rehme, K., 1996, "Large Eddy Simulation and Measurement of the Structure of Turbulence in Two Rectangular Channels Connected by a Gap," *Engineering Turbulence Modeling and Experiments*, edited by Rodi and Bergeles, Vol. 3, pp. 249–258.
- [21] Lee, K. B. and Jang, H. G., 1997, "A Numerical Prediction on the Turbulent Flow in Closely Spaced Bare Rod Arrays by a Nonlinear  $k-\epsilon$  Model," *Nucl. Eng. Des.* **172**, pp. 351–357.
- [22] Tavoularis, S., Madrane, A. and Vaillancourt, R., 2002, "Numerical Simulation of Coherent Structures in Axial Flow through a Rectangular Channel containing a Cylindrical Rod," *Proc. 10th Ann. Conf. CFD Society of Canada*, June 9–11, Windsor, Ontario, pp. 105–110.
- [23] Chang, D., and Tavoularis, S., 2004, "Identification of Coherent Structures in Axial Flow in a Rectangular Channel Containing a Rod," *Proc. 12th Ann. Conf. CFD Society of Canada*, May 9–11, Ottawa, Ontario, pp. 303–309.
- [24] Barth, T. J. and Jespersen, D. C., 1989, "The Design and Application of Upwind Schemes on Unstructured Meshes," AIAA Paper89-0366, *AIAA 27th Aerospace Sciences Meeting*, Reno, Nevada.
- [25] Rhie, C. M. and Chow, W. L., 1983, "Numerical Study of the Turbulent Flow Past an Airfoil with Trailing Edge Separation," *AIAA J.* **21**, pp. 1523–1532.
- [26] Van Doormal, J. P. and Raithby, G. D., 1984, "Enhancements of the SIMPLE Method for Predicting Incompressible Fluid Flows," *Numer. Heat Transfer* **7**, pp. 147–163.
- [27] Gresho, P. M., Lee, R. L. and Sani, R. L., 1980, "On the Time-Dependent Solution of the Incompressible Navier–Stokes Equations in Two and Three Dimensions," *Recent Advances in Numerical Methods in Fluids*, edited by C. Taylor and K. Morgan, Pineridge Press, Swansea, U.K., Chap. 2.
- [28] Wilcox, D. C., 2000, *Turbulence Modeling for CFD*, DCW Industries, Inc., La Canada, California, Chap. 6.
- [29] Gibson, M. M. and Launder, B. E., 1978, "Ground Effects on Pressure Fluctuations in the Atmospheric Boundary Layer," *J. Fluid Mech.* **86**, pp. 491–511.
- [30] Launder, B. E., 1989, "Second-Moment Closure: Present... and Future?," *Int. J. Heat Fluid Flow* **9**(4), pp. 963–985.
- [31] Lien, F. S. and Leschziner, M. A., 1994, "Assessment of Turbulent Transport Models Including Non-Linear RNG Eddy-Viscosity Formulation and Second-Moment Closure," *Comput. Fluids* **23**(8), pp. 983–1004.
- [32] Chen, H. C., and Patel, V. C., 1988, "Near-Wall Turbulence Models for Complex Flows including Separation," *AIAA J.* **26**(6), pp. 641–648.
- [33] Launder, B. E. and Shima, N., 1989, "Second-Moment Closure for the Near-Wall Sublayer: Development and Application," *AIAA J.* **27**(10), pp. 1319–1325.
- [34] Yakhot, V., Orszag, S. A., 1986, "Renormalization Group Analysis of Turbulence: I. Basic Theory," *J. Sci. Comput.* **1**, pp. 3–51.
- [35] Hussain, F., 1986, "Coherent Structures and Turbulence," *J. Fluid Mech.* **173**, pp. 303–356.
- [36] Robinson, S. K., 1991, "Coherent Motions in the Turbulent Boundary Layer," *Annu. Rev. Fluid Mech.* **23**, pp. 601–639.
- [37] Jeong, J. and Hussain, F., 1995, "On the Identification of a Vortex," *J. Fluid Mech.* **285**, pp. 69–94.
- [38] Hunt, J. C. R., Wray, A. A. and Moin, P., 1988, "Eddies, Streams, and Convergence Zones in Turbulent flows," Center for Turbulence Research Report CTR-S88, Stanford Univ., pp. 193–207.



# Three-Dimensional Numerical Simulation and Performance Study of an Industrial Helical Static Mixer

**Ramin K. Rahmani**

Research Assistant  
Department of Mechanical,  
Industrial and Manufacturing Engineering,  
The University of Toledo, Toledo, OH 43606  
e-mail: rkrahmani@yahoo.com

**Theo G. Keith**

Distinguished University Professor  
ASME Fellow  
Department of Mechanical,  
Industrial and Manufacturing Engineering,  
The University of Toledo, Toledo, OH 43606  
e-mail: tkeith@eng.utoledo.edu

**Anahita Ayasoufi**

Research Assistant  
Department of Mechanical,  
Industrial and Manufacturing Engineering,  
The University of Toledo, Toledo, OH 43606  
e-mail: aayasoufi@yahoo.com

*In many branches of processing industries, viscous liquids need to be homogenized in continuous operations. Consequently, fluid mixing plays a critical role in the success or failure of these processes. Static mixers have been utilized over a wide range of applications such as continuous mixing, blending, heat and mass transfer processes, chemical reactions, etc. This paper describes how static mixing processes of single-phase viscous liquids can be simulated numerically, presents the flow pattern through a helical static mixer, and provides useful information that can be extracted from the simulation results. The three-dimensional finite volume computational fluid dynamics code used here solves the Navier-Stokes equations for both laminar and turbulent flow cases. The turbulent flow cases were solved using  $k-\omega$  model and Reynolds stress model (RSM). The flow properties are calculated and the static mixer performance for different Reynolds numbers (from creeping flows to turbulent flows) is studied. A new parameter is introduced to measure the degree of mixing quantitatively. Furthermore, the results obtained by  $k-\omega$  and RSM turbulence models and various numerical details of each model are compared. The calculated pressure drop is in good agreement with existing experimental data.*

[DOI: 10.1115/1.1899166]

## Introduction

Mixing is an essential component of nearly all industrial chemical processes, ranging from simple blending to complex multi-phase reaction systems for which the reaction rate, the yield, and the selectivity are highly dependent upon the mixing performance. Consequences of improper mixing include nonreproducible processing conditions and lowered product quality, resulting in the need for more elaborate downstream purification processes and increased waste disposal costs.

The *static mixer* has increased in popularity within the chemical industry over recent years. The mixing elements, which are called *segments*, as one could imagine, appear to have been cut from a long periodic structure. Several of these segments are inserted in-line at various locations, and housed in a pipe that squeezes the liquid through the resulting mixing element. Because of a very broad range of applications for static mixers, a variety of segment designs is available [1–3]. The *helical static mixer* consists of left- and right-twisting helical elements at right angles to each other. Each element twists through an angle of  $180^\circ$ . The complete mixer consists of a series of elements of alternating clockwise and counterclockwise twist arranged axially within a pipe so that the leading edge of an element is at right angles to the trailing edge of the previous element. Figure 1 shows a six-element helical static mixer. The leading and the trailing edges of the second mixing element are shown in Fig. 1.

Despite widespread usage, the way these mixers work is still not fully understood. The design and optimization of mixers are traditionally performed by trial and error, with much depending on previous experience and wide safety margin. For a given application, besides experimentation, the modern approach is to use powerful computational fluid dynamics (CFD) tools to study the mix-

ing process. In fact, while complex, three-dimensional geometries typical of most industrial mixers make analytic determinations of the velocity field in such equipment impractical, a high quality numerical solution of the velocity field can provide a suitable starting point to characterize mixing performance.

In recent years, significant progress has been made in the characterization of fluid-mechanical mixing using Lagrangian tracking techniques and tools from dynamical systems theory, particularly those related to chaos. Early efforts at CFD modeling of the flow within static mixers were reported in the 1980s. Shintre and Ulbrecht [4] developed a Navier-Stokes-based model for the flow within two sheets of a Koch-Sulzer SMX mixer for  $Re \sim 0$  and 1. Shintre [5] also extended the model to pseudo-plastic fluids.

For helical static mixers, several groups of researchers [6–11] tried to simplify the mathematics of the governing equations (Navier-Stokes equations) by the usage of the natural helical geometry of the mixer. Each study reports transforming reduced forms of the Navier-Stokes equations into nonorthogonal, helical coordinates, and emphasizes that the previous one made a mistake in the coordinate transformation, which shows the difficulty of this approach. Despite the differences between each these researches, all of them were limited to creeping flows ( $Re \sim 0$ ) or in the case of Dackson and Nauman [8] to  $Re < 10$  and to assuming fully developed flow within the mixer. The application of such calculations is restricted to mixer geometries with sufficiently long mixing segments and also small influence of the segments junctions. The paper by Arimond and Erwin [6,7] is notable because even though their flow solution was based on the fully developed assumption, they recognized the importance of the end effects and attempted to account for them.

The majority of the previous work has focused on model flows that are two-dimensional and time periodic, not three-dimensional, spatially periodic flows. Furthermore, each of the studies, mentioned above, focused on fully developed flow within one mixer element. Nauman [12] demonstrated that this assumption is seriously flawed because it violates the conservation of mass; residence time distributions computed from these flowfields

Contributed by the Fluids Engineering Division for publication in the JOURNAL OF FLUIDS ENGINEERING. Manuscript received by the Fluids Engineering Division November 16, 2003. Final manuscript received January 4, 2005. Associate Editor: Malcolm Andrews.

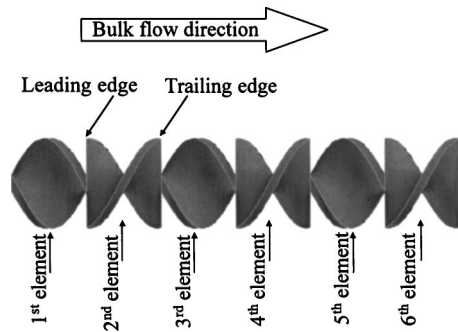


Fig. 1 A six-element static mixer

have an infinite mean. Moreover, recent experiments by Kusch and Ottino [13] suggest that flow in this idealized mixer is highly three-dimensional and dominated by entrance and exit effects.

The most extensive and significant studies in recent years were performed by Byrde [14], Hobbs [15] and Jones [16] using commercial/academic CFD packages on very powerful multiprocessor machines. An investigation by Rauline et al. [17] of the mixing performance of five different static mixers using a commercial CFD code is in this category.

The primary objective of the Byrde study was to develop a computational technique to compute mixing and flowfields using massively parallel supercomputers. A large portion of this study focused on the details of the computational efficiency distributing the computational workload over many processors, i.e., 256 processors. Byrde used the Eulerian approach to solve the flowfield on a block-structured mesh. A Lagrangian approach was used to examine the mixing process [14].

Hobbs [15] studied the mixing performance of a static mixer under laminar flow conditions for alternative mixer geometries and concluded that: the flow in a mixer in which all elements have the same twist direction contains large segregated regular regions that do not exchange material with the remainder of the flow; the extent of mixing per segment and energy efficiency are independent of segment length to diameter ratio, allowing shorter segments to be used to obtain equivalent mixing in a smaller space with a shorter residence time; and for tracer mixing, the injection location has a strong effect on the extent of mixing only for the first few mixing segments, after which the rate of mixing is independent of injection location.

The work of Hobbs et al. [18,19] and Byrde and Sawley [20,21] represent two substantial and important studies in the effort to correctly predict and understand the mixing behavior of helical static mixers. However, the conclusions of their work are contradictory in several important respects. The most glaring contradiction is that Hobbs and Muzzio report that mixing is the poorest for Reynolds numbers of the order of 100, whereas, Byrde and Sawley determine that it is the most efficient for these Reynolds numbers. Further, Byrde and Sawley claim that the grid density needed to obtain physically realistic results are far in excess of the grid density used by Hobbs and Muzzio. Since neither study fully investigated the predicted flowfields, both overlooked potentially important and useful information, e.g., effects of the geometrical parameters such as element twist angle and the ratio of element length to element diameter on the mixer performance [15,20]. One particular point of agreement between the two studies is that, for creeping flows, the most stretching, and therefore, the most mixing, occurs at the intersection of the mixing elements. This result demonstrates the importance CFD-based studies and the inadequacy of those earlier studies that ignored the developing flows within the mixer elements.

One of the most recent numerical studies on helical static mixers have been done by Jones et al. [22] for water treatment. The model they used solves the three-dimensional, Reynolds-averaged

Table 1 Mixer geometrical parameters

Mixer	
Diameter ( $d$ )	4.80 mm
Segment (element) length	4.06 mm
Thickness	0.89 mm
Entrance length	9.60 mm
Exit length	9.60 mm

Navier-Stokes (RANS) equations, closed with the  $k-\omega$  turbulence model, using a second-order finite volume method. The model is applied to a two-element helical static mixer. The Reynolds number is 100,000 and the working fluid is water. What distinguished this study from the work done by Hobbs [18] and Byrde [20,21] is that they considered high Reynolds number flows in helical static mixer. However, the geometry considered in this case is relatively a simple one and only two mixing elements were considered. In addition, they did not investigate the effects of different turbulence models on the prediction of the CFD code.

To obtain accurate numerical results, the computational grid must be sufficiently refined. A coarse mesh can lead the solver to converge to a misleading result; however, over-refinement of the computational grid can lead to unneeded computational expenses. Therefore, it is necessary to study grid refinement to determine the appropriate grid size. Moreover, computational grid type and grid quality have a significant impact on the quality of numerical results and computational expenses needed to obtain these results. In this study a novel technique is used that leads to a very high mesh quality and accelerates the flow solver convergence rate; it also makes the particle trajectory calculations easier and much faster.

In the present paper, Lagrangian techniques are applied on a PC (An Intel 2 GHz processor with computational memory up to 3.35 GB was used in this study) to model a fully three-dimensional flow in an industrial helical static mixer: the TAH static mixer (Robbinsville, NJ) with no simplification on the mixer geometry. The mixer geometrical parameters are shown in Table 1. The solid material thickness of the mixer is about 22% of each segment length, which makes the zero thickness assumption of the mixer, as was done in previous studies, questionable. In addition, the ratio of the each segment length to the mixer diameter is about 0.846. In other words, the static mixer considered here is very compact; in a standard Kenics mixer, the segment length is 1.50 times the mixer diameter [20]. The range of Reynolds numbers is from  $Re=0.01$  up to  $Re=5000$ .

The following sections (1) briefly present the governing equations and describe the numerical techniques used to obtain the velocity field and to characterize mixing at various Reynolds numbers, (2) present results and discussion, and (3) summarize the outcomes of this work.

## Analysis

**Governing Equations.** For steady incompressible flow, the mass conservation equation can be written as

$$\frac{\partial u_i}{\partial x_i} = 0 \quad (1)$$

and the momentum conservation equation can be written as

$$\rho \frac{\partial(u_i u_j)}{\partial x_j} + \frac{\partial p}{\partial x_i} = \frac{\partial \tau_{ij}}{\partial x_j} + \rho g_i + F_i \quad (2)$$

In the absence of a gravitational body force and any external body force, the two last terms on the right side of Eq. (2) are zero. The stress tensor,  $\tau_{ij}$ , in Eq. (2) is given by

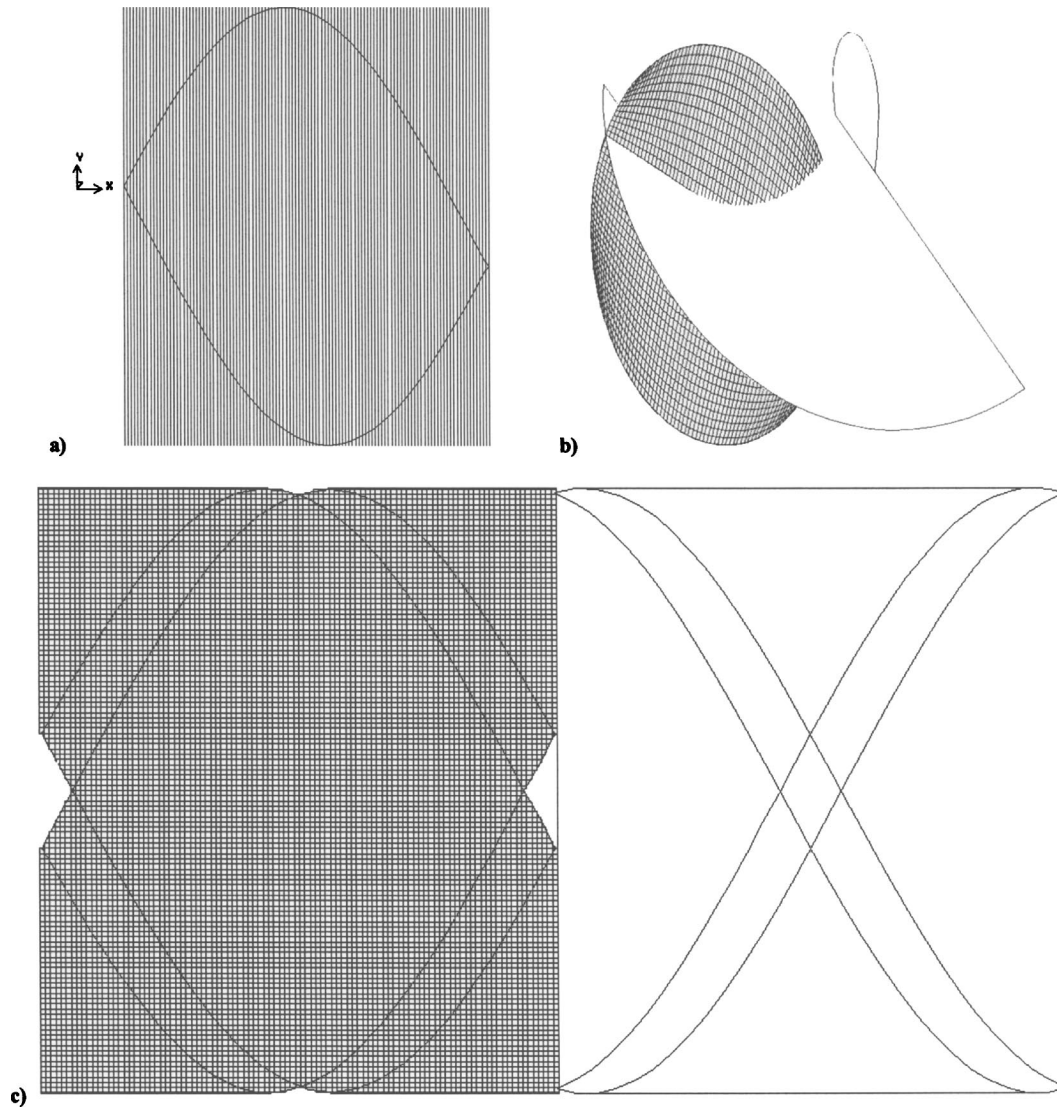


Fig. 2 (a) Computational domain across one helical surface is cut by a large number of parallel planes perpendicular to the flowfield centerline. (b) Cross-sectional mesh. (c) Volume mesh for one mixing element

$$\tau_{ij} = \mu \left( \frac{\partial u_i}{\partial x_j} + \frac{\partial u_j}{\partial x_i} \right) - \frac{2}{3} \mu \frac{\partial u_k}{\partial x_k} \delta_{ij} \quad (3a)$$

Considering the conservation of mass for incompressible flow,  $\partial u_k / \partial x_k = 0$ , gives

$$\tau_{ij} = \mu \left( \frac{\partial u_i}{\partial x_j} + \frac{\partial u_j}{\partial x_i} \right) \quad (3b)$$

**Turbulence Model.** Although there is no complete and sufficient definition of turbulent flow, it may be useful to describe its nature. Turbulent flows represent an intrinsically three-dimensional, time- and space-dependent phenomenon, which have a large number of spatial degrees of freedom. They carry a wide range of vorticities from large- to small-scale vorticities, which have a random nature; of course turbulent flow is a continuum phenomenon. Turbulent flows are characterized by fluctuating velocity fields. These fluctuations mix transported quantities of mass, momentum, and energy, and in turn cause the transported quantities to fluctuate as well. These fluctuations can be of small scale and high frequency; therefore, they are too expensive to simulate directly. Different turbulence modeling techniques can be found in the literature, e.g., [23–26]. In this study, for turbulent

cases ( $Re=3000$  and  $Re=5000$ ), the three-dimensional, steady state Reynolds-averaged, Navier-Stokes equations are solved. The momentum equation can be written as

$$\rho \frac{\partial (u_i u_j)}{\partial x_j} = \frac{\partial}{\partial x_j} \left[ \mu \left( \frac{\partial u_i}{\partial x_j} + \frac{\partial u_j}{\partial x_i} \right) - \frac{2}{3} \mu \frac{\partial u_k}{\partial x_k} \delta_{ij} \right] - \frac{\partial p}{\partial x_i} + \frac{\partial}{\partial x_j} (-\overline{\rho u'_i u'_j}) \quad (4a)$$

For the incompressible flow, Eq. (4a) is reduced to the following:

$$\rho \frac{\partial (u_i u_j)}{\partial x_j} = \frac{\partial}{\partial x_j} \left[ \mu \left( \frac{\partial u_i}{\partial x_j} + \frac{\partial u_j}{\partial x_i} \right) \right] - \frac{\partial p}{\partial x_i} + \frac{\partial}{\partial x_j} (-\overline{\rho u'_i u'_j}) \quad (4b)$$

The **Reynolds stresses**,  $-\overline{\rho u'_i u'_j}$ , must be modeled in order to close the set of equations. A common method employs the Boussinesq hypothesis to relate the Reynolds stresses to the mean velocity gradients. The alternative approach is to solve transport equations for each of the terms in the Reynolds stress tensor, known as Reynolds stress model (RSM) [27–30]. Details regarding these two groups of models can be found in [24,26]. In this study the,  $k-\omega$ , as a Boussinesq approach model, [24,31–33] and the RSM models are employed to solve the turbulent flow and the

**Table 2 Mesh quality tests result**

Maximum volume ratio	1.000058
Maximum face ratio	1.008443
Aspect ratio	1.0083895–1.008390
Diagonal ratio	0.999999–1.000001
Edge ratio	1.008389–1.009009
Midangle skewness	<0.000001
Equal-size skewness	<0.000001

obtained results are contrasted to each other.

The  $k-\omega$  model, which was introduced by Kolmogorov [31] in 1942, in this study was selected for two reasons. First, the  $k-\omega$  model is valid all the way to the wall boundary, and thus the **wall-function approach** that bridges the gap between the fully turbulent region and the viscous sublayer is not needed. Turbulence models that rely on the wall-function approach, although expedient from a computational standpoint, are not suitable for quantitatively accurate predictions of complex, three-dimensional flows with strong vortices [34]. Second, the  $k-\omega$  model has been validated extensively in complex, three-dimensional shear flows and has been shown to be superior to  $k-\varepsilon$  type models [35,36]. The  $k-\omega$  model used in this study has been introduced by Menter in 1994 [37], which is a modified version of the original  $k-\omega$  model of Wilcox [38]. One problem with the original  $k-\omega$  model is that it does not correctly predict the asymptotic behavior of the turbulence in near-wall regions, because of the fact that the eddy viscosity is much smaller than the molecular viscosity close to solid surface [37]. Menter developed two new versions of the  $k-\omega$  model. The first model utilized Wilcox's  $k-\omega$  model in the inner region of the boundary layer and switches it to the standard version of the  $k-\varepsilon$  model in the outer region and in free shear flows. The second model, referred to as shear-stress transport model or the SST  $k-\omega$  model, is a modification of the first model. This model is based on the philosophy underlying the Johnson-King model [39], which holds that the transport of the principal turbulent shear stress is of vital importance in the prediction of severe adverse pressure gradient flows. This new model does not consume much more computing time compared to the original version [37]. The  $k-\omega$  model used in this study is the SST  $k-\omega$  model.

In the Reynolds stress model, transport equations are solved for the individual Reynolds stresses and for another quantity that provides either a length-scale or a time-scale for turbulence, e.g., turbulence energy dissipation ( $\varepsilon$ ) or specific dissipation ( $\omega$ ). The individual Reynolds stresses are then used to obtain closure of the Reynolds-averaged momentum equation [29,30]. The exact form of the Reynolds stress transport equations may be derived by taking moments of the exact momentum equation. This is a process wherein the exact momentum equations are multiplied by a fluctuating property and the product is then Reynolds-averaged. Unfortunately, several of the terms in the complete equation are unknown and modeling assumptions are required in order to close the equations.

Whenever nonisotropic effects are important we should consider using the RSM. Note that in a turbulent boundary layer the turbulence is always nonisotropic, but isotropic eddy viscosity models, such as  $k-\omega$  and  $k-\varepsilon$  models, handle this type of flow excellently as far as mean flow quantities are concerned. Of

**Table 3 Mesh information for the turbulent flow cases for the  $k-\omega$  model**

Re	Number of cells	Minimum $y^+$	Maximum $y^+$
3000	2,335,690	0.11	2.96
5000	2,822,681	0.17	4.35

course, a  $k-\varepsilon$  model gives a very poor representation of the normal stresses. In flows with strong curvature and swirling flows nonisotropic effects often are important; therefore, RSM has also been used to predict the flow properties in the static mixer.

The RSM model contains no Reynolds-number dependence except for near-wall treatments [26]. The RSM model is primarily valid for the turbulent core. Consideration therefore needs to be given as to how to make these models suitable for wall-bounded flows. One common approach to modeling the near-wall region is using semi-empirical formulas (wall functions) to bridge the viscosity-affected region between the wall and the fully turbulent region. The use of wall functions obviates the need to modify the turbulence models to account for the presence of the wall. The wall function proposed by Launder and Spalding [40], usually called the "standard wall function", has been most widely used for industrial flows. The use of a wall function decreases the accuracy of the turbulence model prediction in low Reynolds number flows, in flows with a high pressure gradient near the wall region, and in strongly skewed three-dimensional flows. In this study, an enhanced wall treatment is employed and therefore, the viscosity-affected region near the solid wall is entirely resolved all the way to the viscous sublayer. In order to be able to resolve the laminar sublayer, the computational grid in the near wall region needs to be fine enough. The enhanced wall treatment, used in this study, is based on the work of Chen and Patel [41] and the model introduced by Wolfstein [42], which is used to determine the turbulent viscosity in the viscous sublayer region. A blending function is used in order to extend the applicability of the method throughout the laminar sublayer, the fully turbulent region, and the buffer region between the sublayer and the fully turbulent outer region.

## Numerical Simulation

**Mesh Generation.** Numerical mesh generation is the crucial initial step of any computational simulation problem. Effective numerical processes for CFD problems depend on the geometric modeling, grid generation, and grid quality. Hobbs et al. [19] used an unstructured grid of 295,999 tetrahedral cells for a six-segment mixer. Mesh quality tests, if applied, were not mentioned. Based on the authors' experiences, a tetrahedral mesh with no sliver cells for a geometry with highly twisted surface is difficult, if not impossible, to generate. The surface mesh shown in [19] includes surface cells, which can lead to a three-dimensional mesh with sliver cells (which have four, nearly coplanar points). In addition, there is no report on the study of the mesh density and its effects on the obtained results; however, Byrde and Sawley [20] claim that the grid density needed to obtain realistic results is much more than the grid density used by Hobbs et al. Byrde and Sawley used four different mesh densities for a six-segment mixer: 122,880, 376,320, 929,280, and 1,505,280 cells. They used an H-type mesh in the core of the pipe and an O-type mesh near the pipe wall [21]. The problem of using O-type mesh is an unnecessary concentration of small cells near the center of the pipe. Jones et al. [22] used a 1,035,125 cell structured mesh for a two-segment mixer with a long pipe and elbow prior to the mixing elements. The mesh type, the mesh generation algorithm, and the mesh density study are not mentioned; however, unnecessary small cells can be seen in the computational domain. An alternative to a structured mesh, and the concomitant difficulties, is to use a high quality unstructured mesh [43]. Here, an unstructured hexagonal mesh (which compared to a tetrahedral mesh is much more suitable for this kind of problem involving shear flow) was generated to model the six-element static mixer inside a pipe, using a code developed by the authors. The geometry was modeled exactly, with no simplifications. To achieve the most accurate results of the solver, all efforts have been taken to maximize the quality of the mesh. Instead of the traditional approach of three-dimensional unstructured mesh generation, in which the solid and boundary surfaces grid is generated prior to the volume meshing, here a novel technique is introduced. The flowfield geometry is

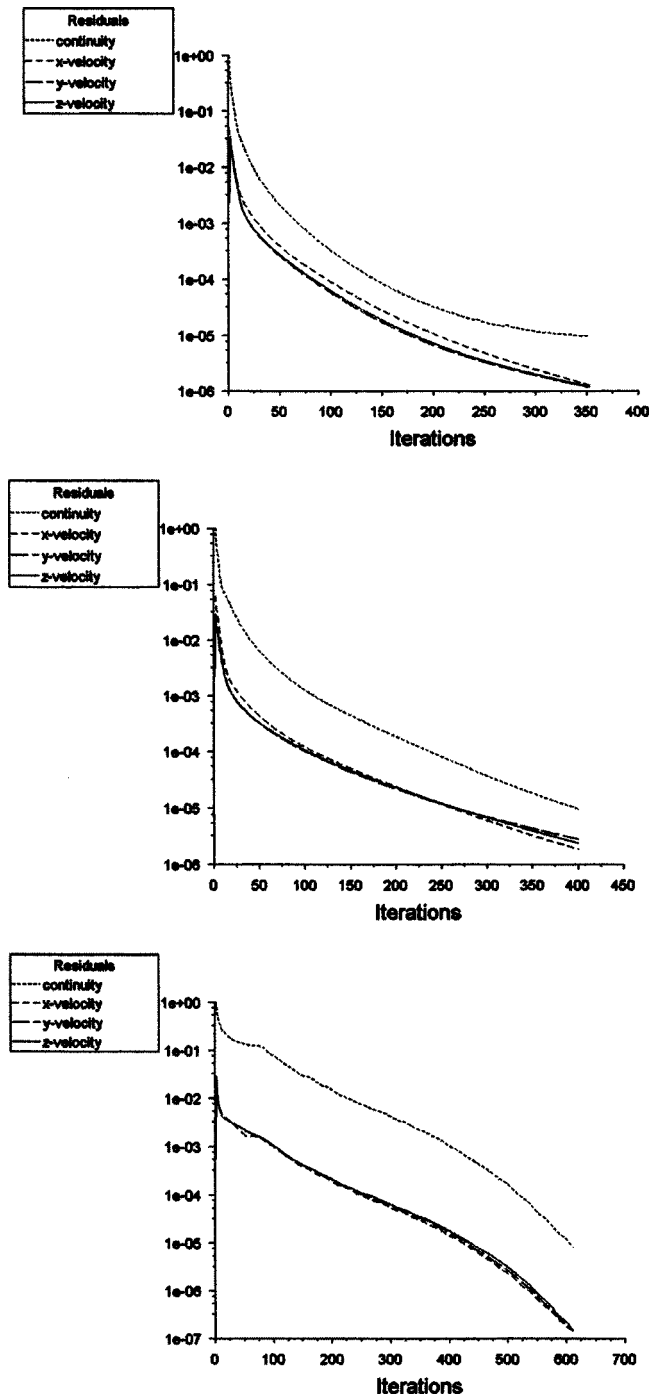


Fig. 3 Residual curves for  $Re=0.01$  (top),  $Re=10$  (middle), and  $Re=1000$  (bottom)

cut by a large number of parallel planes perpendicular to the pipe centerline ( $x_1$  direction). These parallel constant- $x_1$  planes are distributed uniformly with a distance, say  $\Delta s$ , of each other [as illustrated in Fig. 2(a) for one twisted surface equal to the surface of one mixing element]. The cross section of each plane is meshed with an interval size equal to the distance between each two planes,  $\Delta s$ . Figure 2(b) shows the cross-sectional mesh for two surfaces that are two parts of originally one cross-sectional circle cut by the twisted surface. The next step is to mesh the flowfield volume using these cross-sectional surface meshes. This technique leads to a high quality mesh, which in turn improves the rate of convergence of the flow solver. It also, makes the particle tracking

Table 4 Convergence of pressure drop across the mixer

Iterations	Pressure drop ratio	Averaged velocity ratio at the sixth element	Averaged vorticity ratio at the sixth element
3990	1.000424	1.000291	1.000440
4190	0.999913	1.000028	1.000045
4390	1.000018	1.000103	1.000214
4590	0.999998	0.999998	0.999968
4790	0.999999	1.000002	1.000003
4820	<b>1.000000</b>	<b>1.000000</b>	<b>1.000000</b>

calculations much faster and easier. Figure 2(c) shows two helical mixing elements and the result volume mesh on one mixing element. Table 2 shows the results of different mesh quality tests performed on the generated mesh with 1,043,249 cells, used in this study for cases where  $Re \leq 1000$ .

Here, maximum volume ratio means the ratio of the volume of the largest cell to the volume of the smallest one. Maximum face ratio is the ratio of the largest face to the smallest one. The aspect ratio is the maximum value of the average lengths of the edges in three coordinate directions in a cell to the minimum value of the average lengths of the edges in three coordinate directions in that cell. The diagonal ratio is the ratio of the longest diagonal to the shortest diagonal of a cell. The edge ratio is the ratio of the longest edge to the shortest edge of a cell. The midangle skewness is defined by the cosine of the minimum angle formed between the bisectors of the cell faces and is the maximum amount of the cosines of the three angles computed from the face-bisecting lines of the cell. Finally, the equal-size skewness is a measure of skewness, which is defined as follows:

$$\text{Equal-size skewness} = (V_{eq} - V)/V \quad (5)$$

where  $V$  is the volume of the cell, and  $V_{eq}$  is the maximum volume of an equilateral cell, the circumscribing radius of which is identical to that of the mesh element. More details about different computational mesh generation algorithms and different mesh quality tests can be found in [43,44].

*Considerations for Turbulent Flow.* A successful turbulent flow computation requires a sufficiently fine grid, particularly in regions of shear layers with a large rate of strain. For the problem studied here, a large portion of computational domain is in the near-wall region. Depending on the near-wall treatment used in a turbulent flow simulation, different meshing strategies must be used. For example, if wall functions are used, an excessively fine mesh near the walls may increase the error, because the wall functions are not valid in the viscous sublayer. More details can be found in [24]. A very fine, nonuniform mesh is needed to model turbulent flows, as used in this study. A standard approach to measure the fineness of the mesh in the near-wall region is to monitor the distance of the computational cell centroid from the solid wall measured in viscous length,  $y^+ = y\sqrt{\rho \tau_w / \mu}$ . For the methods used in this study, a fine grid with  $y^+$  of order of 1 is desirable in order to obtain an accurate result. Table 3 gives the information related to the computational grid used in this study for the  $k-\omega$  model. For the RSM model, values of  $y^+$  are slightly smaller than the values given in the table.

A uniformly refined mesh leads to an enormous computational cost. Here, an adaptive mesh approach is used, which adds a grid node in the center of an existing computational cell and divides the cell into four new cells. The deviation of orthogonality of the original uniform grid used in this study is negligible and thus this approach does not degenerate the mesh.

*Solver.* The numerical simulation of the flow and mixing in the helical static mixer has been performed via a two-step procedure. In the first step, the flow velocity and the pressure are computed. This has been achieved by the use of a commercial code. These

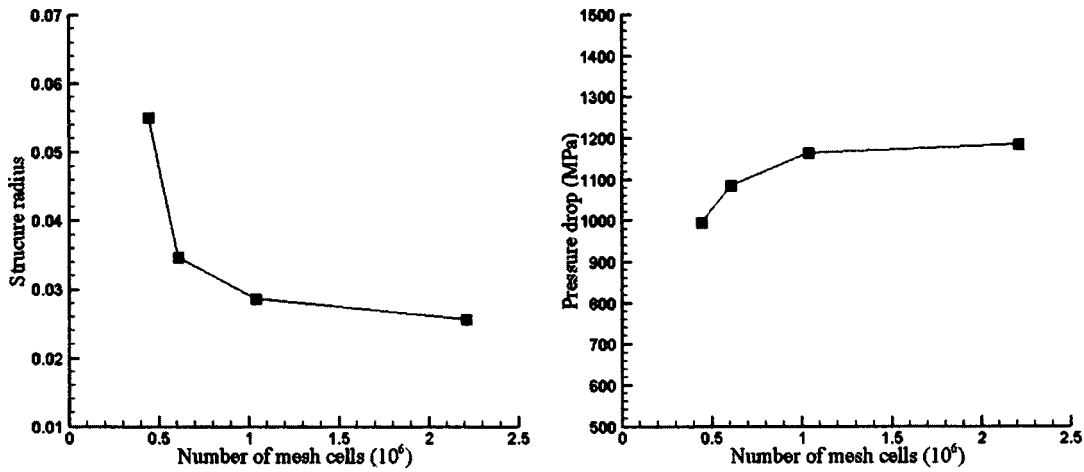


Fig. 4 The obtained structure radius (left) and the computed pressure drop (right) for  $Re=100$

values are then used as input to the second step that consists of the calculation of the particle trajectories within the computed flowfields and other parameters that are subject of interest in the study of a mixer performance. This has been achieved by the use of a code developed by the authors.

**Flow Computation.** The solver used in this study for the flow computation part is a commercial code: FLUENT (Fluent Inc., Lebanon, NH). The employed solver is a segregated, implicit, second-order upwind [45], double precision, finite volume solver. Using the segregated approach, the governing equations are solved sequentially. To obtain second-order accuracy, quantities at cell faces are computed using a multidimensional linear reconstruction approach [45,46]. Pressure-velocity coupling is achieved by using the SIMPLEC (SIMPLE-Consistent) algorithm [47]. The SIMPLEC pressure-velocity coupling scheme, part of the SIMPLE (semi-implicit method for pressure-linked equations) family of algorithms [48], is similar to the SIMPLE procedure, however it has been shown to accelerate the convergence in problems where pressure-velocity coupling is the main deterrent to obtaining a solution. As the convergence criterion, a scaled residual [49] less than  $10^{-5}$  is used here.

**Boundary Conditions.** No-slip boundary conditions are applied to the solid surface of the static mixer and also at the wall of the pipe. A constant mass flow rate constraint is applied at the inlet and outlet boundaries. Different Reynolds numbers for the flow inside the pipe are obtained by varying the mass flow rate at the inlet boundary. The velocity profile for fully developed flow in a pipe (parabolic distribution for laminar flow and one seventh-root law for turbulent flow) is used at the flowfield inlet. The turbulence intensity is used to specify the turbulent boundary conditions at the flow inlet. The turbulence intensity is equal to 6.99% for the case of  $Re=3000$ , and is 6.56% for the case of  $Re=5000$ . Near solid walls, an enhanced wall treatment, as described above, is employed for the case of the RSM turbulent model; and for the  $k-\omega$  model, low-Reynolds-number correction is applied at the near-wall region.

**Particle Tracking.** To determine the efficiency of a mixer, it is necessary to establish means by which the fluid mixing can be gauged both qualitatively and quantitatively. In the present study, this was achieved by calculating the trajectories of fluid particles in the flowfield of the mixer. This method avoids the problem of excessive numerical diffusion that is observed if the species continuity equations are solved [20].

For a steady flow, the particle trajectories correspond to stream-

lines. Therefore, trajectories are tracked by integrating the vector equation of motion, using the numerically computed velocity field as input.

$$\frac{dx_i}{dt} = u_i. \quad (6)$$

Some care must be taken when integrating the equation that describes particle motion in order to retain a sufficient degree of accuracy. Preliminary tests have indicated that while lower-order schemes appear to provide acceptable results, they accentuate the problem of *lost particles*; that is, particles that have trajectories cause them to be trapped near a solid wall, where the local velocity is zero, or leave the computational domain [20]. For the results presented in this paper, a fourth-order Runge-Kutta integration algorithm with adaptive time-step-size control was employed. In addition, to avoid problems near stagnation points, the numerical integration of the streamline equation was performed using a fixed spatial increment rather than a fixed time step. By this method, the trajectory of each fluid particle released at flowfield inlet can be tracked and the particle locations within different cross sections of the flowfield, e.g., at the end of each mixing element, can be obtained.

Some considerations are needed in using the results of a steady state RANS calculation. In turbulent flows, scalar transport and stirring are the result of both the large-scale coherent vortices and the broad range of turbulent eddies. RANS modeling procedure smoothes the flowfield and therefore, particle tracking, using the statistically stationary mean flow as the advecting velocity field, does not take into account the effect of small-scale turbulence on transport. In order to overcome this shortcoming, turbulent Reynolds stresses can be used to generate instantaneous velocity. In the RANS turbulence modeling approach, information about turbulent fluctuations is contained in the time-averaged Reynolds stresses of the form  $\overline{u'_i u'_j}$ . Stochastic techniques can be used in order to generate a random fluctuating velocity field using the turbulence intensities. These fluctuations are superimposed to the calculated time-averaged velocity field and create an instantaneous velocity fields. Fluid particle tracking is carried out using this instantaneous flowfield. A considerable amount of work in random flow generation using the RANS model can be found in the literature, e.g., [50–54]; however, in some of these works, the generated flowfield does not satisfy the requirement of spatial inhomogeneity and anisotropy of turbulent shear stresses or the generated flowfield does not satisfy the continuity conservation law [55]. In this study, a random flow generation technique presented

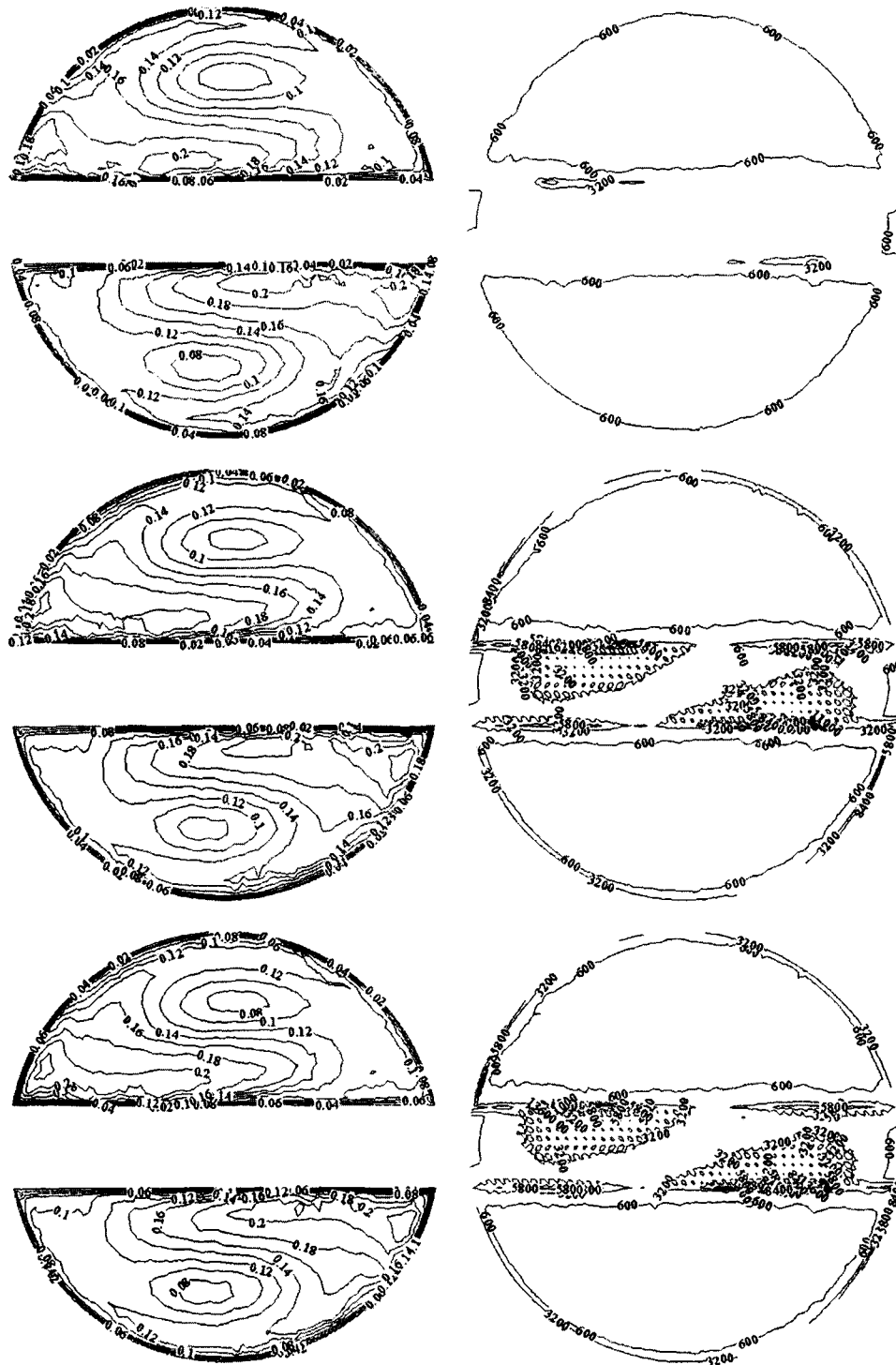


Fig. 5 Velocity contours (m/s) and the vorticity contours (1/s) for  $Re=5000$  (using the  $k-\omega$  model)

by Smirnov et al.[55] is employed. The method is a modified version of Kraichnan's technique [56] and is able to generate a realistic instantaneous flowfield efficiently.

Furthermore, it was found that the mean velocity has an impact on the number of lost particles. The mass flow rate can be written as the following:

$$\dot{m} = \frac{\pi d \mu}{4} Re \quad (7)$$

For a given geometry, the mass flow rate is only a function of viscosity for any specified Reynolds number. Therefore, by changing the values of the working fluid viscosity, different mean velocities can be obtained for the same Reynolds number. For the case of  $Re=5000$ , using the  $k-\omega$  turbulence model, it was found that by decreasing the magnitude of order of the mean velocity by four, the number of lost particles decreased by a factor of 0.7158. It is worthwhile mentioning that this effect is only significant for high Reynolds numbers. With these considerations, the number of

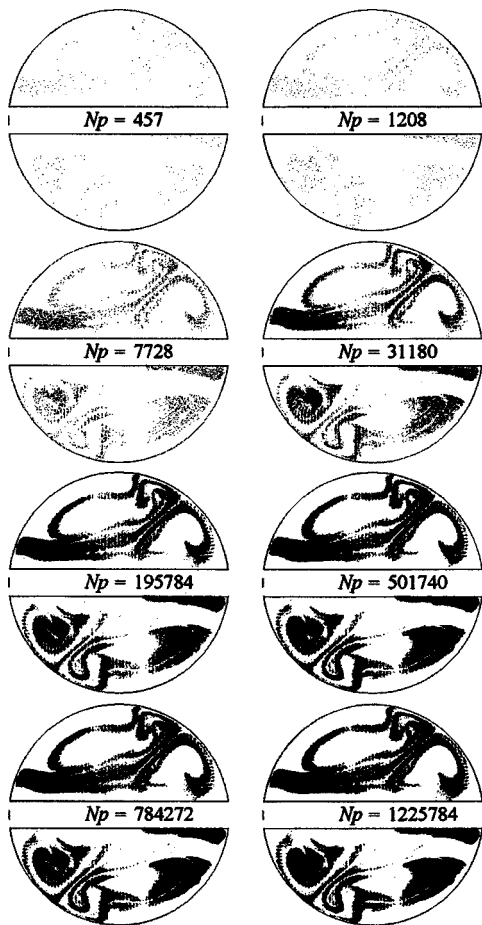


Fig. 6 Images of particle distribution at second element for  $Re=1000$  (for different released particles number,  $N_p$ )

lost particles was minimized to not more than 7.10%. No attempt was made to recuperate lost particles by re-injection into the flowfield, since this may unduly perturb the mixing analysis.

To obtain an accurate evaluation of the mixing, a study of the trajectories of a large number of particles has been undertaken. At the entry of the inlet pipe section, 501,740 zero-volume and zero-mass particles were distributed uniformly over the half-circular plane of the inlet surface. The diameter of this plane is perpendicular to the front edge of the first mixing element in the pipe. This is a simplified model for the diametrical feeding of the mixer with two components fluids. Particle trajectories corresponding to only one of the working fluids are calculated.

The computational grid consists of constant- $x_1$  planes, which can be used as buckets. These buckets are used to find the velocity in each point of flowfield. This search is fast and efficient and increases the speed of integration code of particle tracking. While integrating, the time step is chosen based on the axial velocity ( $u_1$ ) so that the particle currently existing on one constant- $x_1$  plane falls on the next constant- $x_1$  plane. In the next step, a search is performed in this new constant- $x_1$  plane to find the nearest neighboring grid points surrounding the particle. Once these neighboring grid nodes are located, an inverse distance weighted average function can be constructed to calculate the velocity components for the particle. Although for the case of turbulent flow regime the computational grid is not uniform, it is still possible to use the method mentioned here to track the trajectories of particles by the use of a tree data structure.

**Numerical Solution Accuracy.** It is important that the accuracy of the numerical solutions be analyzed before confidence in

the predictive ability of the numerical techniques can be justified. For the present study of mixing under noncreeping flow conditions, there is unfortunately an absence of experimental data sufficiently detailed and accurate to undertake a complete validation of the numerical results. Comparison with certain experimental values of the pressure drop across the mixer, measured for the standard element twist angle, shows very good agreement over a range of flow conditions; however, good agreement with the experimental data for such a global measure is not sufficient to guarantee accurate simulation of the flow in the complex geometry [20]. Therefore, a detailed mesh convergence study has indicated that the computational mesh employed in the present study is sufficiently refined to provide good numerical resolution. A coarse mesh is not able to resolve adequately the complex flow behavior and leads to a considerably large number of lost particles. Moreover, a study conducted using different numbers of particles for the mixing analysis, has shown that the results are independent of the number of particles. The use of an inadequate number of particles to analyze mixing can be misleading and can create a false impression of good mixing in the presence of the fine flow structure [20].

## Results and Discussion

Using the numerical method described above, the flow in a six-element static mixer has been analyzed for a number of different flow conditions. In each case the initial conditions are set so that the axial velocity ( $u_1$ ) is equal to bulk velocity and  $u_2=u_3=0$ . Figure 3 shows the residual history for three different Reynolds numbers. The number of iterations required to obtain a converged solution was found to be a function of the flow regime. For a mesh containing 1,043,249 cells, from 350 (for creeping flows,  $Re=0.01$ ) to 610 (for  $Re=1000$ ) iterations were necessary to reach converged results. For turbulent flows, up to 9700 iterations is needed to obtain a converged solution. The needed computational time varies from few hours (for laminar cases) up to couple days (for turbulent cases). As the convergence criterion, a scaled residual less than  $10^{-5}$  for all scalar equations, is used here. Table 4 shows the values of pressure drop across the mixer, area-weighted average velocities, and area-weighted average vorticity at the end of the sixth mixing element, nondimensionalized by the values as predicted from the converged solution, for the case of the  $k-\omega$  model at  $Re=3000$ .

The results obtained were found to vary negligibly once this condition was reached. For example, for the  $k-\omega$  model at  $Re=3000$ , the convergence criterion of  $10^{-7}$  was also examined; no noticeable changes in the flowfield properties, in the number of lost particles, and also in the particle trajectories, were detected (e.g., the difference between values of the calculated pressure drop is less than 0.00036%).

**Solution Accuracy Evaluation.** For numerical simulations, error estimation is an important and essential task. The validity of the obtained results can be examined via various numerical studies or by comparison with experimental data. In the present study the available experimental data is the pressure drop inside the pipe that includes the mixer. Here, the pressure drop is defined as the absolute difference between the area-weighted average pressure at the computational flowfield inlet and the area-weighted average pressure at the flowfield exit. This is an important quantity for static mixer and provides a measure of the required energy for using the mixer in the pipeline. The maximum difference between the measured value of the pressure drop and the computed pressure drop is for the case of  $Re=5000$ , using the  $k-\omega$  model (4.18%); however, detailed experimental data suitable for comprehensive validation purposes are not available. The effects of the size of the mesh used for the flowfield computations and the influence of the number of particle trajectories calculated to analyze the mixing process have been investigated.

In the present study, the computed pressure drop in the pipe



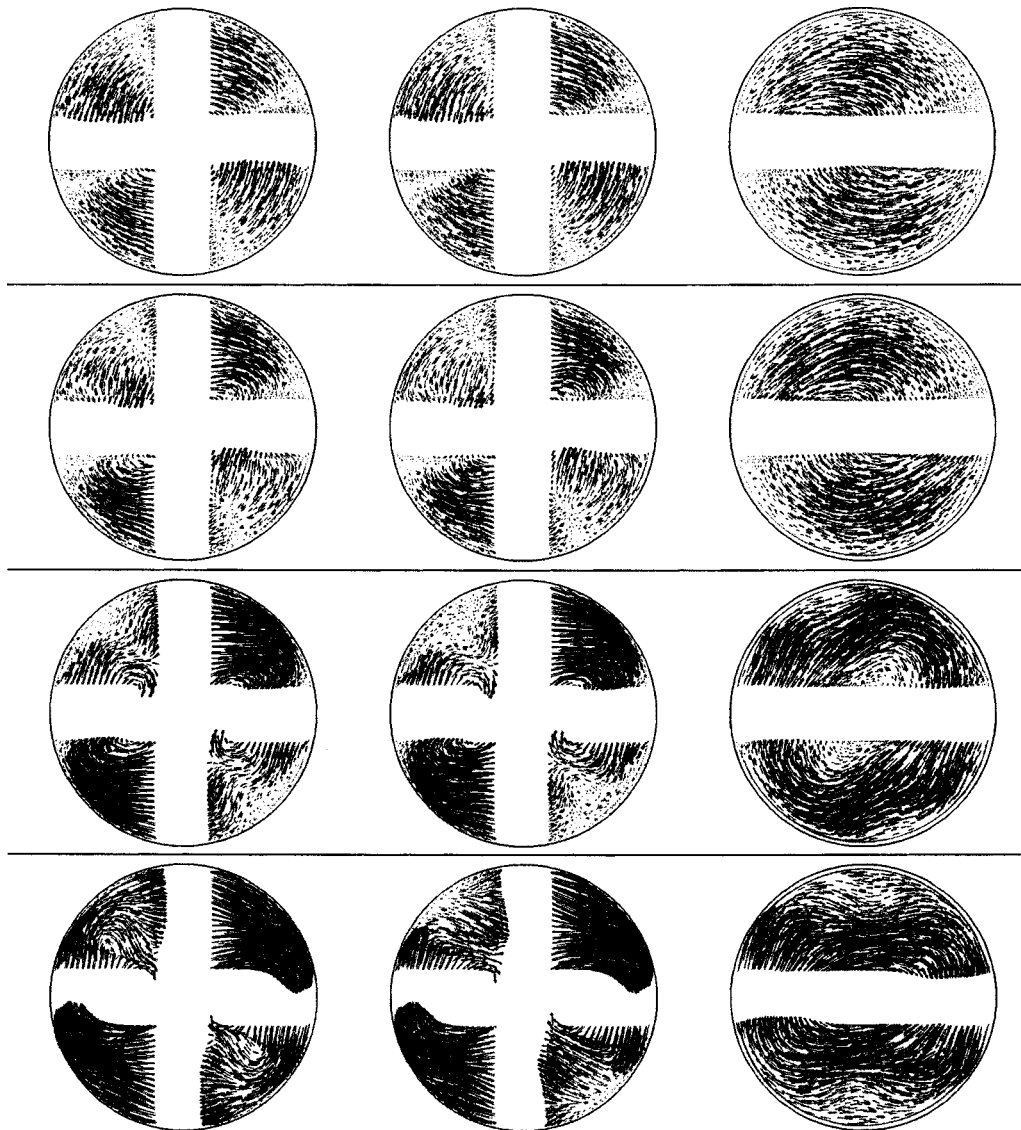


Fig. 7 Velocity field at second, fourth, and sixth elements

along the mixer and velocity contours at the computational flow-field outlet are considered. As a quantitative measure of the fluid mixing, the size of the structures at the flowfield outlet is considered. The two-dimensional structure radius at a given axial location ( $r_s$ ), normalized to the pipe radius, has been defined to correspond to the radius of the largest circle that can be drawn around a particle of one of the fluid components that does not contain any particles of the other fluid component [14]. This structure radius corresponds to the striation thickness, generally measured experimentally [21].

**Mesh Convergence.** Different mesh sizes, which contain 446,489 cells, 613,668 cells, 1,043,249 cells, and 2,210,186 cells,

were used to numerically determine the flowfield. The obtained velocity field in each case was used to calculate the trajectories of 501,740 particles. Figure 4 presents the structure radius (left) and the computed pressure drop (right) values for each of these meshes for  $Re=100$ . As the computational mesh is made finer, the results for both the structure radius and the pressure drop show convergence. The difference in the computed pressure drop for the coarser mesh with 613,668 cells and the finer mesh with 1,043,249 cells is 7.16%; however, the difference between the obtained structure radii for these two meshes is 21.43%. Therefore, the general behavior of the flow is not as dependent on the mesh density as the mixing process is. However, for a mesh

Table 5 Mean axial velocities and velocity magnitudes (m/s)

Re	Averaged axial velocity			Averaged velocity magnitude		
	Second	Fourth	Sixth	Second	Fourth	Sixth
1	0.000278	0.000278	0.000278	0.000307	0.000307	0.000306
10	0.002777	0.002779	0.002123	0.003078	0.003077	0.002457
100	0.027689	0.027698	0.021245	0.038384	0.037648	0.029405
1000	0.275793	0.2761991	0.2125812	0.5210491	0.4995831	0.4377990

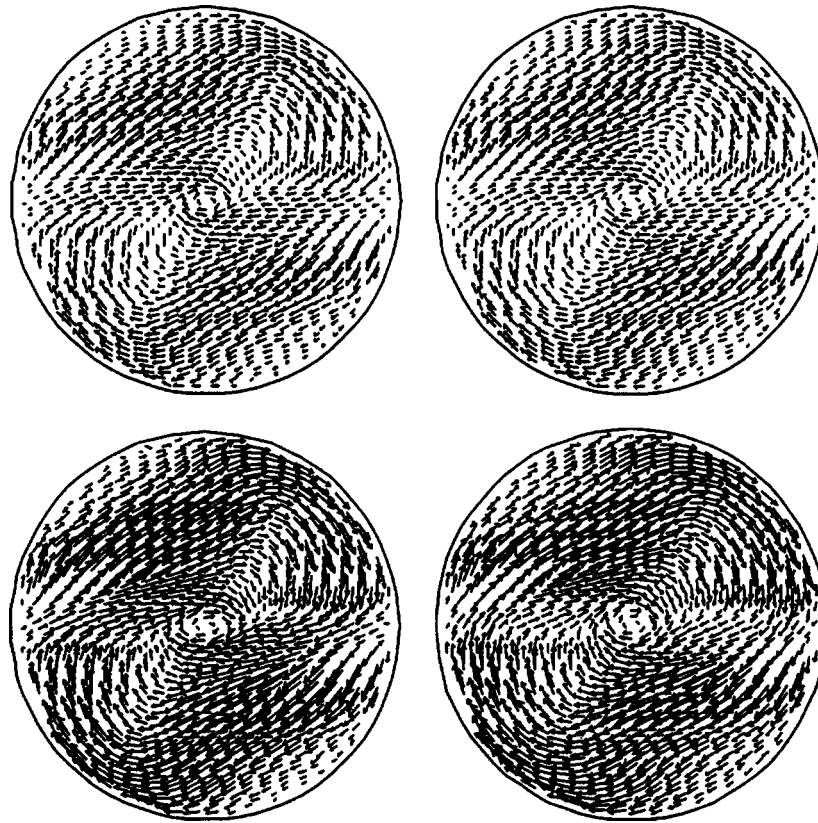


Fig. 8 Velocity field calculated by  $k-\omega$  (left) and RSM (right) models

Table 6 Maximum velocity at the sixth element and total drop in pressure, predicted using different turbulence models

Maximum velocity at the end of the sixth element	
Re=3000, $k-\omega$ model	1.88 m/s
Re=3000, RSM model	1.81 m/s
Re=5000, $k-\omega$ model	3.11 m/s
Re=5000, RSM model	2.92 m/s
Pressure drop in the flow	
Re=5000, $k-\omega$ model	48,758 Pa
Re=5000, RSM model	47,620 Pa
Experimental data	46,800 Pa
Fluid properties	
Density ( $\rho$ )	1000 kg/m <sup>3</sup>
Viscosity ( $\mu$ )	0.001 kg/m s

with 2,210,186 cells, the variation of obtained results is negligible compared to the results obtained using a mesh with 1,043,249 cells. In addition, for the case of Re=10, the difference in the computed pressure drop for the coarser mesh with 613,668 cells and the finer mesh with 1,043,249 cells is 8.26%, and the difference between the obtained structure radius is 38.46%. This is in agreement with the results obtained by Byrde and Sawley [21]. Moreover, the mesh size has a significant impact on the number of lost particles. The number of lost particles is reduced by using a finer mesh, e.g., for the case of Re=10, the number of lost particles for the finer mesh (with 1,043,249 cells) is 90.06% of the number of lost particles for the coarser mesh (with 613,668 cells).

Figure 5 shows the velocity (left) and vorticity (right) contours for Re=5000, predicted by different grids with 1,478,334, 2,086,955, and 2,822,681 cells, respectively, from top to bottom. The pressure drops across the mixer predicted using grids containing 1,478,334 and 2,086,955 cells are 91.19% and 98.33% of the

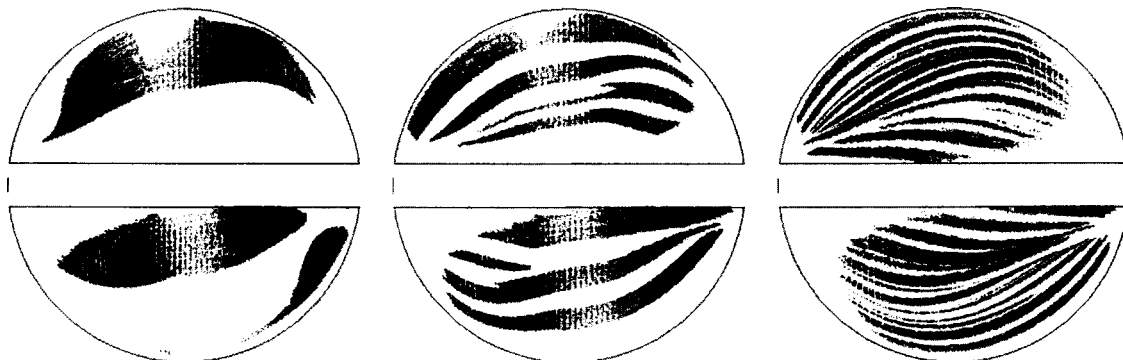


Fig. 9 Particles' locations at second, fourth, and sixth elements (Re=0.01)

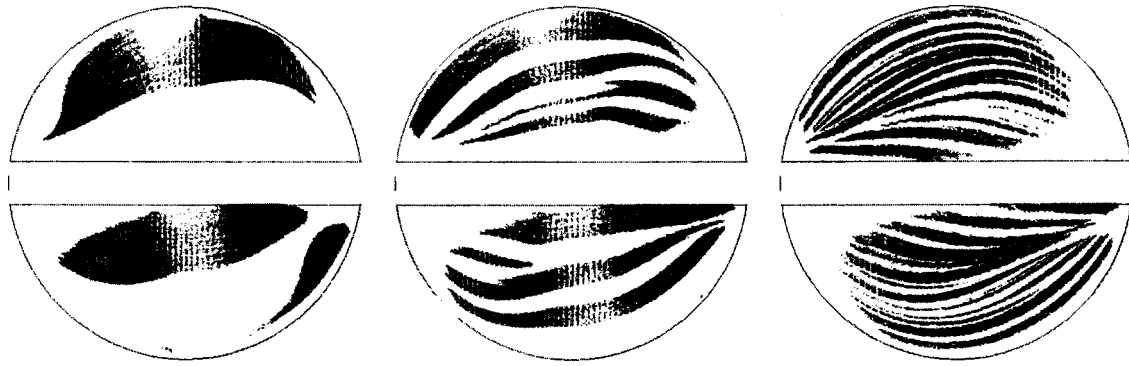


Fig. 10 Particles' locations at second, fourth, and sixth elements (Re=0.1)

pressure drop predicted using a mesh with 2,822,681 cells. The obtained results do not change noticeably after that.

**Number of Particles.** Different numbers of particles ( $N_p=457, 1,208, 7,728, 31,180, 195,784, 501,740, 784,272, \text{ and } 1,225,784$ ) were used to analyze the mixing. By increasing the number of particles released at the flowfield inlet, it is possible to discern finer structures and thus quantify the mixing efficiency with a higher precision. Figure 6 shows the influence of the number of particles released at the flowfield inlet from the reference point of a stationary observer. A relatively small  $N_p$  gives the impression that a high level of mixing has been achieved at the exit of the mixer. As the  $N_p$  is increased, the presence of the striations associated with the mixing process is more and more evident. It can be seen that 501,740 particles at the flow inlet can give a correct image of mixing; although using a higher value for  $N_p$  leads to a more pronounced mixing pattern, but the difference between the obtained results is not that significant to justify the long CPU time needed for calculations.

#### Obtained Numerical Solutions.

**Flowfield Parameters.** The velocity fields for each Reynolds number were obtained. The cross-sectional velocity fields are illustrated in Fig. 7, which show the cross-sectional projection of the velocity vectors at the end of the second, the fourth, and the sixth elements, respectively, from left to right, and correspond to Re=1, Re=10, Re=100, and Re=1000, respectively, from top to bottom. To obtain clear images, the length scale of the product of the velocity vector and the Reynolds number in each case is set to a constant. The cross-sectional velocity fields for Re=1, Re=0.1, and Re=0.01 (not shown in here) are almost identical. Different flow patterns for creeping, laminar, and turbulent flows can be seen. In addition, it is observed that after the second element, four velocity zones are created. These zones combine together and create two velocity zones, as the flow passes through the mixer. The

transition from four zones to two zones occurs sooner, when the Reynolds number is increased. Using water properties ( $\rho = 998.2 \text{ Kg/m}^3$  and  $\mu = 0.001003 \text{ Kg/m s}$ ), the velocity fields were obtained for Re=1, Re=10, Re=100, and Re=1000. Values of mean axial velocities and mean velocity magnitudes at different flow cross sections are shown in Table 5.

As expected from the conservation of mass law, the averaged axial velocity is proportional to Reynolds number, and it is the same for each case at the end of the second and the fourth mixing elements. At the end of the last element, the averaged axial velocity is decreased as the flow cross section is increased. As can be seen, the ratio of the averaged axial velocity to the averaged velocity magnitude is about 0.9 for Re=1 and Re=10 at all flow cross sections, while it is about 0.7 for Re=100, and it is about 0.5 for Re=1000. Therefore, the cross-sectional component of the velocity vectors is increased as the Reynolds number increases, which can lead to a higher degree of mixing.

The velocity fields at the end of the sixth mixing element, obtained by using  $k-\omega$  (left) and RSM (right) turbulence models, are shown in Fig. 8 for Re=3000 (top) and Re=5000 (bottom). Results of both models are very similar; however, they are not identical. Table 6 shows the maximum velocity obtained by each model at the end of the sixth element and also the pressure drop from the flow inlet to the flow outlet, and the existing experimental data for the pressure drop. The fluid properties used to obtain these results are shown in this table. The maximum difference in calculated velocities is 6.37% for the case of Re=5000. For the case of Re=5000, the  $k-\omega$  model overestimates the pressure drop by 4.18%, and the RSM model overestimates the pressure drop by 1.75%.

Using the same initial conditions and the same convergence criteria, the number of iterations needed using the RSM turbulence model to converge is 3.34 to 4.34 times of the iterations needed using the  $k-\omega$  model to converge. Furthermore, memory

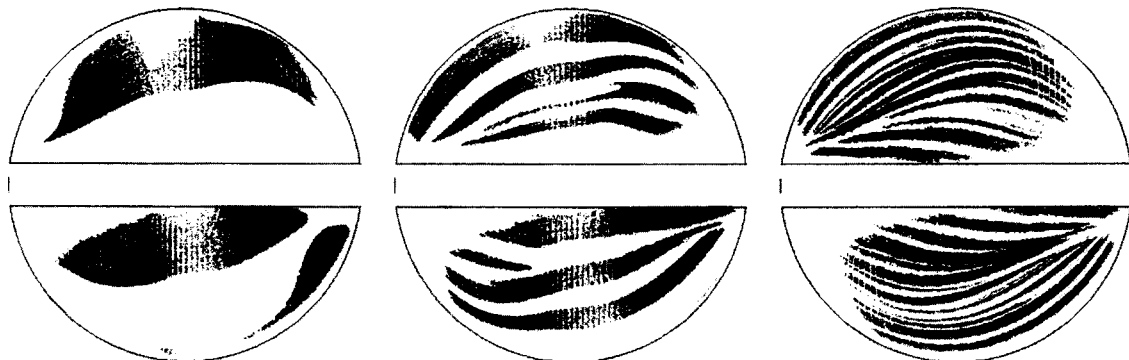


Fig. 11 Particles' locations at second, fourth, and sixth element (Re=1)

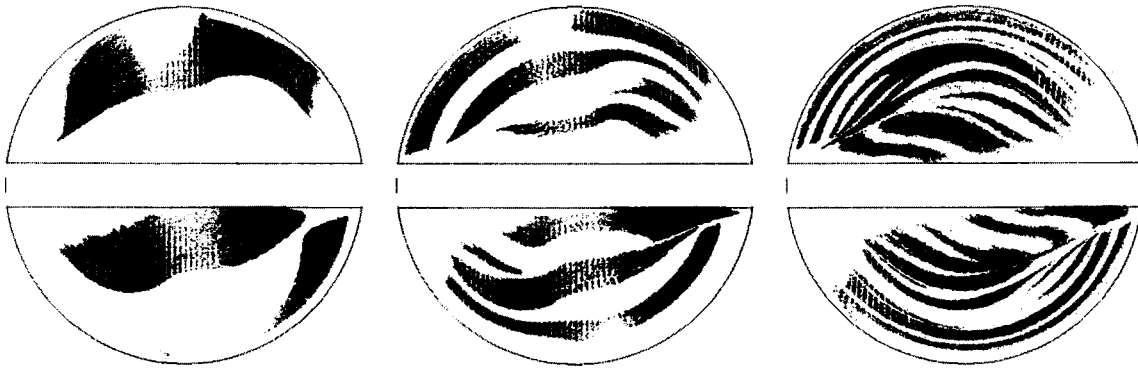


Fig. 12 Particles' locations at second, fourth, and sixth elements (Re=10)

needed by the RSM model is 1.11 times of needed memory using the  $k-\omega$  model. It was also observed that the CPU time per iteration needed by the RSM model is 1.19 times of the CPU time needed using the  $k-\omega$  turbulence model; however, it has been noted that the RSM in FLUENT requires 50–60% more CPU time per iteration compared to the  $k-\omega$  and  $k-\omega$  models, and also 15–20% more memory is needed [57].

**Particles Trajectories.** The trajectories of particles injected into the mixer from the top half of the flow inlet have been calculated. The plots of the positions of fluid particles at the end of the second, the fourth, and the sixth elements, respectively, from left to right, shown in Figs. 9–16, illustrate the redistribution of the released particles via the combined effects of flow division and reversal, resulting in stretching and folding of the observed structures. Separated islands are distinguishable after the flow passes the second mixing element. Increasing the Reynolds number breaks these few large islands into several smaller islands.

The islands, observed after the second elements in low Reynolds number flows, are divided to narrow line shape regions when flow passes the fourth element, which can be still recognized after the sixth element at the lower Reynolds number. Again, increasing the Reynolds number breaks the separated areas and therefore increases the mixing of fluid particles in the same cross-section.

The particles' distributions at the end of the sixth mixing element, obtained by using  $k-\omega$  (left) and RSM (right) turbulence models, are shown in Fig. 17 for Re=3000 (top) and Re=5000 (bottom). Results of both models are similar, however, they are not identical.

**G-value.** About sixty years ago, Camp and Stein [58] developed the root-mean-square  $G$ -value to quantify the mixing in turbulent flocculation basins by analogy with the shear rate in a simple, one-dimensional, laminar shear flow: the Couette flow. The

$G$ -value became a universal measure of mixing in the following decades. However, it has been demonstrated that the original derivation of the  $G$ -value was flawed for three-dimensional flows [59,60] and cannot be universally applied to different types of mixers or different size mixers. Nonetheless, the  $G$ -value remains entrenched in the engineering literature and continues to be used [22]. Because of that and also because it can be calculated easily, it is not entirely futile to use the obtained numerical results to calculate the  $G$ -value and explore it. For any in-line mixer, the  $G$ -value is calculated based on the energy losses that occur in the mixer as follows

$$G\text{-value} = \left( \frac{Q\Delta p}{\mu V_m} \right)^{1/2} \quad (8)$$

For the static mixer studied here, Eq. (8) can be written as

$$G\text{-value} = \frac{1}{2} \left( \frac{\pi D}{V_m} \right)^{1/2} \left( \frac{\text{Re} \Delta p}{\rho} \right)^{1/2} \quad (9)$$

Figure 18 shows the calculated  $G$ -values for different flow conditions. As can be seen, the  $G$ -value increases as the Reynolds number increases. In addition, the rate of increasing of the  $G$ -value is enhanced when the Reynolds number increases, suggesting that the helical static mixers are not very energy efficient in turbulent flows.

As can be seen from Eq. (9), for a given geometry and a specific Reynolds number, the  $G$ -value is a function of material density and the pressure drop of the flow in the mixer. The density of the material used here to calculate the  $G$ -value is  $10^3 \text{ kg/m}^3$ . For the case of Re=1000,  $G$ -value is  $29,279,317.3570 \text{ s}^{-1}$ ; however, for a material with a density of  $10^4 \text{ kg/m}^3$ , the  $G$ -value is  $292.7856 \text{ s}^{-1}$  (for the same Reynolds number), which is  $10^{-5}$

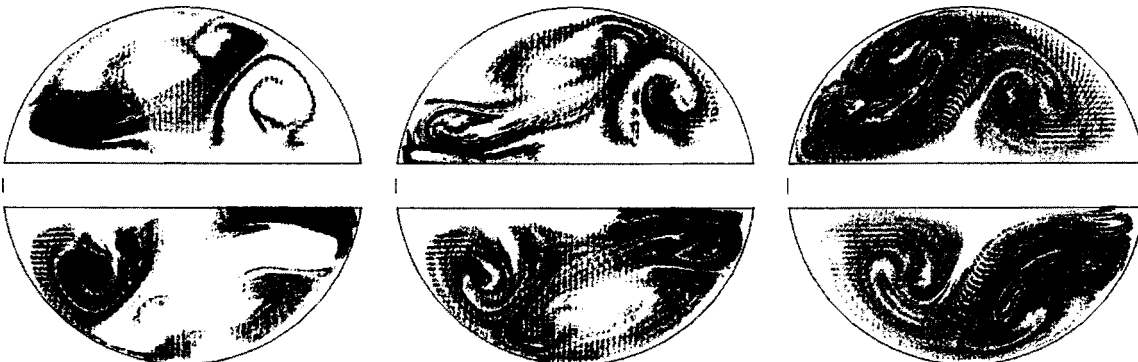


Fig. 13 Particles' locations at second, fourth, and sixth elements (Re=100)

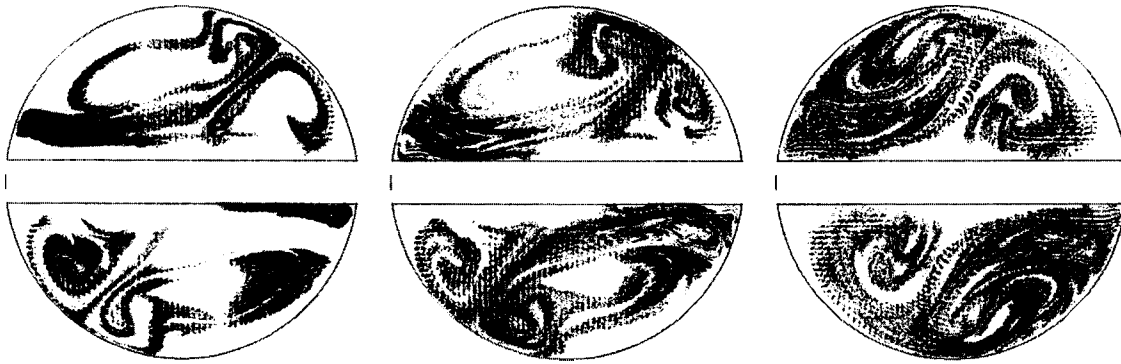


Fig. 14 Particles' locations at second, fourth, and sixth elements (Re=1000)

times smaller than the first value.

**Particle Distribution Uniformity.** The perfect mixing of two fluids can be defined as a uniform distribution of all fluid particles in the flowfield cross section. Based on this concept, a new parameter is introduced to quantify the degree of mixing. First, assume that the cross section of the flow is divided into very small, plane sectors identical in shape and size. If  $N_s$  is the total number of plane sectors, and  $N_{(i)}$  is the number of particles placed in the  $i$ th sector, then the **particle distribution function of the first kind** for the  $i$ th sector is given by

$$pd_1(i) = \frac{\left| \frac{N_p}{N_s} - N_{(i)} \right|}{N_p} \quad (10)$$

If the particles are distributed uniformly at the flow cross section, the value of  $pd_1(i)$  is zero for all the sectors ( $i=1, N_s$ ). If all particles placed in only one sector  $pd_1(i)=1-1/N_s$  for that sector and it is  $1/N_s$  for the rest. Thus,  $0 \leq pd_1(i) \leq 1-1/N_s$ , because of  $N_s \geq 2$ . However, these are two extreme cases.

Now assume the flowfield cross section is divided into equal angles by a large number, say  $N_l$ , of symmetry lines. If the number of particles on the left side of the  $i$ th symmetry line is  $N_{Left}(i)$ , and the number of particles on the right side of this line is  $N_{Right}(i)$ , then the **particle distribution function of the second kind** for the  $i$ th symmetry line is given by

$$pd_2(i) = \frac{|N_{Left}(i) - N_{Right}(i)|}{N_p} \quad (11)$$

If the distribution of the particles is uniform,  $pd_2(i)=0$  for  $i=1, N_l$ . If all the particles are placed between two consecutive symmetry lines, then  $pd_2(i)=1$  for  $i=1, N_l$ .

Using the particle distribution functions of the first and the

second kind, the **particle distribution uniformity (PDU)** can be defined as

$$PDU = \left( 1 - \frac{1}{2 \left( 1 - \frac{1}{N_s} \right)} \sum_{i=1}^{N_s \rightarrow \infty} pd_1(i) \right) \left( 1 - \frac{1}{N_l} \sum_{i=1}^{N_l \rightarrow \infty} pd_2(i) \right) \quad (12)$$

This function varies between zero (a completely nonuniform distribution of particles) and one (a totally uniform distribution of particles). It is worthwhile noticing that to obtain a meaningful value for  $PDU$ ,  $N_s$  should be smaller or equal to  $N_p$  and  $N_l$  should be smaller or equal to  $\frac{1}{2}N_p$ ; also, each of the  $N_s$  and  $N_l$  should be greater than or equal to 2. The calculated  $PDU$  values for different flow conditions and at the different flowfield cross sections (at the end of the second, the fourth, and the sixth mixing elements) are shown in Fig. 19 for  $N_p=501,740$ . The  $PDU$  values obtained for  $Re=0.01$  and  $Re=0.1$  (not shown in the figure) are very close at the same cross sections. The  $PDU$  values obtained for  $Re=0.01$  are very close to these values for  $Re=0.1$  (not shown in the figure) at each flow cross section. For the case of  $Re=10$ , the  $PDU$  value decreases at the end of the last mixing element. For  $Re=0.01$ , the  $PDU$  is slightly less than 0.7 at the end of the second mixing element. By increasing the Reynolds number from 0.01 to 1, and from 1 to 10, and also from 10 to 100, the  $PDU$  value at the end of the second element is found to decrease. As the flow passes through the mixer, the  $PDU$  value slightly decreases at the fourth mixing element for creeping flows and it increases again at the end of the last mixing element. For laminar flows,  $PDU$  values increase upon increasing the number of the mixing elements. It is recognized that by changing the flow pattern from creeping flow to a higher Reynolds number laminar flow, the rate of increasing of the  $PDU$  value is also increased. It can be seen that by increas-

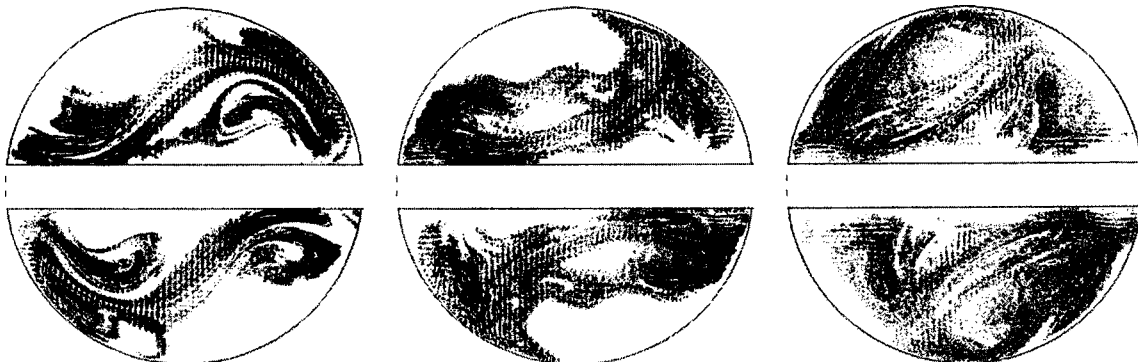


Fig. 15 Particles' locations at second, fourth, and sixth elements (Re=3000)  $k-\omega$  model

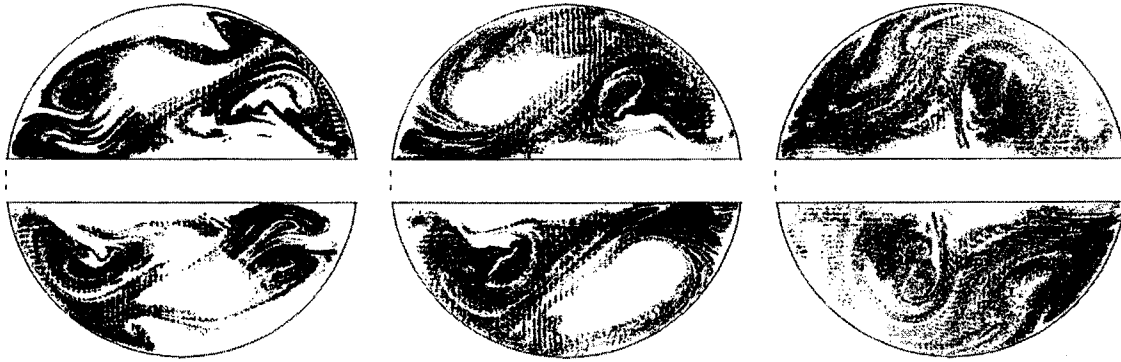


Fig. 16 Particles' locations at second, fourth, and sixth elements ( $Re=5000$ )  $k-\omega$  model

ing the Reynolds number from  $Re$  of the order of  $10^1$  to  $Re$  of the order of  $10^2$ , the rate of increase of  $PDU$  values, based on the number of mixing elements, increases. This suggests that the helical static mixer is more efficient for these Reynolds numbers compared to creeping flows, as it was discussed by Byrde and Sawley [20,21]. Helical static mixer behavior is different for  $Re=10$  and  $Re=1000$ . Although the  $PDU$  increases from the second mixing element to the fourth element, at the end of the last mixing element,  $PDU$  decreases. For  $Re=10$ , the  $PDU$  value at the end of the last element is even less than the  $PDU$  at the end of the second mixing element, which is in contrast with the mixer behavior for all other flow Reynolds numbers. It suggests that helical static mixers are less effective for very low Reynolds number (laminar) flows.

Figure 20 shows the values of  $PDU$  at the fourth mixing element for different Reynolds number from  $Re=0.01$  to  $Re=5000$  using the RSM model for turbulence cases. As can be seen, the values of  $PDU$  is almost the same for creeping flows, it increases as the flow pattern changes from creeping flow to laminar flow

and again when from laminar flow to turbulent flow. By increasing the Reynolds number in laminar flows, the  $PDU$  increases, however, the high rate of changes of  $PDU$  values is around Reynolds number of the order of  $10^2$ . The values of  $PDU$  increase in turbulent flow regime, by increasing the Reynolds number.

Figure 21 compares the  $PDU$  values for  $Re=3000$ , predicted by the  $k-\omega$  and the RSM models. These two models do not predict the same value for  $PDU$ ; however, the results are close to each other. The maximum different, which is 3.65%, occurs at the second mixing element.

If the velocity field obtained by a steady state RANS model is used to predict the particle redistribution in flow cross section, without applying stochastic techniques to generate an instantaneous velocity field, then the predicted  $PDU$  values will be up to 9% different from those predicted using the instantaneous velocity field generated by stochastic techniques.

As expected, the  $PDU$  value is only a function of the Reynolds number for a specific mixer. The density of the material used here to calculate the  $PDU$  value is  $10^3 \text{ kg/m}^3$ . For a material with a

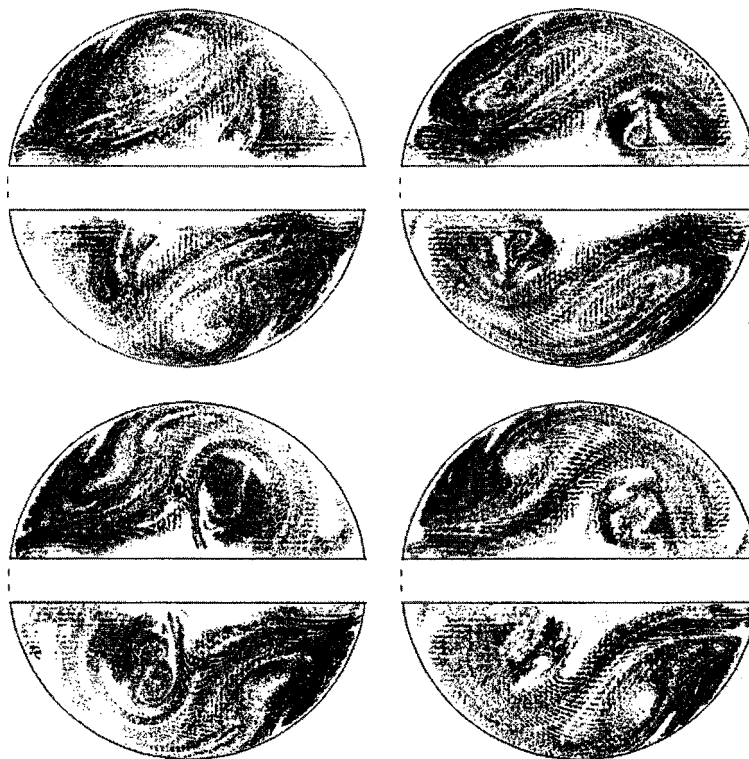


Fig. 17 Particles' locations calculated by  $k-\omega$  (left) and RSM (right) models

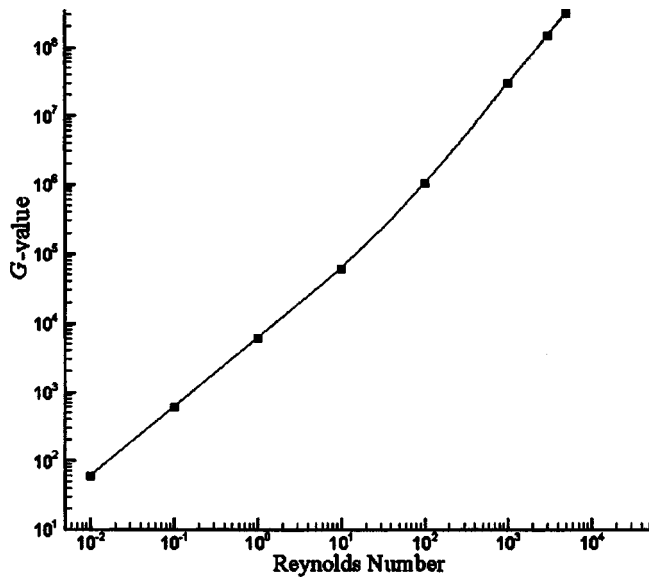


Fig. 18 *G*-value calculated for  $Re=0.01, 0.1, 1, 10, 100, 1000, 3000,$  and  $5000$

density of  $10^4 \text{ kg/m}^3$ , for  $Re=1000$ , *PDU* value changes by 0.2%. The *PDU* value is also changed, when the accuracy of the solver is changed. For example, for the case of  $Re=100$ , the calculated *PDU* value at the fourth mixing element is 28% larger when the second-order flow solver is used compare to the calculated *PDU* value based on the obtained results of the first-order flow solver. Moreover, it may worthwhile noting that the obtained *PDU* value is not very sensitive to the value of  $N_p$ , when  $N_p$  is large enough. For example, for  $N_p=195,784, 501,740,$  and  $784,282$ , the obtained values for *PDU* at the end of the second mixing element for  $Re=1000$  are 99.7%, 99.8%, and 100%, respectively, of the calculated *PDU* value when  $N_p=1,225,784$ . However, for  $N_p=31,180$ , the obtained value for *PDU* is 97.4% of the calculated *PDU* value when  $N_p=1,225,784,784$ .

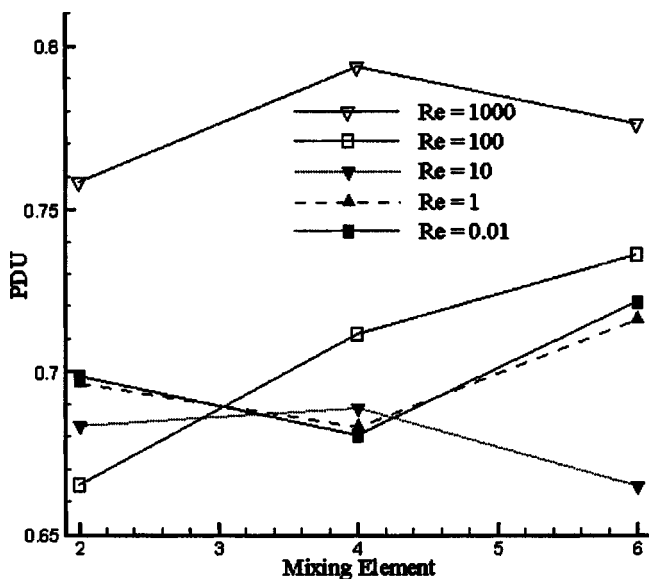


Fig. 19 *PDU* values calculated for  $Re=0.01, 1, 10, 100,$  and  $1000$ , at the second, fourth, and sixth mixing elements

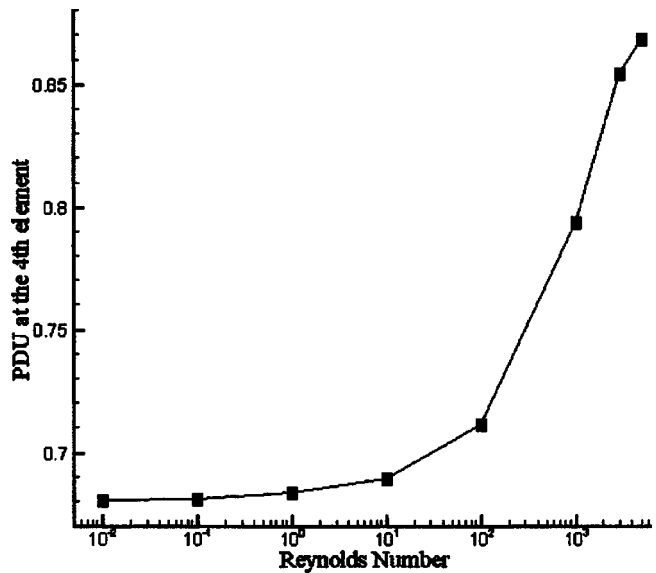


Fig. 20 *PDU* values for  $Re=0.01, 0.1, 1, 10, 100, 1000, 3000,$  and  $5000$  at the fourth mixing elements

### Conclusion

Performance of an industrial helical static mixer was studied efficiently on a PC. Comparison with certain experimental values of the pressure drop across the mixer measured for the standard element twist angle shows very good agreement over a range of flow conditions. However, it is emphasized that further validation is required to quantify the accuracy of mixing patterns predicted; it can be achieved when detailed experimental data is available and when more realistic turbulence models such as large-eddy simulation and direct numerical simulation methods, are applied to the problem.

The effect of Reynolds number on mixing in creeping flow is minimal. In laminar and turbulent flows, the Reynolds number has a major impact on the performance of a static mixer; for low Reynolds number flows, most of fluid particles are separated, whereas, for higher Reynolds number flows, increased mixing of fluid particles occurs. Comparisons between the results obtained by *k- $\omega$*  and RSM turbulent models show that the *k- $\omega$*  has enough

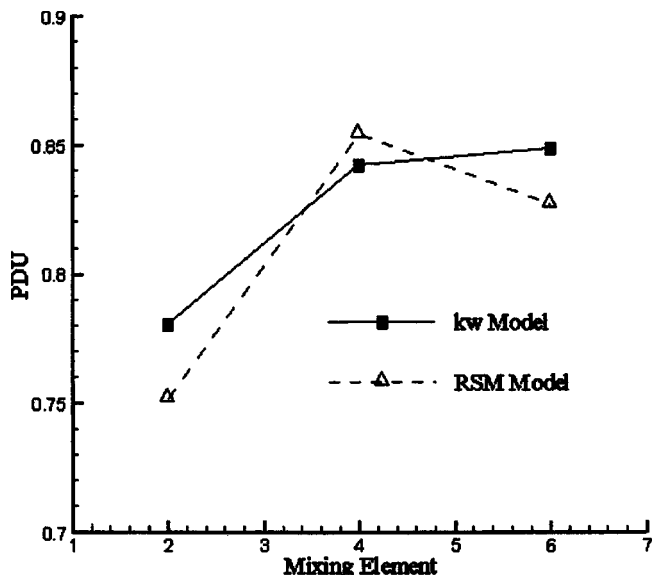


Fig. 21 *PDU* values at the end of even numbered mixing elements ( $Re=3000$ )

accuracy to capture the main aspects of mixing flows, while it is computationally much less expensive than the RSM model.

## Acknowledgment

This research was sponsored by Illinois Tool Works, Inc.

## Nomenclature

- $F_i$  = external force vector ( $i=1,2,3$ )  
 $\dot{m}$  = mass flow rate  
 $N_p$  = particles released at the flowfield inlet  
 $PDU$  = particle distribution uniformity  
 $Q$  = volumetric flow rate  
 $Re$  = Reynolds number ( $=\rho Ud/\mu$ )  
 $U$  = bulk velocity  
 $V$  = grid cell volume  
 $V_m$  = mixer volume  
 $d$  = pipe diameter  
 $\Delta s$  = computational grid interval size  
 $g$  = acceleration due to gravity  
 $k$  = turbulence kinetic energy  
 $p$  = pressure  
 $pd_1(i)$  = particle distribution function of the first kind ( $i=1, \dots, N_s$ )  
 $pd_2(i)$  = particle distribution function of the second kind ( $i=1, \dots, N_l$ )  
 $r_s$  = structure radius  
 $u_i$  = velocity vector ( $i=1,2,3$ )  
 $x_i$  = position vector ( $i=1,2,3$ )  
 $\delta_{ij}$  = Kroncker delta  
 $\varepsilon$  = turbulence energy dissipation  
 $\mu$  = molecular viscosity  
 $\rho$  = density  
 $-\rho u_i' u_j'$  = Reynolds stresses ( $i, j=1,2,3$ )  
 $\tau_{ij}$  = stress tensor ( $i, j=1,2,3$ )  
 $\tau_w$  = wall shear stress  
 $\omega$  = specific dissipation

## References

- Pahl, M. H., and Muschelknautz, E., 1982, "Static Mixers and Their Applications," *Int. Chem. Eng.*, **22**, pp. 197–205.
- Cybulski, A., and Werner, K., 1986, "Static Mixers- Criteria for Applications and Selection," *Int. Chem. Eng.*, **26**, pp. 171–180.
- Myers, K. J., Bakker, A., and Ryan, D., 1997, "Avoid Agitation by Selecting Static Mixers," *Chem. Eng. Prog.*, **93**, pp. 28–38.
- Shintre, S. N., and Ulbrecht, J. J., 1983, "A Model of Mixing in Motionless Mixer," *Chem. Eng. Commun.*, **24**, pp. 115–138.
- Shintre, S. N., 1988, "Mixing of Non-Newtonian (Pseudo-plastic) Fluids in Motionless Mixers," *Proc. Sixth European Conference on Mixing, Pavia, Italy*, pp. 551–556.
- Arimond, J., and Erwin, L., 1985, "Modeling of Continuous Mixers in Polymer Processing," *ASME J. Eng. Ind.*, **107**, pp. 70–76.
- Arimond, J., and Erwin, L., 1985, "A Simulation of a Motionless Mixer," *Chem. Eng. Commun.*, **37**, pp. 105–126.
- Dackson, K., and Nauman, E. B., 1987, "Fully Developed Flow in Twisted Tapes: A Model for Motionless Mixers," *Chem. Eng. Commun.*, **54**, pp. 381–395.
- Ling, F. H., and Zhang, X., 1994, "Chaotic Mixing in the Kenics Static Mixer," *Advances in Computational Methods in Fluid Dynamics*, **FED 196**, pp. 367–374.
- Ling, F. H., and Zhang, X., 1995, "A Numerical Study on Mixing in the Kenics Static Mixer," *Chem. Eng. Commun.*, **136**, pp. 119–141.
- Tung, T., 1976, "Low Re Entrance Flows: A Study of a Motionless Mixer," PhD thesis, University of Massachusetts, Amherst.
- Nauman, E. B., 1991, "On Residence Time and Trajectory Calculations in Motionless Mixers," *Chem. Eng. J.*, **47**, pp. 141–148.
- Kusch, H. A., and Ottino, J. M., 1992, "Experiments on Mixing in Continuous Chaotic Flows," *J. Fluid Mech.*, **236**, pp. 319.
- Byrde, O., 1997, "Massively Parallel Flow Computation with Application to Fluid Mixing," PhD thesis, Ecole Polytechnique Federale de Lausanne, Switzerland.
- Hobbs, D. M., 1998, "Characterization of a Kenics Static Mixer under Laminar Flow Conditions," PhD thesis, Rutgers, The State University of New Jersey, New Jersey.
- Jones, S. C., 1999, "Static Mixers for Water Treatment", PhD thesis, Georgia Institute of Technology, Atlanta.
- Rauline, D., Tanguy, P. A., Le Blevect, J., and Bousquet, J., 1998, "Numerical Investigation of the Performance of Several Static Mixers," *Can. J. Chem. Eng.*, **76**, pp. 527–535.
- Hobbs, D. M., and Muzzio, F. J., 1998, "Reynolds Number Effects on Laminar Mixing in the Kenics Static Mixer," *Comput. J. (Switzerland)*, **70**, pp. 93–104.
- Hobbs, D. M., Swanson, P. D., and Muzzio, F. J., 1998, "Numerical Characterization of Low Reynolds Number Flow in the Kenics Static Mixer," *Chem. Eng. Sci.*, **53**, pp. 1565–1584.
- Byrde, O., and Sawley, M. L., 1999, "Optimization of a Kenics Static Mixer for Non-creeping Flow Conditions," *Chem. Eng. J.*, **72**, pp. 163–169.
- Byrde, O., and Sawley, M. L., 1999, "Parallel Computation and Analysis of the Flow in a Static Mixer," *Comput. Fluids*, **28**, pp. 1–18.
- Jones, S. C., Sotiropoulos, F., and Amirtharajah, A., 2002, "Numerical Modeling of Helical Static Mixer for Water Treatment," *J. Environ. Eng.*, **128**, pp. 431–440.
- Hinze, J. O., 1975, *Turbulence*, McGraw-Hill Publishing Co., New York.
- Wilcox, D. C., 1998, *Turbulence Modeling for CFD*, DCW Industries, Inc., La Cañada, CA.
- Mathieu, J., and Scott, J., 2000, *An Introduction to Turbulent Flow*, The Press Syndicate of The University of Cambridge, Cambridge, UK.
- Pope, B. S., 2000, *Turbulent Flows*, Cambridge University Press, Cambridge, UK.
- Shin, T., Zhu, J., and Lumley, J. L., 1995, "A New Reynolds Stress Algebraic Equation Model," *Comput. Methods Appl. Mech. Eng.*, **5**, pp. 287–302.
- Gibson, M. M., and Launder, B. E., 1978, "Ground Effects on Pressure Fluctuations in the Atmospheric Boundary Layer," *J. Fluid Mech.*, **86**, pp. 491–511.
- Launder, B. E., 1989, "Second-Moment Closure: Present... and Future?," *Int. J. Heat Fluid Flow*, **10**(4), pp. 282–300.
- Launder, B. E., Reece, G. J., and Rodi, W., 1975, "Progress in the Development of a Reynolds-Stress Turbulence Closure," *J. Fluid Mech.*, **68**(3), pp. 537–566.
- Kolmogorov, A. N., 1942, "Equations of Turbulence Motion of Incompressible Fluid," *Izvestia Academy of Sciences, USSR; Physics*, **6**, pp. 56–58.
- Saffman, P. G., and Wilcox, D. C., 1974, "Turbulence-model Predictions for Turbulent Boundary Layers," *AIAA J.*, **12**, pp. 541–546.
- Chou, P. Y., 1945, "On the Velocity Correlations and the Solution of the Equations of Turbulent Fluctuation," *Q. Appl. Math.*, **3**, pp. 38–54.
- Sotiropoulos, F., and Patel, V. C., 1995, "On the Role of Turbulence Anisotropy and Near-wall Modeling in Predicting Three-dimensional Shear-flows," *AIAA J.*, **33**, pp. 504–514.
- Sotiropoulos, F., and Ventikos, Y., 1998, "Flow through a Curved Duct Using Nonlinear Two-equation Turbulence Model," *AIAA J.*, **36**, pp. 1256–1262.
- Lin, F. B., and Sotiropoulos, F., 1997, "Strongly-coupled Multigrad Method for 3-D Incompressible Flows Using Nearwall Turbulence Closures," *J. Fluid Mech.*, **119**, pp. 314–324.
- Menter, F. R. 1994, "Two-Equation Eddy-Viscosity Turbulence Models for Engineering Applications," *AIAA J.*, **32**(8), pp. 1598–1605.
- Wilcox, D. C., 1988, "Reassessment of the Scale-Determining Equation for Advanced Turbulence Models," *AIAA J.*, **26**(11), pp. 1299–1310.
- Johnson, D. A., and King, L. S., 1985, "Mathematically Simple Turbulence Closure Model for Attached and Separated Turbulent Boundary Layers," *AIAA J.*, **23**(11), pp. 2066–2072.
- Launder, B. E., and Spalding, D. B., 1974, "The Numerical Computation of Turbulent Flows," *Comput. Methods Appl. Mech. Eng.*, **3**, pp. 269–289.
- Chen, H. C., and Patel, H. C., 1988, "Near-Wall Turbulence Models for Complex Flows Including Separation," *AIAA J.*, **26**(6), pp. 641–648.
- Wolfstein, M., 1969, "The Velocity and Temperature Distribution of One-Dimensional Flow with Turbulence Augmentation and Pressure Gradient," *Int. J. Heat Mass Transfer*, **12**, pp.301–318.
- Rahmani, R. K., 1997, "Unstructured Three-Dimensional Delaunay Grid Generation and Solving Three-Dimensional Euler Equations," Master's thesis, Sharif University of Technology, Iran.
- Thompson, J. F., Soni, T. B., and Weatherill, N. P., 1999, *Handbook of Grid Generation*, CRC Press LLC, Boca Raton, FL.
- Warming, R. F., and Beam, R. M., 1975, "Upwind Second-order Difference Schemes and Applications in Unsteady Aerodynamic Flows," *Proc. AIAA 2nd Computational Fluid Dynamics Conference, Hartford, Connecticut*, pp. 17–28.
- Barth, T. J., and Jespersen, D., 1989, "The Design and Application of Upwind Schemes on Unstructured Meshes," *Technical Report AIAA-89-0366, AIAA 27th Aerospace Sciences Meeting*, Reno, Nevada.
- Vandoormaal, J. P., and Raithby, G. D., 1984, "Enhancements of the SIMPLE Method for Predicting Incompressible Fluid Flows," *Numer. Heat Transfer*, **7**, pp. 147–163.
- Patankar, S. V., and Spalding, D. B., 1972, "A Calculation Procedure for Heat, Mass and Momentum Transfer in Three-dimensional Parabolic Flows," *Int. J. Heat Mass Transfer*, **15**, pp. 1787–1806.
- FLUENT 6.0 User's Guide, 2001, Vol. 2, Part 22, FLUENT Inc., New Hampshire.
- Li, A., Ahmadi, G., Bayer, R., and Gaynes, M., 1994, "Aerosol Particle Deposition in an Obstructed Turbulence Duct Flow," *J. Aerosol Sci.*, **25**(1), pp. 91–112.
- Mostafa, A. A., and Mongia, H. C., 1988, "On the Interaction of Particles and Turbulent Fluid Flow," *Int. J. Heat Mass Transfer*, **31**(10), pp. 2063–2075.
- Zhou, O. and Leschziner, M., 1991, "A Time-Correlated Stochastic Model for



- Particle Dispersion in Anisotropic Turbulence," *Proc. 8th Turbulent Shear Flows Symposium, Munich, Germany*.
- [53] Fung, J. C. H., Hunt, J. C. R., Malik, N. A., and Perkins, R. J., 1992, "Kinematic simulation of homogeneous turbulence by unsteady random Fourier modes," *J. Fluid Mech.*, **236**, pp. 281–318.
- [54] Bechara, W., Bailly, C., Lafon, P., and Candel, S. M., 1994, "Stochastic approach to noise modeling for free turbulent flows," *AIAA J.*, **32**(3), pp. 455–463.
- [55] Smirnov, A., Shi, S., and Celik, I., 2001, "Random Flow Generation Technique for Large Eddy Simulations and Particle Dynamics Modeling," *ASME J. Fluids Eng.*, **123**, pp. 359–371.
- [56] Kraichnan, R. H., 1970, "Diffusion by a Random Velocity Field," *Phys. Fluids*, **13**, pp.22–31.
- [57] *FLUENT 6.0 User's Guide*, 2001, Vol. 2, Part 10, FLUENT Inc., New Hampshire.
- [58] Camp, T. R., and Stein, P. C., 1943, "Velocity Gradients and Internal Work in Fluid Friction," *J. Boston Soc. Civ. Eng.*, **30**(4), pp. 219–237.
- [59] Clark, M. M., 1985, "Effect of Micromixing on Product Selectivity," *Proc. AWWA Annual Conference, Denver*, pp. 1957–1975.
- [60] Graber, S. D., 1994, "A Critical Review of the Use of the *G*-value (RMS Velocity Gradient) in Environmental Engineering," *Developments in Theoretical and Applied Mechanics*, **17**, pp. 533–556.

# Influence of Bulk Fluid Velocity on the Efficiency of Electrohydrodynamic Pumping

Vishal Singhal

Suresh V. Garimella

e-mail: sureshg@ecn.purdue.edu

School of Mechanical Engineering,  
Purdue University,  
585 Purdue Mall,  
West Lafayette, IN 47907-2088

*The efficiency of conversion of electrical power into fluidic power in an electrohydrodynamic (EHD) pump depends on the bulk fluid velocity. An analytical formulation is developed for calculation of the efficiency of an EHD pump, with and without the presence of a superimposed flow due to an externally imposed pressure gradient. This formulation is implemented into a numerical model, which is used to investigate the effect of bulk fluid velocity on the efficiency of the EHD action. In particular, the net flow due to the combined action of EHD and a positive or negative external pressure gradient is computed. Both ion-drag pumps and induction EHD pumps are considered. Pumps based on the ion-drag principle that are studied include a one-dimensional pump, a two-dimensional pump driven by a stationary potential gradient, and another driven by a traveling potential wave. Two-dimensional repulsion-type and attraction-type induction pumping caused by a gradual variation in the electrical conductivity of the fluid is also investigated. The efficiency of EHD pumps exhibited a strong dependence on bulk fluid velocity: for the two-dimensional steady ion-drag pump, for example, the efficiency increased from less than 2% to 22% under the influence of an external pressure gradient. The corresponding increase in efficiency for a two-dimensional repulsion-type EHD pump was from 0.26% to 24.5%. [DOI: 10.1115/1.1899173]*

## Introduction

Electrohydrodynamics (EHD) as a means of pumping fluids has been under investigation for several decades [1–5]. However, the low efficiency of conversion of electrical power into fluid power has limited the implementation of EHD pumps in practical applications. Recent developments in microfluidics have led to a renewed interest in EHD pumps mainly because of their potential for miniaturization, absence of moving parts, and the resulting high reliability. Miniature ion-drag [6,7], induction EHD [8,9] and electro-osmotic [10,11] pumps have been investigated. However, the efficiency of these devices, seldom greater than 5% and often less than 1%, continues to be a critical issue of concern.

The efficiency of an EHD pump strongly depends on the bulk fluid velocity. Specifically, if an ion-drag pump is operated under an external pressure gradient, causing flow in the same direction as the EHD pump, the efficiency of conversion of electrical power to fluid power is higher than if the external pressure gradient were not present [12]. Conversely, an external pressure gradient in the opposite direction causes a decrease in EHD pumping efficiency. This effect can be used to advantage. For instance, EHD pumping could be used as a booster for existing flow inside pipes or channels. The main pumping action would be carried out by an external pump, while the EHD action helps to increase the fluid velocity. Control of local heat transfer in specific regions or tubes in a heat exchanger, for example, by this means could be of great advantage in specific applications.

Several studies have considered the efficiency of EHD pumps [13–15]. Most, however, have focused on the effect of the electrical properties of the fluid on the efficiency of conversion of electrical power to fluidic power. The role of bulk fluid velocity in increasing the efficiency of EHD pumps has not received much attention. The study of Bondar and Bastien [12] appears to be the only one that has identified the potential increase in the efficiency of EHD action due to increased bulk fluid velocity.

A transient, three-dimensional model of electrohydrodynamics, capable of solving coupled charge transport and Navier–Stokes equations, was recently developed [16,17]. This model is used here to study the effect of bulk fluid velocity on the efficiency of conversion of electrical power into fluidic power in an EHD pumping device. One-dimensional (1D) and two-dimensional ion-drag pumps actuated using a stationary potential gradient as well as a traveling potential wave are studied. Attraction- and repulsion-type induction EHD pumps are also considered.

## Previous Studies

A few studies in the literature have dealt specifically with the efficiency of EHD pumps. Crowley [13] studied the efficiency of EHD induction pumps which use the electrical conductivity jump at the interface between different fluids for inducing charges. This study was confined to the attraction mode, where fluid motion is in the same direction as the traveling potential wave. This would occur when the electric field strength is higher in the fluid with the smaller electrical conductivity. Flow between two parallel plates was studied. Layers of two nonmixing fluids with different electrical properties were present between the plates. A traveling potential wave was applied to the plate which was in contact with the fluid of lower electrical conductivity. The other plate was grounded. An analytical expression was derived for the efficiency of the pump, as a ratio of the product of average shear stress at the interface and velocity of the interface to the time-averaged electrical power input. The effect on pump efficiency of various parameters was analyzed using the expression derived. The efficiency was indicated to be high under the following conditions: the charge relaxation time in the less-conducting fluid is smaller than the time period of the potential wave; the more conducting fluid is highly conductive; and the less-conducting fluid layer is thin, with thickness much smaller than the wavelength of the potential wave.

Bondar and Bastien [12] presented experimental results on the effect of bulk fluid velocity on the efficiency of EHD. Ions were generated by corona discharge from a moving pointed electrode attached to a steel rod. The force due to electrical interaction

Contributed by the Fluids Engineering Division for publication in the JOURNAL OF FLUIDS ENGINEERING. Manuscript received by the Fluids Engineering Division April 20, 2004; revised manuscript received March 5, 2005. Associate Editor: Akira Goto.

between the charges and the rod caused a variation in the acceleration of the steel rod. The resultant change in velocity was measured using an opto-electronic detector. This experiment was performed without and with a pressurized air stream, with the efficiency reaching 2.6% and 7.5% under the former and latter conditions, respectively. This compared to an efficiency of less than 1% without the pressurized air and moving electrode. The efficiency increase was also found to be independent of the electrical power input to the corona discharge. They also presented an integral equation for the efficiency of a steady (constant voltage drop and charge source) EHD pump. Assuming negligible viscous losses in the ionization region, it was shown that the efficiency of EHD can be changed solely by the bulk fluid velocity, without changes in the electrical parameters.

Crowley et al. [14] conducted a theoretical study on the effect of fluid properties on the efficiency and flow rate of a two-dimensional ion-drag EHD pump. Variations in electric field due to the space charge effect were neglected, and the electric field was assumed to be uniform throughout the pump. This facilitated an analytical solution of the governing equations. The efficiency of the EHD pump was defined as  $\eta = 1/(1 + \alpha)$ , where  $\alpha$  is given by  $\alpha = \mu E/v + \sigma E/qv$ . These expressions were obtained from a simplified consideration that the efficiency was equal to the ratio of the electrical power input if fluid mobility and conductivity were zero, to the actual electrical power input, i.e.,  $\eta = qvAV_e/(qvAV_e + \mu qAEV_e + \sigma AEV_e)$ . It was concluded that low electrical conductivity and low ion mobility lead to high efficiency. Limits on flow velocity in an ion-drag EHD pump due to several different factors were also identified. These factors are charge decay by charge conduction and ion mobility, friction forces for laminar and turbulent flow, and breakdown of fluid at high electric fields. Low fluid viscosity and high permittivity were also suggested to lead to high flow rates.

Seyed-Yagoobi et al. [15] presented a theoretical model of steady 1D EHD pumping. Current due to conduction, mobility, and convection of charges was accounted for in the governing equations for EHD. For a 1D flow the EHD equations can be solved without recourse to Navier–Stokes equations. This is because there are no pressure gradients or viscous losses in a 1D flow and hence the flow velocity is the same everywhere. The charge transport equation was solved numerically to obtain electric field and charge density distributions which were then used to calculate efficiency. Results were presented in terms of three non-dimensional numbers: Electric Reynolds number  $Re_{E\ell} = \varepsilon v/\sigma L$ , Electric slip number  $Es\ell = \mu V_e/vL$ , and Electric source number  $Es = q_e L^2/\varepsilon V_e$ ;  $Re_{E\ell}$  is the ratio of free-charge relaxation time of the fluid ( $\varepsilon/\sigma$ ) to the time which characterizes system dynamics ( $L/v$ ),  $Es\ell$  represents the relative motion of charges compared to the bulk fluid velocity, and  $Es$  indicates the influence of space charge on the electric field. The Electric Reynolds number  $Re_{E\ell}$  is also indicative of the efficiency of energy conversion. For a steady 1D EHD pump with an applied voltage difference across a domain and a constant known charge density upstream of the domain, the efficiency of the pump was given by  $\eta = 0.5(E_c^{*2} - E_e^{*2})/(Re_{E\ell} E_c^* + Es\rho_c^* - EsEs\ell\rho_c^* E_c^*)$ , where  $E_c^*$  and  $E_e^*$  are the nondimensional electric fields downstream (at collector) and upstream (at emitter) of the domain and  $\rho_c^*$  is the nondimensional charge density downstream of the EHD pump. The quantities  $E_c^*$ ,  $E_e^*$ , and  $\rho_c^*$  were obtained from numerical analysis. For given values of  $Es$  and  $Es\ell$ , efficiency was shown to increase with  $Re_{E\ell}$ . The efficiency was higher for low values of  $Es\ell$ , which corresponds to low mobility, small voltage difference, or large fluid velocity.  $Es$  was shown to be important only at low values of  $Re_{E\ell}$ . It was thus concluded that low mobility, low conductivity, and high permittivity all lead to higher efficiency.

Most of the related studies in the literature have focused on the effect of electrical properties of the fluid on EHD efficiency. To the authors' knowledge, Bondar and Bastien [12] reported the

only study which identified bulk fluid velocity as a significant parameter in determining the efficiency of EHD. Moreover, the theoretical and numerical analyses in past studies have been limited to very simplified systems, with simplifying approximations frequently made in the governing equations. This was necessitated due to the inability to solve coupled charge transport and Navier–Stokes equations in these studies, which is required to calculate the efficiency of an EHD system.

A theoretical model for EHD pumping is developed below, following which the numerical analysis approach is described, including model validation results. The variation of the efficiency of a number of EHD pump configurations is then explored as a function of bulk fluid velocity.

## Theoretical Analysis

A methodology for the calculation of efficiency of EHD pumping is developed. Alternative definitions for the efficiency of an EHD pump in the presence of an externally imposed bulk fluid velocity are presented. General integral equations are derived for both definitions of efficiency, and then simplified for the particular systems considered here.

**Governing Equations.** Magnetic induction due to moving charges is assumed to be negligible in the following discussion, which means the electric field  $\mathbf{E}$  is irrotational. Gauss's law can be written in terms of the electric potential  $\Phi(V)$  as

$$q = -\nabla \cdot (\varepsilon \nabla \Phi) \quad (1)$$

Conservation of charge  $q$ , in the absence of any charges due to species reaction, is given by

$$\frac{\partial q}{\partial t} + \nabla \cdot \mathbf{J} = 0 \quad (2)$$

Here,  $\mathbf{J}$ , the current density vector is given by

$$\mathbf{J} = \sigma \mathbf{E} + q\mathbf{v} + q\mu \mathbf{E} - D \nabla q \quad (3)$$

The four terms on the right hand side of Eq. (3) represent current due to conduction, convection, ionic mobility, and diffusion of charges, respectively. A detailed explanation of these terms is available in [16,17]. Current due to diffusion of charges is generally negligible, as the diffusion Peclet number is generally much greater than unity, as is assumed in the following analysis [15]. Otherwise, current due to charge diffusion can be significant and should not be neglected.

Combining Eqs. (2) and (3), the charge transport equation can be written as

$$\frac{\partial q}{\partial t} + \nabla \cdot (q\mathbf{v}) = \nabla \cdot (\sigma \nabla \Phi) + \nabla \cdot (q\mu \nabla \Phi) \quad (4)$$

The continuity and Navier–Stokes equations which describe the fluid flow are given below. The Navier–Stokes equations are modified to include pressure generation due to Coulomb forces.

$$\text{Continuity: } \frac{\partial \rho}{\partial t} + \nabla \cdot \rho \mathbf{v} = 0 \quad (5)$$

$$\text{Navier–Stokes: } \frac{\partial \rho \mathbf{v}}{\partial t} + (\mathbf{v} \cdot \nabla) \mathbf{v} = -\nabla p + \nabla \cdot \tau_{ij} + \rho \mathbf{f} - q \nabla \Phi \quad (6)$$

Body forces (other than Coulomb forces) are assumed negligible in the following analysis. The charge transport Eqs. (1) and (4) are solved along with the fluid transport Eqs. (5) and (6) via a numerical analysis to obtain the distribution of potential and charge, as well as the flow characteristics. The electrical and fluidic equations are coupled due to the presence of the charge convection term in the charge transport equation and the Coulomb force term in the Navier–Stokes equations.

**Efficiency Calculation.** The efficiency of a steady-state EHD pump will be shown by the following analysis to vary with bulk fluid velocity. An expression for the efficiency of a general (steady/transient) EHD pump is then derived, and is subsequently simplified for the different pumps considered.

In a steady-state system, the electrical power input to an EHD pump is given by

$$P_i = \iiint_{(\text{Vol})} \mathbf{v}_{\text{ion}} \cdot d\mathbf{F}_{E\ell} \quad (7)$$

Here  $P_i$  is input (electrical) power,  $\mathbf{v}_{\text{ion}}$  is velocity of the ions and  $d\mathbf{F}_{E\ell}$  is electrical force acting on a unit volume of the domain. The electrical force on a unit volume can be further written as  $d\mathbf{F}_{E\ell} = \mathbf{E}dq$ , where  $dq$  is charge density in that unit volume. Hence, Eq. (7) can be written as

$$P_i = \iiint_{(\text{Vol})} \mathbf{v}_{\text{ion}} \cdot \mathbf{E}dq \quad (8)$$

The mechanical power output from the EHD pump,  $P_o$ , can be written as

$$P_o = \iiint_{(\text{Vol})} \mathbf{v}_{\text{fl}} \cdot d\mathbf{F}_m \quad (9)$$

Here,  $\mathbf{v}_{\text{fl}}$  is bulk velocity of the fluid and  $d\mathbf{F}_m$  is that component of the force which contributes to useful work.

The bulk velocity of the ions is related to the velocity of the fluid. When the ions are in equilibrium with the fluid, i.e., when the difference in bulk velocities of the ions and the fluid depends only on local electric field (as would happen when there are no external sources of ions in the domain, i.e., charges are not being created or destroyed due to induction or chemical reactions), this relation can be expressed as

$$\mathbf{v}_{\text{ion}} = \mathbf{v}_{\text{fl}} + \mathbf{v}_{\text{drift}} \quad (10)$$

Here  $\mathbf{v}_{\text{drift}}$  is the drift velocity of the ions and is given by  $\mathbf{v}_{\text{drift}} = \mu\mathbf{E}$ . It should be noted that in the absence of free electrons, external sources of ions or diffusion, the equation for current density [Eq. (3)] reduces to  $\mathbf{J} = q\mathbf{v}_{\text{fl}} + q\mu\mathbf{E}$ . Dividing this equation by charge density  $q$  results in Eq. (10).

The efficiency of an EHD pump can therefore be written as

$$\eta_{E\ell} = \frac{P_o}{P_i} = \frac{\iiint_{(\text{Vol})} \mathbf{v}_{\text{fl}} \cdot d\mathbf{F}_m}{\iiint_{(\text{Vol})} \mathbf{v}_{\text{ion}} \cdot d\mathbf{F}_{E\ell}} \quad (11)$$

If it is assumed that  $d\mathbf{F}_m = d\mathbf{F}_{E\ell}$ , which implies that there are negligible losses due to frictional forces and viscous effects, the efficiency is given by

$$\eta_{E\ell} = \frac{\iiint_{(\text{Vol})} \mathbf{v}_{\text{fl}} \cdot d\mathbf{F}_{E\ell}}{\iiint_{(\text{Vol})} (\mathbf{v}_{\text{fl}} + \mathbf{v}_{\text{drift}}) \cdot d\mathbf{F}_{E\ell}} \quad (12)$$

This expression was first presented by Bondar and Bastien [12]. It can be further rewritten as

$$\eta_{E\ell} = \frac{v_{\text{fl,wa}}}{v_{\text{ion,wa}}} = \frac{1}{1 + v_{\text{drift,wa}}/v_{\text{fl,wa}}} \quad (13)$$

in which  $v_{\text{fluid,wa}}$ ,  $v_{\text{ion,wa}}$ , and  $v_{\text{drift,wa}}$  refer to the weighted average of fluid, ion and drift velocities with respect to the electric force density.

Equation (13) suggests that the efficiency of an EHD pump is related to bulk fluid velocity in the pump. No assumption was made in this analysis regarding the source of this fluid velocity. It may be solely due to the EHD action or may be brought about by an external pressure gradient. In fact, Eq. (13) suggests that the efficiency of an EHD pump can change radically without a change in the electrical conditions of the pump. The pump efficiency would increase with an increase in the fluid bulk velocity (if it is in the same direction as the drift velocity of the ions) and vice versa.

The instantaneous electrical power input  $P_i$  to any EHD pump can be written as

$$P_i = \iiint_{(\text{Vol})} d\mathbf{V} \cdot \mathbf{I} = \int \mathbf{E} \cdot \mathbf{J}d\text{Vol} \quad (14)$$

The above integral would be carried out over the entire region which has a current path to any of the powered electrodes. Introducing  $\mathbf{J} = \sigma\mathbf{E} + q\mathbf{v} + q\mu\mathbf{E}$  in the above equation yields

$$P_i = \int \mathbf{E} \cdot (\sigma\mathbf{E} + q\mathbf{v} + q\mu\mathbf{E})d\text{Vol} \quad (15)$$

In Cartesian coordinates, Eq. (15) reduces to

$$P_i = \iiint_{(\text{Vol})} [(\sigma + q\mu)(E_x^2 + E_y^2 + E_z^2) + q(E_x v_x + E_y v_y + E_z v_z)]dx dy dz \quad (16)$$

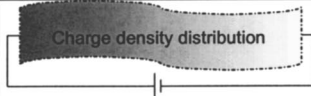
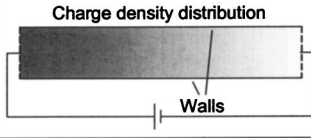
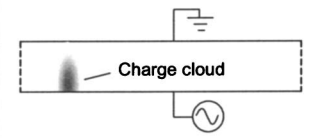
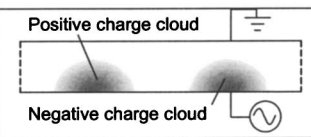
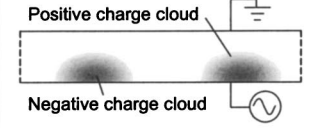
The mechanical work done by an EHD pump causes a pressure gradient in the fluid, which changes its velocity. For a fluid already in motion, the velocity would increase if the Coulomb forces are in same direction as the existing flow, and would decrease otherwise. The pressure gradient is balanced by viscous forces in the fluid and friction forces at the fluid-solid interfaces which act to retard the flow. Hence the mechanical power output  $P_o$  of an EHD pump is given by

$$P_o = \int (\mathbf{s} \cdot \mathbf{v})_{\text{EHD}} - (\mathbf{s} \cdot \mathbf{v})_{\text{No EHD}} dS \quad (17)$$

in which  $\mathbf{s}$  is the stress vector. Subscript ‘‘EHD’’ in the equation refers to flow due to combined action of EHD forces and external pressure gradient, while subscript ‘‘No EHD’’ refers to flow solely due to external pressure gradient. The above integral is executed over the boundary of the domain. The retarding forces are reflected in the velocity gradients in the fluid. Pressure and viscous stresses can be written as  $s_{ij} = -p_{\text{tot}}\delta_{ij} + \mu_{\text{vis}}(v_{i,j} + v_{j,i})$ , where  $p_{\text{tot}}$  is total pressure drop,  $\mu_{\text{vis}}$  is viscosity of the fluid and  $\delta_{ij}$  is the Kronecker delta vector,  $\delta_{ij} = \begin{cases} 1 & \text{if } i=j \\ 0 & \text{if } i \neq j \end{cases}$ . The term  $s_{ij}$  represents stress in the  $j$  direction on a plane in the  $i$  direction. However, flow due to an applied external pressure gradient is not reflected in the above equation, as both the pressure gradient as well as the viscous forces caused by this pressure gradient are included in the equation. The equation for  $s_{ij}$  can be modified as follows to account for flow due to an applied external pressure gradient  $s_{ij} = -p\delta_{ij} + \mu_{\text{vis}}(v_{i,j} + v_{j,i})$ , where  $p = p_{\text{tot}} - p_{\text{app}}$  is net pressure gradient generated by the EHD pump ( $p_{\text{app}}$  is applied external pressure gradient).

The output fluid power can therefore be written as

Table 1 Description of different EHD pumps considered in the present study.

Pump Number	Description	Source of Electric Field	Source of Charges	Comments	Schematic
1	Steady 1-D ion-drag pump	Constant stationary voltage drop	Constant charge density upstream of the pump	Fluid velocity is artificially pinned; same pump as studied in [15]	
2	Steady 2-D ion-drag pump	Constant stationary voltage drop in the direction of flow	Constant uniform charge density upstream of the pump	Flow is fully developed; fluid velocity is varied by applying pressure gradient <sup>i</sup> along length of pump; similar to steady 1-D pump except for viscous losses	
3	Transient 2-D ion-drag pump	Traveling potential wave along one side of the pump with other side grounded	Uniform charge density upstream of the pump for 10% of duration of potential wave starting from time when potential at that cross-section is highest	Flow is periodic in both time and space <sup>ii</sup> ; fluid velocity variation as for steady 2-D ion-drag pump; closely simulates ion-driven air flow device described in [19], except that 1-D geometry was considered in [19]	
4	Repulsion-type induction EHD pump		Induction of charges due to gradual decrease in $\sigma$ from side with potential wave to other side	Flow is periodic in both time and space <sup>iv</sup> ; fluid velocity variation as in steady 2-D ion-drag pump; closely simulates liquid pump described in [16,17]	
5	Attraction-type induction EHD pump		Induction of charges due to gradual increase in $\sigma$ from side with potential wave to other side	Flow is periodic in both time and space <sup>iv</sup> ; fluid velocity variation as in steady 2-D ion-drag pump; similar to repulsion-type EHD pump except that $\sigma$ gradient in opposite direction	

<sup>i</sup> Additional to pressure head generated by EHD

<sup>ii</sup> Time periodicity: Same velocity profile repeated at every cross-section after a time equal to the time-period of the potential wave

Space periodicity: At any given time, same velocity profile repeated after a distance equal to the wavelength of the potential wave

$$P_o = \int \{ (-p\delta_{ij} + \mu_{vis}(v_{i,j} + v_{j,i}))\hat{j} \cdot \mathbf{v} \}_{EHD} - \{ [-p\delta_{ij} + \mu_{vis}(v_{i,j} + v_{j,i})]\hat{j} \cdot \mathbf{v} \}_{No\ EHD} dS \quad (18)$$

In Cartesian coordinates, for a boundary along the  $x$  direction, Eq. (18) reduces to

$$P_o = \int \{ -pv_x + \mu_{vis}[2v_{x,x}v_x + (v_{x,y} + v_{y,x})v_y + (v_{x,z} + v_{z,x})v_z] \}_{EHD} - \{ -pv_x + \mu_{vis}[2v_{x,x}v_x + (v_{x,y} + v_{y,x})v_y + (v_{x,z} + v_{z,x})v_z] \}_{No\ EHD} dS_x \quad (19)$$

Similar expressions may be written for the  $y$  and  $z$  directions.

The efficiency of the EHD pump is the ratio of mechanical power output to electrical power input. From Eqs. (15) and (18), this efficiency can be written as

$$\eta_{El} = \frac{P_o}{P_i} = \frac{\int \{ (-p\delta_{ij} + \mu_{vis}(v_{i,j} + v_{j,i}))\hat{j} \cdot \mathbf{v} \}_{EHD} - \{ [-p\delta_{ij} + \mu_{vis}(v_{i,j} + v_{j,i})]\hat{j} \cdot \mathbf{v} \}_{No\ EHD} dS}{\int \mathbf{E} \cdot (\sigma\mathbf{E} + q\mathbf{v} + q\mu\mathbf{E}) dVol} \quad (20)$$

For two-dimensional EHD pumps, the above equation can be written in Cartesian coordinates as follows

$$\eta_{El} = \frac{\int \{ -pv_x + \mu_{vis}(2v_{x,x}v_x + (v_{x,y} + v_{y,x})v_y) \}_{EHD} - \{ -pv_x + \mu_{vis}(2v_{x,x}v_x + (v_{x,y} + v_{y,x})v_y) \}_{No\ EHD} dy + \int \{ -pv_y + \mu_{vis}(2v_{y,y}v_y + (v_{y,x} + v_{x,y})v_x) \}_{EHD} - \{ -pv_y + \mu_{vis}(2v_{y,y}v_y + (v_{y,x} + v_{x,y})v_x) \}_{No\ EHD} dx}{\iint [(\sigma + q\mu)(E_x^2 + E_y^2) + q(E_xv_x + E_yv_y)] dx dy} \quad (21)$$

For each of the different pumps considered in this work, this equation reduces to the simplified versions developed below. The five pumps considered are described with the help of schematic diagrams in Table 1. It may be noted that in the following three equations, flow without EHD is due to a constant one-dimensional pressure gradient.

$$\text{One-dimensional ion-drag pump: } \eta_{E\ell} = \frac{(pv_x)_{\text{No EHD}} - (pv_x)_{\text{EHD}}}{\int [(\sigma + q\mu)E_x^2 + qE_x v_x] dx} \quad (22)$$

Two-dimensional ion-drag pump due to a stationary one-dimensional potential gradient:

$$\eta_{E\ell} = \frac{\int ((pv_x)_{\text{No EHD}} - (pv_x)_{\text{EHD}}) dy + \int (\mu_{\text{vis}} v_{x,y} v_x)_{\text{EHD}} - (\mu_{\text{vis}} v_{x,y} v_x)_{\text{No EHD}} dx}{\int \int [(\sigma + q\mu)E_x^2 + qE_x v_x] dx dy} \quad (23)$$

Two-dimensional ion-drag pump due to a traveling potential wave, and two-dimensional attraction- and repulsion-type EHD induction pumps:

$$\eta_{E\ell} = \frac{\int [(pv_x)_{\text{No EHD}} - (pv_x)_{\text{EHD}}] dy + \int (\mu_{\text{vis}} v_{x,y} v_x)_{\text{EHD}} - (\mu_{\text{vis}} v_{x,y} v_x)_{\text{No EHD}} dx + \int \{\mu_{\text{vis}} [2v_{x,x} v_x + (v_{x,y} + v_{y,x}) v_y]\}_{\text{EHD}} dy + \int [-pv_y + \mu_{\text{vis}} (2v_{y,y} v_y + v_{y,x} v_x)]_{\text{EHD}} dx}{\int \int [(\sigma + q\mu)(E_x^2 + E_y^2) + q(E_x v_x + E_y v_y)] dx dy} \quad (24)$$

Overall, the efficiency of the flow generation due to several actuating mechanisms which may include both electrical and mechanical forces would be given by the ratio of total fluid power output to total power input. This efficiency can be written as

$$\eta_{\text{tot}} = \frac{P_{o,\text{EHD}}}{P_{i,\text{El}} + P_{i,m}} = \frac{\int ((-p\delta_{ij} + \mu_{\text{vis}}(v_{i,j} + v_{j,i}))\hat{j} \cdot \mathbf{v})_{\text{EHD}} dS}{\int \mathbf{E} \cdot (\sigma\mathbf{E} + q\mathbf{v} + q\mu\mathbf{E}) dVol + \int (p_{\text{app}}\delta_{ij})\hat{j} \cdot \mathbf{v}_{\text{EHD}} dS} \quad (25)$$

In two-dimensional Cartesian coordinates, this may be written as

$$\eta_{\text{tot}} = \frac{\int \{-pv_x + \mu_{\text{vis}}[2v_{x,x}v_x + (v_{x,y} + v_{y,x})v_y]\}_{\text{EHD}} dy + \int (-pv_y + \mu_{\text{vis}}(2v_{y,y}v_y + (v_{y,x} + v_{x,y})v_x))_{\text{EHD}} dx}{\int \int [(\sigma + q\mu)(E_x^2 + E_y^2) + q(E_x v_x + E_y v_y)] dx dy + \int p_{\text{app}} v_{x,\text{EHD}} dy + \int p_{\text{app}} v_{y,\text{EHD}} dx} \quad (26)$$

Equation (26) can be applied to each of the pump designs considered to obtain simplified expressions for  $\eta_{\text{tot}}$ . It is noted that  $\eta_{\text{tot}}$  is the efficiency of the complete fluidic system, which may include both electrical and mechanical actuating forces. On the other hand,  $\eta_{E\ell}$  is the efficiency of solely the electrical forces in causing fluid motion. However,  $\eta_{E\ell}$  is not independent of mechanical forces as the change in bulk fluid velocity due to mechanical forces affects  $\eta_{E\ell}$ .

**Numerical Modeling.** The commercially available computational fluid dynamics software package FIDAP was used for numerical modeling [18]. Flow was assumed to be laminar for all the cases considered. A built-in EHD module in FIDAP was used along with user-defined subroutines developed for calculating the input electrical power and output fluidic power. Validation of the ion-drag and induction EHD models is reported in detail [16], where the ion-drag EHD model was validated by comparison against the results of [15], while the induction EHD model was validated by comparison to [19]. The geometry was modeled using second-order elements. Picard iteration method was used to solve the discretized equations. Mesh-independence tests were performed for potential, charge density, and flow velocity. On doubling the number of elements in each direction, the values of these parameters varied less than 1% for steady-state simulations and less than 2% for transient simulations. Time stepping was done dynamically using the trapezoidal rule, which is a second-order implicit time-integration scheme with maximum relative local time truncation error of 0.1%.

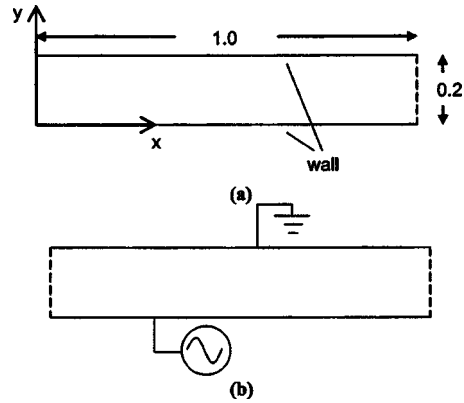


**Fig. 1 (a) Domain under consideration in two-dimensional pumps; (b) potential wave application in pumps with traveling potential wave**

All computations were performed with the following set of parameters. A fluid with  $\epsilon = \sigma = \mu = \mu_{\text{vis}} = 1$  was considered. The two-dimensional domain under consideration in pumps 2–5 (pump numbers identified in Table 1) is shown in Fig. 1. The length of the domain was  $L=1$  for all pumps, and the width was  $w=0.2$  for the two-dimensional pumps. These parameter choices help simplify the nondimensional parameters governing the problem to

Table 2 Comparison of  $\eta$  values for a 1D EHD pump obtained from the present model to values from the literature [15].

Re <sub>E<math>\ell</math></sub>	Es	Esl	$\eta$ (Efficiency)	
			Present work	Results from [15]
200	1	0	0.98	0.98
200	1	0.1	0.89	0.89
200	1	1	0.49	0.49
200	1	10	0.09	0.09
100	0.1	0	0.90	0.90
100	0.1	0.1	0.83	0.83
100	0.1	1	0.47	0.47
100	0.1	10	0.09	0.09

$Re_{E\ell} = v$ ,  $Esl = V_e/v$ , and  $Es = q_e/V_e$ . Also, the units for all the parameter values listed here need only follow a consistent framework, such as those mentioned in the Nomenclature. The results would be valid for any consistent set of units. While the results depend on the choice of these parameter values, the focus here is on the trends of variation obtained.

For the pumps under steady operation (pumps 1 and 2),  $\Phi(x=0, y) = q(x=0, y) = 100$  and  $\Phi(x=1, y) = 0$ . For the pumps in transient operation (pumps 3–5), the initial potential and charge density were zero throughout the domain, i.e.,  $\Phi(x, y, t=0) = 0 = q(x, y, t=0)$ . The potential wave at the electrode wall for all transient pumps was characterized by  $\Phi = 100$ ,  $\omega = k = 2\pi$ , i.e.,  $\Phi(x, y=0) = 100 \cos(2\pi t - 2\pi x)$ . The other wall was grounded, i.e.,  $\Phi(x, y=0.2) = 0$ . For pump 3,  $q = 100$  at  $x=0$  for 10% of the potential wave duration, i.e.,  $q(x=0, y) = \begin{cases} 100, 0 \leq t \leq 0.1/2\pi \\ 0, 0.1/2\pi \leq t < 1/2\pi \end{cases}$ . The constant conductivity gradient for charge induction in pump 4 can be characterized by  $\Delta\sigma = \sigma(x, y=0) - \sigma(x, y=0.2) = 0.1$ , while for pump 5  $\Delta\sigma = \sigma(x, y=0) - \sigma(x, y=0.2) = -0.1$ .

Efficiency values calculated from the present model are compared in Table 2 for several different cases to values read from graphs in [15]; the efficiency of a one-dimensional EHD pump with an applied voltage difference across the domain and a constant charge density upstream of the domain was reported in [15]. The two sets of results, presented in terms of  $Re_{E\ell}$ ,  $Es$  and  $Esl$ , are seen to be identical.

## Results and Discussion

For each of the five pumps considered in this work (as in Table 1), results are presented in terms of the efficiency obtained with EHD action alone, as well as with the combined action of EHD and an external pressure gradient. Efficiency values are presented as a function of the nondimensional average bulk fluid velocity along the length of pump, defined as  $v_{\text{fl}}^* = v_{\text{fl}}/v_{\text{fl},E}$ , where  $v_{\text{fl}}$  is the fluid velocity due to combined action of EHD and pressure gradient and  $v_{\text{fl},E}$  is the fluid velocity due only to the EHD action without any external pressure gradient. This is a more suitable parameter for examining the effect of bulk velocity on pump efficiency since both Reynolds number ( $Re = \rho v_{\text{fl}} h / \mu_{\text{vis}}$ ) and Electric Reynolds number ( $Re_{E\ell} = \varepsilon v / \sigma L$ ) involve parameters which could independently change the results without a change in the bulk fluid velocity. In addition to the efficiency results, variations with bulk fluid velocity of the nondimensional total input power ( $P_{i,\text{tot}}^*$ , which includes both the electrical input power and mechanical input power used to create the pressure gradient), total output power due to combined action of EHD and external pressure gradient ( $P_{o,\text{tot}}^*$ ), electrical input power ( $P_{i,E\ell}^*$ ), and fluidic output power solely due to EHD ( $P_{o,E\ell}^*$ , power transferred to the fluid due to EHD) are also presented. Both the total and the electrical input power as well as the total and the electrical output power are nondimensionalized by the electrical output power in

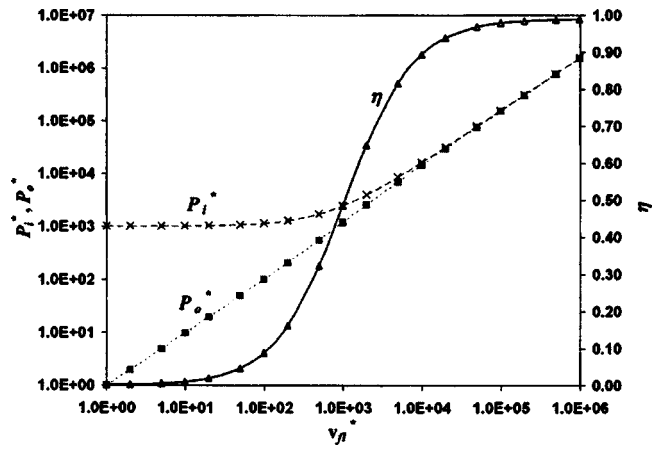


Fig. 2 Effect of variation of nondimensional bulk fluid velocity on nondimensional input power, output power, and efficiency for the steady one-dimensional ion-drag pump

the absence of an external pressure gradient ( $P_{o,E}$ ), i.e.,  $P_{i,\text{tot}}^* = P_{i,\text{tot}}/P_{o,E}$ ,  $P_{i,E\ell}^* = P_{i,E\ell}/P_{o,E}$ ,  $P_{o,\text{tot}}^* = P_{o,\text{tot}}/P_{o,E}$  and  $P_{o,E\ell}^* = P_{o,E\ell}/P_{o,E}$ .

**One-Dimensional Steady-State Ion-Drag Pump.** The variation of nondimensional input and output power ( $P_i^*$  and  $P_o^*$ ) and efficiency ( $\eta$ ) with nondimensional bulk fluid velocity ( $v_{\text{fl}}^*$ ) for a 1D pump is shown in Fig. 2. All input parameters except for  $v_{\text{fl}}^*$  are held constant. The horizontal axis ( $v_{\text{fl}}^*$ ) and left vertical axis ( $P_i^*$  and  $P_o^*$ ) have a logarithmic variation. The right vertical axis ( $\eta$ ) has a linear variation. It may be noted that in a 1D system, the velocity needs to be artificially pinned. Therefore,  $P_i$ ,  $P_o$ , and  $v_{\text{fl}}$  are nondimensionalized with respect to the corresponding values at the lowest  $v_{\text{fl}}$  considered.

Figure 2 shows that  $P_i^*$ ,  $P_o^*$  and  $\eta$  increase with an increase in  $v_{\text{fl}}^*$ . This can be explained as follows. As  $v_{\text{fl}}^*$  increases, the current due to charge convection increases and hence the input electrical power  $P_i^*$  increases. Moreover, since current due to charge conduction and mobility does not vary much with  $v_{\text{fl}}^*$ , the ratio of convection current to total current increases according to Eq. (15). The conversion of electrical power to fluidic power is most efficient for convection current because there is no charge decay as is the case for charge conduction and mobility. This causes an increase in the efficiency of EHD action. Increases in both  $P_i^*$  and  $\eta$  lead to the increase in  $P_o^*$  seen in Fig. 2. Since all the electrical and mechanical parameters except for bulk fluid velocity are fixed, this increase in efficiency is solely due to the increase in  $v_{\text{fl}}^*$ . It may be noted that no distinction is made between  $P_{i,\text{tot}}$ ,  $P_{o,\text{tot}}$ ,  $\eta_{\text{tot}}$ , and  $P_{i,E\ell}$ ,  $P_{o,E\ell}$ ,  $\eta_{E\ell}$  because 1D flow does not offer any pressure gradient or wall friction. Hence subscripts “tot” and “E $\ell$ ” have been dropped from parameters  $P_i$ ,  $P_o$ , and  $\eta$  here.

The 1D case considered above is clearly an idealized situation. It can be thought to represent the ideal operation of an ion-drag EHD pump. Since there is no pressure gradient to be overcome, any pressure head generated by EHD will increase the fluid velocity infinitely unless it is limited by some external means. In the present simulations, these velocities were limited using the inlet velocity boundary condition. A more practical situation would involve flow created using EHD in a pipe or over a plate. In that case, EHD would need to overcome frictional forces at the surface, which would naturally limit the fluid velocity. Such more realistic pumps, with fully developed flow between parallel plates due to differing voltage and charge densities, are considered in the following.

**Two-Dimensional Steady-State Ion-Drag Pump.** The varia-

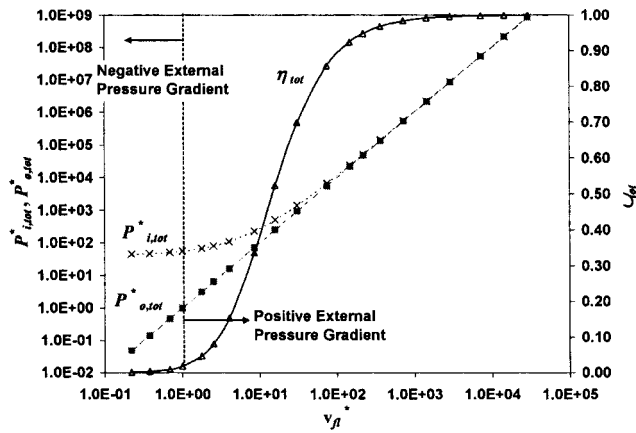


Fig. 3 Variation of nondimensional total input power, total output power, and total efficiency with nondimensional bulk fluid velocity due to combined action of EHD in the steady two-dimensional ion-drag pump and varying external pressure gradient

tion of nondimensional total input power  $P_{i,tot}^*$ , total output power  $P_{o,tot}^*$  and total efficiency  $\eta_{tot}$  with nondimensional average bulk fluid velocity  $v_{fl}^*$  for this pump is shown in Fig. 3. Again the horizontal axis ( $v_{fl}^*$ ) and left vertical axis ( $P_{i,tot}^*$  and  $P_{o,tot}^*$ ) have logarithmic variations, while the right vertical axis ( $\eta_{tot}$ ) has a linear variation. The velocity  $v_{fl}^*$  is varied by applying an external pressure gradient in addition to the EHD action. Both negative and positive pressure gradients are considered. Results for the negative pressure gradient are reported only for cases for which there is still a net flow in the direction of EHD pumping.

For this pump,  $P_{i,tot}^*$  and  $P_{o,tot}^*$  are seen to follow the same trend of variation as for the one-dimensional pump. The monotonic rise in total efficiency  $\eta_{tot}$  with  $v_{fl}^*$  can be attributed to two reasons. A positive pressure gradient causes additional flow in the forward direction, which increases charge convection and hence the output fluid power due to EHD, as was explained above. More importantly for the present pump, a pressure gradient creates flow with perfect efficiency and hence as the ratio of power input due to the pressure gradient to power input from EHD increases, the overall rectification efficiency increases. While the general trend of variation of efficiency for the present pump is similar to that of the previous pump considered,  $P_{o,tot}^*$  varies roughly as the square of  $v_{fl}^*$ . This is expected since the output power from the external pressure gradient varies as square of the pressure gradient ( $P_m \propto p^2$ ) while the fluid velocity varies linearly with pressure gradient ( $v_{fl} \propto p$ ); thus, output power from the external pressure gradient is proportional to the square of fluid velocity ( $P_m \propto v_{fl}^2$ ).

The electrical contributions to the input and output power, as well as the efficiency,  $P_{i,EI}^*$ ,  $P_{o,EI}^*$  and  $\eta_{EI}$  are plotted as a function of  $v_{fl}^*$  in Fig. 4. Again,  $v_{fl}^*$ ,  $P_{i,EI}^*$  and  $P_{o,EI}^*$  are plotted on a logarithmic scale and  $\eta_{EI}$  is on a linear scale. The results are plotted only for cases when the net flow is in the positive direction. In this figure,  $\eta_{EI}$  represents the actual efficiency of the EHD action. While it remains rather small relative to  $\eta_{tot}$  (shown in Fig. 3),  $\eta_{EI}$  increases from less than 0.02 (2% efficient) for no external pressure gradient to more than 0.19 (19% efficient) for  $v_{fl}^* = 147$ ; at this velocity,  $\eta_{tot}$  is 0.92. This increase in  $\eta_{EI}$  is due to the combined effect of an increase in  $P_{i,EI}^*$  and a sharper increase in  $P_{o,EI}^*$ , both due to increased charge convection, as was explained in the case of the one-dimensional pump.

Figure 4 also shows that the output fluid power solely due to EHD action,  $P_{o,EI}^*$ , increases in the presence of the positive external pressure gradient. This implies that the net fluid power achieved from the combined action of EHD and external pressure gradient is greater than the sum of the fluid powers achieved from

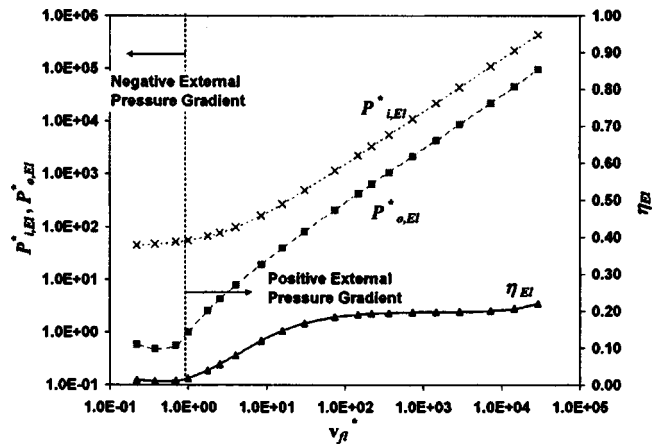


Fig. 4 Variation of nondimensional electrical input power, output power due to EHD, and efficiency due to EHD with nondimensional bulk fluid velocity due to combined action of EHD in the steady two-dimensional ion-drag pump and varying external pressure gradient

their action independent of each other.

The quantity  $P_{o,EI}^*$  is the ratio of output fluid power solely due to EHD to the input electrical power; output fluid power is calculated by subtracting the mechanical fluid power due to the pressure gradient from that due to the combined action of EHD and pressure gradient, i.e.,  $P_{o,EI}^* = (P_{o,tot} - P_{o,m}) / P_{o,EHD}$ . At larger values of  $v_{fl}^*$ , both  $P_{o,tot}$  and  $P_{o,m}$  can be several orders of magnitude larger than  $P_{o,EHD}$ , while  $(P_{o,tot} - P_{o,m})$  is of the same order of magnitude as  $P_{o,EHD}$ . Hence even small numerical inaccuracies in either  $P_{o,tot}$  or  $P_{o,m}$  can result in large discrepancies in the values of  $P_{o,EI}^*$  and  $\eta_{EI}$ . The increase in rate of variation of  $\eta_{EI}$  for  $v_{fl}^* > 10^3$  in Fig. 4 is believed to be due to these numerical inaccuracies.

Results for  $P_{o,EI}^*$  such as those presented above may be employed to generate a pump curve for the system, as is done in the following for each of the two-dimensional pumps considered. The pump curve for the two-dimensional steady-state ion-drag pump is shown in Fig. 5. The inset is a magnified view for small values of  $v_{fl}^*$ . The nondimensional pressure head generated by the pump,  $P_{EI}^*$ , has been obtained using the following expression

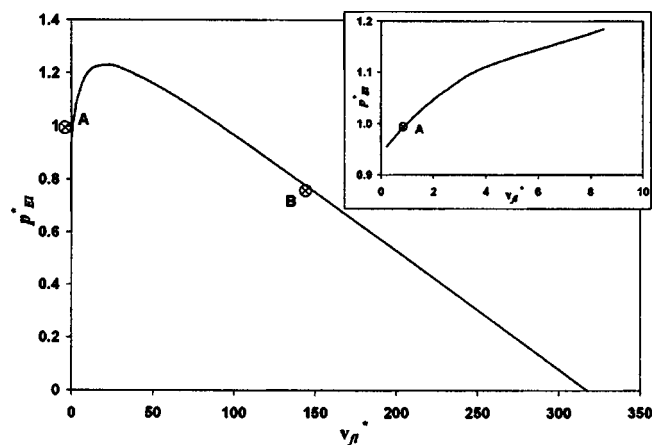


Fig. 5 Nondimensional pump curve for the steady two-dimensional ion-drag pump. (Inset: Magnified view of pump curve for small values of nondimensional bulk fluid velocity.)



$$P_{E\ell}^* = \frac{P_{E\ell}}{P_{EHD}} = \frac{\left( \int \mu_{vis} v_{x,y} v_x dx - \int (p + p_{app}) v_x dy \right) / v_x}{\left[ \left( \int \mu_{vis} v_{x,y} v_x dx - \int p v_x dy \right) / v_x \right]_{EHD}} \quad (27)$$

Here,  $p$  is the pressure head generated by EHD and  $p_{app}$  is applied external pressure gradient. When  $p_{app}=0$ , the EHD pump operates at  $v_{fl}^*=1$ ,  $P_{E\ell}^*=1$ , which is marked as point A in Fig. 5. It is clear that this is not the best operating point for the EHD pump. The maximum output of the pump ( $v_{fl}^* \times P_{E\ell}^*$ ) among the points considered is at  $v_{fl}^*=147.23$ ,  $P_{E\ell}^*=0.76$ . This point is identified as point B in Fig. 5. The output of the EHD pump is more than 112 times higher at this point than at  $v_{fl}^*=1$ ,  $P_{E\ell}^*=1$ , and it decreases on moving away from this point in either direction. This optimal operation at point B is also achieved at lower  $P_{E\ell}^*$  and higher  $v_{fl}^*$

$$P_{o,E\ell}^* = \frac{\left( \int \mu_{vis} v_{x,y} v_x dx - \int p v_x dy \right)_{EHD} - \left( \int \mu_{vis} v_{x,y} v_x dx - \int p v_x dy \right)_{No\ EHD}}{\left( \int \mu_{vis} v_{x,y} v_x dx - \int p v_x dy \right)_E}$$

$$P_{o,tot}^* = \frac{\left( \int \mu_{vis} v_{x,y} v_x dx - \int p v_x dy \right)_{EHD}}{\left( \int \mu_{vis} v_{x,y} v_x dx - \int p v_x dy \right)_E}$$

$$v_{fl}^* \times P_{E\ell}^* = \frac{\left( \int \mu_{vis} v_{x,y} v_x dx - \int (p + p_{app}) v_x dy \right)}{\left( \int \mu_{vis} v_{x,y} v_x dx - \int p v_x dy \right)_E}$$

**Two-Dimensional Transient Ion-Drag Pump.** Simulations for all the transient pumps were run until each pump reached a quasi-steady-state operation, where the results start repeating over the time period of the potential wave. The results shown for these pumps are time averaged over one period of the potential wave after the pumps have reached this quasi-steady state.

Variation of  $P_{i,tot}^*$ ,  $P_{o,tot}^*$  and  $\eta_{tot}$  [Fig. 6(a)],  $P_{i,E\ell}^*$ ,  $P_{o,E\ell}^*$  and  $\eta_{E\ell}$  [Fig. 6(b)] and  $P_{E\ell}^*$  with  $v_{fl}^*$  [Fig. 6(c)] for the two-dimensional transient ion-drag pump are shown in Fig. 6. The trends of variation of  $P_{i,tot}^*$ ,  $P_{o,tot}^*$  and  $\eta_{tot}$  with  $v_{fl}^*$  are the same as for the two-dimensional steady ion-drag pump considered above. On the other hand,  $P_{i,E\ell}^*$ ,  $P_{o,E\ell}^*$  and  $\eta_{E\ell}$  show very different dependence on  $v_{fl}^*$ . The input electrical power  $P_{i,E\ell}^*$  shows a rather small variation with  $v_{fl}^*$ , and that too only at low  $v_{fl}^*$ . This difference in behavior can be explained as follows. Charge is introduced upstream of the pump for a small portion (10%) of the period of the potential wave. For the particular pump considered here, the bulk velocity of the fluid is much higher than the speed of the potential wave; hence, charge is swept out of the pump very quickly and for most of the portion of the period of the potential wave, there is little charge in the domain. The currents due to charge mobility and charge convection are thus limited. Current due to electrical conductivity, however, does not depend on external charge and does not vary. Hence the electrical power input  $P_{i,E\ell}^*$  is limited.

An interesting trend of variation of  $P_{o,E\ell}^*$  with  $v_{fl}^*$  is also seen in

than under conditions where the EHD pump operates without an external pressure gradient. This reinforces the conclusion that an increase in the bulk fluid velocity causes an increase in output power of the pump.

It is important to emphasize the difference between the quantities  $P_{o,E\ell}^*$ ,  $P_{o,tot}^*$  and  $v_{fl}^* \times P_{E\ell}^*$ . The first of these,  $P_{o,E\ell}^*$ , is a measure of the increase in output fluid power due to operation of the EHD pump;  $P_{o,tot}^*$  on the other hand, is a measure of the total output fluid power due to the EHD pump and external pressure gradient. In contrast,  $v_{fl}^* \times P_{E\ell}^*$  is a measure of the net output fluidic power of the EHD pump. It represents how the pump would operate under different hydrodynamic conditions. The equations for  $P_{o,E\ell}^*$ ,  $P_{o,tot}^*$  and  $v_{fl}^* \times P_{E\ell}^*$  are presented explicitly below to clarify their definitions; it may be noted that all three have the same denominator.

Fig. 6(b). The small increase in  $P_{o,E\ell}^*$  when  $v_{fl}^*$  is close to but just greater than 1 is due to an increase in  $P_{i,E\ell}^*$  and  $\eta_{E\ell}$ , which results from an increase in current due to charge convection. The subsequent decrease in  $P_{o,E\ell}^*$  follows the decrease in efficiency of EHD action: a majority of the current at high  $v_{fl}^*$  is due to charge conduction, which has very low efficiency. The slight upturn in  $P_{o,E\ell}^*$  at larger  $v_{fl}^*$  is due to the numerical inaccuracies discussed earlier. The pump curve for this pump is shown in Fig. 6(c). As in Fig. 5, the point of operation of the pump without any external pressure gradient is marked A, while that at which the fluid power output is a maximum (40% higher than at A, where  $v_{fl}^*=1$ ,  $P_{E\ell}^*=1$ ) is marked B. The power output increases significantly with only a modest increase in  $v_{fl}^*$  due to the higher charge convection, and then decreases for larger values of  $v_{fl}^*$  because of the absence of Coulomb forces for a portion of the duration of pump operation.

**Repulsion-Type Induction EHD Pump.** Similar quantities as considered for the pumps above are plotted for a repulsion-type EHD pump in Fig. 7. The flow due to repulsion-type EHD is in a direction opposite to that of the traveling potential wave. The direction of flow is considered positive in the following discussion. Results for negative pressure gradients are presented only for cases in which the resultant flow is in the same direction as that due to EHD alone. The trend of variation for all three parameters in Fig. 7(a) is similar to the other cases considered thus far, with  $P_{o,tot}^*$  showing a quadratic variation with  $v_{fl}^*$ .

The variation of  $P_{i,E\ell}^*$ ,  $P_{o,E\ell}^*$  and  $\eta_{E\ell}$  with  $v_{fl}^*$  is shown in Fig. 7(b). It is seen that the increase in  $P_{i,E\ell}^*$  with increasing  $v_{fl}^*$  is very slight in this case when compared to the steady-state pumps. This is because charge induction results in the creation of equal amounts of negative and positive charges so that the net charge due to induction is zero. An increase in  $v_{fl}^*$  causes an increase in convection of both positive and negative charges and hence there is no change in the convection current. Despite little variation in  $P_{i,E\ell}^*$ , however, the increase in  $P_{o,E\ell}^*$  with  $v_{fl}^*$  is significant:  $P_{o,E\ell}^*$  increases rapidly at small  $v_{fl}^*$ , while the rate of increase drops off at larger  $v_{fl}^*$ . The efficiency  $\eta_{E\ell}$  follows the same trend of variation as  $P_{o,E\ell}^*$ , since there is little variation in  $P_{i,E\ell}^*$ .

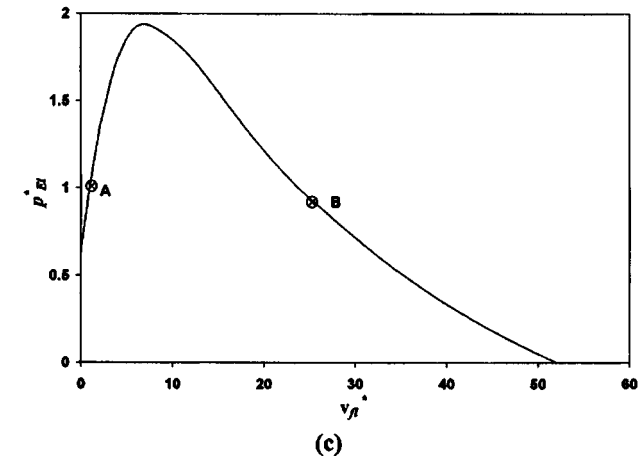
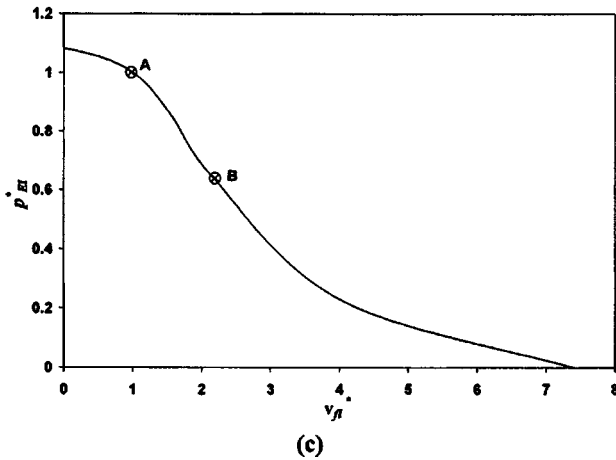
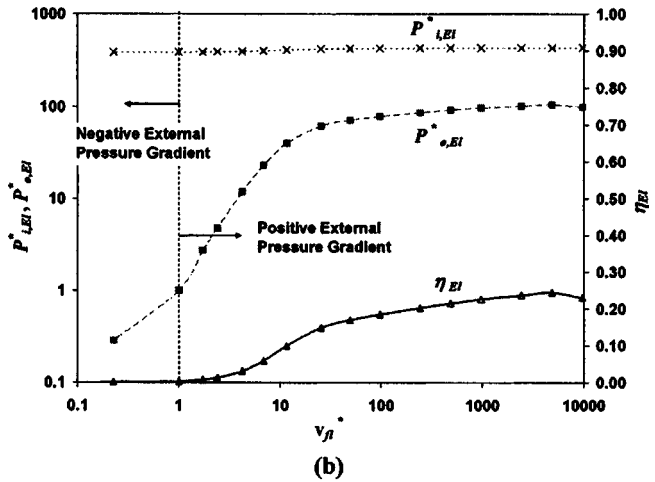
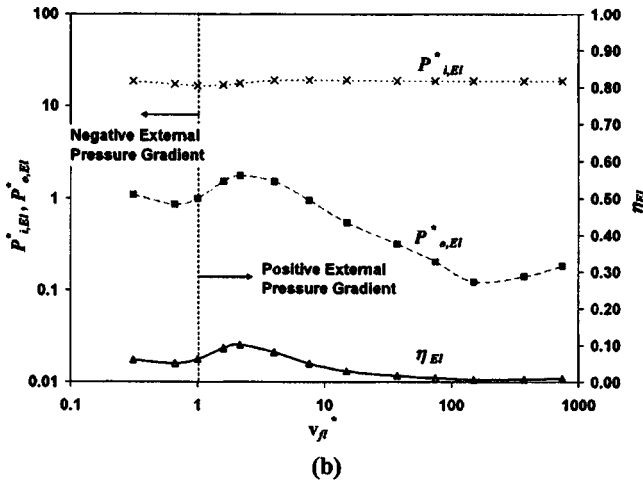
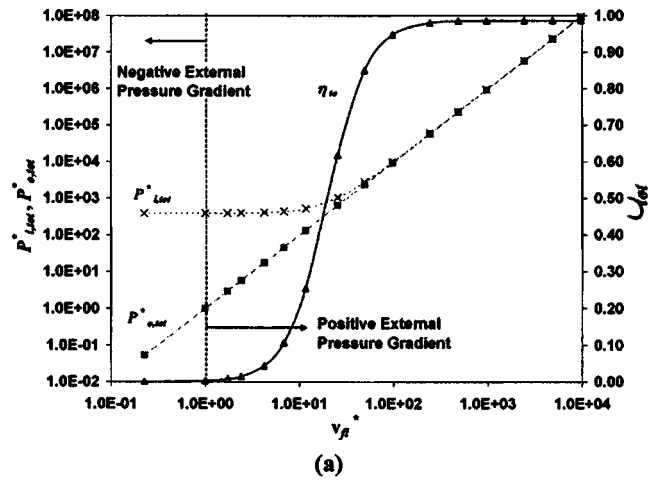
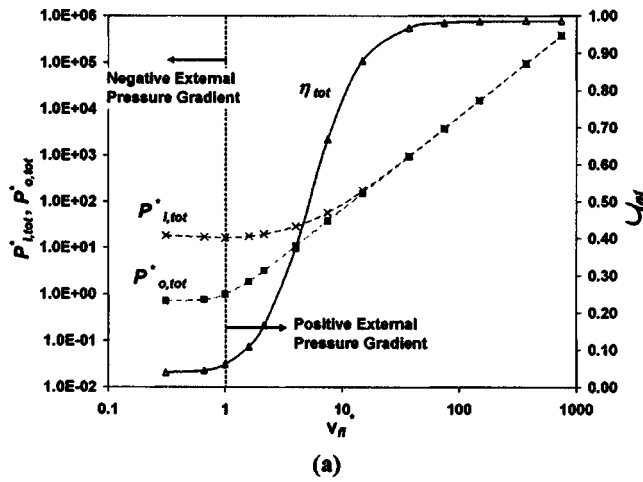


Fig. 6 Variation of (a) nondimensional total input power, total output power, and total efficiency; (b) nondimensional electrical input power, output power due to EHD, and efficiency due to EHD; and (c) pump curve, i.e., nondimensional pressure head generated by the pump with nondimensional bulk fluid velocity due to combined action of EHD in the transient two-dimensional ion-drag pump and varying external pressure gradient

Fig. 7 Variation of (a) nondimensional total input power, total output power, and total efficiency; (b) nondimensional electrical input power, output power due to EHD, and efficiency due to EHD; and (c) pump curve, i.e., nondimensional pressure head generated by the pump with nondimensional bulk fluid velocity due to combined action of the repulsion-type induction EHD pump and varying external pressure gradient

The total fluid power output by the combined action of EHD and pressure gradient for  $v_{fl}^* > 1$  is higher than the sum of the fluid power outputs from EHD and pressure gradient when operated individually. Moreover, this difference increases with an increase in  $v_{fl}^*$ . This observation is similar to that made for the steady two-dimensional ion-drag pump above.

The pump curve (variation of  $P_{fl}^*$  with  $v_{fl}^*$ ) for this pump is shown in Fig. 7(c). The shape of the pump curve is similar to that for the steady two-dimensional ion-drag pump. The fluid output power at its maximum (point B) is approximately 24 times that when there is no external pressure gradient (point A).

**Attraction-Type Induction EHD Pump.** Results for the last of

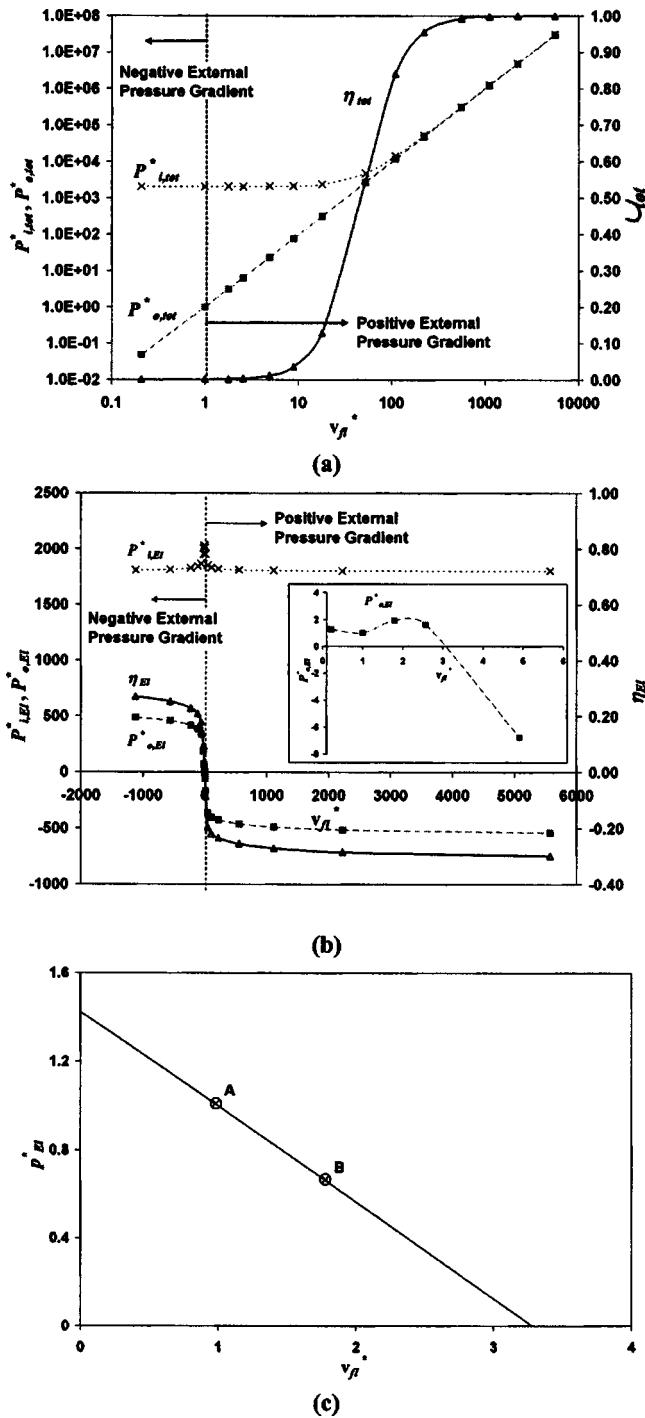


Fig. 8 Variation of nondimensional total input power, total output power, and total efficiency; (b) nondimensional electrical input power, output power due to EHD, and efficiency due to EHD; and (c) pump curve, i.e., nondimensional pressure head generated by the pump with nondimensional bulk fluid velocity due to combined action of the attraction-type induction EHD pump and varying external pressure gradient

the pumps considered, an attraction-type EHD pump, are plotted in Fig. 8. Figure 8(a) shows that  $P_{i,tot}^*$ ,  $P_{o,tot}^*$  and  $\eta_{tot}$  vary with  $v_{fl}^*$  in a manner similar to the behavior of the previously discussed pumps. The variation of  $P_{i,El}^*$ ,  $P_{o,El}^*$ , and  $\eta_{El}$  with  $v_{fl}^*$  is shown in Fig. 8(b); the inset is a magnified view of the behavior at low velocities. The variation of  $P_{i,El}^*$  with  $v_{fl}^*$  is interesting, with its

largest value being very close to  $v_{fl}^* = 1$ , decreasing at both larger and smaller values of  $v_{fl}^*$ . At very large and very small values of  $v_{fl}^*$ , little variation in  $P_{i,El}^*$  is noticed.

The drop in  $P_{i,El}^*$  as  $v_{fl}^*$  increases can be explained as follows. The attraction-type induction EHD pump is a synchronous pump [13]. EHD action tries to move the fluid at the same velocity as the velocity of the potential wave. When the fluid velocity is smaller than the velocity of the potential wave, the pump operates in a "pumping" mode, where it tries to increase the velocity of the fluid, which is limited by the electrical power available and the viscous forces. If the fluid velocity is higher than the wave velocity, the pump goes into a "braking" mode, where it tries to slow down the fluid velocity to the synchronous speed. Here, the pump is limited only by the electrical power available. Hence the largest fluid velocity achievable in an attraction-type induction EHD pump, in the absence of external pressure gradients, is the wave velocity itself. For the present case, the synchronous speed is approximately  $v_{fl}^* = 3.3$ . The output power from EHD ( $P_{o,El}^*$ ) becomes negative at around this value, as can be seen more clearly from the inset. Similarly, if the fluid velocity decreases below the synchronous speed,  $P_{o,El}^*$  increases rapidly. The negligible variation in  $P_{i,El}^*$  at large absolute values of  $v_{fl}^*$  is due to the insignificant effect of variation in charge convection as the net charge in the fluid is zero.

The pump curve for the present pump is shown in Fig. 8(c). The pump generates a net positive pressure gradient along with flow in the positive direction only for  $v_{fl}^* < 3.3$ . The maximum fluid output power in this case (point B) is approximately 20% greater than the power in the absence of an external pressure gradient (point A). It is interesting to note that the pump ceases to generate a net positive pressure gradient at  $v_{fl}^*$  close to 3.3, as it goes into the braking mode beyond this point.

## Conclusions

The efficiency of EHD pumping depends strongly on the bulk fluid velocity. For flow due to a constant, stationary potential gradient, as well as for flow due to repulsion-type induction EHD, the efficiency of EHD pumping increases monotonically with an increase in the bulk fluid velocity. Moreover, the total fluid power output from the combined action of EHD and an externally imposed pressure gradient is larger than the sum of fluid power outputs from their action independent of each other.

The variation of efficiency of an ion-drag EHD pump driven by a traveling potential wave and a transient source of charge density with the bulk fluid velocity depends on the ratio of bulk fluid velocity to the wave velocity. The efficiency of the pump increases with increasing bulk fluid velocity for small values of this ratio and it decreases for large values of this ratio. For attraction-type induction EHD pumps, with flow in the forward direction, the efficiency of EHD action is highest when the fluid velocity is equal to the wave velocity. For fluid velocities in the forward direction larger than the wave velocity, the pump acts to retard the flow.

Results for the input electrical power, output fluid power, and efficiency of EHD action are provided as a function of bulk fluid velocity for the five different EHD pumps considered; graphical pump curves for all the pumps are also developed.

## Acknowledgment

Support in the form of a fellowship for the first author, provided by the Purdue Research Foundation, is gratefully acknowledged.

## Nomenclature

- $A$  = cross-sectional area ( $m^2$ )
- $D$  = charge diffusion coefficient ( $m^2/s$ )
- $E$  = electric field (V/m)
- $E_s$  = electric source number (dimensionless)

$Es_l$  = electric slip number (dimensionless)  
 $f$  = body force per unit mass ( $\text{m/s}^2$ )  
 $F$  = force (N)  
 $h$  = height (m)  
 $I$  = current (A)  
 $J$  = current density in the fluid ( $\text{A/m}^2$ )  
 $k$  = wave number ( $\text{m}^{-1}$ )  
 $L$  = length of the domain (m)  
 $p$  = pressure drop ( $\text{N/m}^2$ )  
 $P$  = power (W)  
 $q$  = charge density in the fluid ( $\text{C/m}^3$ )  
 $Re$  = Reynolds number (dimensionless)  
 $s$  = stress ( $\text{N/m}^2$ )  
 $S$  = surface area ( $\text{m}^2$ )  
 $t$  = time (s)  
 $T$  = temperature (K)  
 $v$  = velocity (m/s)  
 $V$  = voltage (V)  
 $Vol$  = volume ( $\text{m}^3$ )  
 $w$  = width of the domain (m)  
 $x$  =  $x$  direction  
 $y$  =  $y$  direction

### Subscripts and superscripts

$*$  = nondimensional  
 $app$  = applied  
 $c$  = collector  
 $d$  = drift  
 $e$  = emitter  
 $E$  = electric only (without external pressure gradient)  
 $EHD$  = with EHD  
 $El$  = net electric  
 $fl$  = fluid  
 $i$  = input  
 $ion$  = ion  
 $m$  = mechanical  
 $max$  = maximum value (value at the upstream electrode)  
 $No\ EHD$  = without EHD  
 $o$  = output  
 $tot$  = total  
 $wa$  = weighted average  
 $x$  =  $x$  coordinate  
 $y$  =  $y$  coordinate  
 $z$  =  $z$  coordinate

### Greek symbols

$\alpha$  = loss coefficient (dimensionless)  
 $\delta_{ij}$  = Kronecker delta vector (dimensionless)  
 $\varepsilon$  = permittivity of the fluid (F/m)

$\eta$  = efficiency (dimensionless)  
 $\mu$  = electrical mobility of the fluid ( $\text{m}^2/\text{V s}$ )  
 $\mu_{vis}$  = viscosity of the fluid ( $\text{Ns/m}^2$ )  
 $\rho$  = density of the fluid ( $\text{kg/m}^3$ )  
 $\sigma$  = electrical conductivity of the fluid ( $\Omega\ \text{m}$ ) $^{-1}$   
 $\tau$  = charge relaxation time (s)  
 $\tau_{ij}$  = shear stress ( $\text{N/m}^2$ )  
 $\Phi$  = potential (V)  
 $\omega$  = frequency of the potential wave ( $\text{s}^{-1}$ )

### References

- [1] Stuetzer, O., 1959, "Ion Drag Pressure Generation," *J. Appl. Phys.*, **30**, pp. 984–994.
- [2] Robinson, M., 1961, "Movement of Air in the Electric Wind of the Corona Discharge," *J. Am. Inst. Electr. Eng.*, **80**, pp. 143–150.
- [3] Pickard, W., 1963, "Ion Drag Pumping. II. Experiment," *J. Appl. Phys.*, **34**, pp. 251–258.
- [4] Melcher, J. R., 1966, "Traveling-Wave Induced Electroconvection," *Phys. Fluids*, **10**, pp. 1548–1555.
- [5] Gerdt, R. E., Crowley, J. M., and Chato, J. C., 1978, "Electrohydrodynamic Pumping of Cable Oil," *J. Electrostat.*, **5**, pp. 477–488.
- [6] Richter, A., Plettner, A., Hofmann, K. A., and Sandmaier, H., 1991, "A Microfabricated Electrohydrodynamic (EHD) Pump," *Sens. Actuators, A*, **29**, pp. 159–168.
- [7] Ahn, S.-H., and Kim, Y.-K., 1998, "Fabrication and Experiment of a Planar Micro Ion Drag Pump," *Sens. Actuators, A*, **70**, pp. 1–5.
- [8] Bart, S. F., Tavrow, L. S., Mehregany, M., and Lang, J. H., 1990, "Microfabricated Electrohydrodynamic Pumps," *Sens. Actuators, A*, **21–23**, pp. 193–197.
- [9] Fuhr, G., Hagedorn, R., Muller, T., Benecke, W., and Wagner, B., 1992, "Microfabricated Electrohydrodynamic (EHD) Pumps for Liquids of Higher Conductivity," *J. Microelectromech. Syst.*, **1**, pp. 141–146.
- [10] Manz, A., Effenhauser, C. S., Burggraf, N., Harrison, D. J., Seiler, K., and Fluri, K., 1994, "Electroosmotic Pumping and Electrophoretic Separations for Miniaturized Chemical Analysis Systems," *J. Micromech. Microeng.*, **4**, pp. 257–265.
- [11] Zeng, S., Chen, C. H., Mikkelsen, Jr., J. C., and Santiago, J. C., 2001, "Fabrication and Characterization of Electroosmotic Micropumps," *Sens. Actuators B*, **79**, pp. 107–114.
- [12] Bondar, H., and Bastien, F., 1986, "Effect of Neutral Fluid Velocity on Direct Conversion from Electrical to Fluid Kinetic Energy in an Electro-Fluid-Dynamics (EFD) Device," *J. Phys. D*, **19**, pp. 1657–1663.
- [13] Crowley, J. M., 1980, "The Efficiency of Electrohydrodynamic Pumps in the Attraction Mode," *J. Electrostat.*, **8**, pp. 171–181.
- [14] Crowley, J. M., Wright, G. S., and Chato, J. C., 1990, "Selecting a Working Fluid to Increase the Efficiency and Flow Rate of an EHD Pump," *IEEE Trans. Ind. Appl.*, **26**, pp. 42–49.
- [15] Seyed-Yagoobi, J., Bryan, J., and Castaneda, J., 1995, "Theoretical Analysis of Ion-Drag Pumping," *IEEE Trans. Ind. Appl.*, **31**, pp. 469–476.
- [16] Singhal, V., and Garimella, S. V., 2004, "A Novel Micropump for Electronics Cooling," *International Mechanical Engineering Congress and Exposition, IMECE2004-61147*, Anaheim, CA, 1–12.
- [17] Singhal, V., and Garimella, S. V., 2004, "A Novel Valveless Micropump with Electrohydrodynamic Enhancement for High Heat Flux Cooling," *IEEE Trans. Adv. Packag.* (accepted for publication, in press).
- [18] FIDAP 8.7.2, *FIDAP User's Manual*, Fluent, Inc., Lebanon, NH, 2003.
- [19] Melcher, J. R., and Firebaugh, M. S., 1967, "Traveling-Wave Bulk Electroconvection Induced Across a Temperature Gradient," *Phys. Fluids*, **10**, pp. 1178–1185.

Sofiane Khelladi  
e-mail: sofiane.khelladi@paris.enscm.fr

Smaïne Kouidri

Farid Bakir

Robert Rey

Laboratoire d'Energétique et de Mécanique des  
Fluides Interne, Ecole Nationale Supérieure d'Arts  
et Métiers, 151 bd de l'Hôpital, 75013, Paris,  
France

# Flow Study in the Impeller–Diffuser Interface of a Vaned Centrifugal Fan

*In order to better understand the behavior of the fluid flow in vaned centrifugal fans, theoretical and experimental work has been carried out on unsteady three-dimensional (3D) flows. Particular attention is given to the flows located at the rotor–stator interface. This zone is the seat of strong interactions between the moving part and the fixed part. This phenomenon has as consequences: Strongly unsteady flow, fluctuating forces on the stator blades, and an efficiency decrease. This work is part of a project which main objective is the aeroacoustic optimization of high speed centrifugal fans. We present in this paper the first results, mainly aerodynamic ones, which will be used thereafter as an input data to aeroacoustic modeling. A numerical simulation tool was used in order to determine the kinematics and the dynamics of these flows. The measurements of the steady and unsteady flow characteristics allowed a comparison of the theoretical and experimental results. [DOI: 10.1115/1.1900138]*

## Introduction

During the past few years particular attention has been paid to the study of unsteady phenomena related to the complex interactions within the rotor–stator interface of turbomachines. Many experimental and theoretical studies contributed to a better understanding of the nature of the fluctuating flows related to these interactions. Ziegler et al. [1] studied the interaction between the impeller and the diffuser of a centrifugal compressor and its influence on the aerodynamic performance. Wang [2] studied the rotor–stator interaction using a vortex method as well. Sano et al. [3] studied the flow instabilities into a two-dimensional (2D) pump vaned diffuser. In addition, Sinha and Katz et al. [4] made particle image velocimetry (PIV) measurements in order to study the flow structure and turbulence in a centrifugal pump vaned diffuser, in the first stage, and used a passage-averaged approach and large-eddy simulation (LES) modeling [5] to simulate the flows into the vaned machine. Regarding the acoustic field, Jeon et al. [6] used a 2D vortex method for a nonviscous fluid. They considered, in their simulations, only the impeller and the diffuser to analyze the noise generation. Byskov et al. [7] used the LES method to study the kinematics of the flow inside the centrifugal impeller just like Pedersen [8] who used PIV and LDV measurement techniques. Goto [9] proposed a design method based on the study of the unsteady flows between the diffuser blades and within the impeller–diffuser interface. Ardizzon and Pavesi [10] studied a vaned centrifugal fan with a diffuser made up of two parts, the first one is independent and the second one is connected to a return channel.

Centrifugal fans, made up of an impeller, a diffuser, and a return channel, are largely used in the domestic vacuum cleaners. Their high acoustic level constitutes an important criteria of selection for the manufacturers of these appliances. These turbomachines turn at relatively high rotational speeds of about 35000 rpm. The unsteady flow is strong and reaches 250 m/s. Their low efficiency of about 30% is mainly due to the flow disorganization in the impeller–diffuser interface, the junction diffuser – return channel, and the exit of the return channel.

The objective of this paper is the study and the analysis of the aerodynamics of the fluid flow inside the centrifugal fan and par-

ticularly at the impeller–diffuser interface. The emphasis is put on the influence of the axial gap between the impeller and the casing on the overall and local behavior of the flow.

Figures 1 and 2 show the three elements that constitute the fan. The aerodynamic characteristics at operating point are given in Table 1. The geometrical characteristics are presented in Table 2.

## Test Bench

Measurements were carried out on a test bench (see Fig. 3) equipped with an airtight box ( $0.6 \times 0.6 \times 0.6$  m), placed upstream the centrifugal fan, making it possible to vary the flow rate from 12 to 60 l/s by changing the diameter of an orifice plate. The unsteady aerodynamic pressure was measured at various positions within the impeller–diffuser unit. Kulite type dynamic sensors, with a diameter of 1.6 mm and a band-width of 125 kHz were used. They are placed at the impeller inlet [Fig. 3(a)], the impeller–diffuser interface [Fig. 3(b)], the diffuser centerline (Fig. 11), and the return channel outlet [Fig. 3(c)]. This allows the measurement of a static pressure up to 140 mbar and a fluctuating component up to 194 dBA. These aerodynamic data are transmitted to a digital oscilloscope (Gould Nicolet: Sigma 90) with eight simultaneous channels whose band-width is 25 MHz and has a resolution of 12 bits. Figure 3 presents a schematic of the measuring equipment.

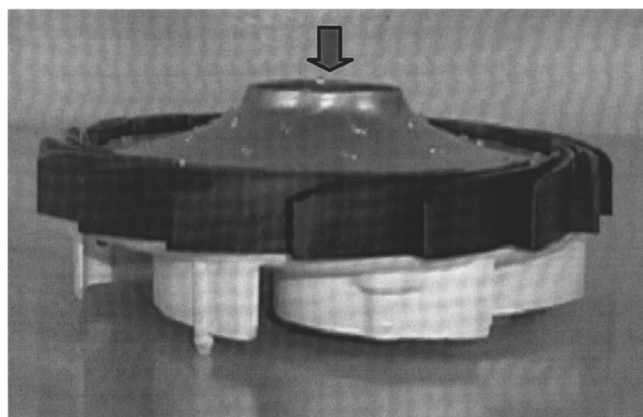


Fig. 1 Impeller, diffuser, and return channel

Contributed by the Fluids Engineering Division for publication in the JOURNAL OF FLUIDS ENGINEERING. Manuscript received June 28, 2004. Final manuscript received March 6, 2005. Associate Editor: Akira GOTO.

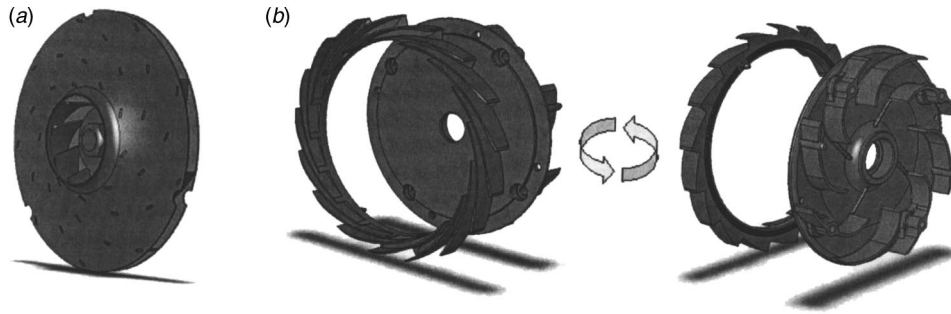


Fig. 2 (a) Centrifugal impeller, (b) diffuser and return channel

Table 1 Aerodynamic characteristics at operating point

Head, $H$ (m)	1300
Flow rate, $Q_v$ ( $m^3/s$ )	$35 \times 10^{-3}$
Rotational speed, $N$ (rpm)	33920
Specific speed $N_s = N\sqrt{Q_v}/H^{3/4}$	29

Table 2 Geometrical characteristics of the centrifugal fan

Description	Impeller	Diffuser	Return channel
Radius of blade inlet (mm)	18	52.7	60
Span of the blade at the entry (mm)	13	6.48	11
Inlet blade angle ( $^\circ$ )	64	85	74
Inclination angle of the blade inlet ( $^\circ$ )	85.8	0	0
Radius of blade exit (mm)	52	66.1	33
Span of the blade at the exit (mm)	5.4	8.43	12
Angle of blade exit ( $^\circ$ )	64	71.6	15
Inclination angle of the blade exit ( $^\circ$ )	0	0	0
Blade number	9	17	8
Blade thickness (mm)	0.8	0.9	1.6

### Numerical Modeling

In order to understand the internal flows and to analyze the fluid behavior of the device, a numerical simulation was carried out. This made it possible to identify the zones with high speed and pressure gradient.

The first step in conducting a numerical simulation is to define the calculation field followed by the generation of the three-dimensional mesh for the selected field. This stage is both the most significant and the most delicate. The costs of calculation

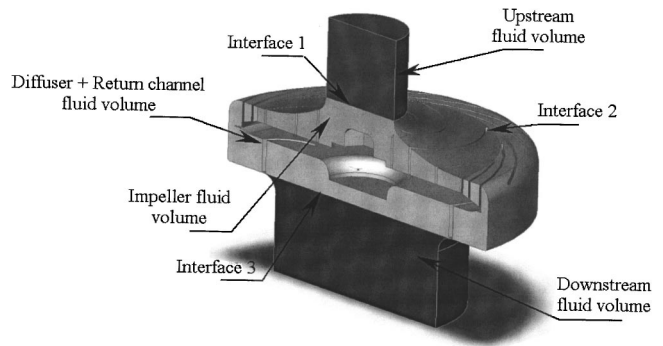


Fig. 4 Fluid volume cross section

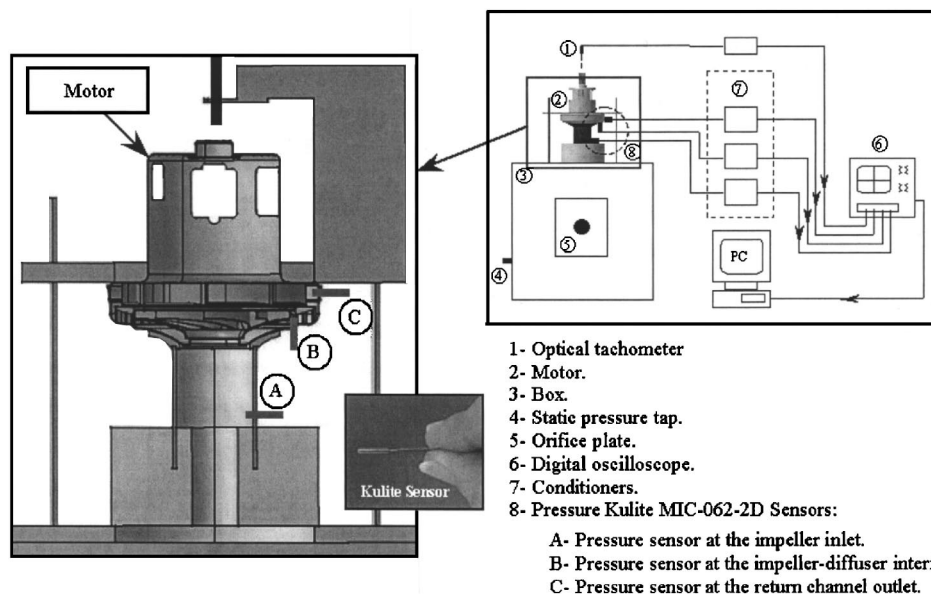


Fig. 3 Diagram of the test bench

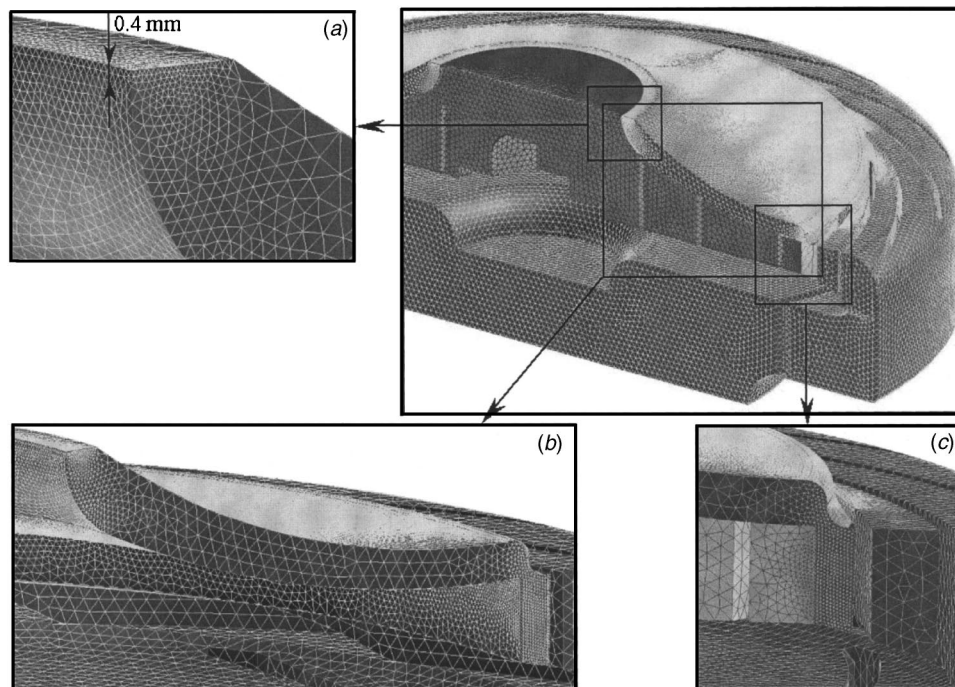


Fig. 5 Cross section of the centrifugal fan meshes

can usually be reduced by considering symmetrical elements and periodicity conditions. Unfortunately, azimuth asymmetry does not allow the benefit of this practice in this case.

The numerical simulations have been carried out with a code that is based on the finite volume numerical method using the commercial code FLUENT 6.1 [11] to solve the full 3D Reynolds average Navier–Stokes equations.

For numerical stability reasons, two fluid volumes, one upstream and one downstream, are added. They do not simulate the actual geometry of the experimental equipment, they are added to the numerical model in order to reduce the effects of the inlet and outlet boundary conditions on the aerodynamic characteristics of the impeller inlet and the return channel outlet.

This configuration results in the three nonconformal interfaces presented in Fig. 4.

As the geometry of the fan is complex, a hybrid mesh is used: Tetrahedral for the impeller and the diffuser-return channel volumes, hexahedral for upstream and downstream fluid volumes. Figure 5 shows grids around the gap (b), around the inlet side (a), and around the impeller–diffuser interface (c).

**Mesh Independence.** Theoretically, the errors in the solution related to the grid must disappear for an increasingly fine mesh. The static pressure at the centrifugal fan inlet was taken as the parameter to evaluate and determine the influence of the mesh size on the solution space (see Table 3). The selected convergence criteria was a maximum residual of  $10^{-6}$ . In Fig. 6, it is observed how the calculated static pressure at the centrifugal fan inlet reaches an asymptotic value as the number of meshes increases.

Table 3 Evaluated grid sizes

Characteristics	Number of meshes
Grid A	800,000
Grid B	1,500,000
Grid C	1,900,000
Grid D	2,300,000
Grid E	3,100,000
Grid F	4,400,000

According to this figure, the grid F ( $4.4 \times 10^6$  meshes) is considered to be sufficiently reliable to ensure mesh independence.

**Turbulence model.** A statistical turbulence model was used within the framework of this numerical simulation. The  $\kappa\text{-}\omega$  SST (shear stress transport) model was adopted. It uses a treatment close to the wall combining a correction for high and low Reynolds number in order to predict separation on smooth surfaces. This model gives a realistic estimation of the generation of the turbulent kinetic energy at the stagnation points. It is more accurate and more robust than the  $\kappa\text{-}\omega$  or  $\kappa\text{-}\epsilon$  standard models [12].

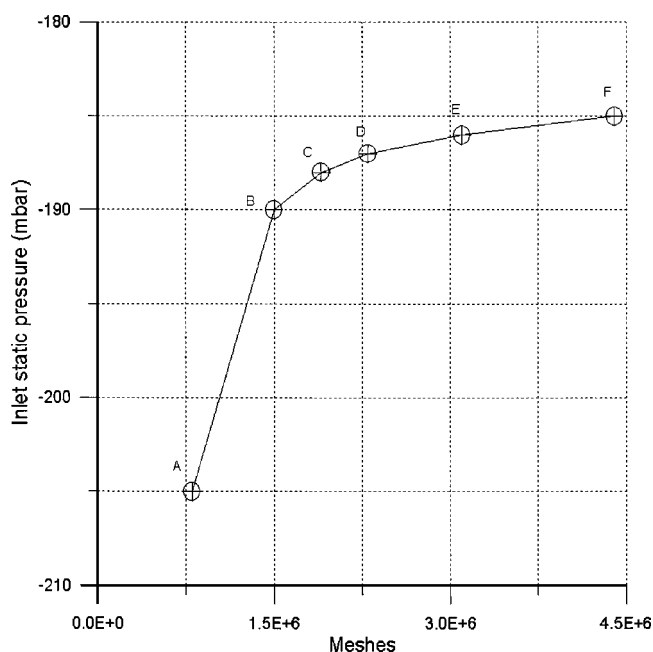


Fig. 6 Influence of grid size on the static pressure at the centrifugal fan inlet

**Table 4 Computation criteria applied to numerical simulation with boundary conditions at operating point**

Characteristic	Description	Value
Simulation	unsteady 3D	-
Fluid	Compressible (air)	Density =1.2
simulation domain	Impeller + diffuser + return channel	(9+17+8) blades
Rotational speed	...	$N=34560$ rpm
Turbulence model	2 equations	$\kappa-\omega$ SST
Equation of energy	Solved	-
Roughness of wall	Smooth	0 [mm]
Inlet boundary condition	velocity	$V=38.17$ [m/s]
Outlet boundary condition	Static pressure.	$P_s=25.1$ [mbar]
Interface	3 nonconformal interfaces	-
Inlet temperature	...	$T=300$ [k]
Average residues	...	$10^{-6}$
Time step	...	$10^{-5}$ s
Computing time	50 iterations per time step	0.4 h (bi-processor) per time step

The SST model performance has been studied in a large number of cases. In a NASA Technical Memorandum [13], SST model was rated the most accurate model for aerodynamic applications.

**Numerical model.** The unsteady terms are implicit second-order discretized. A centered *SIMPLE* algorithm is used for the pressure-velocity coupling and a second-order upwind discretization is used for the convection and diffusion terms. The conservation equations are solved using a segregated solver.

The boundary conditions selected for this simulation are the velocity at the upstream volume inlet and the static pressure at the downstream volume outlet (see Fig. 4 and Table 4). The value of

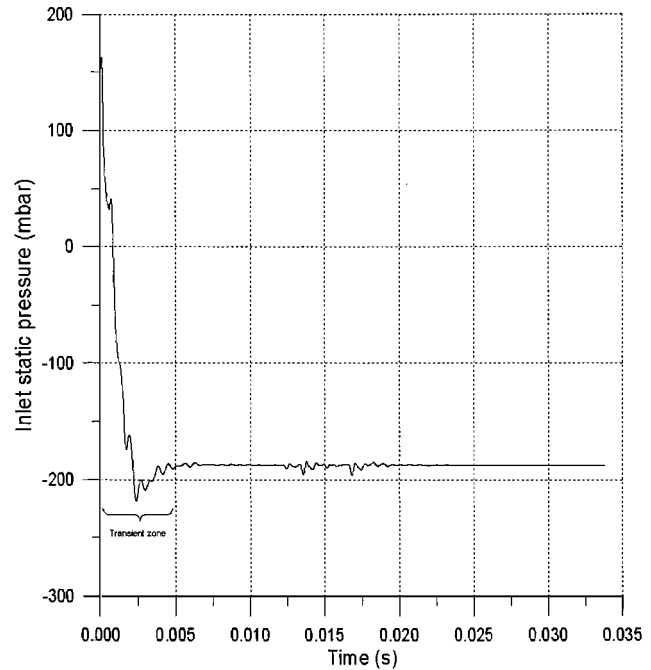


**Fig. 7 Convergence of the static pressure at the inlet of the impeller**

the outlet pressure, applied as boundary condition at the exit part of the downstream volume, comes from the experimental measurement at the outlet side of the engine.

**Convergence.** Figure 7 represents the time history of the static pressure convergence at the impeller inlet. This part of the study

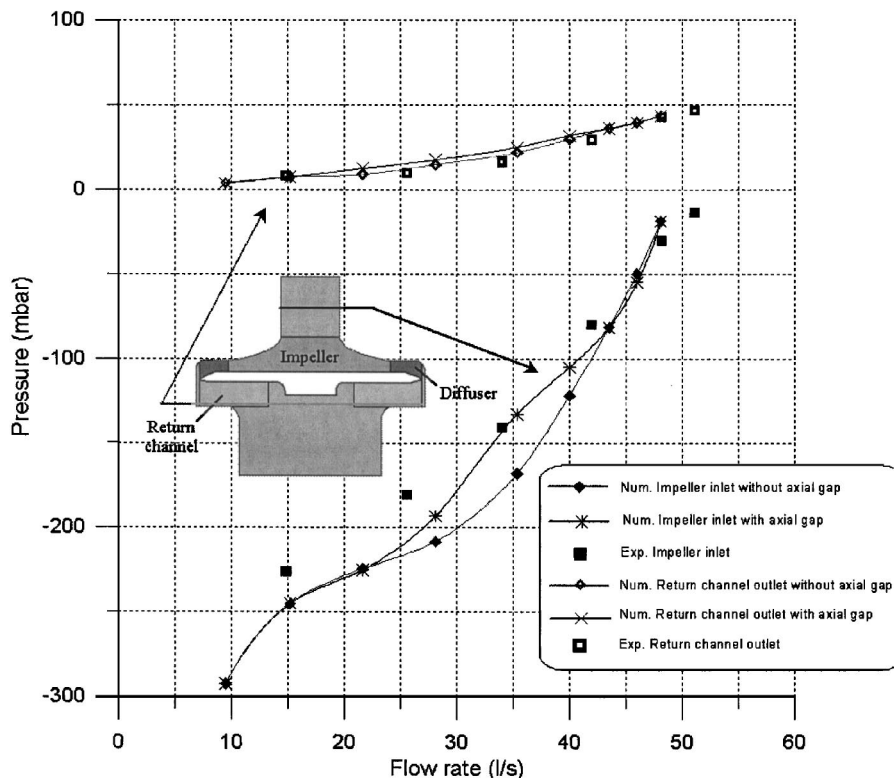


**Fig. 8 Aerodynamic characteristics of the centrifugal fan**



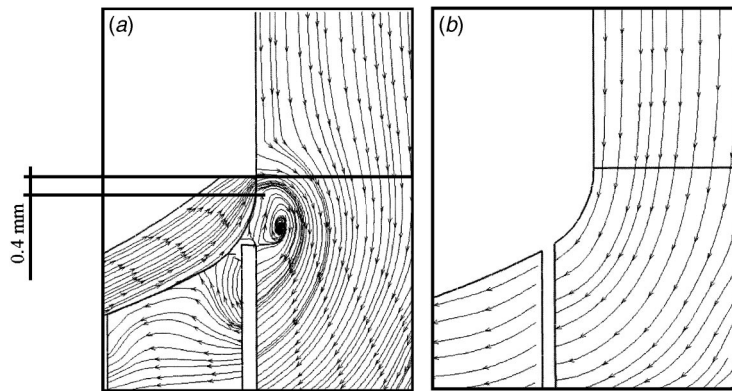


Fig. 9 Streamline pattern at the impeller inlet. With axial gap (a), without axial gap (b) - flow rate =35 l/s

was carried out by using Grid F, with a maximum residue lower or equal to  $10^{-6}$ . It is noticed that the convergence is reached after 0.005 s, which corresponds to three revolutions of the impeller at 34,560 rpm.

### Results and Interpretation

Experimental measurements were conducted in order to get the overall and local air-flow characteristics. Two numerical simulations were carried out, the first one does not take into account the axial gap between the impeller and the casing, while the second one does. The simulation results relating to the pressure development in various parts of the fan are compared with the experimental results.

For all pressure measurements the uncertainty is  $\pm 2.5$  mbar.

Figure 8 represents the evolution of the pressure according to the flow rate with an uncertainty of  $\pm 0.4$  l/s at the inlet of the impeller and the outlet of the return channel. At the outlet of the return channel measurements and numerical results are in good agreement. At the impeller inlet, the theoretical pressure curve not taking into account the axial gap between the impeller and the casing, predicts more depression compared to tests and case with axial gap, particularly with flow rates from 21 to 40 l/s. The pressure rise difference between with and without gap is due to the presence of strong vortex at the impeller entrance which leads to the reduction in total and static pressure rise (pressure difference between the inlet and the outlet), see Fig. 9. The effect of vortices decreases at partial flows. The theoretical pressure curve taking into account the axial gap is in good agreement with the

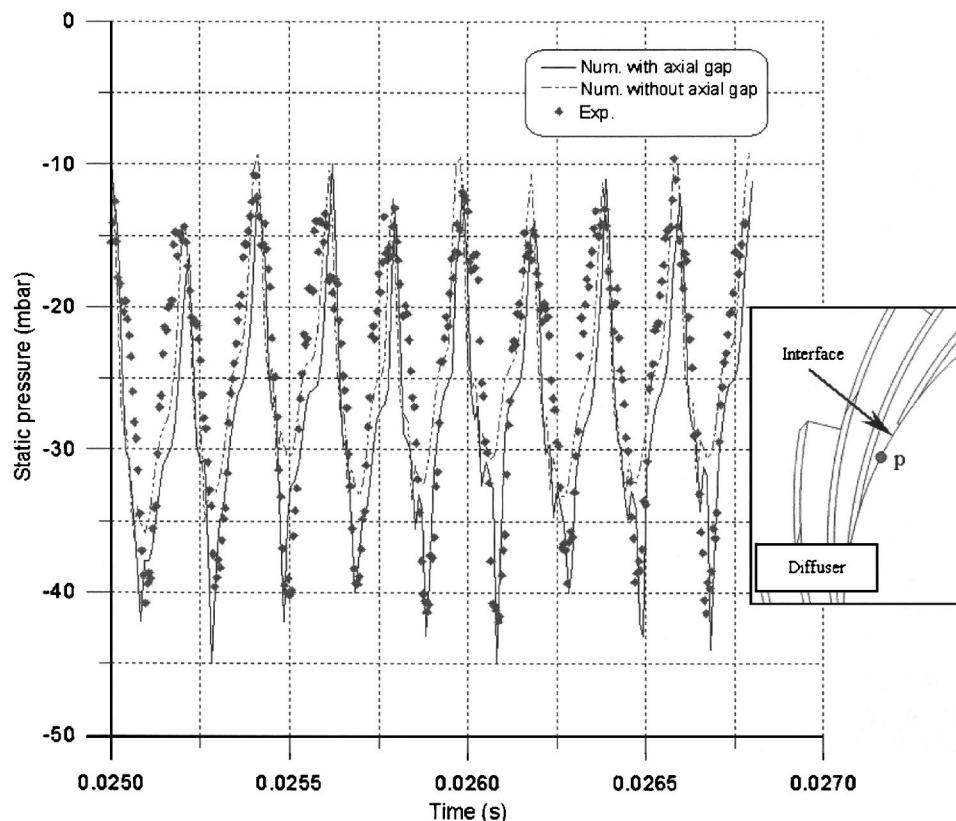
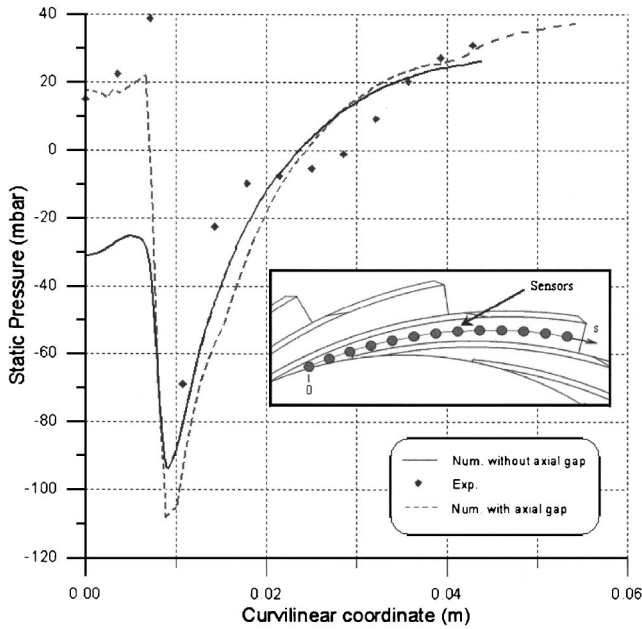


Fig. 10 Variation of the pressure at a point on the impeller-diffuser interface vs time-flow rate =35 l/s.



**Fig. 11 Evolution of the static pressure in the curvilinear direction along the axial clearance of the diffuser—flow rate =35 l/s**

experimental results particularly with flow rates greater or equal to 35 l/s. Numerical simulation gives about 7.5% of leakage flow rate for all flow rates. Figure 10 represents the pressure fluctuation versus time, at point  $p$ , as obtained by calculations and tests at the operating point. The uncertainty in time measurement was  $\pm 2.5 \times 10^{-6}$  s. Notice that the measurement point is located at the midline of two diffuser blades on the impeller–diffuser interface, so that the blade to blade interaction between the impeller and the diffuser and the separation at the blades leading edge of the diffuser do not disturb the measurement.

On the graph, one distinguishes the impeller blade passage as characterized by pressure peaks. The pressure decreases quickly just after the blade passage and increases gradually with the approach of the following blade. The peak to peak pressure gradient due to the blade impeller passing is relatively important (30 mbar). A significant difference between theoretical results with and without axial gap is noted at low pressure peaks. These hollows correspond to a middle distance between two rotor blades. The comparison between tests and numerical simulations validates this result. The calculation result taking into account the axial gap is closer to the tests than that without axial gap. The general shape of the two calculation results are quite similar, the same curvatures are observed at the same time positions. So the axial clearance only affects the peak to peak pressure gradient.

Figure 11 represents the variation of the static pressure along the centerline of the diffuser as measured by flush mounted sensors that do not disturb the flow. The uncertainty in the curvilinear coordinate distance ( $s$ ) is  $\pm 0.1$  mm.

The first three points (curvilinear coordinate =0–0.008 m) of measurement in Fig. 11 are located in a recirculation zone shown in Fig. 12. The position of the sensor in this recirculation zone does not allow an accurate measurement of the static pressure. The noted variation for these points of measurement is probably due to the additional pressure imposed on the static pressure sensor by the flow normal to it. The results of the two numerical simulation show the effect of the axial clearance between the impeller and the casing on the general shape of the curve. In fact, for the first numerical simulation the axial clearance  $j$  is not included in the geometry used to obtain the numerical solution. So the leakage flow which passed through this gap increases the value of

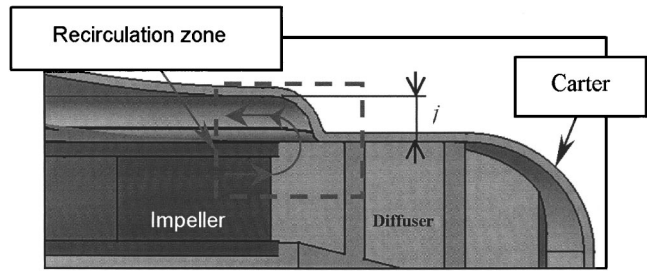
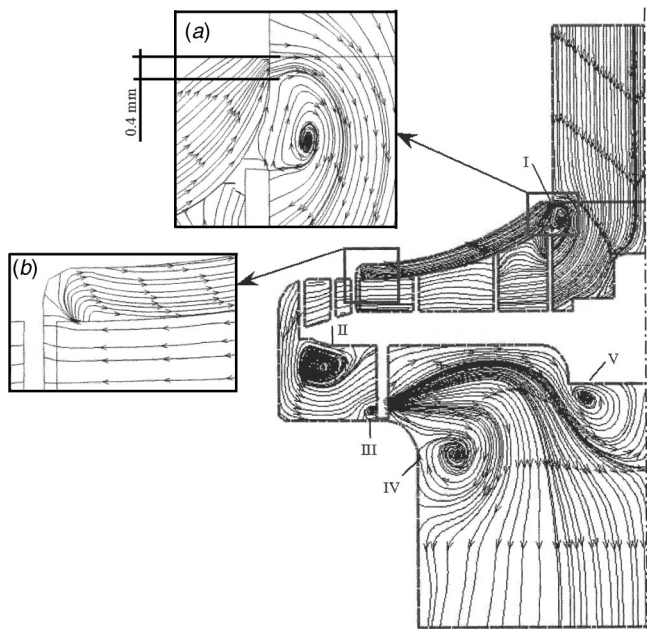


**Fig. 12 Axial clearance between the impeller and the casing**

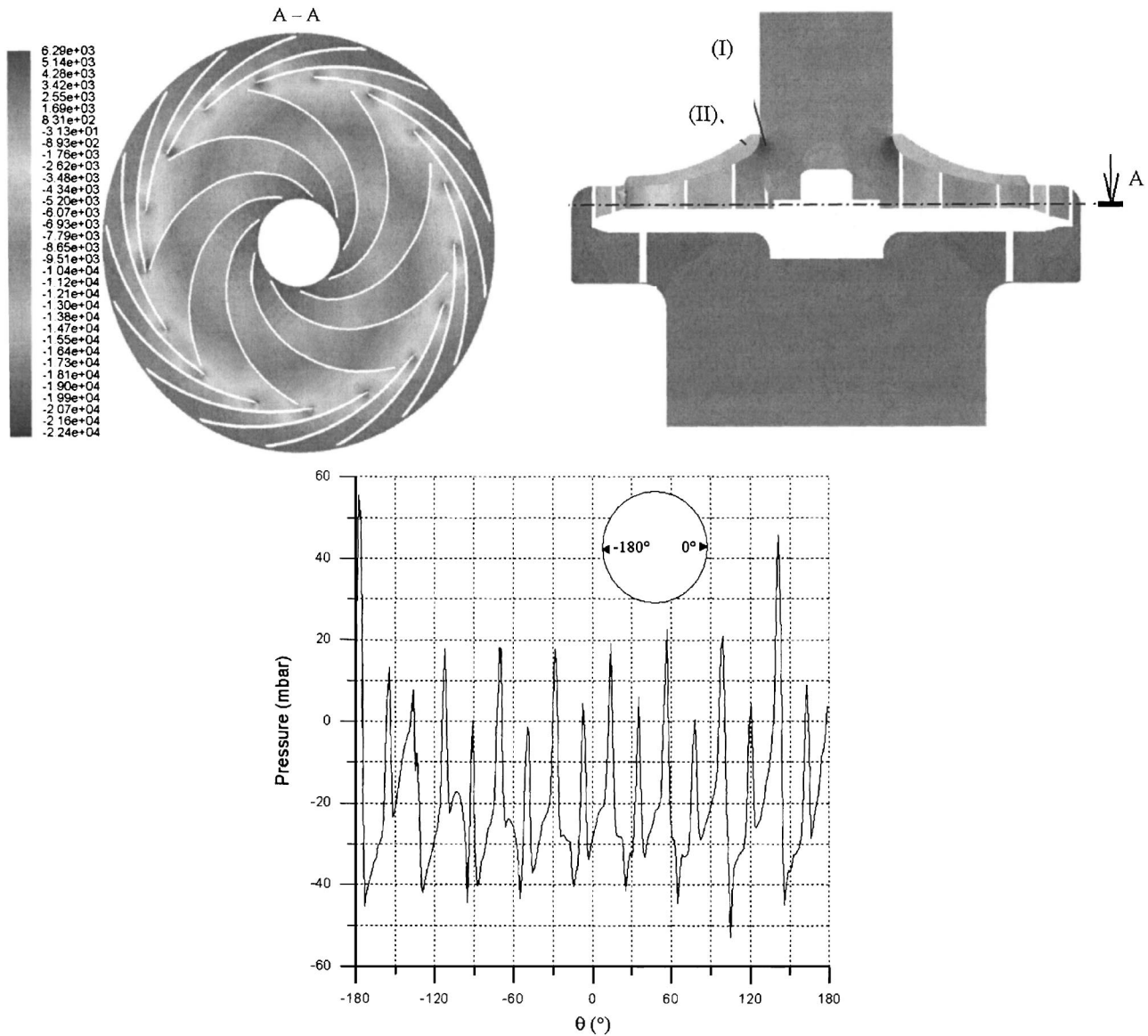
the pressure which ranks from –30 to 20 mbar (at the interface close to the casing). Just after this zone (curvilinear coordinate =0.008–0.01 m) the pressure falls quickly at the leading edge of the diffuser to increase until reaching its maximum value on the outlet side of the diffuser (curvilinear coordinate =0.01–0.045 m). The diffuser transforms a part of the kinetic energy to pressure energy, it increases the pressure from –100 to 30 mbar.

Figure 13 shows the streamline pattern into the centrifugal fan at axial cross section and details around the gap at impeller inlet side (a) and impeller outlet side (b). A portion of the fluid is returned to the impeller inlet through the axial clearance between the impeller and casing. On the figure, five vortices are observed: (i) At the impeller inlet due to leakage flow, (ii) at the cross-over due to the abrupt change of direction, (iii) at the lower side of the return channel blade due to the stagnation point, and finally (iv) and (v) at the downstream duct due to the abrupt change of passage section. These vortices penalize and decrease the overall performances of the centrifugal fan.

Figure 14 shows the static pressure field obtained by numerical simulation at operating point and the azimuth variation of the static pressure obtained by the numerical simulation along the impeller–diffuser interface. The calculations take into account the axial gap. The pressure peaks correspond to the leading edge of the diffuser blades (a max. of 50 mbar). There is a large variation of the pressure over a small angular distance corresponding to the interface (about 60 mbar in some regions). The figure shows that



**Fig. 13 Streamline pattern at axial cross section of the centrifugal fan—flow rate =35 l/s. (a)—The gap at the inlet side. (b)—Recirculation zone**



**Fig. 14** Instantaneous static pressure field and variation of the static pressure at impeller–diffuser interface—Flow rate =35 l/s

in the impeller–diffuser interface the pressure is maximum at an instant of time when the impeller blade is approaching the diffuser. As shown in Fig. 11 also, at the diffuser inlet there is a little zone (a spot) of depression, the pressure falls from 20 to –110 mbar through a very small distance. In Fig. 12, at the impeller inlet the gap between the casing and the impeller creates a big gradient of pressure between the impeller side (i) and the casing side (ii) of about 150 mbar, this difference produces the leakage flow at the impeller outlet.

Figure 15 represents the absolute velocity field inside the centrifugal fan at the same instant of time as Fig. 13. The maximum value of velocity 189 m/s is located at the hub and shroud of the impeller at its outlet side. It decreases considerably at the diffuser outlet, 40 m/s. At point (a) of the impeller inlet the velocity is about 70 m/s; this is due to the abruptness of the section change.

Figure 16 shows the instantaneous turbulence intensity of the flow entering the centrifugal fan at the operating point. The area located between the impeller–diffuser interface and the inlet of the diffuser channels experiences a high level of turbulence intensity (varying from 6% to 11%). At the return channel outlet the turbulence intensity is about 5%. The presence of the axial gap creates

a zone of turbulence at the impeller inlet (with an intensity of 10%). Note that all zones with high turbulence intensity are supposed to be the main source of noise in the centrifugal fan. The flow organization contributes in a narrow way to the mechanism

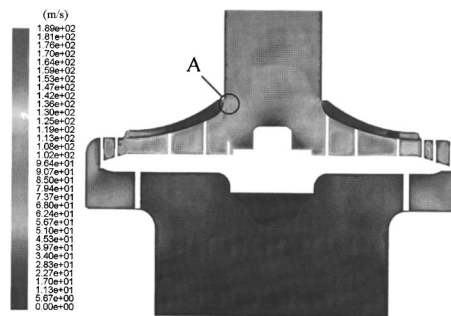


**Fig. 15** Instantaneous velocity magnitude—flow rate =35 l/s

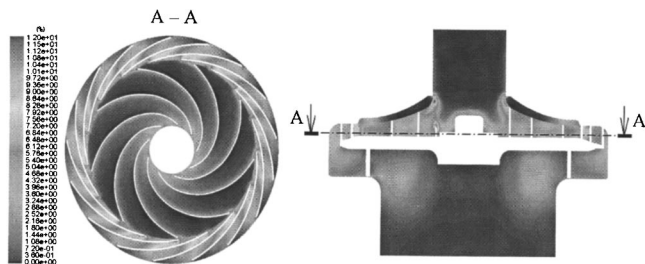


Fig. 16 Instantaneous turbulence Intensity—flow rate =35 l/s

of noise generation. The turbulence intensity can be regarded as a qualitative criterion allowing an aeroacoustic optimization of these machines. The presence of a high level of turbulence at the impeller–diffuser interface allows to predict a generated sound radiation.

### Conclusion

The unsteady flow in a vaned centrifugal fan has been studied. A tool for numerical simulation was used in order to determine the kinematics and the dynamics of the flow field.

A first numerical simulation which did not take into account the axial clearance between the impeller and the casing was carried out. The first comparisons carried out with experimental tests highlighted the importance of taking into account this geometrical parameter. A new modeling of the 3D and unsteady flow of the real geometry of the centrifugal fan was carried out.

Experimental acquisition of the unsteady aerodynamic characteristics allowed the comparison of the theoretical and experimental results, and therefore, the validation of the numerical modeling. Taking into account the axial gap on this numerical simulation allowed a better local and overall behavior of the flow in the centrifugal fan. This modeling gives a satisfactory approach of the centrifugal fan characteristic at operating point flow rate.

The fluctuating pressure at the impeller–diffuser interface was correctly predicted by the numerical simulation only if the axial gap is taken into account. The results of the numerical simulation make it possible to identify the regions with high gradient of pressure located at the impeller–diffuser interface. The significant flow velocity at some points, 189 m/s, involves zones with high shear stress. This result is consolidated by turbulence intensities calculated in this area. The qualitative analysis of the nature of the

flow, high pressure gradient, turbulence intensity and significant velocity, make it possible to release a methodology to design prototypes in the near future.

This study thanks to which our numerical modeling has been validated will be used in a future work in order to determine the necessary aerodynamic characteristics for an aeroacoustic modeling.

### Acknowledgments

The present study is supported by Ministère de l'Industrie. The authors would like to thank the different partners involved in this project and particularly ROWENTA for allowing us to present some results of this work.

### References

- [1] K. U. Ziegler, H. E. Gallus, and R. Niehuis, 2003, "A Study on Impeller-Diffuser Interaction - Part I: Influence on Performance," *ASME J. Turbomach.*, **125**, pp. 173–182.
- [2] H. Wang, and H. Tsukamoto, 2001, "Fundamental Analysis on Rotor-Stator Interaction in a Diffuser Pump by Vortex Method," *ASME J. Fluids Eng.*, **123**, pp. 737–747.
- [3] T. Sano, Y. Yoshida, Y. Tsujimoto, Y. Nakamura, and T. Matsushima, 2002, "Numerical Study of Rotating Stall in a Pump Vaned Diffuser," *ASME J. Fluids Eng.*, **124**, pp. 363–370.
- [4] M. Sinha, and J. Katz, 2000, "Quantitative Visualization of the Flow in a Centrifugal Pump With Diffuser Vanes—I: On Flow Structures and Turbulence," *ASME J. Fluids Eng.*, **122**, pp. 108–116.
- [5] M. Sinha, J. Katz, and C. Meneveau, 2000, "Quantitative Visualization of the Flow in a Centrifugal Pump With Diffuser Vanes—II: Addressing Passage-Averaged and Large-Eddy Simulation Modeling Issues in Turbomachinery Flows," *ASME J. Fluids Eng.*, **122**, pp. 97–107.
- [6] W. H. Jeon, S. J. Baek and C. J. Kim, 2003, "Analysis of the Aeroacoustic Characteristics of the Centrifugal Fan in a Vacuum Cleaner," *J. Sound Vib.*, **268**, pp. 1025–1035.
- [7] R. K. Byskov, C. B. Jacobsen, and N. Pedersen, 2003, "Flow in a Centrifugal Pump Impeller at Design and Off-Design Conditions - Part II: Large Eddy Simulations," *ASME J. Fluids Eng.*, **125**, pp. 73–83.
- [8] N. Pedersen, and C. B. Jacobsen, 2003, "Flow in a Centrifugal Pump Impeller at Off-Design Conditions - Part I: Particle Image Velocimetry (PIV) and Laser Doppler Velocimetry (LDV) Measurements," *ASME J. Fluids Eng.*, **125**, pp. 61–72.
- [9] A. Goto, and M. Zangeneh, 2002, "Hydrodynamic Design of Pump Diffuser Using Inverse Design Method and CFD," *ASME J. Fluids Eng.*, **124**, pp. 319–328.
- [10] G. Ardizzon, and G. Pavesi, 2004, "Analysis of Unsteady Flow in a Vaned Diffuser Radial Flow Pump", *The 10th of International Symposium on Transport Phenomena and Dynamics of Rotating Machinery Honolulu, Hawaii, March 7–11*.
- [11] FLUENT, Fluent, Inc., 1998.
- [12] Menter, F. R., 1993, "Zonal Two Equation  $k-\omega$  Turbulence Models for Aerodynamic Flows," AIAA Pap. 93-2906.
- [13] J. E., Bardina, P. G., Huang and T. J., Coakley, 1997, "Turbulence Modeling, Validation, Testing and Development," NASA Technical Memorandum 110446.

# On the Physics of Flow Separation Along a Low Pressure Turbine Blade Under Unsteady Flow Conditions

**Meinhard T. Schobeiri**

**Burak Öztürk**

Turbomachinery Performance and Flow Research  
Laboratory, Texas A&M University, College  
Station, TX 77843-3123

**David E. Ashpis**

National Aeronautics and Space Administration,  
John H. Glenn Research Center at Lewis Field,  
Cleveland, OH 44135-3191

*The present study, which is the first of a series of investigations dealing with specific issues of low pressure turbine (LPT) boundary layer aerodynamics, is aimed at providing detailed unsteady boundary flow information to understand the underlying physics of the inception, onset, and extent of the separation zone. A detailed experimental study on the behavior of the separation zone on the suction surface of a highly loaded LPT-blade under periodic unsteady wake flow is presented. Experimental investigations were performed at Texas A&M Turbomachinery Performance and Flow Research Laboratory using a large-scale unsteady turbine cascade research facility with an integrated wake generator and test section unit. To account for a high flow deflection of LPT-cascades at design and off-design operating points, the entire wake generator and test section unit including the traversing system is designed to allow a precise angle adjustment of the cascade relative to the incoming flow. This is done by a hydraulic platform, which simultaneously lifts and rotates the wake generator and test section unit. The unit is then attached to the tunnel exit nozzle with an angular accuracy of better than 0.05°, which is measured electronically. Utilizing a Reynolds number of 110,000 based on the blade suction surface length and the exit velocity, one steady and two different unsteady inlet flow conditions with the corresponding passing frequencies, wake velocities and turbulence intensities are investigated using hot-wire anemometry. In addition to the unsteady boundary layer measurements, blade surface pressure measurements were performed at  $Re=50,000, 75,000, 100,000, \text{ and } 125,000$  at one steady and two periodic unsteady inlet flow conditions. Detailed unsteady boundary layer measurement identifies the onset and extent of the separation zone as well as its behavior under unsteady wake flow. The results presented in ensemble-averaged and contour plot forms contribute to understanding the physics of the separation phenomenon under periodic unsteady wake flow. Several physical mechanisms are discussed. [DOI: 10.1115/1.1905646]*

## Introduction

In recent years gas turbine engine aerodynamicists have focused their attention on improving the efficiency and performance of the low pressure turbine (LPT) component. Research at industry, research centers, and academia has shown that reduction in blade count can be achieved without substantially sacrificing the efficiency of the LPT-blading. This reduction contributes to an increase in thrust/weight ratio, thus reducing the fuel consumption. Contrary to the high pressure turbine (HPT) that operates in a relatively high Reynolds number environment, the LPT experiences a variation in Reynolds number ranging from 50,000 to 250,000 dependent on operation conditions. Since the major portion of the boundary layer, particularly along the suction surface, is laminar, the low Reynolds number in conjunction with the local adverse pressure gradient makes it susceptible to flow separation, thus increasing the complexity of the LPT-boundary layer aerodynamics. The periodic unsteady nature of the incoming flow associated with wakes substantially influences the boundary layer development including the onset and extent of the laminar separation and its turbulent re-attachment. Of particular relevance in context of LPT-aerodynamics is the interaction of the wake flow with the suction surface separation zone. While the phenom-

enon of the unsteady boundary layer development and transition in the absence of separation zones has been the subject of intensive research that has led to better understanding the transition phenomenon, comprehending the multiple effect of mutually interacting parameters on the LPT-boundary layer separation and their physics still requires more research.

The significance of the unsteady flow effect on the efficiency and performance of compressor and turbine stages was recognized in the early seventies by several researchers. Fundamental studies by Pfeil and Herbst [1], Pfeil et al. [2], and Orth [3] studied and quantified the effect of unsteady wake flow on the boundary layer transition along flat plates. Schobeiri and his co-workers [4–7] experimentally investigated the effects of periodic unsteady wake flow and pressure gradient on the boundary layer transition and heat transfer along the concave surface of a constant curvature plate. The measurements were systematically performed under different pressure gradients and unsteady wake frequencies using a squirrel cage type wake generator positioned upstream of the curved plate. Liu and Rodi [8] carried out boundary layer and heat transfer measurements on a turbine cascade, which was installed downstream of a squirrel cage type wake generator mentioned previously.

Analyzing the velocity and the turbulence structure of the impinging wakes and their interaction with the boundary layer, Chakka and Schobeiri [7] developed an intermittency based unsteady boundary layer transition model. The analysis revealed a universal pattern for the relative intermittency function for all frequencies and pressure gradient investigated. However, the above

Contributed by the Fluids Engineering Division for publication in the JOURNAL OF FLUIDS ENGINEERING. Manuscript received by the Fluids Engineering Division August 3, 2004; Final manuscript received February 24, 2005. Review conducted by Joseph Katz.

investigations were not sufficient to draw any conclusion with regard to universal character of the relative intermittency function. Further detailed investigations of the unsteady boundary layer along a high Reynolds number turbine blade of the Space Shuttle Main Engine (SSME) by Schobeiri et al. [9] and its subsequent analysis [10–12] verified the universal character of the relative intermittency function. For this purpose, Schobeiri et al. [9] utilized a conceptually different type wake generator, which is also used for the investigation presented in this paper. Fottner and his co-workers [13,14] and Schulte and Hodson [15] used the same wake generating concept for investigating the influence of unsteady wake flow on the LPT-boundary layer. Kaszeta, Simon, and Ashpis [16] experimentally investigated the effect of unsteady wakes on laminar–turbulent transition within a channel with the side walls simulating the suction and pressure surfaces of a LPT-blade. They utilized a retractable cascade of cylindrical rods for generating the unsteady wakes. Lou and Hourmouziadis [17] experimentally investigated the effect of oscillating inlet flow conditions on laminar boundary layer separation along a flat plate under a strong negative pressure gradient which was imposed by the opposite wall.

Using the surface mounted hot film measurement technique, Fottner and his co-workers [13,14], Schröder [18], and Hauelsen, Schröder, and Hennecke [19] documented strong interaction between wakes and the suction surface separation zone on LPT-blades, both in wind tunnel cascade tests and in turbine rig. Furthermore, they investigated the boundary layer transition under the influence of periodic wakes along the LPT-surface and found that the interaction of wakes with the boundary layer greatly affects the loss generation. Investigations by Halstead et al. [20] on a large-scale LP-turbine use surface mounted hot films to acquire detailed information about the quasi-shear stress directly on the blade surface. As investigations by Cardamone et al. [14] and Schröder [18] indicate, the benefit of the wake-boundary layer interaction can be used for design procedure of modern gas turbine engines with reduced LPT-blade number without altering the stage efficiency.

Most of the above mentioned studies on LP-turbine cascade aerodynamics have largely concentrated on the measurement of the signals stemming from hot film mounted on the suction and pressure surfaces of the blades under investigation. Although this technique is effective in qualitatively reflecting the interaction of the unsteady wake with the boundary layer, because of lack of an appropriate calibration method, it is not capable of quantifying the surface properties such as the wall shear stress. The few boundary layer measurements are not comprehensive enough to provide any conclusive evidence for interpretation of the boundary layer transition and separation processes and their direct impact on the profile loss, which is a critical parameter for blade design. Furthermore, numerical simulation of unsteady LPT-blade aerodynamics using conventional turbulence and transition models fails if applied to low Reynolds number cases. Recent work presented by Cardamone et al. [14] shows that in the steady state case at  $Re = 60,000$ , the separation is captured, however, in the unsteady case, the separation zone is not reproduced.

The objective of the present study, which is the first of a series of investigations dealing with specific issues of LPT-boundary layer aerodynamics, is to provide detailed unsteady boundary flow information to understand the underlying physics of the inception, onset, and extent of the separation zone. Furthermore, the unsteady boundary layer data from the present and planned experimental investigations will serve to extend the intermittency based unsteady boundary layer transition model developed by Schobeiri and his co-workers [7,11,12] to the LPT-cases, where separation occurs on the suction surface at low Reynolds number at design and off-design points. Furthermore, the experimental results are intended to serve as a benchmark data for comparison with numerical computation using DNS, LES, or RANS-codes.

It is well known that boundary layer measurement is one of the

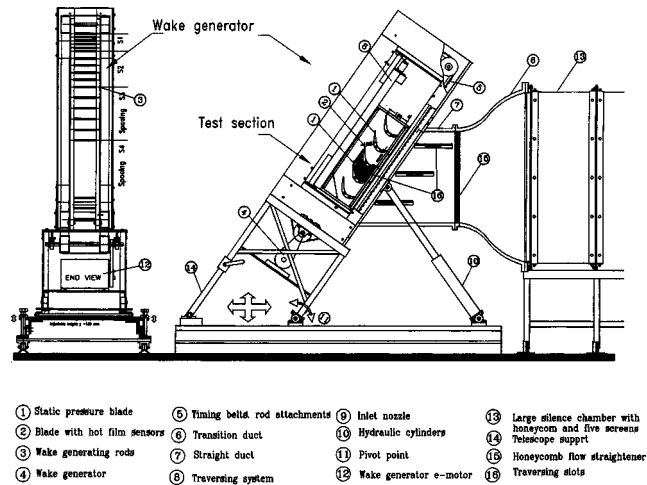


**Fig. 1 Turbine cascade research facility with the components and the adjustable test section**

time consuming aerodynamic measurements. Any attempt to increase the number of parameters to be studied would inevitably result in a substantial increase of the measurement time. Considering this fact, the research facility described in Refs. [9,10] with state-of-the-art instrumentation has been substantially modified to study systematically and efficiently the influence of periodic unsteady and highly turbulent flow on LPT-cascade aerodynamics at the design and off-design incidence angles, where Reynolds number, wake impingement frequency, free-stream turbulence, and the blade solidity can be varied independently.

### Experimental Research Facility

To investigate the effect of unsteady wake flow on turbine and compressor cascade aerodynamics, particularly on unsteady boundary layer transition, a multipurpose large-scale cascade research facility was designed and has been taken into operation since 1993.

Since the facility in its original configuration is described in Refs. [9,10], only a brief description of the modifications and the main components is given below. The research facility consists of a large centrifugal air supplier, a diffuser, a settling chamber, a nozzle, an unsteady wake generator, and a turbine cascade test section (Fig. 1). An air supplier with a volumetric flow rate of  $15 \text{ m}^3/\text{s}$  is capable of generating a maximum mean velocity of  $100 \text{ m/s}$  at the test section inlet. The settling chamber consists of five screens and one honeycomb flow straightener to control the uniformity of the flow.

Two-dimensional periodic unsteady inlet flow is simulated by the translational motion of a wake generator (see Fig. 1), with a series of cylindrical rods attached to two parallel operating timing belts driven by an electric motor. To simulate the wake width and spacing originating from the trailing edge of rotor blades, the diameter and number of rods can be varied. The rod diameter, its distance from the LPT-blade leading edge, the wake width and the corresponding drag coefficient are chosen according to the criteria outlined by Schobeiri et al. [21]. The belt-pulley system is driven by an electric motor and a frequency controller. The wake-passing frequency is monitored by a fiber-optic sensor. The sensor also serves as the triggering mechanism for data transfer and its initialization, which is required for ensemble-averaging. This type of wake generator produces clean two-dimensional wakes, whose turbulence structure, decay and development is to a great extent predictable [21]. The facility was used for many unsteady boundary layer transition and heat transfer investigations [9–12] that serve as benchmark data for validation of turbulence and transition models and for general code assessments.

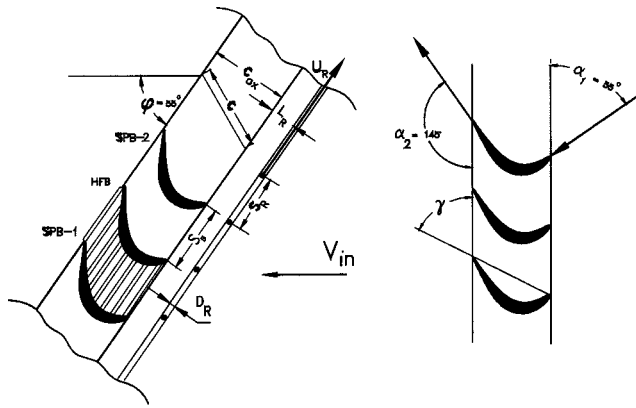


**Fig. 2 Cascade geometry and stagger angle are listed in Table 1. Number of blades=5, SPB-1 and SPB-2 are blades with static pressure taps, HFB is instrumented with surface mounted hot films to be used for future investigations.**

To account for the inlet flow angle and a high flow deflection of LPT-cascade, the entire wake generator and test section unit including the traversing system were modified to allow a precise angle adjustment of the cascade relative to the incoming flow. This is done by a hydraulic platform, which simultaneously lifts and rotates the wake generator and test section unit. The unit is then attached to the tunnel exit nozzle with an angular accuracy less than  $0.05^\circ$ , which is measured electronically.

The special design of the facility and the length of the belts ( $L_{belt}=5,000$  mm) enables a considerable reduction of measurement time. For the present investigation, two clusters of rods with constant diameter of 2 mm are attached to the belts. The two clusters with spacings  $S_R=160$  mm and  $S_R=80$  are separated by a section which does not have any rods, simulating steady state case ( $S_R=\infty$ ). Thus, it is possible to measure sequentially the effect of three different spacings at a single boundary layer point. To clearly define the influence domain of each individual cluster with the other one, the clusters are separated by a certain distance. Using the triggering system mentioned above and a continuous data acquisition, the buffer zones between the data clusters are clearly visible. The data analysis program removes the buffer zones and extracts the data pertaining to each cluster. Comprehensive preliminary measurements were carried out to ensure that the data were exactly identical with the data obtained with an arrangement of rods filling the entire belt at constant spacing.

The cascade test section, located downstream of the wake generator, includes five blades with a height of 200.0 mm and a chord of 203.44 mm, Fig. 2. The airfoil used is the Pratt and Whitney "Pak B" airfoil, whose cascade geometry is given in Table 1. The cascade test section exhibits the essential flow features such as

laminar boundary layer separation that is inherent to typical LPT-blades. The blade geometry was made available to NASA researchers and academia to study the specific problems of LPT-flow separation, its passive and active control and its prevention. As shown in Ref. [9], a minimum blade number of 5 is necessary and sufficient to secure a spatial periodicity for the cascade flow. The periodicity was verified by comparing the pressure distributions of blade number 2 (SPB-1) and 4 (SPB-2) shown in Fig. 2. These blades were specially manufactured for measurement of pressure and showed identical pressure distributions. A computer controlled traversing system is used to measure the inlet velocities and turbulence intensities, as well as the boundary layers on the suction and pressure surfaces. The traversing system is vertically mounted on the plexiglass side wall. It consists of a slider and a lead screw that is connected to a dc-stepper motor with an encoder and decoder. The optical encoder provides a continuous feedback to the stepper motor for accurate positioning of the probes. The system is capable of traversing in small steps up to  $2.5 \mu\text{m}$ , which is specifically required for boundary layer investigations where the measurement of the laminar sublayer is of particular interest.

### Instrumentation, Data Acquisition, and Data Reduction

The data acquisition system is controlled by a personal computer that includes a 16 channel, 12-bit analog-digital (A/D) board (NI, PCI-MIO-16E-1). Time dependent velocity signals are obtained by using a commercial 3-channel (TSI, IFA-100), constant temperature hot-wire anemometer system that has a signal conditioner with a variable low pass filter and adjustable gain. A Prandtl probe, placed upstream of the diffuser, monitors the reference velocity at a fixed location. The pneumatic probes are connected to high precision differential pressure transducers (MKS 220CD, range: 0–10 mmHg) for digital readout. Several calibrated thermocouples are placed downstream of the test section to constantly monitor the flow temperature. The wake generator speed and the passing frequency signals of the rods are transmitted by a fiber-optic trigger sensor. The passage signals of the rods are detected by the sensor using a silver-coated reflective paint on one of the belts. This sensor gives an accurate readout of the speed of the wake generator and the passing frequency of the rods. The signals of the pressure transducers, thermocouples, and trigger sensors are transmitted to the A/D board and are sampled by the computer. The second and fourth blade are each instrumented with 48 static pressure taps. The taps are connected to a scanvalve, which sequentially transferred the pressure signals to one of the transducers that was connected to the A/D board. Using LABVIEW software, the data acquisition system including the computer and the A/D board was upgraded. Two adjacent blades are used for boundary layer measurement.

Steady and unsteady data are taken by angle calibrated, custom designed miniature single hot wire probes. At each boundary layer position samples were taken at a rate of 20 kHz for each of 100

**Table 1 Parameters of turbine cascade test section**

Parameters	Values	Parameters	Values
Inlet velocity	$V_{in}=4$ m/s	Inlet turbulence intensity	$Tu_{in}=1.9\%$
Rod translational speed	$U=5.0$ m/s	Blade Re-number	$Re=110,000$
Nozzle width	$W=200.0$ mm	Blade height	$h_B=200$ mm
Blade chord	$c=203.44$ mm	Cascade solidity	$\sigma=1.248$
Blade axial chord	$c_{ax}=182.85$ mm	Zweifel coefficient	$\Psi_A=1.254$
Blade suction surface length	$L_{SS}=270.32$ mm	Cascade angle	$\varphi=55$ deg
Cascade flow coefficient	$\Phi=0.80$	Cascade spacing	$S_B=163$ mm
Inlet air angle to the cascade	$\alpha_1=0$ deg	Exit air angle from the cascade	$\alpha_2=90$ deg
Rod diameter	$D_R=2.0$ mm	Rod distance to lead. edge	$L_R=122$ mm
Cluster 1 (no rod, steady)	$S_R=\infty$ mm	$\Omega$ -parameter steady case	$\Omega=0.0$
Cluster 2 rod spacing	$S_R=160.0$ mm	$\Omega$ -parameter for cluster 1	$\Omega=1.59$
Cluster 3 rod spacing	$S_B=80.0$ mm	$\Omega$ -parameter for cluster 2	$\Omega=3.18$

revolutions of the wake generator and low pass filtered at 10 kHz. The data were ensemble-averaged with respect to the rotational period of the wake generator. Before final data were taken, the number of samples per revolution and the total number of revolutions were varied to determine the optimum settings for convergence of the ensemble-average.

For the steady state case, the instantaneous velocity components are calculated from the temperature compensated instantaneous voltages by using the calibration coefficients. The instantaneous velocity can be represented in the following form.

$$V = \bar{V} + v \quad (1)$$

Where  $\bar{V}$  is the mean (time-averaged) velocity and  $v$  is the turbulent fluctuation component. The mean velocity, also known as the time-average, is given by:

$$\bar{V} = \frac{1}{M} \sum_{j=1}^M V_j \quad (2)$$

where  $M$  is the total number of samples at one boundary layer location. The root mean square value of the turbulent velocity fluctuation is obtained from the instantaneous and mean velocities by:

$$v = \sqrt{\frac{1}{M} \sum_{j=1}^M (V_j - \bar{V})^2} \quad (3)$$

and the local turbulence intensity is defined as:

$$Tu_{loc} = \frac{v}{\bar{V}} \times 100 = \frac{1}{\bar{V}} \sqrt{\frac{1}{M} \sum_{j=1}^M (V_j - \bar{V})^2} \times 100 \quad (4)$$

The ensemble-averaged velocity, fluctuation velocity, and the turbulence intensity were calculated from the instantaneous velocity samples by:

$$V_i(t_i) \equiv \langle V_i(t_i) \rangle = \frac{1}{N} \sum_{j=1}^N V_{ij}(t_i) \quad (5)$$

$$v_i(t_i) \equiv \langle v_i(t_i) \rangle = \sqrt{\frac{1}{N} \sum_{j=1}^N [V_{ij}(t_i) - \langle V_i(t_i) \rangle]^2} \quad (6)$$

$$\langle Tu_i(t_i) \rangle \equiv \langle Tu_i(t_i) \rangle = \frac{\langle v_i(t_i) \rangle}{\langle V(t) \rangle_{ref}} \times 100 \quad (7)$$

where  $N=100$  is the total number of wake generator periods and  $M$  the number of samples taken per period.  $\langle V(t) \rangle_{ref}$  is the reference ensemble averaged velocity for the particular boundary layer traverse. The ensemble-averaged boundary layer parameters such as displacement thickness  $\langle \delta_1 \rangle$ , momentum thickness  $\langle \delta_2 \rangle$ , and shape factor  $\langle H_{12} \rangle$  are calculated as follows:

$$\delta_1 \equiv \langle \delta_1 \rangle = \int_0^{(\delta)} \left( 1 - \frac{\langle V \rangle}{\langle V \rangle_e} \right) dy \quad (8)$$

$$\delta_2 \equiv \langle \delta_2 \rangle = \int_0^{(\delta)} \frac{\langle V \rangle}{\langle V \rangle_e} \left( 1 - \frac{\langle V \rangle}{\langle V \rangle_e} \right) dy \quad (9)$$

$$H_{12} \equiv \langle H_{12} \rangle = \frac{\langle \delta_1 \rangle}{\langle \delta_2 \rangle} \quad (10)$$

In the above equations the signs  $\langle \rangle$  refer to ensemble averaged quantities. For brevity we will drop  $\langle \rangle$  in the following discussions.

## Experimental Results and Discussion

Detailed surface pressure and boundary layer measurements were performed at three different Re-numbers. For each Reynolds number three different reduced frequencies were applied. For generation of unsteady wakes, cylindrical rods with the diameter  $d_R = 2$  mm were chosen to fulfill the similarity criterion that requires the generation of a drag coefficient  $C_D$  that is approximately equal to the  $C_D$  of the turbine blade with the chord and spacing given in Table 1 (for details we refer to the studies in Refs. [21,22]).

To accurately account for the unsteadiness caused by the frequency of the individual wakes and their spacings, the flow velocity, and the cascade parameters, we define a reduced frequency  $\Omega$  that includes the cascade solidity  $\sigma$ , the flow coefficient  $\varphi$ , the blade spacing  $S_B$ , and the rod spacing  $S_R$ . Many researchers have used Strouhal number as the unsteady flow parameter, which only includes the speed of the wake generator and the inlet velocity. However, the currently defined reduced frequency  $\Omega$  is an extension of Strouhal number in the sense that it incorporates the rod spacing  $S_R$  and the blade spacing  $S_B$  in addition to the inlet velocity and wake generator speed. For surface pressure, measurement rods with uniform spacings as specified in Table 1 were attached over the entire belt length. For boundary layer measurement, however, clusters of rods were used, as described previously.

**Surface Pressure Distributions.** Detailed static surface pressure measurements were taken at Re=50,000, 75,000, 100,000, and 125,000 using the two static pressure blades SPB-1 and SPB-2 shown in Fig. 2. The two blades measured identical static pressure distributions confirming the spatial periodicity.

For each Reynolds number three different reduced frequencies, namely  $\Omega=0.0$ , 1.59, and 3.18, are applied that correspond to the rod spacings  $S_R=\infty$ , 160, and 80 mm. The pressure distributions in Fig. 3, which pertain to SPB-1, show the results of one steady and two unsteady cases. The pressure signals inherently signify the time-averaged pressure because of the internal pneumatic damping effect of the connecting pipes to the transducer. The noticeable deviation in pressure distribution between the steady and unsteady cases, especially on the suction surface, is due to the drag forces caused by the moving rods. The drag forces are imposed on the main stream and cause momentum deficiency that lead to a reduction of the total and static pressure.

The time-averaged pressure coefficients along the pressure and suction surfaces are plotted in Fig. 3. Starting with Re=50,000 and steady state with  $\Omega=0$  shown in Fig. 3(a) the suction surface (upper portion), exhibits a strong negative pressure gradient. The flow accelerates at a relatively steep rate and reaches its maximum surface velocity that corresponds to the minimum  $c_p=-4.0$  at  $s/s_0=0.42$ . Passing through the minimum pressure, the fluid particles within the boundary layer encounter a positive pressure gradient that causes a sharp deceleration until  $s/s_0=0.55$  has been reached. This point signifies the beginning of the laminar boundary layer separation and the onset of a separation zone. As seen in the subsequent boundary layer discussion, the part of the separation zone characterized by a constant  $c_p$ -plateau extends up to  $s/s_0=0.746$ , thus occupying more than 19% of the suction surface.

Passing the plateau, the flow first experiences a second sharp deceleration indicative of a process of re-attachment followed by a further deceleration at a moderate rate. On the pressure surface, the flow accelerates at a very slow rate, reaches a minimum pressure coefficient at  $s/s_0 \approx 0.42$  and continues to accelerate until the trailing edge has been reached. Unlike the suction surface, the pressure surface boundary layer does not encounter any adverse positive pressure gradient that triggers separation. However, close to the leading edge, a small depression in the curve extending from  $s/s_0 \approx 0.08$  to 0.24 indicates the existence of a small size separation zone that might be attributed to a minor inlet flow incidence angle.

Considering the unsteady case with a reduced frequency of  $\Omega$



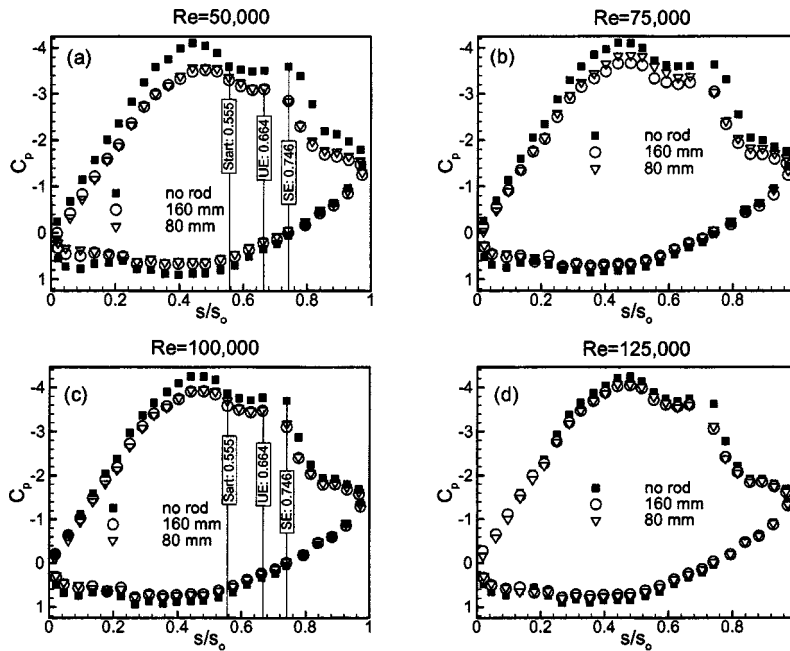


Fig. 3 Static pressure distribution at four different Re-numbers and reduced frequencies  $\Omega=0, 1.59, 3.18$ , (no rod, 160 mm, 80 mm), Start=Separation start for steady and unsteady cases, SE=Separation end for steady case, UE=Separation end for unsteady cases.

$=1.59$  that corresponds to a rod spacing of  $S_R=160.0$  mm, Fig. 3(a) exhibits two distinctive characteristics: (1) A noticeable deviation in pressure distribution between the steady and unsteady cases. As mentioned above, this deviation is attributed to the momentum deficiency that leads to a reduction of the total and static pressure. (2) For  $Re < 125,000$ , the wakes have a substantial reducing impact on the streamwise extent of the separation plateau. As seen in Fig. 3(a), the trailing edge of the plateau has shifted from  $s/s_0=0.746$  to  $s/s_0=0.664$ . This shift has reduced the streamwise extent of the separation plateau from 19% to less than 11% of the suction surface length which is, in this particular case, more than 42% reduction in streamwise extent of the separation plateau. Although the extent of the separation plateau is not necessarily identical with the extent of the separation zone, the relative reductions presented above adequately reflect the relative reduction of the size of the separation zone. Doubling the reduced frequency to  $\Omega=3.18$  by utilizing a rod spacing of  $S_R=80.0$  mm causes a slight shift of the  $c_p$ -distribution compared with the  $\Omega=1.59$ -case. One should bear in mind that pneumatically measured surface pressure distribution represents a time integral of the pressure events only. Detailed information regarding the structure of the separation zone requires a detailed unsteady boundary layer or surface pressure measurement by fast response probes, as will be discussed in the subsequent sections. Increasing the Reynolds number to  $Re=75,000$  has not brought major changes in steady-state  $c_p$ -distribution. This is also true for the subsequent higher Reynolds number cases at steady state, Figs. 3(b)–3(d). However, the combination of higher Re-number with unsteady wakes reveals that the noticeable deviation in pressure distribution between the steady and unsteady cases discussed above is diminishing with increasing the Re-number as shown in Figs. 3(b)–3(d). Two counteracting factors are contributing to this deviation. The first factor is attributed to the momentum deficiency and the associated total pressure losses caused by moving wakes, as discussed above. The second factor pertains to the energizing effect of the impinging wakes on the boundary layer. Although the impinging wakes cause velocity and momentum deficits, their high turbulence intensity vortical cores provide an intensive exchange and transfer

of mass, momentum, and energy to the blade surface, thus energizing the low energetic boundary layer. In conjunction with the surface pressure distribution, the kinetic energy of the normal velocity fluctuation component plays a crucial role. In case of a low Re-number flow, the strong damping effect of the wall shear stress has the tendency to reduce the normal contribution of turbulence kinetic energy, thereby diminishing its surface pressure augmenting effect. Increasing the Reynolds number results in a decrease of the damping effect of the wall shear stress, allowing the kinetic energy of the normal velocity fluctuation component to increase the surface pressure, thus offsetting the wake deficit effects on the pressure distribution. This fact is clearly shown in Figs. 3(a)–3(d), where the pressure distributions of unsteady flow cases at  $\Omega=1.59$  and  $\Omega=3.18$  systematically approach the steady state cases at  $Re=75,000$ , 100,000 and very visibly at  $Re=125,000$ . It is worth noting that the impact of the unsteady wakes on the extent of the separation zone is preserved regardless of the Reynolds number variation performed in this study.

**Time Averaged Velocity Distributions.** Following the surface pressure investigations that mainly addressed the onset and extent of the separation zone discussed previously, comprehensive boundary layer measurements were performed to identify the streamwise and normal extent as well as the deformation of the separation zone under unsteady wake flow. The steady state case serves as the reference configuration.

Boundary layer profiles were taken for one steady and two unsteady inlet flow conditions on the suction surface along 31 streamwise locations parallel to the cascade front. After completing the velocity measurements, the boundary layer coordinates were transformed into a blade orthogonal coordinate system. Velocities at blade normal positions were obtained by interpolating their transformed values. The results showed almost no difference between the interpolated and noninterpolated velocity data. Experimental investigations were performed for three different values of  $\Omega=0.0$ , 1.59, and 3.18. These values cover the reduced frequency range encountered in LPT-design and off-design operation conditions.

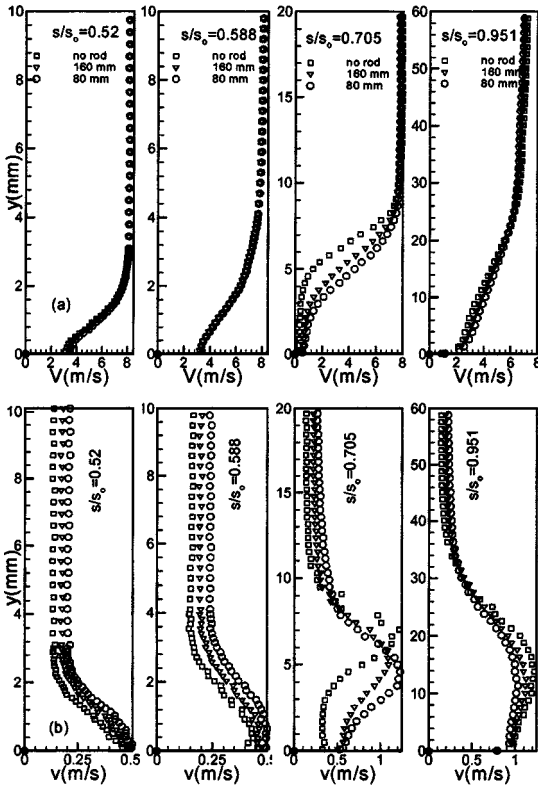


Fig. 4 Distribution of time averaged velocity (a) and fluctuation rms velocity (b) along the suction surface for steady case  $\Omega=0$  ( $S_R=\infty$ ) and unsteady cases  $\Omega=1.59$  ( $S_R=160$  mm) and  $\Omega=3.18$  ( $S_R=80$  mm) at  $Re=110,000$ . Note the changes in  $y$  scale.

The effect of wake frequency on time averaged velocity and turbulence fluctuation distributions is shown in Fig. 4 at four representative streamwise locations for  $Re=110,000$ . Upstream of the separation zone at  $s/s_0=0.52$  and its proximity  $s/s_0=0.588$ , the velocity distributions inside the boundary layer are not affected by wakes. Inside the separation zone at  $s/s_0=0.705$ , a substantial influence of the wake frequency is observed. Higher wake frequency introduces fluctuation kinetic energy into the boundary layer which tends to reverse the separation tendency. Velocity distributions at  $s/s_0=0.767, 0.805, 0.849$ , and  $0.898$  (not presented) clearly show that the wake impingement shortens the streamwise extent of the separation zone compared to the steady case. Downstream of the separation zone, where the flow is fully reattached,  $s/s_0=0.951$ , the impact of wake on the boundary layer is reduced. This effect is clearly shown in the velocity distribution at  $s/s_0=0.951$ . In accord with the previous investigations by Schober et al. [10] on a HP-turbine cascade, an increased wake frequency causes turbulence fluctuations to rise inside and outside the boundary layer as shown in Fig. 4(b). However, once the boundary layer is re-attached and the velocity distribution assumes a turbulent profile, no major changes are observed in velocity as well as fluctuation distribution.

#### Ensemble-Averaged Boundary Layer Velocity Distributions.

Figure 5 displays two representative temporal ensemble-averaged velocity distributions for Fig. 5(a) steady and Fig. 5(b) unsteady flow conditions with their characteristic features. Both figures show the boundary layer development from the freestream to the blade surface at a streamwise position of  $s/s_0=0.0208$ . Approaching the wall surface, both velocities experience a continuous deceleration. The velocity gradient in both cases causes generation and formation of vortices that transform the steady nature of case (a) into an unsteady one as clearly demonstrated in Fig. 5(a). The

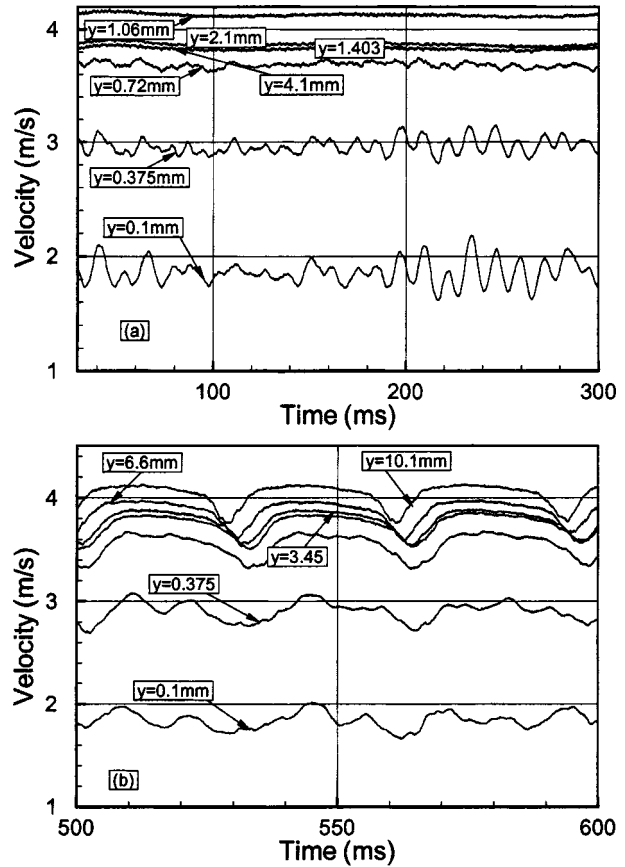


Fig. 5 Ensemble averaged velocity as a function of time for (a) steady flow case  $\Omega=0$  ( $S_R=\infty$ ) and (b) unsteady case  $\Omega=1.59$  ( $S_R=160$  mm) at  $s/s_0=0.0208$  and  $Re=110,000$

unsteady case displayed in Fig. 5(b) is characterized by its deterministic temporal periodicity. Approaching the wall surface from  $y=10.1$  to  $3.45$  mm, the traveling periodic wake experiences a phase shift, while maintaining its deterministic nature. However, by penetrating into the boundary layer, the interaction between wake and boundary layer causes the deterministic nature to degenerate into a stochastic one. The results presented in Fig. 5 are in full agreement with those discussed in Refs. [7,12].

#### Temporal Behavior of the Separation Zone Under Unsteady Wake Flow.

Velocity distributions on the suction surface with time as the parameter are plotted in Fig. 6. The nondimensional time ( $t/\tau$ ) values are chosen so that they represent the temporal states within one full period of wake passing. As Figs. 6(a)–6(e) show, the velocity distributions inside and outside the boundary layer at fixed  $s/s_0$ -locations experience moderate to pronounced changes. Figure 6(a) represents the instantaneous velocity distribution upstream of the separation zone followed by Figs. 6(b)–6(e) which represent the velocity distributions inside the separation zone. The last Fig. 6(f) exhibits the instantaneous velocity distribution downstream of the separation zone. In discussing the following results, we simultaneously refer to the wake distribution as well as the turbulence fluctuation results.

Figure 6(a) exhibits the velocity distribution on the suction surface at  $s/s_0=0.402$ . At this streamwise position, the laminar boundary layer is subjected to a strong negative pressure gradient. The boundary layer distributions at different ( $t/\tau$ ) experience changes in magnitude that reflect the corresponding changes of the impinging periodic wake velocity. It is worth noting, that despite the injection of turbulence kinetic energy by the impinging wakes, no local instantaneous boundary layer transition occurs.

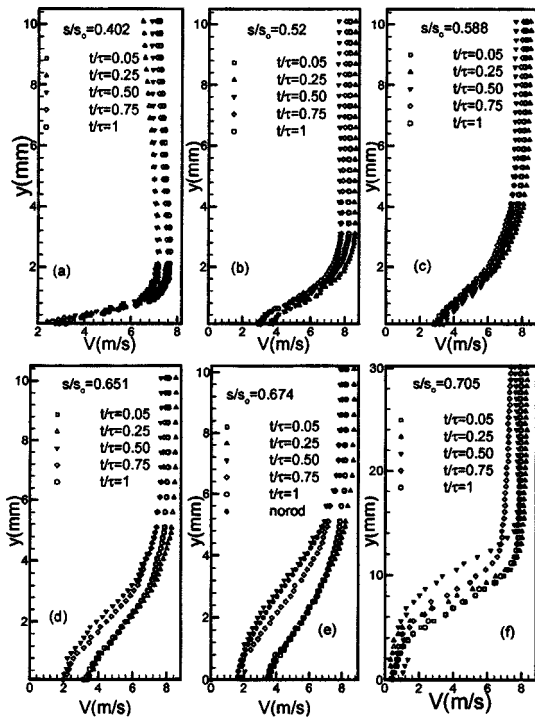


**Fig. 6** Distribution of the ensemble averaged velocity development along the suction surface for different  $s/s_0$  with time  $t/\tau$  as parameter for  $\Omega=1.59$  ( $S_R=160$  mm) and  $Re=110,000$ , note scale change in (f)

This is because of the strong negative pressure gradient that prevents the boundary layer from becoming instantaneously transitional. Instantaneous velocity distributions inside the separation zone are shown in Figs. 6(b)–6(f).

As a representative case, we discuss the results plotted in Fig. 6(e) at  $s/s_0=0.674$ . During the time interval from  $t/\tau$  close to 0.5 (1.5, 2.5, etc.) to about  $t/\tau=0.75$  (1.75, 2.75, etc.), the separation zone is exposed to the wake external flow being under the influence of relatively lower turbulence. This flow does not have the capability to suppress the separation zone. Thus the separation region is clearly shown by the velocity distributions at  $t/\tau=0.5$  and  $t/\tau=0.75$ . As the wake passes over the blade at  $s/s_0=0.674$  introducing high turbulence kinetic energy into the boundary layer, the boundary layer is energized causing the separation zone to partially reduce or disappear. This leads to an instantaneous re-attachment. This time interval corresponds to the case where the flow is completely under the influence of wake and correspondingly the re-attached velocity distribution assumes a turbulent profile characterized by the curves at  $t/\tau=1.0$ ,  $t/\tau=0.05$ , and  $t/\tau=0.25$  shown in Fig. 6(e). To emphasize this statement, the steady state velocity distribution at the same streamwise position is also plotted in Fig. 6(e) using full circles. It shows clearly the separated nature of the boundary layer which coincides with the instantaneous velocity profile at  $t/\tau=0.5$ . Intermediate times reflect the gradual change between the separation and re-attachment as the flow is undergoing the influence of the oncoming wake. Moving to the trailing edge of the separation zone, at  $s/s_0=0.705$ , Fig. 6(f), a partial reduction in boundary layer thickness as the result of wake impingement is visible, however, the separation zone does not seem to disappear.

**Temporal-Spatial Resolution of the Separation Zone.** To better understand the underlying physics of the LPT-flow separation, detailed unsteady flow measurements are performed to identify the onset and extent of the separation zone discussed previously. The separation zone can be thought of as a curve that connects the

velocity inflection points along the suction surface. Starting with a reduced frequency of  $\Omega=1.59$  ( $S_R=160$  mm) at  $s/s_0=0.520$ , Fig. 7(a) exhibits the start of the separation zone with a normal extent of less than 1.0 mm. The impingement of the periodic wake vertical core with the high turbulence intensity causes a local periodic contraction of the zone in normal direction. Convecting downstream, the normal extent increases, thus the contraction appears more pronounced, Figs. 7(b)–7(d). Substantial contraction occurs toward the trailing edge of the separation zone as shown in Figs. 7(e) and 7(f). Similar flow picture is observed when operating at a reduced frequency of  $\Omega=3.18$  ( $S_R=80$  mm).

Studying the temporal distribution of the turbulence fluctuations along the streamwise extension of the separation zone, it is proposed that, in conjunction with the pressure gradient and periodic wakes, there is another crucial mechanism responsible for the normal and streamwise decrease of the separation zone. This mechanism constitutes a combination of the high turbulence fluctuation level and its gradient. It is the temporal gradient of the turbulence fluctuation, or more precisely, the fluctuation acceleration  $\partial v_{rms}/\partial t$  that provides higher momentum and energy transfer into the boundary layer energizing the separation zone and causing it to partially or entirely disappear.

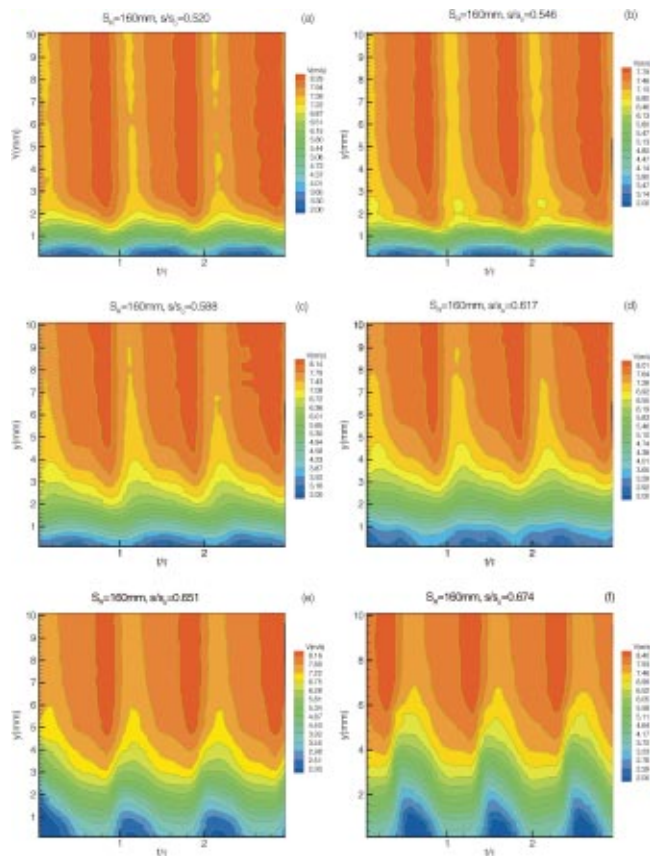
For better understanding this phenomenon, we present the wake and the fluctuation velocity in Fig. 8 for the streamwise position  $s/s_0=0.651$  indicated in Fig. 7(e). For the sake of clarity, we scale up the fluctuation velocity with a factor of 4 and choose an arbitrary normal position of  $y=2.85$  mm to be sufficiently above the separation zone.

Figure 8 exhibits two distinct regions: (1) A wake vortical core, occupied by vortices that originate from the moving cylindrical rods and generate high turbulence fluctuations, and (2) a wake external region between the adjacent vortical cores with relatively low turbulence activities. The wake configuration is asymmetric as discussed in Ref. [21]. Figure 7(e) is enlarged in Fig. 9 to reveal further details.

As Fig. 9 shows, the separation zone starts to contract at  $t/\tau=1.25$  (2.25, etc.). This point coincides with the streamwise position of the velocity maximum, which exactly corresponds to the position of the fluctuation minimum, as shown in Figs. 8 and 10. At this point, the fluctuation within the vortical core starts to increase while the velocity continuously decreases. This process continues until the end contraction at  $t/\tau=1.41$  has been reached. Thereafter, the separation zone is subjected to a process of intensive exchange of momentum and energy that causes the separation to diminish, as shown in Fig. 9. The process of separation contraction, suppression, and regeneration is summarized in Fig. 10. It shows more details of separation contraction and suppression. In this context, it is necessary to subdivide the vortical core shown in Fig. 8 into four distinct regions, separated by thick dashed lines, as presented in Fig. 10. Region (a) is characterized by the initial positive gradient of the fluctuation  $\partial v/\partial t > 0$  marked with an upward arrow. Region (b) represents the substantial part of the vortical core with an intense turbulence activity. Region (c) serves as a transition region between region (b) and the relatively calm region (d) characterized by  $\partial v/\partial t < 0$ .

For an initial fluctuation gradient  $\partial v/\partial t > 0$ , the separation zone begins to contract at  $t/\tau=1.25$ . This initial gradient is crucial for initiating the contraction process. Once the maximum fluctuation velocity with the temporal gradient  $\partial v/\partial t=0$  at  $t/\tau \approx 1.41$  is reached [Fig. 10(a)], the process of energizing the separation zone starts transferring momentum and energy into the separation zone, thereby preventing its regeneration [Fig. 10(b)]. Passing the transition region [Fig. 10(c)], the process of suppression continues until the end of the vortical region at  $t/\tau \approx 2.0$  is reached. At this point the external wake region with its low turbulence content arrives causing a regeneration of the separation zone, thus reversing the entire suppression process.

While turbulence fluctuation expressed in terms of higher turbulence intensity is well known for influencing the flow separa-



**Fig. 7 Contour plot of the ensemble averaged velocity distribution showing the effect of periodic wakes on the separation zone at different streamwise positions and  $Re=110,000$**

tion, its gradient enhances the effect of delaying the onset and reducing the extent of the separation zone. The fluctuation gradient is an inherent feature of the incoming periodic wake flow and does not exist in a statistically steady flow that might have high turbulence intensity.

The results clearly indicate that for the particular blade under investigation, one has to deal with a large separation on the suction surface. These observations in comparison with the steady-state reference case suggest that, once a separation zone is manifested, its size can be significantly reduced by periodic wake impingement, but it cannot be completely removed. The results presented here are valid for blades with a similar pressure distribution discussed earlier. Since the onset and extent of the separation zone is uniquely associated with the pressure gradient, blades can be designed with less local adverse pressure gradient, whose separation onset can completely be suppressed by impinging wakes.

#### Boundary Layer Ensemble Averaged Integral Quantities.

The integral parameters, such as momentum thickness and shape factor, are of particular interest to a turbine designer, since they provide an accurate first estimation of the quality of the designed blade. The ensemble-averaged distributions of the momentum deficiency thickness and shape factor for the suction surface are shown in Figs. 11(a)–11(c) for  $\Omega=1.59$  at different  $s/s_0$ -locations. The momentum thickness values are nondimensionalized with respect to the value corresponding to the steady case with  $\Omega=0$ . The period  $\tau$  represents the wake-passing period that is specific to the individual wake generating cluster, which is characterized by the  $\Omega$ -value under investigation. The periodic behavior of the ensemble-averaged momentum thickness over the entire suction surface as a result of the embedded periodic wake flow is clearly visible from Fig. 11. It represents the momentum thickness behav-

ior at different  $s/s_0$ -locations upstream, within and outside the separation zone. The relative momentum thickness distribution upstream of the separation zone in Fig. 11(a) integrally exhibits a slight increase, whereas inside the zone shown in Fig. 11(b), a substantial decrease is apparent. At the immediate vicinity of the separation zone trailing edge,  $s/s_0=0.705$  close to re-attachment, Fig. 11(c), the momentum thickness experiences a noticeable increase, which by convecting downstream decreases again and approaches the integral values that are close to the steady state case.

The ensemble averaged relative shape factor  $H_{12}$ -distributions on the suction surface at the same streamwise locations are plotted in Figs. 12(a)–12(c). Upstream of the separation zone, Fig. 12(a), they experience a similar periodic change with an average value that is close to the value of the steady case. Moving into the separation zone, Figs. 12(b) and 12(c), each streamwise location presents its own form parameter that is specific to the velocity distribution we discussed.

#### Conclusions

A detailed experimental study on the behavior of the separation zone on the suction surface of a highly loaded LPT-blade under periodic unsteady wake flow was presented. One steady and two different unsteady inlet wake flow conditions with the corresponding passing frequencies, wake velocity, and turbulence intensities were investigated utilizing a new large-scale, subsonic research facility. The results of the unsteady boundary layer measurements were presented in ensemble-averaged, and contour plot forms. Surface pressure measurements were performed at  $Re=50,000$ ,  $75,000$ ,  $100,000$ , and  $125,000$ . At each Reynolds number, one steady and two periodic unsteady inlet flow measurements were performed. The surface pressure distribution showed no major changes with respect to the above  $Re$ -number changes. Noticeable

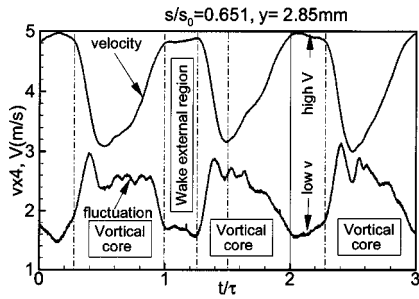


Fig. 8 Wake velocity and fluctuation rms distribution,  $Re=110,000$

changes occurred while operating at unsteady flow conditions. Detailed unsteady boundary layer measurement identified the onset and extent of the separation zone as well as its behavior under unsteady wake flow. Passing the wake flow with its highly turbulent vortical core over the separation region caused a periodic contraction and expansion of the separation zone. It was proposed that, in conjunction with the pressure gradient and periodic wakes, the temporal gradient of the turbulence fluctuation, or more precisely the fluctuation acceleration  $\partial v_{rms}/\partial t$  provides higher momentum and energy transfer into the boundary layer energizing the separation zone and causing it to partially or entirely disappear. We found that for  $\partial v_{rms}/\partial t > 0$ , the separation zone starts to contract whereas for  $\partial v_{rms}/\partial t < 0$  it gradually assumes the shape before the contraction. The existence of higher turbulence fluctuations expressed in terms of higher turbulence intensity is well known for influencing the flow separation; its gradient is of crucial importance in suppressing or preventing the onset and the extent of the separation zone. The fluctuation gradient is an inherent feature of the incoming periodic wake flow and does not exist in a statistically steady flow that might have high turbulence intensity.

### Uncertainty Analysis

The Kline and McClinton [23] uncertainty analysis method was used to determine the uncertainty in the velocity after calibration and data reduction for the single-wire probe. The Kline and McClinton method determines the uncertainty for a 95% confidence level. The uncertainty in velocity for the single-wire probe after data reduction is given in Table 2. As shown, the uncertainty in velocity increases as the flow velocity decreases. This is due to the pneumatic pressure transducer having a large uncertainty during calibration.

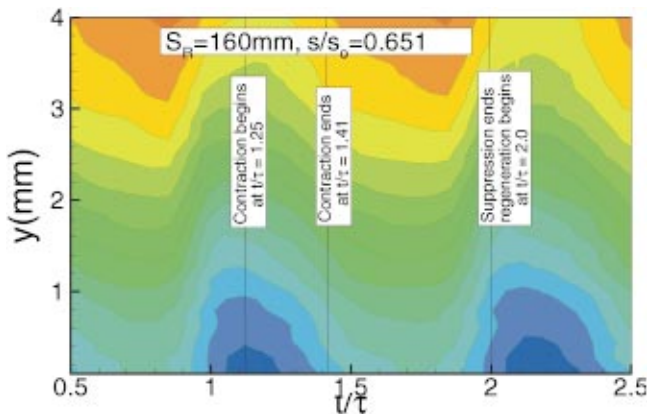


Fig. 9 Separation zone, definition of contraction begin, contraction end, suppression, and regeneration

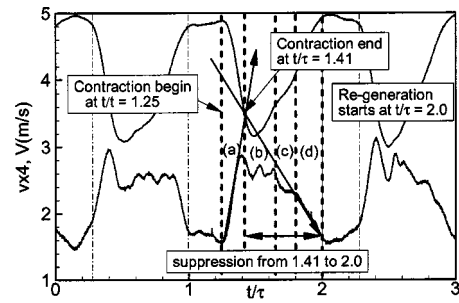


Fig. 10 Separation contraction, suppression, and regeneration,  $Re=110,000$

### Acknowledgments

The presented study is a part of the NASA Glenn Research Center Low Pressure Turbine Flow Physics Program. The first two authors acknowledge the support by NASA Cooperative Agreement NCC 3-793. The authors also gratefully acknowledge Pratt and Whitney for providing the blade coordinates.

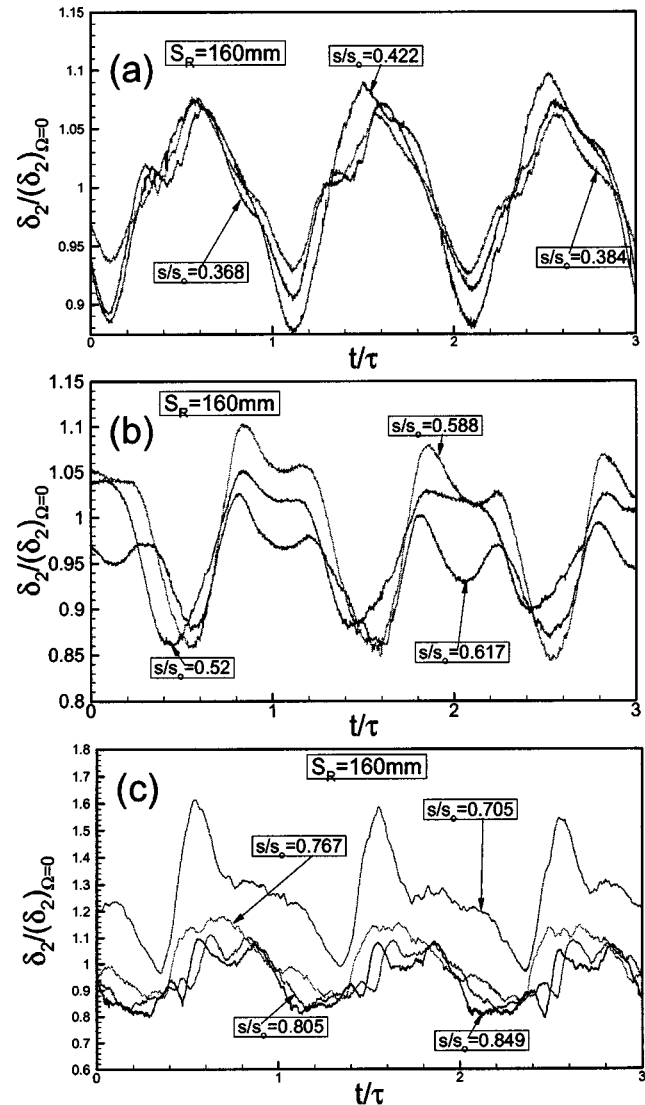


Fig. 11 Ensemble-averaged relative momentum thickness distribution along the suction surface for  $\Omega=1.59$  ( $S_R=160$  mm) and  $Re=110,000$

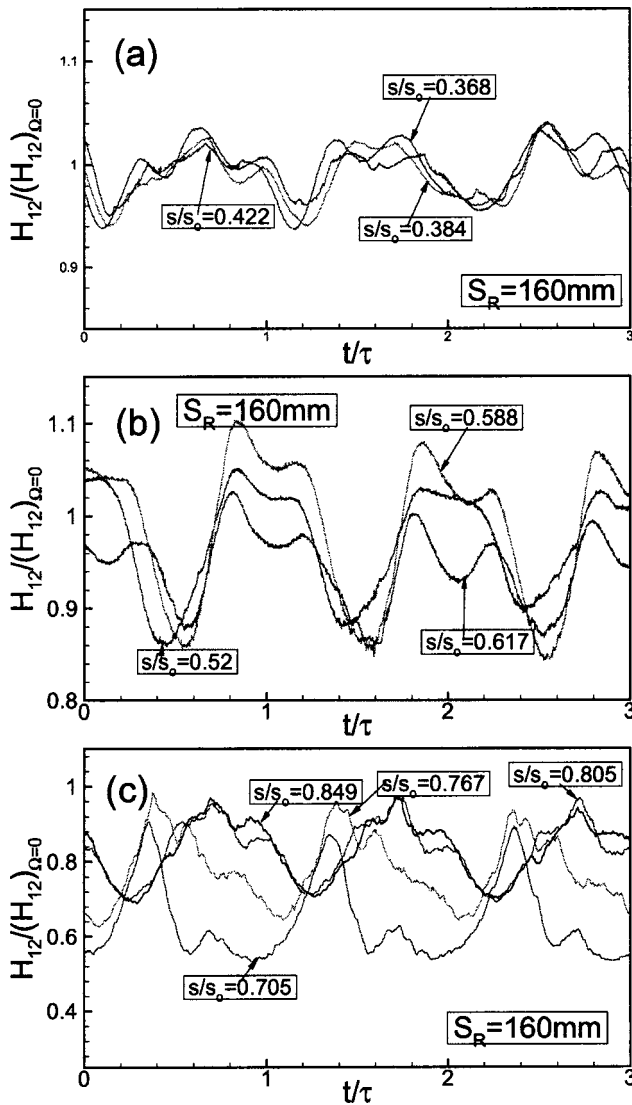


Fig. 12 Ensemble averaged relative form parameter distribution along the suction surface for  $\Omega=1.59$  ( $S_R=160$  mm),  $Re=110,000$

### Nomenclature

$c$	= blade chord
$c_{ax}$	= axial chord
$C_p$	= pressure coefficient, $C_p = (p - p_1) / (p_t - p)_{inl}$
$d_R$	= rod diameter
$M$	= number of samples
$N$	= number of wake cycles
$p, p_t$	= static, total pressure
$p_1$	= static pressure of first tap on suction surface
$Re$	= Reynolds number $Re = S_0 V_{exit} / \nu$
$S_B$	= blade spacing
$S_R$	= rod spacing
$s$	= streamwise distance from blade leading edge
$s_0$	= blade suction surface arc length

Table 2 Uncertainty in velocity measurement for hot-wire probe

$\bar{U}$ (m/s)	3	5	12
$\omega \bar{U} / \bar{U}$ (%) <sub>red</sub>	5.78	2.41	1.40

$t$	= time
$Tu$	= turbulence intensity
$U$	= belt translational velocity
$V_{ax}$	= axial velocity
$V_{exit}$	= exit velocity
$V$	= velocity
$v$	= fluctuation velocity
$y$	= normal distance from the surface
$\gamma$	= blades stagger angle
$\nu$	= kinematic viscosity
$\tau$	= one wake-passing period
$\sigma$	= cascade solidity, $\sigma = c / S_B$
$\varphi$	= flow coefficient, $\varphi = V_{ax} / U$
$\psi_A$	= Zweifel coefficient
	$\psi_A = 2 \sin^2 \alpha_2 (\cot \alpha_2 - \cot \alpha_1) S_B / c_{ax}$
$\Omega$	= reduced frequency $\Omega = c / S_R U / V_{7ax} = \sigma \varphi S_B / S_R$

### Subscripts

$ax$	= axial
$B$	= blades
$R$	= rod
1,2	= stations

### References

- [1] Pfeil, H., and Herbst, R., 1979, "Transition Procedure of Instationary Boundary Layers," ASME Paper, 79-GT-128.
- [2] Pfeil, H., Herbst, R., and Schröder, T., 1983, "Investigation of the Laminar Turbulent Transition of Boundary Layers Disturbed by Wakes," ASME J. Eng. Power, **105**, pp. 130–137.
- [3] Orth, U., 1993, "Unsteady Boundary Layer Transition in Flow Periodically Disturbed by Wakes," ASME J. Turbomach., **115**, pp. 707–713.
- [4] Schobeiri, M. T., and Radke, R. E., 1994, "Effects of Periodic Unsteady Wake Flow and Pressure Gradient on Boundary Layer Transition along the Concave Surface of a Curved Plate," ASME Paper 94-GT-327, presented at the International Gas Turbine and Aero-Engine Congress and Exposition, Hague, Netherlands, June 13–16, 1994.
- [5] Schobeiri, M. T., Read, K., and Lewalle, J., 2003, "Effect of Unsteady Wake Passing Frequency on Boundary Layer Transition, Experimental Investigation and Wavelet Analysis," ASME J. Fluids Eng., **125**, pp. 251–266.
- [6] Wright, L., and Schobeiri, M. T., 1999, "The Effect of Periodic Unsteady Flow on Boundary Layer and Heat Transfer on a Curved Surface," ASME J. Heat Transfer, November 1998, **120**, pp. 22–33.
- [7] Chakka, P., and Schobeiri, M. T., 1999, "Modeling of Unsteady Boundary Layer Transition on a Curved Plate under Periodic Unsteady Flow Condition: Aerodynamic and Heat Transfer Investigations," ASME J. Turbomach., **121**, pp. 88–97.
- [8] Liu, X., and Rodi, W., 1991, "Experiments on Transitional Boundary Layers with Wake-Induced Unsteadiness," J. Fluid Mech., **231**, pp. 229–256.
- [9] Schobeiri, M. T., Pappu, K., and Wright, L., 1995, "Experimental Study of the Unsteady Boundary Layer Behavior on a Turbine Cascade," ASME 95-GT-435, presented at the International Gas Turbine and Aero-Engine Congress and Exposition, Houston, Texas, June 5–8, 1995.
- [10] Schobeiri, M. T., John, J., and Pappu, K., 1997, "Experimental Study on the effect of Unsteadiness on Boundary layer Development on a Linear Turbine Cascade," Journal of Experiments in Fluids, **23**, pp. 303–316.
- [11] Schobeiri, M. T., Wright, L., and Chakka, P., 2000, "Periodic Unsteady Flow Aerodynamics and Heat Transfer Studies on a Curved Surface, Combined Part I and II," Int. J. Rotating Mach., **6**, pp. 393–418.
- [12] Schobeiri, M. T., and Chakka, P., 2002, "Prediction of Turbine Blade Heat Transfer and Aerodynamics Using Unsteady Boundary Layer Transition Model," Int. J. Heat Mass Transfer, **45**, pp. 815–829.
- [13] Brunner, S., Fottner, L., and Schiffer, 2000, "Comparison of two highly loaded turbine cascade under the influence of wake-induced transition," ASME 2000-GT-268, presented at the International Gas Turbine and Aero-Engine Congress and Exposition, Munich, Germany, May 8–11, 2000.
- [14] Cardamone, P., Stadtmüller, Fottner, L., and Schiffer, 2000, "Numerical Investigation of the Wake-Boundary Layer Interaction on a Highly Loaded LP-Turbine Cascade Blade," ASME 2002-GT-30367, presented at the International Gas Turbine and Aero-Engine Congress and Exposition, Amsterdam, Netherlands, June 3–6, 2002.
- [15] Schulte, V., and Hodson, H. P., 1996, "Unsteady Wake-Induced Boundary Layer Transition in High Lift LP Turbines," ASME Paper 96-GT-486.
- [16] Kaszeta, R. W., Simon, T. W., and Ashpis, D. E., 2001, "Experimental Investigation of Transition to Turbulence as Affected by Passing Wakes," ASME Paper 2001-GT-0195.
- [17] Lou, W., and Hourmouziadis, J., 2000, "Separation bubbles under Steady and Periodic Unsteady Main Flow Conditions," ASME Paper 200-GT-270.
- [18] Schröder, Th., 1989, "Measurements with hot-film probes and surface mounted hot film gages in a multi-stage low-pressure turbine," European Propulsion Forum, Bath, UK.

- [19] Hauieisen, V., Schröder, Th., and Hennecke, D., 1997, "Advanced Non-Intrusive for propulsion engines," AGARD-CP-598.
- [20] Halstead, D. E., Wisler, D. C., Okiishi, T. H., Walker, G. J., Hodson, H. P., and Shin, H.-W., 1997, "Boundary layer development in axial compressors and turbines: Part 3 of 4," *ASME J. Turbomach.*, **119**, pp. 225–237.
- [21] Schobeiri, M. T., John, J., and Pappu, K., 1996, "Development of Two-Dimensional Wakes Within Curved Channels, Theoretical Framework and Experimental Investigation," *ASME J. Turbomach.*, **118**, pp. 506–518.
- [22] Eifler, J., 1975, "Zur Frage der freien turbulenten Strömungen, insbesondere hinter ruhenden und bewegten Zylindern," Dissertation D-17, Technische Hochschule Darmstadt, Germany.
- [23] Kline, S. J., and McClintock, F. A., "Describing Uncertainties in Single-Sample Experiments," *Mech. Eng. (Am. Soc. Mech. Eng.)*, **75**, pp. 3–8.

# Experimental and Numerical Investigation on the Effects of the Seeding Properties on LDA Measurements

Angelo Algieri<sup>1</sup>

Sergio Bova<sup>2</sup>

Carmine De Bartolo<sup>3</sup>

Dipartimento di Meccanica,  
Università della Calabria - 87036  
Arcavacata di Rende (CS)

*The characteristics of the seeding particles, which are necessary to implement the laser Doppler anemometry (LDA) technique, may significantly influence measurement accuracy. LDA data were taken on a steady-flow rig, at the entrance of the trumpet of the intake system of a high-performance engine head. Five sets of measurements were carried out using different seeding particles: samples of micro-balloons sieved to give three different size ranges (25–63 μm, 90–200 μm, and standard as received from the manufacturer 1–200 μm), smoke from a “home-made” sawdust burner (particle size ≤1 μm), and fog from a commercial device (particle size around 1 μm). The LDA data were compared with the results of two-phase computational fluid dynamics simulations. The comparison showed a very good agreement between the experimental and numerical results and confirmed that LDA measurements with particle dimensions in the order of 1 μm or less represent the actual gas velocity. On the contrary, quite large particles, which are often used because of their cost and cleanliness advantages, introduce non-negligible errors. [DOI: 10.1115/1.1899167]*

## Introduction

The most advanced experimental techniques for accurately measuring local instantaneous velocity make use of optical methods: laser Doppler anemometry, phase Doppler anemometry, and particle image velocimetry [1]. However, the result of these measurements is not the actual fluid velocity but the velocity of particles (seeding) that are dispersed in the fluid and that scatter the light. Both gases and liquids must therefore be carefully seeded with particles of appropriate characteristics.

The properties of the particles are a fundamental requisite for measurement accuracy. In particular, the seeding particles should have two main characteristics: they have to carefully follow the fluid flow and they have to scatter an adequate light quantity in order to give a strong signal with respect to background noise. Regarding the first, small, low-density particles are preferred. In regard to the light scattering performance, identification of an optimum particle diameter, which maximizes the signal-to-noise ratio, is possible. The goodness of a seeding system, however, is also judged in connection with other properties, which, after all, determine its actual utilization. The seeding system must be capable of continuously generating large volumes of seeding particles. The particles must have a low degree of toxicity, corrosiveness, abrasiveness, and both a low tendency to soil the optical surfaces and to evaporate or to aggregate. Sometimes the possibility of their operating in aggressive environments (e.g., combustion) is also mandatory, and, finally, their cost must be acceptable [2,3].

As a result of the above considerations, a wide interest exists in the evaluation of the difference between fluid and particle velocity as a result of the seeding characteristics, particularly in those applications where considerable measurement is required, so that cost and soiling considerations suggest the use of inexpensive and

clean even if relatively large and heavy particles [4]. A previous work evaluated the performance of a sample of particles in a particular size range [5]. The present paper exposes LDA measurements, which were taken on a steady-flow rig, at the entrance to the intake system of a high-performance internal combustion engine, by using particles of different size and origin: micro-balloons sieved in three different dimensions and smoke and fog generated by means of two different techniques. At the same time, CFD simulations of a two-phase flow of air and a small quantity of particles (<10% in volume, with the same size and density as the ones used in the experiments) were performed. The simulations correctly predicted the velocity of both the particles and the main flow (air) and showed that in the investigated conditions the error associated with quite big particles can reach 10–16%, while the smaller particles follow gas flow with absolutely negligible differences.

## Background

Seeding particles must have two basic properties in order to be adapted to LDA applications: they must be able to follow the flow and they must scatter enough light to produce a good signal-to-noise ratio [2,3]. In addition, other more “handy” aspects of a seeding system are also relevant.

**Fluid Dynamic Considerations.** The LDA technique measures the velocity of the particles which are dispersed in the fluid. This velocity depends on the shape, size, and density of the particles as well as on the fluid velocity, density, and viscosity. In the case of spherical particles, which are dispersed in a gas and whose density is much greater than that of the gas, the force acting on them can be expressed as [6]

$$F = m_p \frac{dv_p}{dt} = 3\mu\pi d(v_f - v_p) \quad (1)$$

or, equivalently,

<sup>1</sup>a.algieri@unical.it

<sup>2</sup>s.bova@unical.it

<sup>3</sup>c.debartolo@unical.it

Contributed by the Fluids Engineering Division for publication in the JOURNAL OF FLUIDS ENGINEERING. Manuscript received November 25, 2003. Final manuscript received December 6, 2004. Associate Editor: Sivaram Gogenini.



$$\frac{1}{6} \pi d^3 \rho_p \frac{dv_p}{dt} = 3 \mu \pi d (v_f - v_p) \quad (2)$$

If the fluid velocity is a constant, the particle velocity will be given by

$$v_p(t) = v_f + [v_p(0) - v_f] e^{-t/\tau} \quad (3)$$

where

$$\tau = \frac{m_p}{3 \pi \mu d} = \frac{\rho_p d^2}{18 \mu} \quad (4)$$

is a time constant. The time that a particle needs to reach the fluid velocity, therefore, decreases as particle density and size decrease and as the fluid viscosity increases. These are also the conditions in order that the particle can follow rapid velocity variations of the flow.

**Optical Considerations.** Even though small particles follow the fluid velocity more easily, larger particles scatter more light. The light signal is therefore stronger, but the background noise level usually also increases, so that the improvement of the signal-to-noise ratio is not guaranteed. As matter of fact, the optical signal quality drops if the particle size becomes comparable with the  $s$  fringe spacing of the control volume. In such a case, the particle occupies both bright and dark fringes at the same time, so that the modulation of the light signal may be poor. The modulation depth or visibility factor:

$$F_v = \frac{y_{max} - y_{min}}{y_{max} + y_{min}}, \quad (5)$$

where  $y_{min}$  and  $y_{max}$  are, respectively, the minimum and maximum level of the light signal, in the case of spherical particles of diameter  $d$  is equal to [2]

$$F_v = \left| \frac{2J_1(\varepsilon)}{\varepsilon} \right| \quad (6)$$

where

$$\varepsilon = \frac{\pi d}{s} \quad (7)$$

and  $J_1(\varepsilon)$  is a Bessel function of the I type. In this case, the signal-to-noise ratio is proportional to  $J_1(\varepsilon)$  and becomes maximum when  $\varepsilon=1.841$ ; i.e., when the ratio of the particle diameter to the fringe spacing is 0.586 [2].

**Practical Remarks.** Besides good fluid dynamic and optical behavior, the seeding particle should also possess other practical characteristics. The seeding must be compatible with the other equipment involved in the application, so it should not be corrosive, toxic, scratching, or soiling; in addition, it should be continuously and inexpensively generated even in quite large quantities. Many of the particle properties are closely related to the generation technique used. Often, aerosol, or atomization, techniques are adopted, which generate monodisperse seeding; i.e., uniform particle size. Aerosols, however, are not easily generated in large quantities [6]. Another frequently used technique is the evaporation and condensation of water-based fog liquid. In some applications, however, the generated fog tends to condense along ducts and on the optical accesses. In addition, the liquid used in the fog generators is quite expensive.

Among the possible generation techniques, the fluidization procedure is often adopted in internal combustion engine investigations, since the other techniques usually produce soiling problem for ducts and optic accesses [4,7]. With this type of seeding generator the particles size depends on the adopted powder. Very small particles are difficult to use, because of their aggregation tendency due to electrostatic attraction [8]. Furthermore, high quality seeding particles are available on the market for fluidization equipments, but their cost is usually very high. Low-cost

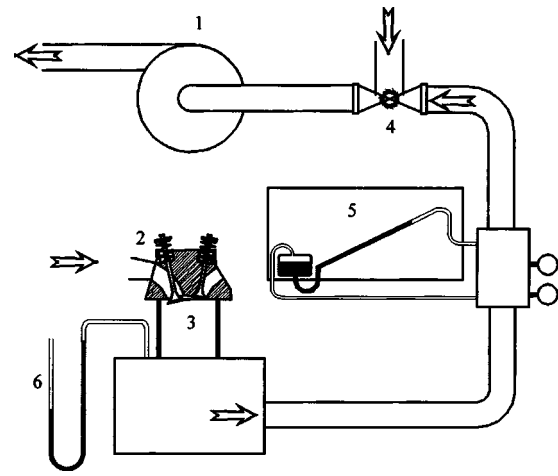


**Fig. 1 Scheme of the steady-flow test rig: (1) blower, (2) engine head, (3) cylinder, (4) bypass valve for flow regulation, (5) flow meter, and (6) differential manometer.**

particles are therefore often adopted, in spite of their dimensions, when large amounts of experimental data are necessary.

## LDA measurements

**Experimental Apparatus.** The experimental investigation was carried out by means of a steady-flow rig, enabling air to be forced through the intake system of an engine head by means of a blower, while the valve lift is fixed to a selected value (Fig. 1). The flow rig can deliver flow rates in the range 40–600 m<sup>3</sup>/h for ambient; cylinder pressure drops up to about 10 kPa at low flow rates and 5 kPa at the highest flow rates. In addition to global mass flow rate, the facility also enables local velocity measurements with LDA [9].

The LDA system is a one-color system (i.e., capable of measuring one component of the velocity) in a backscattering configuration, with a Bragg-cell frequency shifter. The system uses an argon-ion laser as a light source (2 W on the green line, at  $\lambda = 514.5$  nm) and optical fibers for both transmitting and collecting optics. The main geometrical data of the optical system are:

- beam spacing 38 mm
- focal length 400 mm
- probe volume width 0.194 mm
- probe volume length 4.09 mm
- number of fringes 35
- fringe spacing 5.42  $\mu$ m

If a frequency shifter module is used, the number of fringes depends on other parameters, such as record length, center frequency, and band width used by the signal processor. In the case of the reported measurements, the resulting number of fringes was 48.

The movement of the LDA probe is obtained by using a micrometer X-Y traversing system. The probe can also be rotated around its axis and moved vertically (Z axis). A dedicated signal processor, which performs fast-Fourier transform processing of the original signal in order to extract the Doppler frequency, is used for the analysis of the Doppler signal and ensures rejection of the signal produced by different particles that may be present within the measuring volume at the same time. The processor is linked to a computer in order to store and analyze the data.

Three different seeding systems were employed during the investigation. The first one adopts a fluidized bed-like scheme. A fraction of the inlet air is first dried and then passed through a horizontal porous diaphragm on the top of which a layer of silica micro-balloons is deposited. Figures 2 and 3 show the polydis-

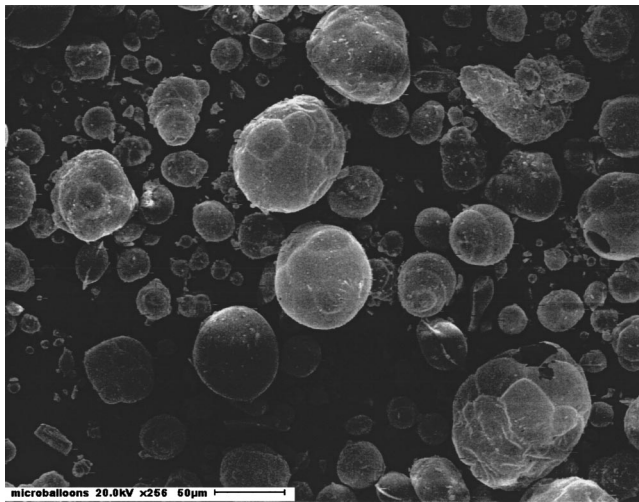


Fig. 2 Microscope photograph of micro-balloons

persed nature of these particles, 80% of which have a size in the range 10–100  $\mu\text{m}$ . The air stream then carries the particles and is subsequently mixed with the main intake air at the engine inlet [7,10]. A second seeding system, a custom-made [11] smoke generator, was tested. No specific size measurement was made on these particles. However, data from literature show that major part of the particles generated by wood combustion is in the range 30–300 nm and that the particle distribution of manually operated burners varies considerably during a burning cycle [12]. Smoke generators usually soil the optical accesses quite rapidly. This was not a problem in the reported tests because the measurements were taken in a free stream at the entrance to the engine intake system. The third seeding system is a commercial device, which generates a fog of very small droplets (mean size around 1  $\mu\text{m}$ ) by evaporation and condensation of a water-based liquid. Figure 4 shows the droplet size distribution, provided by the manufacturer.

**Measuring Conditions.** The measurements with all the different seeding particles were performed on a grid on the middle plane at the entrance of the trumpet of the intake system of a high performance engine head [4]. On the trumpet axis, the measuring points were located at a distance of 5, 10, 15, 20, 25, and 30 mm from the entrance (Fig. 5(a)), while additional measuring points were selected along lines orthogonal to the trumpet axis at dis-

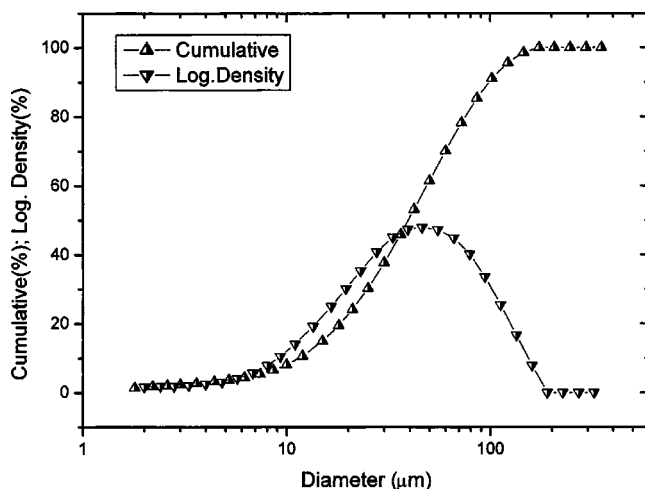


Fig. 3 Cumulative distribution and logarithmic density of micro-balloons

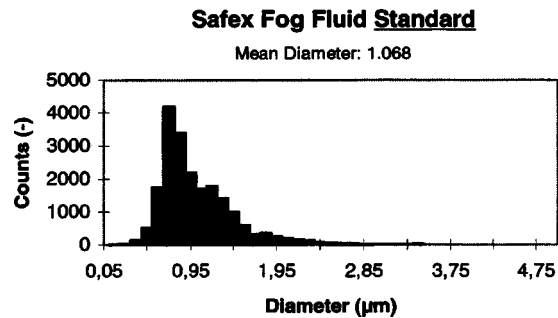


Fig. 4 Size distribution of the fog droplets, as provided by the manufacturer

tances of 5, 15, and 30 mm from the entrance, spaced 6 mm one from the other (Fig. 5(b)). Finally, measurements were taken at all points of the measuring grid by using the commercial fog generator only. One velocity component was measured at a time and at a given point, thus assuming that the flow conditions of both air and particles do not vary with time. In addition, it was assumed that the particle flow does not influence the continuous phase. Tests were carried out at the fixed mass flow rate 0.166 kg/s. Figure 5(c) shows a view of the experimental setup.

Five sets of measurements were carried out, by using different seeding particles: samples of micro-balloons sieved to give three different size ranges (25–63  $\mu\text{m}$ , 90–200  $\mu\text{m}$ , and standard as received from the manufacturer 1–200  $\mu\text{m}$ ), smoke from a custom-made sawdust burner (particle size less than 1  $\mu\text{m}$ ), and fog from a commercial device (particle size around 1  $\mu\text{m}$ ). In all the conditions, the particle-to-air ratio was kept less than 10% in volume. At each measuring point 3000–10,000 realizations were acquired for each velocity component both in the case of the microballoons and of the commercial fog generator and about 3000 in the case of the smoke. Typical mean data rate values of 0.8–1.2 kHz were acquired for the LDV measurements with 70–95% of the data valid.

The relative uncertainty of the experimental velocity measurements, which is due mainly to the setup of the electronics system, is  $\leq 2.1\%$ . The uncertainty of the mass flow rate measurements is  $\leq 1.5\%$ . More details on experimental uncertainty are given in the Appendix.

### CFD simulations

As the geometry and the boundary conditions of the physical system are axis-symmetric and the body forces can be considered negligible, the numerical analysis of the two-phase flow (particle-laden flow) at the entrance to the intake system was carried out by means of three-dimensional (3D) axis-symmetric Navier-Stokes equations, which take advantage of the hypothesis of symmetry in order to reduce the computational effort, without losing the 3D features and without any assumption about the velocity profile.

**Geometric Domain.** The computational domain consists of an intake plenum and of the trumpet entrance, at the end of which a duct of constant diameter was added. Figure 6 shows the 3D axis-symmetric geometric domain and its two-dimensional section. The diameter and the height of the step, as well as the bending radius at the entrance to the trumpet are the same as the real ones. On the contrary, the end of the geometric domain was fictitiously placed at a distance 218 times the height of the step to the intake plenum, in order to enable constant pressure conditions at the exit section to be fixed. Three different structured grids with four node elements were used for the geometric domain “discretization” and a grid-independent solution [13].

**Boundary Conditions.** Axis-symmetric boundary conditions, with zero angular components were set for the continuous phase

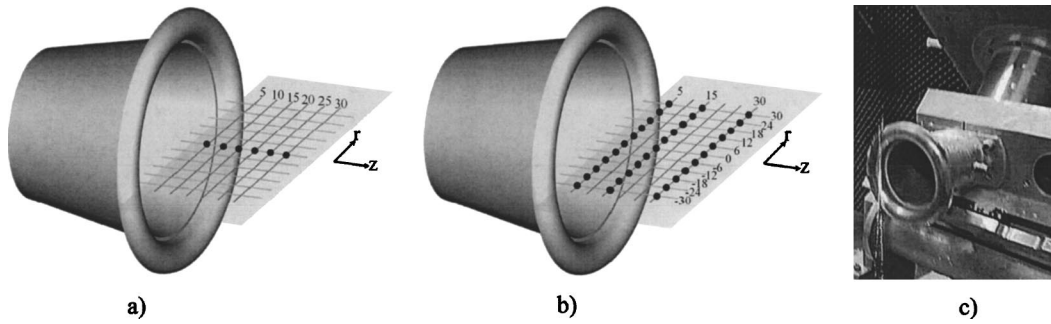


**Fig. 5 Measurement location at the entrance of the intake trumpet. (a) Location of the measuring points along the trumpet axis (b). Location of the measuring points along lines orthogonal to the trumpet axis. (c) Experimental setup.**

flow. A uniform velocity value of the dispersed particles, normal to the inlet boundary (Fig. 6), was evaluated on the basis of the plenum external area  $A$  and of the particle volumetric flow rate  $q^p$ . In addition, at this boundary the values of all turbulence quantities were set to zero, since in the intake plenum the flowfield is laminar. As for the pressure values at the inlet section, ambient experimental ones were used. Conversely, at the exit section, the pressure value that resulted in a mass flow rate equal to the experimental one.  $\dot{m}_{\text{exp}}$  was selected by means of an iterative procedure. Furthermore, on the wall of the duct, the velocity components were set to zero for the continuous phase and the reflection condition was adopted for the dispersed particles. Table 1 summarizes the boundary conditions for the particle-laden flow.

The overall uncertainty of the CFD calculations is  $\leq 0.2\%$ . The issue of the numerical accuracy is discussed in more detail in the Appendix.

**Numerical Procedure.** The simulations were carried out by means of a finite volume commercial code [14]. Because of the low volumetric ratio between the solid (particles) and the fluid (air) phases ( $< 10\%$ ), a two-phase Eulerian-Lagrangian model

was used to calculate the trajectory of the particles. This model besides solving the transport equations for the continuous phase:

$$\frac{\partial(\rho\phi)}{\partial t} + \nabla \cdot (\rho\phi\vec{v}) = \nabla \cdot (\Gamma \nabla \phi) + S_\phi \quad (8)$$

also allows a discrete second phase in a Lagrangian frame of reference to be simulated. This second phase consists of spherical particles dispersed in the continuous phase. The trajectory calculations are based, in this particular case, on the force balance on the particle, by using the local conditions of the previously calculated continuous phase flowfield (uncoupled approach):

$$\frac{dv_i^p}{dt} = \frac{18\mu C_D \text{Re}}{\rho_p d_p^2} (v_i^f - v_i^p) + \frac{g_i(\rho_p - \rho)}{\rho_p} + F_i^p \quad (9)$$

At the entrance to the intake system the flowfield is laminar, as the intake air comes from the rest and no turbulence generator exists before the trumpet. On the contrary, near the exit section the flow is turbulent, due to the presence of a step within the trumpet ( $\text{Re} = 1.8 \times 10^5$ , calculated using the medium velocity and the diameter of the duct at the exit section). The problem was solved for

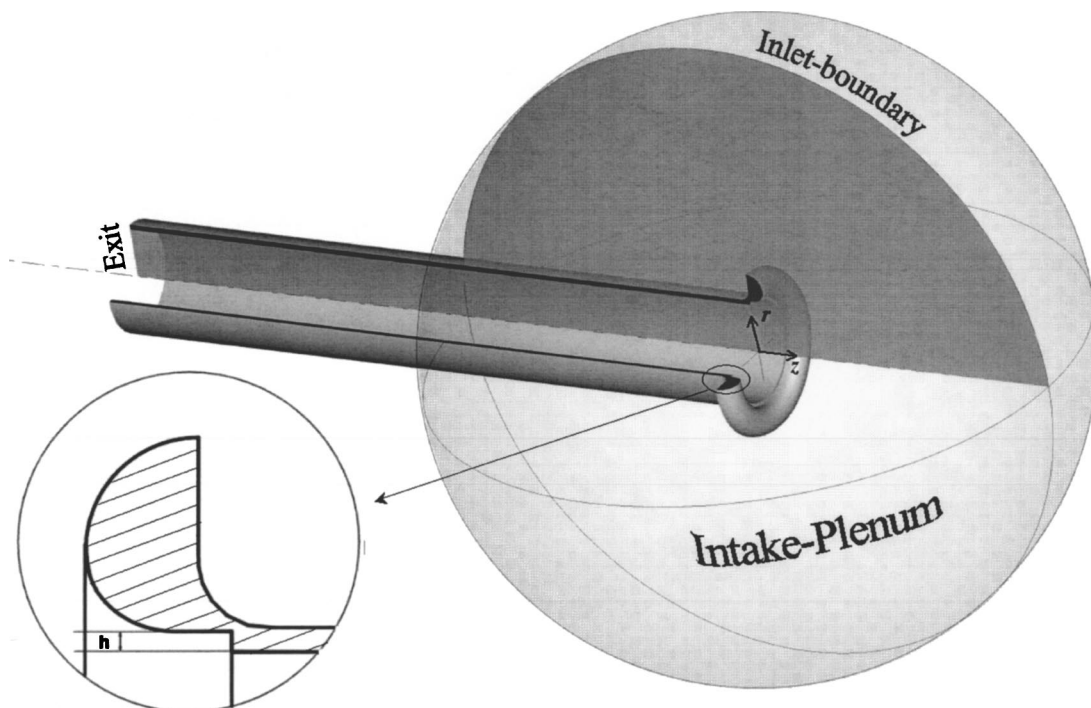


**Fig. 6 Axis-symmetric geometric model**

**Table 1 CFD boundary conditions**

Boundary conditions:	Continuous phase	Discrete phase
On solid walls	$v=v_w=0$ (no slip condition) Heat flow =0 (adiabatic flow)	Reflection condition
On fluid boundaries	Inlet: $p=\text{const}$ (Experim. values) $l=0$ $\mu/\mu_i=0$ Outlet: $p=\text{const}=p(\dot{m}_{exp})$	Inlet: $ v^p  = \frac{Q^p}{A} = \text{const}$ direction: $n$ (normal to the boundary)
On symmetry axis	$\partial()/\partial n=0$ , for all dependent variables	

the turbulent case and at the inlet boundary section the values of all turbulence quantities were set to zero. For the continuous phase, the  $k-\varepsilon$  *realizable* turbulence model was applied. This overcomes the deficiencies of the traditional  $k-\varepsilon$  model (turbulent normal stress less than zero; violation of the Schwarz inequality) by adopting a new eddy-viscosity formula and a new equation for the dissipation term  $\varepsilon$  [15,16]. In order to accurately represent the flow near the wall of the duct, a very fine mesh was adopted in this region. As the Mach number was  $\leq 0.13$ , compressibility effects were neglected and the density value of the continuous phase was set equal to the experimental one. In addition, the governing equations of the two-phase field flow were solved sequentially (segregated solution method).

**Results**

The symbols of Fig. 7 clearly state the problem of the dependence of LDA results on the seeding characteristics. The figure presents the axial LDA velocity measurements<sup>1</sup>, which were taken along the axis of the intake trumpet, one at a 5 mm distance from the other (Fig. 5(a)), in the case of two different seeding particles: standard microballoons with diameter in the range 1–200  $\mu\text{m}$ , and smoke ( $\leq 1 \mu\text{m}$ ). The micro-balloon velocity is significantly lower than the smoke velocity and the difference slightly increases as the measuring point approaches the trumpet entrance, where the pressure gradients are bigger and the flow acceleration higher.

<sup>1</sup>The axial velocity is positive if directed toward the trumpet entrance; the radial velocity is positive if directed toward the trumpet axis.

The causes of these velocity differences were investigated by using particles of different size and by means of CFD simulations. The standard micro-balloon sample was divided into two smaller subsamples (25–63  $\mu\text{m}$  and 90–200  $\mu\text{m}$ ) by a sieving procedure. This firstly aims to reduce the granulometric dispersion of the silica seeding, secondly to evaluate the effect produced by the particle dimension on LDA measurements, and finally to validate the two-phase flow model at the entrance to the intake system. The CFD code [14] was used to simulate of the two-phase flow of 25 and 63  $\mu\text{m}$  particles dispersed in air. The air velocity is the same, both in the case of a flow of air only and in the case of a two-phase flow. This is due to the very low particle volumetric fraction. The measurements (symbols) and the results of the simulations (lines) are compared in Fig. 8 again for the case of the axial velocities along the trumpet axis (measuring points of Fig. 5(a)). Like the experimental evidence, the simulations predict that the particle velocity at a fixed distance from the entrance grows as the particle size decreases, and that the difference between continuous and discrete phase slightly augments as the distance from the entrance diminishes. The figure shows that the experimental data, obtained using the smallest micro-balloon powders, lie well in between the CFD results for the 25 and 63  $\mu\text{m}$  cases and that the smoke experimental data are in good agreement with the air velocity obtained from the simulation. The agreement between experimental and numerical results is also confirmed in the other measuring points. As an example, Fig. 9 compares the axial velocity of the small micro-balloons along three lines orthogonal to the trumpet axis, 5, 15, and 30 mm away from the intake entrance (Fig. 5(b)).

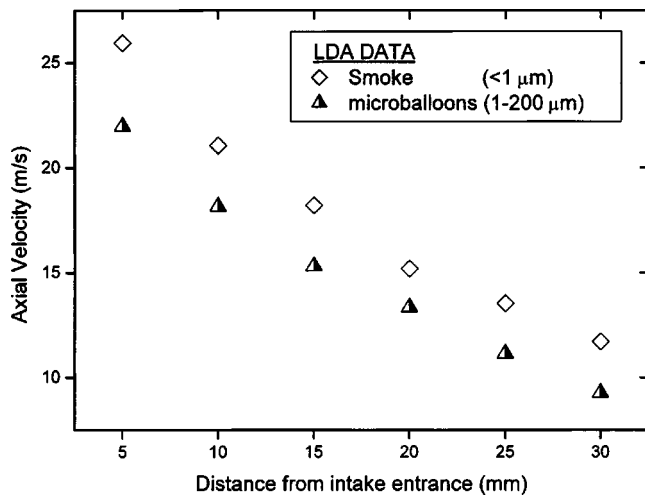


**Fig. 7 LDA measurements taken using micro-balloons and smoke**

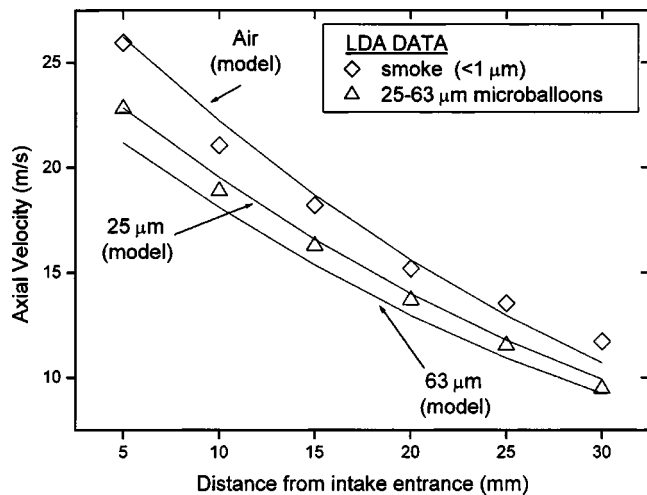


**Fig. 8 Comparison of the LDA data and CFD simulation results (trumpet axis)**

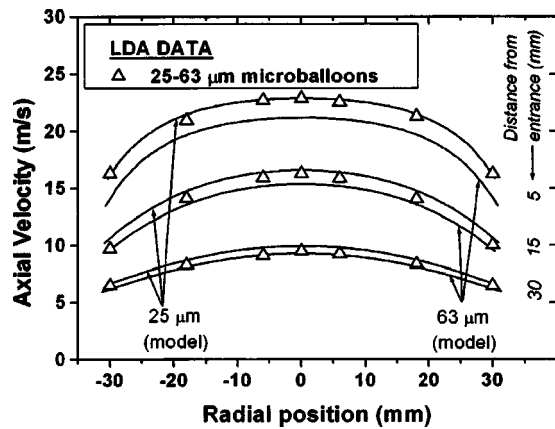


Fig. 9 Comparison of the LDA data and CFD simulation results (radial direction).

The effect of the sieving procedure on the velocity measurements is shown in more detail in Fig. 10. The particle selection technique has a positive effect. In fact, the adoption of the smallest powders allows a better characterization of the air flow. At the highest pressure gradient, a spur in the axial velocity between the smallest and the standard silica particles of about 4% is recorded. Even though this spur is comparable with the measurement uncertainty ( $\sim 2.1\%$ ), the fact that the velocity obtained with the smaller particles is systematically higher than the velocity obtained with the larger ones, makes this difference meaningful. However, the gap relative to the continuous phase remains significant. This difference is better illustrated in Fig. 11, which outlines how the gap rises as the measuring point approaches the trumpet entrance. The relative difference, i.e., the former difference divided by air velocity, falls in the 11–15% range.

The preceding analysis (Fig. 8) showed that smoke is a good tracer for air. Nevertheless, two drawbacks have been found: first of all, soiling problems localized on ducts exist; second, control the particle dimensions is impossible. For these reasons, the performances of a new fog generator were evaluated. Fog and smoke data along the trumpet axis are compared in Fig. 12. Both the fog and the smoke generators produce measurements in good agreement with CFD calculations. The comparison shows that smoke determines a slight increase in data dispersion relative to the numerical results. This is probably due to greater difficulty in controlling the size of the particles. As an example, Fig. 13 illustrates the velocity distribution obtained at the point located on the trum-

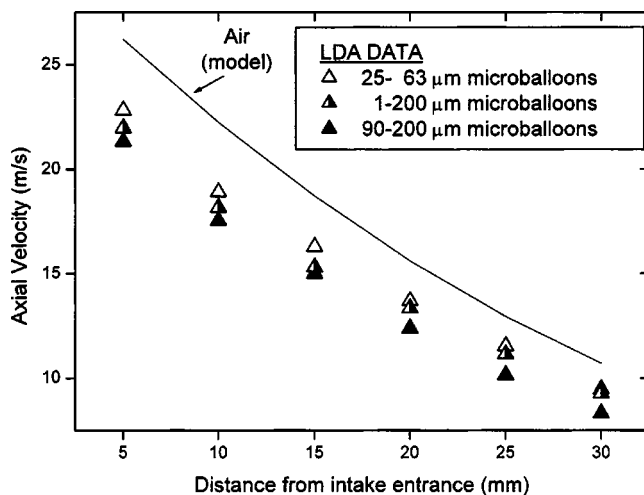


Fig. 10 Effect of the sieving procedure

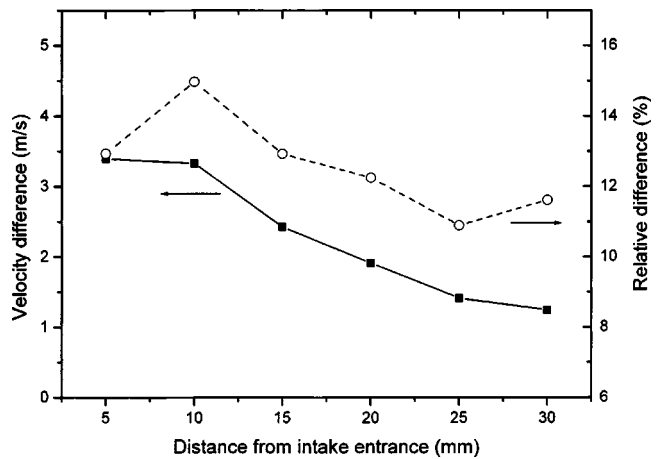


Fig. 11 Absolute and relative differences in the axial component of the velocity along the trumpet axis between microballoons (LDA measurements) and air (model)

pet axis, at a distance 20 mm from the entrance, by using the two seeding techniques. The standard deviation registers a larger value when smoke particles are used. For these reasons, the fog system was adopted to characterize the flowfield at the trumpet intake entrance and to evaluate the influence of the seeding properties on LDA measurements. To this purpose, the experimental investigation was carried out by acquiring the axial and radial velocity components in all the grid measuring points (Fig. 5). Figure 14 shows the comparison between fog and the smallest microballoons in terms of axial velocities. For simplicity, the plot refers only to the measurements acquired along three parallel lines (5, 15, and 30 mm away from the intake entrance). The differences remain almost constant moving in a radial direction. This is probably due to the fact that, in the radial direction, the axial pressure gradients can be considered uniform  $\partial(\partial p / \partial z) / \partial r \approx 0$ . As already observed, the silica powders have greater difficulty following the continuous phase as the measuring point approaches the trumpet entrance. On the contrary, smaller velocity differences are registered on the radial components (Fig. 15) owing to the very low radial pressure gradients ( $|\partial p / \partial r| \sim 1 \text{ kPa/m}$  versus  $|\partial p / \partial z| \sim 20 \text{ kPa/m}$ ).

In order to investigate the influence of the pressure gradients on the LDA measurements, new CFD simulations were performed for 25 and 63  $\mu\text{m}$  particle diameters. All the boundary conditions

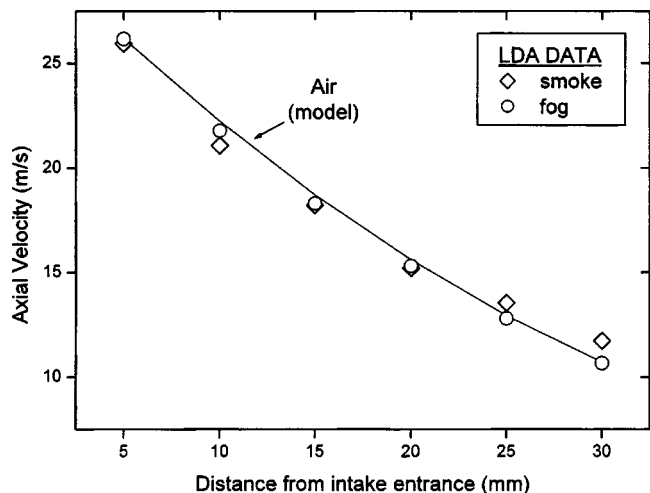


Fig. 12 Comparison of the LDA data (smoke and fog) and CFD results (air) along the trumpet axis

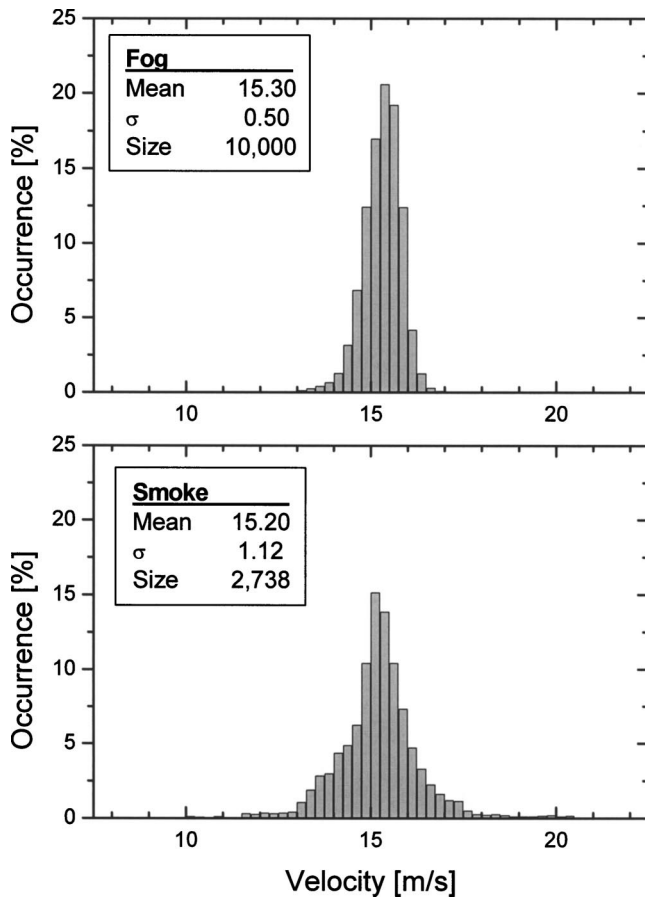


Fig. 13 Comparison of the velocity distributions by using smoke and fog particles

were maintained except for the pressure value at the exit section. This value was chosen as  $\frac{1}{4}, \frac{1}{2}, \frac{3}{4}$ , and 2 times the pressure outlet used in the previous simulations.

Figure 16 shows the axial pressure gradient as a function of the velocity difference between the continuous and discrete phase. Data refer to the measuring points along the trumpet axis. A unique trend is present for each powder sample (parabolic curves are obtained). This means that, for the investigated conditions, the

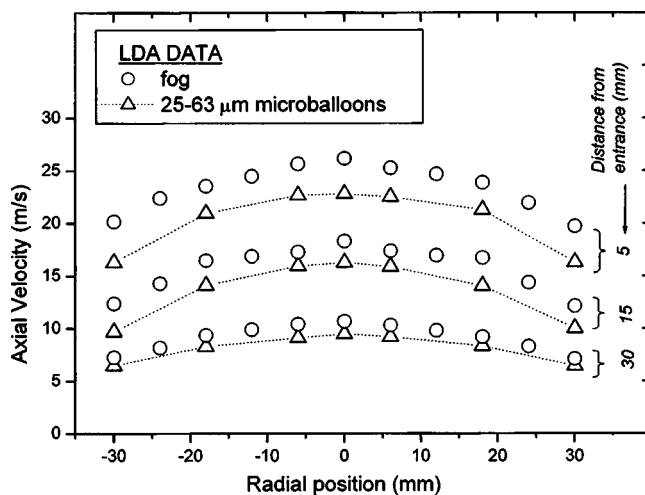


Fig. 14 Axial velocities comparison by using fog and smaller micro-balloons

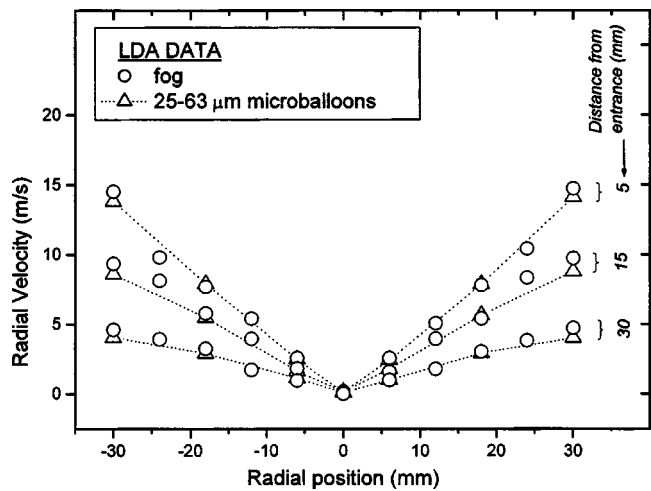


Fig. 15 Radial velocities comparison by using fog and smaller micro-balloons

slip along the axis is mainly a function of the local pressure gradient. Once the pressure gradient is fixed, the gap between continuous and discrete phase raises as the particle dimension increases due to a largest inertia effect. Furthermore, the difference between the two curves grows with the pressure gradient. Ultimately, numerical data lie on the same curves (i.e., logarithmic laws have been found) by considering the percentage velocity differences as function of axial pressure gradient (Fig. 17). In particular, the figure shows that initially the difference between the two curves increases with the pressure gradients, afterwards, this gap remains almost constant and equal to 6% for  $|\partial p / \partial z| > 20$  kPa/m.

## Conclusion

The flow at the entrance to the trumpet of the intake system of a high-performance engine head was investigated by means of the LDA technique and of CFD simulations. The LDA measurements were accomplished with seeding particles of very different sizes, and the CFD analysis simulated the different two-phase flows. The outcomes of the two approaches were compared in order to assess the influence of the seeding characteristics on the LDA measurements. The comparison has shown a very good agreement between the experimental and numerical results and has confirmed

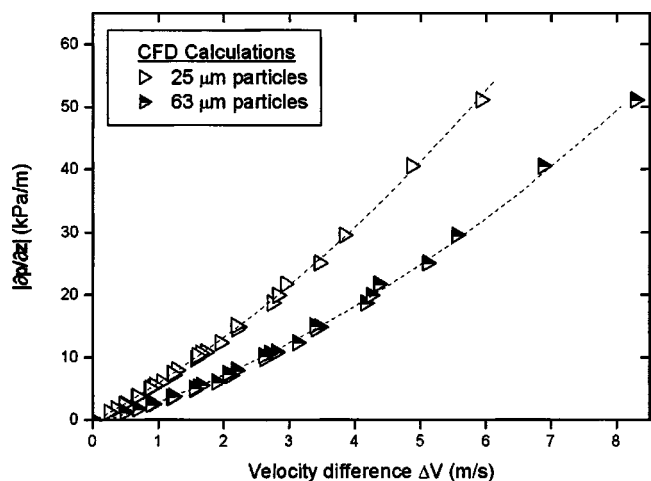


Fig. 16 Axial pressure gradient as a function of the velocity difference between the continuous and discrete phase along the trumpet axis

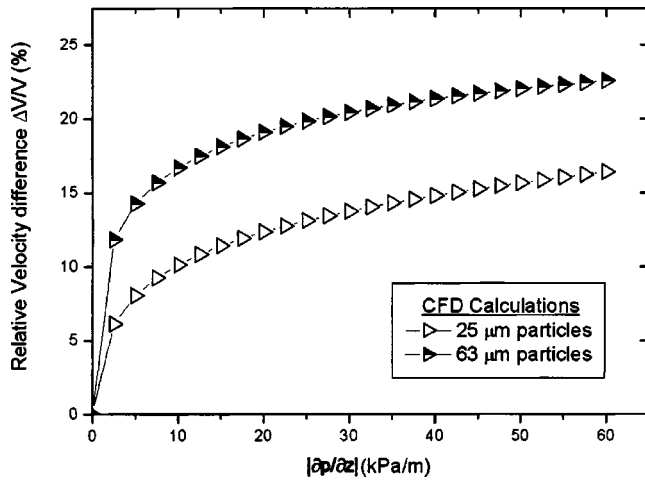


Fig. 17 Percentage velocity differences as function of the axial pressure gradient (25 and 63  $\mu\text{m}$  particles)

that LDA measurements with particle dimensions of the order of 1  $\mu\text{m}$  or less represent the actual gas velocity. On the contrary, quite large particles, which are often used because of their lower cost and cleanliness, introduce non-negligible errors, which in the case of the reported tests were in the 13–16% range. Even if the same particles are sieved the measurement error only decreases slightly.

Finally, the results obtained with a commercial fog generator are far superior. Taking into account that the cost of the LDA equipment is inherently high, the use of a professionally made fog generator is, therefore, recommended in all the application where the presence of the fog is compatible with the phenomenon to be analyzed.

### Acknowledgments

Some of the measurements were taken by L. Castellucci, D. Pellicanò, and part of the CFD simulations were performed by T. Castiglione as part of their thesis work; data of ambient pressure were provided by CRATI s.c.r.l.; the particle size characterization and the sieving procedure were performed by Prof. B. Formisani. Their contribution is gratefully acknowledged.

### Nomenclature

$A$	= plenum boundary area
$C_D$	= drag coefficient
$F_p$	= viscous force acting on the particle
$F$	= additional force acting on the particle
$F_v$	= visibility factor
$I$	= turbulence intensity
$J_I$	= Bessel function of the $I$ type
$N$	= measurements number
Re	= Reynolds number
$S$	= source term
$d$	= particle diameter
$g$	= gravitational acceleration
$h$	= step height
$k$	= turbulence kinetic energy
$m$	= mass
$\dot{m}$	= mass flow rate
$n$	= normal direction
$n_f$	= fringe number
$r$	= radial coordinate
$q$	= volumetric flow rate
$s$	= fringe spacing
$t$	= time

$v$	= absolute velocity
$w$	= wall
$y$	= level of the light signal
$z$	= axial coordinate
$\Gamma$	= diffusion coefficient
$\delta$	= uncertainty on the general variable
$\varepsilon$	= turbulent dissipation
$\mu$	= molecular viscosity of the fluid
$\mu_t$	= turbulent viscosity
$\rho$	= density
$\sigma$	= standard deviation
$\tau$	= time constant
$\phi$	= general variable

### Subscripts and Superscripts:

$exp$	= experimental
$f$	= fluid
$i$	= generic spatial direction
$max$	= maximum
$min$	= minimum
$p$	= particle
$\phi$	= general variable

### Abbreviations

CFD	= computational fluid dynamics
LDA	= laser Doppler anemometry
d.c.e.	= discrete conservation equation

## APPENDIX: Error Analysis

### A. Numerical Accuracy

In order to reduce the numerical discretization error (numerical diffusion), the mesh was generated aligned with the flow as much as possible. Furthermore, the use of quadrilateral grid elements, with second-order space discretization for the diffusive and convective terms of the governing equations allowed accurate results to be obtained in the more complex flow zones of the computational domain. To obtain a mesh-independent solution, two grid refinements were used. Table 2, shows the main characteristics of the three different meshes (M1, M2, M3) that were employed.

Table 3, compares the percentage variation of the continuous phase axial velocity component,  $[(V_{ax_{M_i}} - V_{ax_{M_{i+1}}}) / V_{ax_{M_i}}] \cdot 100$ , calculated at six locations along the trumpet axis, for the two grid refinements: M1  $\rightarrow$  M2, M2  $\rightarrow$  M3.

Unlike the first refinement

$$\frac{V_{ax_{M_i}} - V_{ax_{M_{i+1}}}}{V_{ax_{M_i}}} \cdot 100 < 3,$$

the second one improves the numerical solution only marginally

$$\frac{V_{ax_{M_i}} - V_{ax_{M_{i+1}}}}{V_{ax_{M_i}}} \cdot 100 \leq 0.2.$$

The same is true at all locations within the computational domain. In other words, the two steady axis-symmetric numerical solutions that were obtained with the M2 and M3 meshes are essentially the same, and therefore it can be concluded that the calculations, which make use of the M2 mesh, are grid independent.

As for the solving procedure, the numerical solution to the viscous incompressible flow was obtained by the pressure correction technique (Simple). The convergence check was performed by examining the decay of the residuals  $R$  and by monitoring the variations of the mass flow rate  $\dot{m}$  at the exit section as a functions of the iterations. The residuals were defined as the sum of the absolute imbalance of the discrete conservation equation (d.c.e.) for a general variable  $\phi$  over all the computational cells. This was scaled with a scaling factor ( $S = (\dot{m} \phi)_{in}$ ), representative of the  $\phi$  flow rate through the domain. The residuals can be written:

$$R_\phi = \frac{1}{S} \sum_{\text{cells}} |\text{imbalance d.c.e.}| \quad (\text{A1})$$

where  $R_\phi$  is the residual for the variable  $\phi$  (i.e.,  $\phi=v_r$ , radial momentum equation). As a stopping criterion for the iterative calculations process, the occurrence of constant residual values for several iterations (say 100 or more) was adopted. Besides, a very low percentage variation between inlet and outlet mass flow rate was imposed:

$$\frac{\dot{m}_{\text{in}} - \dot{m}_{\text{out}}}{\dot{m}_{\text{in}}} 100 < 0.005.$$

Table 4 shows typical residuals levels when convergence was achieved.

## B. Experimental Uncertainty

**Velocity.** The uncertainty on LDA measurements is a function of the fringe number  $n_f$  in the control volume [2]:

$$\frac{\delta v}{v} < \pm \frac{1}{n_f} \quad (\text{B1})$$

As the LDA experimental setup uses 48 fringes, the velocity measurement uncertainty is

$$\frac{\delta v}{v} < \pm 2.1\% \quad (\text{B2})$$

Using a different approach [17,18], the mean velocity uncertainty and the rms velocity uncertainty with  $z=1.96$  (95% confidence level) are, respectively,

$$\delta v = \pm \frac{z\sigma}{\sqrt{N-1}}; \quad \delta\sigma = \pm \frac{z\sigma}{\sqrt{2N}} \quad (\text{B3})$$

Applying Eqs. (B3), it follows that the relative uncertainty on the mean and rms velocity values ranges from  $\delta v/v \approx 0.04\%$  and  $\delta\sigma/\sigma \approx 1.4\%$  in the case of fog and 10,000 velocity data, respectively, recorded to  $\delta v/v \approx 3.7\%$  and  $\delta\sigma/\sigma \approx 2.5\%$  in the case of micro-balloons and smoke with 3000 velocity data recorded. The lowest value is obtained at the maximum axial velocity point, on the trumpet axis, whereas the highest one refers to the small tangential velocity, near the trumpet axis; this analysis does not take into account the tangential velocity values on the trumpet axis, which are  $\approx 0$ .

**Mass flow rate.** If a quantity  $F=F(x_1, x_2, \dots, x_n)$ , the uncertainty can be expressed as [2]

$$\delta F = \sqrt{\left(\frac{\partial F}{\partial x_1} \delta x_1\right)^2 + \left(\frac{\partial F}{\partial x_2} \delta x_2\right)^2 + \dots + \left(\frac{\partial F}{\partial x_n} \delta x_n\right)^2} \quad (\text{B4})$$

where  $\delta x_i$  is the uncertainty in parameter  $x_i$ .

As the mass flow rate has been calculated as  $\dot{m}=\rho q$ , the relative uncertainty is

$$\frac{\delta \dot{m}}{\dot{m}} = \sqrt{\left(\frac{\delta \rho}{\rho}\right)^2 + \left(\frac{\delta q}{q}\right)^2} \quad (\text{B5})$$

Applying Eq. (B4) and knowing the uncertainty on the quantities related to the mass flow rate measurements, it is found that

$$\frac{\delta \dot{m}}{\dot{m}} \approx \pm 1.3\% . \quad (\text{B6})$$

## References

- [1] Doebelin, E. O., 1990, *Measurement System, Application and Design*, McGraw-Hill New York.
- [2] Drain, L. E., 1990, *The Laser Doppler Technique*, John Wiley & Sons, New York.
- [3] Meyer, J. F., 1991, "Generation of Particles and Seeding," Lectures Series 1991-08, Von Karman Institute for Fluid Dynamics, pp. 1-42.
- [4] Bova, S., and Amelio, M. 2001, "LDA Investigation on Valve-Wall and Valve-Valve Flow Interaction in High-Performance 4-Valve I.C.E.," SAE paper no. 2001-01-1309.
- [5] A. Algieri, M. Amelio, C. De Bartolo, and S. Bova, 2003, "Influence of the Seeding Characteristics on LDA Measurements at the Intake Entrance of an ICE," in *Proc. of 6th Int. Conf. on Engines for Automobile, ICE2003, SAE-NA 2003-01-29, Capri, 14-19 Sept.*
- [6] Durst, F., Melling, A., and Whitelaw, J. H., 1976, *Principles and Practice of Laser Doppler Anemometry*, Academic Press, New York.
- [7] Amelio, M., Bova, S., and De Bartolo, C., 2000, "The Separation between Turbulence and Mean Flow in ICE LDV Data: The Complementary Point-of-View of Different Investigation Tools," *ASME J. Eng. Gas Turbines Power*, **122**, No. 4, pp. 505-698.
- [8] Geldart, D., and Wong, A. C., 1985, "Fluidization of Powders Showing Degrees of Cohesiveness—Bed Expansion," *Chem. Eng. Sci.*, **9**, pp. 481-488.
- [9] Barbieri, G., and Zagami, S., 2000, "Progettazione e Realizzazione di un Banco di Flussaggio Stazionario per Rilievi LDA su Teste di M.C.I.," *National ATI congress [Italian]*.
- [10] Amelio, M., Belli, M., Bova, S., and Florio, G., 1994, "LDA Flow Field Characterisation in a Motored Reciprocating Engine," in *PD-Vol. 64- 8.3, Engineering Systems Design and Analysis (ESDA) Conference*, Vol. 8, Part C, pp. 597-604, ASME PD.
- [11] Castellucci, L., 2002, "Progettazione, Realizzazione e Sperimentazione di un Sistema di Inseminazione per Anemometria Laser Doppler," Tesi di Laurea, Dip. Meccanica, Univ. Calabria [Italian].
- [12] Wiese, U., and Gaegauf, C. K., 2000, "Nanoparticle Emission of Wood Combustion Processes," *1st World Conf. and Exhib. on Biomass for Energy and Industry, Sevilla (Spain), June*.
- [13] Castiglione, T., 2003, "Simulazioni CFD di un Flusso Bifase all'Ingresso del Sistema di Aspirazioni di un MCI. Confronto con Rilievi Sperimentali LDA," Tesi di Laurea, Dip. Meccanica, Univ. Calabria [Italian].
- [14] FLUENT v. 6.0.12, 2001, Fluent, Inc., Lebanon.
- [15] Wilcox, D. C., 2000, "Turbulence Modeling for CFD, 2nd ed., DCW Industries Inc., La Canada, CA.
- [16] Shih, T. H., Liou, W. W., Shabbir, A., and Zhu, J., 1995, "A New  $k-\epsilon$  Eddy-Viscosity Model for High Reynolds Number Turbulent Flows—Model Development and Validation," *Comput. Fluids*, **24**(3), pp. 227-238.
- [17] Riethmuller, M. L., and Boutier, A., 1991, "Laser Velocimetry," von Karman Institute for Fluid Dynamics.
- [18] Gasparetti, M., Paone, N., and Tomasini, E. P., 1996, "Laser Doppler technique for the combined measurement of inlet flow and valve motion in IC engines," *Meas. Sci. Technol.*, **7**, pp. 576-591.



**Stephen J. LaPointe**  
Graduate Research Assistant  
Department of Mechanical  
and Aerospace Engineering,  
North Carolina State University,  
Campus Box 7910,  
Raleigh, NC 27695

**Nancy Ma<sup>1</sup>**  
Assistant Professor  
Department of Mechanical  
and Aerospace Engineering,  
North Carolina State University,  
Campus Box 7910,  
Raleigh, NC 27695

**D. W. Mueller, Jr.**  
Assistant Professor  
Department of Engineering,  
Indiana University -  
Purdue University,  
Ft. Wayne, IN 46805

# Growth of Binary Alloyed Semiconductor Crystals by the Vertical Bridgman-Stockbarger Process with a Strong Magnetic Field

*This paper presents a model for the unsteady species transport for the growth of alloyed semiconductor crystals during the vertical Bridgman-Stockbarger process with a steady axial magnetic field. During growth of alloyed semiconductors such as germanium-silicon (GeSi) and mercury-cadmium-telluride (HgCdTe), the solute's concentration is not small, so that density differences in the melt are very large. These compositional variations drive compositionally driven buoyant convection, or solutal convection, in addition to thermally driven buoyant convection. These buoyant convections drive convective transport, which produces nonuniformities in the concentration in both the melt and the crystal. This transient model predicts the distribution of species in the entire crystal grown in a steady axial magnetic field. The present study presents results of concentration in the crystal and in the melt at several different stages during crystal growth. [DOI: 10.1115/1.1899169]*

## 1 Introduction

During crystal growth without a magnetic field or with a weak magnetic field, turbulent or oscillatory melt motions can produce undesirable spatial oscillations of the concentration, or microsegregation, in the crystal [1]. Turbulent or oscillatory melt motions lead to fluctuations in the heat transfer across the growth interface from the melt to the crystal. Since the local rate of crystallization depends on the balance between the local heat fluxes in the melt and the crystal, fluctuations in the heat flux from the melt create fluctuations in the local growth rate that create microsegregation. A moderate magnetic field can be used to create a body force that provides an electromagnetic (EM) damping of the melt motion and to eliminate oscillations in the melt motion and thus in the concentration of the crystal. Unfortunately, the elimination of mixing and a moderate or strong EM damping of the residual melt motion may lead to a large variation of the crystal's composition in the direction perpendicular to the growth direction (radial macrosegregation).

On the other hand, if the magnetic field strength is so strong that the melt motion is reduced sufficiently so that it has no effect on the composition in the crystal, then this diffusion-controlled species transport may produce a radially and axially uniform composition in the crystal grown by the Bridgman-Stockbarger process or directional solidification [2]. In order to achieve diffusion-controlled species transport, the species transport Péclet number  $Pe_m = UR/D$  must be small, where  $U$  is the characteristic velocity for the magnetically damped melt motion and is inversely proportional to the square of the magnetic flux density  $B$ , while  $R$  is the characteristic dimension of the melt and  $D$  is the diffusion coefficient for the species in the molten semiconductor. If  $Pe_m \ll 1$ , then the characteristic ratio of convection to diffusion of species is small and the species transport is diffusion controlled. However,

since typical values of  $D$  are extremely small [3], i.e., 1 to  $2 \times 10^{-8}$  m<sup>2</sup>/s, it would not be practical to grow a crystal in the extremely large field strength that would be required to achieve diffusion-controlled species transport. Even for the strongest magnetic fields available with superconducting magnets,  $Pe_m > 1$ . As the magnetic field strength decreases, the of  $Pe_m$  increases. Therefore, the objective is to identify a magnetic field that is strong enough to eliminate flow oscillations but which moderately damps the melt motion in order to improve both radial and axial uniformity in the crystal.

For alloyed semiconductor crystal growth, the density differences due to compositional variations in the melt are very large. During the growth of alloyed semiconductor crystals such as silicon-germanium (GeSi) or mercury-cadmium-telluride (HgCdTe), both compositional and thermal variations in the melt create density differences that drive solutal convection. This solutal convection drives species transport, which causes segregation in the crystal. In germanium-silicon, for example, the mole fraction of germanium may vary from 0.95 in the melt that has not yet received any rejected germanium to 0.99 near the interface, and this compositional difference corresponds to a density difference of nearly 300 kg/m<sup>3</sup>. During the growth of alloyed semiconductor crystals, the application of magnetic fields has shown great promise. For example, Watring and Lehoczyk [4] have shown that the radial variation between the maximum and minimum concentrations can be decreased by more than a factor of 3 with the application of a 5 T magnetic field, arising because the magnetic field retards the sinking of the heavier melt to the center of the ampoule, which results in less radial segregation. Ramachandran and Watring [5] reported a reduction in the radial segregation in all of their samples that were grown in a magnetic field. Alboussiere et al. [6] also experimentally investigated the influence of a magnetic field on segregation in a metallic alloy.

For a typical crystal growth process, resolution of thin species-diffusion boundary layers having an  $O(Pe_m^{-1})$  thickness is often very challenging because the species transport Péclet number can have very large values. Several grid points must be concentrated inside each layer in order to give accurate results because these

<sup>1</sup>Corresponding author: 919-515-5231 (phone), 919-515-7968 (fax), nancy\_ma@ncsu.edu (e-mail).

Contributed by the Fluids Engineering Division for publication in the JOURNAL OF FLUIDS ENGINEERING. Manuscript received January 12, 2004; revised January 4, 2005. Associate Editor: Dennis Siginer.

boundary layers play critical roles in the transport. As the magnetic flux density  $B$  of the externally applied magnetic field is increased, the value of  $Pe_m$  decreases and the species-diffusion boundary layers become thicker, but the value of the Hartmann number  $Ha=BR(\sigma/\mu)^{1/2}$  increases, where  $\sigma$  and  $\mu$  are the electrical conductivity and dynamic viscosity of the melt, respectively. Therefore, there are thin species-diffusion or viscous boundary layers for every value of  $B$ . Therefore, the simultaneous numerical solution of the full Navier-Stokes, internal energy, and species transport must always have a very fine spatial grid and a very small time step. Models that accurately predict the species distribution in an entire crystal for any combination of process variables are needed to facilitate process optimization.

In a previous study [7], we presented an asymptotic and numerical solution for the dilute species transport during the solidification of a doped crystal by the Bridgman-Stockbarger process with a steady axial magnetic field. This study considered only pure crystals with very small dopant concentrations so that there was only thermally driven buoyant convection. During the growth of alloyed semiconductor crystals, the velocity and mole fraction of either species are intrinsically coupled because the buoyant convection is driven by both the thermal and compositional variations in the melt. In the 1970s, Hart [8] presented an asymptotic and numerical solution for the motion of a stratified salt solution with both thermally driven and compositionally driven buoyant convection, or solutal convection, and without a magnetic field or solidification in a rectangular cavity. Ma [9] and Wang and Ma [10] presented an asymptotic and numerical solution for the motion of a molten semiconductor with solutal convection, with a magnetic field and with solidification in a rectangular cavity. Liu et al. [11] numerically studied solutal convection during the traveling heater method with a magnetic field. Several important studies [12–15] have numerically investigated the effects of solutal convection on segregation during solidification without magnetic fields. In the present study, we treat the species transport during the solidification of a germanium-silicon alloy during a realistic process; namely, the vertical Bridgman-Stockbarger process with a uniform, steady, axial magnetic field. The present study eliminates the need for impractical computing resources by using an asymptotic approach to treat the entire period of time needed to grow a crystal. This approach involves an analytic solution to the internal energy equation, and a hybrid solution for the simplified coupled Navier-Stokes, electromagnetic, and species transport equations. The purpose of this paper is to illustrate a method that can be used to optimize the benefits of a magnetic field for a given crystal growth situation.

Researchers have reviewed the literature on crystal growth in the presence of magnetic fields. Garandet and Alboussière [16] reviewed the literature on experimental studies of Bridgman-Stockbarger growth of semiconductor crystals, and Walker [17] reviewed the use of asymptotic methods in modeling of semiconductor crystal growth.

## 2 Temperature

This paper treats the unsteady, axisymmetric species transport of silicon in a germanium melt during the vertical Bridgman-Stockbarger process with an externally applied, uniform, steady, axial magnetic field  $B\hat{z}$ . Here,  $\hat{r}$ ,  $\hat{\theta}$ , and  $\hat{z}$  are the unit vectors for the cylindrical coordinate system. During the Bridgman-Stockbarger process, the ampoule is moved from an isothermal hot zone where the germanium-silicon has been melted, through an adiabatic or thermal-gradient zone where the melt solidifies, and into a cold zone where the crystal is cooled. Our dimensionless problem is sketched in Fig. 1. The coordinates and lengths are normalized by the ampoule's inner radius  $R$ , and  $a$  is the dimensionless length of the ampoule.

Experiments [4] have shown that magnetic fields can control compositionally driven buoyant convection so that the electro-

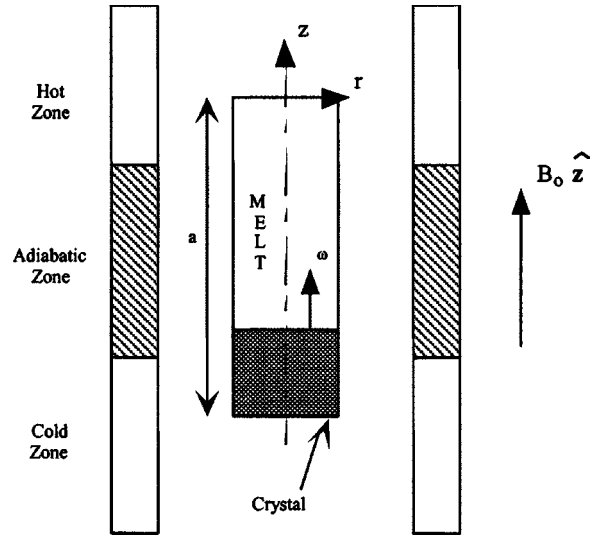


Fig. 1 Vertical Bridgman-Stockbarger ampoule with a uniform, steady, axial magnetic field  $B\hat{z}$  and with coordinates normalized by the ampoule's inner radius

magnetic body force must be comparable to the characteristic gravitational body force associated with compositional variations. Since the electric currents only arise from the melt motions across the magnetic field, the magnetic field can damp the melt motion but cannot completely suppress it. Therefore, this balance gives a characteristic velocity for the magnetically damped, compositionally driven, buoyant or solutal convection [9],

$$U = \frac{\rho_o g \beta_c C_o}{\sigma B^2}, \quad (1)$$

where  $\rho_o$  is the melt's density at the solidification temperature  $T_o$ ,  $g$  is gravitational acceleration,  $\beta_c$  is the compositional coefficient of volumetric expansion, and  $C_o$  is the initial uniform mole fraction of silicon in germanium. Thus, we can expect the melt motion to decrease roughly as  $B^2$  as the magnetic field strength is increased.

The crystal-melt interface moves at a constant velocity  $U_g = \omega U$ , where  $\omega$  is the dimensionless interface velocity. The planar crystal-melt interface lies at  $z=-b$ , where the instantaneous dimensionless axial length  $b(t)=a-\omega t$  decreases during growth. With time  $t$  normalized by  $R/U$ , the dimensionless time to grow the entire crystal is  $a/\omega$ .

The characteristic ratio of the convective to conductive heat transfer is the thermal Péclet number  $Pe_t = \rho_o^2 g \beta_c C_o c_p R / k \sigma B^2$ , which varies as  $B^{-2}$ . Here,  $c_p$  and  $k$  are the specific heat and the thermal conductivity of the melt, respectively. For a sufficiently large value of  $B$  and for practical growth rates, convective heat transfer and the heat released by the cooling melt are negligible compared to the conductive heat transfer [18]. Ma and Walker [19] investigated the effects of convective heat transfer on the temperature distribution and on the thermally driven buoyant convection are negligible for  $Pe_t < 15.0$ . For molten germanium-silicon with  $R=7.5$  mm,  $B=0.5$  T and  $C_o=0.10$ ,  $Pe_t=3.44$ . This value of  $Pe_t$  is sufficiently small that convective heat transfer is negligible.

As long as the furnace is axisymmetric, the melt's temperature is independent of  $\theta$ , and  $T(r, \zeta)$  is the deviation of the melt's dimensional temperature from the hot-zone temperature, normalized by  $(\Delta T)_o$  where  $(\Delta T)_o$  is the difference between the hot-zone temperature and  $T_o$ . Here,  $\zeta=1+2z/b$  is a rescaled axial coordinate, so that  $-1 \leq \zeta \leq +1$  for all time. For each instantaneous melt depth, the temperature is given by a separation-of-variables solution [7],

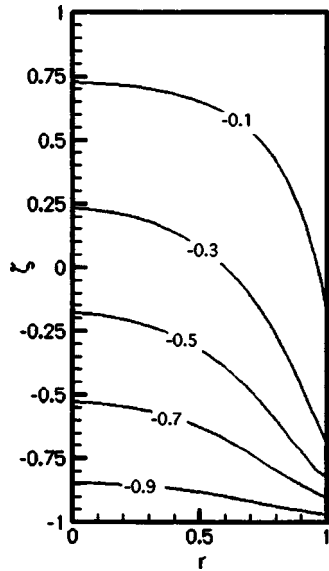


Fig. 2 Temperature  $T(r, \zeta, t=0)$  for  $Bi=10$ , and  $d=0.1$ , and  $a=1.0$

$$T = \frac{1}{2}(\zeta - 1) + \sum_{n=1}^{\infty} \chi_n I_0 \left( \frac{n\pi r}{b} \right) \sin \left[ \frac{n\pi}{2}(\zeta - 1) \right], \quad (2a)$$

$$\chi_n = \frac{\frac{2b}{dn^2\pi^2} \sin \left[ \frac{n\pi}{b}(-b+d) \right]}{\frac{n\pi}{bBi} I_1 \left( \frac{n\pi}{b} \right) + I_0 \left( \frac{n\pi}{b} \right)}, \quad (2b)$$

where  $I_0$  or  $I_1$  is the modified Bessel function of the first kind and zeroth or first order. Here,  $d$  is the dimensionless vertical distance between the crystal-melt interface and the vertical position where the adiabatic and hot-zone meet, while  $Bi$  is the Biot number for the heat transfer from the furnace through the ampoule wall. Some typical isotherms for  $Bi=10$ ,  $d=0.1$ , and  $b=1.0$  are presented in Fig. 2. The thermal gradients are concentrated in a region of the melt near the crystal-melt interface because this region of the ampoule is adjacent to the furnace's thermal-gradient zone. The remainder of the melt, which lies adjacent to the hot-zone is isothermal at the hot-zone temperature.

The model is idealized because we have assumed that the crystal-melt interface is planar. The heat flux is primarily axial in the thermal-gradient zone where the crystal-melt interface lies. Since the thermal conductivity of the solid germanium is less than half that of the melt, the crystal represents a thermal barrier causing some of the heat flux to flow radially outward to the ampoule wall near the interface. This local radial heat flux causes the local isotherms and the crystal-melt interface to be concave into the crystal [5]. Future research will investigate the effect of the curved crystal-melt interface on the solutal convection.

### 3 Solutal Convection

We assume that the temperature differences and compositional variations are sufficiently small that all the thermophysical properties of the melt can be considered uniform and constant except for the density in the gravitational body force term of the momentum equation. In this Boussinesq-like approximation, the characteristic temperature difference  $(\Delta T)_o$  and characteristic mole fraction variation  $(\Delta C)_o$  are assumed to be sufficiently small that the melt's density is a linear function of temperature and composition, given by

$$\rho = \rho_o [1 - \beta_T(T^* - T_o) - \beta_c(C^* - C_o)], \quad (3)$$

and that  $\beta_T(\Delta T)_o \ll 1$  and  $\beta_c(\Delta C)_o \ll 1$ , where  $T^*$  is the temperature in the melt,  $C^*$  is the mole fraction of one species in the melt, and  $C_o$  is the initially uniform mole fraction in the melt before crystal growth begins.

The electric current in the melt produces an induced magnetic field, which is superimposed on the applied magnetic field produced by the external magnet. The characteristic ratio of the induced to the applied magnetic field strengths is the magnetic Reynolds number,

$$R_m = \mu_p \sigma UR, \quad (4)$$

where  $\mu_p$  is the magnetic permeability of the melt. For all crystal-growth processes,  $R_m \ll 1$ , and the additional magnetic fields produced by the electric currents in the melt are negligible.

In the Navier-Stokes equation, the characteristic ratio of the EM body force term to the inertial terms is the interaction parameter  $N = \sigma^2 B^4 R / \rho_o^2 g \beta_c C_o$ , which varies as  $B^4$ . Ma and Walker [19] investigated the role of inertia on the thermally driven buoyant convection during crystal growth and determined the errors associated with the neglect of inertial effects for interaction parameters between  $N=1.307$  and  $N=6803.5$ . We found that inertia significantly affects the buoyant convection for which  $N=1.037$ . As the interaction parameter is increased from this value, the ratios of the inertial force to the EM body force decrease. We found that the error due to neglect of inertial effects is only 2.7% for  $N=16.59$ . For molten germanium-silicon with  $R=7.5$  mm,  $B=0.5$  T, and  $C_o=0.10$ ,  $N=57.3$ . This value of  $N$  is sufficiently small that inertial effects are negligible.

In an asymptotic solution for  $Ha \gg 1$ , the melt is divided into an inviscid core, Hartmann layers with  $O(Ha^{-1})$  thickness adjacent to the boundaries at  $\zeta = \pm 1$ , and a parallel layer with an  $O(Ha^{-1/2})$  thickness adjacent to the ampoule surface at  $r=1$ . The Hartmann layers have a simple, local, exponential structure, which matches any radial core or parallel-layer velocities at  $\zeta = \pm 1$ , which satisfies the no-slip conditions at the solid-liquid interface and at the surface of the ampoule, and which indicates that  $v_z$  in the core or parallel layer is  $O(Ha^{-1})$  at  $\zeta = \pm 1$ . Analysis of the parallel layer reveals that its thickness is actually  $O[(b/Ha)^{1/2}]$  while the axial velocity is  $O[(Ha/b)^{1/2}]$ . Since  $b$  can be as large as 35 at the beginning of the Bridgman-Stockbarger process, the parallel layer is not actually thin as assumed in the formal asymptotic expansion for  $Ha \gg 1$ . While a formal asymptotic analysis for  $Ha \gg 1$  is not appropriate, the numerical solution of the inertialess Navier-Stokes equation with all viscous terms is not necessary. The Hartmann layers represent an extremely small fraction of the melt length and have a simple exponential structure. There is no need to numerically duplicate this simple exponential structure. Therefore, we use a composite core-parallel-layer solution that does not assume that the parallel-layer thickness is small [20]. We discard the viscous terms  $Ha^{-2} \partial^2 \mathbf{v} / \partial \zeta^2$  in the Navier-Stokes equation, we relax the no-slip conditions at  $\zeta = \pm 1$  because they are satisfied by the Hartmann layers that are not part of the composite solution, and we apply the boundary conditions

$$v_z = 0, \quad \text{at } \zeta = \pm 1. \quad (5)$$

Here,  $\mathbf{v} = v_r \hat{\mathbf{r}} + v_z \hat{\mathbf{z}}$  is the velocity normalized by  $U$ , where  $\hat{\mathbf{r}}$  and  $\hat{\mathbf{z}}$  are the unit vectors for the cylindrical coordinate system. Since these conditions neglect the  $O(Ha^{-1})$  perturbation velocity due to the Hartmann layers, we also discard the other viscous terms in the radial component of the Navier-Stokes equation because they are  $O(Ha^{-1})$  compared to the radial pressure gradient in both the core and the parallel layer, and we already have an  $O(Ha^{-1})$  error. There are  $O(Pe_m^{-1})$  species-diffusion boundary layers adjacent to the crystal-melt interface and adjacent to the surfaces of the ampoule. Matching the solutions for  $C$  in the Hartmann layers, the

boundary conditions at the crystal-melt interface and at the top of the ampoule are

$$\frac{2}{b} \frac{\partial C}{\partial \zeta} = \text{Pe}_g(k_s - 1)C, \quad \text{at } \zeta = -1, \quad (6a)$$

$$\frac{\partial C}{\partial \zeta} = 0, \quad \text{at } \zeta = +1, \quad (6b)$$

where  $\text{Pe}_g = U_g R/D = \omega \text{Pe}_m$  is the growth Péclet number and  $k_s$  is the segregation coefficient.

Therefore the dimensionless equations governing the composite core-parallel-layer solution, which assumes that the Hartmann layers have negligible thickness and which has an  $O(\text{Ha}^{-1})$  relative error, are

$$\text{Ha}^{-2} \left( \frac{\partial^4 \psi}{\partial r^4} - \frac{2}{r} \frac{\partial^3 \psi}{\partial r^3} + \frac{3}{r^2} \frac{\partial^2 \psi}{\partial r^2} - \frac{3}{r^3} \frac{\partial \psi}{\partial r} \right) - \frac{4}{b^2} \frac{\partial^2 \psi}{\partial \zeta^2} = \gamma r \frac{\partial T}{\partial r} + r \frac{\partial C}{\partial r}, \quad (7a)$$

$$\gamma = \frac{\beta_T (\Delta T)_o}{\beta_c C_o}, \quad (7b)$$

$$\frac{\partial C}{\partial t} + \mathbf{v} \cdot \nabla C = \text{Pe}_m^{-1} \nabla^2 C, \quad (7c)$$

where  $C$  is the mole fraction of silicon in the germanium-silicon mixture normalized by the initial uniform mole fraction  $C_o$ . The boundary conditions along the impermeable surfaces of the ampoule are  $\hat{\mathbf{n}} \cdot \nabla C = 0$ .

We use a Chebyshev spectral collocation method in order to solve Eqs. (7a) and (7c) with Gauss-Lobatto collocation points in  $r$  and  $\zeta$ . We use a sufficient number of collocation points in order to resolve the large velocity and concentration gradients near  $r=1$ . All values of  $B$  require a significant number of collocation points since  $\text{Ha}$  is proportional to  $B$ , while  $\text{Pe}_m$  is proportional to  $B^{-2}$ . For the time derivative in Eq. (7c), we use a second-order implicit time integration scheme to integrate from  $t=0$  to a time which is slightly less than  $a/\omega$ . We chose a large enough number of time steps so that the results are not changed by increasing the number of time steps. We found 41 collocation points in the radial direction, 41 collocation points in the axial direction, and 12,800 time steps were enough to resolve the velocity and concentration gradients in the melt. Further increasing these numbers did not change the results.

At the beginning of crystal growth, the melt concentration, normalized by the initial uniform concentration, is  $C(r, \zeta, t=0) = 1$ . Thus, the amount of solute initially in the melt is obtained by integrating across the ampoule's volume, giving a total solute concentration equal to  $\pi a$ . We verify that the sum of the total solute in the melt and in the crystal is equal to  $\pi a$  at each time step.

Assuming that there is no diffusion of solute in the solid crystal, the solute distribution in the crystal,  $C_s(r, z)$ , normalized by the initial uniform solute concentration in the melt, is given by

$$C_s(r, z) = k_s C \left( r, \zeta = -1, t = \frac{z}{\omega} \right), \quad (8)$$

where  $k_s = 4.2$  for silicon in a germanium melt.

## 4 Results

We present results for  $B = 0.5$  T,  $C_o = 0.10$ , and  $U_g = 23 \mu\text{m/s}$ , for which  $U = 0.008334$  m/s,  $\text{Ha} = 165.9$ ,  $\text{Pe}_m = 3,125$ ,  $\text{Pe}_g = 8.625$ ,  $\gamma = 0.09246$ , and  $\omega = 0.00276$ . For  $a = 1$ , the dimensionless time to grow a crystal is  $a/\omega = 362.3$ .

Initially at  $t=0$ , the concentration in the melt is uniform and the buoyant convection is driven entirely by thermal gradients as reflected in Fig. 2 for  $B = 0.5$  T and  $b = 1$ . At this time, the maximum value of the streamfunction is 0.00686. In Fig. 3, the hot fluid

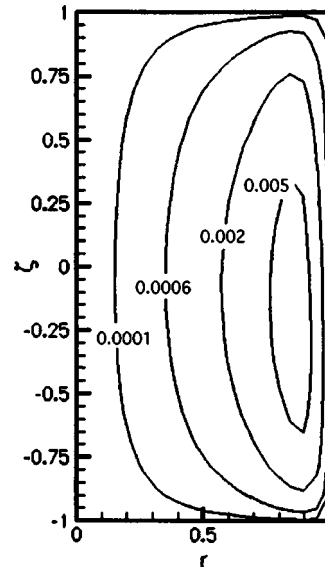


Fig. 3 Streamfunction  $\psi(r, \zeta, t=0)$  for  $B = 0.5$  T and  $a = 1$

risers near the periphery of the melt, flows radially inward along the top of the ampoule, axially downward along the centerline of the ampoule, and either solidifies or flows radially outward along the crystal-melt interface. The  $O(\text{Ha}^{1/2})$  axially upward flow in the parallel layer is reflected in the crowded streamlines adjacent to  $r = 1$ .

Once crystal growth begins, the crystal-melt interface absorbs silicon and the melt adjacent to the interface is silicon depleted. When 0.25% of the crystal has grown at  $t = 0.9059$ , the crystal has absorbed some silicon as reflected in the contours of the concentration in the melt in Fig. 4, in which the minimum value of the concentration is 0.636. The silicon-depleted melt has only diffused or convected a short distance from the crystal-melt interface at this early stage of growth and most of the melt remains at the initial concentration  $C = 1$ . At this early stage, the contours of the concentration are nearly horizontal due to diffusion of the silicon-rich melt towards the interface. The strong axially upward flow adjacent to  $r = 1$  has convected the silicon-depleted melt axially

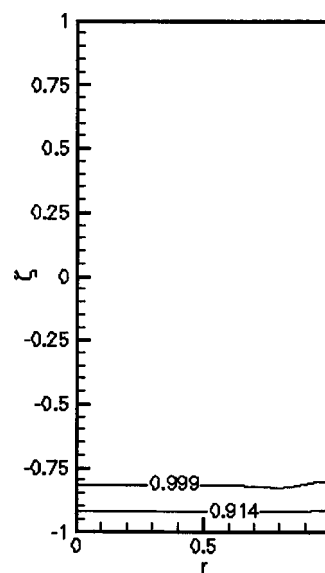


Fig. 4 Concentration in the melt  $C(r, \zeta, t = 0.9059)$  for  $B = 0.5$  T and  $C_o = 0.10$

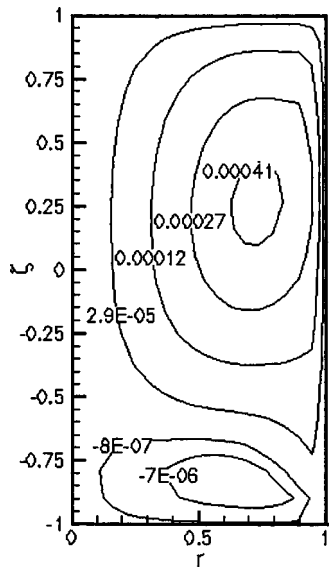


Fig. 5 Streamfunction  $\psi(r, \zeta, t=72.47)$  for  $B=0.5$  T and  $C_0=0.10$

upward so that the concentration near the periphery is lower than the concentration near the centerline. The shapes of the streamlines resemble those of Fig. 2. With solutal convection alone, the lighter fluid adjacent to the centerline would rise while the heavier fluid adjacent to the periphery would sink, thus creating a clockwise circulation that opposes the counterclockwise thermal convection. Therefore, the maximum value of the streamfunction has reduced to 0.00678, which is lower than that for a doped melt in which the melt motion is driven entirely by thermal convection [21].

We present the streamfunction and concentration in the melt at  $t=72.47$ , when 20% of the crystal has grown, in Figs. 5 and 6, respectively. In Fig. 5, the maximum value of the streamfunction has decreased to 0.000442. In Fig. 6, the minimum and maximum values of the concentration are 0.255 and 1.0, respectively. The minimum value of the concentration is small because the segregation coefficient is large. By this stage of growth for a doped crystal, the maximum value of the concentration is  $C < 1$  because

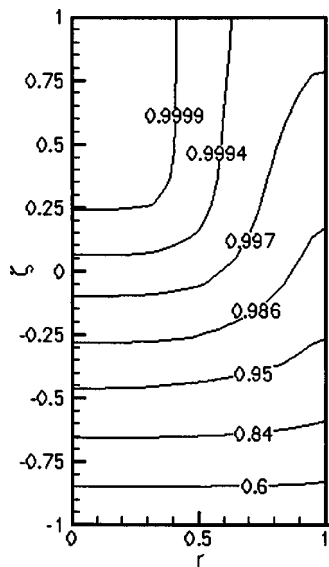


Fig. 6 Concentration in the melt  $C(r, \zeta, t=72.47)$  for  $B=0.5$  T and  $C_0=0.10$

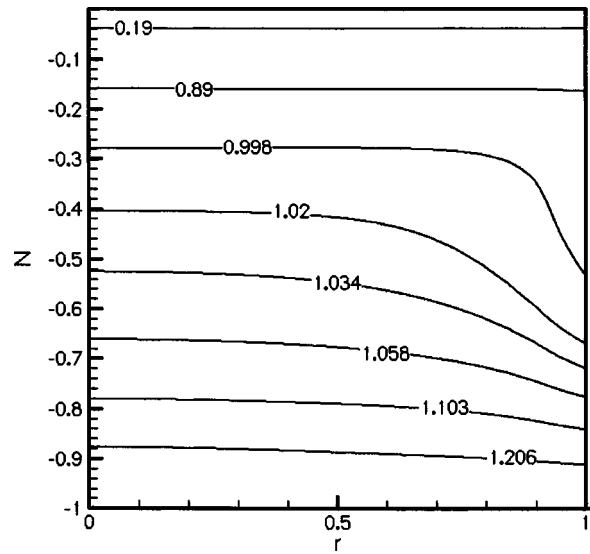


Fig. 7 Concentration in the crystal  $C_s(r, z)$  for  $B=0.5$  T and  $C_0=0.10$

the thermal convection would have convected the silicon-depleted melt over the entire melt [21]. However, for the present alloyed crystal, the opposing solutal convection has decreased the convective species transport so that a pocket of the melt near  $r=0$  and  $\zeta=+1$  still remains at the initial uniform concentration  $C=1$ . The axial position corresponding to the maximum value of the streamfunction in Fig. 5 has moved to axially upward. In Fig. 5, there is an opposing circulation adjacent to the crystal-melt interface caused by the concentration gradient.

For most of the remainder of growth, the shapes of the contours of streamfunction and concentration resemble those of Figs. 5 and 6, respectively. The average concentration in the melt continues to decrease as the crystal-melt interface absorbs silicon continuously throughout growth. Near the end of growth, the melt is left totally depleted of silicon because the segregation coefficient is large.

In Fig. 7, we present the contours of the concentration in the crystal. The bottom of the crystal solidified with a relatively radially uniform composition because the silicon-depleted melt did not have time to convect away. As growth progressed, the contours of the concentration became more curved because the axially upward flow near  $r=1$  convected the silicon-depleted melt away from the interface. Near the end of growth, the average concentration in the melt is small due to the absorption at the interface. In addition, the compositional variations in the melt are small compared with earlier stages of growth so that the crystal is relatively radially uniform near  $z=0$ . The axial composition in the crystal decreases as  $z$  increases.

## 5 Conclusions

We have developed a method to treat buoyant convection and species transport for alloyed crystal growth in a strong magnetic field. We found that the buoyant convection due to compositional variations opposes the buoyant convection due to thermal variations. Thus, the alloyed germanium-silicon crystal solidified with less radial segregation than a doped crystal grown under the same conditions. Because of the large value of the segregation coefficient, the axial variation of the crystal composition is large. Future research will compare asymptotic model predictions to experimental results.

## Acknowledgments

This research was supported by the U.S. Air Force Office of Scientific Research under Grant No. FA9550-04-1-0249. The cal-

culations were performed on the Cray X1 and the SGI Origin 3000 Complex provided by the DoD High Performance Computing Modernization Program under Grant No. AFSNH2487 and on the IBM pSeries 690 provided by the National Computational Science Alliance under grant DMR030015.

## Nomenclature

$B$  = magnetic flux density  
 $Bi$  = Biot number for the heat transfer from the furnace through the ampoule wall  
 $C$  = dimensionless concentration in the melt  
 $C^*$  = concentration or mole fraction of solute in the melt  
 $C_o$  = initial uniform mole fraction of the solute in the melt  
 $D$  = diffusion coefficient for the solute in the molten semiconductor  
 $Ha$  = Hartmann number  
 $I_0$  = modified Bessel function of the first kind and zeroth order  
 $I_1$  = modified Bessel function of the first kind and first order  
 $N$  = interaction parameter  
 $Pe_g$  = growth Péclet number  
 $Pe_m$  = species transport Péclet number  
 $Pe_T$  = thermal Péclet number  
 $R$  = radius of the crystal  
 $R_m$  = magnetic Reynolds number  
 $T$  = dimensionless temperature in the melt  
 $T^*$  = temperature in the melt  
 $T_o$  = solidification temperature  
 $U$  = characteristic velocity for the magnetically damped solutal convection  
 $U_g$  = growth rate or velocity of the crystal-melt interface  
 $a$  = initial dimensionless melt depth  
 $b$  = dimensionless melt depth  
 $c_p$  = specific heat of the melt  
 $d$  = dimensionless vertical distance between the crystal-melt interface and the vertical position where the adiabatic and hot-zone meet  
 $g$  = gravitational acceleration  
 $k$  = thermal conductivity of the melt  
 $k_s$  = segregation coefficient for silicon in germanium  
 $n$  = summation index  
 $\hat{n}$  = unit normal vector  
 $r$  = dimensionless radial coordinate in the melt  
 $\hat{r}$  = unit vector in the radial direction  
 $t$  = dimensionless time  
 $\mathbf{v}$  = dimensionless velocity in the melt  
 $v_r$  = dimensionless radial velocity in the melt  
 $v_z$  = dimensionless axial velocity in the melt  
 $z$  = dimensionless axial coordinate in the melt  
 $\hat{z}$  = unit vector in the axial direction

## Greek Symbols

$(\Delta C)_o$  = characteristic mole fraction variation  
 $(\Delta T)_o$  = difference between the hot-zone temperature and the solidification temperature  
 $\beta_C$  = compositional coefficient of volumetric expansion  
 $\beta_T$  = thermal coefficient of volumetric expansion  
 $\gamma$  = characteristic ratio of thermally driven buoyant convection to compositionally driven buoyant (solutal) convection  
 $\zeta$  = dimensionless rescaled axial coordinate in the melt

$\theta$  = dimensionless azimuthal coordinate in the melt  
 $\hat{\theta}$  = unit vector in the azimuthal direction  
 $\mu$  = dynamic viscosity of the melt  
 $\mu_p$  = magnetic permeability of the melt  
 $\pi$  = 3.14159 radians  
 $\rho$  = density of the melt  
 $\rho_o$  = density of the melt at the solidification temperature  
 $\sigma$  = electrical conductivity of the melt  
 $\phi$  = dimensionless electric potential function  
 $\chi$  = coefficient in the separation-of-variables solution for temperature  
 $\psi$  = dimensionless streamfunction in the melt  
 $\omega$  = dimensionless interface velocity

## References

- [1] Walker, J. S., Henry, D., and BenHadid H., 2002, "Magnetic Stabilization of the Buoyant Convection in the Liquid-Encapsulated Czochralski Process," *J. Cryst. Growth*, **243**(1), pp. 108–116.
- [2] Flemings, M. C., 1974, *Solidification Processing*, McGraw-Hill, New York.
- [3] Khine, Y. Y., Banish, R. M., and Alexander, J. I. D., 2002, "Convective Effects during Diffusivity Measurements in Liquids with an Applied Magnetic Field," *Int. J. Thermophys.*, **23**(3), pp. 649–666.
- [4] Watring, D. A., and Lehoczy, S. L., 1996, "Magneto-hydrodynamic Damping of Convection during Vertical Bridgman-Stockbarger Growth of HgCdTe," *J. Cryst. Growth*, **167**(3/4), pp. 478–487.
- [5] Ramachandran, N., and Watring, D. A., 1997, "Convection Damping by an Axial Magnetic Field during Growth of HgCdTe by Vertical Bridgman Method — Thermal Effects," 35th AIAA Aerospace Sciences Meeting and Exhibit, Paper No. 97-0450, Reno, NV.
- [6] Alboussière, T., Moreau, R., and Camel, D., 1991, "Influence of a Magnetic Field on the Solidification of Metallic Alloys," *Comptes Rendus de l'Académie des Sciences*, **313**(7), pp. 749–755.
- [7] Ma, N., and Walker, J. S., 2000, "A Model of Dopant Transport during Bridgman Crystal Growth with Magnetically damped Buoyant Convection," *ASME J. Heat Transfer*, **122**(1), pp. 159–164.
- [8] Hart, J. E., 1971, "On Sideways Diffusive Instability," *J. Fluid Mech.*, **49**, pp. 279–288.
- [9] Ma, N., 2003, "Solutal Convection during Growth of Alloyed Semiconductor Crystals in a Magnetic Field," *J. Thermophys. Heat Transfer*, **17**(1), pp. 77–81.
- [10] Wang, X., and Ma, N., 2004, "Strong Magnetic Field Asymptotic Model for Binary Alloyed Semiconductor Crystal Growth," *J. Thermophys. Heat Transfer*, **18**(4), pp. 476–480.
- [11] Liu, Y., Dost, S., Lent, B., and Redden, R. F., 2003, "A Three Dimensional Numerical Simulation Model for the Growth of CdTe Single Crystals by the Traveling Heater Method under Magnetic Field," *J. Cryst. Growth*, **254**(3/4), pp. 285–297.
- [12] Timchenko, V., Chen, P. Y. P., Leonardi, E., Davis, G. D., and Abbaschian, R., 2002, "A Computational Study of Binary Alloy Solidification in the ME-PHISTO Experiment," *Int. J. Heat Fluid Flow*, **23**(3), pp. 258–268.
- [13] Brailovskaya, V. A., Zilberberg, V. V., and Feoktistova, L. V., 2000, "Numerical Investigation of Natural and Forced Solutal Convection above the Surface of a Growing Crystal," *J. Cryst. Growth*, **210**(4), pp. 767–771.
- [14] LeMarec, C., Guerin, R., and Haldenwang, P., 1997, "Pattern Study in the 2-D Solutal Convection above a Bridgman-type Solidification Front," *Phys. Fluids*, **9**(11), pp. 3149–3161.
- [15] LeMarec, C., Guerin R., and Haldenwang, P., 1996, "Radial Macro-segregation Induced by 3D Patterns of Solutal Convection in Upward Bridgman Solidification," *J. Cryst. Growth*, **169**(1), pp. 147–160.
- [16] Garandet, J. P., and Alboussière, T., 1999, "Bridgman Growth: Modelling and Experiments," *The Role of Magnetic Fields in Crystal Growth, Progress in Crystal Growth and Characterization of Materials* Vol. 38, K. W. Benz, ed., Elsevier Science Publishers, New York, pp. 73–132.
- [17] Walker, J. S., 1999, "Models of Melt Motion, Heat Transfer, and Mass Transport during Crystal Growth with Strong Magnetic Fields," *The Role of Magnetic Fields in Crystal Growth, Progress in Crystal Growth and Characterization of Materials* Vol. 38, K. W. Benz, ed., Elsevier Science Publishers, New York, pp. 195–213.
- [18] Ma, N., and Walker, J. S., 1997, "Dopant Transport during Semiconductor Crystal Growth with Magnetically Damped Buoyant Convection," *J. Cryst. Growth*, **172**(1/2), pp. 124–135.
- [19] Ma, N., and Walker, J. S., 2001, "Inertia and Thermal Convection during Crystal Growth with a Steady Magnetic Field," *J. Thermophys. Heat Transfer*, **15**(1), pp. 50–54.
- [20] Hirtz, J. M., and Ma, N., 2000, "Dopant Transport during Semiconductor Crystal Growth. Axial Versus Transverse Magnetic Fields," *J. Cryst. Growth*, **210**(4), pp. 554–572.
- [21] Ma, N., and Walker, J. S., 2000, "A Parametric Study of Segregation Effects during Vertical Bridgman Crystal Growth with an Axial Magnetic Field," *J. Cryst. Growth*, **208**(1/4), pp. 757–771.

# Behavior of Short Lateral Dead Ends on Pipeline Transients: A Lumped Parameter Model and an Analytical Solution

**Xiao-Jian Wang**

Project Engineer  
Tonkin Consulting,  
5 Cooke Terrace, Wagville,  
SA 5041, Australia  
e-mail: xiao-jian.wang@tonkin.com.au

**Martin F. Lambert**

Senior Lecturer

**Angus R. Simpson**

Associate Professor

Center for applied modelling in Water  
Engineering (CAMWE) School of Civil and  
Environmental Engineering  
The University of Adelaide, Adelaide, SA 5005,  
Australia

*By integrating the continuity equation over a short lateral dead end, the effects of a short lateral dead end side branch on pipeline fluid transients can be lumped into a node. The analytical solution to a linearized equation shows that a pipeline transient can be expressed as a Fourier series and presence of a lateral dead end reduces the frequencies of the harmonic components. The impact of the lateral dead end on the observed transients depends on a parameter  $S_d$ , which is related to the location of the lateral dead end, the relative volume, and the wave speed of the lateral dead end with respect to the pipeline. A lumped parameter approach that can be incorporated into the method of characteristics has also been developed in this paper. It has been found that it is possible to take account of the effects of a short lateral dead end in an accurate and computational efficient manner. [DOI: 10.1115/1.1899171]*

## 1 Introduction

When a branch in a network is closed (for example, by shutting a valve), a lateral dead end is created. In steady state analysis, a lateral dead end in a network system can be ignored since the flow in it is zero and the lateral dead end has no influence on the other parts of the network. In transient analysis, the lateral dead ends should normally not be neglected. Pezzinga [1] and Karney and McInnis [2] have shown that lateral dead ends in a pipe system can amplify the transients under some conditions. In addition, applications of the inverse transient analysis for leak detection and pipe system calibration require accurate and efficient forward simulation of transients in a pipe system that may include lateral dead ends. If the length of a lateral dead end is close to the normal pipe sections in a pipe network, the lateral dead end can be included in a transient simulation model as a normal pipe section [3]. However, very short lateral dead ends, not uncommon in pipe systems, can cause difficulties for the transient analysis in relation to the number of computational reaches. For example, if a control valve at a branch as shown in Fig. 1 is closed, a very short lateral dead end section is created. If this short dead end is considered to be the normal computation unit in a numerical model, e.g., the method of characteristics (MOC), the entire network must be divided into many computational sections of very small lengths if the Courant number is to be close to unity. Otherwise, the accuracy of the numerical solution is not guaranteed due to the error induced by the interpolations [4]. As a result, alternative ways must be found in a transient model to consider the effects of lateral dead ends on a transient event both efficiently and effectively. In this paper, a lumped parameter (LP) model that can take account of the effects of a short lateral dead end is developed. In addition, a linear analytical solution is developed and this analytical solution provides an explanation about the effects of a short lateral dead end on a transient event. The analytical solution and the lumped parameter model are compared to the typical numerical model in which the lateral dead end is simulated by dividing the pipeline into a great number of computational units.

Contributed by the Fluids Engineering Division for publication in the JOURNAL OF FLUIDS ENGINEERING. Manuscript received by the Technical Committee on Vibration and Sound April 7, 2004. Revised manuscript received December 9, 2004. Associate Editor: J. Katz.

## 2 Lumped Parameter Numerical Model

The unsteady flow behavior of a fluid in a pipeline can be described using conservation of continuity (mass) and momentum [3]. The simplified equation of continuity for unsteady pipe flow is

$$\frac{\partial H}{\partial t} + \frac{a^2}{gA} \frac{\partial Q}{\partial x} = 0 \quad (1)$$

and the simplified equation of motion for unsteady pipe flow is

$$\frac{\partial H}{\partial x} + \frac{1}{gA} \frac{\partial Q}{\partial t} + \frac{fQ|Q|}{2gDA^2} = 0 \quad (2)$$

where  $H$ =piezometric head,  $Q$ =average flow rate,  $t$ =time,  $x$ =distance,  $g$ =gravitational acceleration,  $f$ =the steady state Darcy-Weisbach friction factor,  $D$ =internal pipe diameter,  $A$ =pipe cross-sectional area, and  $a$ =wave speed. The value of wave speed in a pipe can be calculated as [3,5]

$$a = \sqrt{\frac{\frac{K}{\rho}}{1 + \frac{KD}{Ee}c_1}} \quad (3)$$

where  $E$ =Young's modulus of pipe material,  $e$ =thickness of pipe wall,  $K$ =bulk modulus of fluid,  $\rho$ =density of fluid, and  $c_1$ =coefficient related to the pipe anchorage [3,5].

For a short lateral dead end, the distribution of the pressure can be assumed uniform along the dead end during a transient event [3]. Integrating the continuity equation Eq. (1) along a dead end gives

$$Q_d = - \frac{\partial H_d}{\partial t} \frac{gW_d}{a_d^2} \quad (4)$$

where  $a_d$ =wave speed in the lateral dead end section,  $W_d = \pi D_d^2 L_d / 4$ =volume of the lateral dead end,  $D_d$ =diameter of lateral dead end,  $L_d$ =length of lateral dead end,  $Q_d$ =flow rate into the lateral dead end and  $H_d$ =pressure head in the lateral dead end, which is assumed uniform along the lateral dead end. The continuity equation at the node, where the lateral dead end is connected as shown in Fig. 1, is

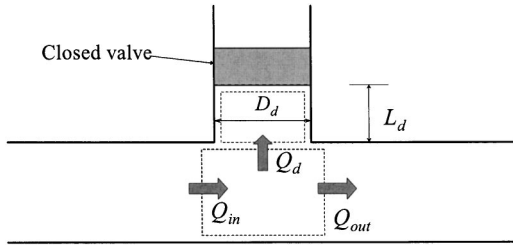


Fig. 1 A pipe section with a short lateral dead end

$$Q_{in} = Q_d + Q_{out} \quad (5)$$

Equation (5) can be incorporated into the method of characteristics [3,5], in which  $Q_d$  is treated as a node flow (demand) boundary condition. The validity of this lumped parameter is investigated against the typical numerical model, in which the lateral dead end is considered as a short pipe section by dividing the pipeline into a greater number of computational units. Two numerical examples are given in Sec. 4.

### 3 Analytical Solution

For the pipeline with a short lateral dead end branch as shown in Fig. 1, the continuity equation for the unsteady flow in the pipeline may be expressed as [6]

$$\frac{\partial H}{\partial t} + \frac{Q}{A} \frac{\partial H}{\partial x} + \frac{a^2}{gA} \frac{\partial Q}{\partial x} - \frac{a^2}{gA} Q_d \delta(x - x_d) = 0 \quad (6)$$

where  $\delta(x - x_d)$  = Dirac delta function,  $x_d$  = location of the lateral dead end along the pipeline. For a pipe with a lateral dead end branch perpendicular to the pipe axis, the conservation of  $x$ -direction momentum is

$$\frac{\partial H}{\partial x} + \frac{1}{gA} \frac{\partial Q}{\partial t} + \frac{1}{gA^2} \frac{\partial Q}{\partial x} + \frac{fQ^2}{2DgA^2} - \frac{Q}{gA^2} Q_d \delta(x - x_d) = 0 \quad (7)$$

The following dimensionless quantities are used to nondimensionalize Eqs. (6) and (7):

$$H^*(x^*, t^*) = \frac{H(x, t)}{H_s}, \quad Q^*(x^*, t^*) = \frac{Q(x, t)}{Q_0}, \quad t^* = \frac{t}{L/a}, \quad (8)$$

$$x^* = \frac{x}{L}, \quad \delta(x^* - x_d^*) = \delta(x - x_d)L$$

in which  $H^*$  = a nondimensional piezometric head,  $H_s = aQ_0/gA$  = Joukowski pressure rise,  $Q^*$  = a nondimensional flow,  $Q_0$  = steady state flow,  $L$  = the pipe length,  $x^*$  = dimensionless distance,  $t^*$  = dimensionless time, and  $x_d^* = x_d/L$  = dimensionless location of the lateral dead end.

Substituting Eqs. (4) and (8) into Eqs. (6) and (7) gives

$$\frac{\partial H^*}{\partial t^*} + \frac{V_0}{a} Q^* \frac{\partial H^*}{\partial x^*} + \frac{aQ_0}{gAH_s} \frac{\partial Q^*}{\partial x^*} + \frac{a^2 Wd}{ALa_d^2} \delta(x^* - x_d^*) \frac{\partial H^*}{\partial t^*} = 0 \quad (9)$$

$$\begin{aligned} \frac{\partial H^*}{\partial x^*} + \frac{aQ_0}{gAH_s} \frac{\partial Q^*}{\partial t^*} + \frac{V_0}{a} Q^* \frac{\partial Q^*}{\partial x^*} + \frac{fLQ_0^2}{2gDA^2H_s} Q^{*2} \\ + \frac{V_0}{a} Q^* \frac{\partial H^*}{\partial t^*} \frac{a^2 Wd}{ALa_d^2} \delta(x^* - x_d^*) = 0 \end{aligned} \quad (10)$$

in which  $V_0 = Q_0/A$  = steady state velocity. Because  $V_0/a$  is normally small, the second term in Eq. (9) and the third and the last terms in Eq. (10) can be neglected. The dimensionless equations become

$$[1 + C\delta(x^* - x_d^*)] \frac{\partial H^*}{\partial t^*} + \frac{\partial Q^*}{\partial x^*} = 0 \quad (11)$$

$$\frac{\partial H^*}{\partial x^*} + \frac{\partial Q^*}{\partial t^*} + RQ^{*2} = 0 \quad (12)$$

in which

$$R = \frac{fLQ_0}{2DAa} \quad \text{and} \quad C = \frac{a^2 Wd}{a_d^2 AL} \quad (13)$$

where  $R$  = friction damping factor,  $C$  = lateral dead end parameter.

Expressing  $H^*$  and  $Q^*$  as steady state values plus transient fluctuations gives

$$H^* = H_0^* + h^*, \quad Q^* = Q_0^* + q^* = 1 + q^* \quad (14)$$

Substituting Eq. (14) into Eqs. (11) and (12), and assuming that the transient magnitude is small ( $q^* \ll 1.0$ ) gives

$$[1 + C\delta(x^* - x_d^*)] \frac{\partial h^*}{\partial t^*} + \frac{\partial q^*}{\partial x^*} = 0 \quad (15)$$

$$\frac{\partial h^*}{\partial x^*} + \frac{\partial q^*}{\partial t^*} + 2Rq^* = 0 \quad (16)$$

Applying  $\partial[\text{Eq. (15)}]/\partial t^* - \partial[\text{Eq. (16)}]/\partial x^*$  gives

$$[1 + C\delta(x^* - x_d^*)] \frac{\partial^2 h^*}{\partial t^{*2}} - \frac{\partial^2 h^*}{\partial x^{*2}} - 2R \frac{\partial q^*}{\partial x^*} = 0 \quad (17)$$

Noticing that  $\partial q^*/\partial x^* = -[1 + C\delta(x^* - x_d^*)] \partial h^*/\partial t^*$  from Eq. (15), Eq. (17) is simplified as

$$\frac{\partial^2 h^*}{\partial x^{*2}} = [1 + C\delta(x^* - x_d^*)] \left( \frac{\partial^2 h^*}{\partial t^{*2}} + 2R \frac{\partial h^*}{\partial t^*} \right) \quad (18)$$

For a pipeline connected between two reservoirs with constant water levels, the boundary conditions for the problem defined by Eq. (18) are

$$h^*(0, t^*) = 0, \quad \text{and} \quad h^*(1, t^*) = 0 \quad (t^* > 0) \quad (19)$$

Supposing a transient is initiated in the pipeline, such initial conditions are

$$h^*(x^*, 0) = f(x^*) \quad \text{and} \quad \frac{\partial h^*(x^*, 0)}{\partial t^*} = g(x^*) \quad (20)$$

in which  $f(x^*)$  and  $g(x^*)$  are known piecewise continuous functions in the range of  $0 < x^* < 1$ . By applying a Fourier expansion (details are given in the Appendix), the solution to Eq. (18) is

$$h^*(x^*, t^*) = \sum_{n=1}^{\infty} \left\{ e^{-Rt^*} [A_n \cos(\lambda t^*) + B_n \sin(\lambda t^*)] \sin(n\pi x^*) \right\} \quad (21)$$

$$\text{in which } \lambda = n\pi/\sqrt{1 + S_d} \quad (n = 1, 2, 3, \dots) \quad (22)$$

and the lateral dead end parameter is

$$S_d = 2C \sin^2(n\pi x_d^*) \quad (23)$$

The values of Fourier coefficients  $A_n$  and  $B_n$  in Eq. (21) are calculated using the initial conditions as

$$A_n = 2 \int_0^1 f(x^*) \sin(n\pi x^*) dx^* \quad (n = 1, 2, 3, \dots) \quad (24)$$

$$B_n = \frac{1}{\lambda} \left[ \int_0^1 2g(x^*) \sin(n\pi x^*) dx^* + A_n R \right] \quad (n = 1, 2, 3, \dots) \quad (25)$$

The analytical solution in Eq. (21) shows that the presence of a lateral dead end in a single pipeline reduces the frequencies of the Fourier components. The magnitude of the frequency reduction depends on the parameter  $S_d$  defined in Eq. (23), which is related



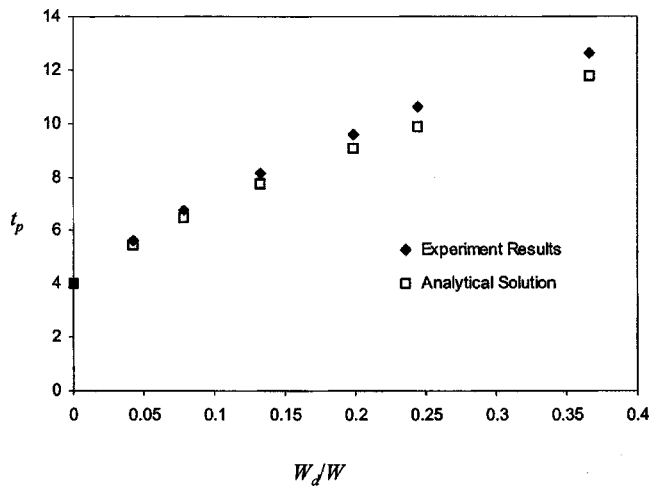


Fig. 2 Comparison of the experimental periods [1] and the analytical results

to the location of the lateral dead end, the relative volume and wave speed of the lateral dead end with respect to those properties in the pipeline. A lateral dead end with a greater length and larger cross-sectional area, and smaller wave speed will have stronger influence on the frequency reduction.

As a lateral dead end pipe can reduce the frequencies of a transient event, a flexible pipe connected into a pipeline system is frequently employed as a method for transient control by reducing the system's wave speed [1,3]. As the frequencies of a transient can be calculated from Eq. (23), this analytical solution provides a simple method to estimate the wave speed in a pipeline with a short lateral dead end. The wave speed of a transient is determined by the fundamental frequency ( $n=1$ ) while higher frequencies influence the shape of the transient. For the experimental results of Pezzinga and Scandura [1], the analytical solution calculated using Eqs. (22) and (23) are given in Fig. 2, where  $t_p = T_d / (L/a)$  and  $T_d$  = transient period with the lateral dead end. Given that viscoelastic influence is not considered in the analytical solution, the analytical solutions are reasonably accurate compared to the experimental results.

In addition to the volume and wave speed of the lateral dead end, location of a dead end also has a significant influence on a transient event. The influences by the lateral dead end location for the different frequencies are different as shown in Fig. 3. For the frequency of  $n=1$ , the maximum influence occurs in the middle ( $x^*=0.5$ ) of the pipeline, while the influences are zero at two ends

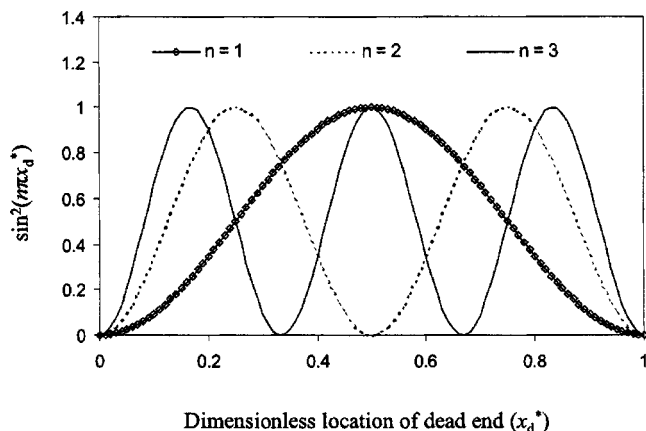


Fig. 3 Influence of the lateral dead end location

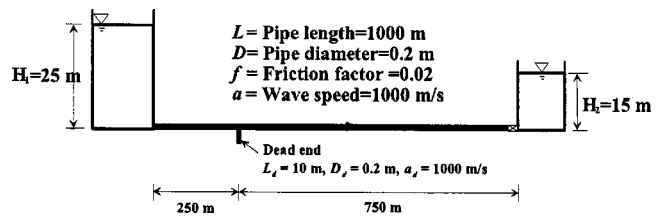


Fig. 4 A single pipeline with a lateral dead end

( $x^*=0.0$  and  $x^*=1.0$ ) of the pipeline. Because the wave speed is mainly influenced by the low frequency, for a tank-pipeline-valve system, a lateral dead end adjacent to the tank ( $x_d^*=0.0$ ) has no influence on the transient speed while a lateral dead end close to the valve ( $x_d^*=0.5$ ) has the maximum influence.

#### 4 Numerical Examples

Two numerical examples including a slow and a fast transient event are presented in this section to visualize the effects of a short lateral dead end on fluid transients. In addition, the accuracy of the lumped parameter (LP) model and analytical solution presented in the previous sections are verified by comparison with the traditional MOC approach in which the lateral dead end is considered as a normal pipe section and the pipeline is divided into a large number of reaches. Details of the MOC approach can be found in many textbooks [3,5].

For the pipeline connecting two constant-head reservoirs as shown in Fig. 4, there is a lateral dead end located 250 m from the upstream reservoir. The length of the lateral dead end is 1% of the pipeline length ( $L_d=10$  m,  $L=1000$  m), and the diameter of the lateral dead end is the same as the diameter of the pipeline ( $D_d=D=0.2$  m). The wave speed in the lateral dead end is the same as that in the pipeline ( $a_d=a=1000$  m/s). To include such a lateral dead end in a normal MOC simulation and keep the Courant number close to unity, the longest pipeline reach in the pipeline should be close to the length of the lateral dead end. In this example, the pipeline is divided into 100 reaches and the lateral dead end is divided into one reach giving a Courant number of  $C_r=1.0$ .

In the first example, a slower transient event is generated by changing the water level at the downstream reservoir in a manner by which a sinusoidal transient is generated in the pipeline. For the convenience of comparison a sinusoidal format transient is chosen here. The variation in water level at the downstream reservoir is defined as

$$H_2 = 15 + 5 \sin^2(0.5\pi t) \quad (0 \leq t \leq 2.0) \quad (26)$$

in which units of  $H_2$  are meters and the dimensionless magnitude of transient ( $q^*$ ) is 0.035. The mean velocity in the pipeline is  $V_0=1.40$  m/s giving the friction damping coefficient  $R=(fLV_0)/(2Da)=0.070$ . The lateral dead end parameter  $C$  and  $S_d$  are calculated as  $C=a^2W_d/a_d^2W=0.010$  and  $S_d=2C \sin^2(n\pi x_d^*)=0.010$  given  $n=1$ . The dominant frequency ( $n=1$ ) of the pipe transient is  $1.0\pi$  without the lateral dead end and  $0.995\pi$  with the lateral dead end based on the analytical solution [Eq. (22)]. The transients calculated by the MOC are presented in Fig. 5 for both cases of with and without the short lateral dead end. The effect of the lateral dead end on the transient is not very significant. However, by zooming in, a phase shift between two cases is evident. The total time shift within 40 s (20 periods) is 0.2 s giving the frequency difference of  $0.005\pi[2\pi/(40/20)-2\pi/(40.2/20)]$  for the two events. This frequency difference is in agreement with the analytical solution in Eq. (21) for  $n=1$ .

The effects of the lateral dead end can be considered by a lumped parameter (LP) model, in which a smaller number of reaches can be used for the pipeline. In this example, the pipeline is divided into 16 reaches. The transients calculated using the LP

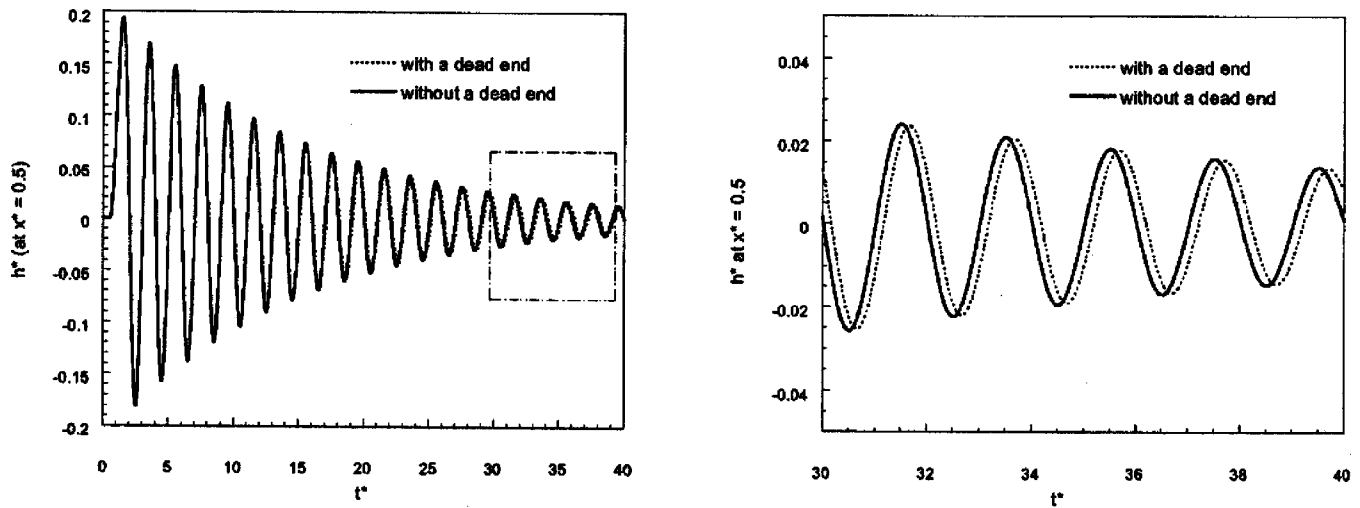


Fig. 5 Effect of lateral dead end on a slow transient (MOC)

model, the MOC, and the analytical solution are given in Fig. 6. The results based on these three methods are virtually identical, which shows that the effect of a lateral dead end on a slower transient event can be adequately considered by the LP model, and the linearized analytical solution is accurate given  $q^* \ll 1.0$  (in this example  $q^* < 0.035$ ). Because the LP model can use a much smaller number of reaches, the computational time used in LP model is significantly less than the normal MOC model. For this example, the computational time used in the highly discretized MOC model (101 reaches and simulation time period of 40.0 s) is 163.64 s on a Pentium III 600 MHz personal computer, and in the LP model (16 reaches and simulation time period of 40.0 s) it is 0.41 s, which is approximately 400 times faster. This improvement is more important when the transient model is used in an inverse calculation in which a great number of transient runs are involved.

In the second example, a faster transient event is initiated by closing the valve at the downstream end of the pipeline as depicted in Fig. 4. The valve is closed instantaneously from a partially open position that gives the steady flow of  $Q_0 = 0.005 \text{ m}^3/\text{s}$ . The transients calculated using the MOC are given in Fig. 7 for both cases with and without a lateral dead end. The

effects of the lateral dead end on the fast transient event are more significant than for the slow transient event case. A reflection from the lateral dead end is obvious, and the transient form becomes complex after several periods due to the interaction of the reflected and transmitted transients by the lateral dead end. The maximum pressure in the pipeline with a lateral dead end is larger than that in the pipeline without the lateral dead end.

The effects of the lateral dead end on a faster transient event calculated using the MOC and the LP model are presented in Fig. 8. For a faster transient event, the effects of unsteady friction are important. Therefore, an unsteady friction model [7] was applied to the MOC and LP model. The large value of  $q^*$  ( $q^* = 1.0$  in this example) invalidates the assumption of  $q^* \ll 1$ ; as a result, the analytical solution is not suitable for this example and is not included in Fig. 8. Generally speaking, the results based on the LP model are in good agreement with those based on the normal MOC model.

## 5 Conclusions

The presence of a short lateral dead end may significantly influence a transient event. A linear solution expressed as a Fourier

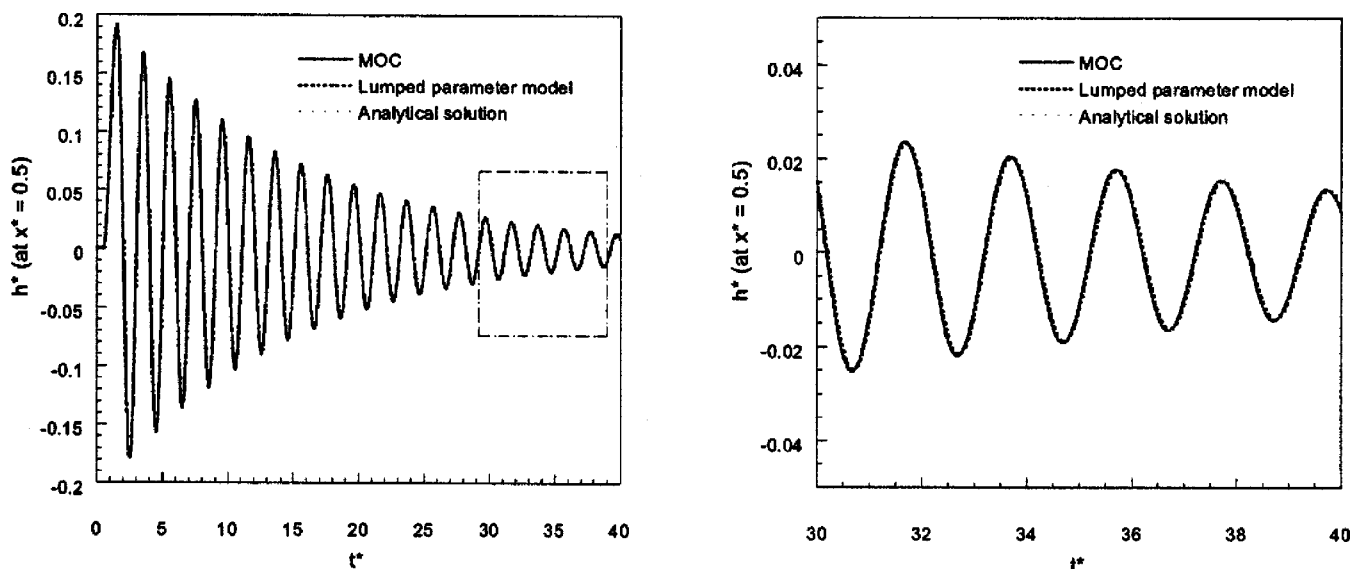


Fig. 6 Comparison of the lumped parameter (LP) model and analytical solution with the MOC for a slow transient

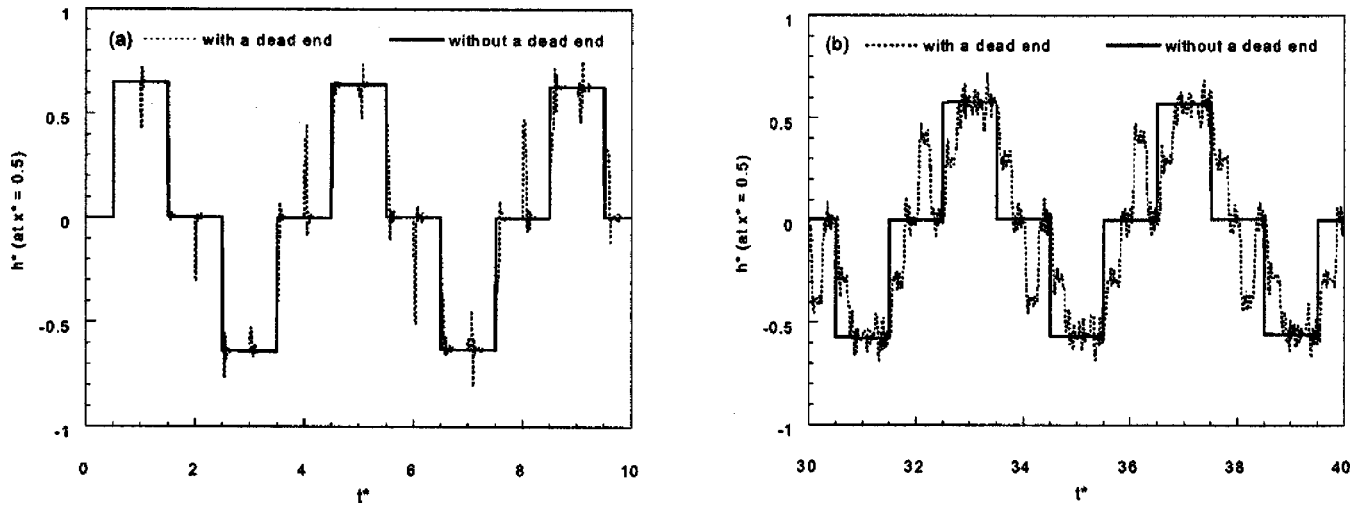


Fig. 7 Effects of lateral dead end on a fast transient event (a):  $0 < t^* < 10$ , (b):  $30 < t^* < 40$

series has been developed for transients in a pipeline with a short lateral dead end. The analytical solution shows that the presence of a lateral dead end changes the frequencies of the harmonic components. The significance of the effect depends on the parameter  $S_d$  defined in Eq. (22), which is related to the location of the lateral dead end, relative volume, and wave speed of the lateral dead end compared to the pipeline. In a tank-pipeline-valve system, a lateral dead end closer to the constant head tank has less influence on the pipeline transients compared to a lateral dead end close to the valve. For slower (smoother) transient events that have less harmonic components, the effect of a lateral dead end appears as the reduction of wave propagation speed. For faster (sharper) transient events that have more harmonic components, the presence of a lateral dead end significantly changes the transient shape and may amplify the transient magnitude. A lumped parameter model, which can be easily included in the MOC solution and can use larger computational reaches, has been developed to effectively simulate effects of a lateral dead end on a transient event.

#### Acknowledgments

The writers would like to acknowledge financial support from the Australian Research Council and an overseas student scholar-

ship provided by the University of Adelaide for the first author, both of which are gratefully appreciated.

#### Nomenclature

- $A$  = internal pipe cross-sectional area ( $m^2$ )
- $A_n, B_n$  = Fourier coefficients
- $a$  = wave speed ( $m/s$ );
- $C$  = dimensionless lateral dead end parameter
- $c_1$  = coefficient related to pipe anchorage
- $C_r$  = Courant number
- $D$  = diameter of pipe ( $m$ )
- $E$  = Young's modulus of elasticity ( $N/m^2$ )
- $f$  = friction factor
- $g$  = gravitational acceleration ( $m/s^2$ )
- $H$  = piezometric head ( $m$ )
- $H_0$  = steady state piezometric head ( $m$ )
- $H_1, H_2$  = heads at reservoirs ( $m$ )
- $H_d$  = head at a lateral dead end ( $m$ )
- $H_s$  = Joukowski pressure rise ( $m$ )
- $H^*$  = dimensionless piezometric head
- $h^*$  = dimensionless head disturbance

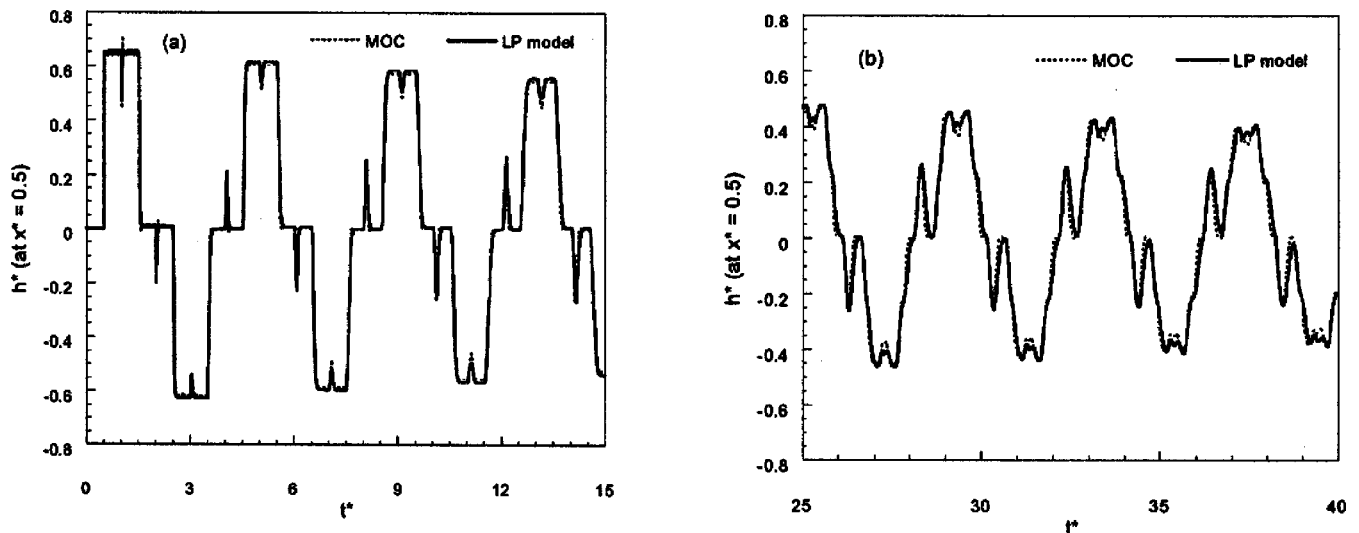


Fig. 8 Comparison of the lumped parameter (LP) model with the MOC for a faster transient (a):  $0 < t^* < 15$ , (b):  $25 < t^* < 40$

- $K$  = bulk modulus of fluid (N/m<sup>2</sup>)  
 $L$  = length of pipeline (m)  
 $n$  = component number in a Fourier series  
 $Q$  = flow rate (m<sup>3</sup>/s)  
 $Q_{in}, Q_{out}$  = upstream and downstream discharges (m<sup>3</sup>/s)  
 $Q_d$  = flow rate into a lateral dead end during a transient event (m<sup>3</sup>/s)  
 $Q^*$  = dimensionless flow rate =  $Q/Q_0$   
 $q$  = discharge ratio in a pipe junction  
 $q^*$  = dimensionless flow rate disturbance  
 $R$  = pipeline friction damping factor; linear regression parameter  
**Re** = Reynolds number  
 $S_d$  = lateral dead end parameter  
 $T$  = natural period of pipeline (s)  
 $T^*$  = dimensionless period of transient =  $T/(L/a)$   
 $t$  = time (s)  
 $t^*$  = dimensionless time =  $t/(L/a)$   
 $T_d$  = transient period with the lateral dead end (s)  
 $t_p$  = dimensionless period =  $T_d/(L/a)$   
 $V_0$  = steady state flow velocity in the pipe (m/s)  
 $W$  = volume of the pipeline (m<sup>3</sup>)  
 $W_d$  = volume of a lateral dead end (m<sup>3</sup>)  
 $x$  = distance along pipeline (m)  
 $x^*$  = dimensionless distance =  $x/L$   
 $x_d$  = position of a lateral dead end (m)  
 $x_d^*$  = dimensionless lateral dead end position =  $x_d/L$   
 $\delta$  = Dirac delta function  
 $\lambda$  = angular frequency  
 $\rho$  = density of fluid (kg/m<sup>3</sup>)

## Appendix

The partial differential equation (P.D.E.), boundary conditions (B.C.), and initial conditions (I.C.) for the transients in a pipeline (with a short lateral dead end) under constant boundary conditions are repeated here

$$\text{P. D. E. } \frac{\partial^2 h^*}{\partial x^{*2}} = [1 + C\delta(x^* - x_d^*)] \left[ \frac{\partial^2 h^*}{\partial t^{*2}} + 2R \frac{\partial h^*}{\partial t^*} \right] \quad (\text{A1})$$

$$\text{B. C. } h^*(0, t^*) = 0, \text{ and } h^*(1, t^*) = 0 \quad (\text{A2})$$

$$\text{I. C. } h^*(x^*, 0) = f(x^*) \quad \frac{\partial h^*(x^*, 0)}{\partial t^*} = g(x^*) \quad (\text{A3})$$

For a pipeline with a lateral dead end, the pipeline can be considered as two portions divided by the lateral dead end with a small neighborhood  $2\varepsilon$  as shown in Fig. 9.

For all points in the pipe except the position of the lateral dead end, the linearized equation Eq. (A1) becomes a wave equation

$$\frac{\partial^2 h^*}{\partial x^{*2}} = \frac{\partial^2 h^*}{\partial t^{*2}} + 2R \frac{\partial h^*}{\partial t^*} \quad (\text{A4})$$

Noticing the boundary condition as those in Eq. (A2) and the continuity of pressure at the lumped lateral dead end [3], the transients in the pipeline can be expressed as [8]

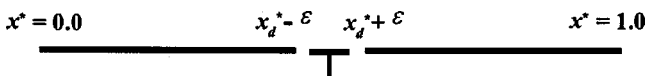


Fig. 9 A pipeline with a lateral dead end

$$h^*(x^*, t^*) = \sum_{n=1}^{\infty} T_n(t^*) \sin(n\pi x^*) \quad (0 \leq x^* \leq 1) \quad (\text{A5})$$

Integrating Eq. (A1) over a small neighborhood on either side of the lateral dead end gives

$$\int_{x_d^* - \varepsilon}^{x_d^* + \varepsilon} \frac{\partial^2 h^*}{\partial x^{*2}} dx^* = \int_{x_d^* - \varepsilon}^{x_d^* + \varepsilon} \left( \frac{\partial^2 h^*}{\partial t^{*2}} + 2R \frac{\partial h^*}{\partial t^*} \right) dx^* + \int_{x_d^* - \varepsilon}^{x_d^* + \varepsilon} C \left( \frac{\partial^2 h^*}{\partial t^{*2}} + 2R \frac{\partial h^*}{\partial t^*} \right) \delta(x^* - x_d^*) dx^* \quad (\text{A6})$$

Letting  $\varepsilon$  approach zero, the first integral on the right-hand side of Eq. (A6) is zero. Thus Eq. (A6) becomes

$$\frac{\partial h^*}{\partial x^*} \Big|_{x_d^* + \varepsilon} - \frac{\partial h^*}{\partial x^*} \Big|_{x_d^* - \varepsilon} = \left( C \frac{\partial^2 h^*}{\partial t^{*2}} + 2RC \frac{\partial h^*}{\partial t^*} \right) \Big|_{x_d^*} \int_{x_d^* - \varepsilon}^{x_d^* + \varepsilon} \delta(x^* - x_d^*) dx^* \quad (\text{A7})$$

Given the definition of Dirac delta function of  $\int_{x_d^* - \varepsilon}^{x_d^* + \varepsilon} \delta(x^* - x_d^*) dx^* = 1$ , substituting Eq. (A5) into the right-hand side of Eq. (A7) gives

$$\frac{\partial h^*}{\partial x^*} \Big|_{x_d^* + \varepsilon} - \frac{\partial h^*}{\partial x^*} \Big|_{x_d^* - \varepsilon} = \sum_{n=1}^{\infty} \left[ \left( C \frac{d^2 T_n}{dt^{*2}} + 2RC \frac{dT_n}{dt^*} \right) \sin(n\pi x_d^*) \right] \quad (\text{A8})$$

The coefficient function  $T_n$  in Eq. (A5) can be expressed by integrals as [8]

$$\begin{aligned} T_n(t^*) &= 2 \int_0^1 h^*(x^*, t^*) \sin(n\pi x^*) dx^* \\ &= 2 \int_0^{x_d^* - \varepsilon} h_\ell^*(x^*, t^*) \sin(n\pi x^*) dx^* \\ &\quad + 2 \int_{x_d^* + \varepsilon}^1 h_r^*(x^*, t^*) \sin(n\pi x^*) dx^* = T_{n\ell}(t^*) + T_{nr}(t^*) \end{aligned} \quad (\text{A9})$$

where

$$T_{n\ell}(t^*) = 2 \int_0^{x_d^* - \varepsilon} h_\ell^*(x^*, t^*) \sin(n\pi x^*) dx^* \quad (\text{A10})$$

$$T_{nr}(t^*) = 2 \int_{x_d^* + \varepsilon}^1 h_r^*(x^*, t^*) \sin(n\pi x^*) dx^* \quad (\text{A11})$$

and the subscript  $\ell$  on the  $h^*(x^*, t^*)$  refers to the region to the left of the lateral dead end, and subscript  $r$  refers to the region to the right of the lateral dead end.

Differentiating Eq. (A10) twice leads to

$$\frac{d^2 T_{n\ell}}{dt^{*2}} = 2 \int_0^{x_d^* - \varepsilon} \frac{\partial^2 h_\ell^*(x^*, t^*)}{\partial t^{*2}} \sin(n\pi x^*) dx^* \quad (\text{A12})$$

Differentiating Eq. (A10) and multiplying  $2R$  leads to

$$2R \frac{dT_{n\ell}}{dt^*} = 2 \int_0^{x_d^* - \varepsilon} 2R \frac{\partial h_\ell^*(x^*, t^*)}{\partial t^*} \sin(n\pi x^*) dx^* \quad (\text{A13})$$

Adding Eqs. (A12) and (A13), and substituting Eq. (A4) gives

$$\frac{d^2 T_{n\ell}}{dt^{*2}} + 2R \frac{dT_{n\ell}}{dt^*} = 2 \int_0^{x_d^* - \varepsilon} \frac{\partial^2 h_\ell^*(x^*, t^*)}{\partial x^{*2}} \sin(n\pi x^*) dx^* \quad (A14)$$

Applying integration by parts twice to Eq. (A14) gives

$$\begin{aligned} \frac{d^2 T_{n\ell}}{dt^{*2}} + 2R \frac{dT_{n\ell}}{dt^*} = 2 \left[ \frac{\partial h_\ell^*(x^*, t^*)}{\partial x^*} \sin(n\pi x^*) \right]_0^{x_d^* - \varepsilon} \\ - (n\pi) h_\ell^*(x^*, t^*) \cos(n\pi x^*) \Big|_0^{x_d^* - \varepsilon} \\ - (n\pi)^2 \int_0^{x_d^* - \varepsilon} h_\ell^*(x^*, t^*) \sin(n\pi x^*) dx^* \end{aligned} \quad (A15)$$

in which

$$\frac{\partial h_\ell^*(x^*, t^*)}{\partial x^*} \sin(n\pi x^*) \Big|_0^{x_d^* - \varepsilon} = \frac{\partial h_\ell^*(x^*, t^*)}{\partial x^*} \Big|_{x_d^* - \varepsilon} \sin(n\pi x_d^*) - 0 \quad (A16)$$

$$(n\pi) h_\ell^*(x^*, t^*) \cos(n\pi x^*) \Big|_0^{x_d^* - \varepsilon} = (n\pi) h_\ell^*(x_d^*, t^*) \cos(n\pi x_d^*) - 0 \quad (A17)$$

due to  $h^*(0, t^*) = 0$  according to the boundary conditions in Eq. (A2) and

$$(n\pi)^2 \int_0^{x_d^* - \varepsilon} h_\ell^*(x^*, t^*) \sin(n\pi x^*) dx^* = (n\pi)^2 \frac{x_d^*}{2} T_{n\ell}(t^*) \quad (A18)$$

Substituting Eqs. (A16)–(A18) into Eq. (A15) gives

$$\begin{aligned} \frac{d^2 T_{n\ell}}{dt^{*2}} + 2R \frac{dT_{n\ell}}{dt^*} = 2 \left[ \frac{\partial h_\ell^*(x^*, t^*)}{\partial x^*} \Big|_{x_d^* - \varepsilon} \sin(n\pi x_d^*) \right. \\ \left. - (n\pi) h_\ell^*(x_d^*, t^*) \cos(n\pi x_d^*) \right] - (n\pi)^2 T_{n\ell} \end{aligned} \quad (A19)$$

Similarly for Eq. (A11) that applies on the right side of the lateral dead end,

$$\begin{aligned} \frac{d^2 T_{nr}}{dt^{*2}} + 2R \frac{dT_{nr}}{dt^*} = 2 \left[ - \frac{\partial h_r^*(x^*, t^*)}{\partial x^*} \Big|_{x_d^* + \varepsilon} \sin(n\pi x_d^*) \right. \\ \left. + n\pi h_r^*(x_d^*, t^*) \cos(n\pi x_d^*) \right] - (n\pi)^2 T_{nr} \end{aligned} \quad (A20)$$

Adding Eq. (A19) and Eq. (A20), and noticing that  $T_{n\ell} + T_{nr} = T_n$  gives

$$\begin{aligned} \frac{d^2 T_n}{dt^{*2}} + 2R \frac{dT_n}{dt^*} = -2 \left[ \frac{\partial h_\ell^*(x^*, t^*)}{\partial x^*} \Big|_{x_d^* - \varepsilon} \right. \\ \left. - \frac{\partial h_r^*(x^*, t^*)}{\partial x^*} \Big|_{x_d^* + \varepsilon} \right] \sin(n\pi x_d^*) - (n\pi)^2 T_n \end{aligned} \quad (A21)$$

Substituting for the term in square brackets on the right-hand side of Eq. (A21) from Eq. (A8)

$$\begin{aligned} \frac{d^2 T_n}{dt^{*2}} + 2R \frac{dT_n}{dt^*} = -2 \sum_{k=1}^{\infty} \left[ \left( C \frac{d^2 T_k}{dt^{*2}} + 2RC \frac{dT_k}{dt^*} \right) \sin(k\pi x_d^*) \right] \sin(n\pi x_d^*) \\ - (n\pi)^2 T_n \end{aligned} \quad (A22)$$

Taking the  $n$ th term out of the summation and rearranging

$$\begin{aligned} [1 + 2C \sin^2(n\pi x_d^*)] \frac{d^2 T_n}{dt^{*2}} + 2R [1 + 2C \sin^2(n\pi x_d^*)] \frac{dT_n}{dt^*} + (n\pi)^2 T_n \\ = -2 \sin(n\pi x_d^*) \sum_{k=1, k \neq n}^{\infty} \left[ \left( C \frac{d^2 T_k}{dt^{*2}} + 2RC \frac{dT_k}{dt^*} \right) \sin(k\pi x_d^*) \right] \end{aligned} \quad (A23)$$

The general solution of Eq. (A23) is

$$\begin{aligned} T_n(t^*) = e^{-Rt^*} \left[ A_n \cos \sqrt{\frac{(n\pi)^2}{1+S_d} - R^2} t^* + B_n \sin \sqrt{\frac{(n\pi)^2}{1+S_d} - R^2} t^* \right] \\ + T_{ns}(t^*) \end{aligned} \quad (A24)$$

in which

$$S_d = 2C \sin^2(n\pi x_d^*) \quad (A25)$$

is the lateral dead end parameter, and  $T_{ns}(t^*)$  is a particular solution to Eq. (A23) and has no influence on the solution of  $h^*(x^*, t^*)$  due to orthogonality. Since normally the value of  $R$  is much smaller than unity, Eq. (A24) can be simplified as

$$T_n(t^*) = e^{-Rt^*} (A_n \cos \lambda t^* + B_n \sin \lambda t^*) + T_{ns}(t^*) \quad (A26)$$

$$\text{in which } \lambda = \frac{n\pi}{\sqrt{1+S_d}} \quad (A27)$$

Substituting Eq. (A26) without  $T_{ns}(t^*)$  into Eq. (A5) gives the general solution

$$h^*(x^*, t^*) = \sum_{n=1}^{\infty} \left\{ e^{-Rt^*} [(A_n \cos(\lambda t^*) + B_n \sin(\lambda t^*)) \sin(n\pi x^*)] \right\} \quad (A28)$$

which is Eq. (21).

## References

- [1] Pezzinga, G., and Scandura, P. (1995). "Unsteady Flow in Installations with Polymeric Additional Pipe." *J. Hydraul. Eng.* **121**(11), 802–810.
- [2] Karney, B. W., and McInnis, D. (1990). "Transient Analysis of Water Distribution Systems." *J. Am. Water Works Assoc.*, **82**(2), 62–70.
- [3] Wylie, E. B., and Streeter, S. L. (1993). *Fluid Transients in Systems*, Prentice-Hall, Englewood Cliffs, NJ.
- [4] Chen, L.-C. (1995). "Pipe Network Transient Analysis—the Forward and Inverse Problems." Ph.D. thesis, Dept. of Civil and Environmental Engineering, Cornell University, Ithaca, New York.
- [5] Chaudhry, M. H. (1986). *Applied Hydraulic Transients*, Van Nostrand Reinhold, New York.
- [6] Wang, X.-J. (2002). "Leak and Blockage Detection in Pipelines and Pipe Network Systems Using Fluid Transients." Ph.D. thesis, School of Civil & Environmental Engineering, The University of Adelaide, Adelaide, Australia.
- [7] Bergant, A., Vítkovský, J. P., and Simpson, A. R. (2001). "Developments in Unsteady Friction Modeling." *J. Hydraul. Res.* **39** (3), 249–257.
- [8] Levine, H. (1997). *Partial Differential Equations*, American Mathematical Society, Providence, RI.

# The Effects of Polymer Solution Preparation and Injection on Drag Reduction

R. Sun Chee Fore

J. Szwalek

A. I. Sirviente<sup>1</sup>

Department of Naval Architecture and Marine Engineering, University of Michigan, Ann Arbor, MI 48109-2145

*The understanding of drag reduction by injection of polymer solutions requires an adequate and accurate polymer solution preparation process as well as a thorough understanding of the effects that the delivery system might have on the polymer flow. Mass production of polymer solutions for engineering applications could be more cost effective if large batches of highly concentrated polymer solutions are prepared and then diluted to the final concentrations of interest. However, as shown in this study, depending on the type of polymer used this procedure might be more or less adequate. This study also corroborates that the presence of macro-molecular polymer structures induced by injecting highly concentrated polymer solutions into a shear flow translates into a drag increase and substantial degradation endurance especially at high Reynolds numbers in comparison to homogeneous polymer solutions. [DOI: 10.1115/1.1905644]*

## 1 Introduction

The pioneering work of Toms [1] documented the ability of a small amount of soluble polymer additives to reduce the friction resistance of turbulent pipe flows of Newtonian fluids. Many theories have been developed since then to explain the way in which polymers reduce drag. The approach that has found support in most of the experimental results that followed those of Toms, is that of Lumley [2] who proposed that the mechanism for drag reduction was an increased viscosity near the wall, caused by elongational deformation of the molecules by the turbulence. New arguments based on the kinetics of the molecules have been recently introduced in the development of drag reduction theories (Ryskin [3], De Gennes [4] and Tabor et al. [5]).

The drag-reducing abilities of polymer solutions are known to be triggered by a critical level of shear stress parameterized by the so-called "onset Reynolds number." Such condition should be enough for the flow to stretch the polymer, which in turn introduces an anisotropic effect by which the turbulence structure is changed, and drag reduction induced. The behavior of polymer solutions is governed by many parameters. The most obvious ones being the solvent type, the polymer concentration (very dilute polymer solutions have been shown to have viscosity that is very close to that of water (Koskie and Tiederman [6]), the velocity and length scales governing the flow and the type of polymer (characterized by its chemical composition, molecular weight distribution, and polydispersity index among others).

A large number of studies reported in the literature regarding polymer drag reduction are concerned with homogeneous polymer solutions. Most of them involve the study of fully developed turbulent channel flows where either a polymer ocean is established (Den Toonder et al. [7], Vlachogiannis and Hanratty [8] among others) or polymer is injected in such a way to achieve a homogeneous distribution of the polymer at the test section (Fortuna and Hanratty [9], Reischman and Tiederman [10], McComb and Rabie [11], Tiederman et al. [12], Willmarth et al., [13], Luchik and Tiederman [14], Wei and Willmarth [15], among others). Most of the numerical studies in this area consist of direct numerical simulation (DNS) of polymer flows in turbulent channels (i.e.,

Sureshkumar et al. [16], Dimitropoulos et al. [17], among others). A few experimental studies have also been conducted on polymer drag reduction on external flows, such as flow over a flat plate (i.e., Fontaine et al. [18], Somandepalli et al. [19]).

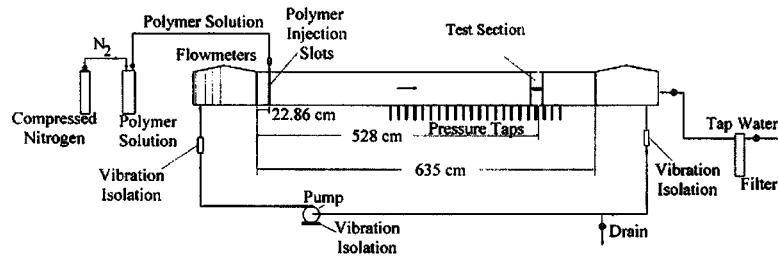
Experimental studies concerning heterogeneous drag reduction in internal flows have also received attention in the past (Vleggaar and Tels [20], Smith and Tiederman [21], Bewersdorff et al. [22], among others). In these studies, highly concentrated polymer solutions of long chain, high molecular weight polymer, were injected into the core region of a turbulent pipe or channel. For a certain range of concentrations, it was observed that a single coherent thread was formed that preserved its identity for long distances after injection. The recent studies by Shen et al. [23] and Kim et al. [24] address comparisons of homogeneous and heterogeneous drag reduction cases for the same concentration at the channel test section but with the polymer injected at the wall. The latter studies concluded that a substantial increase of drag reduction could be accomplished by heterogeneous polymer solution versus the homogeneous polymer solution. Those studies also showed that polymer structures, even if not present in the prepared solution, could be induced by the injection system. The work of Vlachogiannis and Hanratty [8] concludes that lower concentrations of Hydrolyzed Polyacrylamide can achieve very large levels of drag reduction when polymer structures are present in the solutions prior to injection.

Today, PAM and PEO are probably the most widely used water-soluble polymers in commercial applications. Both are linear, flexible molecules, which can be obtained in a wide range of molecular weights. Studies indicate that PAM is able to endure shear degradation better than PEO (Hoyt, [25]). Experimental results with hydrolyzed or partially hydrolyzed polyacrylamides (HPAM) can also be found in the literature, though not as frequently (Warholic et al. [26], Den Toonder et al. [27], Gampert et al. [28], among others).

In general, the procedures followed by different research groups to prepare the polymer solutions are different even for the same type of polymers. Little information is however reported in the literature regarding preparation procedures of polymer solutions and tests designed to ensure their consistency. Also little attention is given to the shelf life of the prepared polymer solutions. The majority of the studies performed in the past in channel and pipes, aimed at establishing homogeneous polymer solutions at the test section. This is generally accomplished by continuously injecting the polymer solution in the flow to always have fresh, undegraded polymer in a certain region of the flow. As pointed out by Den

<sup>1</sup>Corresponding author (asirv@engin.umich.edu); Tel: (734)-647-9411; Fax: (734)-936-8820.

Contributed by the Fluids Engineering Division for publication in the JOURNAL OF FLUIDS ENGINEERING. Manuscript received by the Fluids Engineering Division March 4, 2004; final manuscript received March 16, 2005. Associate Editor: Dennis Siginer.



Not to scale

Fig. 1 Schematic of the recirculating channel

Toonder et al. [7] this can be fairly impractical from an economical point of view. In their work, special attention was paid to the effect of the pump as a main degradation contributor and, the investigators were able to find that with a disc pump a constant drag reduction could be attained after an initial period of degradation, which was not possible with a centrifugal pump. Effectively a polymer ocean was established in their experiment following the initial injection of the polymer solution. Most of the experimental setups reported in the literature make use of centrifugal pumps. Establishing a polymer ocean with such pumps is not simple although possible, (Vlachogiannis and Hanratty [8]) and consequently continuous polymer injection is the alternative that has been most commonly followed in the past.

One of the most obvious consequences of injection is the possibility of inducing degradation of the injected polymer solution. Degradation translates into the loss of the polymer drag reducing abilities. Mechanical degradation refers to the shearing effect induced by solid surfaces, walls, pumps, etc., which potentially can translate into the breaking of the polymer, thus reducing its molecular weight and drag-reducing effectiveness. Chemical reactions could potentially induce changes in the polymer structure as well, and contribute detrimentally to their drag-reducing behavior. Consequently, it is important to assess if degradation is induced by the injection system, the pump, etc. and then to adequately

optimize the setup. However, it has been argued by Kim et al. [24] that the shear induced in the polymer delivery system might also contribute to the formation of macro-molecular polymer structures and these have been shown to improve the drag reduction performance of the polymer solutions. It has also been argued that the presence of such structures prior to injection can contribute to improve the drag reduction abilities of the polymer solutions (Vlachogiannis and Hanratty, [8]).

The aim of this paper is to first establish a preparation procedure of polymer solutions that is consistent and translates into long enough shelf-life for the solutions. This procedure will be compared for three different types of commercially available polymers PEO, PAM, and HPAM. First, the study reports on the inconsistencies found for solutions with concentrations lower than 100 ppm for the ionic polymers tested (i.e., PEO and HPAM). Secondly, the effect of the polymer delivery system and the mixing process that takes place in a channel prior to the test section is evaluated for different injection concentrations yielding the same test section concentration. It is corroborated that the presence of macro-molecular polymer structures induced by injecting highly concentrated polymer solutions into a shear flow increases drag reduction with respect to homogeneous polymer solutions. More importantly it is shown that the endurance to degradation of such

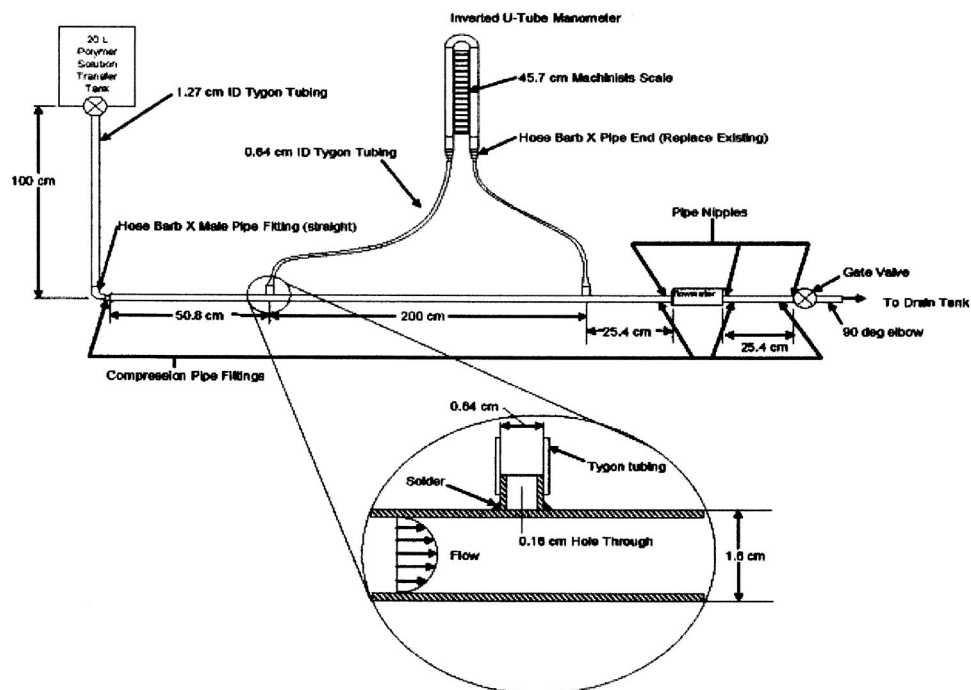


Fig. 2 Schematic of the polymer consistency apparatus

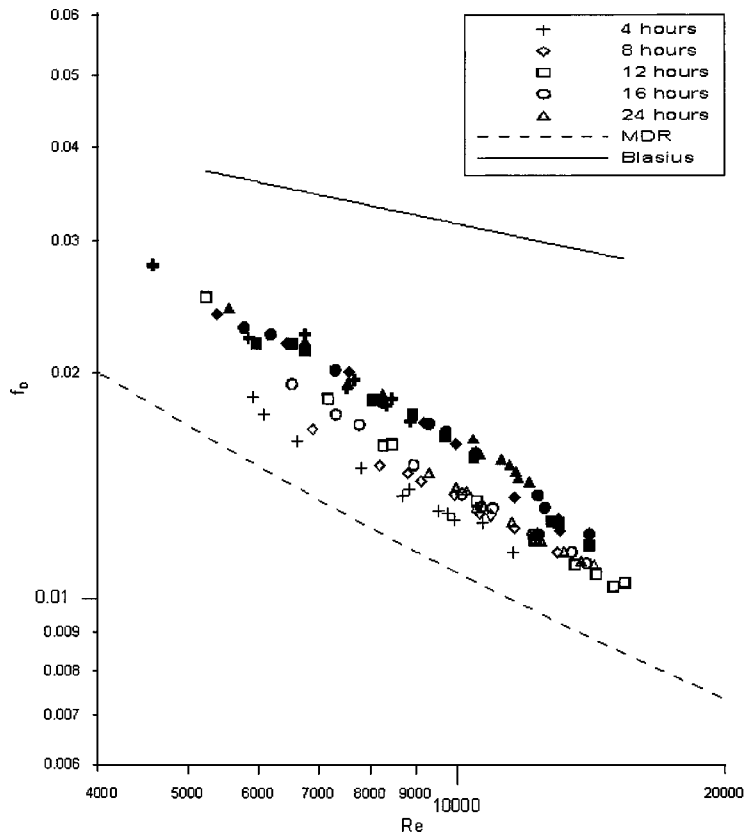


Fig. 3 Hydration test for a 10,000 ppm PAM (open symbols) and HPAM (solid symbols) master solutions

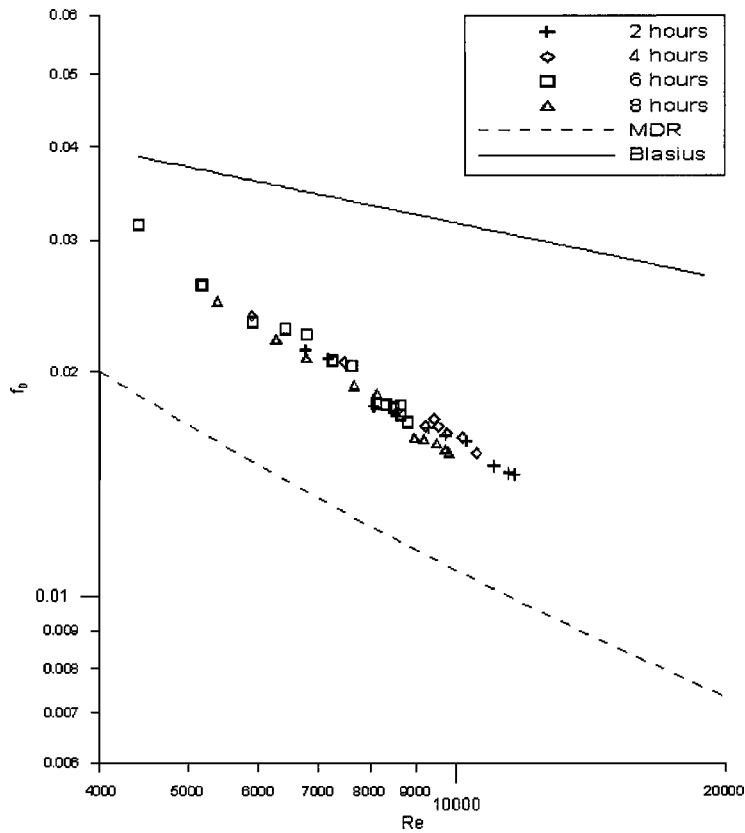
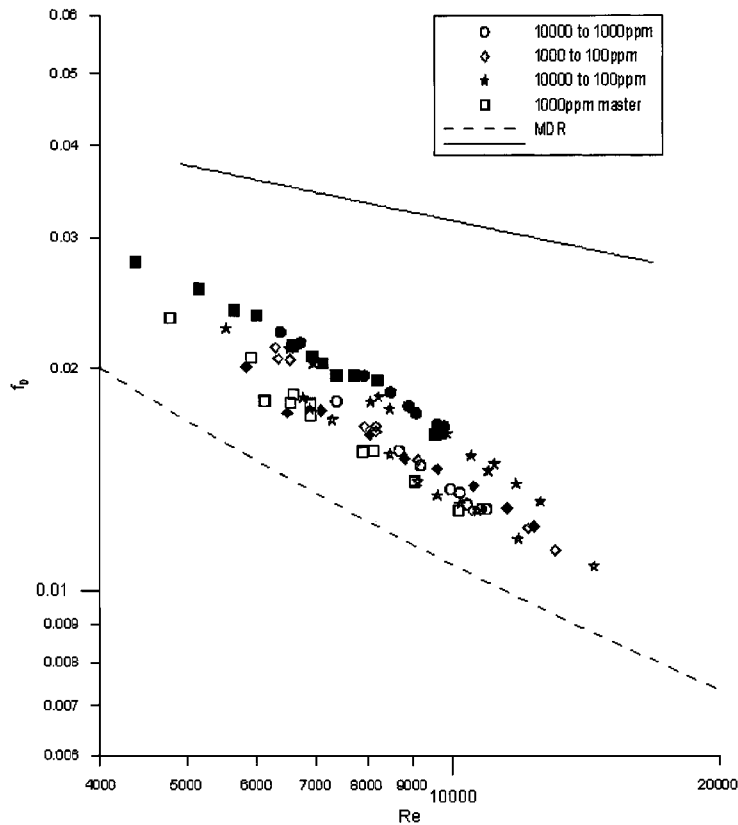


Fig. 4 Hydration test for a 1,000 ppm PEO master solution





**Fig. 5 Comparison of drag reduction abilities of 100 ppm solutions obtained by diluting 10,000 and 1,000 ppm master batches: PAM (open symbols) and HPAM (solid symbols). Data represents stable solutions for each dilution.**

structured solutions is significant especially for large Reynolds numbers. It should be noted that a detailed flow characterization including laser doppler velocimetry (LDV) measurements, as well as turbidity and birefringence measurements for a structured and a nonstructured polyacrylamide polymer solution was presented by the authors in Kim et al., [24] and Shen et al. [23]. The present study builds upon the findings presented in those studies. It, however, focuses on the implications related to procedures followed to prepare consistent highly concentrated polymer solutions, and it also demonstrates the better ability that structured polymer solutions have to sustain degradation.

## 2 Experimental Apparatus and Procedures

The experiments reported in this study were conducted at the Marine Hydrodynamics Laboratory of the University of Michigan. One of the facilities was a recirculating water channel, where the flow is driven by a 1200 gallons per minute ( $0.076 \text{ m}^3/\text{s}$ ) centrifugal pump into the 5.99 cm wide by 59.94 cm high and 6.35 m long channel test section. The bulk velocity in the test section can be up to 2.11 m/s, leading to Reynolds numbers based on the channel's width up to  $1.26 \times 10^5$ . Settling chambers are located at each end of the test section and connected to it through a one-dimensional planar contraction-expansion. In the upstream settling chamber, there are two stainless steel screens to help break up large eddies, reduce small scale turbulence and produce a turbulent wake to aid in the development of fully developed turbulent flow in the test section. Twenty-one equally spaced pressure taps are located on one of the test section walls to monitor the pressure gradient. The test section aspect ratio is 10:1, and the measurement station located 88.5 channel widths (5.28 m) downstream of the test section entrance. The polymer injection slots are

located on both sides of the channel at 22.86 cm downstream of the test section entrance. They are 0.25 cm wide, 59.94 cm high and are inclined at an angle of 25 deg to the wall. A pneumatic system drives the polymer solution from storage tanks to the injection slots. A schematic of the channel can be found in Fig. 1.

The polymer solution is injected during a short period of time to ensure that no polymer build-up takes place in the channel. This is monitored by measuring the pressure drop at the test section of the channel and making sure it remains constant. Before it starts to drift, the injection is stopped and the polymer is run through the pump until it is fully degraded. The channel reference velocity is monitored continuously with a GF-Signet 5100 flowmeter. The pressure taps are connected to a W0602/IP-24T Scanivalve and a Digi-Key 287-1027-ND temperature compensated pressure sensor, with  $\pm 4$  in  $\text{H}_2\text{O}$  range and a Pentium II PC is used to collect and process the signals. During the experiments, the temperature is held constant at  $22 \pm 1^\circ \text{C}$ . The channel water, polymer solution, and room temperatures are measured using Type K thermocouples with  $0.1^\circ \text{C}$  resolution. More detailed information regarding the channel setup and the polymer injection process can be found in Shen et al. [23] and Kim et al. [24].

A different experimental setup was used to test the polymer solutions and conduct degradation tests. It consists of a copper pipe of 1.6 cm in diameter through which the polymer is gravity fed. The pressure drop and flow rate measurements in this pipe give a quick measurement of the wall shear stress and consequently of the drag reduction induced by the polymer. This setup allows for a quick and reliable way to test the consistency of the various polymer solutions prepared throughout the life of this experimental work. The measurements involve the use of a U-tube manometer with  $\pm 2 \text{ mm}(\text{H}_2\text{O})$  error and an Omega Engineering

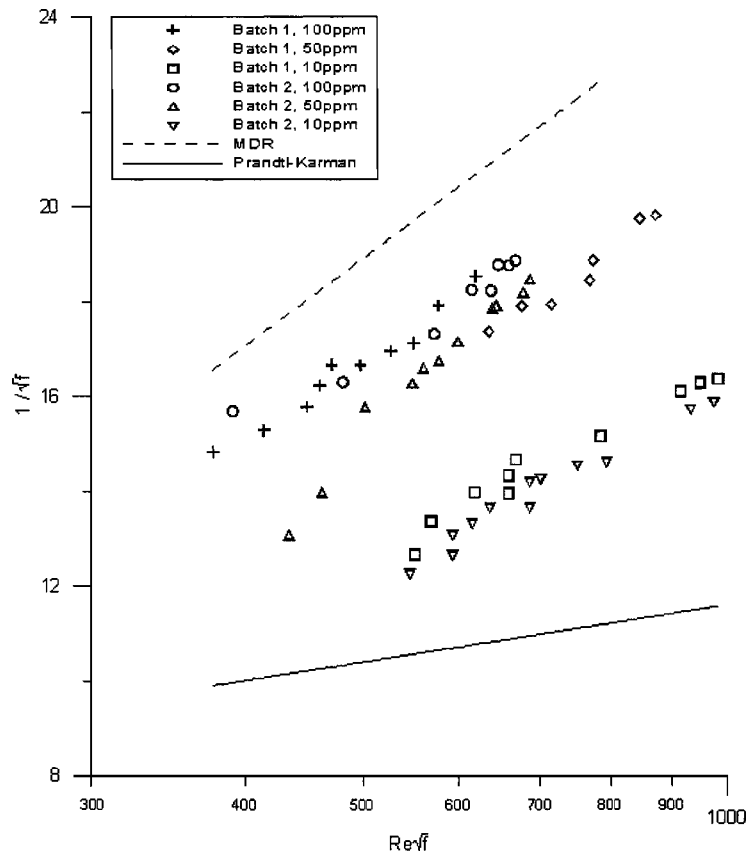


Fig. 6 Consistency test for 10, 50, and 100 ppm PAM solutions

Model FTB791 flowmeter with a linear range of 1–10 gpm ( $6.3 \times 10^{-5}$ – $6.3 \times 10^{-4}$  m<sup>3</sup>/s) with  $\pm 0.04$  gpm ( $0.25 \times 10^{-5}$  m<sup>3</sup>/s) error. The errors related to the calculations of the corresponding friction factor coefficient and Reynolds number are well within 4.5% for all cases reported in the study. A schematic of this apparatus, referred to as the polymer consistency apparatus, is shown in Fig. 2. Koskie and Tiederman [6] used a similar procedure to ensure consistency of the prepared polymer solutions by ensuring that the drag reduction obtained was within 10% for each batch tested.

### 3 Polymer Solution Study

**3.1 Polymer Type.** In this study three commercially available polymers were used, a polyacrylamide (PAM), a polyethylene oxide (PEO) and a hydrolyzed polyacrylamide (HPAM). The weight average ( $M_w$ ) molar mass and  $z$  average radius of gyration ( $R_{g,z}$ ) of PAM was measured by multi-angle laser light scattering (Dawn EOS, Wyatt Technologies). Further details of this procedure can be found in Kim et al. [24] for the results concerning PAM, and in Islam et al. [29] for the results concerning PEO. No such measurements were conducted for the HPAM.

The nonionic polyacrylamide used in this study is Hyperfloc NF301 purchased from Hychem Inc. (Tampa, FL). The molar mass moments reported in Kim et al. [24] are summarized herein. The weight average molecular weight is  $7.5 \times 10^6$  g/mole, and the  $R_{g,z} = 170$  nm.

The polyethylene oxide (PEO) used in this study is purchased from Polysciences, Inc. (Warrington, PA). The number average molecular weight is  $3.27 \times 10^6$  g/mole, the weight average molecular weight is  $4.71 \times 10^6$  g/mole, and the polydispersity index ( $M_w/M_n$ ) is 1.44.

The ionic polyacrylamide (HPAM) used in this study is Superfloc A-110 Flocculant purchased from Cytec (West Paterson, NJ).

No molecular characterization of this polymer was done and consequently only the information reported by the manufacturer is included herein. The number average molecular weight is  $15 \times 10^6$  g/mole.

**3.2 Polymer Solution Preparation and Assessment.** The preparation of the aqueous solution of Hyperfloc used in this study follows a procedure similar to the one followed by Kim et al. [24]. Preparation of the polymer solution involves the preliminary de-aeration of filtered tap water by heating it to 34–38°C while stirring magnetically and subsequently allowing it to settle. The polymer in granular form is suspended on a small percentage of isopropanol and then mixed into filtered tap water to produce a solution of the desired concentration. The mixing is done with a Nuova magnetic stirrer for the first ten minutes and then rolled by a Bellco Cell Production Roll Apparatus. The rollers need to provide enough agitation to avoid clumping without causing shear degradation of the polymer solution. The time the solution is allowed to hydrate while being rolled has proven to be a critical factor. Isopropyl alcohol is an anti-microbial agent and the purpose behind its use is to avoid biological degradation to the furthest extent possible and increase the stability of the solution. The polymer solution is stored at ambient conditions in the laboratory

(22°C).

**3.2.1 Effects of Hydration Time.** The effects of hydration while stirring the prepared polymer solution or master batch were tested by extracting samples from the solution after selected rolling times. This helped to determine the period of time required for this process to yield a stable condition. The tests were performed by gravity feeding the samples through the polymer consistency apparatus and measuring the corresponding pressure drop and flow-rate to determine the drag reduction induced by the polymer

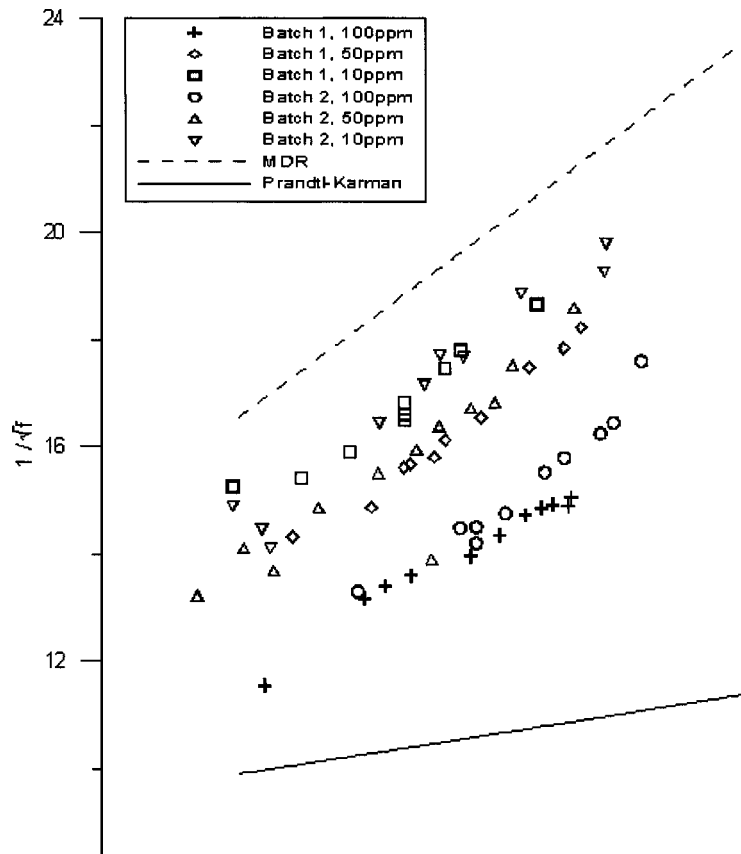


Fig. 7 Consistency test for 10, 50, and 100 ppm HPAM solutions

solution. Tests were performed at different Reynolds numbers and water characteristics were used in the calculations of the Fanning friction factor and Reynolds numbers.

The results obtained for the nonionic Polyacrylamide (PAM) showed that a stirring time of at least twelve hours was needed to yield adequate mixing and stable characteristics in time, for a 10,000 ppm solution. Such results are shown in Fig. 3 for a 100 ppm sample obtained from a 10,000 ppm master solution allowed to roll for 4, 8, 12, 16, and 24 h. The samples were tested right after dilution was performed. The figure shows the variation of the Darcy friction factor, defined as  $f_D = (2d\Delta p) / (\rho LV^2)$ , (based on the pipe diameter,  $d$ , the pressure drop  $\Delta p$ , the length,  $L$ , of the pipe, the fluid density,  $\rho$ , and the bulk velocity,  $V$ ) with the Reynolds number, (based on the pipe diameter,  $D$ , and the bulk velocity). Such results correspond to a Reynolds number range of  $5.23 \times 10^3 < Re < 1.54 \times 10^4$ . The analytical solution developed by Blasius for water pipe flow ( $f_D = 0.316 Re_d^{-1/4}$ ) is also shown in the figure for reference. The results indicate that at low Reynolds numbers, the hydration time required to achieve consistent levels of drag reduction seems to be slightly longer. Overall consistent results (within  $\pm 5\%$  for  $5000 < Re < 15,000$ ) seem to be achieved after twelve hours.

Similar results for the ionic Polyacrylamide (HPAM) are also shown in Fig. 3 for 100 ppm samples from a 10,000 ppm master batch. The samples were obtained in the same way as explained earlier for PAM. It is remarkable to note that the rolling time did not seem to have much effect on the drag reduction abilities of this polymer in the range of Reynolds numbers tested. However, it should be noted that visual inspection of the solution throughout the first eight hours of the stirring period indicated that the solution was not fully mixed. It is possible that the polymer aggregates early on in the preparation process, due to its charged character, and the rolling time is not sufficient to affect this state.

The PolyEthylene Oxide (PEO) displayed a strong tendency towards clustering when preparation of highly concentrated solutions was attempted following the same preparation procedure as with PAM and HPAM. Such solutions required rolling times of at least two weeks in order for them to become visually homogeneous. Consequently only solutions with concentrations of 1,000 ppm and lower were tested when using PEO. Additionally, the polymer preparation procedure was slightly altered regarding the conditions of the solvent, since PEO has higher phase instability with increased solution temperature. As a result all PEO solutions were prepared with cold deionized tap water. Results corresponding to a 100 ppm sample diluted from a 1,000 ppm solution of PEO are shown in Fig. 4 for a period of two to eight hours of rolling time. A zero-hour test was not conducted due to the visual nonhomogeneity observed in the solution. The data show that after two hours of mechanical mixing and hydration drag reduction consistency is achieved. Similarly to HPAM the results are consistent throughout all Reynolds numbers tested.

Assessment of the experimental error associated with the polymer solution preparation process is important to properly interpret polymer drag reduction results. Turbidity measurements conducted on the most concentrated (10,000 ppm) quiescent solution of PAM employed in this study did not show appreciable polymer structure formation (Kim et al. [24]). Consequently if the process of preparation of the polymer solution indeed yields homogeneous solutions, it should be expected that samples of the same concentration prepared either directly or from 10,000 or 1,000 ppm master batches, or from a 1,000 ppm solution obtained by diluting a 10,000 ppm master batch should yield consistent results. Such a study was done by comparing the performance of corresponding 100 ppm samples in the polymer consistency apparatus.

To conduct the latter experiment however, tests assessing the hydration time needed to consistently dilute concentrated polymer

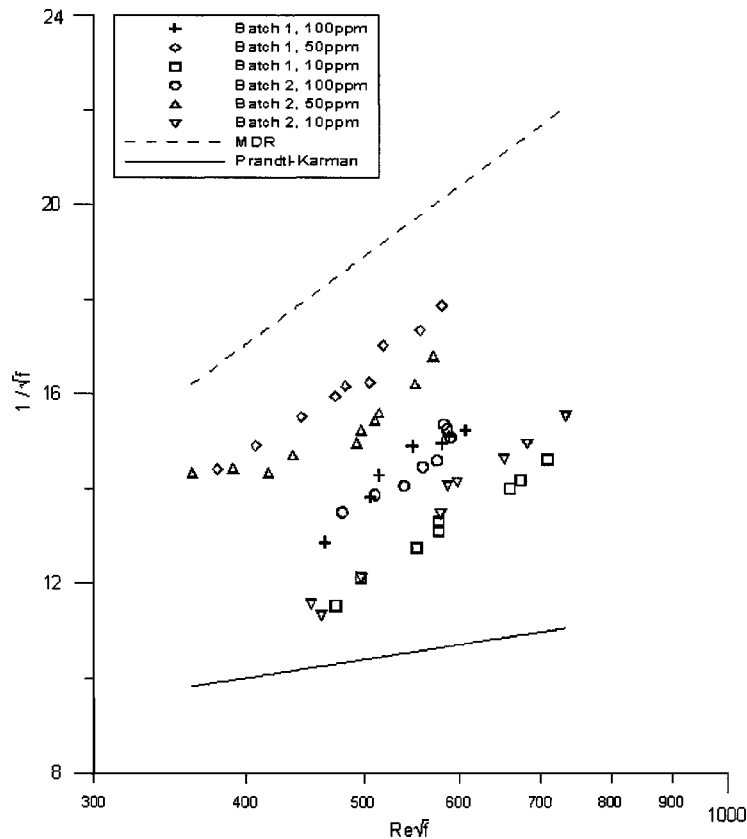


Fig. 8 Consistency test for 10, 50, and 100 ppm PEO solutions

solutions to a lower concentration were done similarly to what was described earlier for 100 ppm samples from 10,000 ppm master batches of PAM and HPAM and 100 ppm samples from a 1,000 ppm PEO master batch. These tests were needed to rule out the effects of dilution time due to differences in initial concentration. It was found that 100 ppm solutions of PAM obtained by diluting a 10,000 ppm master batch give consistent results (within  $\pm 10\%$  for  $5500 < Re < 15,000$ ) right after dilution and up to six hours thereafter. A 100 ppm solution obtained from a 1,000 ppm showed consistent results (within  $\pm 5\%$  for  $4000 < Re < 15,000$ ) right away and up to at least three hours of hydration. The results showed more consistent agreement, that is less scattered data in time by comparison to the results from the 100 ppm solution obtained by diluting a 10,000 ppm master batch. They were also more consistent at the lower range of Reynolds numbers (4000–8500). A 100 ppm sample taken from a 1,000 ppm solution obtained by diluting a 10,000 ppm master batch was also studied. The hydration time to get consistent results (within  $\pm 6\%$  for  $7000 < Re < 15,000$ ) for the 1,000 ppm solution was two hours. The corresponding 100 ppm samples from the 1,000 ppm solution were consistent (within  $\pm 5\%$  for  $4000 < Re < 15,000$ ) for at least three hours. The final results for each of the 100 ppm solutions mentioned are plotted together in Fig. 5, along with the analytical results from Blasius for water as a reference. The limit of stable drag reduction is slightly different for each dilution case, but these results are all consistent within  $\pm 5\%$  for  $7000 < Re < 15,000$ .

The results obtained for 100 ppm solutions of HPAM diluted from 10,000 and 1,000 ppm are also compared in Fig. 5. The hydration time for both 100 ppm solutions obtained by diluting 10,000 and 1,000 ppm batches, respectively, does not seem to be a critical factor since consistent results (within  $\pm 4\%$  for  $6000 < Re < 14,000$ ) are obtained right away and throughout the period tested, at least eight hours. For 100 ppm solutions, testing the hydration time required for dilution of the 10,000 ppm master

batch down to 1,000 ppm, also included in Fig. 5, showed consistency (within  $\pm 3\%$  for  $5500 < Re < 10,000$ ) right away and up to at least twenty-seven hours thereafter, despite the fact that within eight hours of hydration the solution was not visually homogeneous. Figure 5 gives a comparison of all the 100 ppm solutions mentioned above and shows that all 100 ppm solutions are consistent within  $\pm 7\%$  for  $6500 < Re < 10,000$ .

Similar tests to those indicated earlier were not conducted for PEO due to the long time required to prepare highly concentrated solutions as indicated earlier in this section.

**3.2.2 Polymer Solution Consistency for Concentrations Lower than 100 ppm.** Once the procedure for preparation of the polymer solutions was sorted out, tests were conducted to ensure batch to batch consistency for various concentrations, lower than 100 ppm, for the three polymers used in this study. A preliminary study to assess the proper hydration time required was conducted whenever pertinent. While the results for PAM followed the expected trends, the ones corresponding to PEO and HPAM did not.

Figure 6 shows the changes of the Fanning friction factor,  $f$ , [defined as  $f = (1/4)f_D$ ] with Reynolds number in Prandtl–Karman coordinates (i.e.,  $1/\sqrt{f}$  versus  $Re\sqrt{f}$ ) for 10, 50, and 100 ppm solutions. These solutions were obtained by diluting samples from different 10,000 ppm PAM polymer solutions (two of these, denoted as batches 1 and 2, are shown in the figure). Figure 6 also shows the drag reduction interval as that between the Prandtl–Karman curve for water [ $1/\sqrt{f} = 4 \log(Re\sqrt{f}) - 0.4$ ] and the Virk's Maximum Drag Reduction Asymptote [MDRA;  $1/\sqrt{f} = 19 \log(Re\sqrt{f}) - 32.4$ ]. The results showed drag reduction consistency within 4%, among the samples from the different batches with the same concentrations. They also reflect the expected trend of higher drag reduction with higher concentrations.

The results obtained for similar tests performed with HPAM are presented in Fig. 7. Drag reduction consistency among samples

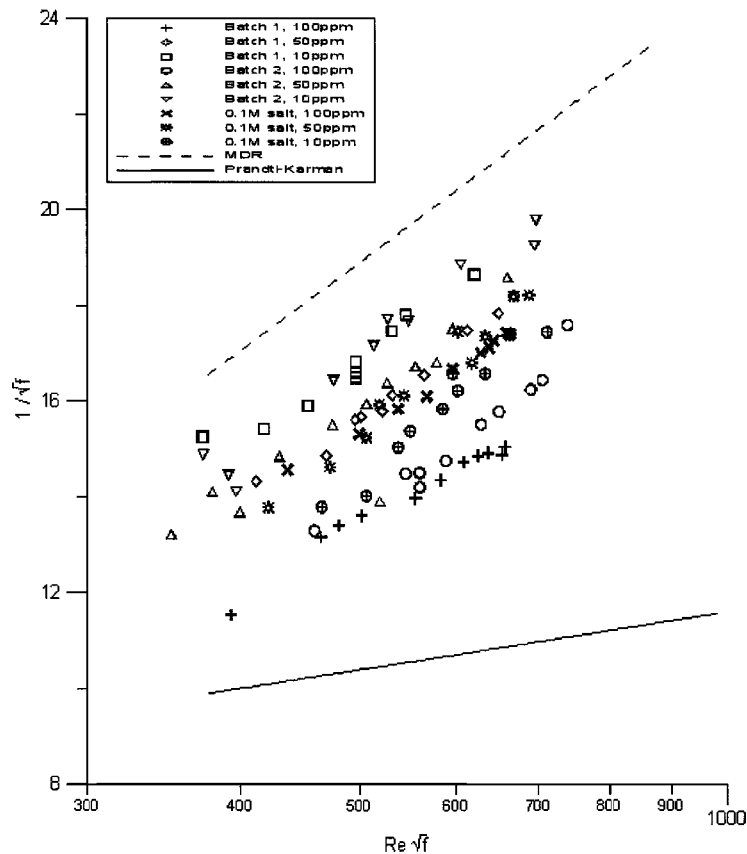


**Fig. 9 Consistency test for 10, 50, and 100 ppm HPAM solutions with and without 0.1 molar concentrations of salt**

from different batches is within 5%. They show consistency for solutions with the same concentration (for instance, batches 1 and 2 shown in the figure), but inconsistent overall drag reduction trends. Data corresponding to 10 ppm solutions were closer to the MDR than that corresponding to 100 ppm, which was closer to the water results. The results corresponding to the 50 ppm solutions fall in between the 100 and 10 ppm results. The influence of the hydration times for the 10 and 50 ppm was tested and did not appear to be an issue. The same trends and quantitative data (drag reduction within 7% for all concentrations) were obtained for 10, 50, and 100 ppm solutions diluted from 1,000 ppm solutions. Further confirmation of this unusual trend was evident from testing 25 and 75 ppm samples. Their results showed the drag reduction corresponding to the 75 ppm solution between the data corresponding to 50 and 100 ppm and the drag reduction for the 25 ppm solution between the 10 and 50 ppm. The sensitivity of Superfloc to changes in the solvent conditions due to its ionic nature was thought to be a potential explanation for this anomaly. However, the pH levels corresponding to the solutions with concentrations in the range 10–100 ppm were within the interval  $9.31 < \text{pH} < 9.36$  and the temperature differences well within  $\pm 1^\circ\text{C}$ . These changes in the solvent conditions did not seem to be significant enough to explain the reported unexpected trend.

The tests conducted for PEO also showed unexpected results of a similar nature to that seen for HPAM. Drag reduction consistency within 6% was found among batches of the same concentration obtained by diluting 1,000 ppm polymer solutions to 10, 50, and 100 ppm. The measured data is shown in Fig. 8 where the maximum drag reduction asymptote and the Prandtl–Karman law are also shown for reference. Two different 1,000 ppm solutions are shown in the figure and denoted as batches 1 and 2. However, the drag reduction measured for the 100 ppm solutions falls in

between that corresponding to 10 and 50 ppm with 50 ppm giving the largest drag reduction. Hydration tests were performed for the 10 and 50 ppm solutions to assess the proper time for solution homogeneity to rule out this variable as the one responsible for the inconsistent results. The pH levels corresponding to the 10, 50, and 100 ppm solutions were within the interval  $9.27 < \text{pH} < 9.35$  and the temperature differences well within  $\pm 1^\circ\text{C}$ .

The ionic character of these polymers (i.e., HPAM and PEO) might translate into the formation of polymer aggregates. It is possible that such aggregates are not disrupted by the gentle rolling process to which the solution is subjected during mixing, explaining the very consistent data obtained throughout the hydration process shown earlier in Section 3.2.1. If that is indeed the case, the size of these aggregates versus the size of the pipe of the polymer consistency apparatus where these solutions were tested might play a significant role on the overall drag reduction obtained. The consistency on the results corresponding to different batches of the same concentration is remarkable. To test this speculation an attempt was made to neutralize the ionic behavior of the polymers (both PEO and HPAM) by preparing polymer solutions with salt water instead of tap water. The preparation process of such solutions involved premixing small amounts of water with salt and slowly adding polymer solution while stirring to ensure that the salt does not settle to the bottom. The results for HPAM with 0.1 molar concentration of salt solution are shown in Fig. 9. The effect of the salt is to increase the drag reduction for the 100 ppm to be within error of the 50 ppm. The results for the 50 ppm solution are practically unchanged with salt addition and the 10 ppm data has decreased drag reduction such that it is slightly above the 100 ppm solution without salt. The salt test shows that the ionic behavior is partially responsible for the reverse trend associated with the HPAM solutions. Tests were also

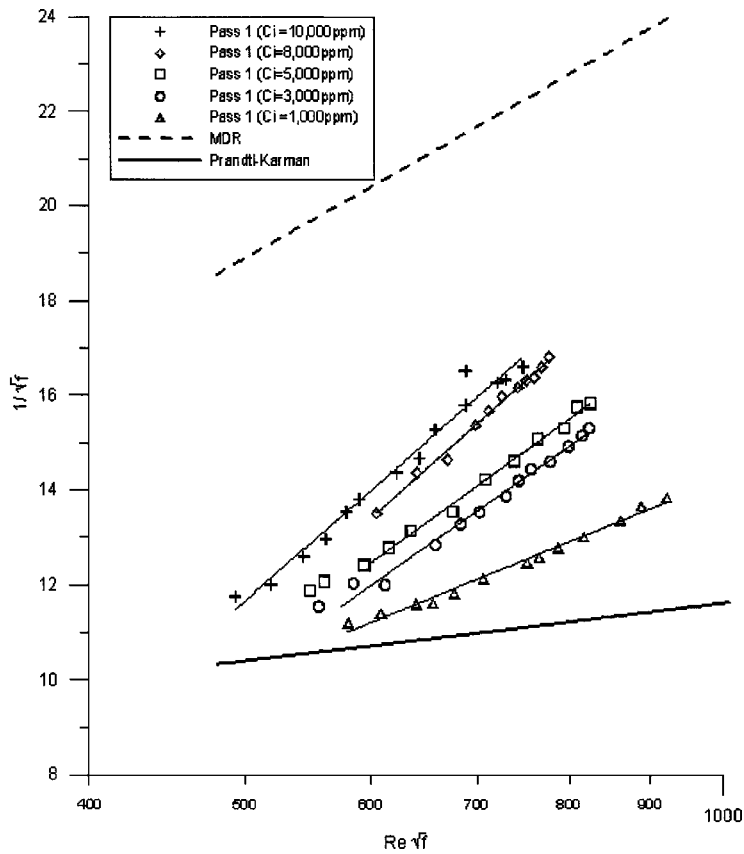


Fig. 10 Comparison of degradation for the first pass of 14 ppm PAM solutions obtained by injecting into the channel

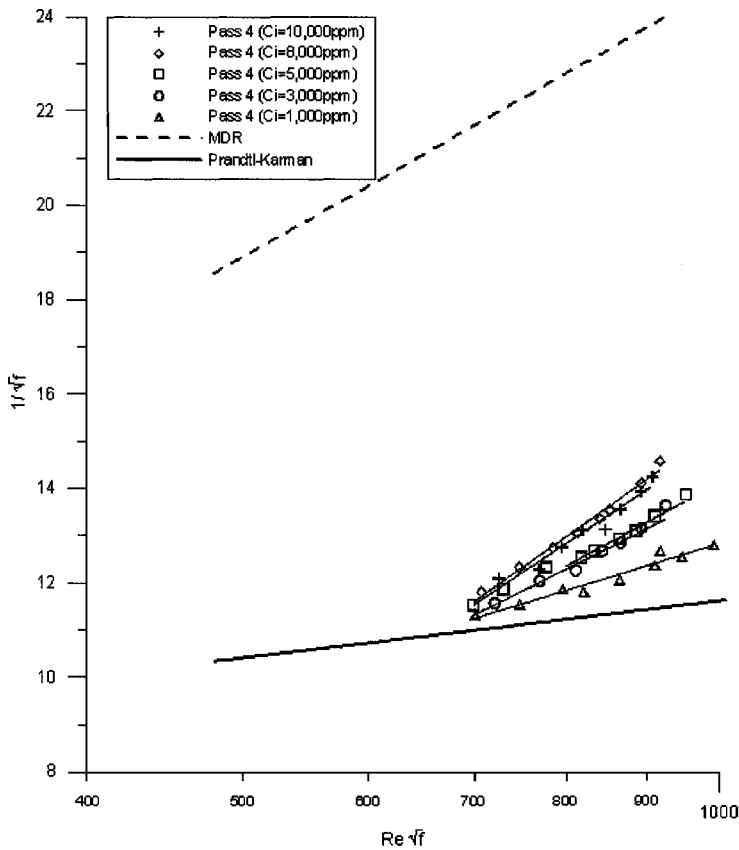


Fig. 11 Comparison of degradation for the fourth pass of 14 ppm PAM solutions obtained by injecting into the channel

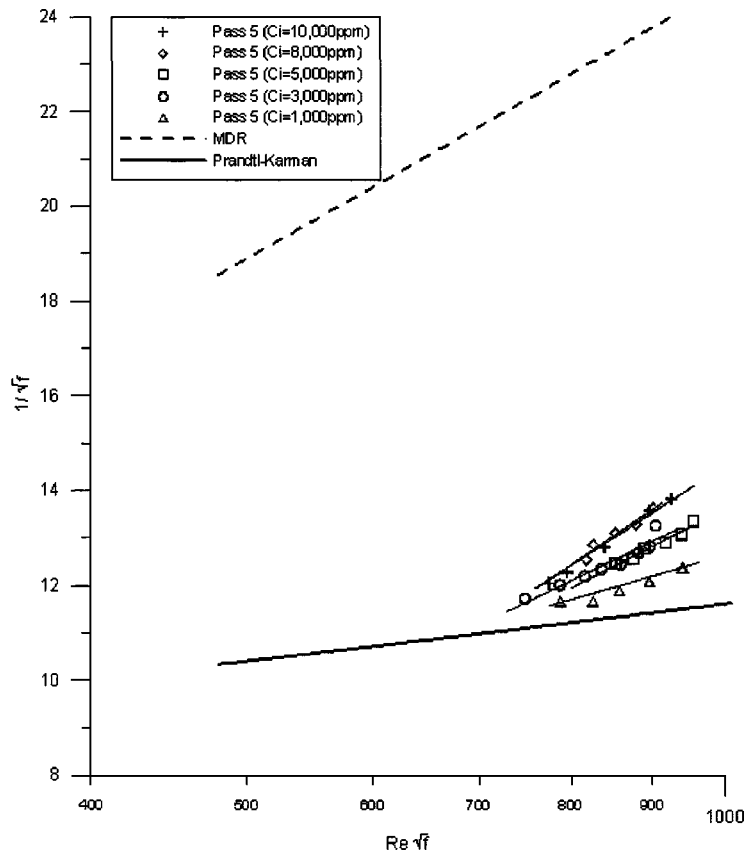


Fig. 12 Comparison of degradation for the fifth pass of 14 ppm PAM solutions obtained by injecting into the channel

performed with PEO solutions with 0.02 molar concentration of salt in anticipation of the weaker ionic bonds compared to HPAM. No effect on the drag reduction results shown in Fig. 8 was seen and, therefore, a larger salt concentration corresponding to 0.1 molar concentration of salt was tested. However, the results again did not change substantially with respect to those shown in Fig. 8 and the same trends were obtained. The abnormality in the high levels of drag reduction obtained from the 50 ppm solutions compared to the 100 ppm did not seem to be associated with the weakly ionic properties of PEO. Further studies are required to characterize with certainty the reasons for the abnormal trends observed with both HPAM and PEO for concentrations lower than 100 ppm when obtained by diluting highly concentrated solutions in the range 1,000–10,000 ppm.

**3.2.3 Shelf-Life Tests.** The shelf-life of the prepared solutions is considered an important parameter both to designing time-efficient experiments involving polymer injection and also to assess the practicality of polymers as drag reduction agents in real engineering applications. Tests were conducted to try to capture the life span of polymer solutions prepared following the steps indicated earlier and stored at lab conditions (22°C) in sealed containers. Polymer solutions of PAM, 1000 and 10,000 ppm were prepared and tested in the polymer-consistency apparatus every few days. The results showed consistency for at least 15 and 52 days, respectively. Solutions of PEO, 1,000 ppm showed consistency for at least 16 days. The tests conducted for 10,000 and 1,000 ppm solutions of HPAM showed stable drag reduction characteristics for at least 31 and 16 days, respectively. All the shelf-life experiments were conducted in the range of Reynolds numbers corresponding to  $4 \times 10^3 < Re < 1.6 \times 10^4$ .

#### 4 Effects of Injection of Polymer Solutions

Injection of homogeneous highly concentrated polymer solutions into shear flows can result into the formation of macromolecular polymer structures. The studies of Shen et al. [23] and Kim et al. [24] associate the presence of macro-molecular PAM polymer structures with a substantial enhancement in drag reduction when compared to that corresponding to an equivalent average homogeneous polymer concentration at the test section. In those studies the polymer structures were induced by injecting a homogeneous highly concentrated polymer solution into the same water channel flow used in this study to achieve a concentration of 14 ppm at the test section for a Reynolds number of  $5.6 \times 10^4$  based on the channel width and the centerline velocity. The presence of such macro-molecular polymer structures was proved in the above mentioned studies via laser induced fluorescence visualization and Birefringence measurements for injection concentrations above 3,000 ppm. No appreciable polymer structures were detected for lower concentrations even though that does not preclude their existence. If present, however, their size should be much smaller than the wavelength of light as explained by Kim et al. [24].

A degradation study consisting of measuring the drag reduction corresponding to homogeneous and heterogeneous polymer solutions with the same average concentration after passing them several times through a pipe was performed. This study was conducted to further assess the impact that formation of polymer structures have on the overall performance of polymer solutions for various Reynolds numbers. The study was done only for PAM and the injection concentrations were chosen based on the results of Kim et al. [24] that established the injection concentration

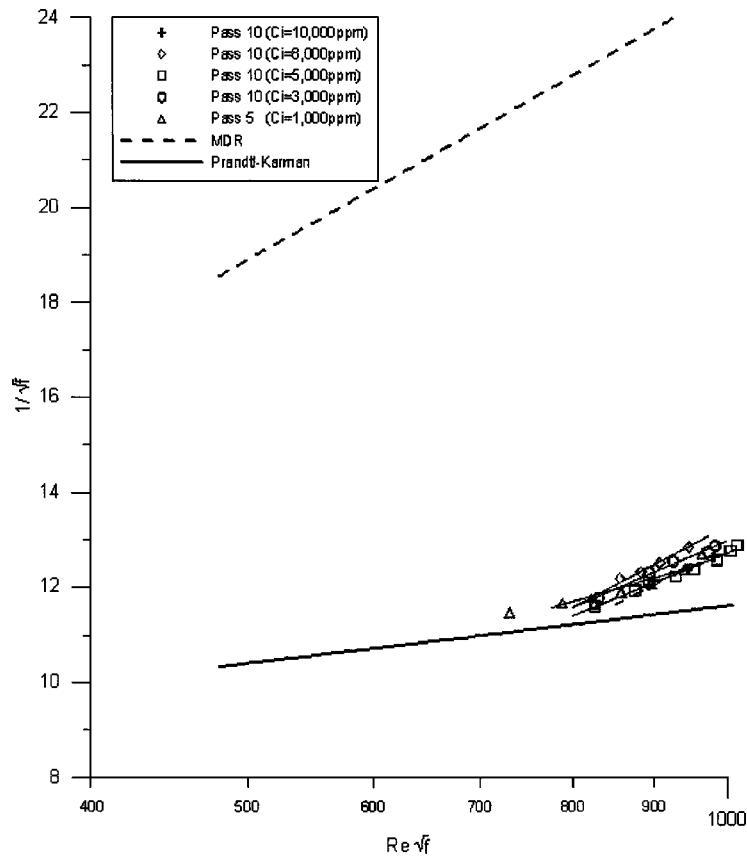


**Fig. 13 Comparison of degradation for 14 ppm PAM solutions for the tenth pass obtained by injecting 10,000, 8,000, 5,000, 3,000 ppm solutions into the channel along with the fifth pass from injection of 1,000 ppm**

threshold needed for macro molecular polymer structures to be present in this channel flow. The solution without polymer structures was induced by injecting a 1,000 ppm polymer solution in the channel at an injection rate corresponding to an average test section concentration of 14 ppm, following the conclusions of the mentioned study. The solution with the polymer structures was induced by injecting polymer solutions in the range of 3,000–10,000 ppm in the channel. The injection was done at both channel walls well upstream the test section at a flow rate corresponding to an average 14 ppm concentration at the test section. Samples were extracted from the channel just downstream of the test section. Samples from both polymer solutions with and without polymer structures were then tested in the polymer consistency apparatus. Flow rates and pressure drops were measured for each case and the results from several passes through the pipe recorded and compared.

The outcome from such degradation tests are shown in Figs. 10–13 for injection concentrations of 10,000, 8,000, 5,000, 3,000, and 1,000 ppm and a corresponding average concentration of 14 ppm at the test section. Each figure (Figs. 10–12) shows the drag reduction versus Reynolds number (in Prandtl–Karman, PK, coordinates) achieved by each of the polymer solutions for passes one, three and five through the pipe. Figure 13 shows the results corresponding to ten passes through the pipe.

The results shown in Fig. 10 corresponding to the first pass through the polymer consistency apparatus show that the level of drag reduction attained by the structured polymer solutions is drastically different from that achieved by the nonstructured polymer solution for all Reynolds numbers tested. The results corresponding to the largest injection concentration translate into roughly double the drag reduction of that achieved by the non-

structured polymer solution. As shown in the figure the data can be quite well approximated by the straight lines indicated, corresponding to least-squares regressions of the data with correlation coefficients,  $r$ , of at least 0.94. The difference between the slope of the curves corresponding to the polymer solution and the solvent was referred to as slope increment,  $\delta$ , by Virk (1975). The slope increments corresponding to the first pass of the structured samples tested for injection concentrations  $C_i = (10,000, 8,000, 5,000, \text{ and } 3,000 \text{ ppm})$  are  $\delta = (25.5, 25.8, 20.4, 19.5)$ . The slope increment corresponding to the nonstructured solution is 9.6. For injection concentrations within  $3,000 \text{ ppm} \leq C_i \leq 10,000 \text{ ppm}$ ,  $\delta$  is at least double that corresponding to the nonstructured polymer solution ( $C_i = 1,000 \text{ ppm}$ ) for the same average concentrations. As expected, the results confirm that the level of polymer structure formation is highly dependent on the injection concentration. For the same Reynolds numbers, lower drag reduction is obtained at the lower injection concentrations. The mean value of  $Re\sqrt{f}$  corresponding to the onset of drag reduction,  $Re\sqrt{f}_o$ , and the slope increments of the curves shown in Fig. 10, corresponding to  $C_i = 10,000$  and 8,000 ppm are  $459 \pm 13$  and  $25.65 \pm 0.15$ . Similarly the mean results for  $C_i = 5,000$  and 3,000 ppm are  $504 \pm 11.5$  and  $19.95 \pm 0.45$  for both intercept and slope. The mean values of  $\delta$  and  $Re\sqrt{f}_o$  corresponding to all the structured cases tested and shown in Fig. 10, is  $22.8 \pm 3.3$  and  $481.75 \pm 35.75$ . The change with respect to the corresponding values for the nonstructured solution is 40% and 5%, respectively. In other words, trends shown in Fig. 10 indicate that the onset of drag reduction for the nonstructured solution takes place at a slightly higher Reynolds number or corresponding critical wall shear stress,  $\tau_{wc}$ , than that required for the structured polymer solutions to become effective



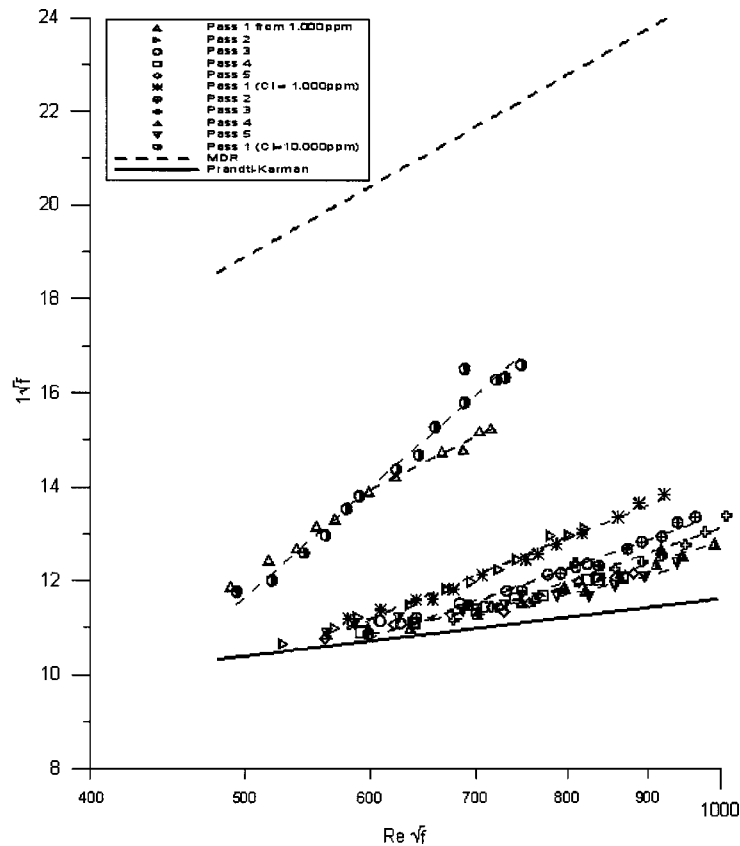


**Fig. 14 Degradation for 14 ppm PAM solutions obtained by diluting 1,000 ppm compared to a samples taken from injection of 1,000 and 10,000 ppm into the channel**

drag reduction additives. The most striking outcome, however, is the similarity in both slope increment and  $Re\sqrt{f}_o$  for all the structured solutions and the substantial change in slope with respect to the nonstructured solution while the onset of drag reduction is very comparable.

The overall endurance to degradation is considerably better for the samples with polymer structures as it is shown in the results corresponding to consecutive passes through the pipe (Figs. 10–13). For all passes, the structured polymer solutions show higher levels of drag reduction for all Reynolds numbers tested than those corresponding to the nonstructured solution. The onset of drag reduction becomes relatively closer between the various structured samples and the nonstructured one the more passes through the pipe. In fact by the third (Fig. 11), and fourth pass (not shown due to space constraints) the results corresponding to all of the structured samples indicate a very comparable onset of drag reduction to that corresponding to the nonstructured sample. For the first two passes the critical wall shear stress corresponding to the nonstructured polymer solution is larger than that corresponding to the structured samples. By pass four the trend has reversed and the onset of drag reduction takes place now at higher critical wall shear stresses for all the structured solutions with respect to the nonstructured solutions.

The process of degradation of the structured polymer solutions and that corresponding to the nonstructured polymer solutions are deemed to be substantially different. In the case of the structured polymer, it is speculated that the majority of the degradation comes initially from the breakup, or disentanglement, of the polymer structures while some breakup of the individual polymer molecules will most likely also happen. In the case of the homogeneous polymer solution, degradation comes from the breakup of the polymer molecules, which in turn comes associated with a

change in the molecular weight of the solution and a consequent increase of the critical wall shear stress and decrease of the slope (Virk [30]). While the critical wall shear stresses also increase with more passes through the pipe for the structured samples the change is much larger compared to that endured by the nonstructured sample for the same number of passes.

Figure 13 shows the results corresponding to  $C_i=1,000$  ppm after five passes through the pipe in comparison with the data corresponding to all the other injection concentrations tested after ten passes through the pipe. The slope increments corresponding to all the structured polymer solutions after ten passes are still at least double of that corresponding to the nonstructured polymer solution after five passes. On the other hand the onset of all the structured samples are within 2%, and within 12% of the onset corresponding to the nonstructured solution after five passes which takes place at a lower wall shear stress. The latter translates into the structured solutions still being more effective after ten passes at larger Reynolds numbers ( $Re > 14,000$ ) than the ones tested in this study. For the range of Reynolds numbers shown in Fig. 13 ( $6,000 < Re < 14,000$ ) the percentages of drag reduction shown by the structured solution after five passes and the nonstructured polymer solutions after five are comparable.

Figure 14 shows the data corresponding to a similar degradation test to those mentioned earlier, but now performed on a 14 ppm sample obtained from direct dilution of a 1,000 ppm polymer solution. These results are compared in Fig. 14 with those corresponding to the channel test section sample for an injection concentration of 1,000 ppm and an average test section of 14 ppm. The data corresponding to the first pass through the pipe of a sample from the channel test section corresponding to an injection concentration of 10,000 ppm, is also shown in Fig. 14

**Table 1 Summary of slope increments, onset points, and correlation statistics for all PAM 14 ppm solutions both structured and unstructured**

Pass	$C_i$ [ppm]	Onset Ref <sup>0.5</sup>	$f^{0.5}$	Slope increment	$\tau_{wc}$ [N/m <sup>2</sup> ]	$r$
1	10,000 prepared	364	9.8	15.6	0.3573	0.9832
1	1,000 prepared	337	9.7	12.9	0.3056	0.9795
1	10,000	446	10.2	25.5	0.5377	0.9885
1	8,000	472	10.3	25.8	0.6006	0.9965
1	5,000	493	10.4	20.4	0.6545	0.9967
1	3,000	516	10.5	19.5	0.7186	0.9935
1	1,000	533	10.5	9.6	0.7657	0.9937
2	1,000 prepared	539	10.5	10.1	0.7841	0.9896
2	10,000	552	10.6	21.0	0.8227	0.9934
2	8000	557	10.6	22.6	0.8367	0.9918
2	5,000	570	10.6	15.9	0.8757	0.9946
2	3,000	590	10.7	15.5	0.9396	0.9892
2	1,000	600	10.7	8.3	0.9711	0.9903
3	1,000 prepared	596	10.7	8.2	0.9593	0.9680
3	10,000	612	10.7	20.7	1.0111	0.9940
3	8,000	606	10.7	21.6	0.9917	0.9897
3	5,000	635	10.8	15.8	1.0875	0.9906
3	3,000	635	10.8	15.4	1.0862	0.9922
3	1,000	622	10.8	7.0	1.0451	0.9722
4	1,000 prepared	552	10.6	4.2	0.8233	0.9925
4	10,000	652	10.9	18.1	1.1464	0.9772
4	8,000	651	10.9	19.6	1.1422	0.9931
4	5,000	662	10.9	13.9	1.1832	0.9949
4	3,000	659	10.9	12.7	1.1712	0.9926
4	1,000	634	10.8	6.2	1.0852	0.9777
5	1,000 prepared	547	10.6	3.8	0.8072	0.9722
5	10,000	682	10.9	17.6	1.2557	0.9952
5	8,000	688	11.0	18.7	1.2776	0.9725
5	5,000	702	11.0	13.1	1.3309	0.9904
5	3,000	674	10.9	12.0	1.2247	0.9538
5	1,000	652	10.9	5.6	1.1466	0.9448
10	10,000	801	11.2	12.5	1.7286	1.0000
10	8,000	750	11.1	13.5	1.5171	0.9913
10	5,000	762	11.1	9.5	1.5664	0.9932
10	3,000	751	11.1	10.3	1.5198	0.9944

for comparison. The results corresponding to the first pass through the polymer consistency apparatus for the directly prepared 14 ppm sample and that corresponding to the nonstructured channel sample show important quantitative differences in their levels of drag reduction. This is to be expected due to the degradation endured by the nonstructured channel polymer solution from injection to the channel test section located 84.3 channel widths downstream from the injection slot. The slope increments corresponding to both first passes are 12.9 and 9.6, respectively. Despite the initial difference in drag reduction levels, it is interesting to note that the results corresponding to subsequent passes through the pipe render very similar trends and characteristics. On the other hand the comparison of the results corresponding to the first pass of the directly prepared sample and the structured polymer sample for the channel test section display what might seem at first quantitative similarities. However, quantitative comparisons are not justified, as mentioned earlier, due to the fact that the channel samples endure degradation from injection to the test section. It is interesting to note though, the similarity in the slopes of the cases corresponding to the nonstructured solutions and their discrepancy with respect to the slope increment corresponding to the structured polymer sample,  $\delta=25.5$ .

Similar results to those obtained from the directly prepared sample from a 1,000 ppm solution were obtained from a directly prepared 14 ppm sample by diluting a 10,000 ppm solution (not shown in Fig. 14). The results corresponding to the first pass through the polymer consistency apparatus of both samples show slope increments of 12.9 and 15.6, respectively, and the results obtained from their subsequent passes through the polymer consistency apparatus show again good consistency. This is to be expected as discussed earlier in Section 3, where the consistency of prepared PAM polymer solutions was addressed.

The data corresponding to  $\delta$ ,  $Re \sqrt{f}_o$  and  $\tau_{wc}$  for injection concentrations of 10,000, 8,000, 5,000, 3,000, and 1,000 ppm versus

the number of passes through the pipe is shown in Table 1. In the same table, the data corresponding to the 14 ppm solution obtained by direct dilution of a 1,000 ppm sample for passes one through five is also included. From the data presented in Table 1 it can be observed that after ten passes the slope increment corresponding to the structured solutions is roughly double than that corresponding to the nonstructured solution after five passes. This translates into larger drag reduction efficiency on the part of the structured solutions, roughly an average 10% higher for all Reynolds numbers tested by pass five. The change in slope increment for all structured solutions is larger in the first pass than afterwards when the changes become very comparable from pass to pass in the range tested. The nonstructured solutions experienced very similar changes for all passes. The only exception being possibly passes 4 and 5 of the directly prepared solution when  $\delta$  practically remains constant. It is also noticeable that the critical shear stress is larger for all the channel samples and for all passes shown in comparison to that obtained for the directly prepared polymer solution. The range of change of the critical shear stress throughout the degradation process corresponding to the nonstructured channel sample is considerably smaller than that corresponding to all the structured samples.

## 5 Conclusions

Preparation procedures as well as solution stability and shelf life have been examined for three different polymer types (PAM, HPAM, and PEO). It is found that it is crucial to determine the proper hydration or rolling time needed to produce a fully mixed, homogeneous and hence consistent polymer solution. Hydration time changes with polymer type and with concentration. A consistent, repeatable procedure was established and tested. The perti-

ment errors associated with the process were also assessed and discussed. The shelf lives of all polymer solutions prepared in this study were at least fifteen days.

When attempting to produce polymer solutions of concentrations 100 ppm and lower of PEO and HPAM from highly concentrated solutions (i.e., 10,000 ppm and lower) it was found that the expected monotonic trend of larger drag reduction for larger concentrations was not followed. Such unusual behavior could not be traced to temperature changes or the pH effect of the solvent. Tests to neutralize the ionic character of both polymers were attempted by using a small concentration of salt. These results do not seem to be fully conclusive but it does seem plausible that if polymer aggregates are present in the highly concentrated solution despite the mixing process, the process of dilution will result in heterogeneous solutions with an average concentration that will be difficult to determine.

The effect of polymer structures induced by injecting a highly concentrated polymer solution into a channel flow was studied for various Reynolds numbers. It was found that the slope increment was increased substantially when compared to samples of non-structured, homogeneous, solutions of the same average concentrations. Degradation tests were performed with nonstructured and structured polymer samples of PAM with the same average concentration by running the samples several times through the polymer consistency apparatus. It was found that more than double the number of passes are needed from the structured sample to attain the same level of drag reduction for all Reynolds numbers tested in this experiment. It is speculated that the process of degradation endured by the structured polymer solutions could mostly be due to the breakup of the polymer structures. The change in the critical shear stress throughout the degradation process is larger for the structured samples than it is for the nonstructured solutions.

While the results presented in the degradation study discussed herein are particular for a certain type of polymer and flow characteristics, they nonetheless highlight the importance of polymer structures as drag reduction agents and their remarkable endurance to degradation. Inducing polymer structures through polymer solution preparation or injection might be a powerful and controllable mechanism to substantially increase the levels of drag reduction obtained with polymers.

## Acknowledgments

This work was supported by the Defense Advance Research Projects Agency (DARPA) under Grant No. MDA972-01-1-0014, as part of the Friction Drag Reduction Program and partially by a grant from the NSF-Advance Program at the University of Michigan. This support is gratefully acknowledged.

## References

- [1] Toms, B. A., 1948, "Some Observations on the Flow of Linear Polymer Solutions through Straight Tubes at Large Reynolds Numbers," *Proceedings First International Congress in Rheology*.
- [2] Lumley, J. L., 1977, "Drag Reduction in Two Phase and Polymer Flows," *Phys. Fluids*, **20**, pp. S64-S71.
- [3] Ryskin, G., 1987, "Turbulent Drag Reduction by Polymers: A Quantitative Theory," *Phys. Rev. Lett.*, **59**, p. 2059-2062.
- [4] DeGennes, P. G., 1986, "Towards a Scaling Theory of Drag Reduction," *Physica A*, **140**, pp. 9-25.
- [5] Tabor, M., Durning, C. J., and O'Shaughnessy, B., 1989, "The Microscopic Origins of Drag Reduction," Internal Report of the Department of Applied Physics, Columbia University, New York.
- [6] Koskie, J. E., and Tiederman, W. G., 1991, "Turbulence Structure and Polymer Drag Reduction in Adverse Pressure Gradient Boundary Layers," Technical Report PME-FM-91-3, Purdue University, West Lafayette, Indiana.
- [7] Den Toonder, J. M., Draad, A. A., Kuiken, G. D. C., and Nieuwstadt, F. T. M., 1995, "Degradation Effects of Dilute Polymer Solutions on Turbulent Drag Reduction in Pipe Flows," *Appl. Sci. Res.*, **55**, pp. 63-82.
- [8] Vlachogiannis, M., and Hanratty, T. J., 2003, "Influence of Wavy Structured Surfaces and Polymer Aggregation on Drag Reduction," *Exp. Fluids*, **36**(5), pp. 685-700.
- [9] Fortuna, G., and Hanratty, T. J., 1972, "The Influence of Drag-Reducing Polymers on Turbulence in the Viscous Sublayer," *J. Fluid Mech.*, **53**, pp. 575-586.
- [10] Rieschman, M. M., and Tiederman, W. G., 1975, "Laser-Doppler Anemometer Measurements in Drag-Reducing Channel Flows," *J. Fluid Mech.*, **70**, pp. 369-392.
- [11] McComb, W. D., and Rabie, L. H., 1982, "Local Drag Reduction Due to Injection of Polymer Solutions into Turbulent Flow in a Pipe," *AIChE J.*, **28**, pp. 547-557.
- [12] Tiederman, W. G., Luchich, T. S., and Bogard, D. G., 1985, "Wall Layer Structure and Drag Reduction," *J. Fluid Mech.*, **156**, pp. 419-437.
- [13] Willmarth, W. W., Wei, T., and Lee, C. O., 1987, "Laser Anemometer Measurements of Reynolds Stress in a Turbulent Channel Flow with Drag Reducing Polymer Additives," *Phys. Fluids*, **30**, pp. 933-935.
- [14] Luchik, T. S., and Tiederman, W. G., 1988, "Turbulent Structure in Low-Concentration Drag-reducing Channel Flows," *J. Fluid Mech.*, **190**, pp. 241-263.
- [15] Wei, T., and Willmarth, W. W., 1992, "Modifying Turbulent Structure with Drag-Reducing Polymer Additives in Turbulent Channel Flows," *J. Fluid Mech.*, **245**, pp. 619-641.
- [16] Sureshkumar, R., Beris, A. N., and Handler, R. A., 1997, "Direct Numerical Simulation of the Turbulent Channel Flow of a Polymer Solution," *Phys. Fluids*, **9**, pp. 743-755.
- [17] Dimitropoulos, C. D., Sureshkumar, R., Beris, A. N., and Handler, R. A., 2001, "Budgets of Reynolds Stress, Kinetic Energy and Streamwise Enstrophy in Viscoelastic Turbulent Channel Flow," *Phys. Fluids*, **13**(4), pp. 1016-1027.
- [18] Fontaine, A. A., Petrie, H. L., and Brungart, T. A., 1992, "Velocity Profile Statistics in a Turbulent Boundary Layer with Slot-Injected Polymer," *J. Fluid Mech.*, **238**, pp. 435-466.
- [19] Somandepalli, V. S. R., White, C. M., and Mungal, M. G., 2003, "Boundary Layer Studies on Polymer Drag Reduction Using PIV and PLIF," *Proceedings 4th ASME/JSME Joint Fluids Engineering Conference*, Hawaii.
- [20] Vlegaar, J., and Tels, M., 1973, "Drag Reduction by Polymer Threads," *Chem. Eng. Sci.*, **28**, pp. 965-968.
- [21] Smith, R. E., and Tiederman, W. G., 1991, "The Mechanism of Polymer Thread Drag Reduction," *Rheol. Acta*, **30**, pp. 103-113.
- [22] Bewersdorff, H. W., Gyr, A., Hoyer, K., and Tsinober, A., 1993, "An Investigation of Possible Mechanisms of Heterogeneous Drag Reduction in Pipe and Channel Flows," *Rheol. Acta*, **32**, pp. 140-149.
- [23] Shen, X., Kim, K., Miller, J., Sun-Chee-Fore, R., and Sirviente, A. I., 2003, "Experimental Study of Polymer Drag Reduction in a Turbulent Channel Flow," *Proceedings 4th ASME/JSME Joint Fluids Engineering Conference*, Hawaii.
- [24] Kim, K., Islam, M. T., Shen, X., Sirviente, A. I., and Solomon, M. J., 2003, "Effect of Macro-Molecular Polymer Structures on Drag Reduction in a Turbulent Channel Flow," *Phys. Fluids*, **16**(11), pp. 4150-4162.
- [25] Hoyt, J. W., 1986, "Drag Reduction," *Encyclopedia of Polymer Science and Engineering*, edited by H. F. Mark et al., 5, pp. 129, Wiley, New York.
- [26] Warholic, M. D., Massah, H., and Hanratty, T. J., 1999, "Influence of Drag-Reducing Polymers on Turbulence: Effects of Reynolds Number, Concentration and Mixing," *Exp. Fluids*, **27**, pp. 461-472.
- [27] Den Toonder, J. M., Hulsen, M. A., Kuiken, G. D. C., and Nieuwstadt, F. T. M., 1997, "Drag Reduction by Polymer Additives in a Turbulent Pipe Flow: Numerical and Laboratory Experiments," *J. Fluid Mech.*, **337**, pp. 193-231.
- [28] Gampert, B., Braemer, T., Eich, T., and Dietmann, T., 2003, "Some Experimental Results on Laser Doppler Velocimetry (LDV) and Birefringence (FIB) Studies of Non-Newtonian Fluids Flow through Rectangular Channels," *Proceedings of the 4th ASME/JSME Joint Fluids Engineering Conference*, Hawaii.
- [29] Islam, M. T., Vanapalli, S. A., and Solomon, M. J., 2003, "Inertial Effects on Polymer Chain Scission in Planar Elongational Cross-Slot Flow," *Macromolecules*, **37**(3), pp. 1023-1030.
- [30] Virk, P. S., 1975, "Drag Reduction Fundamentals," *AIChE J.*, **21**, pp. 625-653.

# Optimum Bifurcating-Tube Tree for Gas Transport

Tianshu Liu

Department of Mechanical  
and Aeronautical Engineering,  
Western Michigan University,  
Kalamazoo, MI 49008  
e-mail: tianshu.liu@wmich.edu

*This paper describes optimality principles for the design of an engineering bifurcating-tube tree consisting of the convection and diffusion zones to attain the most effective gas transport. An optimality principle is formulated for the diffusion zone to maximize the total diffusion mass-transfer rate of gas across tube walls under a constant total-volume constraint. This optimality principle produces a new diameter distribution for the diffusion zone in contrast to the classical distribution for the convection zone. In addition, this paper gives a length distribution for an engineering tree based on an optimality principle for minimizing the total weight of the tree under constraints of a finite surface and elastic criteria for structural stability. Furthermore, the optimum branching angles are evaluated based on local optimality principles for a single bifurcating-tube branch. [DOI: 10.1115/1.1899168]*

## Introduction

A biological respiratory system for gas transport can be considered as a bifurcating-tube tree (bronchial tree) consisting of a number of branching generations of tubes [1,2]. Hence, a bifurcating-tube tree can serve as a biologically inspired model for gas transport in engineering applications. Here, we want to devise an engineering bifurcating-tube tree for the most effective gas transport based on optimality principles and scaling analyses. As shown in Fig. 1, the diameter, length, and wall thickness of a bifurcating tube are three basic metric quantities, and the branching angle is an angular quantity characterizing the geometric structure of a bifurcating-tube tree. Since trees are not necessarily planar to avoid intersection with each other, another parameter is the azimuthal rotational angle of a tube branch relative to the preceding branch. The biggest tube is designated as the generation 0. The successive left and right branches are designated as the first generation, and so on. Therefore, the total number of tubes in the  $n$ th generation is  $2^n$ . Consider an engineering bifurcating-tube tree in which tubes are circular and tree bifurcation is symmetrical, and steady flow through it is driven by a constant pressure difference between the generation 0 and the end generation (unlike periodic flow in bronchial trees). An engineering tube tree is distinctly divided into the convection and diffusion zones. Tubes are bigger in the convection zone where the generation number is lower than a critical value for division. Since the Péclet number is large, the dominant physical process is convection while diffusion is negligible. For simplicity, it is assumed that tube walls in the convection zone are impermeable. As the generation number exceeds a certain critical value for division, diffusion becomes a dominant physical mechanism in the diffusion zone (higher generations) where tubes are fine and highly permeable. Separation of a tree into two distinct zones where different physical mechanisms prevail is convenient for an engineering analysis. The critical number for division between the two zones depends on the Péclet number indicating the relative importance of convection to diffusion. The core problem is to determine the diameter, length, wall thickness, and branching angle of tubes as a function of the generation number.

Strikingly, a diameter distribution in the convection zone has been obtained based on simple optimality principles without con-

sidering hydrodynamic details [3–9]. An optimality principle for the minimum power gives a classical diameter-generation relation [3]

$$d_n \propto 2^{-n/3}, \quad (1)$$

where  $d_n$  is the tube diameter in the  $n$ th generation and  $n$  is the generation number. This result has also been derived based on similar optimality principles for the minimum volume [4], minimum entropy production [7], and minimum resistance [10–12]. In fact, Eq. (1) is an asymptotic distribution in the convection zone where resistance (entropy production or work) is a legitimate target for minimization. Naturally, a question is whether we can derive another asymptotic distribution of the diameter in the diffusion zone based on appropriate optimality principles.

The objective of this work is to formulate appropriate optimality principles for designing an engineering bifurcating-tube tree for gas transport rather than providing a teleological explanation for the architecture of bronchial trees. Based on these optimality principles, we deduce a diameter distribution for the diffusion zone of a tube tree and a length distribution for the entire tree. Moreover, the optimum branching angles are determined for both the convection and diffusion zones.

## Diameter Distribution and Maximum Gas Diffusion

An optimality principle for the diffusion zone of an engineering bifurcating-tube tree is formulated based on scaling analyses of surface, volume, and gas concentration. We consider the ad hoc solutions  $d_n \propto 2^{-pn}$  and  $l_n \propto 2^{-qn}$  for the diameter and length, respectively, and  $V_n \propto 2^{\beta n}$  for the total volume of the  $n$ th generation, where the parameter  $\beta$  is defined as  $\beta = 1 - 2p - q$ . Clearly, the main task is to determine the parameters  $p$  and  $q$ .

For thin and permeable tube walls in the diffusion zone, according to Fick's law, the diffusion mass-transfer rate of gas from the inside to the outside of tubes in the  $n$ th generation is

$$\dot{m}_n = D_{diff}(A_{eff})_n \Delta C_n / h_n, \quad (2)$$

where  $D_{diff}$  is the gas diffusion coefficient of wall material,  $h_n$  is the wall thickness,  $(A_{eff})_n$  is the effective diffusion area,  $\Delta C_n$  is a change in the gas concentration across a tube wall, and the subscript  $n$  denotes the  $n$ th generation. For simplicity, it is assumed that the gas concentration outside tubes is zero; i.e.,  $\Delta C_n = C_n$ . Generally, to consider nonhomogeneous diffusion surfaces, the effective diffusion area is expressed as a power-law function of the total surface of tubes, i.e.,  $(A_{eff})_n \propto A_n^\alpha$ , where  $A_n$  is the total surface area in the  $n$ th generation. The positive exponent  $\alpha = A_n(A_{eff})_n^{-1}[d(A_{eff})_n/dn]/(dA_n/dn)$  represents the increasing rate

Contributed by the Fluids Engineering Division for publication in the JOURNAL OF FLUIDS ENGINEERING. Manuscript received: December 31, 2003. Final manuscript received: January 24, 2005. Review conducted by: Joseph Katz.

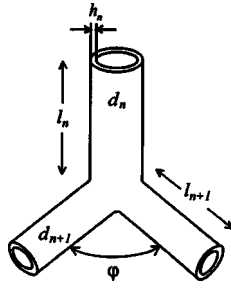


Fig. 1 Geometry of tube bifurcation

of the effective diffusion area relative to that of the total surface area in the  $n$ th generation. For homogeneous permeable surfaces, the exponent is simply  $\alpha=1$ .

In addition, we generally consider the fractal surface of tubes; hence, an area-volume relation is  $A_n \propto V_n^{D_2/3}$  [13], where  $D_2$  is the fractal dimension of the surface of tubes and  $V_n$  is the total volume of tubes in the  $n$ th generation. The non-fractal surface is treated as a special case of  $D_2=2$ . Therefore, the effective diffusion area is  $(A_{eff})_n \propto V_n^{\alpha D_2/3}$ . According to structural stability criteria for a tube described in the subsequent section, the tube wall thickness should be proportional to the tube diameter; i.e.,  $h_n \propto d_n$ . Furthermore, using a length distribution  $l_n \propto 2^{-n/4}$  ( $q=1/4$ ) derived in the subsequent section, we have a relation between the total volume  $V_n$  of tubes in the  $n$ th generation and the wall thickness  $h_n$ ; i.e.,  $V_n \propto 2^n d_n^2 l_n \propto 2^{3n/4} d_n^2 \propto 2^{3n/4} h_n^2$ .

Using the estimates  $(A_{eff})_n \propto V_n^{\alpha D_2/3}$ ,  $h_n \propto 2^{-3n/8} V_n^{1/2}$ , and  $C_n \propto V_n^{-\gamma}$  given in Appendix A for the concentration distribution, we have a power-law relation between the total diffusion mass-transfer rate and the total volume of tubes in the  $n$ th generation

$$\dot{m}_n = B_1 2^{3n/8} V_n^{1/s}, \quad (3)$$

where the parameter  $s$  is defined as  $s = (\alpha D_2/3 - \gamma - 1/2)^{-1}$  and  $B_1$  is a positive proportional constant. Setting  $x_n = V_n^{1/s}$ , we have the total diffusion mass-transfer rate of gas across tube walls in the diffusion zone

$$\dot{m}_T = \sum \dot{m}_n = \sum w_n x_n, \quad (4)$$

where the weight coefficients are  $w_n = B_1 2^{3n/8}$ . Thus, an optimization problem is to maximize the cost function  $\dot{m}_T$  subjected by a total volume constraint

$$\sum V_n = \sum x_n^s = B_2, \quad (5)$$

where  $B_2$  is a positive constant.

As shown in Appendix B, for  $s > 1$ , there is an optimum solution to maximize the total mass-transfer rate  $\dot{m}_T$  in the diffusion zone

$$(V_n)_{op}^{1/s} = B_2^{1/s} w_n^{1/(s-1)} \left( \sum w_n^{s/(s-1)} \right)^{-1/s}. \quad (6)$$

Substitution of Eq. (6) into Eq. (3) gives an optimum solution for  $\dot{m}_n$

$$(\dot{m}_n)_{op} = B_1 B_2^{1/s} 2^{3n/8} w_n^{1/(s-1)} \left( \sum w_n^{s/(s-1)} \right)^{-1/s}. \quad (7)$$

Because of  $\dot{m}_n = (\dot{m}_n)_{op}$  at the optimum state, we know the consequences of  $s \rightarrow +\infty$  and  $\gamma = \alpha D_2/3 - 1/2$ . For  $s \rightarrow +\infty$ , the condition  $s > 1$  for the maximum value is always satisfied. Therefore, at the optimum state, the total volume of tubes in the  $n$ th generation is  $(V_n)_{op} \propto 2^{3n/8}$ . Using the relation  $V_n \propto 2^n d_n^2 l_n \propto 2^{3n/4} d_n^2$ , we obtain a diameter distribution at the optimum state for the diffusion zone

$$d_n \propto 2^{-3n/16}. \quad (8)$$

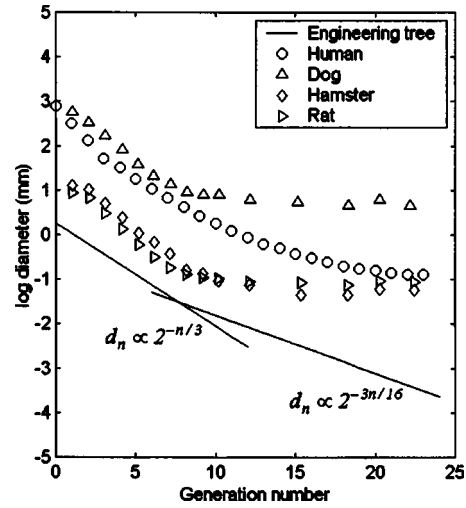


Fig. 2 The theoretical diameter distributions for an engineering bifurcating-tube tree along with measured data for bronchial trees

Interestingly, this result does not depend on the intermediate parameters introduced in the analyses. Figure 2 show the diameter distributions  $d_n \propto 2^{-n/3}$  for the convection zone and  $d_n \propto 2^{-3n/16}$  for the diffusion zone in an engineering tree along with measured data for the bronchial trees of human, dog, hamster, and rat [2,8]. Obviously, unlike the human's bronchial tree, the bronchial trees of dog, hamster, and rat do not follow the theoretical distribution for the diffusion zone in an optimal engineering tree.

We should examine the underlying assumptions made in the above analyses. First, we assume the ad hoc exponential distributions for the diameter and length ( $d_n \propto 2^{-pn}$  and  $l_n \propto 2^{-qn}$ ) in the diffusion zone. From a viewpoint of engineering design, these distributions enjoy simplicity that makes analytical solutions possible. However, we cannot exclude the existence of more complicated solutions for the same optimization problems; therefore, the uniqueness problem of solution is worth further investigation. In Appendix A, to estimate the concentration distribution, a bifurcating-tube tree is considered as a discrete system in which the cross-section-area-averaged concentration is constant in each generation. Further, using an approximation  $C_n \approx (C_{n-1} + C_{n+1})/2$ , we find that the diffusion mass-transfer fluxes into and out a tube along the axial direction are approximately equal; i.e.,  $\Delta f_{n,ax} \approx 0$ . These results are reasonable as first-order approximations. A power-law estimate  $C_n \propto V_n^{-\gamma}$  for the gas concentration in the diffusion zone is another major approximation (see Appendix A). This is based on an exponential function approximation for the asymptotic behavior of a complicated product function in higher generations ( $n \in [0.5N, N]$ ). The fitting error is typically 1–4% in a semi-log plot.

### Length Distribution, Minimum Weight, and Structural Stability

From the viewpoint of structural mechanics, a bifurcating-tube tree can be modeled as an elastic tree on which a single segment is idealized as an elastic tube. Similar to McMahon's analysis of a botanical tree [14], we suppose that an elastic tube must satisfy two necessary elastic criteria to form a stable tree structure under the gravitational force. One criterion is that a tube should be stable when its outer wall is pressed by a certain amount of force. This requires the wall thickness  $h$  of a tube proportional to the tube diameter  $d$ , i.e.,  $h \propto d$ , where the prefactor is related to the critical pressure [15]. Another criterion is that a cantilever tube on a tree cannot exceed a critical length beyond which the tube no longer extends further due to the bending force by its own weight. The

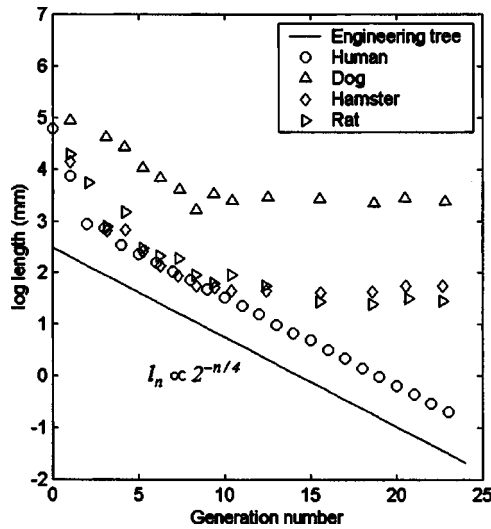


Fig. 3 The theoretical length distribution for an engineering bifurcating-tube tree along with measured data for bronchial trees

critical length for bending obeys a power-law relation  $l_{cr} \propto h^{2/3}$  [14]. If tubes in a tree tend to achieve the maximum length to occupy as large space as possible, a combination of these criteria leads to a length-diameter relation for a single tube  $l \propto l_{cr} \propto h^{2/3} \propto d^{2/3}$ . Furthermore, since the weight of a single tube is  $W \propto ld^2$ , a length-weight relation for a single tube is  $l \propto W^{1/4}$ , which is valid for tubes in all the generations.

An appropriate optimization problem is to minimize the total weight of a tree

$$W_T = \sum (W_T)_n, \quad (9)$$

while the total surface area remains constant, where  $(W_T)_n$  is the net weight of tubes in the  $n$ th generation. According to a area-weight relation  $A_n \propto V_n^{D_2/3} \propto (W_T)_n^{D_2/3}$ , the total surface constraint can be written as

$$\sum (W_T)_n^{D_2/3} = \text{const}, \quad (10)$$

where  $D_2$  is the fractal dimension of the surface. This weight minimization problem is the same max-min problem discussed in B. Because of  $D_2/3 < 1$ , there is an optimum solution to minimize the total weight  $W_T$ , i.e.,

$$[(W_T)_n]_{\text{opt}} = 2^n W_n = \text{const} \quad (11)$$

where  $W_n$  is the weight of a single tube in the  $n$ th generation. Combination of Eq. (11) with a length-weight relation  $l_n \propto W_n^{1/4}$  for structural stability yields a length distribution for a bifurcating-tube tree

$$l_n \propto 2^{-n/4}. \quad (12)$$

Figure 3 show a length distribution  $l_n \propto 2^{-n/4}$  for an engineering tree along with measured data for bronchial trees (human, dog, hamster, and rat) [2,8]. Equation (12) is in good agreement with data for the human bronchial tree, but deviates significantly from data for dog, hamster, and rat.

### Branching Angles

An optimization problem for the branching angle  $\varphi$  is generally formulated for a single bifurcation branch [16–18]; in this sense, the optimum branching angle can be determined independently when the diameter distribution is given a priori. In a study of arterial branching geometry, Zamir [16] proposed four local optimality principles that minimize surface, volume, power, and drag,

respectively. For a symmetrical bifurcation, the optimum branching angles given by the four principles are, respectively,

$$\cos(\varphi) = R_A^{-1} - 1, \quad (\text{min. surface}), \quad (13)$$

$$\cos(\varphi) = 2R_A^{-2} - 1, \quad (\text{min. volume}), \quad (14)$$

$$\cos(\varphi) = R_A^4/2 - 1, \quad (\text{min. power}), \quad (15)$$

$$\cos(\varphi) = R_A^2/2 - 1, \quad (\text{min. drag}), \quad (16)$$

where  $R_A = 2d_{n+1}^2/d_n^2$  is a ratio of the total cross-sectional areas between successive generations. In the convection zone ( $d_n \propto 2^{-n/3}$  and  $R_A \approx 1.26$ ) where all the four principles are plausible, Eqs. (13) and (16) predict the same optimum branching angle  $\varphi \approx 102^\circ$ , while both Eqs. (14) and (15) give  $\varphi \approx 75^\circ$ . For simplicity of design, a single branching angle, such as the average value of the branching angles  $\varphi \approx (75^\circ + 102^\circ)/2 \approx 89^\circ$ , could be used for the convection zone in an engineering bifurcating-tube tree.

For the diffusion zone in which gas diffusion is the dominant physical process, three of the four principles can be excluded. The optimality principles for the minimum power and drag are not strong constraints for the diffusion zone where the Reynolds number (as well as the Péclet number) is small. In addition, the optimality principle for the minimum surface is clearly inapplicable to the diffusion zone where the total mass-transfer rate of gas across tube surfaces should be maximized. Hence, the optimality principle for the minimum volume is the remaining one that seems plausible; in the diffusion zone ( $d_n \propto 2^{-3n/16}$  and  $R_A \approx 1.54$ ), the optimum branching angle given by Eq. (14) is  $\varphi \approx 99^\circ$ .

At the branching angle of  $89^\circ$ , tree branches may intersect with each other after some bifurcations if a tree is strictly two dimensional. Therefore, to avoid such intersections, a tree must be constructed in three-dimensional space by choosing a suitable distribution of the azimuthal rotational angle of a branch with respect to the preceding branch. Since no physical mechanism constrains the azimuthal angle, the determination of a distribution of this angle in a tree can be considered as a pure geometric problem to construct the most compact tree without intersections. This non-trivial problem will be investigated in the future.

### Conclusions

A biologically inspired engineering bifurcating-tube tree, which is divided into the convection and diffusion zones, is designed based on the proposed optimality principles to achieve the most effective gas transport. In the convection zone, the classical diameter distribution  $d_n \propto 2^{-n/3}$  holds for minimizing the energy expenditure of gas transport. In the diffusion zone, the diameter distribution  $d_n \propto 2^{-3n/16}$  is derived based on the optimality principle for maximizing the total diffusion mass-transfer rate of gas across tube walls under a constant total-volume constraint. In addition, the length distribution  $l_n \propto 2^{-n/4}$  is given for the whole tree based on the optimality principle for minimizing the total weight of a tree under a constant total-surface constraint while the elastic criteria for structural stability are satisfied. The estimated optimum branching angles for the convection and diffusion zones are  $89^\circ$  and  $99^\circ$ , respectively.

### Appendix A: Gas Concentration in Bifurcating-Tube Tree

To estimate the gas concentration  $C_n$  in the  $n$ th generation, we consider an ideal cascade process in which a bulk of gas mass sequentially distributes from a lower generation into a higher generation of tubes. From the continuity equation  $\nabla \cdot \mathbf{u} = 0$  for steady incompressible flow, we give a relation for the cross-section-area-averaged axial velocity  $u_n$  in the  $n$ th generation

$$u_n/u_0 = 2^{-n}(d_0/d_n)^2, \quad (\text{A1})$$

where  $d_n$  denotes the tube diameter in the  $n$ th generation. Integrating the mass-transfer equation  $\nabla \cdot (\mathbf{u}C) = -\nabla \cdot \mathbf{f}$  over a volume of a tube in the  $n$ th generation, and applying Gauss theorem and a zero-normal-velocity condition on the periphery wall, we obtain the diffusion mass-transfer flux across the periphery wall for a single tube

$$f_{n,peri} = (d_n/4l_n)\{u_n(C_{n-1} - C_{n+1}) + \Delta f_{n,ax}\}, \quad (\text{A2})$$

where  $\Delta f_{n,ax}$  is a difference between the diffusion mass-transfer fluxes into and out a tube along the axial direction. Here, the flux  $\mathbf{f} = -D_{diff}\nabla C$  is the diffusion mass transfer rate per unit area. When a tube tree is considered as a discrete system in which the cross-section-area-averaged concentration is constant in each generation, an estimate is  $\Delta f_{n,ax} \propto (C_{n-1} - C_n) - (C_n - C_{n+1})$ . Using an approximation  $C_n \approx (C_{n-1} + C_{n+1})/2$ , we know  $\Delta f_{n,ax} \approx 0$ . This means that the diffusion mass-transfer fluxes into and out a tube along the axial direction are approximately equal. Therefore, we have the mass-transfer rate across the effective diffusion surface of tube walls in the  $n$ th generation ( $2^n$  tubes)

$$\dot{m}_n \propto (A_{eff})_n(d_n/l_n)u_n(C_{n-1} - C_n). \quad (\text{A3})$$

As pointed out in the main text, the diffusion mass-transfer rate across tube walls in the  $n$ th generation is also  $\dot{m}_n \propto (A_{eff})_n C_n / h_n \propto (A_{eff})_n C_n V_n^{-1/2} 2^{3n/8}$ . Using the exponential relations  $d_n \propto 2^{-pn}$  and  $l_n \propto 2^{-qn}$  for the diameter and length and  $V_n \propto 2^{\beta n}$  for the total volume of the  $n$ th generation, we have a relation  $C_{n-1} = \varepsilon^{-1}(V_n^\lambda + \varepsilon)C_n$ , where the parameters are  $\lambda = (11/8 - p - q)/\beta - 1/2$  and  $\beta = 1 - 2p - q$ , and  $\varepsilon$  is a positive constant. The parameters  $p$  and  $q$  are to be determined in optimization problems. Furthermore, we have a relation

$$C_0 = \varepsilon^{-n} \prod_{k=1}^n (V_k^\lambda + \varepsilon) C_n, \quad (\text{A4})$$

which describes a cascade process of mass transfer through successive generations of a bifurcating-tube tree. We calculate the function  $\varepsilon^{-n} \prod_{k=1}^n (V_k^\lambda + \varepsilon)$  over a range of generations ( $n \in [0, N]$ ) for different values of the parameters  $\lambda$  and  $\varepsilon$ , and find that the asymptotic behavior of this function for sufficiently higher generations ( $n \in [0.5N, N]$ ) can be reasonably approximated by an exponential function of the generation number  $n$ . The fitting error is typically 1–4% in a semi-log plot. Hence, we have an estimate for the gas concentration in the diffusion zone

$$C_n \propto V_n^{-\gamma}, \quad (\text{A5})$$

where  $\gamma$  is an empirical constant.

## Appendix B: Max-Min Problem

The optimality of an engineering bifurcating-tube tree is related to the following max-min problem. Consider a cost function (per-

formance measure)  $P = \sum_{n=1}^N w_n x_n$  for a system that is characterized by a set of the positive quantities  $\{x_n\} (n=1, 2, \dots, N)$ , where  $\{w_n\}$  are the positive weight coefficients. We want to find the optimum state to maximize or minimize the cost function  $P$  subject to a constraint  $\sum_{n=1}^N x_n^s = B$ , where  $B$  is a positive constant and  $s$  is a positive exponent. For  $s \neq 1$ , the use of the Lagrange-multiplier method gives an optimum solution

$$(x_n)_{op} = B^{1/s} w_n^{1/(s-1)} \left( \sum_{n=1}^N w_n^{s/(s-1)} \right)^{-1/s}, \quad (n=1, 2, \dots, N). \quad (\text{B1})$$

When  $s > 1$ , Eq. (B1) gives the optimum state maximizing the cost function  $P$ , while it minimizes  $P$  when  $s < 1$ . Particularly, for  $w_n = 1$ , the optimum solution is simply  $(x_n)_{op} = B^{1/s} N^{-1/s} = \text{const}$ . The consequence of the above analysis is used to formulate the optimality principles for the design of an engineering bifurcating-tube tree.

## References

- [1] Weibel, E. R., and Gomez, D. M., 1962, "Architecture of the Human Lung," *Science*, **137**, pp. 577–585.
- [2] Weibel, E. R., 1963, *Morphometry of the Human Lung*, Academic, New York.
- [3] Murray, C. D., 1926, "The Physiological Principle of Minimum Work," *Proc. Natl. Acad. Sci. U.S.A.*, **12**, pp. 207–214.
- [4] Horsfield, K., and Cumming, G., 1967, "Angles of Branching and Diameters of Branches in the Human Bronchial Tree," *Bull. Math. Biophys.*, **29**, pp. 245–259.
- [5] Horsfield, K., Dart, G., Olson, D. E., Filley, G. F., and Cumming, G., 1971, "Models of the Human Bronchial Tree," *J. Appl. Physiol.*, **31**, pp. 201–217.
- [6] Horsfield, K., 1990, "Diameters, Generations, and Orders of Branches in the Bronchial Tree," *J. Appl. Physiol.*, **68**, pp. 457–461.
- [7] Wilson, T. A., 1967, "Design of the Bronchial Tree," *Nature (London)*, **18**, pp. 668–669.
- [8] West, B. J., Bhargava, V., and Goldberger, A. L., 1986, "Beyond the Principle of Similitude: Renormalization in the Bronchial Tree," *J. Appl. Physiol.*, **60**, pp. 1089–1097.
- [9] West, B. J., and Goldberger, A. L., 1987, "Physiology in Fractal Dimensions," *Am. Sci.*, **75**, pp. 354–365.
- [10] Rashevsky, N., 1960, *Mathematical Biophysics—Physico-mathematical Foundation of Biology*, Dover, New York, Vol. 2, Chap. XXVI.
- [11] LaBarbera, M., 1990, "Principles of Design of Fluid Transport Systems in Zoology," *Science*, **249**, pp. 992–1000.
- [12] LaBarbera, M., 1993, "Optimality in Biological Fluid Transport Systems," In *Fluid Dynamics in Biology, Contemporary Mathematics*, A. Y. Cheer and C. P. van Dam, eds., American Mathematical Society, Providence, RI, Vol. 141, pp. 565–586.
- [13] Mandelbrot, B. B., 1982, *The Fractal Geometry of Nature*, Freeman, New York, Chaps. 12 and 17.
- [14] McMahon, T., 1973, "Size and Shape in Biology," *Science* **179**, pp. 1201–1204.
- [15] Timoshenko, S., and Goodier, N., 1951, *Theory of Elasticity* (2nd ed.), McGraw-Hill, New York.
- [16] Zamir, M., 1976, "Optimality Principles in Arterial Branching," *J. Theor. Biol.*, **62**, pp. 227–251.
- [17] Uylings, H. B. M., 1977, "Optimization of Diameters and Bifurcation Angles in Lung and Vascular Tree Structures," *Bull. Math. Biol.*, **39**, pp. 509–520.
- [18] Roy, A. G., and Woldenberg, M. J., 1982, "A Generalization of the Optimal Models of Arterial Branching," *Bull. Math. Biol.*, **44**, pp. 349–360.

# New Physically Based Approach of Mass Conservation Correction in Level Set Formulation for Incompressible Two-Phase Flows

**Snehamoy Majumder**

Department of Mechanical Engineering,  
Jadavpur University,  
Calcutta-700032, India

**Suman Chakraborty**

Member, ASME  
Department of Mechanical Engineering,  
Indian Institute of Technology,  
Kharagpur-721302, India  
e-mail: suman@mech.iitkgp.ernet.in

*A novel physically based mass conservation model is developed in the framework of a level set method, as an alternative to the Heaviside function based formulation classically employed in the literature. In the proposed "volume fraction based level set approach," expressions for volume fraction function for each interfacial computational cell are developed, and are subsequently correlated with the corresponding level set functions. The volume fraction function, derived from a physical basis, is found to be mathematically analogous to the Heaviside function, except for a one-dimensional case. The results obtained are compared with the benchmark experimental and numerical results reported in the literature. Finally, transient evolution of a circular bubble in a developing shear flow and rising bubbles in a static fluid, are critically examined. The Cox angle and the deformation parameter characterizing the bubble evolution are critically examined. An excellent satisfaction of the mass conservation requirements is observed in all case studies undertaken. [DOI: 10.1115/1.1899172]*

## 1 Introduction

A large variety of engineering problems involves interaction of two fluid phases across a continuously evolving interface, which includes motion of droplets and bubbles in channels, motion of blood cells in capillary tubes, free surface deformation of a molten arc-weld pool, evolution of active interfaces under chaotic mixing conditions of two immiscible fluids, etc. A common characteristic of all such problems is that a jump in the flow properties like density and/or viscosity exists across the interface, and transient evolution of the field variables strongly depends on the resultant inter-fluid interaction mechanisms. Therefore, an accurate and physically based computation of interface evolution is critical for successful solution of these problems.

Classically, two broad types of interface-evolution algorithms have been employed by researchers in their multiphase flow prediction procedures [1], namely, the "front-tracking method" [2], and the "volume tracking approach." The so-called "volume-of-fluid (VOF) method" [3] evolved as a variant of the volume tracking approach, which tracks the motion of the interior region rather than the boundary of the evolving front. Although complicated topological boundaries can be handled in this method, it is difficult to calculate curvature of the front from such representation of boundaries. Additionally, extension of this algorithm to three-dimensional problems is not straightforward. Such limitations are greatly overcome through a class of techniques commonly known as the "level set method," originally introduced in this context by Osher and Sethian [4]. This method relies on a level set partial differential equation to describe the motion of a propagating interface, which may be approximated by borrowing technology from numerical solution of hyperbolic conservation laws. By viewing the interface as a level set, this method handles topological complexities of the evolving front naturally, yielding a correct limiting entropy-satisfying solution. Sussman et al. [5] used this approach for computing solutions of incompressible and immiscible two-phase flow. However, mass of the bubble was not con-

served in their implementation. Chang et al. [6] first proposed an effective conservation of mass approach appropriate for level set formulation. Kaliakatos and Tsangaris [7] employed the Heaviside-function approach as a measure of the pertinent level set "distance function" that effectively interpolates fluid properties for simulation of motion of deformable drops in pipes and channels. Sussman et al. [8] further improved the level set method by introducing an iterative procedure to conserve mass locally. However, their formulations were not very successful in ensuring mass conservation. Bourlioux [9] introduced a coupled level set and volume-of-fluid (CLSVOF) method for tracking material interfaces, and exploited a combination of the superior mass preservation characteristic of the VOF approach with a superior topology preservation property of the level set method. Sussman and Puckett [10] subsequently developed a three-dimensional and axisymmetric CLSVOF method for computing incompressible two-phase flows with large density ratios, utilizing the inherent essence of CLSVOF. Son and Hur [11] also developed a CLSVOF approach for buoyancy driven flows. Later, Sussman [12] proposed a second order CLSVOF method, in an effort to obtain more accurate solutions to generic interface evolution problems. It can be noted here that all the above authors effectively used the Heaviside function to correct local mass imbalances, without resorting to any kind of physical basis. Further, major difficulties can be encountered in the implementation of the CLSVOF method, with respect to the reconstruction of the interface, for accurate advection of the VOF function and reinitialization of the level set function.

Deviating from the abovementioned Heaviside function based approach, Shin and Juric [13] modeled a three-dimensional multiphase flow involving changes in phase, using a front tracking method. Their mass correction procedure essentially employed the continuity equation, coupled with an interfacial mass flux [14]. However, for evaluation of the material properties, they used an indicator function, which is equivalent to the Heaviside function. Enright et al. [15], for the first time, used a hybrid particle level set method for interface capturing. Their method employed Lagrangian marker particles to rebuild the level set function, based on a basic principle that the marker particle should not cross the interface unless it is computed wrongly. However, this method is not easy and convenient to implement.

Contributed by the Fluids Engineering Division for publication in the JOURNAL OF FLUIDS ENGINEERING. Manuscript received by the Fluids Engineering Division April 8, 2004; revised manuscript received March 7, 2005. Associate Editor: S. Balachandra.



It can be noted here that although the mass correction approaches, mentioned as above, mathematically smoothen out discontinuities across the artificially smeared interface, no pertinent physical basis can be directly established. Consequently, the resultant “correction” terms employed for enforcing local mass conservation in the vicinity of the interface are not physically based, although they are mathematically “intuitive.” The aim of the present work, accordingly, is to develop and establish a new physically based approach (which can be termed as a volume-fraction level set approach) as an alternative mathematical formulation of the Heaviside function classically employed for property evaluation and mass conservation correction. This is effectively achieved by developing expressions for volume fraction in each computational cell that can distinctively identify the pertinent phases and their properties, and effectively replace the Heaviside function. In other words, role of each phase on the physical behavior and mathematical calculations is directly represented by identifying their relative quantitative presence in an elemental control volume. The physical basis of this approach lies in the fact that logically the volume fraction, which is a relative quantitative measure of amount of fluid in a control volume, is much more relevant than any other physical quantities to be used for interpolation of physical properties.

## 2 Mathematical and Numerical Modeling

For mathematical analysis, we assume a system of two fluid phases constituting a two-dimensional domain. The individual fluid phases are assumed to be incompressible, but deformable in shape on account of shear stresses prevailing between various fluid layers as well as fluid-solid interfaces. We assume the flow field to be two dimensional and laminar.

### 2.1 Governing Equations. Continuity:

$$\frac{\partial \rho}{\partial t} + \frac{\partial(\rho u_j)}{\partial x_j} = 0 \quad (1)$$

**Momentum:**

$$\rho \frac{\partial u_i}{\partial t} + \rho u_j \frac{\partial u_i}{\partial x_j} = \frac{\partial}{\partial x_j} \left( \mu \frac{\partial u_i}{\partial x_j} \right) - \frac{\partial p}{\partial x_i} + \rho g_i + \sigma \kappa(\phi) \nabla \phi \delta(\phi) \quad (2)$$

( $i, j = 1, 2$ )

It can be noted here that the Dirac delta function is replaced by volume fraction in our formulation. In this formulation, a scalar variable, called the level set function, is used to identify the interface between the two phases, and consequently, to act effectively as the distance function. Since the interface between the two fluid phases may be assumed to be advected by the fluid motion, the equation governing “transport” of the interface can be written as

$$\frac{\partial \phi}{\partial t} + u_j \frac{\partial \phi}{\partial x_j} = 0 \quad (3)$$

where  $\phi(x_j, t)$  is the so-called “level set function” prescribing position of interface at any specified time instant. Following the suggestion of Sussman et al. [8],  $\phi$  is taken here to be the normal distance of the pertinent location from the interface. To be specific, if the value of  $\phi$  at the interface is taken to be zero (as adopted in the present study),  $\phi$  effectively becomes a “distance function” satisfying

$$|\nabla \phi| = 1 \quad (4)$$

Since the value of  $\phi$  at the interface is zero,  $\phi$  has opposite signs in the two phases of concern. It is extremely important to recognize here that for the level set formulation to work properly,  $\phi$  must remain a distance function at all instants of time within the time domain of interest. Although this seems to be rather obvious, this is by no means trivially satisfied by the mathematical formulation, since the physical notion of distance function is not explicitly justified by sole description of the governing differential equa-

tion for advection of  $\phi$ . In fact, this can only be ensured at the initial time when the location of the interface is explicitly known and the values of  $\phi$  at all other points of interest are accordingly calculated. The values of  $\phi$  at subsequent time instants are calculated by using Eq. (3). Although the interface is still represented by the reference value, the other values of  $\phi$  as obtained out of solution of the abovementioned equation might not be the corresponding distances from the interface. In order to resolve this situation, another scalar variable needs to be introduced and subsequently solved. This variable ( $\psi$ ) must be physically constrained to constitute a distance function having the same interface value as  $\phi$ . In effect, a physically realistic and consistent solution for  $\psi$  at the end of a discretized time step can be arrived at by obtaining a pseudo steady state solution for the following transient transport equation of  $\psi$  ( $\bar{T}$  being a pseudo-time variable):

$$\frac{\partial \psi}{\partial \bar{T}} = \text{Sign}(\psi)(1 - |\nabla \psi|) \quad (5)$$

$$\text{where } |\nabla \psi| = \sqrt{(\psi_x^2 + \psi_y^2)} \quad (6)$$

Equation (5) is subjected to the following initial condition:

$$\psi(\mathbf{x}, 0) = \phi(\mathbf{x}, t + \Delta t) \quad (7)$$

It is clear from Eq. (5) that the “pseudo steady state” solution of the same satisfies Eq. (3), and hence it can be interpreted as the desired distance function. The initial value of  $\psi$  effectively ensures that the interface value of the same is identical to the interface value of  $\phi$ . As a result, the pseudo steady state values of  $\psi$  are the values of  $\phi$  at the time instant  $t + \Delta t$ .

**2.2 Interpolation of Interface Properties and Formulation for Mass Correction.** It can be noted here that the success of mass correction effected by Eq. (5) depends on the accuracy of interpolation of physical properties such as density across the interface and representation of the same in mass correction formula. Classically, this has been mathematically postulated by calculating a property  $\xi$  (such as density, viscosity etc.) within a control volume as

$$\xi = [1 - H(\phi)]\xi_1 + H(\phi)\xi_2 \quad (8)$$

where  $H(\phi)$  is the so-called Heaviside function. The exact value of a property in a control volume, however, depends on the choice of the Heaviside function. In the literature, to date, different approximations have been followed in this regard leading to various forms of the Heaviside function [6,8]. It can well be recognized here that although different choices of Heaviside function satisfy certain mathematical requirements for accommodating jump conditions across an interface, they are, by no means, obtained from any physical basis. Therefore, there is no guarantee that a mass correction formula incorporating such a function would automatically lead to the desired mass conservation, although mathematically they might all ensure asymptotic stability criteria. Accordingly, in place of the Heaviside function, we propose to use the concerned phase volume fractions as appropriate interpolating parameters. The basic idea of this proposition is based on the fact that the mass within a control volume is proportional to the volume fraction and density. Therefore, the basic task here boils down to correlate the volume fraction  $H_V$  to the distance function  $\phi$ . In the present work, this is systematically developed as follows. First, the volume fraction for a one-dimensional control volume is presented. This is followed by the formulation of the volume fraction for a two-dimensional control volume.

**2.2.1 One-Dimensional Control Volume.** Figure 1 illustrates the one-dimensional geometry for a control volume whose size is  $\Delta X$ . Cartesian coordinates are used in this demonstration. For the purpose of demonstration and without loss of generality, let us consider a situation where phase 1 occupies the  $\phi < 0$  region and phase 2 occupies the  $\phi > 0$  region. In Fig. 1,  $\mathbf{w}$  and  $\mathbf{e}$  represent the

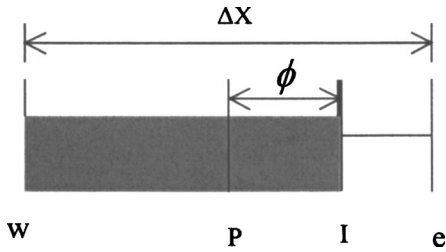


Fig. 1 One-dimensional control volume with fluid interface at I

left (west) boundary, and right (east) boundary of the control volume. **P** and **I** represent the central node of the control volume and position of the interface, respectively. The fluid for which the volume fraction is being sought fills up the space between **I** and **w** and the distance between **P** and **I** is the distance function  $\phi$ .

The equation for the one-dimensional volume fraction for Fig. 1 is given by

$$H = 0.5 + \frac{\phi}{\Delta X} \quad (9)$$

**2.2.2 Two-Dimensional Control Volume.** The control volume in a two-dimensional flow field has the length and breadth as  $\Delta X$  and  $\Delta Y$ , respectively. The volume fraction for such case is dependent on the orientation of the interface (the interface is considered to be linear within the cells) in the control volume. The orientation can be of different type depending how the interface intersects the control volume sides and accordingly the angle ( $\theta$ ) between the vertical central line of the control volume and perpendicular from the center of the control volume to the interface changes. There can be two major orientations, namely, when the interface intersects adjacent sides and when it intersects opposite sides. Each of these two orientations may again correspond to different interface configurations, which need to be addressed separately, and the resultant conclusions are to be combined to develop a generalized formulation that is valid under all situations. This is achieved in the present study by detailed analysis of the various possible cases, to be described as follows.

**Case I (Refer to Fig. 2 for pertinent interfacial orientation).** In Fig. 2, the perpendicular from  $O$  to  $A_1A_3$  (i.e., the interface) or the perpendicular distance  $OA_1$  is the level set value at the center of the control volume (i.e., at  $O$ ) and it is denoted by  $\phi$ . The angle between the centerline of the control volume  $OO_1$  and  $OA_1$  is denoted by  $\theta$ . In effect, the volume fraction  $H_V$  needs to be prescribed as  $H_V = f(\phi, \theta)$ . First, let us consider  $\phi > 0$ , so that we have  $H_V > 0.5$ . Now, volume of the triangle  $A_1A_2A_3 = \frac{1}{2}(B+C)E$ , where,  $B = A_2A_0$ ,  $C = A_0A_1$ , and  $E = A_2A_3$ .

Or, volume of the fluid  $= \frac{1}{2}(B+C)^2 \tan \theta$

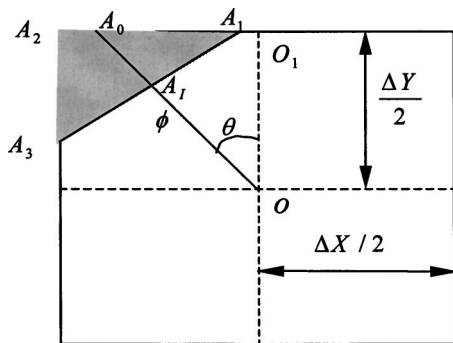


Fig. 2 Orientation of an interface cutting the adjacent sides of the control volume,  $A_1A_2 > A_2A_3$  and  $A_1A_2 < \Delta X/2$ ,  $A_2A_3 < \Delta Y/2$

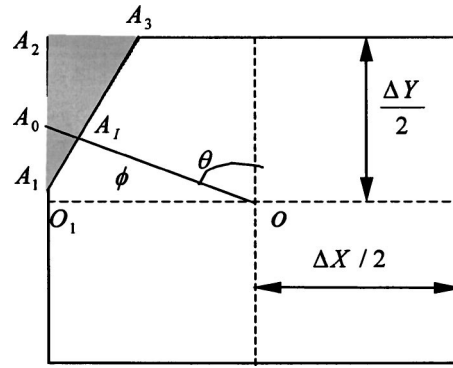


Fig. 3 Orientation of an interface cutting the adjacent sides of the control volume,  $A_1A_2 > A_2A_3$  and  $A_1A_2 < \Delta X/2$ ,  $A_2A_3 < \Delta Y/2$

Hence,  $H_V = 1.0 - \frac{1}{2}(B+C)^2 \tan \theta / (\Delta X \Delta Y)$   
On further simplification, we obtain

$$H_V = 1.0 - H_1, \quad \text{where}$$

$$H_1 = a(|\phi|)^2 + b(|\phi|) + c \quad (10)$$

In the above expression

$$a = \frac{1}{\sin 2\theta(\Delta X \Delta Y)}, \quad b = -\frac{(\Delta Y \cos \theta + \Delta X \sin \theta)}{\sin 2\theta(\Delta X \Delta Y)} \quad \text{and}$$

$$c = \frac{(\Delta Y \cos \theta + \Delta X \sin \theta)^2}{4 \sin 2\theta(\Delta X \Delta Y)}$$

It also follows from the above that

$$\text{or } \phi = \left( \frac{\Delta X}{2} - \frac{\Delta Y}{2} \tan \theta + \frac{\Delta Y}{2 \sin \theta \cos \theta} \mp \sqrt{2(1.0 - H_V)(\Delta X \Delta Y) / \tan \theta} \right) \sin \theta \quad (10a)$$

Next, let us consider  $\phi < 0$ , so that we have  $H_V < 0.5$ . Here,

$$H_V = \frac{1}{2} \left( \frac{\Delta X}{2} - \frac{\Delta Y}{2} \tan \theta + \frac{\Delta Y}{2 \sin \theta \cos \theta} - \frac{|\phi|}{\sin \theta} \right)^2 \tan \theta / (\Delta X \Delta Y) \quad (11)$$

Now, following analogous inverse methods for reevaluation of  $\phi$  (as depicted for  $\phi > 0$  case), we get

$$|\phi| = \left( \frac{\Delta X}{2} - \frac{\Delta Y}{2} \tan \theta + \frac{\Delta Y}{2 \sin \theta \cos \theta} \mp \sqrt{2H_V(\Delta X \Delta Y) / \tan \theta} \right) \sin \theta \quad (12)$$

where  $\phi = -|\phi|$ .

**Case II (Refer to Fig. 3 for pertinent interfacial orientation).** First, let us consider  $\phi > 0$ , so that,  $H_V > 0.5$ .

Here,

$$H_V = 1.0 - \frac{1}{2}(B+C)^2 \cot \theta / (\Delta X \Delta Y)$$

Substitution of various geometrical parameters in the above expression, as before, yields

$$H_V = 1.0 - \frac{1}{2} \left( \frac{\Delta Y}{2} - \frac{\Delta X}{2} \cot \theta + \frac{\Delta X}{2 \sin \theta \cos \theta} - \frac{\phi}{\cos \theta} \right)^2 \cot \theta / (\Delta X \Delta Y) \quad (13)$$

Now, following inverse methods for reevaluation of  $\phi$ , we get from Eq. (13)

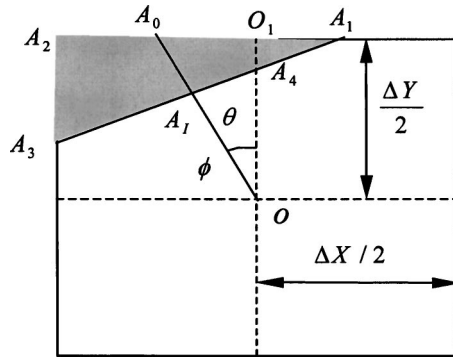


Fig. 4 Orientation of an interface cutting the adjacent sides of the control volume,  $A_1A_2 > A_2A_3$  and  $A_1A_2 > \Delta X/2$ ,  $A_2A_3 < \Delta Y/2$

$$\phi = \cos \theta \left( \frac{\Delta Y}{2} - \frac{\Delta X}{2} \cot \theta + \frac{\Delta X}{2 \sin \theta \cos \theta} \mp \sqrt{2(1.0 - H_V)\Delta X \Delta Y / \cot \theta} \right) \quad (14)$$

Next, let us consider  $\phi < 0$ , so that  $H_V < 0.5$ . Here,

$$H_V = \frac{\cot \theta}{2} \left( \frac{\Delta Y}{2} - \frac{\Delta X}{2} \cot \theta + \frac{\Delta X}{2 \sin \theta \cos \theta} - \frac{|\phi|}{\cos \theta} \right)^2 / (\Delta X \Delta Y) \quad (15)$$

Now, following analogous inverse methods for reevaluation of  $\phi$ , we get from Eq. (15)

$$|\phi| = \left( \frac{\Delta Y}{2} - \frac{\Delta X}{2} \cot \theta + \frac{\Delta X}{2 \sin \theta \cos \theta} \mp \sqrt{2H_V \Delta X \Delta Y / \cot \theta} \right) \cos \theta \quad (16)$$

and  $\phi = -|\phi|$

Case III (Refer to Fig. 4 for pertinent interfacial orientation). When,  $\phi > 0$ ,  $H_V > 0.5$ , we have, for this case

$$H_V = 1.0 - \frac{1}{2}(B + C + D)^2 \tan \theta / (\Delta X \Delta Y)$$

Proceeding in a similar manner as outlined before, for the present case it follows that

$$H_V = 1.0 - \frac{1}{2} \left( \frac{\Delta X}{2} + \frac{\Delta Y}{2 \tan \theta} - \frac{\phi}{\cos \theta \tan \theta} \right)^2 \tan \theta / (\Delta X \Delta Y) \quad (17)$$

Now, following analogous inverse methods for reevaluation of  $\phi$  as before, we get from Eq. (17)

$$\phi = \sin \theta \left( \frac{\Delta X}{2} + \frac{\Delta Y}{2 \tan \theta} \mp \sqrt{2(1 - H_V)\Delta X \Delta Y / \tan \theta} \right)$$

Next, let us consider  $\phi < 0$ ,  $H_V < 0.5$ . Here,

$$H_V = \frac{1}{2} \left( \frac{\Delta X}{2} + \frac{\Delta Y}{2 \tan \theta} - \frac{|\phi|}{\cos \theta \tan \theta} \right)^2 \tan \theta / (\Delta X \Delta Y) \quad (18)$$

The inverse methods for reevaluation of  $\phi$ , as applied to Eq. (18), yield

$$|\phi| = \sin \theta \left( \frac{\Delta X}{2} + \frac{\Delta Y}{2 \tan \theta} \mp \sqrt{2H_V \Delta X \Delta Y / \tan \theta} \right) \quad (19)$$

i.e.,  $\phi = -|\phi|$ .

Case IV (Refer to Fig. 5 for pertinent interfacial orientation). First, let us consider  $\phi > 0$ , i.e.,  $H > 0.5$ . For this case, we get

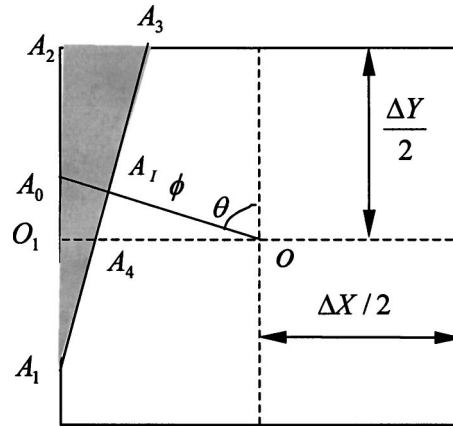


Fig. 5 Orientation of an interface cutting the adjacent sides of the control volume,  $A_1A_2 > A_2A_3$  and  $A_1A_2 < \Delta X/2$ ,  $A_2A_3 > \Delta Y/2$

$$H_V = 1.0 - \frac{1}{2} \left( \frac{\Delta Y}{2} + \frac{\Delta X}{2 \cot \theta} - \frac{\phi}{\sin \theta \cot \theta} \right)^2 \cot \theta / (\Delta X \Delta Y) \quad (20)$$

Now, applying inverse method for reevaluation of  $\phi$  on Eq. (20) we get

$$\phi = \cos \theta \left( \frac{\Delta Y}{2} + \frac{\Delta X}{2 \cot \theta} \mp \sqrt{2(1 - H_V)\Delta X \Delta Y / \cot \theta} \right)$$

Next, let us consider the case with  $\phi < 0$ , i.e.,  $H_V < 0.5$ .

Necessary evaluation of pertinent geometrical parameters, for this case, reveals

$$H_V = \frac{1}{2} \left( \frac{\Delta Y}{2} + \frac{\Delta X}{2 \cot \theta} - \frac{|\phi|}{\sin \theta \cot \theta} \right)^2 \cot \theta / (\Delta X \Delta Y) \quad (21)$$

Also, applying the inverse method for reevaluation of  $\phi$ , we get

$$|\phi| = \cos \theta \left( \frac{\Delta Y}{2} + \frac{\Delta X}{2 \cot \theta} \mp \sqrt{2H_V \Delta X \Delta Y / \cot \theta} \right) \quad (22)$$

and,  $\phi = -|\phi|$ .

Case V (Refer to Fig. 6 for pertinent interfacial orientation). From Fig. 6 it can be observed that Case V is identical with Case III, so far as formulation of the Heaviside function is concerned.

Case VI (Refer to Fig. 7 for pertinent interfacial orientation). This case, as apparent from Fig. 7, is identical with case IV, and the same Heaviside functions hold good here.

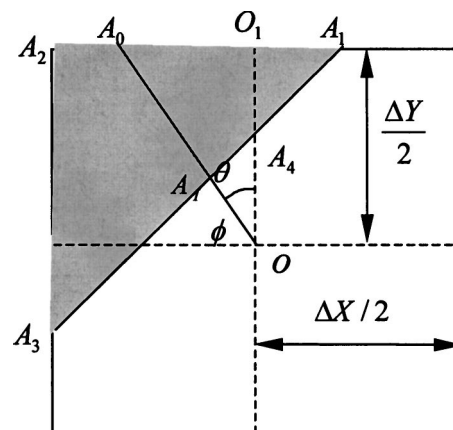


Fig. 6 Orientation of an interface cutting the adjacent sides of the control volume,  $A_1A_2 > A_2A_3$  and  $A_1A_2 > \Delta X/2$ ,  $A_2A_3 > \Delta Y/2$

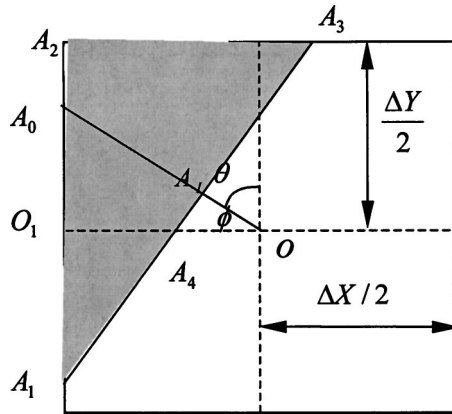


Fig. 7 Orientation of an interface cutting the adjacent sides of the control volume,  $A_1 A_2 > A_2 A_3$  and  $A_1 A_2 > \Delta X / 2$ ,  $A_2 A_3 > \Delta Y / 2$

Case VII (Refer to Fig. 8 for pertinent interfacial orientation). For this case, first let us consider  $\theta > 0$ , so that,  $H_V > 0$ . Carrying out the necessary steps, it follows that

$$H_V = \frac{1}{2} + \frac{\phi}{\sin \theta \Delta X} \quad (23)$$

For the situation of interface cutting vertically opposite sides, we may refer to Fig. 9, and analogous calculations reveal that

$$H_V = \frac{1}{2} + \frac{\phi}{\Delta Y \cos \theta} \quad (24)$$

**2.3 Mass Correction.** As already mentioned, solution of Eqs. (3) and (5) does not guarantee the satisfaction of conservation of mass. To account the mass loss or gain out of numerical artifacts in interface representation, a new methodology is introduced here. In this situation, a mass correction term ( $M_{cor}$ ) needs to be formulated that enforces satisfaction of conservation of mass to the limit of computational precision desired. For the purpose of this discussion, let the reference phase be the phase with  $\phi \geq 0$  and  $\rho = \rho_2$ . The total mass of this phase of the fluid is

$$M = \sum \rho_2 (H_V) \Delta X \Delta Y \quad (25)$$

In the case of mass imbalance, there are two possible cases. These are:

- (i) mass loss, in which case addition of mass ( $M_{cor} > 0$ ) will ensure mass conservation, and
- (ii) mass surplus, in which case removal of mass ( $M_{cor} < 0$ ) will lead to mass conservation. Therefore  $M_{cor}$  can be written as

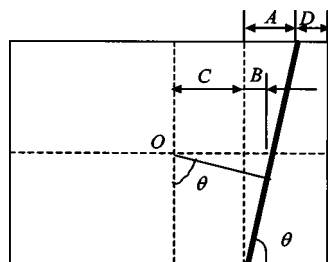


Fig. 8 Interface cutting opposite horizontal sides

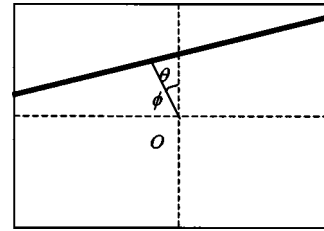


Fig. 9 Interface cutting vertical opposite sides

$$M_{cor} = M_O - M_C = \sum \rho_2 H_{VO} \Delta X \Delta Y - \sum \rho_2 H_{VC} \Delta X \Delta Y \quad (26)$$

where  $M_O$ ,  $M_C$  and  $H_{VO}$ ,  $H_{VC}$  are mass and volume fraction function at time,  $t=0$  and  $t=t+\Delta t$  respectively. It can be noted here that since the function  $H_V$  is now physically derived from basic considerations of volume fraction, the mass correction formula represented by Eq. (26) is a physically consistent measure of the satisfaction of mass conservation for constituent phases present in the domain. The concerned mass correction procedure can be broadly outlined as follows:

- (1) First, the control volumes containing the interface are identified. Let the number of such control volumes be  $N$ ;
- (2) The volume fractions at the above control volumes are calculated by the appropriate expressions;
- (3) Current instantaneous mass ( $m_{ins}$ ) of each such control volumes and total current mass ( $M_{ins}$ ) of all  $N$  such control volumes are calculated using Eq. (25), and the mass correction ( $M_{cor}$ ) is obtained;
- (4) A fraction of the correction mass ( $=m_{ins}/M_{cor}M_{ins}$ ) proportional to its current instantaneous mass is added or deducted to each such control volume depending on whether  $M_{cor}$  is positive or negative, respectively;
- (5) The volume fractions are re-calculated with the new mass (old mass+distributed or deducted mass); and
- (6) From the updated volume fraction, the corrected distance function is reevaluated by inverse method.

It can be noted here that in this entire mass correction procedure the interface geometry is modeled by piecewise line segments, which is first order accurate [i.e.,  $O(\Delta X)$ ], intercepting some of the computational control volumes. However, while redistributing the deficit mass or subtracting the excess mass for implementation of the mass correction formulation, position of the interface may change. In that respect, the mass balance (correction) may have to be distributed to the more than one adjacent control volumes, depending on the respective interface conditions after redistribution of the excess or less mass. This is because, while adding or subtracting the mass, the new volume fraction may become more than unity or less than zero, which is physically unrealistic, and this issue needs to be addressed with care. For example, in Fig. 10(a), the "dashed line" indicates the position of

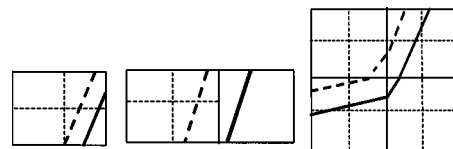


Fig. 10 (a) Change of interface within control volume. (b) Change of interface to the next control volume. (c) Change of interface adjacent control volumes

interface without mass correction, while the continuous thick line represents the corrected interface. Similar adjustments need to be made in other cases as well.

**2.4 Overall Solution Procedure.** The solution procedure adopted for the coupled equations consistent with the present formulation can be summarized as follows:

- (1) specify the location of the interface(s) at time  $t=0$ ;
- (2) calculate the normal distance for all nodes from the interface;
- (3) specify the properties at all nodes using Eq. (8);
- (4) solve the continuity and momentum conservation equations [given by Eqs. (1) and (2)] at  $t=t+\Delta t$ ;
- (5) solve for  $\phi$  [Eq. (3)] using the velocities obtained in step 4;
- (6) solve for the pseudo steady state  $\psi$  [Eq. (5)] using the values of  $\phi$  from step 5 as the initial values;
- (7) set  $\phi(\mathbf{x}, t+\Delta t) = \psi(\mathbf{x})$ ; and
- (8) Repeat steps 3–7 for all time steps.

It can be noted here that the governing differential equations, coupled with appropriate boundary conditions, are solved using a pressure based finite volume method, as per the SIMPLER algorithm [16]. Convection-diffusion terms in the conservation equations are discretized using the power law [16] scheme.

### 3 Results and Discussions

**3.1 Comparisons of Heaviside Function and Volume Fraction Function.** In order to mathematically compare the Heaviside function and the corresponding volume fraction developed in the present study, they are plotted against the normalized distance functions for various cases investigated, as shown in Figs. 11–14. In constructing all of the figures, the following parameters are considered:  $h=0.001$ ,  $\Delta X=\Delta Y=h$ . It is apparent from Fig. 11(b) that even with the same interface width, the two functions are not matching each other, for the one-dimensional case. However, an

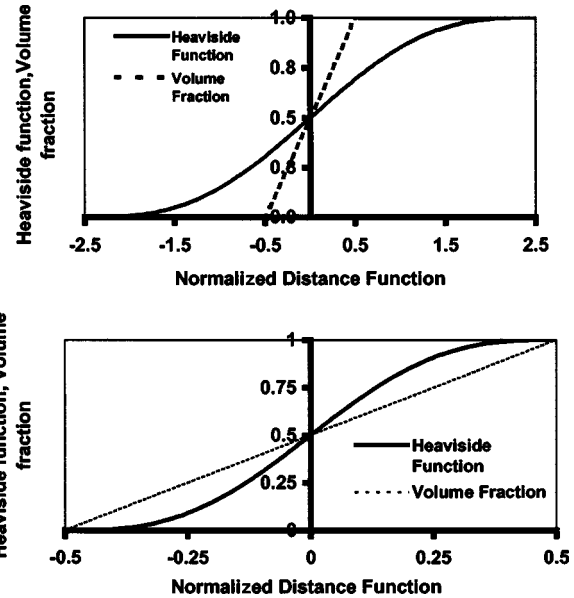


Fig. 11 (a) Distribution of Heaviside function and volume fraction function for one-dimensional case. Interface width is taken as  $2.5h$  for Heaviside function and  $h$  for volume fraction function. (b) Distribution of Heaviside function and volume fraction function for one-dimensional case. Interface width is taken as  $h$  for both Heaviside function and volume fraction function.

excellent agreement of these two functions for the same interface width can be obtained for the two-dimensional cases, as apparent from Figs. 12(b), 13(b), and 14(b). A strong dependence of the above two functions on interface width is also very clear from Figs. 12(a), 13(a), and 14(a).

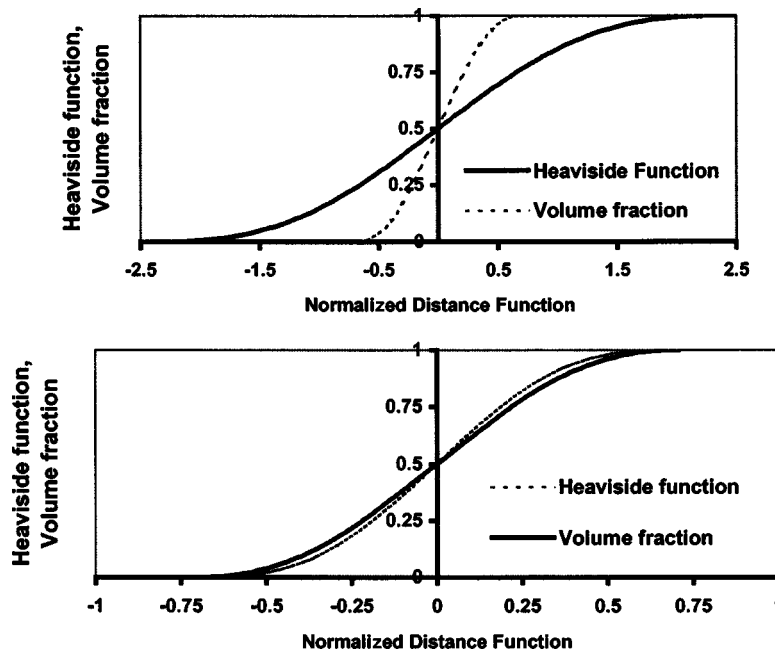


Fig. 12 (a) Distribution of Heaviside function and volume fraction function for two-dimensional case with  $\theta=30^\circ$ . Interface width is taken as  $2.5h$  for Heaviside function and  $h$  for volume fraction function. (b) Distribution of Heaviside function and volume fraction function for two-dimensional case with  $\theta=30^\circ$ . Interface width is taken as  $h$  for both Heaviside function and volume fraction function.

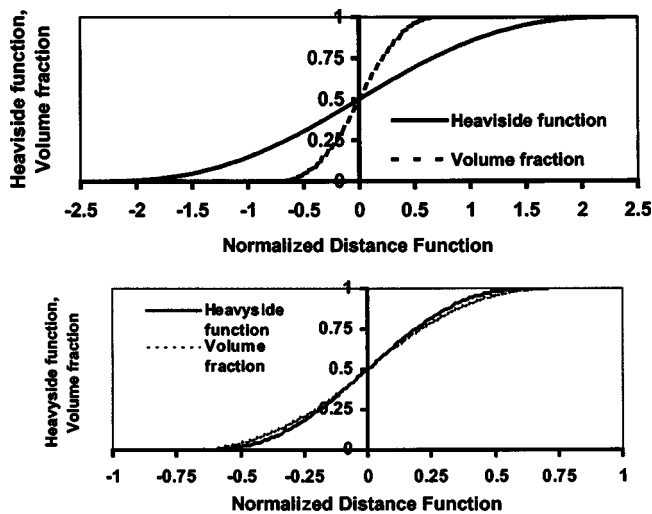


Fig. 13 (a) Distribution of Heaviside function and volume fraction function for two-dimensional case with  $\theta=45^\circ$ . Interface width is taken as  $2.5 h$  for Heaviside function and  $h$  for volume fraction function. (b) Distribution of Heaviside function and volume fraction function for two-dimensional case with  $\theta=45^\circ$ . Interface width is taken as  $h$  for both Heaviside function and volume fraction function.

**3.2 Model Validation and Representative Case Studies.** In order to validate the mathematical model developed here, results from the present method are compared with reported experimental data on collapsing water column by Martin and Moyce [17] and Koshizuka et al. [18]. Figure 15 shows the dimensions and features of the experimentation. In Fig. 16, the nondimensional height of the collapsing water column is plotted with respect to the nondimensional time. The numerical solutions are carried out using  $41 \times 22$  and  $82 \times 44$  grids. Although at  $t=2$  the experimental column height began to decrease slightly faster, it is observed that

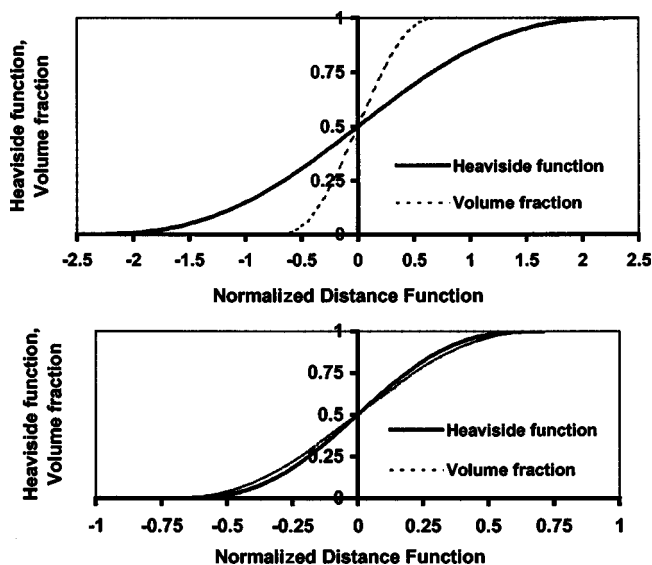


Fig. 14 (a) Distribution of Heaviside function and volume fraction function for two-dimensional case with  $\theta=60^\circ$ . Interface width is taken as  $2.5 h$  for Heaviside function and  $h$  for volume fraction function. (b) Distribution of Heaviside function and volume fraction function for two-dimensional case with  $\theta=60^\circ$ . Interface width is taken as  $h$  for both Heaviside function and volume fraction function.

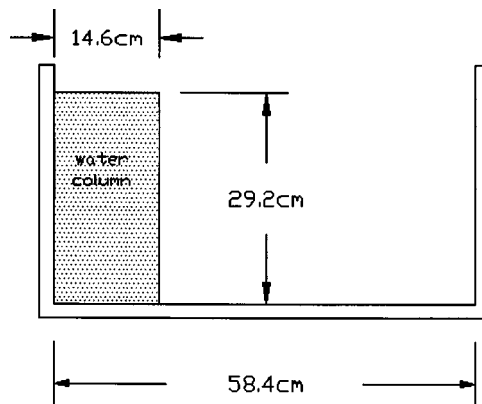


Fig. 15 Experimental arrangement for studying collapsing of water column

the present results are matching very well with the experimental results. Furthermore, a comparison of the leading edge of the water column is carried out between the present method and the results from Koshizuka et al. [18]. In Fig. 17, the nondimensional leading edge of the collapsing water column is plotted against the nondimensional time. Again, the comparison of both numerical and experimental results is found to be quite satisfactory. Additionally, in order to study of the effects of variable density ratio, the collapsing water column is studied for different combinations of fluids with density ratios of 10:1, 100:1 and 1000:1. From the numerical results presented in Fig. 18, it can be seen that the fluid systems with higher density ratios collapse at a somewhat faster rate. This is quite consistent with the physical intuition, since a lower-density secondary fluid should have a slower free fall than a heavier fluid under the same conditions.

In our next numerical experiment, we have computed merging

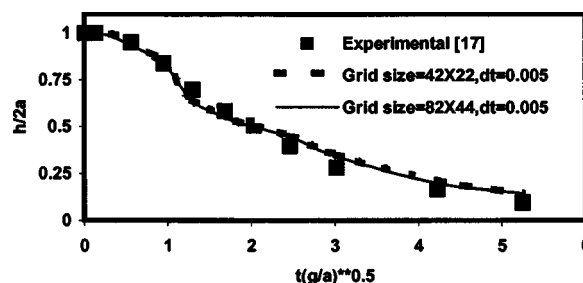


Fig. 16 Height of the collapsing water column,  $h$  = instantaneous height, initial height =  $2a$

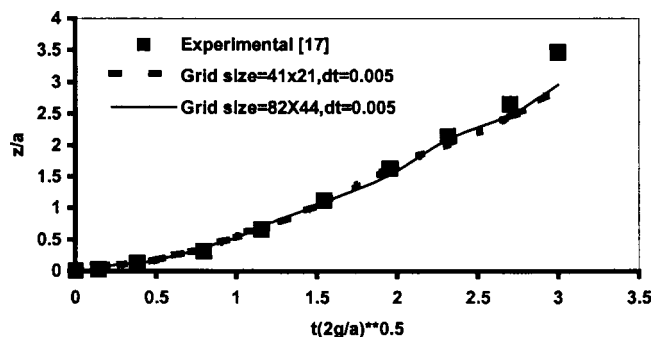


Fig. 17 Position of leading edge of the collapsing water column,  $z$  = instantaneous leading edge position

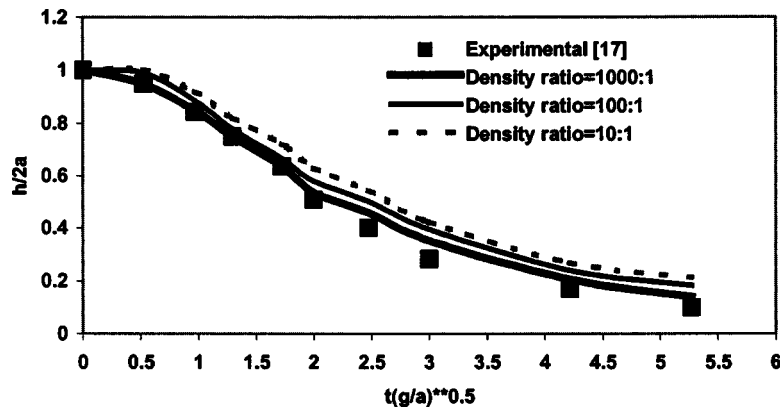


Fig. 18 Effects of density ratio on the collapsing water column height

of two fluid bubbles with the same density under the influence of gravity. The fluid is at rest initially. Viscosity of the fluid inside the two bubbles is equal to  $\mu=0.00025$  and that of outside fluid is  $\mu=0.0005$ . The radius of lower bubble is 0.10 units and it is placed at (0.5,0.35) of a rectangular domain of  $1.0 \times 1.0$  unit dimension. The radius of the upper bubble is 0.15 units and it is placed at (0.5,0.65) of the same geometry. The density of the bubbles is 1.0 and that of the background is 10. The grid size is  $256 \times 256$ . We have also checked a few results with  $512 \times 512$  grid size, and have found no perceptible changes in results in comparison to those obtained by using  $256 \times 256$  grids. Since the bubbles are lighter than the background fluid, the bubbles will eventually rise with time, and the different configurations at different times are shown in the Fig. 19. Literally, the same numerical experiment has been conducted by Chang et al. [6], and the present results have matched excellently with their solutions, which establishes the validity of present method. Further, we have also executed a convergence study for a single rising bubble, by employing exactly the same set of problem data as that reported in Sussman et al. [5]. The comparison is depicted in Fig. 20, which depicts a reasonable good agreement. The bubble radius for this problem is 2.5 length units, density of the bubble is 1.0 units, and that of the background is 1000 units. The viscosity of the bubble is 0.00025 units and that of the background is 0.0005 units.

As another case study to test the proposed methodology, we simulate the evolution of a spherical (circular in two dimensions) bubble in a bulk flow field. Fluid entrapped in the bubble and the

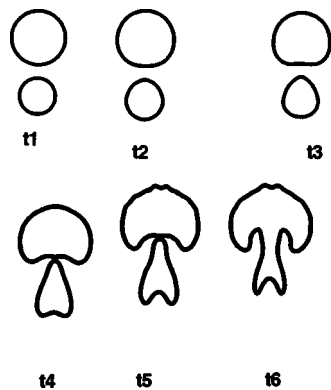


Fig. 19 Two bubbles of same density rising up. Density ratio between the bubbles and the background is 1:10, grid size is  $256 \times 256$ , viscosity of the bubbles is 0.00025 units and that of the background is 0.0005 units,  $t_1=0$  s,  $t_2=0.1$  s,  $t_3=0.18$  s,  $t_4=0.24$  s,  $t_5=0.28$  s,  $t_6=0.32$  s.

outer fluid are taken to be of the same density ( $1 \text{ kg/m}^3$ ), whereas their viscosities are assumed to be different ( $0.1 \text{ kg/m s}$  for the bulk fluid and  $0.001 \text{ kg/m s}$  for the bubble). The flow domain is assumed to be rectangular in nature (length=2.5 m, width=1 m), with the inlet (left boundary) velocity distribution being subjected to a shear flow (inlet velocity varying linearly from 0 to 1.0 as one moves from bottom to the top). Top and bottom boundaries are taken to be rigid walls while the right boundary is assumed to act as an outlet for the bulk flow. Initial circular shape of the bubble becomes deformed and is displaced with the evolution of the flow. Some of the intermediate transients are depicted in Fig. 21. It can be noted here that the deformation of the bubble, as applicable in such a situation, can be quantified with the formation of Cox angle [19], which can be very nicely captured by the present method. It can be observed here that as the “originally circular” bubble confronts an imposed shear flow, it experiences a “lift” force (similar to that of an airplane wing perpendicular to the velocity of shear), and thereby, the stable configuration (with minimum surface energy) is disturbed. The resultant shape and configuration of the bubble is a combined consequence of this lift force, the net buoyancy force, and the drag forces acting on it. In the simulation results presented here, the bubble is neutrally buoyant with the flow, and therefore, the lift and drag forces are the fundamental factors influencing the bubble evolution. It is also important to note here that such physical situations can be potential sources of mass imbalance in a numerical scheme, predominantly because of the variable nonzero orientation angle subtended by the bubble with the respective coordinate directions. As a check of the rigor-ousness of the mass correction approach proposed here, we have numerically calculated mass of the system as a function of time during the flow transients, as well. It has been observed that mass

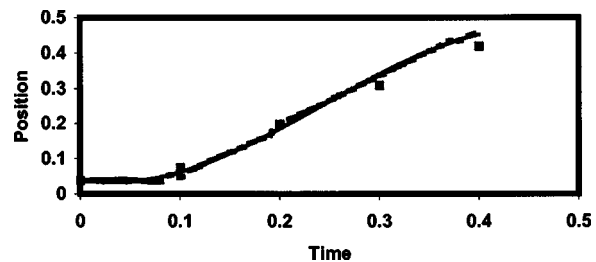
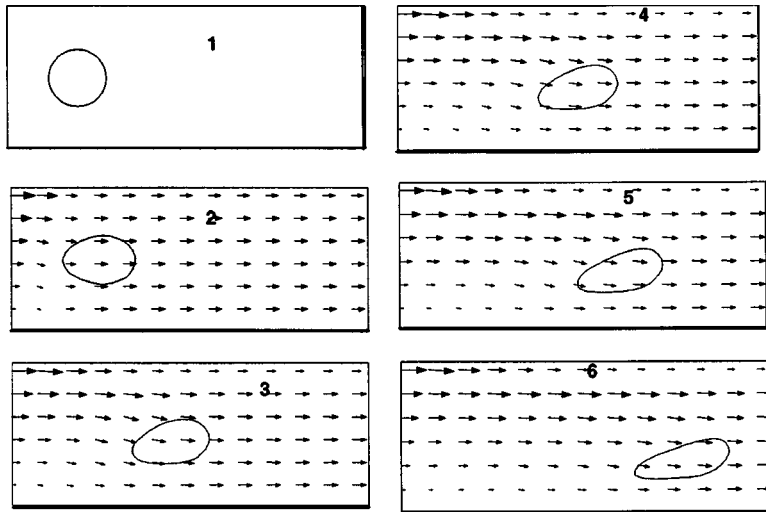


Fig. 20 Position versus time curve corresponding problem data reported in Sussman et al. [5]. The continuous and dotted lines correspond to results obtained using the present method, by employing a  $72 \times 72$  and  $36 \times 36$  square grid, respectively, while the square marks represent numerical results reported in Sussman et al. [5].



**Fig. 21** Transient evolution of a circular bubble in a developing flow field with inlet shear flow. The different snapshots are computed at the following instances of time:  $t_1=0$  s,  $t_2=0.0027$  s,  $t_3=0.0054$  s,  $t_4=0.0081$  s,  $t_5=0.0108$  s,  $t_6=0.0135$  s

conservation requirements are excellently satisfied over the entire time domain of simulation, up to a machine precision of  $10^{-16}$ .

#### 4 Conclusions

A new physically based volume fraction level set approach is developed and established, as an alternative to the Heaviside function based mathematical formulation classically employed for property evaluation and mass correction enforcement in a multiphase flow situation. Expressions for volume fraction function for each pertinent computational cell are established using concepts of computational geometry, and with an inverse analysis the same is correlated with the level set (distance) function. This ensures that physical characteristics of each phase are directly represented in terms of their respective quantitative presence in the respective control volumes, leading to physically consistent evaluation of interfacial properties and a robust implementation of the mass conservation requirements. Like all other mass preserving methodologies, the present method also possesses some limitations, especially in the sense that it corrects the mass globally and there is a probability of ill distribution of masses in certain cases. However, the method is physically simple and understandable, computationally cheap and fast. Future research, therefore, needs to be directed towards further improvement of this method, especially in an effort to derive a more appropriate local mass redistribution strategy, without sacrificing the underlying physical basis.

#### Nomenclature

$\phi$  = levelset function, m  
 $\theta$  = angle between the vertical central line of a control volume and normal direction of the interface in, *radian*  
 $\varepsilon$  = half thickness of the interface as assumed in relation with Heaviside function, m  
 $\xi$  = fluid properties such as density, viscosity, etc.  
 $\psi$  = dummy variable of level-set function, m  
 $\delta$  = Dirac delta function  
 $\lambda$  = Cox angle, *radian*  
 $\sigma$  = surface tension coefficient, N/m  
 $\rho$  = density of the fluid, kg/m<sup>3</sup>  
 $\mu$  = viscosity of the fluid, N s/m<sup>2</sup>  
 $\kappa$  = curvature, m<sup>-1</sup>  
 $D_{\text{ef}}$  = deformation parameter  
 $H$  = Heaviside function

$H_V$  = volume fraction

$u_j$  = velocity, m/s

$p$  = pressure, N/m<sup>2</sup>

$Pe$  = Peclet number

$\Delta X$  = width of the control volume along the X axis, m

$\Delta Y$  = width of the control volume along the Y axis, m

$N$  = number of control volumes containing the interface

$g$  = acceleration due to gravity, m/s<sup>2</sup>

$M_C$  = corrected mass, kg

$M_O$  = original mass, kg

$M$  = instantaneous mass, kg

$H_{VO}$  = original volume fraction

$H_{CO}$  = corrected volume fraction

$L_B$  = length of the deformed bubble, m

$B_B$  = width of the deformed bubble, m

$t$  = time, s

$\Delta t$  = small time step, s

#### References

- [1] Patankar, S. V., 1992, "Review of Calculation Methods for Single-Phase and Multiphase Flows," UMSI Report No. 92/53.
- [2] Unverdi, S., and Tryggvason, G., 1992, "A Front Tracking Method for Viscous, Incompressible, Multi-Fluid Flows," *J. Comput. Phys.*, **100**, pp. 25–37.
- [3] Hirt, C. W., and Nichols, B. D., 1981, "Volume of Fluid (VOF) Method for the Dynamics of Free Boundaries," *J. Comput. Phys.*, **39**, pp. 201–225.
- [4] Osher, S., and Sethian, J. A., 1988, "Fronts Propagating with Curvature-Dependent Speed: Algorithms Based on Hamilton-Jacobi Formulations," *J. Comput. Phys.*, **79**, pp. 12–49.
- [5] Sussman, M., Smereka, P., and Osher, S., 1994, "A Level Set Approach For Computing Solutions to Incompressible Two-Phase Flow," *J. Comput. Phys.*, **114**, pp. 146–159.
- [6] Chang, Y. C., Hou, T. Y., Merriman, B., and Osher, S., 1996, "A Level Set Formulation of Eulerian Interface Capturing Methods for Incompressible Fluid Flows," *J. Comput. Phys.*, **124**, pp. 449–464.
- [7] Kaliakatos, C., and Tsangaris, S., 2000, "Motion of Deformable Drops in Pipes and Channels Using Navier–Stokes Equations," *Int. J. Numer. Methods Fluids*, **34**, pp. 609–626.
- [8] Sussman, M., Fatemi, E., Smereka, P., and Osher, S., 1998, "An Improved Level Set Method for Incompressible Two-Phase Flows," *Comput. Fluids*, **27**(5–6), pp. 663–680.
- [9] Bourlioux, A., 1995, "A Coupled Level-Set Volume-of-Fluid Algorithm for Tracking Material Interfaces," *Proc. 6th Int. Symp. on Computational Fluid Dynamics*, Lake Tahoe, CA, pp. 15–22.
- [10] Sussman, M., and Puckett, G., 2000, "A Coupled Level Set and Volume of Fluid Method for Computing 3D and Axisymmetric Incompressible Two-Phase Flows," *J. Comput. Phys.*, **162**, pp. 301–337.
- [11] Son, G., and Hur, N., 2002, "A Coupled Level Set And Volume-Of-Fluid Method for the Buoyancy-Driven Motion of Fluid Particles," *Numer. Heat*



- Transfer, Part B, **42**, pp. 523–542.
- [12] Sussman, M., 2003, “A Second Order Coupled Level Set And Volume of Fluid Method For Computing Growth And Collapse of Vapor Bubbles,” *J. Comput. Phys.*, **187**, pp. 110–136.
- [13] Shin, S., and Juric, D., 2002, “Modeling Three-Dimensional Multiphase Flow Using a Level Contour Reconstruction Method for Front Tracking Without Connectivity,” *J. Comput. Phys.*, **180**, pp. 427–470.
- [14] Juric, D., and Tryggvason, G., 1998, “Computations of Boiling Flows,” *Int. J. Multiphase Flow*, **24**, pp. 387.
- [15] Enright, D., Fedkiw, R., Ferziger, J., and Mitchell, I., 2002, “A Hybrid Particle Levelset Method for Improved Interface Capturing,” *J. Comput. Phys.*, **183**, pp. 83–116.
- [16] Patankar, S. V., 1981, *Numerical Heat Transfer and Fluid Flow*, McGraw-Hill, New York.
- [17] Martin, J. C., and Moyce, W. J., 1952, “An Experimental Study of the Collapse of Liquid Columns on a Rigid Horizontal Plane,” *Philos. Trans. R. Soc. London*, **244**, pp. 312–324.
- [18] Koshizuka, S., Tamako, H., and Oka, Y., 1995, “A Particle Method for Incompressible Viscous Flow with Fluid Fragmentation,” *Comput. Fluid Dyn. J.*, **4**, pp. 29–46.
- [19] Tsakalos, V. T., Navard, P., and Peuvrel-Disdier, E., 1998, “Deformation and Breakup Mechanisms of Single Drops During Shear,” *J. Rheol.* **42**, pp. 1403–1417.

# Population Balance Modeling of Turbulent Mixing for Miscible Fluids

**Giridhar Madras**

Department of Chemical Engineering,  
Indian Institute of Science,  
Bangalore 560 012, India  
e-mail: giridhar@chemeng.iisc.ernet.in

**Benjamin J. McCoy**

Department of Chemical Engineering, Louisiana  
State University,  
Baton Rouge, LA 70803.

*Blending one fluid into another by turbulent mixing is a fundamental operation in fluids engineering. Here we propose that population balance modeling of fragmentation-coalescence simulates the size distribution of dispersed fluid elements in turbulent mixing. The interfacial area between dispersed and bulk fluids controls the transfer of a scalar molecular property, for example, mass or heat, from the dispersed fluid elements. This interfacial area/volume ratio is proportional to a negative moment of the time-dependent size distribution. The mass transfer coefficient, in the form of a Damkohler number, is the single geometry- and state-dependent parameter that allows comparison with experimental data. The model results, easily realized by simple computations, are evaluated for batch and flow vessels. [DOI: 10.1115/1.1899174]*

*Keywords: Mixing, Diffusion, Dispersion, Mathematical, Modeling, Turbulence, Blending*

## 1 Introduction

Mixing is an essential unit operation in chemical processes, and also a challenging problem in fluids engineering science. Laminar and turbulent mixing, involving fluid mechanics and either mass transfer (concentration blending) or heat transfer (temperature blending), has been the subject of scores of empirical and modeling studies [1]. The difficulty lies in describing how the tracer-containing fluid is dispersed into the bulk fluid, and how tracer diffuses from the dispersed fluid to the bulk [2,3]. The wide-ranging literature on mixing of miscible turbulent fluids has been extensively reviewed [1]. Joshi and Renade [4] appraised the expectations, but also the problems, of applying computational fluid dynamics for designing process equipment. Ottino et al. [5] assessed the literature on laminar mixing.

Brodkey's [2] explanation of mixing clearly outlined the important issues, including Danckwerts's [6] seminal proposals. Mixing in fluids is characterized by two interdependent processes: (1) dispersion of fluid elements, measured by a scale of segregation, and (2) molecular diffusion, measured by intensity of segregation. This division corresponds roughly with the concepts of macromixing, due to bulk fluid motion, and micromixing, due to local turbulence and diffusion. The discrepancy becomes important in modeling mixing processes. Dispersion, which can occur even if molecular diffusion is negligible, enhances mixing by providing an increased area for diffusion [2]. Turbulent eddies are much larger than molecular dimensions, and homogeneity cannot be attained in the absence of molecular diffusion [2]. According to this conception, turbulence and diffusion should be treated separately, rather than as a single micromixing process.

The present investigation of miscible-fluid mixing is based on our recent proposal [7,8] to describe dispersive turbulent reactive mixing in liquids by population balance modeling of concurrent breakage coalescence of the dispersed fluid. The work combined chemical kinetics and hydrodynamics so that dispersed reactants interact with the bulk fluid at evolving fluid-element interfaces. For the batch reactor the dispersed fluid elements are fragmented in a cascade of increasingly smaller sizes and larger interfacial area [9]. The reversible fragmentation coalescence was described

by a population dynamics equation with an exact self-similar solution for the size distribution as a function of time. The similarity solution [10,11] was also used to investigate two-phase mixing of a tracer [8,12]. Two types of competitive reaction kinetics incorporating a diffusion-limited fast reaction were shown to satisfy nonlinear differential equations written in terms of moments of the time-dependent dispersed-fluid size distribution. Applying a compressed time variable to transform to a simple system of differential equations readily solved the nonlinear equations. The straightforward solutions displayed realistic effects of dispersed fluid volume fraction, rate parameters, and initial concentrations. Final fractional conversions, occurring when the limiting reactant is depleted, are functions of the molecular diffusivity through a Damkohler number, volume fraction of dispersed reactant, and scaled initial conditions. Our present objective is to apply this approach in the absence of chemical reaction to turbulent blending operations.

A central quantity in mixing is the mixing time, defined as the time required to achieve a given degree of mixing when a tracer is dispersed into a bulk fluid. We can define the degree of mixing at time  $t$  for the tracer in terms of the initial concentration ( $c_0$ ) in the dispersed fluid and the perfectly mixed concentration ( $c_\infty$ )

$$E_m(t) = [c_0 - c(t)]/[c_0 - c_\infty] \quad (1.1)$$

where  $c(t)$  is the concentration of the tracer in the dispersed fluid at time  $t$ . For example,  $E_m(t_m) = 0.95$  is typically chosen to define the mixing time [13],  $t_m$ .

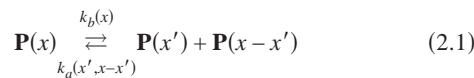
Generalized micromixing models for unsteady state flow reactors have been developed using population balance equations [14]. Our model departs from other mixing models by employing a population balance approach to characterize the fluid eddy size distribution. For the batch mixer, this allows compressing the time variable with a moment relationship representing the interfacial area of fluid eddies. Then the governing equations for mixing are transformed into standard well-stirred flow-reactor form. We propose a general approach for either laminar or turbulent systems whereby the dispersed fluid element area per volume,  $a(t)$ , enters into the mass balance. In laminar mixing very long striations are created by smooth stretching [5,15,16], whereas in fluctuating turbulent flow the fluid elements are fragmented and merged (coalesced). *According to this view, mixing is effected by increasing the contact area between the dispersed and bulk fluid, allowing*

Contributed by the Fluids Engineering Division for publication in the JOURNAL OF FLUIDS ENGINEERING. Manuscript received July 20, 2004; revised manuscript received December 17, 2004. Associate Editor: Ugo Piomelli.

diffusion to occur between them. Obviously if regions of characteristic size  $\delta$  in the fluid remain undispersed, then the mixing time will scale as  $\delta^2/D_M$ , where  $D_M$  is the molecular diffusivity. Once the interfacial area as a function of time is determined, molecular diffusion from the dispersed fluid into the bulk can be formulated. We attempt to develop these ideas in a straightforward and computationally efficient manner. The result is an approach that embodies the essential ideas of mixing in an unexpectedly simple manner, yet captures the important behavior previously described only by empirical methods. The central concepts are population balance modeling and mass transfer. The model is readily converted to heat transfer and the blending of fluids of different temperature.

## 2 Population Balance Modeling

We have previously reported that fluid elements  $\mathbf{P}(x)$  undergoing shearing and merging during turbulent stirring processes can be described quantitatively by population balance modeling. We consider that fragmentation and coalescence are uncorrelated, and that the simultaneous binary processes can be represented as



where  $k_b(x)$  and  $k_a(x',x-x')$  represent the rate coefficients for fragmentation (breakage) and coalescence (aggregation), respectively. The number of dispersed fluid elements at time  $t$  in the mass range  $(x, x+dx)$  is the distribution  $p(x,t)dx$ , and the mass of such elements is  $xp(x,t)dx$ . Moments can be defined as

$$p^{(v)}(t) = \int_0^\infty p(x,t)x^v dx \quad (2.2)$$

such that the number of fluid elements is  $p^{(0)}(t)$ , and their average mass is  $p^{\text{avg}}(t) = p^{(1)}/p^{(0)}$ .

The population balance equation (PBE) for Eq. (2.1) is first order for breakage and second order for aggregation [17]

$$\begin{aligned} \partial p(x,t)/\partial t = & -k_b(x)p(x,t) + 2 \int_x^\infty k_b(x')p(x',t)\Omega(x,x')dx' \\ & - 2p(x,t) \int_0^x k_a(x,x')p(x',t)dx' \\ & + \int_0^x k_a(x',x-x')p(x',t)p(x-x',t)dx' \end{aligned} \quad (2.3)$$

The initial distribution is  $p(x,t=0) = p_0(x)$ , which by Eq. (2.2) has moments,  $p_0^{(v)}$ . The PBE 2.3 reduces to pure fragmentation or pure aggregation, respectively, when  $k_a$  or  $k_b$  is zero. The stoichiometric kernel,  $\Omega(x,x')$ , gives the product mass distribution for the binary fission and satisfies symmetry and normalization conditions [18]. A general breakage kernel has been proposed [18] that can represent the entire range of product distributions from random to midpoint fragmentation, respectively,  $1/x'$  (chosen here) and  $\delta(x-x'/2)$ . For a well-stirred fluid the aggregation rate coefficient should be relatively independent of the masses of the coalescing eddies, thus, in the present work we let  $k_a(x',x-x') = k_a$ , a constant. More general rate coefficients can be handled by solving Eq. (2.3) numerically. An analytical similarity solution [10,11] is found when the fragmentation rate coefficient,  $k_b(x)$ , is proportional to  $x$ . Other expressions for fragmentation and coalescence rate coefficient expressions require numerical solutions to the PBE. We define a reference breakage rate coefficient for elements of mass  $p_0^{\text{avg}} = p_0^{(1)}/p_0^{(0)}$ , such that  $k_{b0} = k_b(x=p_0^{\text{avg}})$  and scale the distributions with the initial conditions,  $p_0^{(0)}$  and  $p_0^{\text{avg}}$ .

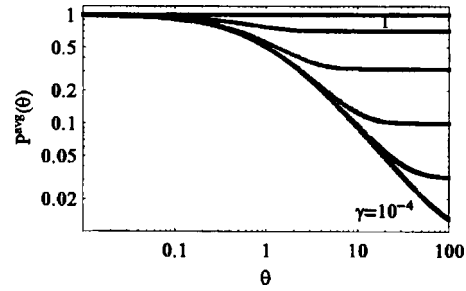


Fig. 1 Variation of  $P^{\text{avg}}(\theta)$  with time  $\theta$  for  $\gamma = 10^{-4}, 10^{-3}, 10^{-2}, 0.1, 0.5$  and  $1$  on a log-log plot showing the asymptotes,  $\gamma^{1/2}$ , at large time  $\theta$  and the asymptotic behavior,  $(1+\theta)^{-1}$ , for small and intermediate time

We have previously expressed the solution to the PBE for Eq. (2.1) as dimensionless variables and parameters (see Nomenclature). The initial distribution with  $P^{\text{avg}}(\theta=0) = p^{\text{avg}}(t=0)/p_0^{\text{avg}} = 1$ , containing a given concentration of tracer solution, evolves to the exact self-similar exponential solution [8,17] in terms of the average element mass,  $P^{\text{avg}}(\theta)$ ,

$$P(\xi, \theta) = [P^{\text{avg}}(\theta)]^{-2} \exp[-\xi/P^{\text{avg}}(\theta)] \quad (2.4)$$

whose moments are simply

$$P^{(v)}(\theta) = (P^{\text{avg}})^{v-1} \Gamma(v+1) \quad (2.5)$$

The similarity variable  $\xi/P^{\text{avg}}(\theta)$  in Eq. (2.4) combines scaled mass  $\xi$  and time  $\theta$ . The time dependence is thus governed by  $P^{\text{avg}}(\theta)$ , which satisfies the differential equation

$$dP^{\text{avg}}/d\theta = -(P^{\text{avg}})^2 + \gamma \quad (2.6)$$

with unity as initial condition. The parameter  $\gamma$  represents the relative rates of coalescence and fragmentation. Increasing or decreasing  $\gamma$  shows how coalescence or fragmentation of fluid eddies affects the processes. The solution to Eq. (2.6) is [10,17],

$$P^{\text{avg}}(\theta) = \gamma^{1/2} \tanh[\theta\gamma^{1/2} + \tanh^{-1}(\gamma^{-1/2})] \quad (2.7)$$

For  $\gamma < 1$ , the quantity  $P^{\text{avg}}(\theta)$  decreases with time at a rate depending on the parameter  $\gamma$ , the ratio of rate coefficients for coalescence and fragmentation, which in turn decreases with increased turbulence. The asymptotic values for small and large values of time are clearly shown in Fig. 1, a log-log plot of  $P^{\text{avg}}$  versus  $\theta$ . Figure 1 shows that the average eddy size at equilibrium decreases as  $\gamma$  decreases. When  $\theta \ll \gamma^{-1/2} \tanh^{-1}(\gamma^{-1/2})$  in Eq. (2.7), we have  $P^{\text{avg}} \sim 1$ , whereas for large time,  $\tanh \sim 1$  and  $P^{\text{avg}} \sim \gamma^{1/2}$ . For small  $\gamma$ , fragmentation dominates coalescence and the intermediate asymptotic time dependence [19] is

$$P^{\text{avg}}(\theta) \sim 1/(1+\theta) \quad (2.7a)$$

## 3 Mixing in Stirred Vessels

In either laminar or turbulent flow, mixing is facilitated if the dispersed fluid elements increase their interfacial area in contact with the bulk fluid, thus allowing diffusion of the tracer into the adjoining bulk fluid. For generality we formulate the mixing equations for a continuous-flow stirred vessel, and thus include the case of tracer entering the vessel during a finite time. We define the average residence time as the ratio of the vessel volume to the volume flow rate,  $t_r = V/Q$ . The mass balance equations for the dispersed fluid concentration,  $c(t)$ , and the bulk fluid concentration,  $c_b(t)$ , that incorporate mass transfer at the dispersed fluid interface can be written as

$$a dc/dt = c_{in}/t_r - k_M a a(t)[c(t) - c_b(t)] \quad (3.1)$$

$$(1 - \alpha)dc_b/dt = -(1 - \alpha)c_b(t)/t_r + k_M \alpha a(t)[c(t) - c_b(t)] \quad (3.2)$$

which reduce to the batch case if  $1/t_r=0$ . For consistency, because Eqs. (2.3)–(2.7) are for batch dispersal, we formulate Eq. (3.1) so that no dispersed fluid exits the vessel. Initial conditions are  $c(t=0)=c_0$  and  $c_b(t=0)=c_{b0}$ , where  $c_{b0}=0$  if the bulk fluid is initially free of tracer. The mass transfer coefficient  $k_M=D_M/\delta$  is related to the molecular diffusivity  $D_M$  and the diffusion distance  $\delta$ . It is clear that interfacial mass transfer is determined by this diffusion distance and by the interfacial area,  $a(t)$ , both representing complex physical processes. The appearance of a mass transfer or diffusion coefficient is to be expected, as a Damkohler number is essential to interpreting mixing behavior. For heat transfer, one substitutes a relative temperature for concentration and a heat transfer coefficient for  $k_M$ .

In a recent study of competitive reactions during turbulent mixing, Madras and McCoy [7] showed how to formulate  $a(t)$  in terms of the dispersed fluid volume per vessel volume,  $\alpha$ . For spherical elements of mass  $x$  and radius  $r$ , the ratio of area to volume is  $3/r=3(3x/4\pi\rho)^{-1/3}=g x^{-1/3}$ , where  $g=(36\pi\rho)^{1/3}$  and the dispersed-fluid area per vessel volume for elements in the range  $(x, x+dx)$  is  $\alpha g x^{-1/3} p(x, t) dx$ . When integrated over all  $x$ , the total area/volume ratio is

$$a(t) = g p^{(\nu)}(t) \quad (3.3)$$

in terms of the negative fractional moment ( $\nu < 0$ ), defined by Eq. (2.2), and where  $\nu=-1/3$  for spherical elements. Because the fluid elements are not spherical for turbulent mixing, the coefficients of  $x^\nu$  have other forms. For example, for fragmentation occurring by stretching cylindrical fluid elements of radius  $r(t)$  and then severing them into two random segments of area/volume= $2/r$ , the cylinder mass in terms of its length  $z$  is  $x=\pi r^2 z \rho$ , from which  $2/r=g x^{-1/2}$ , where  $g=(\pi z \rho)^{1/2}$ . If fragmentation occurs by stretching flat slabs and then cutting them into two, and if the ribbon-like sheets, or striations, are thin with thickness  $y$  and surface  $2S$ , then edge areas can be neglected and the element area per element volume is  $2/y$ . In terms of the element mass  $x=S y \rho$ , we have  $2/y=g/x$  with  $g=2S\rho$ . In this case the moment with  $\nu=-1$  in Eq. (2.2) diverges, but we can compute the moment for  $\nu$  arbitrarily close to  $-1$ . Thus,  $\nu=-1/3, -1/2$ , and  $-1$  for the spherical, cylindrical, and sheet geometries, respectively, represent  $a(t)$  in Eq. (3.3), and govern mass transfer in the mixing system. As the negative moments increase strongly when fragmentation dominates the mixing process [8], the results are quite sensitive to  $\nu$ . The vortex structure of eddies in turbulent motion suggests a value of  $\nu$  between  $-1/2$  and  $-1$ , and for most of the illustrative computations herein,  $-2/3$  is chosen.

The mass balance equations can be cast in dimensionless form (see Nomenclature)

$$\alpha dC/d\theta = C_{in}/\theta_r - \kappa_M \alpha P^{(\nu)}(\theta)[C(\theta) - C_b(\theta)] \quad (3.4)$$

$$(1 - \alpha)dc_b/d\theta = -(1 - \alpha)c_b(\theta)/\theta_r + \kappa_M \alpha P^{(\nu)}(\theta)[C(\theta) - C_b(\theta)] \quad (3.5)$$

where

$$k_M a(t) = \kappa_M P^{(\nu)}(\theta) \quad (3.6)$$

As indicated by the definition,  $\kappa_M$  is based on the ratio of the mass transfer coefficient ( $k_M$ ) to the fragmentation coefficient ( $k_{b0}$ ), and thus can be termed a Damkohler number. With the asymptotic expression, Eq. (2.7a), the mass transfer term is written simply as

$$k_M a(t) \approx \kappa_M \Gamma(1 + \nu)(1 + \theta)^{1-\nu} \quad (3.6a)$$

For the *batch mixer* ( $\theta_r \rightarrow \infty$ ), the ordinary differential Eq. (3.4) and (3.5) are homogeneous. The solutions are considerably simplified if we define a dimensionless time variable

$$d\tau = P^{(\nu)}(\theta) d\theta \quad (3.7)$$

such that

$$\tau(\theta) = \int_0^\theta P^{(\nu)}(\theta) d\theta = \Gamma(1 + \nu) \int_0^\theta [P^{avg}(\theta)]^{\nu-1} d\theta \quad (3.8)$$

when Eq. (2.5) is substituted. Replacing  $\theta$  with  $\tau$  in Eqs. (3.4) and (3.5) yields the equations for a well-mixed flow vessel

$$\alpha dC/d\tau = -\alpha \kappa_M [C(\tau) - C_b(\tau)] \quad (3.9)$$

$$(1 - \alpha)dc_b/d\tau = \alpha \kappa_M [C(\tau) - C_b(\tau)] \quad (3.10)$$

These simplified equations can be solved analytically. Batch blending of a tracer into a bulk fluid thus has the solution

$$C(\tau) = 1 + (1 - \alpha)(C_{b0} - 1)\{1 - \exp[-\tau \kappa_M/(1 - \alpha)]\} \quad (3.11)$$

and for initially tracer-free bulk fluid ( $C_{b0}=0$ ),

$$C(\tau) = \alpha + (1 - \alpha)\exp[-\tau \kappa_M/(1 - \alpha)] \quad (3.11a)$$

with

$$C_b(\tau) = \alpha\{1 - \exp[-\tau \kappa_M/(1 - \alpha)]\} \quad (3.11b)$$

This is an advantage of the present approach to turbulent mixing: by resolving the problem into dispersion and diffusive transfer, we are able to convert a complex process into equations that are familiar in chemical reaction engineering. The assumptions that allow this simplification are (1) uncorrelated eddy distributions describe binary fragmentation and coalescence, (2) immiscible continuous and dispersed phases are well mixed in the vessel, (3) concentrations in the continuous and dispersed phases are uniform.

The integral (3.8) is also related to the intensity of segregation, which can be defined [2] for a stirred vessel as

$$I_s(\theta) = [C(\theta) - C_\infty]^2/[1 - C_\infty]^2 = [(C(\theta) - \alpha)/(1 - \alpha)]^2 \quad (3.12)$$

where for perfect mixing,  $C_\infty=\alpha$ . Substituting Eq. (3.11) into Eq. (3.12) and rearranging yields

$$I_s(\theta) = \exp[-2 \kappa_M \tau(\theta)/(1 - \alpha)] \quad (3.13)$$

The exponential decrease with time and diffusivity agrees generally with earlier results [2]. As explained by Brodkey [2], Beek and Miller [20] related  $I_s$  to the energy spectrum  $E(k, \theta)$ , which decays exponentially with time

$$I_s(\theta) = (1 - \alpha)^{-2} \int_0^\infty E(k, \theta) dk \quad (3.14)$$

According to Brodkey [2],  $I_s$  is a function only of the Reynolds number, which defines the turbulent field, and the Schmidt number, which defines the relative rate of molecular diffusion. In Eq. (3.13) the product  $\kappa_M \tau$  depends on the Reynolds and Schmidt numbers. The degree of mixing at time  $\tau$  for the batch is simply related to the intensity of segregation,  $E_m(\tau) = 1 - I_s(\tau)^{1/2}$ .

An expression for the degree of mixing follows by substituting  $C(\tau)$  from Eq. (3.11a) into Eq. (1.1)

$$E_m(\theta) = 1 - \exp[-\kappa_M \tau(1 - \alpha)] \quad (3.15)$$

This has the proper limits,  $E_m(\theta=0)=0$  and  $E_m(\theta \rightarrow \infty)=1$ . Significantly,  $E_m$  exponentially approaches complete mixing as mixing time increases [13], a well-known result in blending technology. The mixing time realistically decreases as the mass transfer coefficient and hence the molecular diffusivity increases. According to Eq. (3.15), we can compute the time  $\theta$  for given  $E_m$  and  $\alpha$  if we have a relationship for  $\kappa_M$  and for  $P^{avg}(\theta)$ .

The integral of Eq. (3.8) can be evaluated analytically when Eq. (2.7) is substituted for  $P^{avg}(\theta)$

$$\begin{aligned} \tau(\theta) = & \gamma^{-1} \Gamma(\nu) [- {}_2F_1(1, \nu/2, 1 + \nu/2, 1/\gamma) \\ & + [P^{\text{avg}}(\theta)]^\nu {}_2F_1(1, \nu/2, 1 + \nu/2, P^{\text{avg}}(\theta)^2/\gamma) ] \end{aligned} \quad (3.16)$$

The tabulated hypergeometric function has the series representation [21]

$${}_2F_1(a, b; c; d) = \sum_{k=0}^{\infty} \frac{(a)_k (b)_k d^k}{(c)_k k!} \quad (3.16a)$$

where the Pochhammer symbol is defined as  $(a)_k = \Gamma(a+k)/\Gamma(a)$ . Alternatively, a straightforward numerical integration can be used to evaluate Eq. (3.8) for the stretched time  $\tau$ .

The integral of Eq. (3.8) is readily evaluated when the asymptotic behavior, Eq. (2.7a), is substituted for  $P^{\text{avg}}(\theta)$

$$\tau(\theta) = [(1 + \theta)^{2-\nu} - 1] \Gamma(1 + \nu) / (2 - \nu) \quad (3.17)$$

For long times ( $\theta \gg 1$ )

$$\tau(\theta) \approx \theta^{2-\nu} \Gamma(1 + \nu) / (2 - \nu) \quad (3.17a)$$

For realistic negative values,  $-1 < \nu \leq -1/2$ ,  $\tau$  varies with  $\theta$  to a power between 5/2 and 3. According to Eq. (3.8) the direct exponential dependence used in previous work [1] is obtained when  $\nu=1$  so that  $\tau(\theta) = \theta$ .

One can plot  $\theta$  versus  $\tau$  with  $\gamma$  as a parameter, so that for known values of  $E_m$  and  $\kappa_M$  on the right-hand side of Eq. (3.16), one has a value for  $\tau$  and can read  $\theta$  on the vertical axis. We can also relate  $\tau$  and  $\theta$  by differentiating Eq. (3.16)

$$d\tau/d\theta = \Gamma(1 + \nu) [P^{\text{avg}}(\theta)]^{\nu-1} \quad (3.18)$$

which shows that the slope of the mixing-time curve is proportional to a power of the scaled average eddy size. According to the asymptotic limits discussed following Eq. (2.7), the short- and long-time asymptotes of the slope,  $d\tau/d\theta$ , are  $\Gamma(1 + \nu)$  and  $\Gamma(1 + \nu) \gamma^{(\nu-1)/2}$ , respectively. For small  $\gamma$ , Eq. (2.7a) can be substituted for  $P^{\text{avg}}(\theta)$  in Eq. (3.18).

For the case of steady injection of a tracer into a stirred vessel of constant volume the vessel has a constant volume of liquid when the injection rate equals the outflow rate. If the exit stream contains only bulk fluid (the same condition required for the similarity solution to the PBE for dispersed fluid), then for the continuous-flow stirred tank mixer, Eqs. (3.4) and (3.5) become

$$\alpha(\theta) dC/d\theta = C_{\text{in}}/\theta_r - \kappa_M \alpha(\theta) \Gamma(1 + \nu) [P^{\text{avg}}(\theta)]^{\nu-1} [C(\theta) - C_b(\theta)] \quad (3.19)$$

and

$$\begin{aligned} [1 - \alpha(\theta)] dC_b/d\theta = & -[1 - \alpha(\theta)] C_b(\theta) / \theta_r + \kappa_M \alpha(\theta) \Gamma(1 + \nu) \\ & \times [P^{\text{avg}}(\theta)]^{\nu-1} [C(\theta) - C_b(\theta)] \end{aligned} \quad (3.20)$$

where the volume fraction  $\alpha$  of dispersed fluid now varies with time. For a constant injection rate, we have  $\alpha = Qt/V = t/t_r = \theta/\theta_r$ , which is substituted into Eqs. (3.19) and (3.20). Although the substitution (3.8) is not helpful here because of the nonhomogeneous term  $C_{\text{in}}/\theta_r$ , the two nonlinear differential Eqs. (3.19) and (3.20) are readily solved numerically with  $P^{\text{avg}}(\theta)$  given by Eq. (2.7), or the approximation, Eq. (2.7a).

#### 4 Computations and Results

The computations were performed with the software MATHEMATICA® on an ordinary desktop computer. No difficulties were encountered in applying routine numerical procedures for solving ordinary differential equations. The CPU time required on a Pentium® IV machine for solving the system of Eqs., (3.19) and (3.20), was less than 5 s. The effortlessness of the computations is an obvious attribute of the population balance modeling approach.

Population dynamics yields the fluid-element (eddy) size distribution, and hence an average eddy size, which is simply related to the mixing length through the fluid density. Kolmogorov's scaling

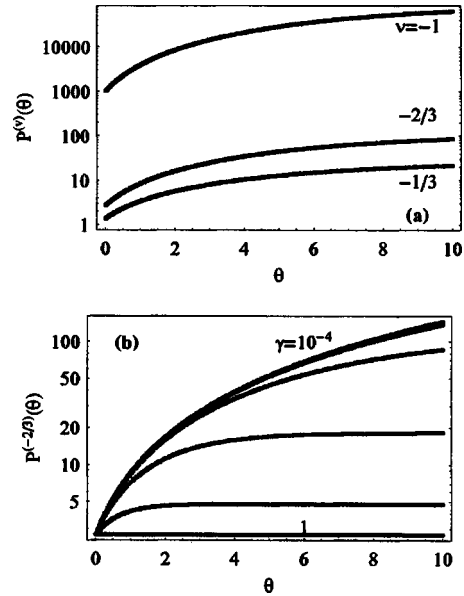


Fig. 2 Variation of the  $\nu$ th moment,  $P^{(\nu)}(\theta)$ , with scaled time  $\theta$  for (a)  $\nu = -1, -2/3$ , and  $-1/3$  with  $\gamma = 0.01$ ; (b)  $\gamma = 10^{-4}, 10^{-3}, 10^{-2}, 0.1, 0.5$  and  $1$  with  $\nu = -2/3$

theory shows how the mixing length is related to the vessel Reynolds number. This suggests a relationship for the fragmentation rate parameters in terms of the vessel Reynolds number, thus providing a connection between fragmentation kinetics and reactor vessel parameters. The log-log plot of  $P^{\text{avg}}(\theta)$  versus  $\theta$  for various values of  $\gamma$  (Fig. 1) shows the asymptotic time dependence at large and small  $\theta$  for the average fluid eddy sizes. The equilibrium eddy size,  $\gamma^{1/2}$ , roughly equates to the Kolmogorov microscale at which viscous dissipation occurs. As moments are based on mass, or volume, we have at equilibrium  $P^{\text{avg}} \sim (\eta/L)^3$ , where the ratio of the microscale length  $\eta$  to the macroscale length  $L$  can be shown [3] to be  $\eta/L \sim \text{Re}_L^{-3/4}$  in terms of a Reynolds number based on the length scale  $L$ . It follows that  $\gamma \sim \text{Re}_L^{-9/2}$ , which ensures that  $\gamma$  is very small for moderate values of  $\text{Re}_L$ . Thus, the precise value of  $\gamma \ll 1$  is not critical in determining mixing efficiency.

The plot of  $P^{(\nu)}(\theta)$  [Eq. (2.5)] for negative values of  $\nu$  [Fig. 2(a)] shows the moments increasing with time for  $\gamma = 0.01$ . Substitution of either Eq. (2.7) or Eq. (2.7a) gives identical plots. These negative moments are a measure of the area for mass transfer. The value  $\nu = -1$  is the highest curve, indicating that shearing of the dispersed fluid into thin sheets is an efficient way to increase the area of mass transfer. Figure 2(b) shows the variation of  $P^{(-2/3)}(\theta)$  with time  $\theta$  for various  $\gamma$ . As fragmentation becomes more significant,  $\gamma$  decreases, and  $P^{(\nu)}(\theta)$  increases more strongly with time. For  $\gamma \leq 10^{-3}$ , the curves in Fig. 2(b) coincide.

The intensity of segregation,  $I_s$ , plotted in Fig. 3 as a function of scaled time,  $\theta$ , was determined from Eq. (3.13). Substitution of either Eq. (3.16) or Eq. (3.17) gives identical plots, indicating that Eq. (2.7a) is a valid simplification for Eq. (2.7) for small  $\gamma$ . The parameter  $\kappa_M$  is proportional to the mass transfer coefficient and thus is related to the Schmidt number,  $\text{Sc}$ , and Reynolds number,  $\text{Re}_L$ . As found previously [2,20], the difference between gases and liquids (small and large  $\text{Sc}$ ) is huge in Fig. 3. Changing  $\kappa_M$  by an order of magnitude changes the intensity of segregation by several orders of magnitude. The requirement of no mixing in the limit of infinite Schmidt number ( $\kappa_M = 0$ ) is satisfied, giving  $I_s = 1$  for all time [2]. A similar plot of Beek and Miller [20] suggests the

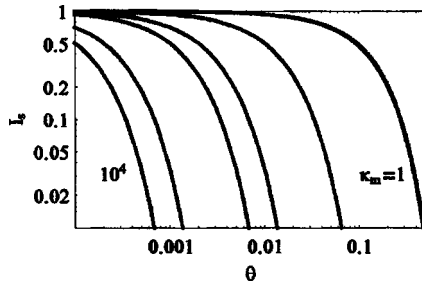


Fig. 3 Variation of the intensity of segregation,  $I_s$ , with time,  $\theta$ , [Eq. (3.13)] for  $\kappa_M=1, 10, 50, 100, 500, 10^3$  and  $10^4$  and  $\alpha=0.2, \nu=-2/3, \gamma=0.01$

magnitudes  $\kappa_M=1$  for liquids and  $\kappa_M=10^4$  for gases. These values are nearly proportional to diffusivity, and as expected, differ by a factor of  $10^4$ .

The effects of the parameters on extent of mixing,  $E_m$ , are displayed in Fig. 4. Figure 4(a) shows the variation of  $E_m$  with  $\kappa_M \tau_m$  [based on Eq. (3.15)] on a loglinear scale with the volume fraction  $\alpha$  of dispersed fluid as the parameter. As mixing time increases,  $E_m$  increases from zero to unity exponentially, consistent with earlier studies [13]. To determine the variation of the extent of mixing with the scaled mixing time,  $\theta_m$ , Eq. (3.16) is substituted into Eq. (3.15). Figures 4(b) and 4(c) show the variation of  $E_m$  as a function of the mixing time  $\theta_m$ , for various  $\kappa_M$  and  $\gamma$  and fixed values of  $\nu$  and  $\alpha$ . Figure 4(c) shows that for large  $\kappa_M$  the precise value of  $\gamma \ll 1$  is not critical in determining mixing efficiency. Small  $\kappa_M$  means that diffusive contributions to mixing are reduced, allowing turbulent fragmentation ( $\gamma$ ) and its enhancement of mass transfer area to have a greater influence on mixing. As Fig. 4(d) indicates, smaller  $\gamma$  diminishes the effect of  $\kappa_M$  on  $E_m$ . Therefore, for strong turbulence, where  $\gamma$  is small, the effect of further decreasing  $\gamma$  is insignificant. This agrees with the experimental observation [1,22] that the circulation time is constant and independent of Reynolds number above  $10^4$ . One infers, as rec-

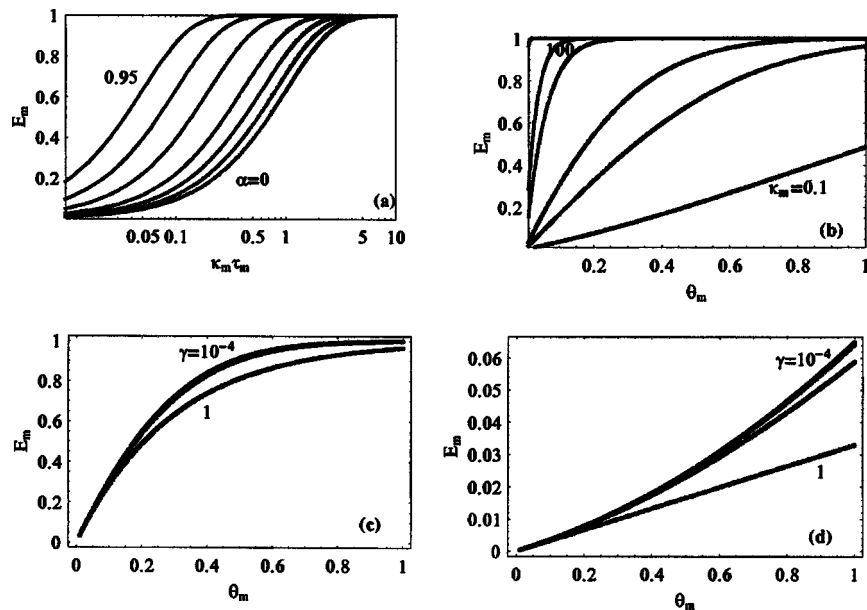


Fig. 4 Variation of the extent of mixing,  $E_m(\theta)$ , (a) with  $\kappa_M \tau_m$  [Eq. (3.15)] for  $\alpha=0, 0.2, 0.4, 0.6, 0.8, 0.9$  and  $0.95$ ; (b) with  $\theta_m$  for  $\kappa_M=0.1, 0.5, 1, 5, 10$  and  $100$  and  $\alpha=0.2, \nu=-2/3, \gamma=0.01$ ; (c) with  $\theta_m$  for  $\gamma=10^{-4}, 10^{-3}, 10^{-2}, 0.1, 1$  and  $\alpha=0.2, \nu=-2/3, \kappa_M=1$ ; (d) with  $\theta_m$  for  $\gamma=10^{-4}, 10^{-3}, 10^{-2}, 0.1, 1$  and  $\alpha=0.2, \nu=-2/3, \kappa_M=0.01$

ommended by other investigators, that increasing the turbulence (decreasing  $\gamma$ ) above the optimum Reynolds number is not an efficient use of energy.

Figures 5(a)–5(c) show the variation of  $\tau$  with scaled time,  $\theta$ , with  $\gamma$  as a parameter for  $\nu$  equal to  $-1, -2/3$ , and  $-1/3$ , respectively. The plots, independent of  $\alpha$ , indicate the strong effect of increased (less negative)  $\nu$ .

Dispersed and bulk fluid concentrations in a flow vessel [Eqs. (3.19) and (3.20)] for a constant injection rate ( $\alpha=\theta/\theta_c$ ) are displayed in Fig. 6. Figure 6(a) shows the time evolution of  $C$  and  $C_b$  in a continuous stirred tank reactor (CSTR) mixer for given values of  $\gamma, \nu$ , and  $\kappa_M$ . While the dispersed phase concentration,  $C(\theta)$ , initially decreases and then increases, the bulk concentration,  $C_b(\theta)$ , continuously increases with time. At long times, the concentrations are equal.

For the CSTR with  $C_0=C_{in}=1.0$ , Fig. 6(b) shows the time evolution of  $C_b$  when  $\kappa_M$  is changed from 0.1 to 1000. The graph indicates that the influence of  $\kappa_M$  on the time evolution of the concentration is substantial. The magnitude of the influence will be determined by how mass transfer (Sherwood number) depends on Reynolds number.

Figure 6(c) shows the variation of the bulk concentration with time when  $\nu$  is changed from  $-1/3$  to  $-1$ . The concentrations are highly influenced by the value of  $\nu$ , consistent with Fig. 5. Figure 6(d) shows that the time evolution of the concentration is independent of turbulent fragmentation when  $\gamma$  is less than 0.1, consistent with Figs. 4(c) and 4(d).

A method for relating the present theory to existing mixing correlations can be devised by relating the mixing time to  $\kappa_M$ . When the asymptotic result of Eq. (3.17) is substituted into Eq. (3.15), the mixing time can be expressed in terms of the mixing efficiency

$$\theta_m \approx [1 - \kappa_M^{-1}(1 - \alpha)(2 - \nu)\ln(1 - E_m)/\Gamma(1 + \nu)]^{1/(2-\nu)} - 1 \quad (3.21)$$

allowing easy computation of  $\theta_m$ . The mixing time is usually taken to be 3–5 times the circulation time [23] and thus the circulation-path models [1,13] are typically based on  $\theta_m/\theta_c \approx 3.0$ . The dimen-

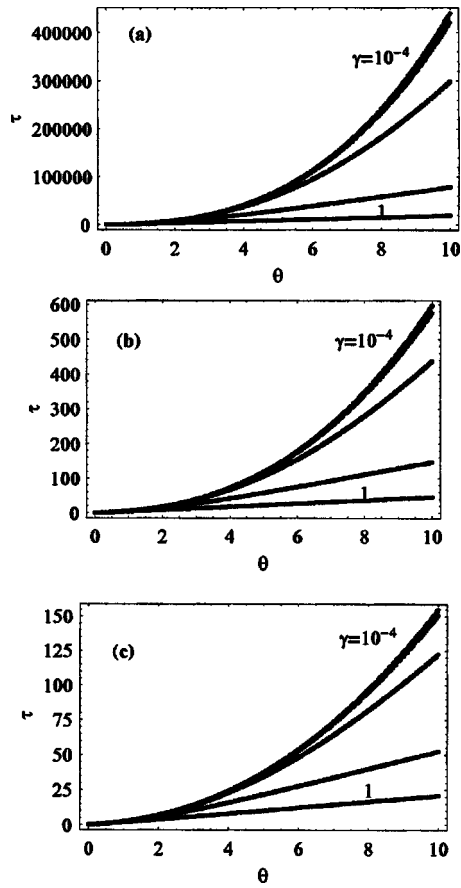


Fig. 5 Variation of  $\tau$  with time,  $\theta$ , [Eq. (3.16)] with  $\gamma (=10^{-4}, 10^{-3}, 10^{-2}, 0.1, 0.5$  and  $1$ ) as a parameter for  $\nu=-1, -2/3$ , and  $-1/3$

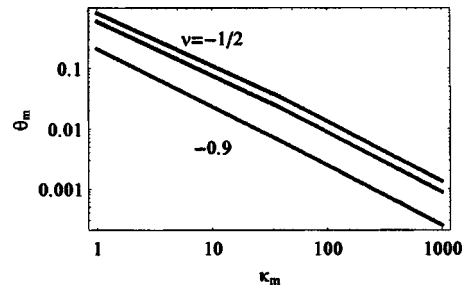


Fig. 7 Variation of the mixing time with  $\kappa_M$  for  $\nu=-1/2, -2/3$ , and  $-0.9$  and  $\alpha=0.2, E_m=0.95$

sionless circulation time,  $\theta_c$ , has been related to power input and primary and secondary flow numbers for particular impellers. By setting  $\theta_m=3.0 \theta_c$  in Eq. (3.21), one can find a relationship for  $\kappa_M$  in terms of  $\theta_c$ , for given values of  $E_c$  and  $\nu$ . Eq. (3.21) thus provides correlations for the key parameter in our model and permits one to relate the present model to other correlations. Figure 7 shows the variation of the mixing time with  $\kappa_M$  for various values of  $\nu$ .

The parameter  $\kappa_M$  is a power law function of Reynolds number,  $\kappa_M \sim \text{Re}^\psi$ . For small  $\kappa_M (< 1)$ , a relationship between the mixing time and Reynolds number, deduced from Eq. (3.21), is  $\theta_m+1 = \phi \text{Re}^{-\psi/(2-\nu)}$ , where  $\phi$  is a constant dependent on  $\alpha$  and  $\nu$ . For large  $\kappa_M$ , the mixing time is close to zero, consistent with experimental observations [1,22]. Fang and Lee [24] observed a power law dependence of mixing time with Reynolds number,  $\theta_m = \phi \text{Re}^{-1}$ , consistent with that observed in this study when  $\psi=(2-\nu)$ . The power was found to vary between  $-1.69$  and  $-2.12$  by application of the incorporation model [25] to experimental data [24]. Such powers can be obtained by choosing appropriate values for  $\psi$  and  $\nu$  in our proposed model. Further, a wide range of mixing times reported in the literature [1,24] can be obtained by choosing appropriate values for the parameters in the model. For

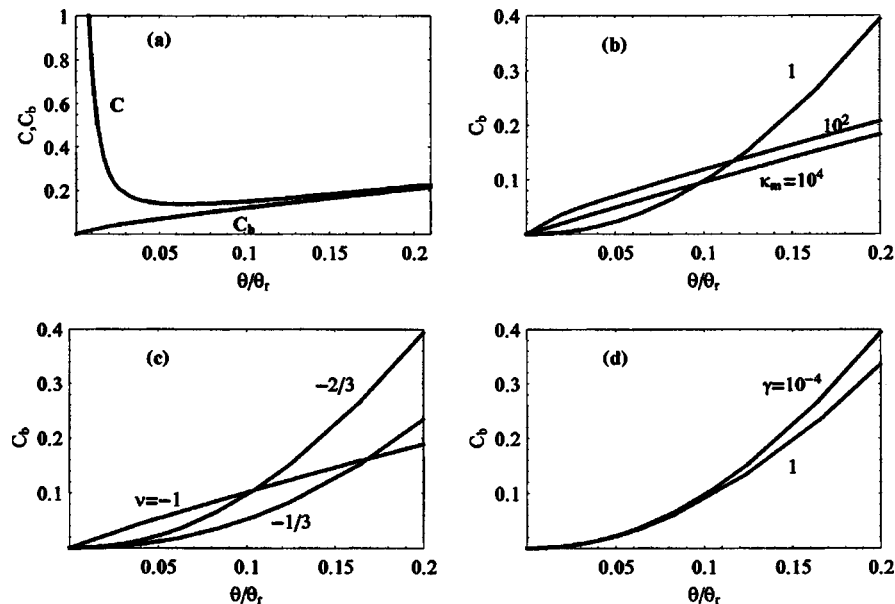


Fig. 6 Dispersed and bulk fluid concentrations in a CSTR: (a) Time variation of the dispersed phase concentration,  $C(\theta)$ , and bulk fluid concentration,  $C_b(\theta)$ , in a CSTR for  $\gamma=0.01, \nu=-2/3$ , and  $\kappa_M=100$ ; (b) Time variation of the bulk fluid concentration,  $C_b(\theta)$ , in a CSTR for  $\kappa_M=0.1, 10, 1000$  with  $\gamma=0.01, \nu=-2/3$ ; (c) Time variation of the bulk fluid concentration,  $C_b(\theta)$ , in a CSTR for  $\nu=-1/3, -2/3, -1$  with  $\gamma=0.01$ , and  $\kappa_M=1$ ; (d) Time variation of the bulk fluid concentration,  $C_b(\theta)$ , in a CSTR for  $\gamma=10^{-4}, 10^{-2}, 1$  with  $\nu=-2/3$  and  $\kappa_M=1$

**Table 1** Experimental parameters<sup>a</sup> and values of  $\theta_r$  and  $\kappa_M$  used to fit the data<sup>a</sup> in Figs. 8(a)–8(c)

Figure	rpm <sup>a</sup>	$\nu$ , mL/s <sup>a</sup>	$t_r$ , s <sup>a</sup>	$\theta_r = t_r k_{b0}$	$\kappa_M$
8(a)	600	1.0	900	90	6
8(b)	600	0.5	1800	180	6
8(c)	200	1.0	900	90	2

<sup>a</sup>Reference [26].

example, choosing  $\kappa_M=1$  and 6 with  $k_{b0}=0.1 \text{ s}^{-1}$ ,  $\alpha=0.2$ , and  $\nu=-2/3$  yields typical mixing times of 1–5 s, that are observed experimentally [1].

We next investigate how the model agrees with experimental observations. Tracer dispersion experiments [26] have been performed to assess mixing in a Taylor–Couette cell. Both the rotation speed of the inner cylinder and the input flow rate were varied in the experiments (Table 1). Increasing the rotation speed decreases  $\gamma$  and increases  $\kappa_M$  causing a more rapid breakup and lower values of the bulk concentration. As discussed earlier, the influence of  $\gamma$  on the time evolution of the bulk concentration is minimal. Therefore,  $\kappa_M$  was chosen as adjustable and proportional to the rotation speed. The experiments were conducted at two flow rates of 0.5 and 1 mL/s corresponding to residence times of approximately 1800 and 900 s, respectively. For  $k_{b0}=0.1 \text{ s}^{-1}$ ,  $\theta_r = t_r k_{b0}$  is 180 and 90 for the two flow rates. Figures 8(a)–8(c) show that the model results match the experimental data satisfactorily when  $\kappa_M$  is 6 and 2, respectively, for the 600 and 200 rpm

rotational speeds. The experimental variables and the parameters selected for the model are listed in Table 1. The values of  $\kappa_M$  are consistent<sup>1</sup> with Eq. (3.21) for typical mixing times of 1–5 s, so that for  $k_{b0}=0.1 \text{ s}^{-1}$ ,  $\alpha=0.2$ , and  $\nu=-2/3$ , we have  $\kappa_M=1$  and 6.

## 5 Conclusion

We have proposed a population balance approach to quantitatively represent the fluid eddy size distribution and to characterize the time-dependent average interfacial area of fluid eddies by a moment relationship. Our objective was to explore the hypothesis to assess (1) if such computations can be executed rapidly and efficiently, and (2) if general experimental observations can be explained by the model. The relationships with other models that we have discussed are also relevant. We find the model is a straightforward approach that elucidates experimental and modeling observations for blending and reactive mixing processes. A distinct advantage is the computational ease of implementing the theory. The model assumes that uncorrelated eddy distributions describe binary fragmentation and coalescence, concentrations in the continuous and dispersed phases are uniform and that the immiscible continuous and dispersed phases are well mixed in the vessel.

Models can be judged by the types of parameters that appear in the governing equations. In the current theory several parameters are given by the conditions of the problem: the volume fraction of dispersed fluid,  $\alpha$ , the initial and inlet dispersed fluid concentration,  $C_0$  and  $C_{in}$ , and the initial bulk fluid concentration,  $C_{b0}$ . The computational results are relatively insensitive to the coalescence-fragmentation ratio  $\gamma$  less than 0.1. The parameter  $\nu$  is related to the shape of turbulent fluid eddies, and thus is likely to be in the range  $-1/2$  to  $-0.9$ . The Damkohler number,  $\kappa_M$ , which is a ratio of mass transfer coefficient to fragmentation coefficient, is determined by comparison with one experimental point, as demonstrated here and in our previous report on the population balance modeling approach to turbulent reactive mixing [7]. We have assumed certain conditions for the population balance equation, namely, coalescence with constant rate coefficient and random-kernel fragmentation with rate coefficient proportional to fluid element size. These conditions lead to an analytical (similarity) solution for the size distribution with time dependence incorporated in the average size and determined by a single parameter,  $\gamma$ . A surprisingly simple asymptotic time dependence of the average eddy size,  $P^{avg} \sim (1 + \theta)^{-1}$ , governs the moment behavior and thus the mass transfer, allowing a straightforward computation of the mixing time in terms of the two significant parameters,  $\nu$  and  $\kappa_M$ . Although based on concepts familiar to chemical engineers, the new approach described here diverges significantly from other mixing theories and simulations, but realistically describes key behavior of turbulent blending.

## Nomenclature

- $c$  = concentration of the dispersed fluid, mol/m<sup>3</sup>
- $c_b$  = concentration of the bulk fluid, mol/m<sup>3</sup>
- $C = c/c_0$  = concentration of the dispersed fluid (dimensionless)
- $C_b = c_b/c_0$  = concentration of the bulk fluid (dimensionless)
- $\alpha$  = volume fraction of dispersed fluid

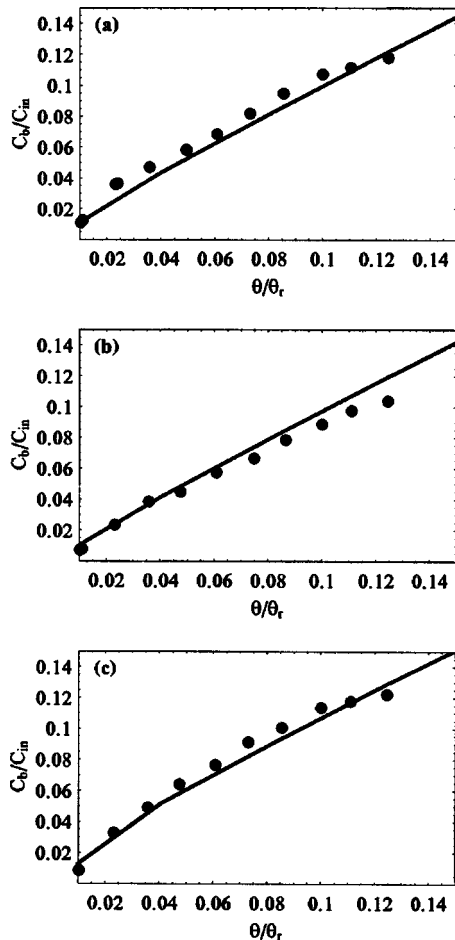


**Fig. 8** Comparison of the model [Eqs. (3.19) and (3.20)] with  $\gamma=0.01$  and  $\nu=-2/3$  and the experimental data of Marchisio et al. [26]. The other parameters are listed in Table 1.



$$\begin{aligned} \kappa_M &= k_{Mg} p_0^{(0)} (p_0^{\text{avg}})^{\nu} / k_{bo} \\ \gamma &= k_a p_0^{(0)} / k_{bo} \\ \theta &= t k_{bo} \\ \xi &= x / p_0^{\text{avg}} \\ \tau &= \int_0^\theta p^{(\nu)}(\theta) d\theta \\ a(t) &= g p^{(\nu)}(t) \text{ interfacial area/volume} \\ P(\xi, \theta) &= p(x, t) p_0^{\text{avg}} / p_0^{(0)}, \\ P^{(\nu)}(\theta) &= p^{(\nu)}(t) / p_0^{(0)} (p_0^{\text{avg}})^{\nu} \\ p^{\text{avg}} &= p^{(1)} / p^{(0)} \\ t &= \text{time} \\ x &= \text{fluid element mass} \end{aligned}$$

### Subscripts:

$M$  = molecular  
 $m$  = mixing, as in mixing time  
 $r$  = average residence time, as in  $t_r = V/Q$   
in = inlet condition  
0 = initial condition

### References

- [1] Nere, N. K., Patwardhan, A. W., and Joshi, J. B., 2003, "Liquid-Phase Mixing in Stirred Vessels: Turbulent Flow Regime." *Ind. Eng. Chem. Res.*, **42**, pp. 2661–2698.
- [2] Brodkey, R. S., 1967. *The Phenomena of Fluid Motions*, Addison–Wesley, Reading, MA, pp. 327, 335, 339.
- [3] Baldyga, J., and Bourne, J. R., 1999. *Turbulent Mixing and Chemical Reactions*, Wiley, Chichester.
- [4] Joshi, J. B., and Renade, V. V., 2003. "Computational Fluid Dynamics for Designing Process Equipment: Expectations, Current Status, and Path Forward," *Ind. Eng. Chem. Res.*, **42**, pp. 1115–1128.
- [5] Ottino, J. M., DeRoussel, P., Hansen, S., and Khakhar, D. V., 1999, "Mixing and Dispersion of Viscous Liquids and Powdered Solids," *Adv. Chem. Eng.*, **25**, pp. 105–204.
- [6] Danckwerts, P. V., 1953, "The Definition and Measurement of Some Characteristics of Mixtures," *Appl. Sci. Res.*, pp. 279–296.
- [7] Madras, G., and McCoy, B. J., 2004, "Chemical Kinetics and Reactive Mixing: Fragmentation and Coalescence in Turbulent Fluids," *AIChE J.*, **50**, pp. 835–847.
- [8] McCoy, B. J., and Madras, G., 2003, "Chemical Kinetics in Dispersed-Phase Reactors: Effects of Fragmentation and Coalescence," *Int. J. Chem. Reaction*

- Eng. **1**, A10.
- [9] Frisch, U., and Orszog, S. A., 1990, "Turbulence: Challenges for Theory and Experiment," *Phys. Today*, **43**, pp. 24–32.
- [10] Madras, G., and McCoy, B. J., 2002, "Numerical and Similarity Solutions for Reversible Population Balance Equations With Size-Dependent Rates," *J. Colloid Interface Sci.*, **246**, pp. 356–365.
- [11] McCoy, B. J., and Madras, G., 2003, "Analytical Solution for a Population Balance Equation with Aggregation and Fragmentation," *Chem. Eng. Sci.*, **58**, pp. 3049–3051.
- [12] McCoy, B. J., and Madras, G., 2002, "Tracer Mixing Dynamics during Aggregation and Fragmentation," *AIChE J.*, **48**, pp. 2167–2178.
- [13] Patwardhan, A. W., and Joshi, J. B., 1999, "Relation between Flow Pattern and Blending in Stirred Tanks," *Ind. Eng. Chem. Res.*, **38**, p. 3131.
- [14] Chen, M. S. K., 1971, "The Theory of Micromixing for Unsteady State Flow Reactors," *Chem. Eng. Sci.*, **26**, pp. 17–29.
- [15] Alvarez, M. M., Zalc, J. J., Shinbrot, T., Arratia, P. E., and Muzzio, F. J., 2002, "Mechanisms of Mixing and Creation of Structure in Laminar Stirred Tanks," *AIChE J.*, **48**, pp. 2135–2148.
- [16] Ottino, J. M., 1985, *The Kinetics of Mixing, Stretching, Chaos, and Transport*, Cambridge University Press, Cambridge.
- [17] McCoy, B. J., and Madras, G., 1998, "Evolution to Similarity Solutions for Fragmentation and Aggregation," *J. Colloid Interface Sci.*, **201**, pp. 200–209.
- [18] McCoy, B. J., and Wang, M., 1994, "Continuous-Mixture Fragmentation Kinetics: Particle Size Reduction and Molecular Cracking," *Chem. Eng. Sci.*, **49**, pp. 3773–3785.
- [19] Ziff, R. M., 1991, "New Solutions to the Fragmentation Equation," *J. Phys. A*, **24**, pp. 2821–2828.
- [20] Beek, J., and Miller, R. S., 1959, "Turbulent Transport In Chemical Reactors," *Chem. Eng. Prog., Symp. Ser.*, **55**, pp. 23–28.
- [21] Abramowitz, M., and Stegun, I. A., 1965, *Handbook of Mathematical Functions*, Dover, New York.
- [22] Voncken, R. M., Holmes, D. B., and Den Hartog, H. W., 1964, "Fluid Flow in Turbine Stirred, Baffled Tanks—II: Dispersion During Circulation," *Chem. Eng. Sci.*, **19**, pp. 201–298.
- [23] Patwardhan, A. W., Pandit, A. B., and Joshi, J. B., 2003, "The Role of Convection and Turbulent Dispersion in Blending," *Chem. Eng. Sci.*, **58**, pp. 2951–2962.
- [24] Fang, J. Z., and Lee, D. J., 2001, "Micromixing Efficiency In Static Mixer," *Chem. Eng. Sci.*, **56**, pp. 3797–3802.
- [25] Fournier, M. C., Falk, L., and Villermaux, J., 1996, "A New Parallel Competing Reaction System For Assessing Micromixing Efficiency—Determination Of Micromixing Time By A Simple Model," *Chem. Eng. Sci.*, **51**, pp. 5187–5192.
- [26] Marchisio, D. L., Barresi, A. A., and Fox, R. O., 2001, "Simulation of Turbulent Precipitation in a Semi-batch Taylor-Couette reactor Using CFD," *AIChE J.*, **47**, pp. 664–676.

# Unstructured Grid Based Reynolds-Averaged Navier-Stokes Method for Liquid Tank Sloshing

**Shin Hyung Rhee**

Lead Engineer  
Member ASME  
Fluent, Inc., 10 Cavendish Ct.,  
Lebanon, NH 03766  
e-mail: shr@fluent.com

*The present study is concerned with liquid tank sloshing at low filling level conditions. The volume of fluid method implemented in a Navier–Stokes computational fluid dynamics code is employed to handle the free-surface flow of liquid sloshing. The geometric reconstruction scheme for the interface representation is employed to ensure sharpness at the free surface. The governing equations are discretized by second order accurate schemes on unstructured grids. Several different computational approaches are verified and numerical uncertainties are assessed. The computational results are validated against existing experimental data, showing good agreement. The capability is demonstrated for a generic membrane-type liquefied natural gas carrier tank with a simplified pump tower inside. The validation results suggest that the present computational approach is both easy to apply and accurate enough for more realistic problems. [DOI: 10.1115/1.1906267]*

## Introduction

Sloshing in hydrodynamics can be defined as a free-surface flow in a container that is subjected to a forced motion. Tank sloshing problems in ships or offshore structures are increasingly of concern to naval architects and ocean engineers, as they are directly related to the safety of the ocean structure as well as to its cargo. The recent increase in demand for midsize tankers and liquefied natural gas (LNG) carriers entails more attention on the accurate prediction of sloshing fluid behavior inside tanks, whereby ship motions are more reactive to the external disturbances and the natural periods of sloshing are longer due to growing individual tank sizes. Moreover, the popularity of moored floating production storage offloading units, which need to be designed to withstand severe sea states and eventually severe sloshing load inside, warrants more complete and general tools for tank sloshing analysis. Besides ship/offshore hydrodynamics, liquid sloshing is also an important physical phenomenon that needs to be considered in many applications; for example, fuel tanks on spacecraft, liquid tanks on highway trucks and railroad cars, and large oil storage tanks and nuclear reactors under the influence of earthquakes, to name a few.

Experimental studies have been the most popular approach for liquid sloshing and have provided valuable insights into the physics, e.g., Abramson et al. [1]; however, it is difficult to scale down all the physics involved and extend the model test measurements to full scale predictions. Moreover, it takes a huge amount of time and effort to carry out the tests even for relatively simple geometries and motions. In the following, therefore, only analytic and numerical approaches in relevant studies are reviewed.

In the early days of sloshing studies, when computer simulation was in its infancy, several analytic methods were proposed, and a good review of studies at that time in the 1960s is available in Abramson [2]. Later Faltinsen [3] proposed a nonlinear analytic method using a perturbation technique applied to a potential flow formulation and many variations followed. Simple and mild sloshing problems were targets of these methods and a great deal of

fundamental understanding of sloshing was obtained through the studies. However, liquid sloshing involves in most cases highly nonlinear and transient motions and therefore requires numerical simulation methods that can handle unsteady nonlinear free-surface flows. For those practical situation problems, analytic methods have clear limitations.

There have been four major approaches to the numerical simulation of liquid sloshing: (1) boundary element integral methods, (2) finite element methods for potential flow, (3) finite difference/volume methods solving the Euler/Navier–Stokes equations, and (4) the smoothed particle hydrodynamics method. As of the end of the last millennium, Cariou and Casella [4] provided a comparative study of various numerical simulation results, and the performance of a variety of numerical methods was presented. It should be noted that there are other methods certainly worth being mentioned, but not included in Cariou and Casella [4].

The boundary element integral methods [3,5,6] are the most efficient way of handling liquid sloshing as long as the liquid motion is very mild and the container geometry is simple. Recently, an effort to couple one of these methods with ship motion prediction analysis has shown the viability of these methods in some limited applications [7].

Another approach based on potential flow methods is solving the governing equations by the finite element formulation. Okamoto and Kawahara [8,9] and Kim et al. [10] provide good theoretical background of the finite element method for free-surface flows and show fairly good results. However, a large number of empirically determined formulas and parameters are involved and only limited validations are presented. Moreover, their free-surface solution is limited to mildly varying, single-valued interface and cannot allow overturning and/or multiple liquid volumes in the domain.

The most popular approach for liquid sloshing today is solving the Navier–Stokes equations with a solution method for moving free surface employing the finite difference or finite volume discretization schemes [11–18]. Many of them present detailed descriptions of numerical methods and show good comparison with experimental data and/or analytical solutions. Both interface tracking and capturing methods are used for free-surface solution in those studies, but for truly general free-surface motion like sloshing, it is acknowledged that interface capturing methods,

Presented at the 23rd International Conference on Offshore Mechanics and Arctic Engineering (OMAEE), Vancouver, Canada, June 2004. Submitted to ASME Journal of Fluids Engineering, October 8, 2004. Revised manuscript submitted, February 15, 2005. Associate Editor: S. P. Vanka.

such as the volume of fluid (VOF) method, are desired. With the recent advent of high speed computing, application of these methods is warranted for more general problems, in which the traditional potential flow based methods have difficulties, e.g., ones involving violent free-surface motion, complex geometries, air entrainment, liquid vaporization, and significant viscous flow effects.

Last, the smoothed particle hydrodynamics (SPH) method was applied quite recently to sloshing flows. The primary advantage of employing this method is that its initial volume grid generation is relatively simple, as the SPH method is based on the Lagrangian tracking of fluid particles in the computational domain. Applications of the method show flexibility in free-surface solutions with favorable comparison to experimental data [19,20]. Yet more thorough validations are desired and anticipated.

As Kim et al. [10] have pointed out, operating LNG carriers and oil tankers at all filling level conditions has become common in recent years, and issues with the sloshing motion at low filling level are raised as a hot topic for the design of those vessels. Although many studies have been done for high filling level conditions, for which the sloshing motion is of a standing wave type, only few studies [10,19] have been found for low filling level conditions, i.e., less than 20% of the tank length or width, for which the sloshing motion is of a progressive wave type and is accompanied by hydraulic jumps and wave breaking. However, rigorous validation and generalization of the computational methods are lacking in those studies: only free-surface shape and/or peak impact pressure are considered for simple geometries and simple motions. In order to address all these issues, the present study focuses on the liquid sloshing motion at low filling level conditions. The objectives are therefore; (1) presenting a computational method that can efficiently handle liquid sloshing, (2) verifying the various computational approaches, (3) assessing the numerical uncertainties, (4) validating the computational results against experimental data [21] including the whole pressure histories, and (5) demonstrating the capability by applying it to a generic membrane-type LNG carrier tank with a simplified pump tower inside.

The present paper is organized as follows. The mathematical modeling and numerical method are described in the next section. Then the model problem description and grid generation are presented, followed by the validation and results discussion. Last, some concluding remarks are made with recommendations for future work.

## Mathematical Modeling and Numerical Method

The computations were carried out using FLUENT, a general purpose computational fluid dynamics (CFD) software. The governing equations are written for the mass and momentum conservation, such that

$$\frac{\partial \rho}{\partial t} + \nabla \cdot (\rho \mathbf{v}) = 0 \quad (1)$$

$$\frac{\partial}{\partial t}(\rho \mathbf{v}) + \nabla \cdot (\rho \mathbf{v} \mathbf{v}) = -\nabla p + \nabla \cdot (\bar{\tau}) + \mathbf{F} \quad (2)$$

where  $\mathbf{v}$  is the velocity vector in the Cartesian coordinate system,  $p$  the static pressure, and  $\bar{\tau}$  the stress tensor given by

$$\bar{\tau} \equiv \mu \left[ (\nabla \mathbf{v} + \nabla \mathbf{v}^T) - \frac{2}{3} \nabla \cdot \mathbf{v} I \right] \quad (3)$$

where  $\mu$  is the molecular viscosity,  $I$  the unit tensor, and the second term on the right hand side the effect of volume dilation. In the present study, a moving reference coordinate system with its origin at the tank center was used. Therefore, an external force momentum source term is incorporated to take the proper transformation between the earth-fixed and tank-fixed coordinate systems into consideration. The external force,  $\mathbf{F}$ , can be written as

$$\mathbf{F} = \mathbf{g} - \frac{d\mathbf{U}}{dt} - \frac{d\mathbf{\Omega}}{dt} \times \mathbf{r} - 2\mathbf{\Omega} \times \mathbf{v} - \mathbf{\Omega} \times (\mathbf{\Omega} \times \mathbf{r}) \quad (4)$$

where  $\mathbf{g}$  is the gravitational acceleration vector,  $\mathbf{U}$  and  $\mathbf{\Omega}$  the translational and rotational velocity vectors of the tank-fixed coordinate system, respectively, and  $\mathbf{r}$  is the position vector in the tank-fixed coordinate system.  $\mathbf{U}$  and  $\mathbf{\Omega}$  are obtained by sinusoidal motion formula with given amplitudes and periods.

Once the Reynolds averaging approach for turbulence modeling is applied, the Navier–Stokes equations can be written in Cartesian tensor form as

$$\frac{\partial \rho}{\partial t} + \frac{\partial}{\partial x_i}(\rho u_i) = 0 \quad (5)$$

$$\begin{aligned} \frac{\partial}{\partial t}(\rho u_i) + \frac{\partial}{\partial x_j}(\rho u_i u_j) = & -\frac{\partial p}{\partial x_i} + \frac{\partial}{\partial x_j} \left[ \mu \left( \frac{\partial u_i}{\partial x_j} + \frac{\partial u_j}{\partial x_i} - \frac{2}{3} \delta_{ij} \frac{\partial u_l}{\partial x_l} \right) \right] \\ & + \frac{\partial}{\partial x_j}(-\overline{\rho u'_i u'_j}) + F_i \end{aligned} \quad (6)$$

where  $\delta_{ij}$  is the Kronecker delta, and  $-\overline{\rho u'_i u'_j}$  the Reynolds stresses. The Reynolds stress term is related to the mean velocity gradients, i.e., turbulence closure, by the Boussinesq hypothesis as

$$-\overline{\rho u'_i u'_j} = \mu_t \left( \frac{\partial u_i}{\partial x_j} + \frac{\partial u_j}{\partial x_i} \right) - \frac{2}{3} \left( \rho k + \mu_t \frac{\partial u_l}{\partial x_l} \right) \delta_{ij} \quad (7)$$

where  $\delta_{ij}$  is the Kronecker delta. It is generally accepted that the Reynolds averaging approach is valid in most unsteady flow problems, as long as the characteristic time scale is much larger than the turbulence fluctuation time scale, which is the case considered in the present study. The standard  $k$ - $\epsilon$  turbulence model [22], which is based on the Boussinesq hypothesis with transport equations for the turbulent kinetic energy,  $k$ , and its dissipation rate,  $\epsilon$ , was used for turbulence closure. The turbulent viscosity  $\mu_t$  was computed by combining  $k$  and  $\epsilon$  as  $\mu_t = \rho C_\mu k^2 / \epsilon$ , where  $C_\mu$  is an empirical constant set to 0.09 here, and inserted in Eq. (7) to close Eq. (6). The standard  $k$ - $\epsilon$  model is a workhorse of practical engineering flow calculations since the time it was proposed. Robustness, economy, and reasonable accuracy for a wide range of turbulent flows explain its popularity in industrial flow simulations.

As mentioned in the first section, the VOF method was employed to handle the free-surface flow of the sloshing liquid. The VOF formulation relies on the fact that two or more fluids/phases are not interpenetrating. For each additional phase, a new variable that is the volume fraction of the phase in the computational cell is introduced. In each cell, the volume fractions of all phases sum to unity. The fields for all variables and properties are shared by the phases and represent volume-averaged values, as long as the volume fraction of each of the phases is known at each location. Thus the variables and properties in any given cell are either purely representative of one of the phases or representative of a mixture of the phases, depending upon the volume fraction values. Based on the local volume fraction of the  $q$ th fluid,  $\alpha_q$ , the appropriate variables and properties are assigned to each cell within the domain. The tracking of the interfaces between the phases is accomplished by the solution of a continuity equation for the volume fraction of phases. For the  $q$ th phase, this equation has the following form:

$$\frac{\partial \alpha_q}{\partial t} + \mathbf{v} \cdot \nabla \alpha_q = 0 \quad (8)$$

Note that the volume fraction equation is not solved for the primary phase, but based on the following constraint:

$$\sum_{q=1}^n \alpha_q = 1 \quad (9)$$

A single momentum equation is solved throughout the domain, and the resulting velocity field is shared among the phases. The momentum equation is dependent on the volume fractions of all phases through the fluid properties, which are determined by the presence of the component phases in each control volume, e.g.,  $\rho = \sum_{q=1}^n \alpha_q \rho_q$ . The surface tension can be handled as a body force in the interface cells, but is not included in the present study. In the case of turbulence quantities, a single set of transport equations is solved, and the turbulence variables are shared by the phases throughout the field. Imposing boundary conditions was simple; no-slip condition on the tank walls.

The present CFD code employs a cell-centered finite-volume method that allows use of computational elements with arbitrary polyhedral shape. Convection terms are discretized using the second order accurate upwind scheme, while diffusion terms are discretized using the second order accurate central differencing scheme. For unsteady flow calculations, time derivative terms are discretized using the first order accurate backward implicit scheme. Currently, the first order accurate scheme is the only one available for temporal discretization of the volume fraction equation, and its drawbacks are discussed in Rhee and Koutsavdis [23] and Rhee and Makarov [24]. However, it should be noted that the thrust of the present study is the application of the VOF method to liquid sloshing and efforts are being made to enable higher order accurate schemes for the volume fraction equation. The velocity-pressure coupling and overall solution procedure are based on a SIMPLE-type segregated algorithm adapted to unstructured grid. The discretized equations are solved using pointwise Gauss-Seidel iterations, and an algebraic multigrid method accelerates the solution convergence. For large computations, parallel processing based on message passing is possible.

For the calculation of face fluxes for the VOF model, the geometric reconstruction (GR) [25] and high-resolution interface capturing (HRIC) [26] schemes were employed. These two schemes have produced the most desirable solutions for various types of free-surface flow in the author's other studies [24,27,28]. Note that the standard interpolation schemes are used to obtain the face fluxes whenever a cell is completely filled with one phase or another. When the cell is near the interface between two phases, one of the following schemes is used.

The GR scheme represents the interface between fluids using a piecewise-linear approach. It assumes that the interface between two fluids has a linear slope within each cell and uses this linear shape for calculation of the advection of fluid through the cell faces. The first step in this reconstruction scheme is calculating the position of the linear interface relative to the center of each partially filled cell, based on information about the volume fraction and its derivatives in the cell. The second step is calculating the advecting amount of fluid through each face using the computed linear interface representation and information about the normal and tangential velocity distribution on the face. The third step is calculating the volume fraction in each cell using the balance of fluxes calculated during the previous step.

The HRIC scheme is a blend of upwind and downwind discretizations, so that the computed fluxes of volume fraction do not overflow or underflow the cells. The blending of the upwind and downwind discretizations is determined by the local distribution of volume fraction, the relative free-surface position to the cell face where the flux is computed, and the local Courant number. Two modifications were applied to the original HRIC scheme such that (1) the explicit integration of the volume fraction equation is done within a subiteration loop, and (2) instead of using first order upwind discretization, the one-dimensional bounded version of QUICK [29] is used, when the flow is parallel to the interface.

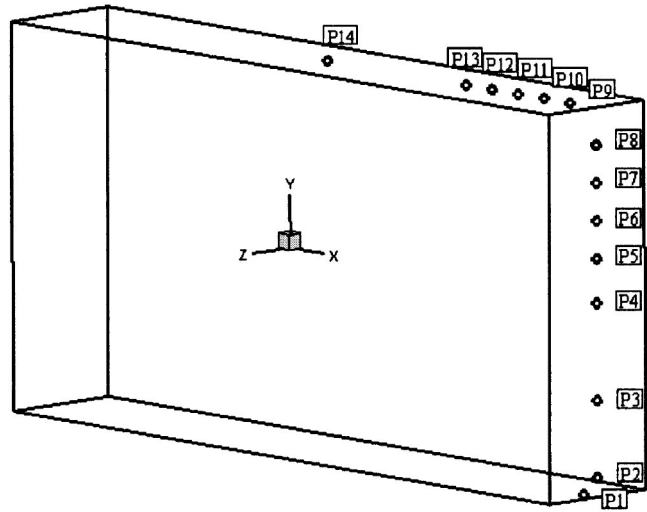


Fig. 1 Geometry of the tank and positions of pressure taps shown in the x-y plane

### Model Problems and Grid Generation

Two model problems were considered in the present study; one for validation and the other for capability demonstration. In both model problems, fresh water and air at 20°C were selected as the liquid and gas in the tank, respectively. For the validation purposes, the experiments carried out at the National Maritime Research Institute of Japan were selected [21]. The apparatus used in these experimental studies of sloshing allows sway, pitch, heave, and roll motion to be imposed on the tank, either separately or in any combination. The roll motion is centered at the coordinate system origin that is located at the tank center. The dimensions of the tank are 1.2 m wide, 0.6 m tall, and 0.2 m deep, as shown schematically in Fig. 1. It was confirmed during the experiments that the flow can be considered nearly two-dimensional (2D). Pressure taps for recording pressure variation with time were installed at 14 locations on one sidewall and on the bottom and top walls. In Fig. 1, these pressure taps are labeled P1–P14, and their coordinates are presented in Table 1. Note that only the data from three pressure taps, P1–P3, were considered in the present study, considering the low filling level that is even below P3 when there is no motion. In addition to pressure measurements, video recording was conducted over many periods of motion, allowing visual comparison of free-surface deformation between experiments and simulations.

The pure sway (translation along the  $x$  axis) and pure roll (rotation with respect to the  $z$  axis) motions were considered in the present study. The motions are simply sinusoidal. For all the

Table 1 Coordinates of pressure taps in  $m$

	$x$	$y$	$z$
P1	0.57	-0.3	0.0
P2	0.6	-0.27	0.0
P3	0.6	-0.15	0.0
P4	0.6	0.0	0.0
P5	0.6	0.068	0.0
P6	0.6	0.126	0.0
P7	0.6	0.184	0.0
P8	0.6	0.242	0.0
P9	0.542	0.3	0.0
P10	0.484	0.3	0.0
P11	0.426	0.3	0.0
P12	0.368	0.3	0.0
P13	0.31	0.3	0.0
P14	0.0	0.3	0.0

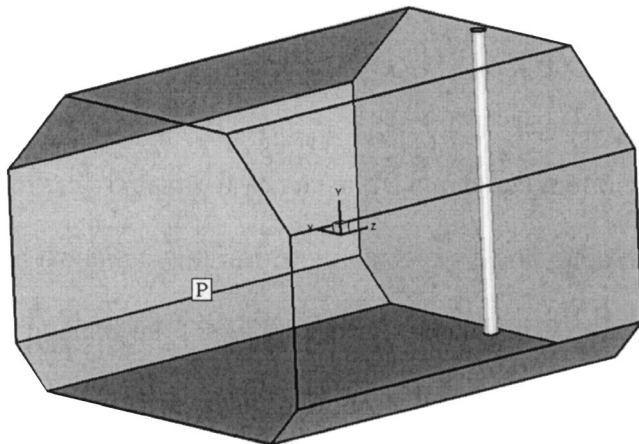
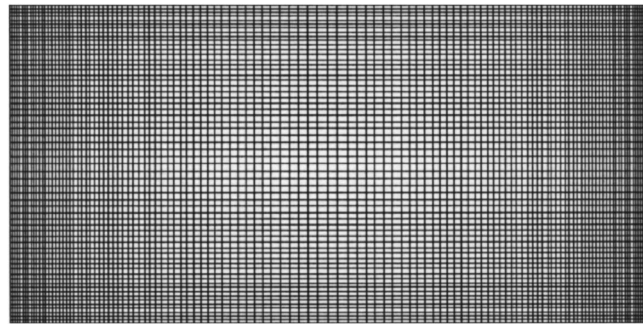
**Table 2 Computational conditions for rectangular tank cases**

Name	Motion	Filling level	Amplitude	Period
<i>Sway-base</i>	Sway	20% Height	0.06 m	1.94 s
<i>Sway-short</i>	Sway	20% Height	0.06 m	1.74 s
<i>Roll-base</i>	Roll	20% Height	10°	2.25 s
<i>Roll-short</i>	Roll	20% Height	10°	1.85 s

cases, the filling level was 20% of the tank height. Two cases for pure sway motion with a sway amplitude,  $A$ , of 0.06 m were considered; one with period,  $T$ , of 1.94 s and the other with  $T$  of 1.74 s, referred to as *sway-base* and *sway-short* cases, respectively. Similarly, two cases for pure roll motion with a roll amplitude,  $\theta$ , of 10 deg were considered; one with  $T$  of 2.25 s and the other with  $T$  of 1.85 s, referred to as *roll-base* and *roll-short* cases, respectively. These cases were deemed appropriate for the present study, as they reveal the physics associated with sloshing at low filling level conditions, the primary concern of the present study. Table 2 summarizes the conditions for these cases.

For demonstration purposes, sloshing at a low filling level condition in a generic LNG carrier was considered. It is a simplified geometry of a typical membrane-type LNG tank with a pump tower inside as shown in Fig. 2. The tank shape was taken from Abramson et al. [1]; the 2D tank shape in Fig. 5 of their paper was extruded in the third direction and a cylinder representing a simplified pump tower was added. The dimensions of the tank were 1.38 m wide, 1.02 m tall, and 1.5 m deep with upper and lower chamfers. The upper chamfer's width and height were both 0.295 m, while those of lower chamfers were both 0.14 m. A cylinder of 0.1 m diameter, which represented a simplified pump tower, was inserted at 0.05 m from one of the walls along the center plane. A model scale condition with low filling level was considered, i.e., with a filling level equal to 12% of tank breadth, 0.166 m, and a combined motion of sway (translation along the  $x$  axis), roll (rotation with respect to the  $z$  axis), and pitch (rotation with respect to the  $x$  axis). Each mode of motion with respect to the center of the tank was sinusoidal with sway amplitude of 0.015 m, sway period of 2 s, roll amplitude of 10 deg, roll period of 2.5 s, pitch amplitude of 1 deg, and pitch period of 30 s. The static pressure history was recorded at the halfway point along the knuckle of the lower chamfer, P, in Fig. 2.

Multiple grids were generated to check the validity of the chosen mathematical modeling as well as to evaluate the grid dependence of the solutions. For the rectangular tank cases, four 2D grids and one three-dimensional (3D) grid were generated. The base line 2D structured grid, shown in Fig. 3, consisted of  $120 \times 60 = 7200$  cells with the first cell size off the tank wall being 0.005 m. The 3D grid was a simple extension of this grid in the third direction, with  $120 \times 60 \times 20 = 144,000$  cells. The coarse and fine structured grids were generated by doubling and halving the grid spacing of the base line 2D structured grid in each direction, resulting in  $60 \times 30 = 1800$  and  $240 \times 120 = 28,800$  cells, respectively. A 2D unstructured grid was also generated to evaluate the performance of the code on unstructured grids in terms of efficiency and accuracy. Four quadrilateral cell layers were attached to the tank wall to resolve boundary layers and triangular cells filled the remaining region of the domain, as shown in Fig. 4. The overall grid resolution is comparable to the base line 2D structured grid, but with a larger number of cells, 13,074. For the generic LNG tank cases, an unstructured grid with 918,830 prism cells was generated. The first cell size off the tank wall was approximately 0.001 m. Figure 5 shows a partial view of the grid.

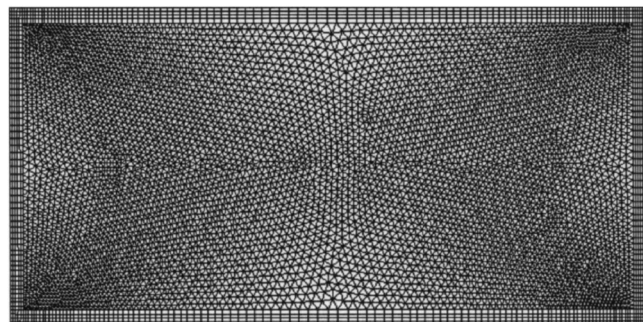
**Fig. 2 Geometry of the generic LNG tank****Fig. 3 Base line 2D structured grid for rectangular tank cases**

$\times 60 = 7200$  cells with the first cell size off the tank wall being 0.005 m. The 3D grid was a simple extension of this grid in the third direction, with  $120 \times 60 \times 20 = 144,000$  cells. The coarse and fine structured grids were generated by doubling and halving the grid spacing of the base line 2D structured grid in each direction, resulting in  $60 \times 30 = 1800$  and  $240 \times 120 = 28,800$  cells, respectively. A 2D unstructured grid was also generated to evaluate the performance of the code on unstructured grids in terms of efficiency and accuracy. Four quadrilateral cell layers were attached to the tank wall to resolve boundary layers and triangular cells filled the remaining region of the domain, as shown in Fig. 4. The overall grid resolution is comparable to the base line 2D structured grid, but with a larger number of cells, 13,074. For the generic LNG tank cases, an unstructured grid with 918,830 prism cells was generated. The first cell size off the tank wall was approximately 0.001 m. Figure 5 shows a partial view of the grid.

## Validation and Discussion

First of all, for the *sway-base* case, evaluation results of computational approaches are presented. Then numerical uncertainties are assessed in terms of grid and time step size dependence of the solutions for the *sway-base* case. In the last subsection, the computational results for both the rectangular tank and generic LNG tank cases are presented and discussed, along with validation results against the experimental data.

**Computational Approaches.** For the *sway-base* case, four different sets of computational approaches were evaluated; laminar flow versus turbulent flow, 2D versus 3D, structured grid versus unstructured grid, and GR scheme versus HRIC scheme. This evaluation is deemed to be an essential prerequisite for rigorous validations, as these issues need to be understood clearly prior to the final validation runs. Other computational parameters, e.g., under-relaxation factors, turbulence model constants, etc., were set based on the author's experience from previous studies, and their influence on solutions was found to be insignificant in problems of the present kind. Note that the baseline setup is the GR

**Fig. 4 A 2D unstructured grid for rectangular tank cases**

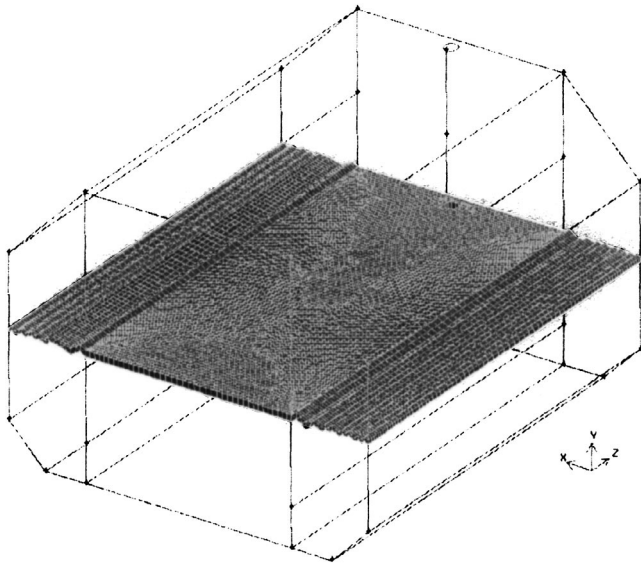


Fig. 5 Partial view of the generic LNG tank grid

scheme employed for turbulent flow on the baseline 2D structured grid with a time step size,  $\Delta t$ , of 0.001 seconds. It takes 1.2 seconds per time step to run the *sway-base* case with the baseline setup on a 2.6 GHz Linux desktop PC.

First, Fig. 6 displays the comparison of static pressure histories at P1 with and without turbulence. Note that the initial hydrostatic pressure values are subtracted for the static pressure presented throughout this study. Only small differences are seen between two curves; however, the laminar solution sometimes shows unphysical fluctuations, which seem to be due to numerical instabilities that resulted from ignoring turbulence effects. The same tendency is also observed in the free-surface shape. As shown in Fig. 7, the free-surface shape from the laminar flow solution exhibits unphysical irregularities and instabilities. Moreover, the contours of the root mean square of the turbulent velocity fluctuation,  $q = \sqrt{k}$ , displayed in Fig. 8, indicate pockets of non-negligible turbulence levels in both air and water regions, wherein the free surface is represented by the thick solid line in the domain. Including turbulence effects is, therefore, necessary especially for low filling level sloshing cases, in which violent fluid motion brings about significant turbulence.

Second, Fig. 9 shows the free-surface shape at a certain instant in a 3D simulation. Except for the small areas near the sidewalls, the free-surface shape is nearly two dimensional, confirming the experimental observation. Figure 10 displays the comparison of

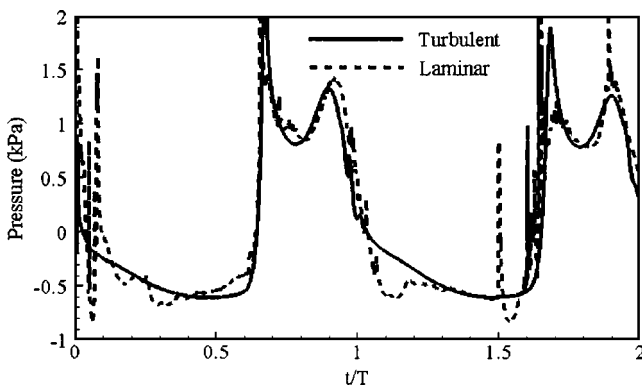


Fig. 6 Comparison of static pressure histories at P1 with and without turbulence

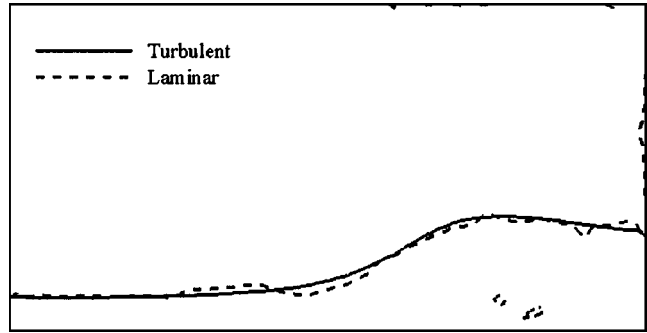


Fig. 7 Comparison of 2D free-surface shapes from solutions with and without turbulence

static pressure histories at P1 from 2D and 3D solutions. The two lines are very close to each other and suggest that the 3D effects are not significant in these rectangular tank cases.

Third, the free-surface shapes from solutions on the base line structured and unstructured grids are shown in Fig. 11. The VOF solutions are nearly the same on both grids, assuring that the VOF method of the present study performs equally well on triangular cells. The static pressure histories are also close to each other. However, the unstructured grid consists of larger number of cells

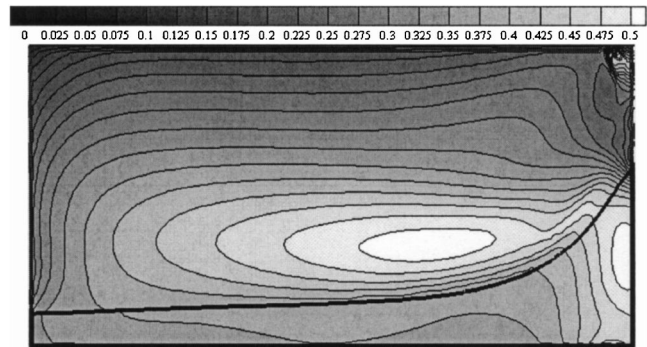


Fig. 8 Contours of turbulent fluctuation

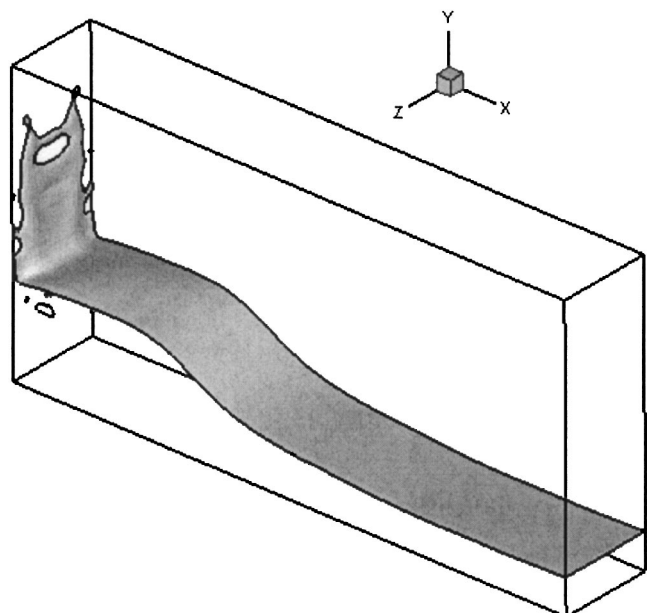


Fig. 9 A 3D free-surface shape at a certain instant

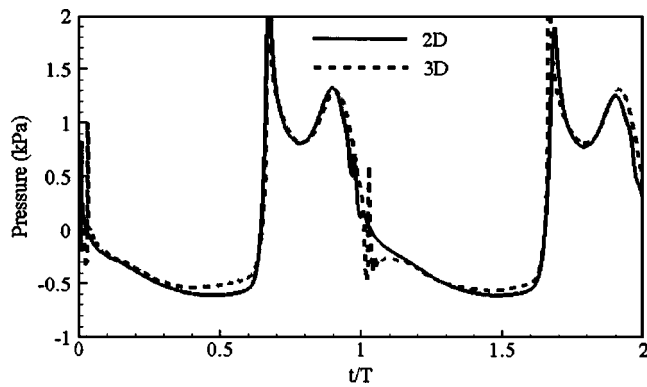


Fig. 10 Comparison of static pressure histories at P1 from 2D and 3D solutions

and accordingly requires more CPU time. For geometries that can be meshed easily using the structured grid generation approach, it is recommended to utilize this advantage as much as possible.

Last, the comparison of the static pressure histories at P1 from the solutions by the GR and HRIC schemes is shown in Fig. 12. The HRIC scheme solution appears smoother and under predicts the pressure peaks, suggesting that the scheme is more diffusive and perhaps more suitable for mild unsteady or steady flows. This behavior is confirmed in Table 3, which presents the comparison of the averaged impact pressure at P1. The definition of the averaged impact pressure is presented in the section for Results and Comparison with Data. It is interesting to see that while the motion of the free surface is not very different for the two schemes, the pressure prediction reveals considerable difference. This observation is congruent with the general notion that the GR scheme produces a more accurate solution for unsteady flow.

Based on these computational approach evaluation results, the base line setup, i.e., the GR scheme for turbulent flow on 2D structured grids, was employed for the rest of the rectangular tank

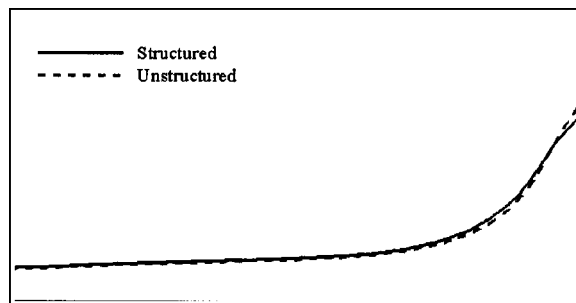


Fig. 11 Comparison of 2D free-surface shapes from solutions on the base line structured and unstructured grids

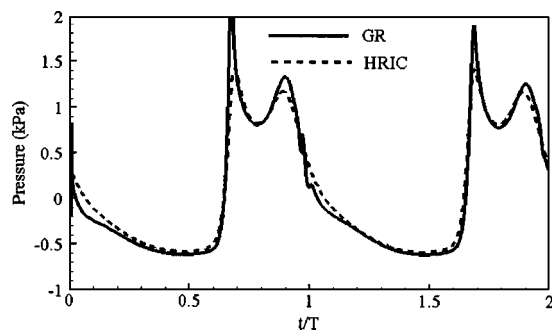


Fig. 12 Comparison of static pressure histories at P1 from GR and HRIC solutions

Table 3 Averaged impact pressure at P1 from GR and HRIC solutions

	Averaged impact pressure (kPa)	Error (% measured)
Measured	1.533	
GR	1.490	2.80
HRIC	1.328	13.4

cases. For the *sway-base* case with the base line setup, the local Courant number, which is based on the tank width, motion period, and individual cell size, ranges from  $4.5 \times 10^{-4}$  to 0.12, well within the known upper limit of 0.7. It does not necessarily mean, however, that the base line setup provides the most accurate computational results possible by the present method.

**Numerical Uncertainty Assessment.** In order to ensure high quality solutions, both grid and time step size dependence tests were carried out. The variable selected for the tests is the averaged impact pressure at P1. The grid dependence in terms of the relative difference,  $\varepsilon$ , between base line and fine grids is less than 6.2%. Note that  $\varepsilon$  is the relative difference in the solutions obtained at two grid or time step size levels considered and defined as  $\varepsilon = (\varphi_{\text{coarser}} - \varphi_{\text{finer}}) / \varphi_{\text{finer}}$ , where  $\varphi_{\text{coarser}}$  and  $\varphi_{\text{finer}}$  represent the solutions at the coarser and finer levels of the two, respectively. The results obtained on the coarse grid show 15.3% difference from the corresponding results obtained on the base line grid and were not considered for analysis. Similarly, the time step size dependence was estimated with three different  $\Delta t$ 's, base line,  $\Delta t = 0.001$ , large,  $\Delta t = 0.002$ , and extra large,  $\Delta t = 0.004$ . In each time step, subiterations were carried out until the solution residuals drop at least three orders of magnitude, which proved sufficient for general unsteady flow solutions. Normally it takes 10–20 subiterations to achieve the solution convergence within each time step. The time step size dependence in terms of  $\varepsilon$  is less than 2.5%. Table 4 summarizes the grid and time step size dependence results. Both of the dependence test results provide evidence that the solutions are practically insensitive to the grids and time step sizes in the considered range. Table 4 also presents the estimated order of accuracy,  $p$ , which is defined as  $p = \ln[(\varphi_{\text{medium}} - \varphi_{\text{coarse}}) / (\varphi_{\text{fine}} - \varphi_{\text{medium}})] / \ln(r)$ , where  $\varphi_{\text{coarse}}$ ,  $\varphi_{\text{medium}}$ , and  $\varphi_{\text{fine}}$  are solutions at coarse, medium, and fine levels, respectively, and  $r$  is the refinement ratio [30]. Even though the theoretical orders of accuracy are two and one in space and time, respectively, the values of  $p$  based on the selected variable are somewhat different and indicate that the present computational approach has an order of accuracy somewhere between one and two, which is the general tendency also observed in other CFD codes, e.g., see Wilson et al. [31]. In the following sections, the results obtained on the base line grid and with base line  $\Delta t$  are presented and validated.

**Results and Comparison with Data.** In this section, the computed results for the rectangular tank cases are presented first with comparison to corresponding experimental results, especially in detail for the *sway-base* case, and then discussed with respect to

Table 4 Grid and time step size dependence results

Grid	Averaged impact pressure (kPa)	$\varepsilon$
Fine	1.588	6.17%
Base line	1.490	15.3%
Coarse	1.262	$p = 1.22$
Time step size	Averaged impact pressure (kPa)	$\varepsilon$
Base line	1.490	0.94%
Large	1.504	2.46%
Extra large	1.541	$p = 1.40$

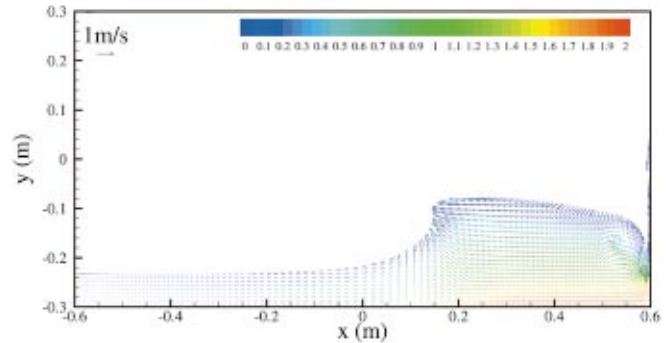
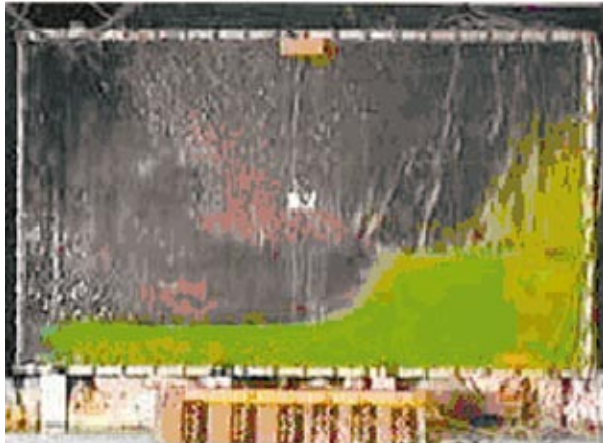
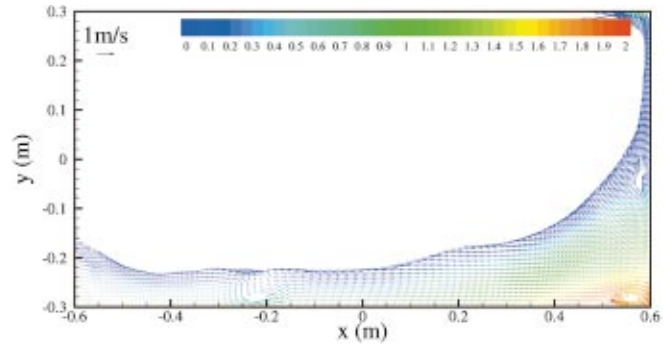


Fig. 13 Comparison of 2D free-surface shapes from the experiment and computation

the effects of different modes of motion and lengths of the period. The results for the generic LNG tank case are presented next to round off the demonstration of the capability.

The predicted free-surface shapes at different times are compared with experimental visualization. Although the free-surface deformation varies from one period to another, observation of the flow over several periods suggests that these variations are relatively small and that no important new features appear in different periods. Therefore, figures showing instantaneous free-surface shape from the simulation are compared with experimental visualization at approximately the same time within one period. Figure 13 shows typical results for the *sway-base* case. The figures of computed results also display velocity vectors colored by static pressure. The agreement is very good in terms of free-surface shape. Also in the computational results, the regions of high pressure are identifiable and the fluid motion due to the traveling wave is clearly observed in the liquid region.

For the *sway-base* case, Fig. 14 shows the comparison of static pressure histories at three pressure taps, P1–P3, which are located inside the region where the effects on the wall of the sloshing liquid are large. The overall agreement is very good both quantitatively and qualitatively. Note that there are two spikes in each period, which represent the impact of the sloshing liquid when there is the first hit by the traveling wave and the second by the momentum change due to the liquid falling down that once climbed up along the sidewall. Another point to note is the pressure history at P3 in which the pressure is zero for approximately 0.7 T in each period. This zero pressure indicates the time when the pressure tap is above the free surface and dry.

The comparison of averaged impact pressure from the experiment and computation is presented in Table 5. The averaged impact pressure is obtained by averaging the highest 10% pressure values for the periods considered, which is over at least five periods. It is well known that there is a need to filter out the noise in

both measurements and computations, as pointed out in Abramson et al. [1] and Kim [16]. The above averaging, which is similar to the measure used by the Bureau Veritas, is a relatively simple, yet quite meaningful, measure for structural design, as it is crucial in structural design to have comprehensive and reliable information of both the probable impact pressure and whole time histories of local pressure and total force on the walls. The raw pressure histories show that, at a given location, peak pressure values are generally in the range of 1.5 and 5.5 times the averaged impact pressure. As for the whole histories, the agreement between measured and computed values is excellent.

In addition to the pressure histories at individual pressure taps, the force histories on the tank walls were also recorded. As individual pressure histories at specific points are important for the structural analysis aspect, the total force histories on the tank walls are important for the interaction of liquid sloshing with the motion of the floating body on which the sloshing liquid acts. Figure 15 presents the computed force history in  $N$  on the right hand side wall. It is observed that the force history generally resembles that of the individual pressure histories, but with milder peaks.

The results of the other rectangular tank cases are presented now. Figure 16 shows the comparison of static pressure histories at three pressure taps, P1–P3, for the *sway-short* case. The agreement is as good as for the *sway-base* case.

The same comparison is made for the roll motion cases. Figs. 17 and 18 present the comparison of static pressure histories at the same three pressure taps for the *roll-base* and *roll-short* cases, respectively. For the *roll-base* case, the comparison is fairly good, although the first peak pressure in each period is overpredicted and larger than the second, unlike the trend in measurements. The comparison for the *roll-short* case is the least favorable of the four cases considered for rectangular tank sloshing. This seems to be due to the faster movement of blobs of fluid lumped together by



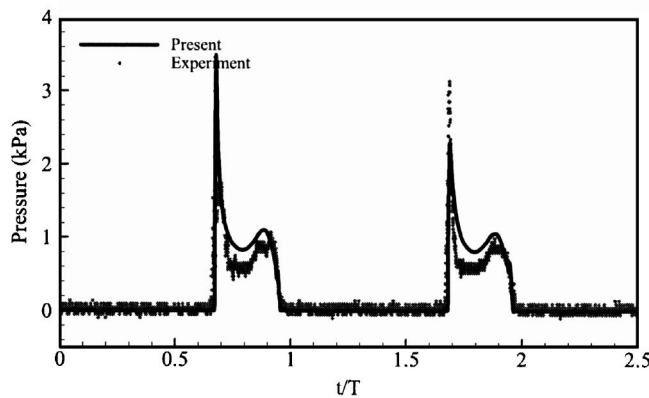
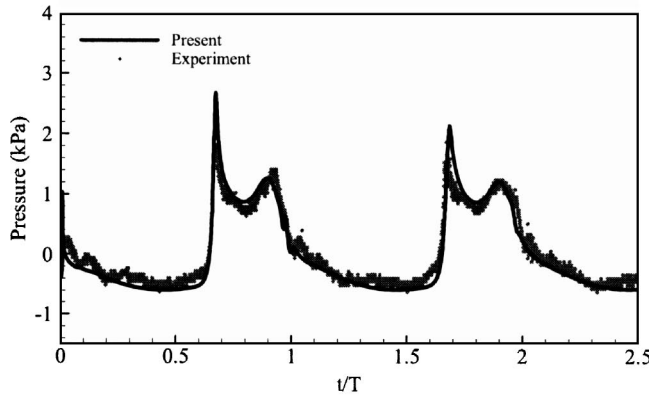
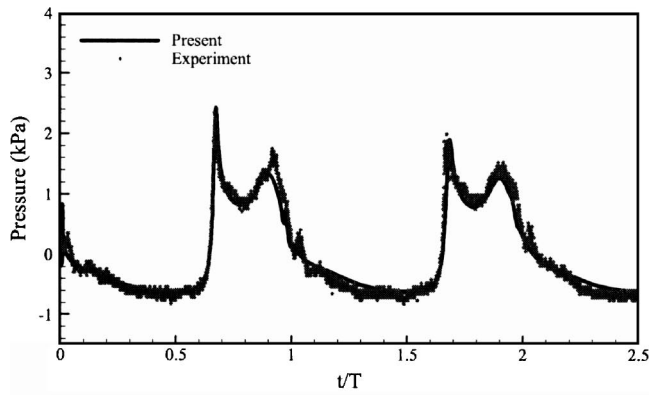


Fig. 14 Comparison of static pressure histories at P1 (top), P2 (middle), and P3 (bottom)—sway-base case

the rolling motion with the shorter period. Finer grids and smaller time step sizes may be required to handle this behavior with the momentum source term, Eq. (4), and produce better simulation results in this case.

Compiling all the results computed for the four cases involving the rectangular tank sloshing, it can be summarized that (a) the effect of different periods is clear; (b) the second pressure peaks are sharper when the period is shorter; (c) the receding speed of fluid from one sidewall is slower when the period is longer, in

Table 5 Comparison of averaged impact pressure from experiment and computation

Location	Measured (kPa)	Computed (kPa)	Error (% measured)
P1	1.533	1.490	2.80
P2	1.355	1.471	8.56
P3	1.398	1.345	3.79

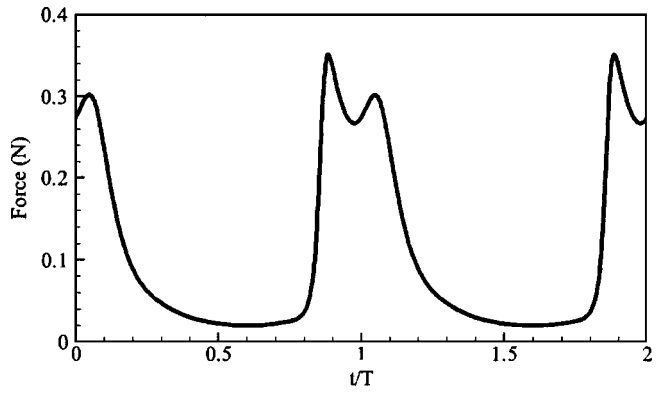


Fig. 15 Total force history on the right hand side wall—sway-base case

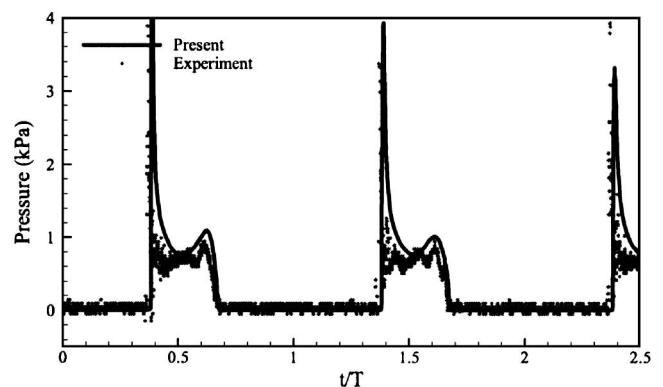
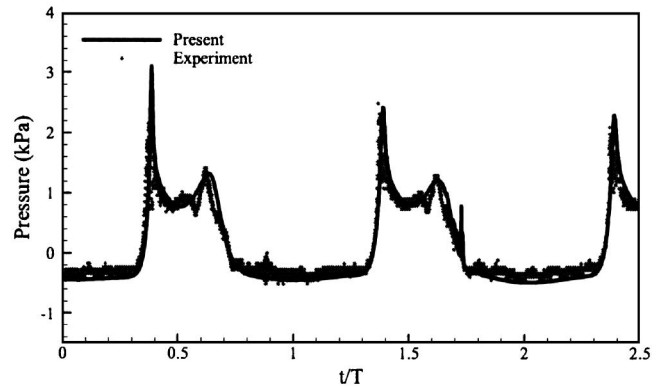
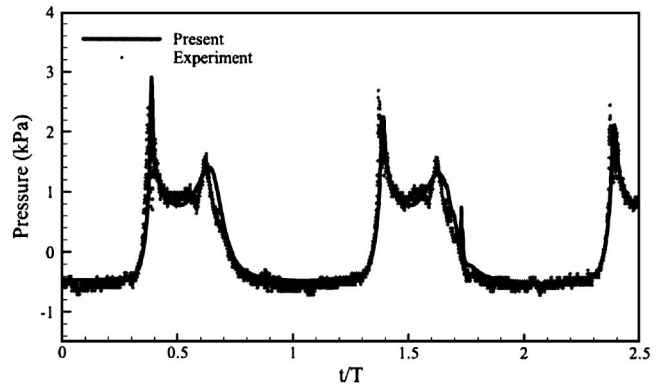


Fig. 16 Comparison of static pressure histories at P1 (top), P2 (middle), and P3 (bottom)—sway-short case

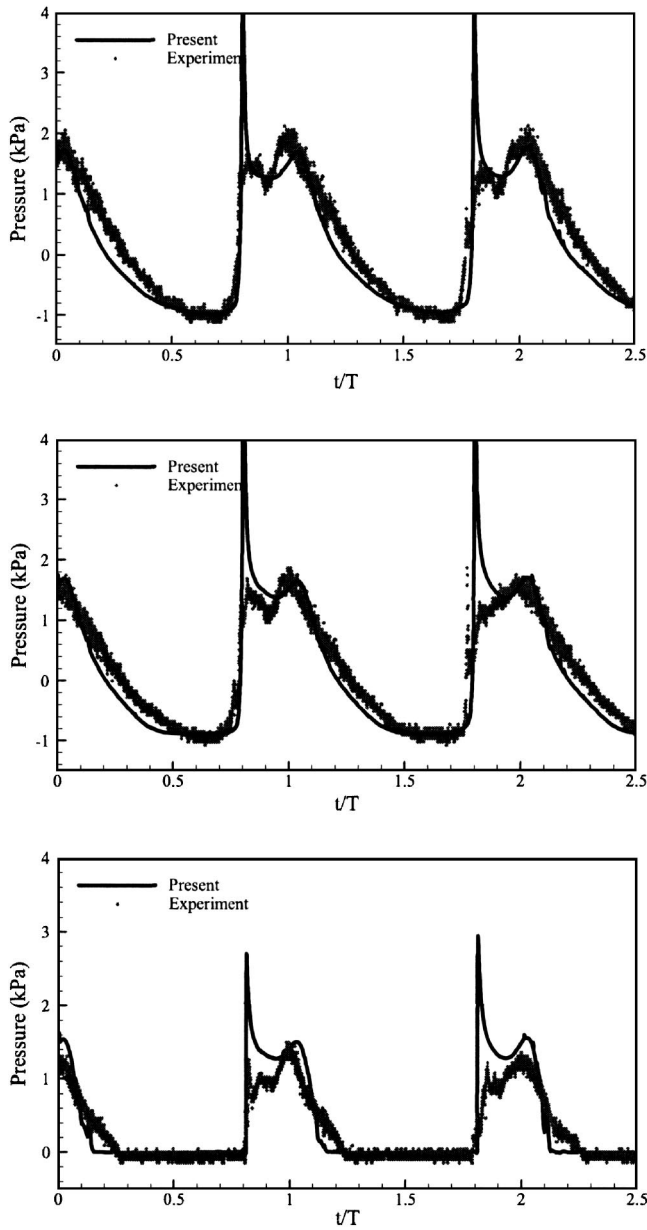


Fig. 17 Comparison of static pressure histories at P1 (top), P2 (middle), and P3 (bottom)—roll-base case

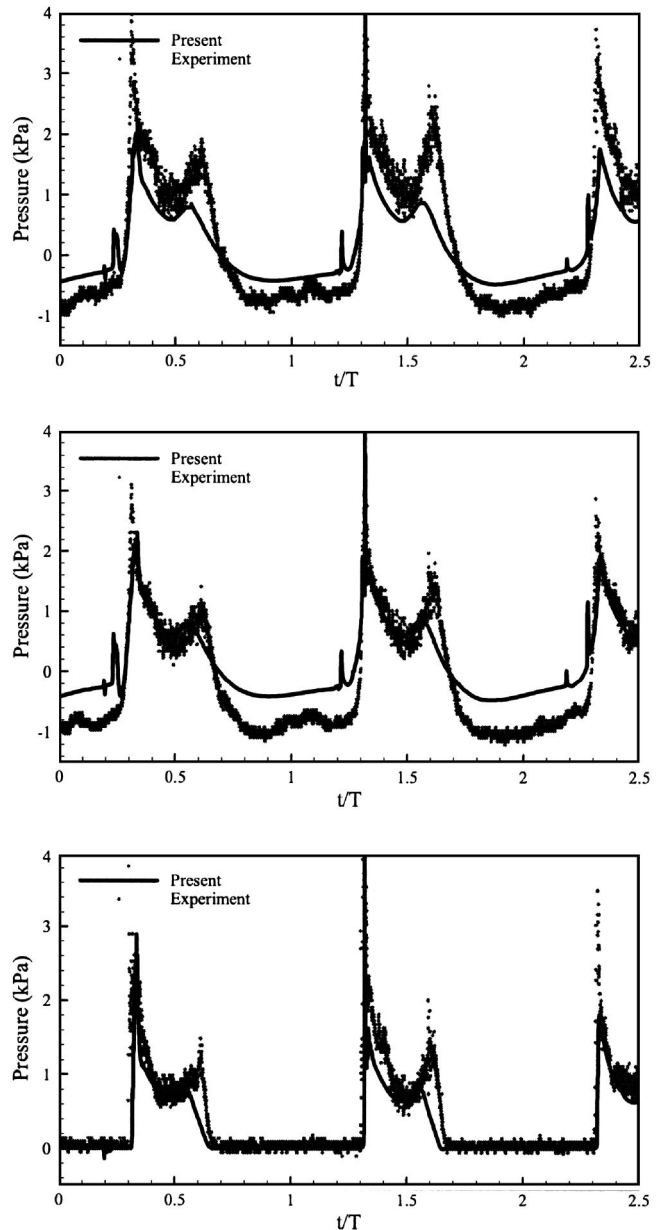


Fig. 18 Comparison of static pressure histories at P1 (top), P2 (middle), and P3 (bottom)—roll-short case

other words, the slope of pressure history after the second pressure peak is milder with a longer period; (d) overall trends in computational prediction agree fairly well with that in experimental measurements; and (e) better agreement is obtained for sway motion cases and it is attributed to the more stringent requirements for grids and time step sizes, which results from the more complicated momentum source term for rotating motions, cf. Eq. (4).

Last, the results of the generic LNG tank case are presented. Unfortunately there are no experimental data available for comparison and only computational results are discussed. Two snapshots of free-surface shape at different time steps are displayed in Fig. 19. Apparently 3D effects are significant, and the influence of the pump tower on the sloshing liquid is clearly seen. Also worth noting is the irregular free surface that reveals the burst of large air bubbles that were trapped during the wave breaking. The static pressure history at P is presented in Fig. 20. The trend is largely the same as that in rectangular tank cases, but the period does not

strictly equal any of the input periods provided by the motion parameters, which is obvious due to the combined motions in three modes, i.e., roll, sway, and pitch.

### Concluding Remarks

Liquid sloshing at low filling level conditions is studied using a Navier–Stokes solver. The VOF method is implemented in the CFD code to handle the free-surface flow of liquid sloshing. The geometric reconstruction scheme for the interface representation is employed to ensure sharpness at the free surface. The governing equations are discretized by second order accurate schemes on unstructured grids. Several different computational approaches are verified and numerical uncertainties are assessed and summarized: for the problems where 3D effects are not significant, 2D results show good comparison with experimental data; because of the pockets of high turbulence due to the violent motion of liquid, turbulence effects should be taken into account in mathematical modeling and computational methods; the present CFD code’s

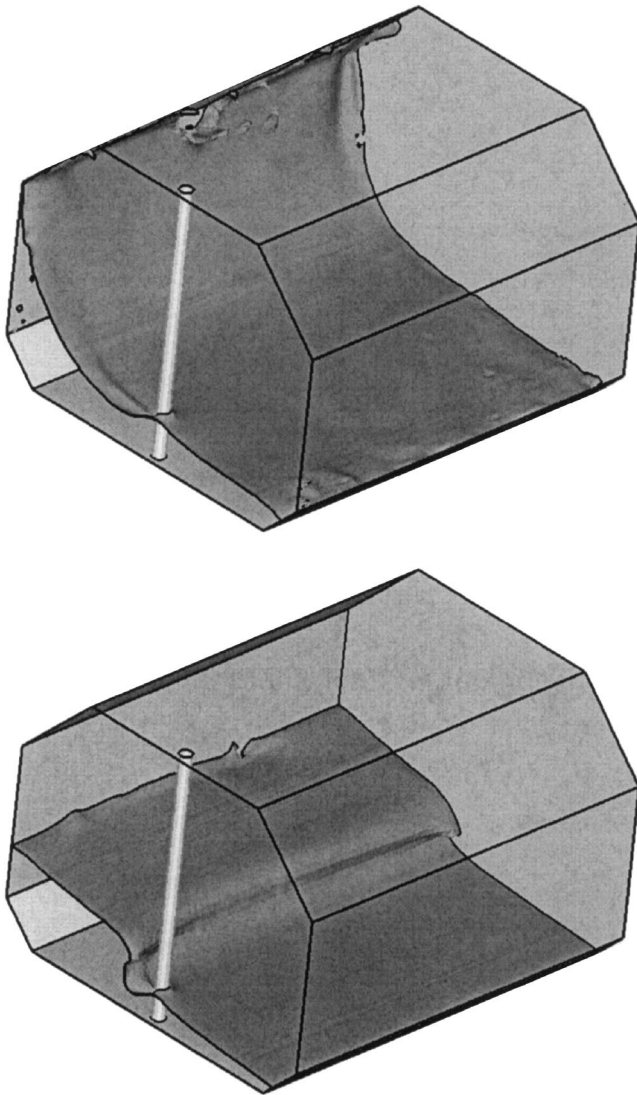


Fig. 19 Snapshots of free-surface shape at different time steps: 8.12 s (upper); 13.52 s (lower)

performance on unstructured grids is as good as on structured grids; the GR scheme appears to produce a more accurate solution for unsteady flow than the HRIC scheme.

The computational results of the rectangular tank cases are validated against existing experimental data, showing good agreement both qualitatively and quantitatively. The validation results sug-

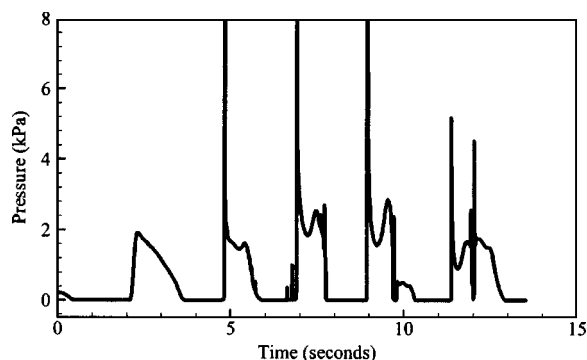


Fig. 20 Static pressure history at P

gest that the sway motion cases are more forgiving in terms of grid and time step size requirements, perhaps due to the simplicity of the momentum source term for coordinate transformation. The capability is demonstrated for a generic membrane type LNG carrier tank with a simplified pump tower inside. Although validations are not possible due to the unavailability of experimental data, the results show fairly reasonable behavior of liquid sloshing under a general tank motion. The overall results suggest that the present computational approach is both easy to apply and accurate enough for more realistic problems. Important outstanding issues for future work include improvement of numerical methods for faster solution procedure, handling of the fluid-structure interaction due to the insulation system on tank walls, modeling of the liquid compressibility and cushioning effect of bubbles, and coupling with external motion of the floating body on which the sloshing liquid acts.

### Acknowledgment

The experimental data were provided by the National Maritime Research Institute (NMRI) of Japan. The author would like to express his sincere gratitude to Dr. Munehiko Hinatsu of NMRI for his help in providing the experimental data.

### References

- [1] Abramson, H. N., Bass, R. L., Faltinsen, O., and Olsen, H. A., 1974, "Liquid Slosh in LNG Carriers," *Proc. Tenth Symp. on Naval Hydrodynamics*, Cambridge, MA, pp. 371–388.
- [2] Abramson, H. N., 1966, "The Dynamic Behavior of Liquids in Moving Containers," NASA SP-106.
- [3] Faltinsen, O. M., 1974, "A Nonlinear Theory of Sloshing in Rectangular Tanks," *J. Ship Res.*, **18**(4), pp. 224–241.
- [4] Cariou, A., and Casella, G., 1999, "Liquid Sloshing in Ship Tanks: A Comparative Study of Numerical Simulation," *Mar. Struct.*, **12**, pp. 183–198.
- [5] Nakayama, T., 1990, "A Computational Method for Simulating Transient Motions of an Incompressible Inviscid Fluid with a Free Surface," *Int. J. Numer. Methods Fluids*, **10**, pp. 683–695.
- [6] Liu, Z., and Huang, Y., 1994, "A New Method for Large Amplitude Sloshing Problems," *J. Sound Vib.*, **175**(2), pp. 185–195.
- [7] Kim, Y., Shin, Y.-S., Lin, W.-M., and Yue, D. K. P., 2003, "Study on Sloshing Problem Coupled with Ship Motion in Waves," *Proc. Eighth Int. Conf. on Num. Ship Hydrodynamics*, Busan, Korea.
- [8] Okamoto, T., and Kawahara, M., 1990, "Two-Dimensional Sloshing Analysis by Lagrangian Finite Element Method," *Int. J. Numer. Methods Fluids*, **11**(5), pp. 453–477.
- [9] Okamoto, T., and Kawahara, M., 1997, "3-D Sloshing Analysis by an Arbitrary Lagrangian-Eulerian Finite Element Method," *Int. J. Comput. Fluid Dyn.*, **8**(2), pp. 129–146.
- [10] Kim, J. W., Shin, Y., and Bai, K. J., 2002, "A Finite-Element Computation for the Sloshing Motion in LNG Tank," *Proc. 12th International Offshore and Polar Engineering Conference*, Fukuoka, Japan.
- [11] Bridges, T. J., 1981, "A Numerical Simulation of Large Amplitude Sloshing," *Proc. Third Int. Conf. on Numerical Ship Hydrodynamics*, Basin d'Essais des Carènes, Paris, France, pp. IV-4-1–VI-4-15.
- [12] Sicilian, J. M., and Tegart, J. R., 1989, "Comparison of FLOW-3D Calculations with Very Large Amplitude Slosh Data," *Proc. ASME/JSME Pressure Vessels and Piping Conference*, Honolulu, HI.
- [13] Kassinos, A. C., and Prusa, J., 1990, "A Numerical Model for 3-D Viscous Sloshing in Moving Containers," *Recent Advances and Applications in Computational Fluid Dynamics*, O. Baysal, ed., ASME FED, New York, Vol. 103, pp. 75–86.
- [14] Armenio, V., 1997, "An Improved MAC Method (SIMAC) for Unsteady High-Reynolds Free Surface Flows," *Int. J. Numer. Methods Fluids*, **24**, pp. 185–214.
- [15] Ushijima, S., 1998, "Three-Dimensional Arbitrary Lagrangian-Eulerian Numerical Prediction Method for Non-Linear Free Surface Oscillation," *Int. J. Numer. Methods Fluids*, **26**, pp. 605–623.
- [16] Kim, Y., 2001, "Numerical Simulation of Sloshing Flows with Impact Load," *Appl. Ocean Res.*, **23**, pp. 53–62.
- [17] Celebi, M. S., and Akyildiz, H., 2002, "Nonlinear Modeling of Liquid Sloshing in a Moving Rectangular Tanks," *Ocean Eng.*, **29**, pp. 1527–1553.
- [18] Sames, A., Marcouly, D., and Schellin, T. E., 2002, "Sloshing in Rectangular and Cylindrical Tanks," *J. Ship Res.*, **46**(3), pp. 186–200.
- [19] Iglesias, A. S., Pavon, C. L., and Frayssé, B., 2003, "SPH Simulations of Free Surface Movements of Passive Stabilizing Tanks for Fishing Vessels," *Proc. Eighth Int. Conf. on Num. Ship Hydrodynamics*, Busan, Korea.
- [20] Landrini, M., Colagrossi, A., and Faltinsen, O. M., 2003, "Sloshing in 2-D Flows by the SPH Method," *Proc. Eighth Int. Conf. on Num. Ship Hydrodynamics*, Busan, Korea.
- [21] Tanaka, Y., Ando, T., and Miyamoto, T., 2000, "Experimental Study on Sloshing Load Measured by Panel-Type Pressure Gauge," *Proc. 74th General Meet-*

- ing of Ship Research Institute, Ship Research Institute, Tokyo, Japan, pp. 137–142.
- [22] Launder, B. E., and Spalding, D. B., 1972, *Lectures in Mathematical Models of Turbulence*, Academic, London, England.
- [23] Rhee, S. H., and Koutsavdis, E., 2005, “Two-Dimensional Simulation of Unsteady Marine Propulsor Blade Flow Using Dynamic Meshing Techniques,” *Computers and Fluids*, (in press).
- [24] Rhee, S. H., and Makarov, B., 2005, “Validation Study for Free-Surface Wave Flows Around Surface-Piercing Cylindrical Structures,” *Proc. 24th International Conference on Offshore Mechanics and Arctic Engineering*, Halkidiki, Greece.
- [25] Youngs, D. L., 1982, “Time-Dependent Multi-Material Flow with Large Fluid Distortion,” in *Numerical Methods for Fluid Dynamics*, K. W. Morton and M. J. Baines, ed., Academic, New York.
- [26] Muzaferija, S., Peric, M., Sames, P., and Schellin, T., 1998, “A Two-Fluid Navier-Stokes Solver to Simulate Water Entry,” *Proc. 22nd Symposium on Naval Hydrodynamics*, Washington, DC, pp. 277–289.
- [27] Rhee, S. H., Makarov, B., Krishnan, H., and Ivanov, V., 2004, “Assessment of Numerical Techniques in Volume of Fluid Method for Free-Surface Wave Flows,” *Proc. Ninth International Symposium on Practical Design of Ships and Other Floating Structures*, Hamburg, Germany.
- [28] Rhee, S. H., and Skinner, C., 2005, “Unstructured Grid Based Navier-Stokes Solver for Free-Surface Flow around Surface Ships,” *Proc. CFD Workshop Tokyo 2005*, Tokyo, Japan.
- [29] Leonard, B. P., 1979, “A Stable and Accurate Convective Modelling Procedure Based on Quadratic Upstream Interpolation,” *Comput. Methods Appl. Mech. Eng.*, **19**, pp. 59–98.
- [30] Roache, P. J., 1997, “Quantification of Uncertainty in Computational Fluid Dynamics,” *Annu. Rev. Fluid Mech.*, **29**, pp. 123–160.
- [31] Wilson, R. V., Stern, F., Coleman, H. W., and Paterson, E. G., 2001, “Comprehensive Approach to Verification and Validation of CFD Simulations-Part 2: Application for RANS Simulation of a Cargo/Container Ship,” *J. Fluids Eng.*, **123**, pp. 803–810.

# Influence of Wall Proximity on the Lift and Drag of a Particle in an Oscillatory Flow

Paul F. Fischer

Gary K. Leaf

Mathematics and Computer Science Division,  
Argonne National Laboratory,  
Argonne, IL 60439

Juan M. Restrepo<sup>1</sup>

e-mail: restrepo@math.arizona.edu  
Department of Mathematics and  
Department of Physics,  
University of Arizona, Tucson, AZ 85721

*We report on the lift and drag forces on a stationary sphere subjected to a wall-bounded oscillatory flow. We show how these forces depend on two parameters, namely, the distance between the particle and the bounding wall, and on the frequency of the oscillatory flow. The forces were obtained from numerical solutions of the unsteady incompressible Navier–Stokes equations. For the range of parameters considered, a spectral analysis found that the forces depended on a small number of degrees of freedom. The drag force manifested little change in character as the parameters varied. On the other hand, the lift force varied significantly: We found that the lift force can have a positive as well as a negative time-averaged value, with an intermediate range of external forcing periods in which enhanced positive lift is possible. Furthermore, we determined that this force exhibits a viscous-dominated and a pressure-dominated range of parameters. [DOI: 10.1115/1.1905647]*

## 1 Introduction

We study the lift and drag forces on a sphere that is held a fixed distance away from an ideally smooth wall. The sphere is immersed in an incompressible fluid that is subjected to time-periodic forcing. This study is a follow-up on Fischer et al. [1] (hereafter referred to as FLR02), in which we explored the dependence of the lift and drag on the Reynolds number and the non-dimensional forcing period, referred to as the Keulegan–Carpenter number. In that study the sphere was also held fixed in time and space; however, it rested on the bounding wall. The methodology followed here is the same as in FLR02: We use time-dependent three-dimensional simulations of the Navier–Stokes equations to obtain the flow from which we can obtain the lift and drag on the particle.

In FLR02, we reported that, for the range of parameters considered, the lift and drag varied more dramatically with changes in the Keulegan–Carpenter number rather than with changes in the Reynolds number. In this study we focus on how these forces depend on the Keulegan–Carpenter number and on the *gap*, which is the shortest distance between the surface of the sphere and the wall, normalized to the diameter of the particle.

Numerous studies have examined oscillatory flows past stationary cylinders (e.g., Bearman et al. [2], Sarpkaya [3], Obajasu et al. [4], Justesen [5]). Many of these studies have been motivated primarily by the need to characterize forces resulting from rhythmic flow around submerged pipes in oceanic settings. Little, however, has appeared in print regarding forces on a spherical particle in an oscillating flow, particularly in proximity to a bounding wall. When one compares the experimental results of Rosenthal and Sleath [6] and FLR02, it becomes clear that the topological differences between two-dimensional cylinder flow and three-dimensional flow past a sphere prevent one from extrapolating the cylinder results to the spherical case.

Our flow configuration is characterized by the three independent flow parameters: The Keulegan–Carpenter number, the Reynolds number, and the gap. The resulting fluid motion due to an oscillating far-field velocity field is unsteady, and thus steady-state

or unidirectional analyses are not generally applicable. Hence, the Keulegan–Carpenter number plays a more prominent role in determining the nature of the flow than does the Reynolds number. Indeed, this was borne out in FLR02: Variations in the flow were significantly more dramatic when the Keulegan–Carpenter number was varied, rather than when the Reynolds number was varied, when the particle was resting on the bounding wall. Our present calculations do not indicate that introducing a gap changes this outcome much. Hence, all results presented here correspond to a fixed Reynolds number of 100. The insensitivity of the lift and drag to the Reynolds number is not totally unexpected: The Reynolds number is defined in terms of the maximum speed of the far-field (bulk) flow, the diameter of the particle, and the fluid viscosity. This choice of Reynolds number is more appropriate for a steady-flow situation; nevertheless, we use it because FLR02 as well as this study were inspired by experimental work due to Rosenthal and Sleath [6] in which the Reynolds number was defined as stated above. The gap parameter, on the other hand, is particularly important because the proximity of a wall to an object subjected to steady flows has a significant influence on the forces experienced by the particle (see Hall [7], Cherukat et al. [8], Asmolov and McLaughlin [9], and references mentioned in these works). It would be reasonable to expect important changes on the lift and drag forces on a particle subjected to a flow in the vicinity of a wall when the gap width is varied, especially if the boundary layers in the neighborhood of the wall and the sphere are comparable to the gap width.

In Sec. 2 we describe the physical configuration of the particle and the flow. We also briefly describe how this flow is computed numerically. In Sec. 3 we present the numerical results of measurements of the drag force and discuss its dependence on the gap and frequency parameters of the flow. In Sec. 4 we discuss the results for the lift force. In Sec. 5 we consider the dynamic implications of combined drag and lift forces. We also describe the qualitative changes that occur in the flow field and how they relate to changes on the lift and drag forces. A summary of the results appears in Sec. 6.

## 2 Computational Model

Our computational model is based on the incompressible Navier–Stokes equations, given in nondimensional form by

$$\frac{\partial \mathbf{u}}{\partial t} + \mathbf{u} \cdot \nabla \mathbf{u} = -\nabla p + \frac{1}{\text{Re}} \nabla^2 \mathbf{u}, \quad (1)$$

<sup>1</sup>Corresponding author. Telephone: (520) 621-4367, Fax: (520) 621-8322.

Contributed by the Fluids Engineering Division for publication in the JOURNAL OF FLUIDS ENGINEERING. Manuscript received by the Fluids Engineering Division May 14, 2004; final revision received December 4, 2004. Associate Editor: S. Balachandrar.

**Table 1 Gap size, domain dimensions, and number of elements**

$\epsilon$	$L_x$	$L_y$	$L_z$	$K$
0.0156	27.5	5.5	7.8156	2836
0.125	27.5	5.5	7.925	2836
0.25	28.0	9.0	10.50	4116
0.50	28.0	9.0	10.75	4116
0.70	28.0	9.0	11.00	4116
1.00	28.0	9.0	11.75	4116

$$\nabla \cdot \mathbf{u} = 0, \quad (2)$$

where  $\mathbf{u}=(u,v,w)$  is the nondimensional velocity and  $p$  is the pressure normalized by the fluid density  $\rho$ . The equations are non-dimensionalized by the characteristic length-scale  $D$ , the particle diameter, and the convective time scale,  $D/U$ , where  $U$  is the amplitude of oscillation in the far-field velocity. The Reynolds number is  $Re:=UD/\nu$ , with  $\nu$  the kinematic viscosity. The results presented below have a fixed Reynolds number of  $Re=100$ .

The discretization of (1) is based on the spectral element method in space and a characteristics-based second-order accurate splitting in time (Maday et al. [10]). Full details of the discretization can be found in FLR02 and Fischer [11]. The computational domain is the parallelepiped  $[-L_x, L_x] \times [-L_y, 0] \times [0, L_z]$ . Homogeneous Dirichlet conditions ( $\mathbf{u}=\mathbf{0}$ ) are applied on the bounding wall, located at  $z=0$ , and on the surface of the unit-diameter sphere centered at  $(x,y,z)=(0,0,\frac{1}{2}+\epsilon)$ . Here,  $\epsilon$  is the nondimensional gap width, referenced to the diameter  $D$  of the sphere. Boundary conditions on the  $y=-L_y$  and  $z=L_z$  planes are free-slip, no-penetration, which correspond to reflection symmetry about the given plane. In order to reduce computational cost, symmetry conditions are also employed about the  $y=0$  plane. A full three-dimensional calculation carried out in FLR02 demonstrated the appropriateness of the bilateral symmetry assumption under the current flow conditions. Table 1 lists the domain sizes and number of elements,  $K$ , employed for each value of  $\epsilon$  considered. All reported cases are run with polynomial degree  $N=5$  in each element. For all cases, the time step size was  $\Delta t=0.05$ , in convective time units. Note that it is the convective timescale that determines the stability and accuracy constraints on  $\Delta t$  and not the period  $\tau$ . The CPU time per simulation period thus scales in direct proportion to  $\tau$ .

Several mesh convergence studies with  $N=8$  and  $N=10$  confirmed mesh independence. The appropriateness of the timestep and domain sizes were also confirmed. For the particular case of  $\epsilon=1$ ,  $\tau=10$ , the mean lift for a simulation with  $N=10$ ,  $K=9632$ ,  $\Delta t=0.025$ , and domain dimensions  $(L_x, L_y, L_z)=(38, 16, 15)$  was found to be within 0.4% of the production simulation run. The maximum difference in the lift coefficient was 0.9% over a given period.

The base flow conditions are such that, in the absence of the particle, the nondimensionalized velocity field would be

$$\mathbf{u}_b = \left( \sin\left(\frac{2\pi t}{\tau}\right) - e^{-z/\delta} \sin\left(\frac{2\pi t}{\tau} - z/\delta\right), 0, 0 \right), \quad (3)$$

which corresponds to a unit-amplitude velocity field oscillating back and forth in the  $x$  direction with nondimensional period  $\tau$ . For viscous flows, this results in a time-periodic boundary layer with characteristic thickness

$$\delta = \sqrt{\frac{\tau}{\pi Re}}.$$

In this study the period is in the range  $10 \leq \tau \leq 300$ , and thus the Stokes layer range is  $0.17 < \delta < 0.98$ , which is comparable to the range of the gap,  $0.0156 \leq \epsilon \leq 1.0$ .

As in FLR02, we use  $\mathbf{u}=\mathbf{0}$  as an initial condition in all cases. The base flow is established in one of two ways, depending on the period. For relatively short periods ( $\tau \leq 40$ ), periodic boundary conditions are used in the  $x$  direction, and the flow is forced by a time-periodic mean pressure gradient. Because (1) is linear in  $p$ , we can write the pressure as

$$p = p'(x,y,z,t) + p_0(x,t), \quad (4)$$

where

$$p_0 := \frac{2\pi x}{\tau} \cos\left(\frac{2\pi t}{\tau}\right) \quad (5)$$

supplies the desired time-dependent mean pressure gradient and  $p'$  is the computed perturbation pressure, which is spatially periodic. Note that drag-coefficient computations must include the full pressure (4) and not just the computed perturbation  $p'$ .

For longer periods, the base flow is established by specifying Dirichlet conditions on either end of the domain. When the far-field base flow is in the positive  $x$  direction, we set  $\mathbf{u}(-L_x, y, z, t) = \mathbf{u}_b$  and use a homogeneous Neumann condition at  $x = +L_x$ . When the far-field base flow is in the negative  $x$  direction, we reverse these conditions. The Neumann condition corresponds to the usual outflow (natural) boundary condition associated with the Stokes subproblem that is solved in each step. Note that the required hydrostatic forcing results directly from application of the boundary conditions and that the auxiliary pressure  $p_0$  is not needed.

We tested the consistency of the results with regard to changing boundary condition strategies. The maximum difference between the lift computed with the periodic boundary conditions and the inflow-outflow boundary conditions for  $\tau=40$  and  $\epsilon=0.5$  was 0.34%.

At each time step, we compute the lift and drag coefficients, given by

$$C_L = \frac{F_z}{\frac{1}{2}A\rho U^2}, \quad (6)$$

$$C_D = \frac{F_x}{\frac{1}{2}A\rho U^2}, \quad (7)$$

respectively, where  $F_x$  and  $F_z$  are components of the dimensional force on the particle and  $A = \pi D^2/4$  is the cross-sectional area. We introduce additional subscripts  $m$ ,  $M$ , and  $A$  to indicate the respective minimum, maximum, and average of (6) and (7) over a single cycle in the time-periodic flow state.

### 3 Drag Calculations

The numerical simulations result in time histories of drag and lift data for each  $(\tau, \epsilon)$  pairing. A typical set of drag histories is shown in Fig. 1 for the case of  $\epsilon=0.5$  and several values of  $\tau$ . Figure 2 shows the constituent viscous and pressure contributions to the drag for the same cases. Over the range of parameters considered, the drag behavior is smooth and essentially monochromatic, with a dominant frequency of  $f=2\pi/\tau$ . The pressure and viscous contributions are slightly out of phase for small  $\tau$ . The phase lag becomes smaller as  $\tau$  increases. These curves also show that only a few oscillations are required to obtain a periodic state, starting from rest, with a somewhat longer time frame for small  $\tau$ . All of the summary data (minimum, maximum, and average) are computed during the final period.

In Fig. 3, we plot  $C_{D_M}(\epsilon, \tau)$ , the peak drag coefficient, for each of the gap values considered. As  $\tau \rightarrow 0$ ,  $C_{D_M}$  exhibits a rapid increase and a similar value for all of the gaps considered. For the

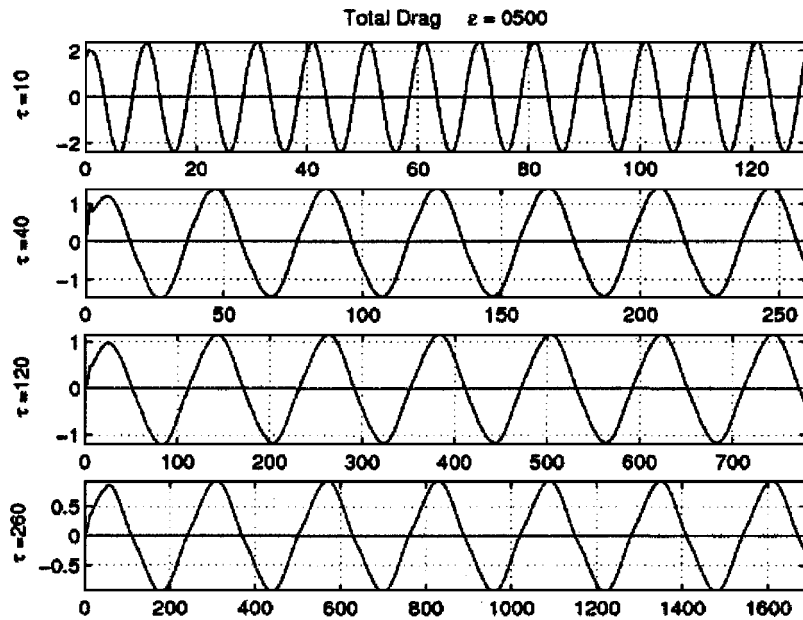


Fig. 1 Drag histories for  $\epsilon=0.5$ ; (a)  $\tau=10$ , (b)  $\tau=40$ , (c)  $\tau=120$ , and (d)  $\tau=260$

larger periods, there is a significant spread in the drag coefficient as a function of the gap, with larger gaps corresponding to increased  $C_{D_M}$ .

The drag behavior can be understood by considering its constituent pressure and viscous components. The pressure drag consists of a term arising from the mean pressure gradient that drives the flow,  $\partial p_0/\partial x$ , and a term associated with the computed perturbation pressure  $p'$ . From (4) and (5), we see that the mean component scales as  $\tau^{-1}$ , and we may expect this term to dominate the overall drag for sufficiently small periods. Because the mean pressure varies linearly with  $x$ , its contribution to drag is simply the pressure gradient times the volume of the particle. When normalized by  $\frac{1}{2}\rho U^2$ , the resulting contribution to  $C_{D_M}$  is

$$C_{D_{M,0}} = \frac{8\pi}{3} \frac{1}{\tau}. \quad (8)$$

While an inverse power-law trend is indicated by the data in Fig. 3, the exponent is not self-evident. In Fig. 4 we plot the  $C_{D_M}$  for  $\epsilon=0.125$ , along with its respective pressure and viscous contributions,  $C_{D_{M,p}}$  and  $C_{D_{M,v}}$ . (Note that  $C_{D_M}$  equals  $C_{D_{M,p}} + C_{D_{M,v}}$  only when the pressure and viscous forces are in phase.) The slope of  $C_{D_{M,p}}$  on this log-log scale indicates an exponent of about  $-0.63$  at  $\tau=10$ , indicating that we are outside of the range where (8) is dominating the overall pressure. An extension to (8) is obtained by accounting for the flow-separation that results in additional

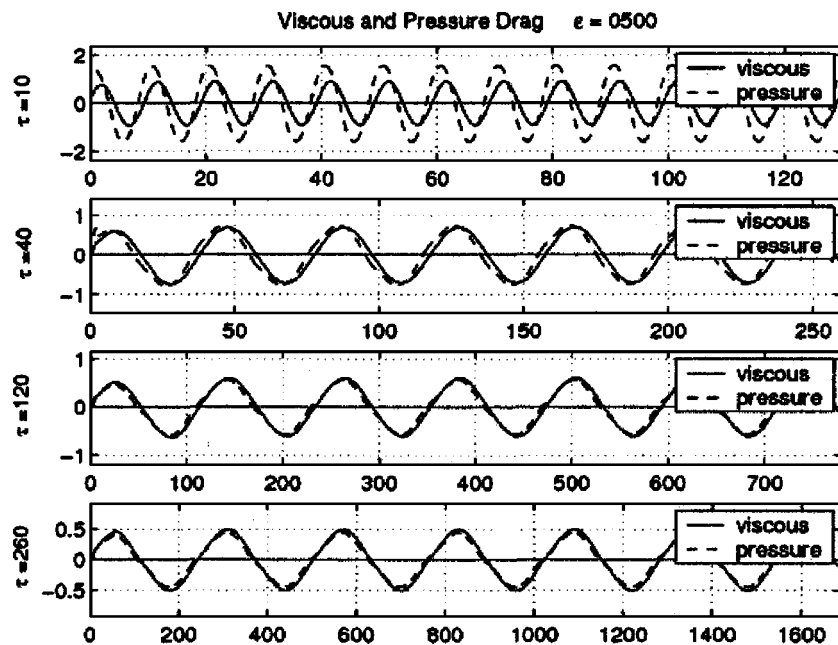


Fig. 2 Pressure and viscous contributions to the drag histories for  $\epsilon=0.5$ ; (a)  $\tau=10$ , (b)  $\tau=40$ , (c)  $\tau=120$ , and (d)  $\tau=260$

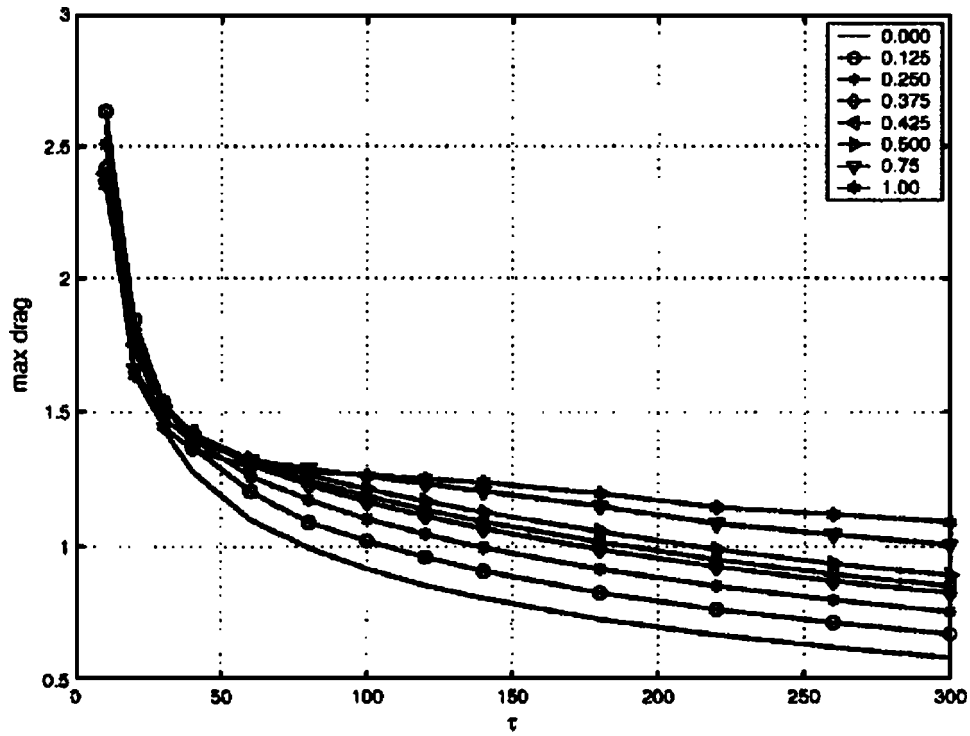


Fig. 3  $C_{D_M}$  as a function of gap  $\epsilon$  and period  $\tau$

pressure drag (the  $p'$  contribution). Supposing the flow is fully separated (i.e.,  $C_{D'} \approx 1$ ),

$$C_{D_p} \approx 1 + \frac{8\pi}{3} \frac{1}{\tau}, \quad (9)$$

which is also plotted in Fig. 4.

The magnitude of (9) is in reasonable agreement with  $C_{D_{M,p}}$  for the smaller periods but is not correct for large  $\tau$ , where (9)  $\rightarrow 1$ , while  $C_{D_{M,p}} \rightarrow 0$  as  $\tau$  increases. This result is to be expected be-

cause the physics in the large- $\tau$  limit is quite different due to the interaction of the Stokes layer with the particle. Figure 4 reveals that  $C_{D_M}$  drops substantially below unity for large  $\tau$ . This drop is explained by the momentum deficit associated with the Stokes layer near the wall, which is growing as  $\tau^{1/2}$ . Particles within the Stokes layer do not "see" the full velocity magnitude,  $U$ . One might, therefore, expect that particles further from the wall would exhibit larger values of  $C_{D_M}$  in the large- $\tau$  limit. Conversely, for

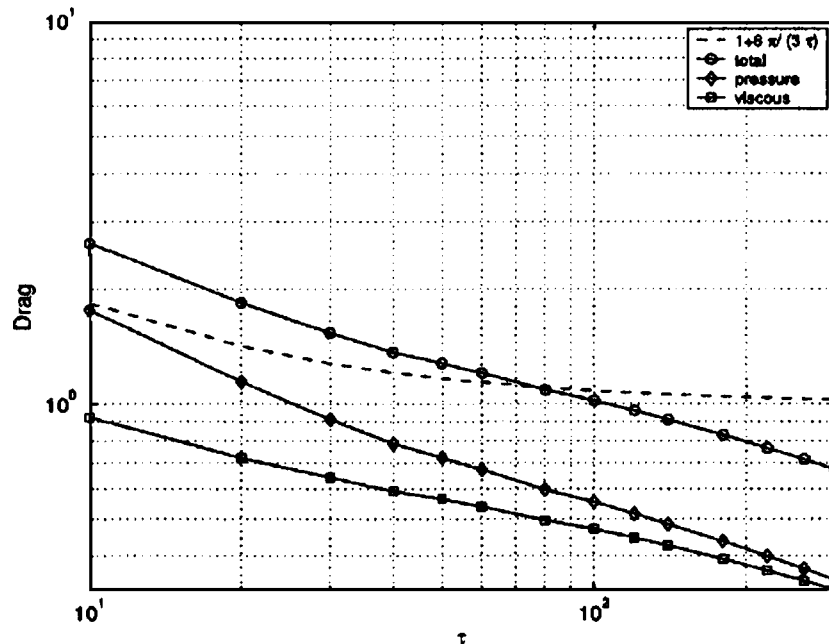


Fig. 4  $C_{D_M}$ ,  $C_{D_{M,p}}$ , and  $C_{D_{M,v}}$  for  $\epsilon=0.125$ . Also plotted are Eqs. (8) and (9)



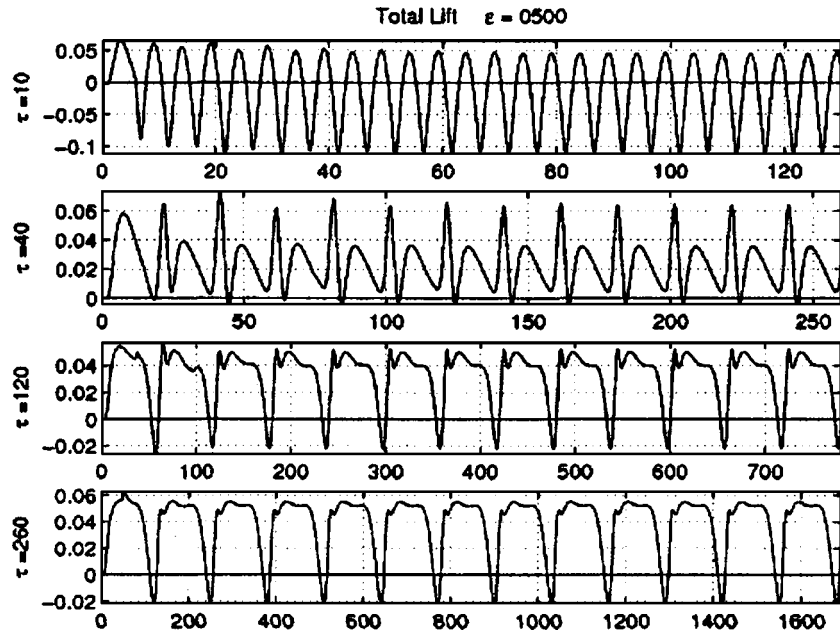


Fig. 5 Lift histories for  $\epsilon=0.5$ ; (a)  $\tau=10$ , (b)  $\tau=40$ , (c)  $\tau=120$ , and (d)  $\tau=260$

small  $\tau$  and, hence, small  $\delta$ , the drag behavior should not be strongly dependent on  $\epsilon$ . These behaviors are indeed evident in Fig. 3.

Regarding the viscous contribution to the drag, one can make arguments similar to that for the pressure in the case of short periods. The peak value of the viscous drag will scale as  $\beta A \rho \nu U / \bar{\delta}$ , where  $A$  is the cross-sectional area,  $\beta$  an order-unity constant, and  $\bar{\delta}$  a characteristic boundary layer thickness on the particle surface. Standard dimensional arguments imply that the boundary layer thickness scales as  $(\nu \bar{t})^{1/2}$ , where  $\bar{t}$  is a relevant viscous time scale. For long periods (neglecting any interaction with the Stokes layer),  $\bar{t}$  is essentially the time of flight for a fluid particle to pass the sphere, which is unity given our choice of

nondimensionalization. For short periods, the time scale will be  $\bar{t} \approx \tau/2$ , which is the length of time that the flow proceeds in a given direction. Thus, in the small- $\tau$  limit, we expect the viscous drag contribution to scale as  $\tau^{-0.5}$ . In fact, we observe in Fig. 4  $C_{D_{M,v}} \approx O(\tau^{-0.4})$  for  $\tau=10$ , which is in reasonable agreement with this analysis.

#### 4 Lift Calculations

Figure 5 shows the lift histories for the  $\epsilon=0.5$  case at values of  $\tau$  corresponding to the drag cases of Fig. 1. Figure 6 shows the viscous and pressure contributions to the lift for the same cases. We see that the time history of the lift does not exhibit the nearly simple harmonic behavior observed in the drag histories. For the

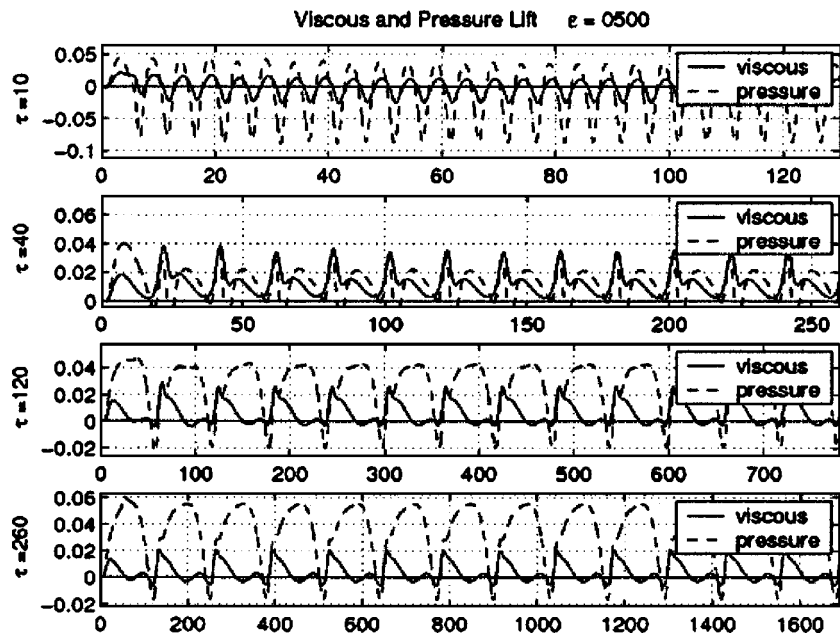


Fig. 6 Pressure and viscous contributions to the lift histories for  $\epsilon=0.5$ ; (a)  $\tau=10$ , (b)  $\tau=40$ , (c)  $\tau=120$ , and (d)  $\tau=260$

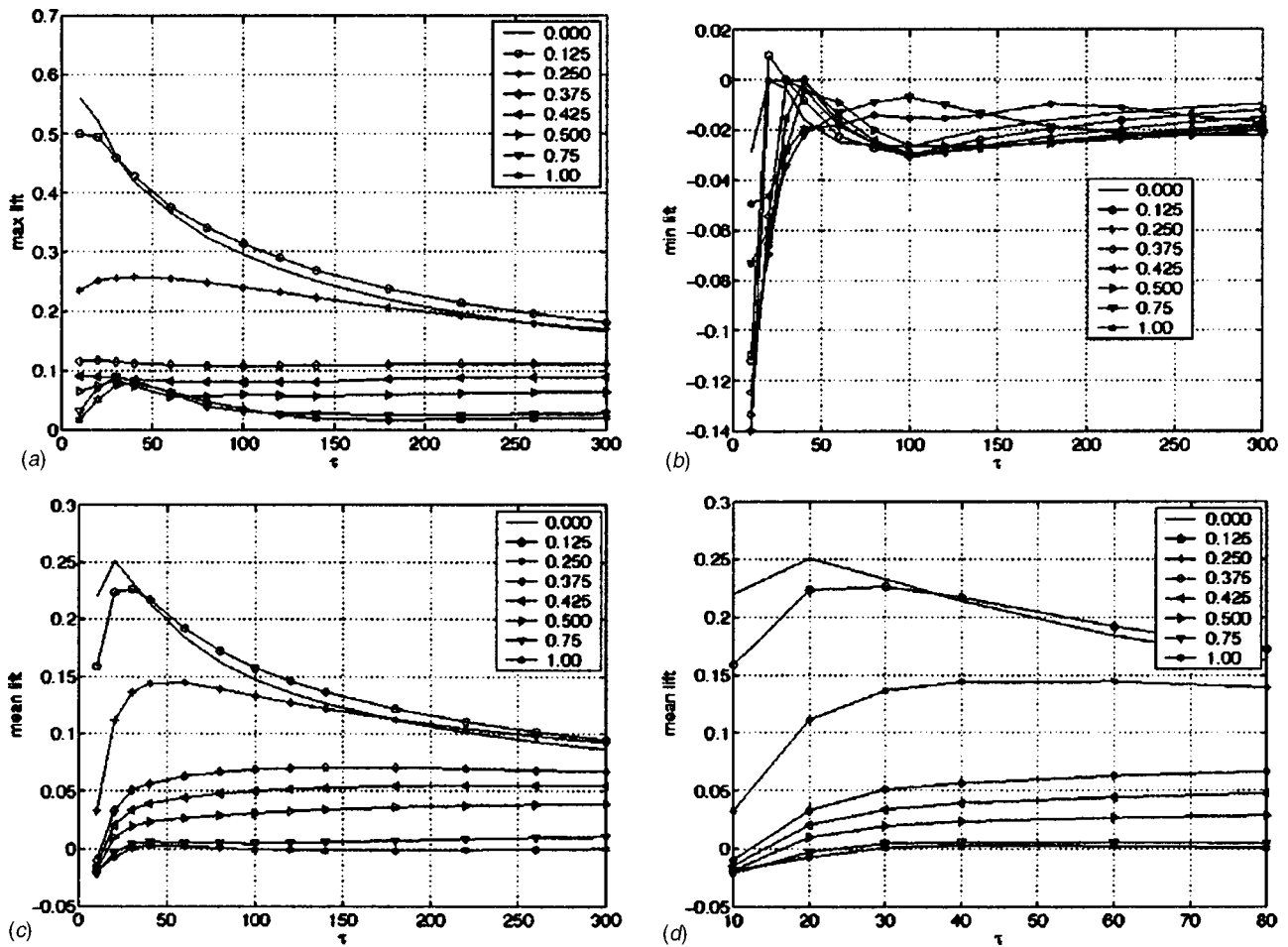


Fig. 7 (a)  $C_{L_M}$ , (b)  $C_{L_m}$ , (c) and (d)  $C_{L_A}$  as a function of gap  $\epsilon$  and period  $\tau$ ; (d) shows small  $\tau$  details of  $C_{L_A}$

shortest period,  $\tau=10$ , the behavior is dominated by a single frequency, which is twice the fundamental frequency due to the fore-aft symmetry of the flow conditions. Nonetheless, the negative extrema are more sharply peaked than the positive extrema, thus indicating the presence of higher harmonics. In Fig. 6 the contrasting sharpness of the peaks is clearly present in both the viscous and pressure lift contributions. For  $\tau=40$ , a strong subharmonic at  $\tau/4$  is present in both the viscous and pressure lift contributions. Finally, for  $\tau=260$ , we return to a strong fundamental signal with period  $\tau/2$ . However, the viscous and pressure peaks are out of phase, such that the total lift is essentially a flat signal with periodic negative spikes. The negative extrema coincide with the change in sign of the bulk velocity field given by (3).

Figure 7 shows the maximum, minimum, and average lift as a function of  $\epsilon$  and  $\tau$ . By symmetry considerations, the lift is expected to go to zero as  $\epsilon$  gets large. The figures clearly show this trend. We examined the  $\epsilon=4$  case (not shown in this paper) to confirm this outcome. We found that the lift becomes nearly simple-oscillatory with period  $\tau/2$  and that its magnitude, for a fixed  $\tau$ , is smaller than all other cases considered here, that is, tending to zero. In addition, the lift is expected to go to zero as  $\tau$  goes to infinity. We return to this point in the subsequent discussion.

A salient feature of Fig. 7 is the appearance of a regime of parameters that exhibit significant positive time-averaged lift,  $C_{L_A}$ , which we refer to as the transitional regime. The transitional range of parameter space ranges from roughly  $\tau=30$  to  $\tau=100$ . The figure shows an increase in the average lift in the transitional regime, particularly for small-gap cases. Below that transitional

regime is one in which the average lift can be negative. That is, for a given gap width, there are values of  $\tau$  small enough for which there is a net suction. On the other side of the transitional regime,  $C_{L_A}$  does not change considerably with  $\tau$  and represents a lift force that, on average, is directed away from the bounding wall. The  $\epsilon=0$  case has the most pronounced transitional region. Figure 7 shows that the maximum lift for  $\epsilon=0$  is positive for all  $\tau > 10$ . In FLR02, however, we found that the maximum quickly tends to zero for values of  $\tau < 10$ . For the larger gap sizes investigated (i.e., for  $\epsilon$  close to unity), the average lift is small and negative at  $\tau=10$ .

Figure 8 shows the viscous and pressure components of the computed average lift as a function of  $\epsilon$  and  $\tau$ . These plots reveal viscous- and pressure-dominated lift regimes which are separated by a cross-over point in  $\epsilon$ - $\tau$  space. For small gap widths, this crossover either does not occur or occurs for periods smaller than the ones examined in this study. In Fig. 8(a) we see no crossover. In the remaining figures we see a crossover between the viscous and pressure components. Furthermore, the crossover point clearly tends to larger values of  $\tau$  as  $\epsilon$  increases. Figure 9 shows the average lift regimes borne out of the numerical simulations. The crossover points were obtained numerically and were connected in the figure by straight lines. The average lift value at which crossover occurs becomes smaller in magnitude as both  $\tau$  and  $\epsilon$  get larger.

As mentioned, for fixed  $\epsilon$ , the lift is expected to go to zero as  $\tau$

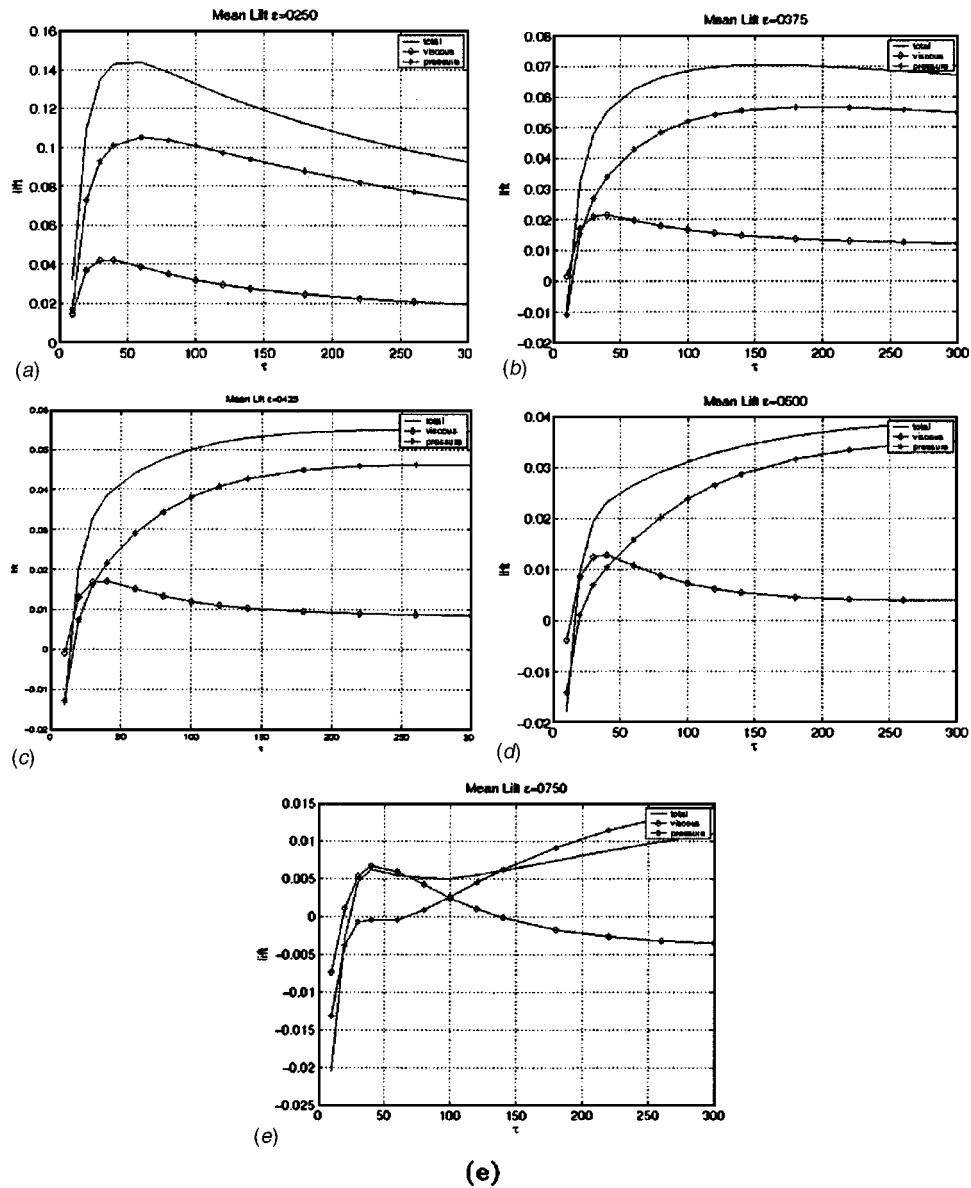


Fig. 8  $C_{L_A}$  (solid), average of the viscous component of the lift (diamonds), average of the pressure component of the lift (stars); as a function of  $\tau$ , for (a)  $\epsilon=0.250$ , (b)  $\epsilon=0.375$ , (c)  $\epsilon=0.425$ , (d)  $\epsilon=0.500$ , and (e)  $\epsilon=0.750$ . Note scales.

goes to infinity. This would be the limit of Stokes flow.<sup>1</sup> Our computational configuration does not allow us to explore this limit, but the tendency is certainly present. It may be somewhat puzzling to consider the Stokes flow limit if we are holding the Reynolds number fixed at 100 in our exploration of parameter space. The apparent contradiction is resolved by realizing the Reynolds number used here, based on the external flow, becomes less relevant in the regime of very large  $\tau$ . As  $\tau$  goes to infinity the Stokes layer thickness gets larger (at a rate proportional to  $\tau^{1/2}$ ); the Stokes layer becomes infinitely large, when compared to  $D$ , and the impinging velocity shear goes to zero.

To gain further insight to the nature of the lift force in the large- $\tau$  limit, we conducted a separate set of steady-state calculations. We considered the lift conditions in the large  $\tau$  limit for the particular case  $\epsilon=0.5$ . As  $\tau \rightarrow \infty$ , we can expect the flow conditions to

<sup>1</sup>Not to be confused with Stokes boundary layer solution to oscillatory bounded flows.

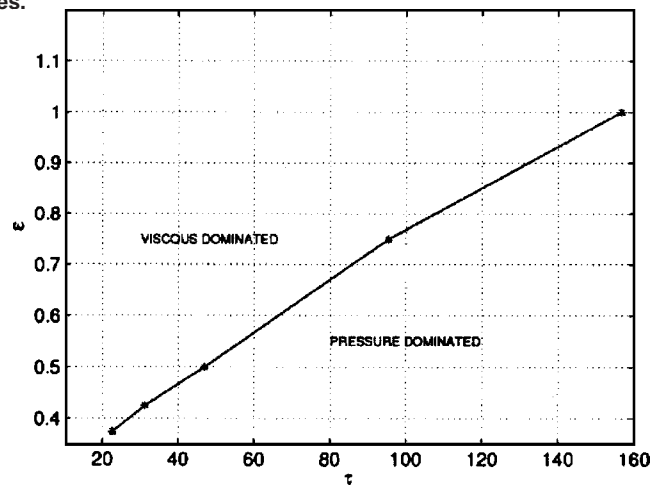


Fig. 9 Boundary line in  $(\epsilon, \tau)$ -space for the pressure and the viscous dominated regimes for the average lift  $C_{L_A}$ . The calculated points have been connected by straight lines.

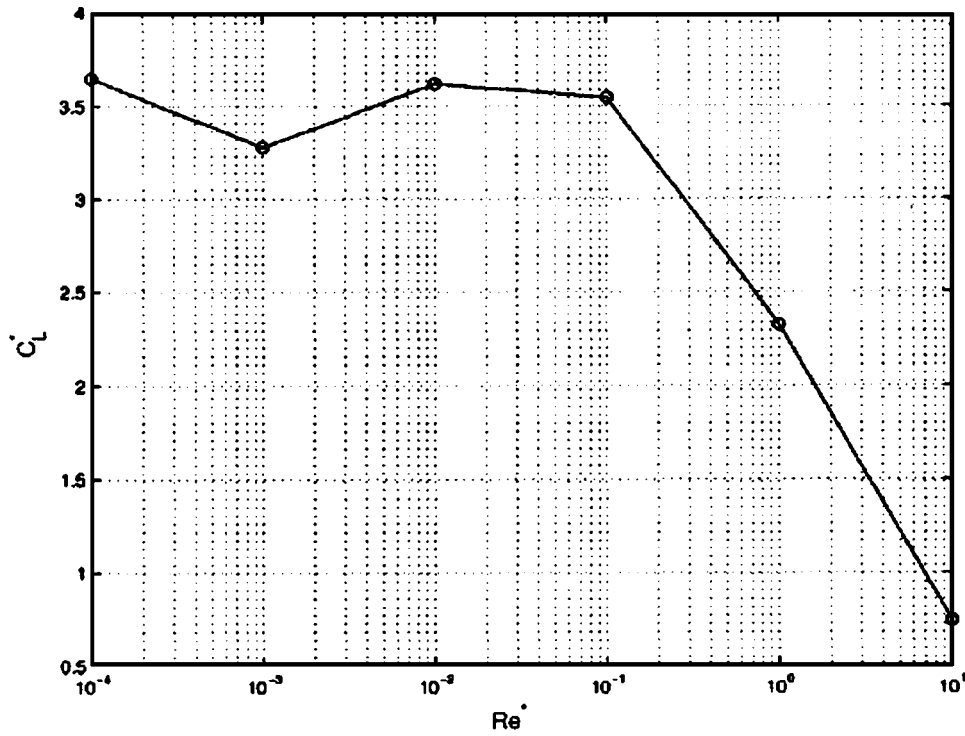


Fig. 10 Lift for a sphere in a plane Couette flow,  $\epsilon=0.5$ , for a  $Re^*=DU^*/\nu$  in the range of  $Re^*=10^{-4}-10^1$

be quasi steady-state and  $\delta \gg 1$ . Under these conditions, the background velocity profile near the wall is  $\mathbf{u} \approx (0, 0, cz)$ . Here,  $c$  is found by differentiating (3),

$$c = \left. \frac{\partial u_b}{\partial z} \right|_{z=0} = \frac{1}{\delta} (\sin(2\pi t/\tau) + \cos(2\pi t/\tau)),$$

which takes as its maximum (over time)

$$c_{\max} = \frac{\sqrt{2}}{\delta} = \sqrt{\frac{2\pi Re}{\tau}}.$$

For  $\epsilon=0.5$ , the center of the sphere is located at  $z=1$  and the velocity at the sphere center is thus  $U^* := c$ . The steady-state calculations used the same computational domain as considered in the oscillatory case but with boundary conditions such that the base flow corresponds to plane Couette flow with  $\mathbf{u} \approx (0, 0, z)$  (i.e., the flow is normalized by the base-flow velocity  $U^*$ ). We considered a series of trial runs with finite Reynolds numbers,  $Re^* := DU^*/\nu$  in the range of  $Re^*=10^{-4}-10^1$ . The computed lift coefficients are shown in Fig. 10 and clearly show a trend toward an order unity constant. From the data,

$$C_L^* := \frac{L^*}{\frac{1}{2}\rho(U^*)^2} \approx 3.6.$$

The dimensional relationship between  $C_L^*$  and  $C_L$  is

$$C_L = \left(\frac{U^*}{U}\right)^2 C_L^* = \frac{2\pi Re}{\tau} C_L^*,$$

from which we conclude that

$$C_{LM} \sim 3.6 \frac{2\pi Re}{\tau}$$

as  $\tau \rightarrow \infty$ , for  $\epsilon=0.5$ . For other values of  $\epsilon$  we would expect a similar trend with a different order unity constant. Note that, for

this limit to apply, we must have  $\delta > 1 + \epsilon$  (the normalized sphere height), which implies  $\tau \gg \pi Re(1 + \epsilon)^2$ .

Figure 11 shows the spectral content of  $C_L(t; \tau; \epsilon)$ , corresponding to the cases considered in Fig. 5. The most prominent feature of these plots is the relatively few degrees of freedom present in the lift signal, which suggests that a simple and practical parametrization of the lift might be possible. Regardless of the forcing period, the spectra will always contain the half-period signal (the lift goes through two cycles per forced oscillation). For short-period forcing, the spectra indicate that nearly all of the energy in the lift is captured by the  $\tau/2$ -period degree of freedom. As  $\tau$  increases, a cascade of subharmonics appears. The overall energy of the signal also decreases (i.e., the lift decreases). For larger values of  $\tau$ , the spectrum becomes more regular; that is, the cascade contains commensurate subharmonics. An example of this is shown in Figs. 11(c) and 11(d). Furthermore, as the gap is increased, the spectrum becomes more regular, and the energy in the subperiods decreases significantly. Examination of all the spectra, particularly for large  $\tau$ , did not yield a power law relationship in the spectrum. For midvalues of the period, say between  $\tau=30$  and  $\tau=100$ , the spectra is more complex: Not only are subharmonics present and large, but other degrees of freedom can be seen in the spectra. In fact the half-period component seen in Fig. 11(b) is smaller than other spectral components for the  $\tau=40$  case.

Figure 6 shows that the phase between the viscous and the pressure components of the lift is not constant across all  $\tau$ . For small values of  $\tau$  the two components are largely in phase, and the two components play nearly equally important roles in determining the lift. In the transitional region, however, the two components exhibit complex phase relationships and comparable magnitudes. For longer periods the magnitude of both components falls dramatically, the pressure component dominates, and the phase is still fairly complex. This situation is illustrated in Fig. 12, where the points represent values of the components of the lift-drag at different times. The trajectory direction is clockwise for advancing time, except for Fig. 12(b), which incidentally, corresponds to

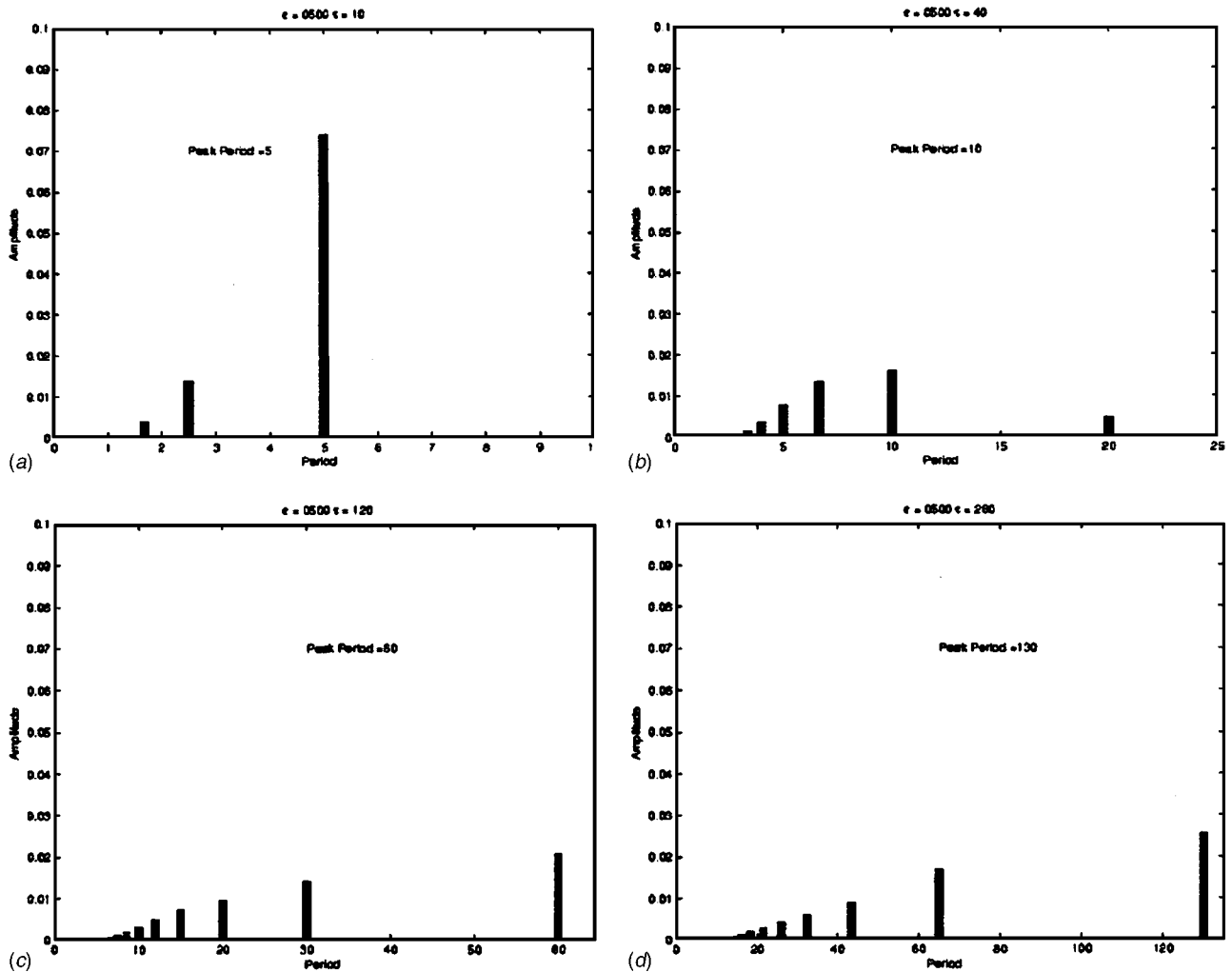


Fig. 11 Spectrum of  $C_L(t; \tau, \epsilon)$  for  $\epsilon=0.500$ ; (a)  $\tau=10$ , (b)  $\tau=40$ , (c)  $\tau=120$ , and (d)  $\tau=260$ . Amplitude scaled to  $C_L$ .

a case in the transitional range. Figure 12(a) corresponds to  $\epsilon=0.5$  and  $\tau=10$ . For the same gap and  $\tau=40$ , Fig. 12(b) shows that the trajectory is a distorted “Fig. 8.” The rightmost portion of the 8 is progressing clockwise. With larger  $\tau$ , the Fig. 8 settles to a shape similar to that shown in Fig. 12(d), the  $\tau=260$  case. Of note is how quickly the pressure component of the lift grows and drops in all cases. In these figures a few spurious points correspond to the early times of the simulation, when transients are present.

## 5 Combined Lift and Drag

We examine next the combined action of the lift and drag forces and relate certain features of these forces to qualitative changes in the vorticity field. To do so, we have computed force phase diagrams. In contrast to Fig. 12, however, these phase diagrams plot the history of the lift against the drag. The phase diagrams are plotted as histories, time being quoted in fractions of the period. In addition, we display the velocity and the magnitude of the vorticity at the associated stages during the cycle. Since the forces are periodic, we display the magnitude of the vorticity only for times after one half-period has transpired.

For  $\epsilon=0.5$  and  $\tau=40$ , we see in Fig. 13 that the maximum lift is attained when the far field velocity magnitude is near zero. The ascent in phase space, from the second smallest value of the lift to the largest, occurs very quickly. As the velocity magnitude increases the drag increases further, the lift quickly reaches its minimal value and is then driven slowly to the maximum drag point. Later, as the asymmetry in the vorticity increases, both the drag

and the lift decrease. The climb to the maximum value of the lift, following the second smallest value of the lift, is characterized by a considerable amount of vorticity in the neighborhood of the bounding wall.

In Fig. 14 we see that the magnitude of the lift in the  $\epsilon=1$  and  $\tau=40$  case is smaller than in the  $\epsilon=0.5$  and  $\tau=40$  case. We also see that the lift is small in comparison to the drag. In this instance, the lift has only one minimum and one maximum. The lift maximum coincides with an increase in the asymmetry in the vorticity distribution. This case, as well as that of Fig. 13, belongs to the viscous-dominated average-lift regime.

Figure 15 shows the phase portrait and velocity–vorticity distributions for the  $\epsilon=0.5$  and  $\tau=120$  case. In contrast to the preceding cases, it corresponds to a pressure-dominated-regime case. Of note is the appearance of two maxima in the lift and one minimum. We observe, as well, that the time progression of the changes in the lift and drag as a function of time occur more smoothly than in the  $\tau=40$  case. We also note that the lift–drag magnitude ratio of this case is similar to the  $\epsilon=1.0$ ,  $\tau=40$  case. The main characteristic that makes this case different from the viscous-dominated cases is the proportion of time the lift is of one sign (in this case positive).

We can relate the spectral analysis of the lift, some of which appears in Fig. 11, to the phase plots. Doing so, we reach the following general conclusions: Over a full period of the forcing, the two largest maxima and minima in the lift are correlated in time with the largest spectral components. The smaller features

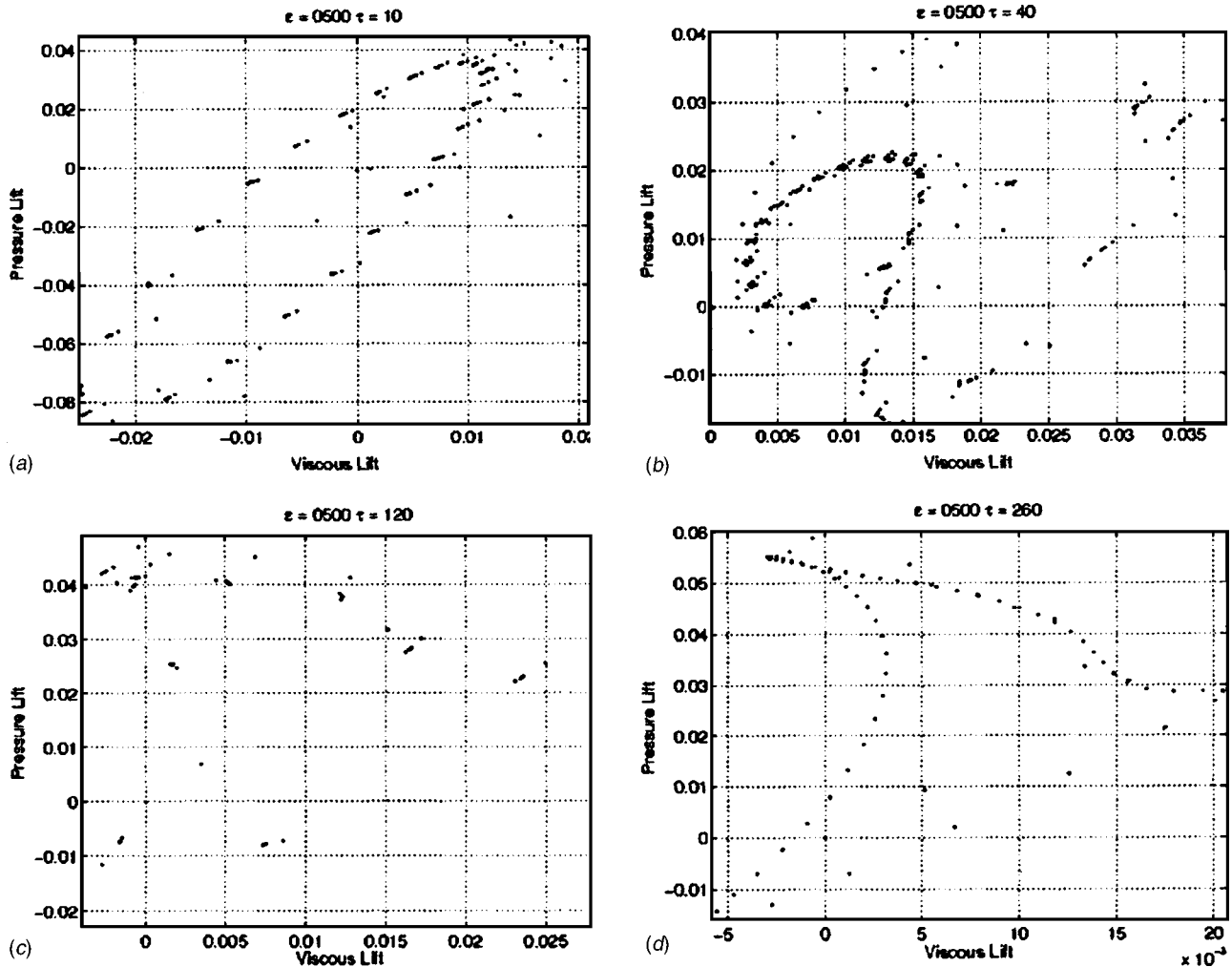


Fig. 12 Phase relationship between the pressure and viscous components of the average lift  $C_{L_A}$ , for  $\epsilon=0.5$ ; (a)  $\tau=10$ , (b)  $\tau=40$ , (c)  $\tau=120$ , and (d)  $\tau=260$ . Shown here is the superposition of 6.5 periods of data, including the initial transient data.

are correlated to the smaller amplitude spectral components as well. Since the phase portraits are periodic, with period equal to half the forcing period, the periods of the spectral components smaller than the dominant one must be additively commensurate in smaller groups, usually two. In the transitional regime, where the largest spectral component is not the half-period of the forcing, the largest extremum is associated with the largest component of the spectrum, the half-period component with the next largest component. Qualitatively, for moderate  $\epsilon$  and the larger- $\tau$  range, the lift is characterized by a smaller but more sustained positive lift. For the same  $\epsilon$  and  $\tau$  in the transitional range, the lift is characterized by more peaked and shorter-lived bursts. One may speculate that this difference in behavior, when comparing the transitional and the larger- $\tau$  regimes, may be associated in an idealized fluid flow as follows: supposing that the buoyancy and lift forces on a particle are comparable in this idealized flow, the transitional regime would be more effective in dislodgement and the longer period regime more effective in keeping a particle in suspension.

## 6 Summary

In Fischer et al. [1] we numerically computed the lift and drag on a stationary sphere in the neighborhood of an ideal wall boundary, subjected to a time-periodic fluid flow. The lift and drag were obtained as a function of the period of external forcing and Rey-

nolds number. Here we explored how the lift and drag forces change as the gap as well as the forcing period parameters are varied.

The drag force is found to be very uniform in character, for a wide range of period and gap values. The drag is the prevalent force, when compared to the lift, if consideration is limited solely to their relative magnitude; nevertheless the complex phase relationship between the lift and drag suggests that in some contexts ignoring one of the components of the total force would yield a poor description of the dynamics of a particle, unless, perhaps, when the buoyancy force is overwhelming.

We found that there are clearly identifiable regimes in which the average lift is primarily described as viscous- or pressure-dominated. We find that the lift has a range in  $(\epsilon, \tau)$  parameter space in which enhancement takes place and that the lift force is qualitatively different when the gap is present, as compared to the situation where the gap is not there.

This study raises several questions, the most important being the following: Why is there a parameter regime of enhanced averaged lift? What is the underlying reason for there being a pressure and viscous dominated regime in the lift?

This study also concludes that one should be able to build a robust and widely applicable model for the combined lift and drag forces on particles subjected to oscillatory flows. To this end this paper provides a fairly complete description of the forces that should be of considerable aid in formulating such a model.

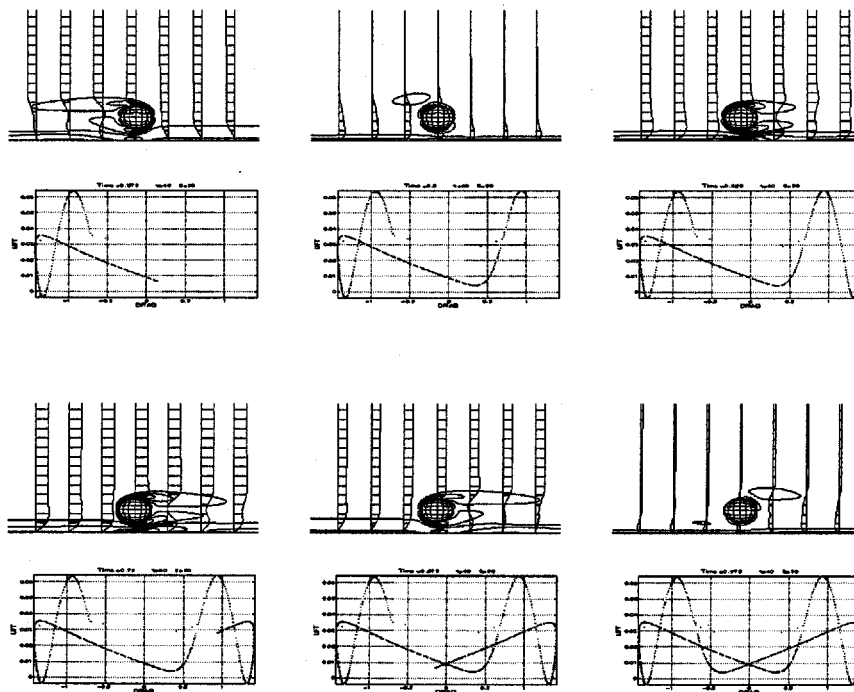


Fig. 13 Vorticity magnitude, velocity profiles, and phase portrait at  $t/\tau=0.375, 0.500, 0.625, 0.750, 0.875,$  and  $0.975$  for  $\epsilon=0.5, \tau=40$

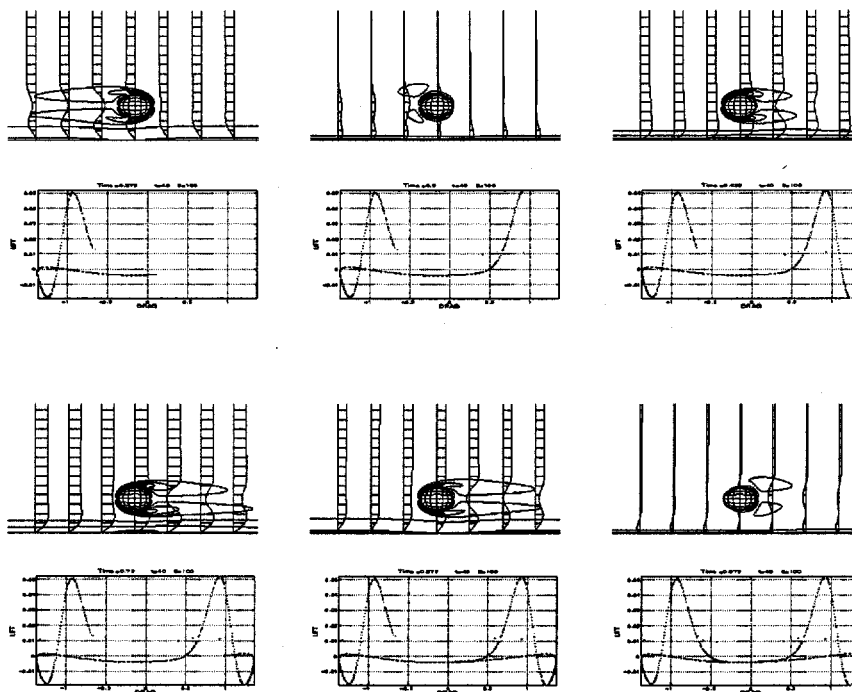


Fig. 14 Vorticity magnitude, velocity profiles, and phase portrait at  $t/\tau=0.375, 0.500, 0.625, 0.750, 0.875,$  and  $0.975$  for  $\epsilon=1.0, \tau=40$

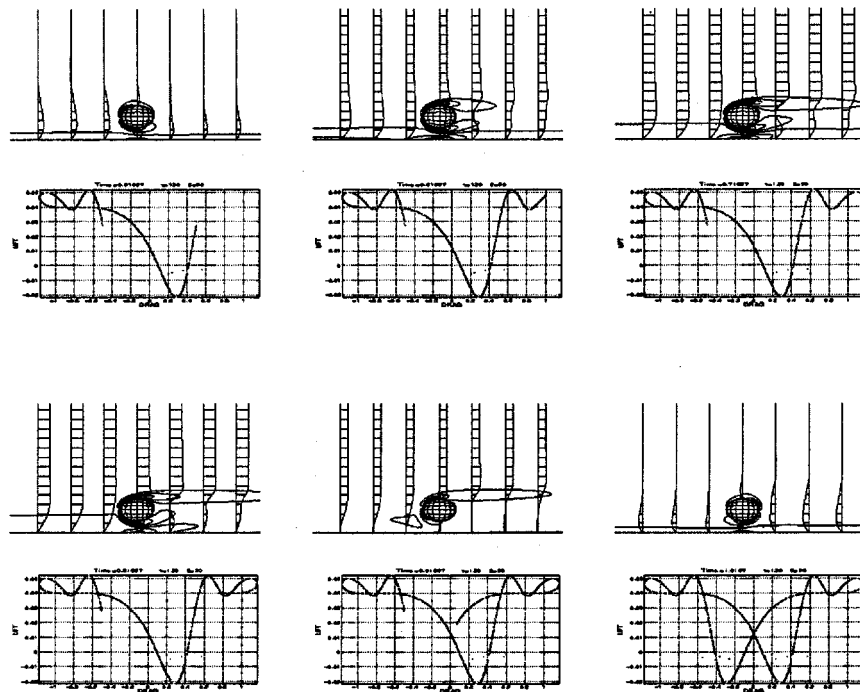


Fig. 15 Vorticity magnitude, velocity profiles, and phase portrait at  $t/\tau=0.500, 0.600, 0.700, 0.800, 0.900,$  and  $1.000$  for  $\epsilon=0.5, \tau=120$

Several authors, among them Rubinov and Keller [12], Honji and Taneda [13], Kurose and Komori [14], and Kim and Choi [15], have found that the estimate on the lift forces of spheres and cylinders in steady flows can be significantly affected by ignoring torque. In a future study we intend to take up this question in the context of oscillatory flows using similar methods to those used in this work. Later, we will also characterize the lift and drag forces on a freely moving particle and determine if there is a preferential combination of parameters that lead to sustained suspension or particle dislodgement.

The computed data for lift and drag as a function of time, for periods  $10 \leq \tau \leq 300$  and gaps  $0 \leq \epsilon \leq 1$ , is available and may be obtained by contacting the authors.

### Acknowledgments

This work was carried out in part at Argonne National Laboratory under the auspices of the Department of Energy under Contract W-31-109-Eng-38. J.M.R. wishes to thank the DEP and the MCS Division at Argonne, as well as the support by DOE through Grant No. 329080.

### References

[1] Fischer, P. F., Leaf, G. K., and Restrepo, J. M., 2002, "Forces on Particles in an Oscillatory Boundary Layer," *J. Fluid Mech.*, **468**, pp. 327–347.  
 [2] Bearman, P. W., Downie, M. J., Graham, J. M. R., and Obajasu, E. D., 1985, "Forces on Cylinders in Viscous Oscillatory Flows at Low Keulegan-Carpenter

Numbers," *J. Fluid Mech.*, **154**, pp. 337–356.  
 [3] Sarpkaya, T., 1986, "Force on a Circular Cylinder in Viscous Oscillatory Flow at Low Keulegan-Carpenter Numbers," *J. Fluid Mech.*, **165**, pp. 61–71.  
 [4] Obajasu, E. D., Bearman, P. W., and Graham, J. M. R., 1988, "A Study of Forces, Circulation and Vortex Patterns Around a Circular Cylinder in Oscillating Flow," *J. Fluid Mech.*, **196**, pp. 467–494.  
 [5] Justesen, P., 1991, "A Numerical Study of Oscillating Flow Around a Circular Cylinder," *J. Fluid Mech.*, **222**, pp. 157–196.  
 [6] Rosenthal, G., and Sleath, J., 1986, "Measurements of Lift in Oscillatory Flow," *J. Fluid Mech.*, **146**, pp. 449–467.  
 [7] Hall, D., 1988, "Measurements of the Mean Force on a Particle Near a Boundary in Turbulent Flow," *J. Fluid Mech.*, **187**, pp. 451–466.  
 [8] Cherukat, P., McLaughlin, J. B., and Graham, A. L., 1994, "The Inertial Lift on a Rigid Sphere Translating in a Linear Shear-Flow Field," *Int. J. Multiphase Flow*, **20**, pp. 339–353.  
 [9] Asmolov, E. S., and McLaughlin, J. B., 1999, "The Inertial Lift on an Oscillating Sphere in a Linear Shear Flow," *Int. J. Multiphase Flow*, **25**, pp. 739–751.  
 [10] Maday, Y., Patera, A. T., and Rønquist, E. M., 1990, "An Operator-Integration-Factor Splitting Method for Time-Dependent Problems: Application to Incompressible Fluid Flow," *J. Comput. Phys.*, **5**, pp. 310–337.  
 [11] Fischer, P. F., 1997, "An Overlapping Schwarz Method For Spectral Element Solution of the Incompressible Navier-Stokes Equations," *J. Comput. Phys.*, **133**, pp. 84–101.  
 [12] Rubinov, S. I., and Keller, J. B., 1961, "The Transverse Force on a Spinning Sphere Moving in a Viscous Fluid," *J. Fluid Mech.*, **11**, pp. 447–459.  
 [13] Honji, H., and Taneda, A., 1969, "Unsteady Flow Past a Circular Cylinder," *J. Phys. Soc. Jpn.*, **27**, pp. 1668–1677.  
 [14] Kurose, R., and Komori, S., 1999, "Drag and Lift Forces on a Rotating Sphere," *J. Fluid Mech.*, **384**, pp. 183–206.  
 [15] Kim, D., and Choi, H., 2002, "Laminar Flow Past a Sphere Rotating in the Streamwise Direction," *J. Fluid Mech.*, **461**, pp. 365–386.



Virginie Gilard

Laurent-Emmanuel Brizzi

Phone: (33) 05 49 49 69 27;

Fax: (33) 05 49 49 69 68;

e-mail: laurent.brizzi@lea.univ-poitiers.fr

Laboratoire d'Etudes Aérodynamiques (UMR 6609), Boulevard Marie et Pierre Curie, Téléport 2, BP 30179, 86960 Futuroscope Chasseneuil Cedex, France

# Slot Jet Impinging On A Concave Curved Wall

*In order to study the aerodynamics of a slot jet impinging a concave wall, flow visualizations, velocity measurements by particle image velocimetry (PIV) (mean velocity fields and the Reynolds stresses) and mean pressure measurements were carried out. Among the studied parameters is the effect of the relative curvature of the wall, in particular the low curvature radius because of the presence of three semistable positions. It is the first time that this type of behavior is observed in fluid mechanics. Thus three flow modes are observed and their behaviors are described. These different behaviors modify considerably the impinging jet structure and the turbulence values. Finally, from the pressure measurements, we were able to determine a criterion that allows us to know the behavior of the jet. [DOI: 10.1115/1.1905643]*

## Introduction

One of the means frequently used by the manufacturers of airplane engines to cool the turbine blades is the impinging jets technique coupled with the film cooling technique, this process improves thermal exchanges between walls and fluid. The aim of this technique is to bring a certain quantity of "fresh" air from the engine compressor level and to restore it to the turbine level. This fluid goes inside the blades and is ejected, through several lines of small holes, on the inner part of the blades. By conduction, the heat of the blade is thus "pumped" by the fluid. Because of the low gap between the internal wall of the blade and the holes, we often model this flow by several lines of jets impinging a plane wall. However, for the leading edge of the blade, this assumption (plane wall) is not true: The jets impinge upon a concave surface.

Also, after many studies of jets impinging on a plane wall, we have chosen to study the influence of several characteristic parameters of jets impinging on a curved wall: The radius of curvature of the wall, the impingement height (jet exit-to-surface spacing), and the Reynolds number.

Even though the subject was studied for many years (first study in 1969), the number of studies concerning one (or several) impinging jet on a curved wall remains low: Less than fifteen in the past three decades. Preceding the Eighties, the majority of the studies done only relate to the thermal aspect of the problem with an estimation of thermal correlations  $Nu=f(Re)$ . During the Eighties the first measurements of pressure appeared, while in the Nineties the interest shifted to visualizations of the physical phenomena. It is only very recently that the studies related to the velocity field of the flow generated by impinging jets on a curved wall (main subject of our study) have appeared. These are summarized below.

**Visualizations.** Gau and Chung [1] carried out smoke wire visualizations for a plane jet impinging on a curved (concave and convex) surface. They observed, like in the plane wall case, the formation of vortices in the mixing layer of the jet. They noticed that, when the slot width increased, the formation of the vortices occurred closer to the slot exit, thus decreasing the potential core of the jet. They estimated that this reduction causes an increase of the heat transfer at the stagnation point. After the impact, these structures are convected downstream of the stagnation point in the wall jet. The flow structure then becomes turbulent and is not easily analyzable.

Cornaro et al. [2] also carried out smoke wire visualizations for a turbulent axisymmetric jet impinging on a semicylindrical concave surface. They studied the effects of the nozzle-to-surface distance and the relative curvature of the surface. Initially, they observed that the flow in the case of a concave surface is very unstable, taking into account the destabilizing effect of the centrifugal force and the interaction which exists between the outgoing flow (wall jet) and the flow exiting the nozzle. This interaction reduces the probability of obtaining stable vortices in the jet. As in the case of the plane surface, two behaviors are distinguished according to the nozzle-to-surface distance: When a surface is placed at the end of the potential core, they observe a random radial oscillation of the stagnation point which destroys the vortical structures and the jet symmetry. For lower distance ( $H/d \approx 1$ ), this instability disappears: The stagnation point no longer oscillates, although a strong axial oscillation of the wall jet is observed. Small vortices are observed in the wall jet and keep their integrity until the end of the curved surface. Their study on the effect of the relative curvature indicates that, when  $Dc/d$  increases, vortices appear in the mixing layers of the jet but they disappear as soon as they interact with the curved surface. Only for nozzle-to-surface distances larger than 5.26 distinct vortices are observed. However, the relative curvature effect is often masked by the strong oscillations of the stagnation point and the wall jet observed for the higher nozzle-to-surface distances ( $H/d > 4$ ) or the lowest nozzle-to-surface distance ( $H/d < 1$ ).

**Pressure.** In 1981, Hrycak [3] indicates that the static pressure along the axis of an axisymmetric jet is independent of the nozzle-to-surface distance or the Reynolds number. However, in the vicinity of the wall, he shows that the static pressure is suddenly increased. Moreover, he observes in the mixing layer of the jet, that the static pressure is negative. He explains this negative pressure by the presence of a pressure gradient which is necessary for jet entrainment.

Similarly for the plane jet, Brahma et al. [4] divided the flow in the vicinity of an axisymmetric jet impinging on a concave hemispherical surface into two zones (stagnation region, wall jet). For each of these regions, Brahma et al. [4] defined two parts: An inner region corresponding to a conventional (laminar) boundary layer and an outer region resembling a turbulent free jet. They evaluated, at the stagnation point, the momentum thickness of the boundary layer in order to estimate (by an extension of Polhausen's approximate method) the thickness of the thermal boundary layer and the local Nusselt number. They observed that these thickness values depend on the distance  $H/b$ .

Lee et al. [5] carried out wall pressure measurements for an axisymmetric jet impinging on a concave hemispherical surface.

Contributed by the Fluids Engineering Division for publication in the JOURNAL OF FLUIDS ENGINEERING. Manuscript received by the Fluids Engineering Division September 23, 2002; final manuscript received January 20, 2005. Associate Editor: M. Plesniak.

They observed that the wall pressure coefficient ( $C_p$ ) is maximum at the stagnation point and decreases along the surface for all the Reynolds number values and all the relative curvature studied. They also observed that all the pressure profiles intersect at  $r/d = 0.8$  and that, beyond this point, the wall pressure becomes unstable. They explain this behavior by the production of an unstable distribution of moment-of-momentum created in the boundary layer which develops on the concave wall. Finally, they noted that the maximum value of the pressure, located at the stagnation point, decreases with the nozzle-to-surface distance.

**Average and Fluctuating Velocity Field.** Hrycak [6] was first interested by the axial velocity of an axisymmetric jet impinging a concave hemispherical surface. He notices that the axial velocity profiles have the same behavior as in the case of a plane surface. He finds a potential core (shorter than in the plane surface case) where the axial velocity is constant and equal to the exit velocity. Approaching the wall, the axial velocity strongly decreases.

Choi et al. [7] carried out velocity measurements with laser doppler anemometry (LDA) for a free jet and an impinging jet. They studied the effect of the nozzle-to-surface distance on the velocity fluctuations in order to explain the heat transfer results from the velocity measurements. First, they notice that the thickness of the stagnation region (defined as the thickness where the axial velocity profile deviates from the free jet velocity profile) is around  $2b$ . They show that the axial velocity fluctuations strongly increase in the stagnation region because of the reduction of the axial velocity when the flow approaches the surface. For a nozzle-to-surface distance around  $10b$  (i.e., higher than the length of the potential core), they noticed that the concave surface makes flow entrainment difficult, inducing a reduction in the turbulence level (compared to the free jet case). For the nozzle-to-surface distance studied, Choi et al. [7] observe that the wall jet grows in the main flow direction but becomes weaker when the nozzle-to-surface distance decreases. They consider that this reduction creates an increase of the heat transfer rate when the nozzle-to-surface distance is small. For the lowest distance ( $H/b < 0.5$ ), they observe an acceleration of the flow in the wall jet leading to radial velocity higher than the velocity jet ( $U_r/U_j > 1$ ). In conclusion, they estimate that the fluctuations of the radial velocity in the wall jet generate the second peak of the heat transfer (at  $s/b = 4$  to 5) observed for lower nozzle-to-surface distances.

Yang et al. [8] specify that the shape of the slot influences the characteristics of the jet. They carried out velocity measurements using hot wire technique for three different slot nozzles [round, rectangular shaped and two-dimensional (2D) contoured nozzle]. They show that the mean and fluctuating velocity profiles are different according to the initial conditions. This difference modifies the characteristics of heat transfer at the stagnation point.

**Thermal Aspect.** Even though this work does not include a thermal part, one of the main interests of this kind of study relates to the heat and mass transfer. Thus, the main application of jets impinging a concave surface remains the cooling of the inner part leading edge of the turbine blade. Because of this application, the major part of previous works only address the thermal problem. In most of the studies, the jets are located along one or several lines and impact a semicylindrical surface. The effects of various aerodynamic parameters (Reynolds number  $Re_d$ ) and geometric parameters (jet diameters, nozzle-to-surface distance, distance between the jets, etc.) are studied. The results are generally presented by mean of correlations relating the Nusselt number to the other parameters (geometrical and dynamic) of the study.

In 1969, Metzger et al. [9] and Chupp et al. [10] gave the first correlations including most of the geometrical and dynamic parameters. Metzger et al. [9] show that, on an equivalent surface, the heat transfer for a round jet [three-dimensional (3D)] is higher than for a slot jet (2D).

Tabakoff and Clevenger [11] compare the efficiency of the heat transfer on a semicylindrical surface for three different injections:

A slot jet, a round jet row and an array of round jets. They show that the average heat transfer is most efficient for an array of round jets and less efficient in the case of a slot jet. These differences are explained from the local distributions: For the slot jet, they observe the presence of a single peak in the vicinity of the stagnation point whereas in the case of a round jet row the distribution is triangular. For the array of round jets, the distribution is almost uniform. Under these conditions, the level of the local heat transfer is lower than in the two other configurations but the exchanges are more efficient.

In 1991, Gau and Chung [1] confirm this study ( $Nu_{jet2D} \ll Nu_{jet3D}$ ) with more accurate measurements. They show that the value of the Nusselt number increases with the curvature because of the appearance of Taylor-Görtler vortices which develop along the surface (confirming Thomann [12] results). They found an optimum height for which the heat transfer is maximum at approximately  $8b$  (according to the results of Gardon and Akfirat [13]). The evolution of the Nusselt number at the stagnation point was first studied by Lee et al. [5] for a round jet impinging on a hemispherical surface. More recently, Choi et al. [7] show that the heat transfer at the stagnation point for a slot jet evolves according to nozzle-to-surface distance. For the lowest heights ( $H/b < 2$  to 3)  $Nu_0$  is maximum but decreases with  $H$ . When the nozzle-to-surface distance increases ( $H/b \in [3; 6]$ ), the impinging surface stays in the potential core but the nozzle-to-surface distance becomes larger than the thickness of the stagnation region. Although the mean velocity remains constant, the fluctuations increase which in turn causes an increase of the heat transfer. When  $H$  becomes higher than the length of the potential core ( $H > 6$ ) the jet velocity decreases, inducing a reduction in heat transfer.

According to the conclusions of Kataona et al. [14], Choi et al. [7] explain the presence of the secondary peak on the Nusselt number graph (near  $s/b = 4$  to 5) by the transition and the creation of vortices in the boundary layer of the wall jet.

After this review, several questions remain. Some points seem to have a very particular importance:

The boundary conditions seem to be very important. Gau and Chung [1] show clearly that, taking into account the geometry, the flow after the impact disturbs the jet flow near the nozzle and modifies the generation of the vortices. The shape of the cavity seems to have a considerable effect on the structure of the flow. Yang et al. [8] show that the slit geometry influences the characteristics of the jet (turbulence level) and modifies the heat transfer at the stagnation point.

The stagnation region thickness was determined by Choi et al. [7], but only from velocities measured on the axis. No information on the spatial velocity distribution or the unsteadiness of the flow is available.

Many vortical structures develop in the vicinity of the impact (shear layer vortices and other secondary structures close to the wall) and if their role in the heat transfer is not any more a doubt (Thomann [12]), the modifications which involve on the aerodynamic field seem relatively misunderstood.

To answer these questions it is necessary to know the unsteady structure of the flow and for this reason we undertook to carry out PIV measurements. Before studying the more complex case of a line of discrete jets, we initially undertook the study of a slot jet in order to highlight the structure of a jet impinging a concave surface.

## Experimental Apparatus

Initially, the main aim of our study is to determine the influence of the curvature of the target wall on the impinging jet flow. Thus, we choose to use the simplest model: A plane jet impinging on a half-cylinder target. Therefore, in order to compare the present results with those obtained during our previous studies on impingement on flat wall, we kept constant most of the geometrical parameters. In the present study, the choice of the jet geometry (3D jet or 2D jet) is posed at first. The case of a plane jet was

initially retained because of more academic geometry allowing to facilitate numerical modeling even if in many industrial applications, and particularly in the turbine blades, the configuration of multiple three-dimensional jets is commonly used. Moreover, the plane jet is a simple, symmetrical, two-dimensional configuration and it is more adapted to known metrologies.

**Dimension of the Injector.** To obtain good spatial resolution, a slot height of 10 mm is retained ( $b=10$  mm). According to Rajaratnam [15], the aspect ratio must be higher than 20 to obtain a quasi two-dimensional flow. We will use an injector channel 300 mm broad ( $L/b=30$ ).

**Type of Injection.** Because of problems of confinement it was not possible to use a converging nozzle as injection device and thus to obtain "Top hat" profiles at the jet exit. We use an injection device with long feeding circuits (plane channel). Under these conditions, we obtain "developed" velocity profiles at the jet exit. (This choice will, however, involve difficulties for the comparison with the literature).

**Impinging Height.** The many preceding studies on of the jets impinging a plane wall showed that the optimal height is always about 5 diameters. We retained three impinging heights around this value ( $H/b=3, 5, \text{ and } 7$ ).

**Impingement Surface.** We retained a half-cylinder because it is a simple geometry. The radius of curvature is more difficult to determine. If it is too large, it approaches the limiting case configuration of jet impinging on a plane wall. It should not be too small for reasons of confinement. In the real turbine blade, it is difficult to define only one curvature radius, the value of the relative curvature (surface diameter divided by the slot height) is about 7. We thus chose to take two values framing this value:  $Dc/b \approx 5.2$  and  $9.4$ .

**Side Walls.** The cylindrical impingement wall is closed at these two ends by side plates. Now the question is to know if the border of this semicylindrical wall must be prolonged by higher and lower plates. With the impinging heights selected ( $H=30, 50, \text{ and } 70$  mm) and curvature radii selected ( $Dc=52$  and  $94$  mm), several flow patterns can arise. In particular, for the lowest relative curvature and the strongest impinging heights, a great part of jet is subjected to the external disturbances. We chose to use additional plates in order to avoid the external disturbances. The two plates impose a more confinement, but which exists in the real blades.

**Dynamic Parameters.** For the comparison between the two configurations (plane jet and 3D jet), we retained an identical reference length [jet diameter ( $d$ )=slot height ( $b$ )=10 mm]. As the section of injection is difference (Surface of injection Jet 2D =  $7.64 \times$  Surface of injection Jet 3D), we have the choice between using the same flow rates (but different jet mean flow velocities) or using same jet mean flow velocities (but different flow rates). From the thermal point of view the first choice would be retained, on the other hand from the aerodynamic point of view the second choice is relevant. We thus chose to take a velocity identical  $U_j$  for the two geometries (thus of identical Reynolds numbers).

The slot is supplied by a right-angled parallelepiped channel (955 mm long, 300 mm wide, and 10 mm high). Thus, the slot is 10 mm high and 300 mm wide. The impingement surface consists of a half cylinder and two plates used as higher and lower boundaries. All these elements are transparent (Altuglas 4 mm thick) in order to do the visualisations and measurements by PIV velocimetry (Fig. 1).

The upstream side of the test section (Fig. 2) is connected to a fan. Flowmeters and valves are inserted between the convergent inlet and the fan to regulate and measure the inlet flow rate  $Q_e$ . A heat exchanger is used to control the jet temperature.

The three main parameters of this study are:

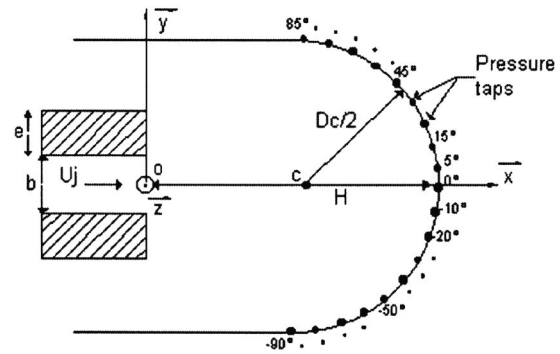


Fig. 1 Test geometry

- The Reynolds number based on the jet mean flow velocity  $U_j$  and the jet height  $b$  ( $Re_b = U_j b / \nu = Q_e / L \nu$ ). ( $Re_b = 1400, 3200, \text{ and } 6400$ );
- the dimensionless impinging height ( $H/b = 3, 5, \text{ and } 7$ );
- the relative curvature of the wall ( $Dc/b = 5.2, 9.4$ ).

Since the same flow structure and the same effect of the curvature radius were observed for each studied Reynolds number and for impinging height ( $H/b$ ) higher than 4, only the results for the configuration where  $Re_b = 3200, H/b = 7$  will be presented.

The free jet and the flow dynamics are characterized by the distributions of the mean velocity and turbulence values at the jet exit (Cornaro et al. [2], Yang et al. [8]). The velocity distributions of the free slot jet are measured with a hot wire anemometer (the sampling rate is 10 KHz, 50,000 samples were recorded). Figure 3 presents the distributions of the mean and root-mean square (rms) values of the velocity for the free jet at ( $x/b=0$ ) and ( $Re_b$

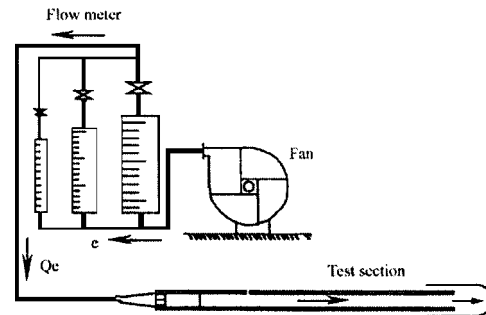


Fig. 2 Experimental device

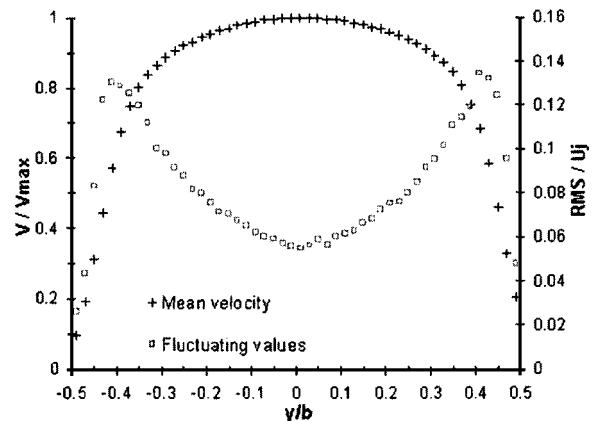
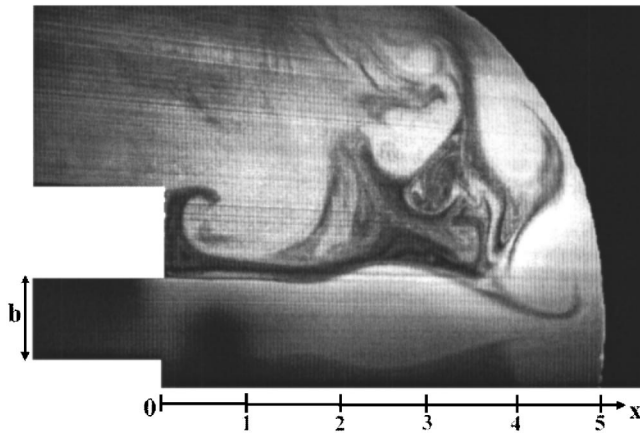


Fig. 3 Distributions of mean and fluctuating values of the velocity for the free jet ( $Re_b=3200$ )



**Fig. 4 Example of image of a jet impinging a curved wall. ( $Re_b=1400$ ,  $H/b=5$ ,  $Dc/b=9.4$ )**

$=3200$ ). The mean velocity is divided by the velocity at the jet axis ( $y/b=0$ ) and the rms values are divided by the jet mean flow velocity ( $U_j$ ). We observe that the velocity fluctuations are very low ( $\approx 0.05 U_j$ ) near the jet axis ( $y/b=0$ ) but at the edge of the nozzle ( $y/b=\pm 0.5$ ), the values are higher ( $\approx 0.13 U_j$ ) due to the mixing layers of the jet.

### Visualizations

The flow visualizations were obtained by laser tomography. The jet flow is seeded with a smoke generator (water and glycerine) and is illuminated with light sheets issuing from an Argon-Ion laser. A digital camera (HCC-1000 Camera,  $1024 \times 1024$  pixels) gives the possibility to record some sequences of images with frequencies up to 1000 frames per second. During the experiments, the jet is seeded only a few seconds at the beginning of the visualizations in order to not pollute the whole field and we waited for the disappearance of the totality of the seeding before doing another recording. Moreover for technical and symmetry reasons, the flow visualizations were only realized on the higher part of the flow and for several experimental configurations.

Figure 4 presents the slot jet impinging the curved wall for the following parameters  $Re_b=1400$ ,  $H/b=5$ , and  $Dc/b=9.4$ . On this "snapshot," we observe that the jet, issuing from the left, impacts the curved wall at its center ( $x/b=5$ ;  $y/b=0$ ). Then the flow separates and each part of the jet follows the curved wall, one part downwards and the other one upwards. The formation of the vortices is also observed in the jet mixing layers. These vortices, characteristic of a shear layer, appear as an undulation (starting from  $x/b=3$ ), and develop into rolls up shapes further downstream. Then they impact the wall and finally convect downstream in the wall jet.

### Velocity Measurements by PIV

The velocity measurements were carried out by the particle image velocimetry (PIV) technique. A SPECTRA-PHYSICS Nd-YAG laser source ( $2 \times 200$  mJ at 10 Hz and 532 nm) is used for measurements with the PIV system (DANTEC Technology) that allows us to obtain several planes of velocity. A laser beam penetrates the bottom of the test rig by means of the "telescopic arm" ERROL allowing us to illuminate the flow in the plane of interest. Seeding is obtained using an atomizer (water and glycerine). The mean size of the particles is less than  $0.7 \mu\text{m}$ .

Pictures are obtained using a Kodak MegaPlus ES 1.0w camera ( $768 \times 484$  pixels double frames) working in cross-correlation mode. The FLOWMANAGER 2.22 software controls the Piv2000 processor which converts pictures into velocity fields.

Measurements are obtained for several experimental configurations. For each configuration, 5000 independent samples of measurement are recorded at 10 Hz, divided into 25 packages of 200 recordings. From an initial velocity field, validation and statistical processes are carried out in order to obtain the mean field ( $\bar{U}$ ,  $\bar{V}$ ) and the ( $\text{rms}_u$ ,  $\text{rms}_v$ , and  $u'v'$ ) values.

**Additional Filtering Process.** To eliminate erroneous measurements during the recording (shaded zones, wall reflections, bad seeding), the data are filtered in each point of measurement, for each acquisition, and each velocity component. Thus each sample of measurement is validated according to several criteria. Then the data processing is carried out in two steps.

In the first processing, each sample is validated according to a significant value of the signal–noise ratio (the threshold is fixed at 2). This corresponds to a signal–noise ratio between the first and the second peak of the correlation function used to determine the velocity. Then starting from these validated values, a velocity histogram at each point and for each velocity component is built and smoothed. A threshold is applied on the bottom part of the velocity histogram. The mean ( $\bar{U}$ ,  $\bar{V}$ ) and fluctuating ( $\text{rms}_u$ ,  $\text{rms}_v$ ) values of the velocity are thus estimated. These estimated values are used to obtain the boundaries of the bandwidth filter ( $\bar{U} \pm K * \text{rms}_u$ ).

In the second processing, the initial measurements are again filtered with a lower threshold than the first processing, (signal–noise ratio at 1.5). Measurements are then filtered by bandwidth re-using the results of the first processing. Supposing that the velocity histogram is Gaussian, only the values included in the interval ( $\bar{U} \pm K * \text{rms}_u$ ) are validated. The  $K$  coefficient is a measure of the confidence level and is equal to 3. The mean values and the fluctuations for each velocity component and each point are finally calculated. After the post processing, only the statistics with more than 3000 validated vectors are retained.

**Velocity Measurement Uncertainty.** The errors inherent in the PIV measurements were quantified according to Westerweel [16] with a 95% confidence level. The errors of the method mainly depends on the scale calibration ( $\approx 0.65\%$ ), the pixel displacement ( $\approx 1.04\%$ ), and the time interval between the two images (negligible uncertainty). To obtain the uncertainty of measurement, it is necessary to add to the precision the various biases of this technique. There are many biases and some of them are not easily quantifiable. For example, we will note the bias related to interpolation sub-pixel (Westerweel [16]) or the bias due to the zones with strong velocity gradient (Keane [17]). However, if we assure that the biases are less the twice of the uncertainty allotted to the precision, the uncertainty is estimated at 3% for the mean values and at 6% for rms.

Most of the measurements are realized in and around the symmetry plane ( $x=0$ ) of the slot jet for all the configurations.

For the reference point ( $x/b=5.3$ ;  $y/b=0.7$ ) and for the configuration where  $Re_b=3200$ ,  $H/b=7$ , and  $Dc/b=5.2$ , we observe that the time evolution of the vertical component  $V$  are mainly distributed between  $\pm 3$  m/s.

For the convergence calculations, only the values validated by the data processing are used. We observe, for the reference point ( $x/b=5.3$ ;  $y/b=0.7$ ), that convergence is reached (within  $\pm 0.5\%$ ) from 150 samples for the mean velocity  $\bar{U}$  and from 2500 for the  $\text{rms}_u$  values. Thus the recording of 5000 instantaneous velocity fields is sufficient to obtain statistical convergence.

### Results

Figure 5 is the mean velocity field obtained by PIV for the following parameters ( $Re_b=3200$ ;  $H/b=7$ ;  $Dc/b=9.4$ ). We observe that the jet issuing from the left impacts the center of the curved wall at ( $x/b=7$  and  $y/b=0$ ). At this location, the flow

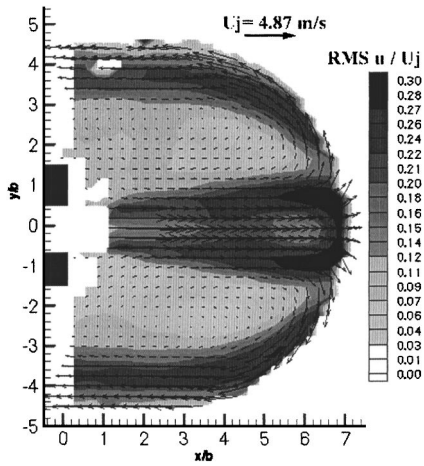


**Fig. 5 Mean velocity field and  $rms_u$  values ( $Re_b=3200$ ;  $H/b=7$ ;  $Dc/b=9.4$ )**

separates in two parts. Each part of the fluid skirts the curved wall and is symmetrical on each side of the horizontal axis ( $y/b=0$ ). Thus we observe clearly an impact on the curved wall. In this configuration, rms values of the horizontal component ( $U$ ) have a rather particular form: The maximum values ( $\approx 0.3 U_j$ ) are reached in the vicinity of the jet shear layer. These two areas located symmetrically about the  $x$  axis meet in the vicinity of the stagnation point and form a horseshoe shape (cf. Fig. 5). For the vertical component ( $V$ ), the intensity of the maximum fluctuations is almost identical to that of the horizontal component ( $\approx 0.15 U_j$ ). On the other hand, the location of these maxima is different: It is close to the impact point ( $x/b=7$ ;  $y/b=0$ ).

For this configuration, we note that, for several aspects, this behavior is similar to the one observed in the case of a single jet impinging a plane wall. It is not the same when the wall curvature radius is modified.

Figure 6 shows the mean velocity field obtained by PIV for the following parameters ( $Re_b=3200$ ;  $H/b=7$ ;  $Dc/b=5.2$ ). We observe now that the jet issuing from the left does not impact directly the center of the curved wall ( $x/b=7$  and  $y/b=0$ ). Indeed, there is a triangular area in the vicinity of this impact point where the velocities are very low. The mean flow is always symmetrical

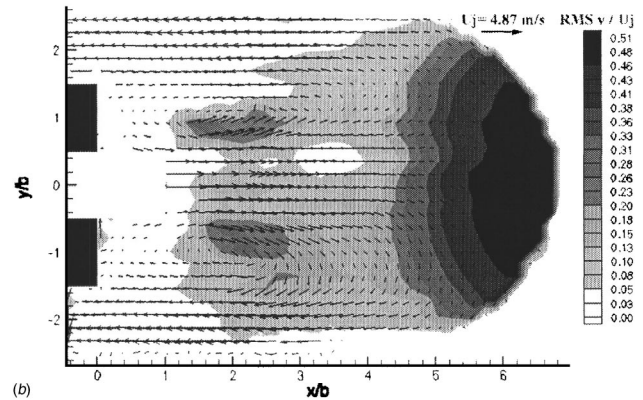
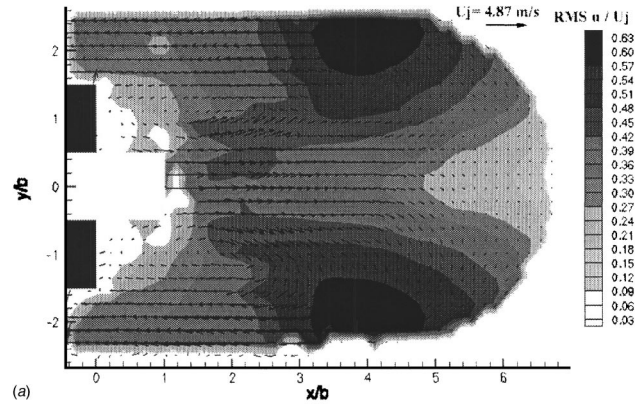


**Fig. 6 Mean velocity fields and rms values of horizontal component  $U$  (a) and vertical component  $V$  (b) ( $Re_b=3200$ ;  $H/b=7$ ;  $Dc/b=5.2$ )**

about the  $x$  axis, but there seems to be a “dead fluid” area which prevents the jet from impacting with the curved wall. Thus, the fluid makes a half-turn and comes out, as mentioned previously, at the top and bottom of the figure. For the horizontal and vertical velocity fluctuations, we also observe many transformations. For the horizontal component ( $rms_u$ ), the position and values of the maxima evolve considerably.

Figure 6(a) also shows two zones with high intensity

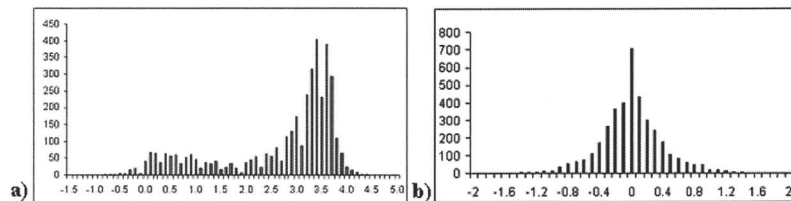


**Fig. 7 Histograms of the horizontal component (a) and the vertical component (b) at the reference point ( $x/b=6.7$ ;  $y/b=0$ ) ( $Re_b=3200$ ,  $H/b=7$ ,  $Dc/b=9.4$ )**

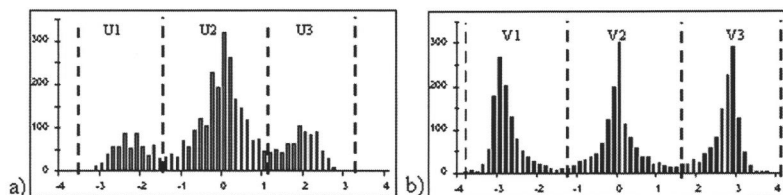


**Fig. 8 Histograms of the horizontal component (a) and the vertical component (b) at the reference point ( $x/b=5.3$ ;  $y/b=0.7$ ) ( $Re_b=3200$ ,  $H/b=7$ ,  $Dc/b=5.2$ )**

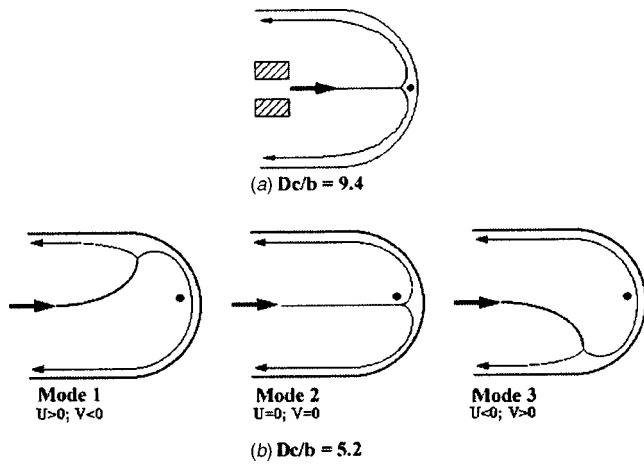


Fig. 9 Scheme of the flow for (a)  $Dc/b=9.4$  and for (b)  $Dc/b=5.2$

( $\approx 0.6 U_j$ ) located symmetrically about the jet axis in  $x/b=4.5$  and  $y/b=\pm 2.5$ . For the vertical component [cf. Fig. 6(b)], we find the same behavior as for large radius of curvature: Only a single zone of maximum in the vicinity of ( $x/b=7$  and  $y/b=0$ ). However, we can notice that the level reached for the lower radius of curvature ( $\approx 0.5 U_j$ ) is much higher than large radius of curvature. At first sight, this behavior can appear surprising since there is no impact at ( $x/b=7$  and  $y/b=0$ ) in the case of the small relative curvature.

In the case of the lower relative curvature ( $Dc/b=5.2$ ), the fact that the jet does not impact the center of the curved wall is a rather surprising phenomenon. Thus in order to understand this different behavior between the two relative curvatures, the histograms of the two components of the velocity, for a point located in the zone of strong  $rms_v$  values, are built for each curvature radius and for the same Reynolds number and impinging height. The histograms of the two components of the velocity for the configuration ( $Re_b=3200$ ,  $H/b=7$ ) are presented in Fig. 7 for  $Dc/b=9.4$  and in Fig. 8 for  $Dc/b=5.2$ . The velocity histograms are built at the reference points ( $x/b=6.7$ ;  $y/b=0$ ) for  $Dc/b=9.4$  and at ( $x/b=5.3$ ;  $y/b=0.7$ ) for  $Dc/b=5.2$ .

For large relative curvature ( $Dc/b=9.4$ ), we observe for the horizontal component a main peak centered around 3.5 m/s and a second peak centered around 0 m/s [cf. Fig. 7(a)]. Therefore, the horizontal component is mainly greater than 0 m/s. For the vertical component only one peak centered around the value 0 m/s is observed [cf. Fig. 7(b)]. In this case, the jet comes to impact the center of the wall [cf. Fig. 9(a)].

For the lower relative curvature ( $Dc/b=5.2$ ), the histograms of the two components show three distinct peaks, centered around the values: (-3, 0, and 3 m/s) for the vertical component [cf. Fig. 8(b)] and (-2.3, 0, +2 m/s) for the horizontal component [cf. Fig. 8(a)]. This can be considered as the superposition of three distinct behaviors. In order to study separately these three configurations, we define three velocity ranges for each component: [-4; -1.5 m/s] (range V1), [ $\pm 1.5$  m/s] (range V2), and [1.5; 4 m/s] (range V3) for the vertical component and [-3; -1.4 m/s] (range U1), [ $\pm 1.4$  m/s] (range U2), and [1.4; 3 m/s] (range U3) for the horizontal component.

The mean velocity and rms values of the two components are then recomputed by keeping only the velocity fields for which, at the reference point, the measurement of the vertical velocity component is included in one of the three ranges. The same filtering as previously used is used to calculate the averages for the velocity fields selected. Then, we observe that each velocity range of the vertical component is connected with only one velocity range of

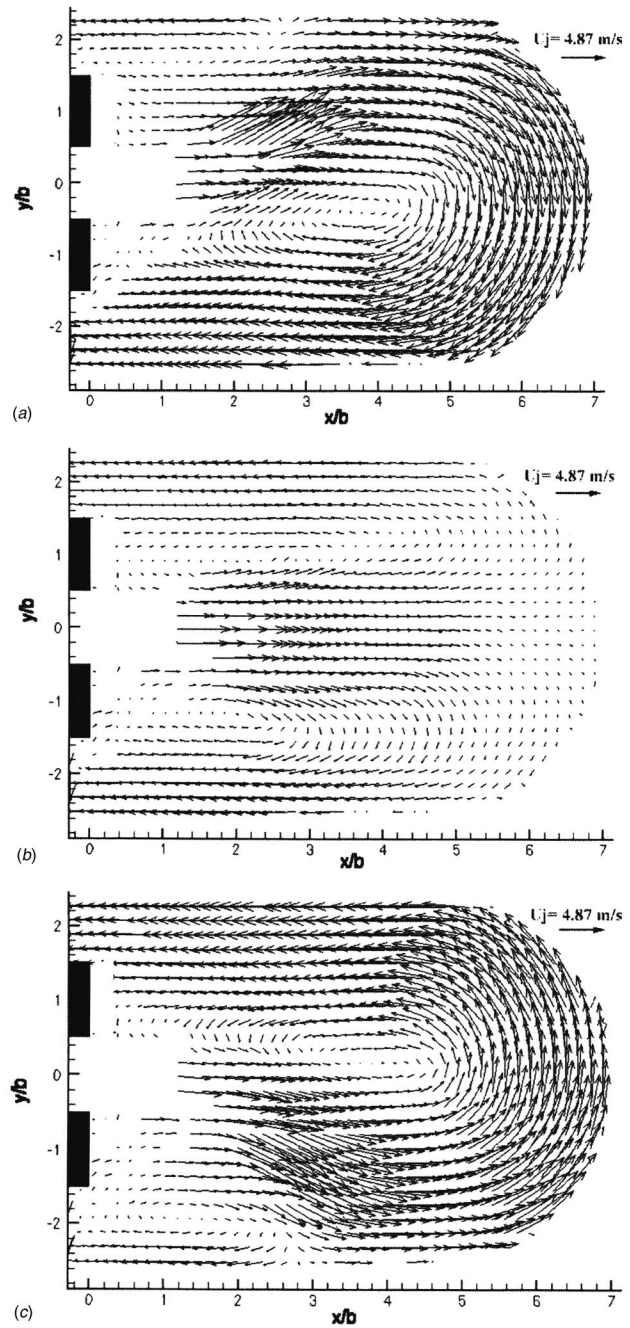


Fig. 10 Mean velocity field for the three modes ( $Re_b=3200$ ,  $H/b=7$ ,  $Dc/b=5.2$ )

the horizontal component (V1 and U3, V2 and U2, V3 and U1). Three flows with different characteristics from the mean velocity field are obtained. We have verified that the mean velocity fields of these three flows (cf. Fig. 10) correspond with the instantaneous velocity fields observed for these behaviors during the measurements (cf. Fig. 11).

Figure 10(a) shows the mean velocity field for the first mode ( $Re_b=3200$ ,  $H/b=7$ ,  $Dc/b=5.2$ ). We observe, contrary to the mean velocity field, that the jet impacts the higher part of the curved surface ( $x/b=2.7$ ;  $y/b=2.6$ ) and then separates in two parts. A significant part of the jet skirts the curved wall to the bottom and another smaller part sets out again directly towards the left [cf. Fig. 9(b)]. In this case, the flow is no longer symmetrical about the horizontal axis.

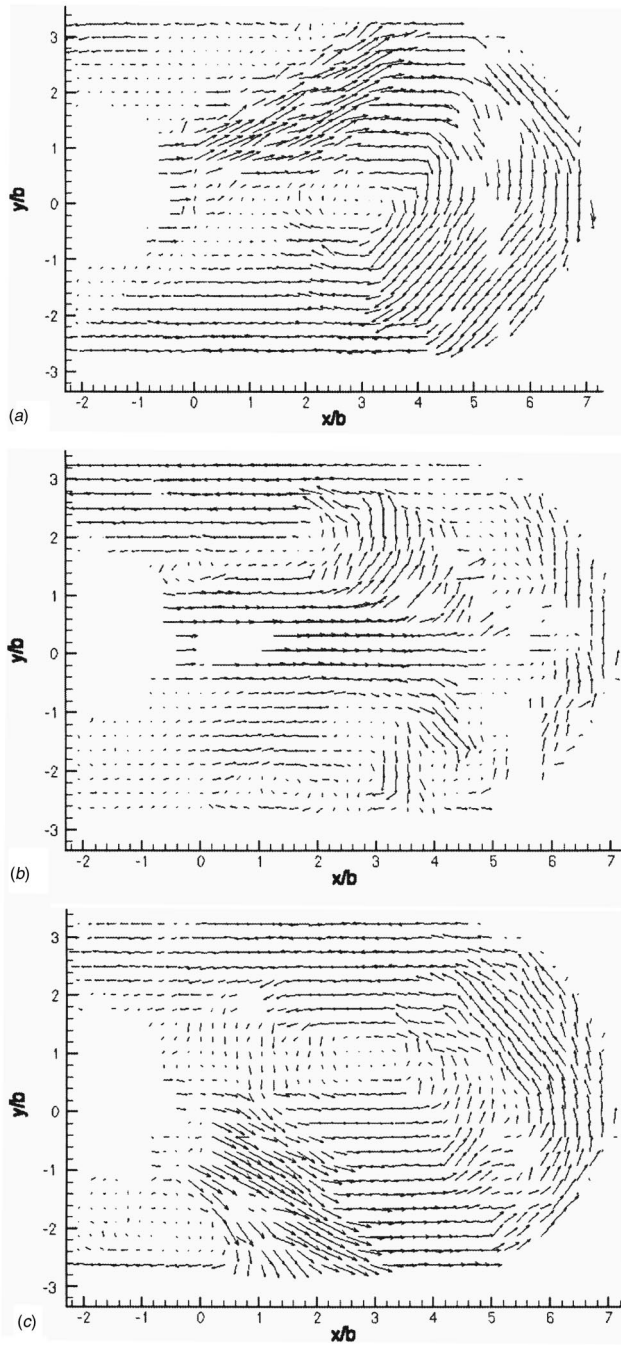


Fig. 11 Instantaneous velocity field for the three modes ( $Re_b = 3200$ ,  $H/b = 7$ ,  $Dc/b = 5.2$ )

For mode 2 [cf. Fig. 10(b)], we notice that the jet impacts the center of the curved wall at  $(x/b=7; y/b=0)$ . The jet separates and each part follows the curved wall on both sides of the stagnation point [cf. Fig. 9(b)]. Then we find a symmetrical flow about the horizontal axis.

Finally, Fig. 10(c) shows the mean velocity field for the third mode. As for mode 1, we observe that the jet impacts the wall, but here on its lower part ( $x/b=2.8; y/b=-2.6$ ), and then separates. In the case, most of the jet flow also follows the curved surface upwards and a small part sets out again directly towards the left [cf. Fig. 9(b)]. Like for the mode 1, the flow is not symmetrical about the horizontal axis.

These three flow patterns show the presence of three semistable positions: For example, the jet remains directed to the top a few

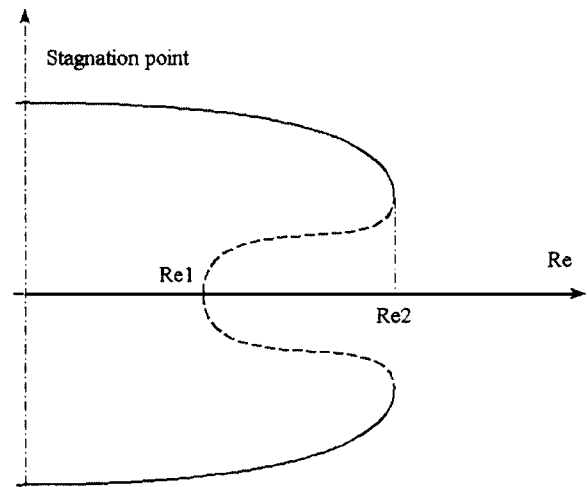


Fig. 12 Bifurcation diagram for  $Dc/b=5.2$

seconds then it moves towards another position (bottom or middle) to be stabilized again. A few seconds later, it starts again.

From our experiments (mainly flow visualizations and some PIV measurements) we can propose a bifurcation diagram (cf. Fig. 12) that we could observe for our configuration. On the graph we observe several stable (solid lines) and unstable (dashed lines) states according to the Reynolds number. For the lower values ( $Re < Re_1 \approx 500$ ) we observe two stable states: The first one characterizes the flow when the jet impacts the upper side of the target plate, the second when the jet impacts the lower side. Experimentally we observe that we need a very strong disturbance to pass from one state to the other. Between the range [ $Re_1; Re_2 > 6400$ ] we have three stable states: the two previous states and the state corresponding to the case when the jet impacts the center of the curved surface. When the Reynolds number increases, the disturbance needed to pass from one state to another seems to decrease, involving the increase of the frequency for the flow structure transition between modes. For the higher Reynolds numbers values, we only find one stable mode corresponding to the jet which impacts the center of the curved target wall.

Computations of the fluctuations of each velocity component for each mode are also carried out. We observe significant modifications for the fluctuations of the horizontal component ( $rms_u$ ) compared to the mean field. Indeed, for the modes 1 and 3 (cf. Figs. 13(a) and 13(c)), only one zone of strong  $rms_u$  values is observed. This zone is located at  $(x/b=2.2; y/b=0.5)$  for the mode 1 and at  $(x/b=2.5; y/b=-0.5)$  for the mode 3. The maximum  $rms_u$  value ( $\approx 0.4 U_j$ ) is definitely weaker than the one for the mean field ( $\approx 0.6 U_j$ ). Moreover, for mode 2 [cf. Fig. 13(b)], a large zone of strong  $rms_u$  values is observed and is located between  $(x/b=1.5; x/b=5)$ . The maximum  $rms_u$  value ( $\approx 0.49 U_j$ ) is once again weaker than the one for the mean field.

For each mode, we find, for the  $rms_v$  values, the same behavior as for the mean field. A large zone of strong  $rms_v$  values located close to the center of the curved wall at  $(x/b=7; y/b=0)$  is also observed. However, the maximum  $rms_v$  value is for each mode weaker than for the mean field ( $\approx 0.5 U_j$ ). Indeed, for modes 1 and 3 the maximum is approximately equal to  $0.3 U_j$  and for mode 2 it is approximately equal to  $0.4 U_j$ .

Thus the mean velocity fields and rms values of the three modes show a different structure of the flow and the maximum rms value for the two components is weaker and is located at different places compared to the whole field computed with all the samples.

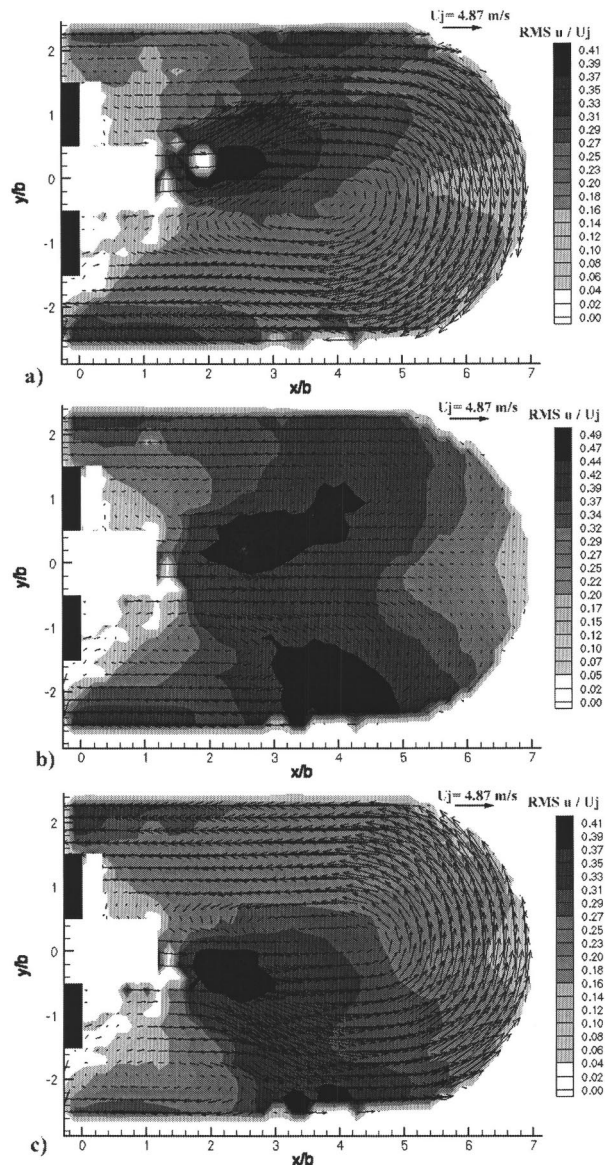


Fig. 13 Mean velocity field and  $rms_u$  values for the three modes ( $Re_b=3200$ ,  $H/b=7$ ,  $Dc/b=5.2$ )

### Pressure Measurements and Results

Measurements of pressures in the curved wall were also carried out. Pressure taps (0.4 mm) were created at different locations only on the curved part of the wall (cf. Fig. 1). For the pressure measurements, differential pressure sensors are connected to an acquisition card and the signal is amplified beforehand. The sampling rate is set at 500 Hz and the time of acquisition is about 10 s. The measurements allow us to calculate the pressure coefficient:  $C_p = 2 \cdot (p_i - p_{ref}) / (\rho U_j^2)$ , where  $p_i$  is the static pressure at the tap number  $i$  and  $p_{ref}$  the pressure reference (here  $p_{ref} = p_{atm}$ ).

Wall pressure was measured using a digital micro-manometer (Furness FC012) whose precision is about 1% of full scale ( $\approx 200$  Pa). The uncertainty of measurement is  $\pm 2$  Pa and thus for the pressure coefficient it is about 15%.

Figure 14 shows the evolution of the mean pressure coefficient  $C_p$  for the two configurations. For the large radius, the distribution of  $C_p$  is the same as that for a plane wall: The maximum is reached at the stagnation point and a symmetrical decrease is observed on each side of the curve from this point. This pressure maximum confirms the impact of the jet in the center of the wall.

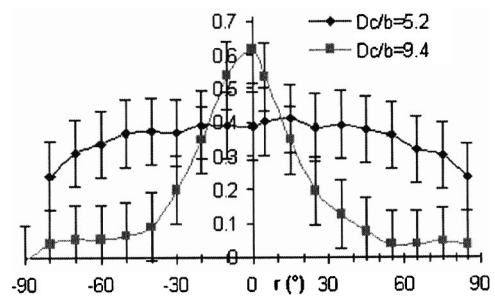


Fig. 14 Mean pressure distribution ( $Re_b=3200$ ,  $H/b=7$ )

For the small radius of curvature, the  $C_p$  has a different shape. We do not observe a distinct maximum but rather a constant value on most of the profile, indicating a uniform zone of pressure. In this case, the lack of the maximum pressure coefficient reaffirms that the jet does not impact the center of the wall but oscillates between three semistable positions. So the superposition of three higher pressure peaks corresponding to the stagnation points of the three modes involves that the mean pressure coefficient is constant along the curved wall.

We observe that, if the jet comes to impact the center of the wall, the pressure coefficient is maximum at the center. When the jet oscillates between three distinct positions, the pressure coefficient does not have a maximum and is constant along the wall. Thus the value of the pressure coefficient at the center of the wall makes it possible to know if the jet impacts directly the curved wall. A maximum pressure coefficient value in the center of the wall is a criterion to indicate impact. Figure 15 presents the results of the mean pressure coefficient for the three studied impinging heights in the case of the small radius. We can observe, for small impinging height ( $H/b=3$ ), that the jet impacts directly the center of the wall unlike for large impinging height ( $H/b > 4$ ). Hence the impinging height also has an effect on the jet structure.

### Conclusion

The measurements of average fields and turbulent values were obtained in the case of a plane jet impinging on a curved wall in order to obtain comparisons (or validations) with numerical studies and to highlight the significant role of the radius of curvature on an impinging plane jet. The results for a lower relative curvature indicate that in spite of the convergence of the statistics, the flow oscillates between three different behaviors which modifies significantly (in level and position) the turbulent values. The statistics obtained for each one of these configurations are all different and are also different to the whole field computed with all the samples gathered from these three configurations. This flow transformation will involve a modification of the thermal transfers in the vicinity of the leading edge of the blade. The knowledge of the jet behavior will make it possible to optimize turbine blade cool-

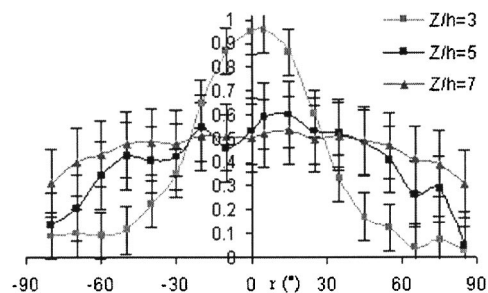


Fig. 15 Mean pressure distributions for the three impinging heights ( $Re_b=3200$ ,  $Dc/b=5.2$ )



ing. In addition, the pressure measurements have confirmed the relative curvature effects and allowed us to know the behavior of the jet. A study of the instability could be carried out according to the other parameters. However, the transition from one configuration to another is not easily foreseeable (a study was just begun) because it seems impossible (for this flow configuration) to dissociate the turbulence and stability study.

## Nomenclature

- $b$  = Slot height ( $b=10$  mm)  
 $c$  = Curvature center  
 $D_c$  = Curvature diameter  
 $H$  = Impinging height  
 $L$  = Slot width  
 $O$  = Slot origin  
 $e$  = Channel wall thickness ( $e=10$  mm)  
 $U, V, W$  = Velocity components  
 $U_j$  = Jet mean flow velocity

## References

- [1] Gau, C., and Chung, C. M., 1991, "Surface Curvature Effect on Slot-Air-Jet Impingement Cooling Flow and Heat Transfer Process," *J. Heat Transfer*, **113**, pp. 858–864.
- [2] Cornaro, C., Fleischer, A. S., and Goldstein, J. R., 1999, "Flow Visualization of a Round Jet Impinging on Cylindrical Surfaces," *Exp. Therm. Fluid Sci.*, **20**, pp. 66–78.
- [3] Hrycak, P., 1981, "Heat Transfer from a Row of Impinging Jets to Concave Cylindrical Surfaces," *J. Heat Transfer*, **24**, pp. 407–419.
- [4] Brahma, R. K., Padhy, I., and Pradham, B., 1990, "Prediction of Stagnation Point Heat Transfer for a Single Round Jet Impinging on a Concave Hemispherical Surface," *Waerme- Stoffuebertrag.*, **26**, pp. 41–48.
- [5] Lee, D. H., Chung, Y. S., and Won, S. Y., 1999, "The Effect of Concave Surface Curvature on Heat Transfer from a Fully Developed Round Impinging Jet," *J. Heat Transfer*, **42**, pp. 2489–2497.
- [6] Hrycak, P., 1982, "Heat Transfer and Flow Characteristics of Jets Impinging on a Concave Hemispherical Plate," 7th Int. Heat Transfer Conference Munich, pp. 357–362.
- [7] Choi, M., Yoo, H. S., Yang, G., and Lee, J. S., 2000, "Measurement of Impinging Jet Flow and Heat Transfer on a Semi-Circular Concave Surface," *J. Heat Transfer*, **43**, pp. 1811–1822.
- [8] Yang, G., Choi, M., and Lee, J. S., 1999, "An Experimental Study of Slot Jet Impingement Cooling on Concave Surface: Effects of Nozzle Configuration and Curvature," *J. Heat Transfer*, **42**, pp. 2199–2209.
- [9] Metzger, D. E., Yamashita, T., and Jenkins, C. W., 1969, "Impingement Cooling of Concave Surfaces with Lines of Circular Air Jets," *J. Eng. Power*, pp. 149–158.
- [10] Chupp, R. E., Helms, H. E., McFadden, P. W., and Brown, T. R., 1969, "Evaluation of Internal Heat Transfer Coefficients for Impingement-Cooled Turbine Airfoils," *J. Aircr.*, **6**, pp. 203–208.
- [11] Tabakoff, W., and Clevenger, W., 1972, "Gas Turbine Blade Heat Transfer Augmentation by Impingement of Air Jets Having Various Configurations," *J. Eng. Power*, pp. 51–60.
- [12] Thomann, H., 1968, "Effect of Streamwise Wall Curvature on Heat Transfer in a Turbulent Boundary Layer," *J. Fluid Mech.*, **33**, pp. 283–292.
- [13] Gardon, R., and Akfirat, J. C., 1966, "Heat Transfer Characteristics of Impinging Two-Dimensional Air Jets," pp. 101–107.
- [14] Kataoka, K., Suguro, M., Degawa, H., Marul, I., and Mihata, I., 1987, "The Effect of Structure Renewal due to Large-Scale Eddies on Jet Impingement Heat Transfer," *Int. J. Heat Mass Transfer*, **30**, pp. 559–567.
- [15] Rajaratnam, N., 1976, *Turbulent Jet*, Elsevier Scientific Publishing Company, New York.
- [16] Westerweel, J., and Willert, C., 1998, "Principles of PIV Techniques. Application of Particle Image Theory and Practice," Course at DRL, Göttingen, Germany.
- [17] Keane, R. D., and Adrian, R. J., 1990, "Optimization of Particle Image Velocimeters. Part 1: Double Pulsed Systems," *Meas. Sci. Technol.*, **1**, pp. 1202–1215.

# Statistical Approach for Estimating Intervals of Certification or Biases of Facilities or Measurement Systems Including Uncertainties

**F. Stern**

IHR Hydrosience and Engineering, The University of Iowa, Iowa City, IA 52242

**A. Olivieri**

INSEAN, Italian Ship Model Basin, Rome, Italy

**J. Shao**

**J. Longo**

IHR Hydrosience and Engineering, The University of Iowa, Iowa City, IA 52242

**T. Ratcliffe**

NSWC/CD, David Taylor Model Basin, Bethesda, MD

*A statistical approach for estimating intervals of certification or biases of facilities or measurement systems including uncertainties is set forth based on  $M \times N$ -order level testing, which is defined as  $M$  repetitions of the same  $N$ -order level experiment in  $M$  different facilities or in the same facility with  $M$  different measurement systems. In the absence of reference values, the mean facility or measurement system is used for assessing intervals of certification or biases. Certification or biases of facilities or measurement systems are defined as processes for assessing probabilistic confidence intervals for facilities or measurement systems for specific tests, data reduction equations, conditions, procedures, and uncertainty analysis. Similarly, subgroup analysis is performed for isolating and assessing levels of differences due to use of different model sizes (scale effects) or measurement systems. An example is provided for towing tank facilities for resistance tests using standard uncertainty analysis procedures based on an international collaboration between three facilities. Although the number of facilities are at a minimum, the results demonstrate the usefulness of an approach and support recommendation of future collaborations between more facilities. Knowledge of intervals of certification or biases is important for design, accrediting facilities or measurement systems, and CFD validation. [DOI: 10.1115/1.1906269]*

## 1 Introduction

Experimental fluid dynamics (EFD) testing in large-scale facilities at research institutes is undergoing change from routine tests for global variables to detailed tests for local variables for model development and computational fluid dynamics (CFD) validation, as design methodology changes from model testing and theory to simulation-based design. Detailed testing requires facilities utilize advanced modern measurement systems (MS) with complete documentation of test conditions, procedures, and uncertainty analysis. The requirements for intervals of uncertainties are even more stringent than required previously since they are a limiting factor in establishing intervals of CFD simulation validation [1] and code certification [2] and ultimately credibility of simulation technology. In addition, routine test data is more likely utilized in house, whereas detailed test data is more likely utilized internationally, which additionally requires use of standard procedures and uncertainty analysis and establishment of benchmark intervals of uncertainties. Detailed testing offers new opportunities for research institutes, as the amount and complexity of testing is increased.

Methodology and procedures for estimating EFD uncertainties have developed and progressed over the past 50 years. Formalization [3–5] is followed by standard procedures with emphasis on simplification and practical application [6,7]. However, rigorous use continues to be a problem in both research and design at university, industry, and government laboratories. Another problem is lack of methodology and procedures for estimating intervals of certification or biases of facilities or MS, i.e., establishing intervals of confidence for facilities or MS arising from systematic

errors due to differences or peculiarities in individual facilities or MS. Such differences or peculiarities arise from detailed facility geometry or MS design, working fluid and flow quality, conditions and procedures, test engineers, specific locations, etc. Adding to the problem is fact that such developments require considerable resources and, in case of facilities, cooperation amongst institutes, which often crosses international boundaries. Estimating intervals of certification or biases of facilities or measurement systems are required for establishing standard intervals of uncertainties for various types of facilities (towing tanks, wind tunnels, flumes, etc.) and tests (forces and moments, motions, waves elevations, mean velocities, turbulence, etc.) and MS (load cells, potentiometers, wave probes, pitot, LDV, PIV, etc.). This is important for design, accrediting facilities or measurement systems, and CFD validation.

Most work on facility or MS biases is for small-scale flow meter calibration facilities with focus on validation of accuracy, comparison of international flow standards, and establishing domestic flow traceability [8]. Proficiency testing programs are used to establish flow measurement traceability, which are largely based on Youden plots [9] requiring two (e.g., tandem and/or upstream and downstream) MS at each facility. This approach is not easily extended to large-scale multipurpose facilities with complex MS, including consideration of individual facility and measurement systems bias and precision limits. Individual facility and measurement systems bias and precision limits are required for use of such data as well as helpful in MS improvements.

For large-scale facilities such as wind tunnels and towing tanks with complex MS, only limited work was done and facility or MS biases not yet considered. The NATO, AGARD, Propulsion and Energetics Panel, Uniform Engine Testing Program, was a remarkable early exercise in large-scale testing in which the same jet engines were tested in a number of jet engine test stands in

Contributed by the Fluids Engineering Division for publication in the JOURNAL OF FLUIDS ENGINEERING. Manuscript received by the Fluids Engineering Division April 8, 2003; final revision received February 10, 2005. Associate Editor: S. Ceccio.

various NATO countries and uncertainties were estimated to explain whether data scatter was within the data uncertainty and conclusions were drawn [10]. Reference [11] compares results from wind tunnel tests for same geometry and conditions at two different institutes, model scales, and using a number of different measurement techniques and extensive error-analysis. The Cooperative Experimental Program of the Resistance Committees of the 17–19 International Towing Tank Conferences (ITTC) [12] compare results from towing tank tests at 22 institutes. Comparisons are made of global (resistance, sinkage and trim, wave profile, wave cut, wake survey, form factor, and blockage) and local (surface pressure and boundary layer traverses) data for a standard geometry (Series 60) of different sizes (1.2–9.6 m). However, uncertainty assessment was not considered. The cooperative uncertainty assessment example for resistance test of the Resistance Committee of the 22nd ITTC [13] compared results from towing tank tests at 7 institutes of resistance test bias and precision limits and total uncertainties following standard uncertainty assessment procedures, but for different model geometries and sizes (Series 60, container ships, and 5415).

In the following, a statistical approach for estimating intervals of certification or biases of facilities or MS including uncertainties is set forth.  $N$ -order level testing is reviewed followed by definitions for  $M \times N$ -order level testing, which is defined as  $M$  repetitions of the same  $N$ -order level experiment in  $M$  different facilities or in the same facility with  $M$  different measurement systems. If reference values are known, present approach are used at either the  $N$ -order or  $M \times N$ -order levels. However, unlike CFD where EFD provides reference values, for EFD reference values are seldom known, e.g., from a standard facility or MS. In the absence of reference values, the mean facility or MS is used for assessing intervals of certification or biases. Herein, certification or biases of facilities or measurement systems are defined as processes for assessing probabilistic confidence intervals for facilities or measurement systems for specific tests, data reduction equations, conditions, procedures, and uncertainty analysis. Similarly, subgroup analysis is performed for isolating and assessing levels of differences due to use of different model sizes (scale effects) or measurement systems. An example is provided for towing tank facilities for resistance tests using standard uncertainty analysis procedures based on an international collaboration between three facilities.

## 2 Estimating Intervals of Certification of Biases of Facilities or MS

Designing tests for estimating intervals of certification or biases of facilities or MS requires special care and consideration. Many factors affect certification or biases of facilities or MS; therefore, as with estimating precision limits (i.e., random errors), only those factors specifically isolated (i.e., turned on) are included. For example, if interest is for certain types of measurements using same MS in different facilities, then model-geometry, tests, data reduction equations, conditions, procedures, and uncertainty analysis should all be the same. Ideally, standard models are used. Otherwise, effects of differences in model geometry are included. If models are geometric similar, but two different scales, then scale effects are included. Similarly, if different MS are used at different facilities, then effects of MS are included and so on. Although approach used for either facilities or MS, presentation that follows is for facilities since same as for the example.

**2.1  $N$ -order Level Testing.** In  $N$ -order level testing,  $N$  repetitions of the same experiment in the same facility conducted

$$X_i = \frac{1}{N} \sum_{j=1}^N X_i^j \quad (1)$$

where  $X_i^j$  and  $X_i$  are single realization and individual facility mean results, respectively. The uncertainty in  $X_i$  is given by the root-

sum-square (RSS) of bias  $B_{X_i}$  and precision  $P_{X_i}$  limits

$$U_{X_i} = \sqrt{B_{X_i}^2 + P_{X_i}^2} \quad (2)$$

The bias limit is obtained by considering all sources for systematic errors, based on 0- or 1-order testing. The precision limit obtained by the standard deviation of the mean

$$P_{X_i} = 2 \frac{S_{X_i^j}}{\sqrt{N}} \quad (3)$$

where  $S_{X_i^j}$  is the standard deviation of the sample population  $X_i^j$

$$S_{X_i^j} = \left[ \frac{1}{N-1} \sum_{j=1}^N (X_i^j - X_i)^2 \right]^{1/2} \quad (4)$$

Under the assumption of a normal distribution for the sample population  $X_i^j$ , 95% confidence level, and  $N \geq 10$ , the estimated true result of the experiment  $X_{ET,N}$  lies inside the intervals

$$X_i^j - U_{X_i^j} \leq X_{ET,N} \leq X_i^j + U_{X_i^j} \quad (5)$$

$$X_i - U_{X_i} \leq X_{ET,N} \leq X_i + U_{X_i} \quad (6)$$

for the single realization and mean experimental result, respectively, where

$$U_{X_i^j}^2 = B_{X_i^j}^2 + (2S_{X_i^j})^2 \quad (7)$$

Additionally, this assumes facility biases  $\beta_{FB} = 0.0$ , otherwise  $X_{ET,N}$  is the biased estimated true value.  $X_{ET,N}$  is referred to as estimated true result of the experiment; since, confidence in Eqs. (5) and (6) relies on confidence in Eqs. (2) and (7). Note that at the  $N$ -order level outliers are often discarded if

$$|D_i^j| = |X_i^j - X_i| > 2S_{X_i^j} \quad (8)$$

**2.2  $M \times N$ -order Level Testing.** In  $M \times N$ -order level testing,  $M$  repetitions of the same  $N$ -order experiment in  $M$  different facilities conducted

$$\bar{X} = \frac{1}{M} \sum_{i=1}^M X_i = \frac{1}{M \times N} \sum_{i=1}^M \sum_{j=1}^N X_i^j \quad (9)$$

where  $\bar{X}$  is the mean facility result. The uncertainty in  $\bar{X}$  is

$$U_{\bar{X}} = \sqrt{B_{\bar{X}}^2 + P_{\bar{X}}^2} \quad (10)$$

The bias limit of the mean  $B_{\bar{X}}$  is the average RSS of the  $M$  bias limits  $B_{X_i}$

$$B_{\bar{X}} = \frac{1}{M} \sqrt{\sum_{i=1}^M B_{X_i}^2} \quad (11)$$

The precision limit  $P_{\bar{X}}$  is the standard deviation of the  $M$  results  $X_i$

$$P_{\bar{X}} = 2S_{\bar{X}} = 2 \frac{S_{X_i}}{\sqrt{M}} = \frac{2}{\sqrt{M}} \left[ \frac{1}{M-1} \sum_{i=1}^M (X_i - \bar{X})^2 \right]^{1/2} \quad (12)$$

or  $P_{\bar{X}}$  is the average RSS of the  $M$  precision limits  $P_{X_i}$  from Eq. (3)

$$P_{\bar{X}} = \frac{1}{M} \sqrt{\sum_{i=1}^M P_{X_i}^2} \quad (13)$$

Under the assumption of normal distribution for the sample population  $X_i$ , 95% confidence level, and  $M \geq 10$ , the estimated true result of the experiment  $X_{ET,MN}$  lies inside the intervals

$$X_i - U_{X_i} \leq X_{ET,MN} \leq X_i + U_{X_i}, \quad (14)$$

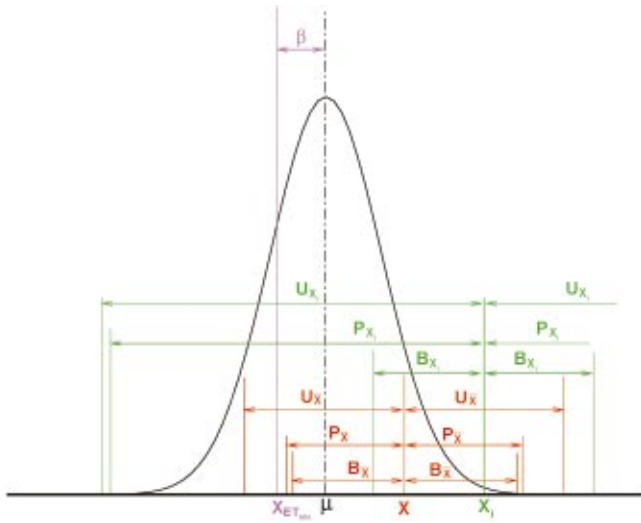


Fig. 1  $M \times N$ -order level testing

$$\bar{X} - U_{\bar{X}} \leq X_{ET_{MN}} \leq \bar{X} + U_{\bar{X}} \quad (15)$$

for the individual and mean facilities, respectively, where

$$U_{X_i}^2 = B_{X_i}^2 + (2S_{X_i})^2 \quad (16)$$

Equation (16) equals Eq. (2) if  $S_{X_i} = S_{X_i} / \sqrt{N}$ . Additionally, this assumes the mean facility biases  $\bar{\beta}_{FB} = 0.0$ , otherwise  $X_{ET_{MN}}$  is the biased estimated true value. Figure 1 displays  $M \times N$ -order level testing, including individual and mean facility results and their bias and precision limits and total uncertainties; biased parent-population mean value  $\mu$ ; and estimated true experimental results  $X_{ET_{MN}}$ .

**2.3 Using Mean Values as Reference Values.**  $D_i$  defined as the difference between the  $N$ -order level individual facility  $X_i$  and  $M \times N$ -order level mean facility  $\bar{X}$  values

$$D_i = X_i - \bar{X} \quad (17)$$

and its uncertainty  $U_{D_i}$  is defined as the RSS of the uncertainties of  $X_i$  and  $\bar{X}$

$$U_{D_i} = \sqrt{U_{X_i}^2 + U_{\bar{X}}^2} \quad (18)$$

$$U_{D_i}^2 = B_{X_i}^2 + P_{X_i}^2 + \frac{\sum B_{X_i}^2}{M^2} + \frac{4S_{X_i}^2}{M} \quad (19)$$

or

$$U_{D_i}^2 = B_{X_i}^2 + P_{X_i}^2 + \frac{\sum B_{X_i}^2}{M^2} + \frac{\sum P_{X_i}^2}{M^2} \quad (20)$$

If the absolute value of  $D_i$  is less than  $U_{D_i}$ ,

$$|D_i| \leq U_{D_i} \quad (21)$$

then the individual facility is certified at interval  $U_{D_i}$ , whereas if the absolute value of  $D_i$  is greater than  $U_{D_i}$ ,

$$|D_i| > U_{D_i} \quad (22)$$

then the facility bias  $U_{FB_i}$  is defined as

$$U_{FB_i}^2 = D_i^2 - U_{D_i}^2 \quad (23)$$

with total uncertainty

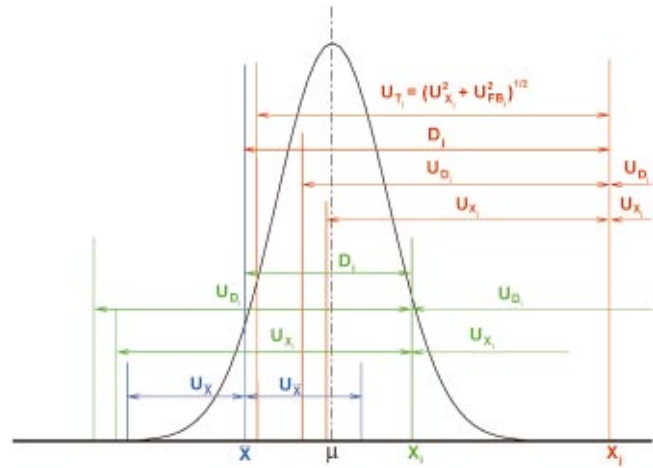


Fig. 2 Estimating intervals of certification or biases of facilities using mean as reference value: facility  $i$  certified at  $U_{D_i}$  and facility  $j$  with facility bias  $U_{FB_j}$

$$U_{T_i}^2 = U_{X_i}^2 + U_{FB_i}^2 \quad (24)$$

If  $|D_i|$  is much greater than  $U_{D_i}$

$$|D_i| \gg U_{D_i} \quad (25)$$

then  $D_i$  approximately equals the individual facility bias error  $\beta_{FB_i}$

$$D_i \cong \beta_{FB_i} \quad (26)$$

such that the biases can be estimated in both sign and magnitude and used for calibration. Figure 2 displays use of mean values as reference values, including both situations of estimation of interval of facility certification and bias.

For certified facilities, interval certification provides additional confidence in accuracy measurements, since it validates  $X_i$  and accounts for  $U_{\bar{X}}$  in assessing the level of certification. For noncertified facilities, accounting for facility biases provides  $U_{T_i}$ , which is an improved estimate than  $U_{X_i}$ . Presumably, design sets the requirements on appropriate intervals for certification or biases of facilities. Comparison of  $U_{X_i}$  with  $U_{\bar{X}}$  and uncertainties from other facilities is useful in developing strategies for reduction  $U_{X_i}$ . Note that for sufficiently large  $M$ ,  $U_{X_i} \gg U_{\bar{X}}$  so  $U_{D_i} \approx U_{X_i}$ . In this case,  $M \times N$ -order level testing primarily provides  $\bar{X}$ . As already mentioned, if reference values are known, present approach can be used at either the  $N$ -order or  $M \times N$ -order levels, which for completeness is included as an Appendix.

**2.4 Subgroup Analysis.** Isolating and assessing levels of differences due to use of different model sizes (scale effects) or measurement systems is of importance. Subgroup differences are assessed by comparison of the subgroup mean to the total mean, with consideration to the uncertainty in the comparison. For  $L$  subgroup facilities, subgroup mean and uncertainty are given by

$$\bar{X}_{SG} = \frac{1}{L} \sum_{i=1}^L X_{SG_i} \quad (27)$$

$$U_{X_{SG}}^2 = B_{X_{SG}}^2 + P_{X_{SG}}^2 \quad (28)$$

where

$$B_{X_{SG}}^2 = \frac{1}{L^2} \sum_{i=1}^L B_{X_{SG_i}}^2 \quad (29)$$

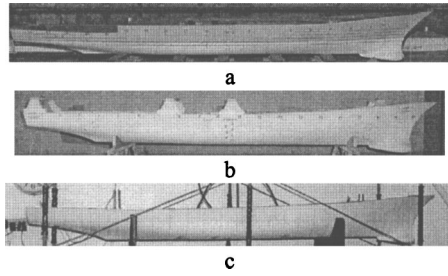


**Fig. 3 Surface-combatant model ships (a) DTMB model 5415 (b) INSEAN model 2340A (c) IIHR model 5512**

$$P_{\bar{X}_{SG}} = \frac{2}{\sqrt{L}} \left[ \frac{1}{L-1} \sum_{i=1}^L (X_{SG_i} - \bar{X}_{SG})^2 \right]^{1/2} \quad (30)$$

The subgroup difference and difference uncertainty are given by

$$D_{SG} = \bar{X}_{SG} - \bar{X} \quad (31)$$

$$U_{D_{SG}}^2 = U_{\bar{X}_{SG}}^2 + U_{\bar{X}}^2 \quad (32)$$

For

$$|D_{SG}| \leq U_{D_{SG}} \quad (33)$$

differences cannot be discerned, i.e., within noise intervals of comparison, whereas for

$$|D_{SG}| > U_{D_{SG}} \quad (34)$$

differences are discernable, which suggests the need for separated certification. The present approach differs from analysis of the means [14], since it takes into account both bias and precision uncertainties for both subgroup and mean in assessing intervals of subgroup differences. Analysis of the mean compares  $|D_{SG}|$  with  $P_{\bar{X}}/\sqrt{L}$ .

### 3 Example for Towing Tank Facilities

It is not easy to provide an example of the proposed approach, since, as already mentioned it requires considerable resources and cooperation amongst institutes often crossing international boundaries. The example provided is based on an international collaboration between three towing tank facilities for purposes of procuring benchmark CFD validation data for ship hydrodynamics resistance and propulsion geometry and conditions. Overlapping tests were conducted for evaluation of facilities; measurement systems; test procedures; uncertainty assessments; model size, offsets, and turbulence stimulation; and facility/model geometry and scale effect biases. The facilities were NSWC/CD David Taylor Model Basin (DTMB), Bethesda, MD USA; Istituto Nazionale per Studi ed Esperienze di Architettura Navale (INSEAN), Rome, Italy; and Iowa Institute of Hydraulic Research (IIHR), Iowa City, IA, USA. Hereafter designated as facilities *A*, *B*, and *C*, respectively. The model geometry is DTMB surface combatant 5415. Between all three facilities, many conditions and physics are under investigation. The data used as one of three test cases at the recent Gothenburg 2000 Workshop on Numerical Ship Hydrodynamics [15]. DTMB 5415 was conceived by USA Navy as a preliminary design for a surface combatant ca. 1980 with a sonar dome bow and transom stern. *A* and *B* used 5.72 m, 1/24.8 scale models, whereas *C* used a 3.048 m, 1/46.6 model, as shown in Fig. 3. Thus, scale effects (subgroup analysis) are considered in comparing *C* with *A* and *B*. The uncertainty assessment procedures closely follow [13] recommendations based on [6,7]. Reference [16] provides an overview of the overall results of the col-

laboration. Although number of facilities is a minimum, the results demonstrate usefulness of approach. Since  $N < 10$ ,  $P_{\bar{X}}$  is estimated using Eq. (13) as opposed to (12).

**3.1 Overlapping Test Design, Data Reduction Equations, Conditions, Procedures, and Uncertainty Analysis.** The most typical towing-tank tests were selected for the overlapping tests, i.e., resistance, sinkage and trim, wave profile, wave elevations, and nominal wake. Each institute followed their usual procedures; however, special consideration was given to integration of uncertainty assessment into all phases of the experimental process, CFD validation, and complementary CFD. Data-reduction equations were defined for residuary resistance  $C_R$ , sinkage  $\sigma$  and trim  $\tau$ , wave profile and elevations  $\zeta$ , and nominal wake mean velocity  $V$  and pressure  $C_p$ . Similar conditions and locations were used at all three facilities: Froude number (Fr) ranges; Fr and spatial locations for uncertainty analysis; and spatial resolution for wave elevations and nominal wake.

Initial analysis of the results and attempt at identification of facility biases were done by [16] using comparisons of differences between facilities (*A*–*B*, *A*–*C*, *B*–*C*) and the RSS of their uncertainties. However, this approach lacks a reference value such that the estimated facility biases depend on which facilities compared. Subsequently all results were reanalyzed according to the present approach. Presentation of the results for all tests is extensive and not necessary for the purpose of demonstration of the usefulness of the present approach. Herein, the results for the resistance test presented.

The data reduction equation for the resistance test is

$$C_R = C_T^{Tm} - C_F^{Tm}(1+k) \quad (35)$$

$$C_T^{Tm} = \frac{M_x^{Tm} g}{0.5\rho U_c^2 S} \quad (36)$$

$$C_F = \frac{0.075}{(\log_{10} \text{Re} - 2.0)^2} \quad (37)$$

The residuary resistance  $C_R$  used since it approximately removes a portion of Reynolds number (Re) scale effects due to skin friction (but not wave breaking).  $C_F^{Tm}$  is the frictional resistance at the measured towing tank temperature *Tm*, *k* is the form factor,  $M_x$  is the force in the axial direction (resistance),  $\rho$  is the towing-tank water density,  $U_c$  is the carriage speed, and *S* is the design-offsets wetted surface area for the static condition.  $M_x$  in kg is converted to Newtons by multiplication with *g* ( $g_A = 9.8009$ ;  $g_B = 9.8033$ ;  $g_C = 9.8031 \text{ m/s}^2$ ) based on the local latitude.  $C_F$  is calculated as recommended by [17] using the model-ship correlation line Eq. (37) and *k* is determined from low-speed resistance tests by Prohaska's method. The form factor approximately accounts for hull form effects on the model-ship correlation line under low speed and no separation assumptions.

Tests at *A* were performed in basin No. 2 (575 m long, 15.5 m wide, 6.7 m deep), which is equipped with an electrohydraulically operated drive carriage and capable of speeds of 10.3 m/s. Sidewall and end wall beaches enable 20-min intervals between carriage runs. Washington Suburban Sanitation Commission supplied the towing-tank water. Tests at *B* were performed in towing tank No. 2 (220 m long, 9 m wide, 3.6 m deep), which is equipped with a single drive carriage that is capable of speeds of 10 m/s. Sidewall and end wall beaches enable 20-min intervals between carriage runs. Natural springs supplied the towing tank water. Tests at *C* were performed in the IIHR towing tank (100 m long and 3.048 m wide and deep), which is equipped with an electric-motor operated drive carriage that is cable driven by a 15-horsepower motor and capable of speeds of 3 m/s. Sidewall and end wall beaches enable twelve-minute intervals between carriage runs. City of Iowa City supplied the towing tank water.

Equation (36) consists of individual MS for resistance, density,

**Table 1 Bias limits for resistance, density, carriage speed, and surface area**

	Calibration	Data Acquisition	Data Reduction
Resistance	Load Cell	Curve fit	Alignment load cell
Density	Thermometer		
Carriage Speed	Encoder	AD conversions	
	Wheel diameter Time base	Curve fit	
Surface area	Template		
	Rulers		
	Weights		

carriage speed, and surface area. Resistance was measured using load cells and PC data acquisition and reduction, including statistical analysis of the sample population (average, standard deviation, minimums, maximums, outliers). Outliers were identified and deleted using Chauvenet's criterion. Density is determined from measured  $T_m$  using fresh water values as recommended by ITTC Quality Manual Procedure 4.9-03-01-03 Density and Viscosity of Water.  $T_m$  is measured daily using thermometers. Carriage speed is measured using encoders and PC data acquisition and reduction. Surface area is measured using templates for estimating accuracy of model offsets and rulers and weights for estimating accuracy of installation depending on whether model installed by waterline or displacement.

A used a variable reluctance, in-house manufactured load cell, signal conditioner, and 16-bit AD card. The load cell, signal conditioner, and carriage PC AD card are statically calibrated on a test stand to determine the voltage–mass relationship. Data acquired by collection of 2000 discrete samples over 5 s at 400 Hz. Data filtered through a 10 Hz low-pass filter. B used a Hottinger Baldwin Messtechnik model U1, 50 kg load cell, signal conditioner, and 16-bit AD card. The load cell, signal conditioner, and AD card statically calibrated on a Kempf and Remmers precision test stand to determine the voltage–mass relationship. Data acquired by collection of 300 discrete samples over 10 s at 30 Hz. Amplified analog voltages are converted to frequency ( $3000 \pm 2500$  Hz) for transmission to the AD card to reduce signal sensitivity to noise. Data are filtered through a 10 Hz low-pass filter. C used a Nisshio strain-gage type 20 kg load cell, signal conditioner, and 12-bit AD card. The load cell, signal conditioner, and AD card statically calibrated on an IIHR test stand to determine the voltage–mass relationship. Data are acquired by a collection of 2000 discrete samples over 10 s at 200 Hz. Data are filtered through a 3 Hz low-pass filter.

Uncertainty in  $C_R$  is equivalent to uncertainty in  $C_T^{Tm}$ , since uncertainties in  $k$  and  $C_F$  not considered. Bias limits were estimated for individual resistance, density, carriage speed, and surface area MS, whereas precision limits were estimated end-to-end using Eq. (36). Table 1 summarizes the calibration, data acquisition, and data-reduction bias limits considered for each MS. Precision limits conducted over a time-period during which test conditions varied and in some cases including reinstallation of the model.

## 4 Results

**4.1 N-Order Level.** Figure 4 compares the individual facility (A, B, C) results for the range of Fr. All three facilities conducted uncertainty analysis for Fr=0.1, 0.28, and 0.41. Table 2 provides N-order level residuary resistance values, bias and precision limits, and total uncertainties. Trends for all three facilities are similar. Bias limits predominate for all Fr. Although not included in Table 2, bias limits for resistance and especially carriage speed are large for all speeds, whereas bias limit for the surface area are only significant for large speed. Precision limits increase for increasing Fr. Total uncertainty decreases for increasing Fr.

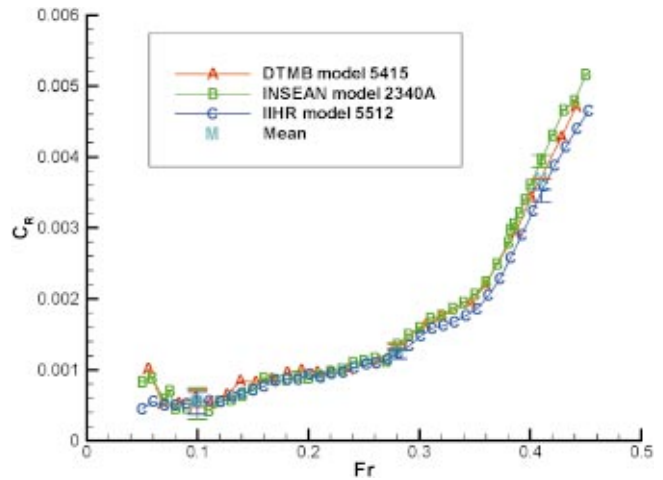


**Fig. 4 Individual facility residuary resistance results and mean facility residuary resistance and individual facility uncertainty bands at Fr=0.1, 0.28, and 0.41.**

**4.2 M×N-Order Level.** In addition, Table 2 provides  $M \times N$ -order level facility uncertainties and mean-facility bias and precision limits and total uncertainties and facility certification or biases. Even for  $M=3$ ,  $U_{X_i} > U_{\bar{X}}$  so  $U_{D_i} \approx U_{X_i}$ . For low speed  $D_i \ll U_{D_i}$  and all three facilities certified, albeit at a large interval (average 17.9%). Reduction interval of certification largely requires reduction individual facility biases for resistance and carriage speed. For medium speed,  $D_i > U_{D_i}$  and all three facilities have facility biases (average 2.3%) and total uncertainties larger than individual facility estimates, especially for C. For high speed,  $D_i > U_{D_i}$  and facility biases and total uncertainties for B and C are large (uncertainty analysis not available for A). Figure 4 and Table 2 suggest scale effects important for C, for medium and high speed, as shown in the next section using subgroup analysis.

**4.3 Subgroup Analysis.** Table 3 is similar to Table 2, but for subgroup analysis in order to isolate scale effects due to smaller model size used at C. In this case mean facility based only on facilities A and B, which used same model size, and subgroup analysis based on facility C. For low speed, scale effects not discernable and facility certification similar as before. For medium and high speed, conclusions different from before, i.e., for medium speed facilities A and B certified at about 2% interval, whereas facility C has nearly 8% interval facility bias. For high speed, facility B has small and facility C large facility biases.

## 5 Summary and Conclusions

A statistical approach is set forth for assessing probabilistic confidence intervals (i.e., intervals of certification or biases of facilities of MS) for facilities or MS for specific tests, data reduction equations, conditions, procedures, and uncertainty analysis based on  $M \times N$ -order level testing and use of mean facility or MS as reference values.  $M \times N$ -order level testing defined as  $M$  repetitions of the same  $N$ -order level experiment in  $M$  different facilities or in the same facility with  $M$  different measurement systems. Similarly, subgroup analysis is performed for isolating and assessing levels of differences due to use of different model sizes (scale effects) or measurement systems.

An example is provided for towing tank facilities for resistance tests using standard uncertainty analysis procedures based on an international collaboration between three facilities: two using larger models and one using smaller model. Although the number of facilities is a minimum, the results demonstrate the usefulness of the approach, including subgroup analysis for isolating differences due to use of different model sizes. For low speed, all three

Table 2 *N*-order level residuary resistance values, bias and precision limits, and total uncertainties; *M*×*N*-order level facility uncertainties and mean-facility bias and precision limits and total uncertainties; and facility certification or biases

Fr & Facility	N-order level (% $X_i$ )				M×N-order level (% $\bar{X}$ )				Facility Certification or biases (% $\bar{X}$ )				
	$X_i$	$B_{X_i}^2$	$P_{X_i}^2$	$U_{X_i}$	$U_{X_i}$	$B_{\bar{X}}^2$	$P_{\bar{X}}^2$	$U_{\bar{X}}$	$D_i$	$U_{D_i}$	$U_{FB_i}$	$U_{T_i}$	
0.10	A	6.00E-04	76.3%	23.7%	10.4%	11.3%			8.6%	14.5%	0	11.3%	
	B	5.23E-04	69.4%	30.6%	21.2%	20.1%	75.7%	24.3%	9.1%	-5.3%	22.0%	0	20.1%
	C	5.34E-04	87.6%	12.4%	14.9%	14.5%				-3.3%	17.1%	0	14.5%
	AVE	5.52E-04	77.8%	22.2%	15.5%	15.3%				0.0%	17.9%	0	15.3%
0.28	A	1.33E-03	45.5%	54.5%	1.1%	1.1%				3.0%	1.6%	2.6%	2.8%
	B	1.32E-03	80.0%	20.0%	2.1%	2.1%	81.6%	18.4%	1.2%	2.2%	2.4%	0	2.1%
	C	1.22E-03	89.2%	10.8%	2.7%	2.6%				-5.3%	2.8%	4.4%	5.1%
	AVE	1.29E-03	71.6%	28.4%	2.0%	1.9%				0.0%	2.3%	2.3%	3.4%
0.41	A	3.69E-03	NA	NA	NA	NA				-0.2%	NA	NA	NA
	B	3.94E-03	66.3%	33.7%	1.1%	1.2%	73.6%	26.4%	0.8%	6.7%	1.4%	6.5%	6.6%
	C	3.45E-03	80.5%	19.5%	1.3%	1.2%				-6.5%	1.4%	6.3%	6.5%
	AVE	3.69E-03	73.4%	26.6%	1.2%	1.2%				0.0%	1.4%	6.4%	6.5%

facilities are certified, but at a large interval (average 17.9%). Reduction interval of certification largely requires reduction individual facility biases for resistance and carriage speed. For medium speed, facilities with larger models certified at about 2%, whereas facility with smaller model shows 7.2% facility bias. For high speed, facilities with larger and smaller models show 2.9% and 9.3% facility biases, respectively. For certified facilities, interval certification provides additional confidence in accuracy

measurements. For noncertified facilities, accounting for facility biases provides improved individual facility uncertainties. Presumably, design sets the requirements on appropriate intervals for certification or biases of facilities. The results are also useful for developing strategies for reduction intervals of individual facility uncertainties and certification or facility biases.

It is reasonable to expect that results from more facilities for same model geometry with uncertainty analysis will in fact pro-

Table 3 Subgroup analysis: *N*-order level residuary resistance values, bias and precision limits, and total uncertainties; *M*×*N*-order level facility uncertainties and mean facility bias and precision limits and total uncertainties; and facility certification or biases

Fr & Facility	N-order level (% $X_i$ )				M×N-order level (% $\bar{X}$ )				Facility Certification or biases (% $\bar{X}$ )				
	$X_i$	$B_{X_i}^2$	$P_{X_i}^2$	$U_{X_i}$	$U_{X_i}$	$B_{\bar{X}}^2$	$P_{\bar{X}}^2$	$U_{\bar{X}}$	$D_i$	$U_{D_i}$	$U_{FB_i}$	$U_{T_i}$	
0.10	A	6.00E-04	76.3%	23.7%	10.4%	11.1%			6.8%	15.9%	0	11.1%	
	B	5.23E-04	69.4%	30.6%	21.2%	19.8%	71.1%	28.9%	11.3%	-6.8%	22.8%	0	19.8%
	C	5.34E-04	87.6%	12.4%	14.9%	14.2%				-4.8%	18.2%	0	14.2%
	AVE	5.61E-04	77.8%	22.2%	15.5%	15.0%				-1.6%	18.9%	0	15.0%
0.28	A	1.33E-03	45.5%	54.5%	1.1%	1.1%				0.4%	1.6%	0	1.1%
	B	1.32E-03	80.0%	20.0%	2.1%	2.1%	72.8%	27.2%	1.2%	-0.4%	2.4%	0	2.1%
	C	1.22E-03	89.2%	10.8%	2.7%	2.5%				-7.7%	2.8%	7.2%	7.6%
	AVE	1.33E-03	71.6%	28.4%	2.0%	1.9%				-2.6%	2.3%	2.4%	3.6%
0.41	A	3.69E-03	NA	NA	NA	NA				-3.3%	NA	NA	NA
	B	3.94E-03	66.3%	33.7%	1.1%	1.1%	66.3%	33.7%	1.1%	3.3%	1.6%	2.9%	3.1%
	C	3.45E-03	80.5%	19.5%	1.3%	1.2%				-9.5%	1.6%	9.3%	9.4%
	AVE	3.81E-03	73.4%	26.6%	1.2%	1.1%				-3.2%	1.6%	6.1%	6.3%

vide confirmation of normal distributions for  $M \times N$ -order level testing and improved estimates for intervals of certification or biases of facilities. This is based on previous work between more facilities using same model geometry but without uncertainty analysis and using uncertainty analysis but with different model geometry. It is also reasonable to expect that situation will be similar for different types of facilities and MS. Both these expectations support recommendation of future collaborations between more facilities. International collaborations are attractive from resource perspective and in achieving ground truth. Knowledge of intervals of certification or biases is important for design, accrediting facilities or measurement systems, and CFD validation.

### Acknowledgments

The Office of Naval Research under 6.1 and 6.2 funding, administered by Dr. Patrick Purtell, sponsored the research at IIHR and DTMB. The research at INSEAN was sponsored by the Italian Ministry of Transportation and Navigation and in part by the Office of Naval Research under NICOP funding.

### Appendix: Estimating Intervals of Certification or Biases of Facilities or MS Using Reference Values

Assume a reference value known for the experimental result designated  $X_R$  with uncertainty  $U_R$  both of which are considered as standard values. Although  $U_R$  is likely much less than  $U_{X_i}$  or  $U_{\bar{X}}$ , it is retained for completeness.

For the mean facility,  $\bar{D}$  is defined as the difference between the mean facility  $\bar{X}$  and reference  $X_R$  values

$$\bar{D} = \bar{X} - X_R \quad (\text{A1})$$

and its uncertainty  $U_{\bar{D}}$  is defined as the RSS of the uncertainties of  $\bar{X}$  and  $X_R$

$$U_{\bar{D}} = \sqrt{U_{\bar{X}}^2 + U_R^2} \quad (\text{A2})$$

If the absolute value of  $\bar{D}$  is less than  $U_{\bar{D}}$

$$|\bar{D}| \leq U_{\bar{D}} \quad (\text{A3})$$

then the mean facility is certified at the interval  $U_{\bar{D}}$ , whereas if the absolute value of  $\bar{D}$  is greater than  $U_{\bar{D}}$

$$|\bar{D}| > U_{\bar{D}} \quad (\text{A4})$$

then the mean facility bias  $U_{\text{FB}}$  is defined as

$$U_{\text{FB}}^2 = \bar{D}^2 - U_{\bar{D}}^2 \quad (\text{A5})$$

with total uncertainty  $U_{\bar{T}}$

$$U_{\bar{T}}^2 = U_{\bar{X}}^2 + U_{\text{FB}}^2 \quad (\text{A6})$$

If  $|\bar{D}|$  is much greater than  $U_{\bar{D}}$

$$|\bar{D}| \gg U_{\bar{D}} \quad (\text{A7})$$

then  $\bar{D}$  approximately equals the mean facility bias error  $\bar{\beta}_{\text{FB}}$

$$\bar{D} \cong \bar{\beta}_{\text{FB}} \quad (\text{A8})$$

such that the biases can be estimated in both sign and magnitude and used for calibration.

For the individual facility,  $D_i$  is defined as the difference between the individual facility  $X_i$  and reference  $X_R$  values

$$D_i = X_i - X_R \quad (\text{A9})$$

and its uncertainty  $U_{D_i}$  is defined as the RSS of the uncertainties of  $X_i$  and  $X_R$

$$U_{D_i} = \sqrt{U_{X_i}^2 + U_R^2} \quad (\text{A10})$$

If the absolute value of  $D_i$  is less than  $U_{D_i}$

$$|D_i| \leq U_{D_i} \quad (\text{A11})$$

then the individual facility is certified at the interval  $U_{D_i}$ , whereas if the absolute value of  $D_i$  is greater than  $U_{D_i}$

$$|D_i| > U_{D_i} \quad (\text{A12})$$

then the individual facility bias  $U_{\text{FB}_i}$  is defined as

$$U_{\text{FB}_i}^2 = D_i^2 - U_{D_i}^2 \quad (\text{A13})$$

with total uncertainty  $U_{T_i}$

$$U_{T_i}^2 = U_{X_i}^2 + U_{\text{FB}_i}^2 \quad (\text{A14})$$

If  $|D_i|$  is much greater than  $U_{D_i}$

$$|D_i| \gg U_{D_i} \quad (\text{A15})$$

then  $D_i$  approximately equals the individual facility bias error  $\beta_{\text{FB}_i}$

$$D_i \cong \beta_{\text{FB}_i} \quad (\text{A16})$$

such that the biases can be estimated in both sign and magnitude and used for calibration.

### References

- [1] Coleman, H. W. and Stern, F., 1997, "Uncertainties in CFD Code Validation," *ASME J. Fluids Eng.*, **119**, pp. 795–803.
- [2] Stern, F., Robert, Wilson, and Shao, J., "Statistical Approach to CFD Code Certification (Invited Paper)," AIAA 2003-410 Applied Aerodynamics Special Session on CFD Uncertainty, 41st Aerospace Sciences Meeting, Reno, Nevada, 6–9 January 2003.
- [3] Kline, S. J. and McClintock, F. A., 1953, "Describing Uncertainties in Single-Sample Experiments," *Mech. Eng. (Am. Soc. Mech. Eng.)*, **75**, pp. 3–8.
- [4] Abernethy, R. B., Benedict, R. P., and Dowdell, R. B., 1985, "ASME Measurement Uncertainty," *J. Fluids Eng.*, **107**, pp. 161–164.
- [5] Coleman, H. and Steele, G., 1999, *Experimentation and Uncertainty Analysis for Engineers*, 2nd ed., Wiley, New York.
- [6] ASME, 1998, "Test Uncertainty: Instruments and Apparatus," PTC 19.1.
- [7] AIAA Standard, (1999), "Assessment Experimental Uncertainty with Application to Wind Tunnel Testing," AIAA S-017A-1999, Washington, D.C.
- [8] Mattingly, G. E., 2001, "Flow Measurement Proficiency Testing for Key Comparisons of Flow Standards among National Measurement Institutes and for Establishing Traceability to National Flow Standards," in Proceedings of the ISA 2001 Conference, Houston, TX:ISA 2001.
- [9] Youden, W. J., 1959, "Graphical Diagnosis of Interlaboratory Test results," *Journal of Industrial Quality Control*, **15**, pp. 24–28.
- [10] Vleghert, J. P. K., 1989, "Measurement Uncertainty Within the Uniform Engine Test Programme," AGARD Dorgaph No. 307.
- [11] Gooden, J. H. M., Gleyzes, C., and Maciel, Y., 1997, "Experimental Study of the Flow Around Two Scaled 3D Swept Wings," 28th AIAA Fluid Dynamics Conference, Snowmass, CO.
- [12] ITTC, 1987, "Report of the Resistance and Flow Committee," 18th International Towing Tank Conference, Kobe, Japan.
- [13] ITTC, 1999, "Report of the Resistance and Flow Committee," 22nd International Towing Tank Conference, Seoul, Korea/Beijing, China.
- [14] Hensch, M., 2002, "Statistical Analysis of CFD Solutions from the Drag Prediction Workshop," AIAA 2002-0842, 40th AIAA Aerospace Sciences Meeting and Exhibit, Reno, NV, 14–17 January.
- [15] Larsson, L., Stern, F., and Bertram, V., editors, in Proceeding Gothenburg 2000, A Workshop on Numerical Ship Hydrodynamics, Chalmers University of Technology, Gothenburg, Sweden, September 2000; *J. Ship Res.*, **47**, March 2003, pp. 63–81.
- [16] Stern, F., Longo, J., Penna, R., Olivieri, A., Ratcliffe, T., and Coleman, H., "International Collaboration on Benchmark CFD Validation Data for Naval Surface Combatant," Invited Paper Proceedings of the 23rd ONR Symposium on Naval Hydrodynamics, Val de Reuil, France, 17–22 September 2000.
- [17] ITTC, 1978, "Report of the Performance Committee," 15th International Towing Tank Conference, Hague, The Netherlands.



## Energy Separation in Steady Separated Wake Flow

**B. W. van Oudheusden**

Department of Aerospace Engineering, Delft University of Technology, The Netherlands PO Box 5058, 2600 GB Delft, The Netherlands  
e-mail: b.w.vanoudheusden@lr.tudelft.nl

### 1 Introduction

The phenomenon that regions of different total enthalpy can develop in an external flow starting from initially homogeneous conditions upstream is known as “energy separation.” Eckert [1,2] discussed its basic mechanisms and introduced the energy separation factor  $S=(H-H_e)/\frac{1}{2}u_e^2$  as descriptive nondimensional parameter. In inviscid flow the only mechanism for energy redistribution is unsteady pressure work and strong energy separation has indeed been observed for a number of unsteady flow phenomena, notably the vortex wake [3–5]. Several studies have provided analytical, experimental, and computational evidence of hot and cold spots formed around the convected vortical structures, at the fast and slow sides, respectively. Diffusive energy redistribution, due to the combined effects of the work by viscous stresses and of thermal conduction, is a second possible mechanism for energy separation. It is, in general, much weaker than the unsteady pressure mechanism discussed above, and best known in the context of thermal recovery in boundary layers.

Energy separation has also been observed experimentally in other free shear flows, like mixing layers and jets [6–8]. With large vortex formation absent in that case, it appears at least partially unclear whether small-scale vortex formation is the governing mechanism, or to what extent the diffusive mechanism is relevant here too. In the computational study by Han et al. [9] of a planar mixing layer it was concluded that also in this case the unsteady pressure effect is dominant over the viscous mechanism. In relation to the above topic, the specific subject of the present note is to report on the occurrence of energy separation in a *steady* separated wake flow and to investigate how in that case the observed particular energy separation signature can indeed be attributed to viscous energy separation alone. In addition, the analysis provides a simple theoretical expression with which the contribution of the viscous energy separation mechanism can be assessed.

### 2 Observation of Energy Separation in Steady Separated Wake Flow

As mentioned above, vortex wakes that are characterized by large-scale flow unsteadiness display a strong energy separation

generated by pressure fluctuations. In contrast to this, the structure of separated wake flow behind a truncated afterbody (“base flow”) at supersonic conditions is quite different and predominantly steady [10]. An illustration of the mean flow field structure, with some details relevant to the geometry considered in the present investigation, is given in Fig. 1. Separation of the boundary layer is fixed at the afterbody corners, where free shear layers are formed that enclose a recirculation region that is terminated by a recompression at shear layer reattachment. Between separation and reattachment, the free shear layers develop in an environment of nearly constant pressure. The energy separation for this kind of flow configuration and under these conditions has not been reported earlier. A particular energy separation feature may be observed in the reversed flow region behind the model base. This is illustrated here with results of the numerical simulation (perfect gas, RANS) of the steady flow around an axisymmetric afterbody in a Mach 3 supersonic free stream, as sketched in Fig. 1. Whereas previous attention was directed only to the velocity and pressure fields [11], further investigation of the temperature data of the simulation (previously unpublished) reveals a pronounced reduction of total temperature in the separated flow region behind the base. Areas of minimum energy are found coinciding with the steady recirculating flow structures in the near wake. This is further quantified in Fig. 2 which displays the distribution of velocity and temperature, taken directly from the numerical flow simulation, as well as the inferred separation factor, plotted along a radial line across the wake at 0.7 base diameters behind the body (approximately halfway between the base and the wake reattachment point).

A very prominent feature of the total temperature profile (hence, the separation factor) is the distinct minimum it attains in the recirculation region. A qualitatively similar profile of the separation factor was observed experimentally in the separated wake behind a thick flat plate by O’Callaghan and Kurosaka at a Mach number of 0.9 [6]. In absolute sense, the energy separation variations in the experiment of O’Callaghan and Kurosaka are however, more pronounced. A maximum overshoot of +0.06 was observed in the outer part of the wake, a minimum of –0.32 inside the wake near the location of mean-flow reversal and an approximate value of –0.11 near the wake center line. In the present simulation the corresponding values are +0.02, –0.17, and –0.13, respectively. In the same paper O’Callaghan and Kurosaka reported on experiments with a screen obstruction in the flow, which generated a mixing layer flow, with low velocity behind the obstruction. For that case the energy separation inside the shear layer was reported to display a maximum  $S=0.06$  and a minimum of –0.16 near the near the high-velocity edge and low-velocity boundaries, respectively, while approximately vanishing ( $S=0$ ) outside the shear layer. Based on the similarity with the energy separation distribution in unsteady vortex wakes, they explained the energy separation in both their wake experiments entirely from the effect of unsteady vortex formation in the unstable shear layer. However, the scale of the energy separation is of a similar order as in the present numerical simulation, whereas the latter contains no unsteady effects: The total variation in the separation factor is

Contributed by the Fluids Engineering Division for publication in the JOURNAL OF FLUIDS ENGINEERING. Manuscript received May 11, 2004; Final manuscript received February 22, 2005. Associate Editor: H. Johari.

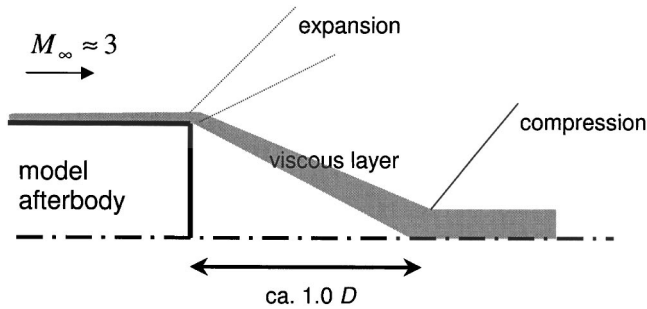


**Fig. 1 Schematic flow field structure of a supersonic base flow**

0.38 in the plate wake experiment and 0.19 in the simulation. If one assumes that the result of the present simulation data is representative of the magnitude of the viscous energy separation effect, overlooking the possible influence of the difference in Mach number regime (transonic vs supersonic), it would seem to account for about half of the total energy separation observed in the transonic wake experiment. In the next section the prominent features of energy separation in *steady* viscous flow are further analyzed, for different free shear layer configurations, in order to investigate how they can account for the particular energy separation signature encountered in the supersonic wake flow simulation, as well as allowing to assess the viscous contribution to the total energy separation in a separated shear flow under more general conditions.

### 3 Analysis of Viscous Energy Separation in Steady Flow

First, as a reference the typical energy separation profile has been computed for three elementary constant-pressure shear layers, viz. the flat-plate boundary layer, the mixing layer between a stream and stagnant environment (jet boundary) and the far wake. For incompressible laminar flow each of these cases displays self-similar solutions for the velocity and temperature distributions with respect to a scaled transverse coordinate  $\eta$  (see [12,13] for details). Computation results obtained from solving the self-similarity flow equations for  $Pr=0.7$  are presented in Fig. 3, showing profiles of the velocity, static temperature, and energy separation factor for the three flows, appropriately normalized. The velocity has been normalized on a scale from 0 to 1, spanning the maximum velocity difference across the shear layer  $\Delta u = u_{\max} - u_{\min}$ , where  $u_{\max}$  is equal to  $u_e$ , while  $u_{\min}$  is zero for the bound-

ary layer and the mixing layer, and equal to the center-line velocity for the wake. Equally, the temperature (enthalpy) and separation factor have been scaled with the maximum kinetic energy difference, being  $\frac{1}{2}u_e^2$  for boundary layer and mixing layer, and  $u_e \Delta u$  for the far wake. A common characteristic of all flow types is that positive energy separation occurs on the high-velocity side of the shear layer, and negative energy separation on the low-velocity side. This produces a pattern that is qualitatively similar to the time-mean action of unsteady vortex formation. Comparing these results to the base flow simulation data of Fig. 2, we observe a combination of features of the mixing layer and the wake. The distribution clearly differs from that of the single mixing layer, in the sense that the “slower stream” does not provide an adiabatic boundary condition, as it is not an independently fed stream, but a result of the recirculating wake flow itself.

A further clarification of energy-separation features under more general conditions can be obtained from the enthalpy-velocity relation that was derived in an earlier study [14], which allows the energy separation to be related analytically to the velocity field, as:

$$H - H_e = (r - 1) \frac{1}{2} (u_e^2 - u^2) + (1 - r) \frac{\psi}{\rho} \frac{\partial u}{\partial y} \quad (1)$$

where  $\psi$  is the stream function and  $r$  the recovery factor. The first and second term represent “incomplete energy recovery” and “diffusive energy redistribution,” respectively. This relation was originally derived for two-dimensional laminar constant-property (incompressible) boundary layer flow, in which case  $r = \sqrt{Pr}$ . The effect of compressibility was found to be relatively small, especially in the absence of pressure gradient [15]. It is easily verified that the above expression also applies to a laminar wake flow, provided that the conditions at both sides of the wake are equal. In addition, the above analysis can be extended to turbulent wake flows, by neglecting viscous terms and assuming a constant turbulent viscosity across the wake [13]. In that case we find that again Eq. (1) applies where in analogy  $r = \sqrt{Pr_T}$ , with  $Pr_T$  the turbulent Prandtl number. Note that the well-known recovery relation for turbulent boundary layer flow,  $r = \sqrt[3]{Pr}$ , does not apply here.

For the application to the base flow data, Eq. (1) is slightly adapted, in the sense that  $u^2$  is replaced by  $u^2 + v^2$  in the recovery term, while the integration for  $\psi$  is started from the center line, using the density data from the simulations (not shown). Good agreement with the numerical data is obtained, when a recovery factor of  $r = 0.86$  is chosen. At this point there is no independent justification for this specific value, but in view of the theoretical analysis, this would correspond to an average turbulent Prandtl number of about 0.75. The continuous line in Fig. 2 represents the

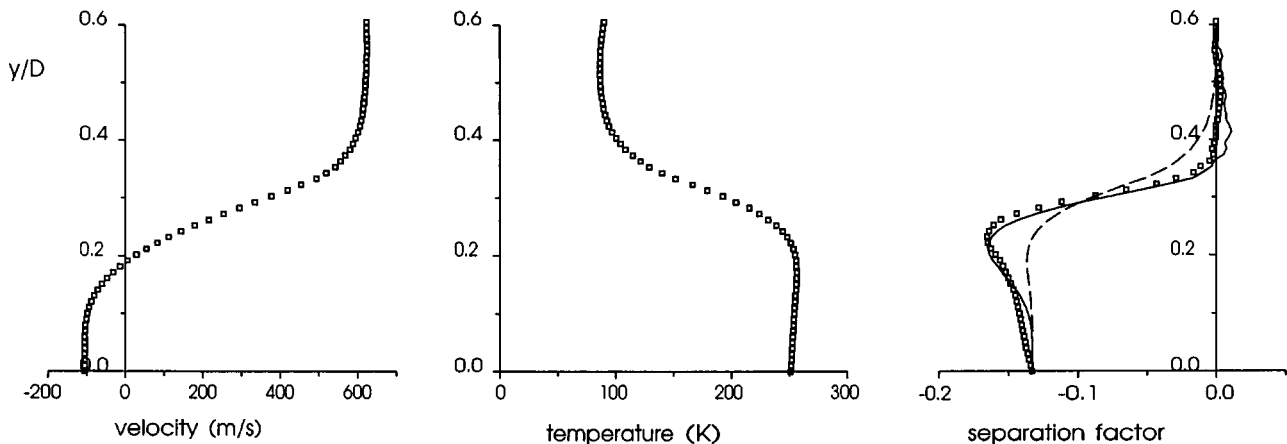


**Fig. 2 Energy separation in compressible base flow (symbols: Numerical data, solid line: Present theory, dashed line: Classic theory)**

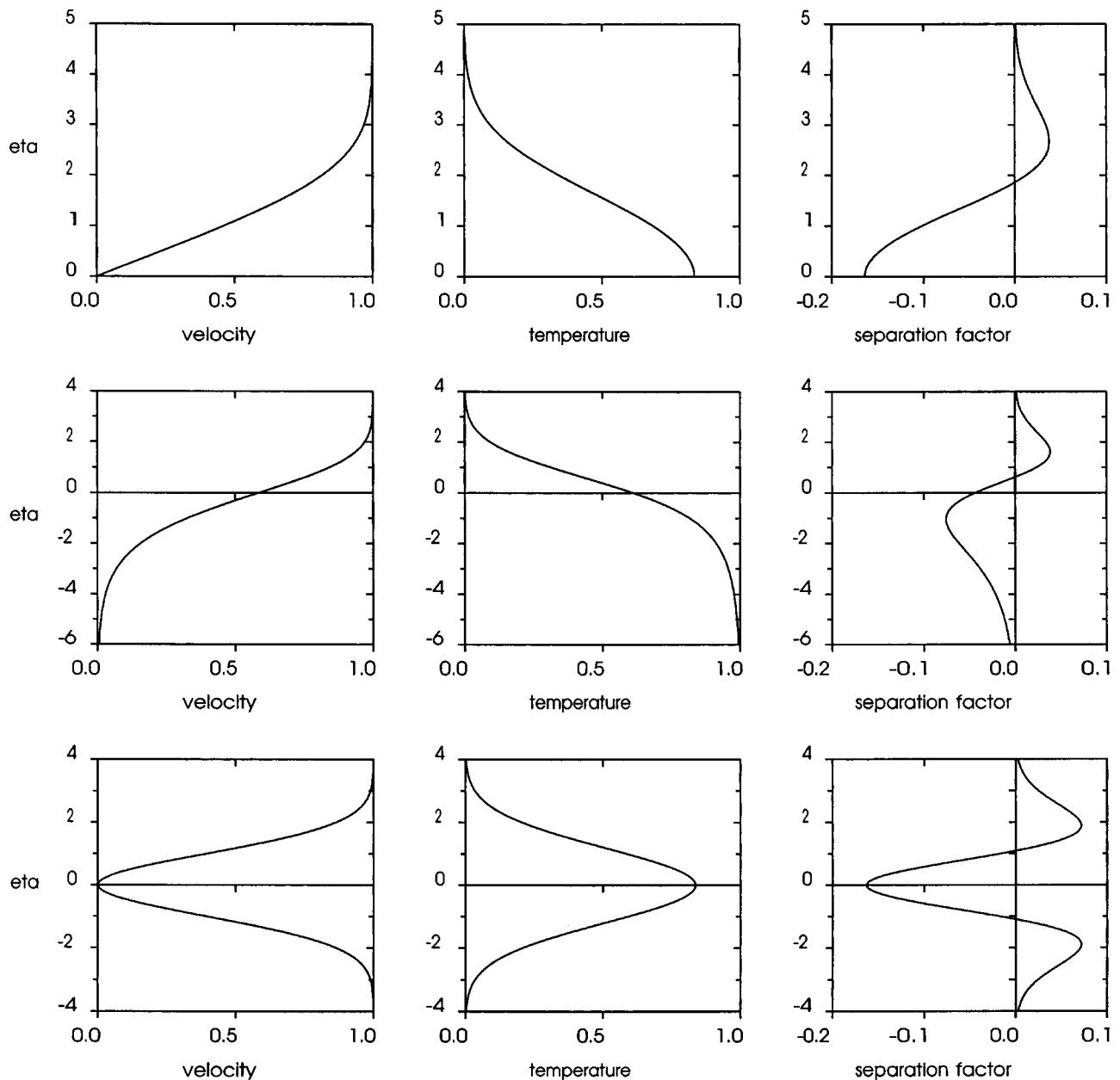


Fig. 3 Energy separation in steady viscous zero-pressure-gradient flow ( $Pr=0.7$ ); boundary layer (top), mixing layer (center) and far wake (bottom)

prediction of the separation factor according to Eq. (1), whereas the broken line is the result of using the classic Crocco–Busemann relation, i.e., omitting the second term from Eq. (1). Most of the prominent features of the energy separation distribution are indeed reproduced. Comparing the two theoretical curves reveals that the local extrema in the energy separation profile are generated by the redistribution term in Eq. (1). In particular the minimum is well predicted, which is related to the effect of flow reversal. Both the “recovery term” and the “additional transport term” reach a minimum near that position. The overshoot in total enthalpy is relatively small, with the mass flux near the outer flow being much higher than in the base flow region. The numerical total temperature data do not properly reproduce this overshoot. A possible explanation is that the enthalpy excess has been redistributed over a larger flow region, due to real or numerical diffusion in the computational domain along the model upstream of the base.

#### 4 Discussion and Conclusions

The occurrence of energy separation was reported for the steady separated wake of an object in a supersonic flow simulation. A particular feature was observed, *viz.* regions with a significant decrease in total energy, that correspond with the locations of steady vortical structures in the recirculation region. As the flow is steady in the simulation only the viscous mechanism can be responsible for this. This motivated a further investigation of viscous energy separation in the context of steady flow. It was shown that indeed the particular pattern can be explained from this mechanism and that the energy separation is enhanced by means of the feedback effect of the flow recirculation in the wake region. An analytical expression was presented that describes the strength of viscous energy separation in relation to the velocity field.

With regard to the plate and screen wake experiments of

O'Callaghan and Kurosaka it can be concluded that a significant part of the energy separation observed in the experiment can be attributed to viscous energy separation. Comparing the screen wake experiment to the theoretical analysis of the mixing layer (Fig. 3), the viscous effect is seen to account for about half of the reported energy separation. For the plate wake the comparison is less straightforward. The theoretical relation of Eq. (1) would allow to assess the viscous contribution more quantitatively, but unfortunately no velocity data are available for evaluating this. Nevertheless, assuming that the simulation results are indicative of the viscous energy separation, the viscous effect is estimated to account again for roughly half the observed energy separation effect.

In conclusion, the viscous effect is found to contribute significantly to the energy separation in free shear layer flow of wakes and mixing layers for the cases considered. The unsteady pressure effect is certainly not to be dismissed, however, and this is most likely responsible for the strongest excursions of the separation factor in the wakes. Finally, it may be remarked that the Mach number regime has probably quite some influence on the presence and strength of the unsteady pressure effect, as transonic wake flow has been observed to be inherently more unsteady than supersonic flow [16].

### Acknowledgment

Mr. H. B. A. Ottens (current address: AOES Advanced Operations and Engineering Services, Leiden, The Netherlands) kindly provided the numerical data of the supersonic base flow simulation.

### References

- [1] Eckert, E. R. G., 1986, "Energy Separation in Fluid Streams," *Int. Commun.*

- Heat Mass Transfer*, **13**, pp. 127–143.
- [2] Eckert, E. R. G., 1987, "Cross Transport of Energy in Fluid Streams," *Wärme- und Stoffübertragung*, **21**, pp. 73–81.
- [3] Kurosaka, M., Gertz, J. B., Graham, J. E., Goodman, J. R., Sundarun, P., Riner, W. C., Kuroda, H., and Hankey, W. L., 1987, "Energy Separation in a Vortex Street," *J. Fluid Mech.*, **178**, pp. 1–29.
- [4] Goldstein, R. J., and He, B., 2001, "Energy Separation and Acoustic Interaction in Flow Across a Circular Cylinder," *J. Heat Transfer*, **123**, pp. 682–687.
- [5] Carscallen, W. E., Currie, T. C., Hogg, S. I., and Gostelow, J. P., 1999, "Measurement and Computation of Energy Separation in the Vortical Wake of a Turbine Nozzle Cascade," *J. Turbomach.*, **121**, pp. 703–708.
- [6] O'Callaghan, J. J., and Kurosaka, M., 1993, "Vortex-Induced Energy Separation in Shear Flows," *AIAA J.*, **31**(6), pp. 1157–1159.
- [7] Seol, W. S., and Goldstein, R. J., 1997, "Energy Separation in a Jet Flow," *J. Fluids Eng.*, **119**, pp. 74–82.
- [8] Han, B., and Goldstein, R. J., 2003, "Instantaneous Energy Separation in a Free Jet. Part II. Total Temperature Measurement," *Int. J. Heat Mass Transfer*, **46**, pp. 3983–3990.
- [9] Han, B., Goldstein, R. J., and Choi, H. G., 2002, "Energy Separation in Shear Layers," *Int. J. Heat Mass Transfer*, **45**, pp. 47–55.
- [10] Delery, J., and Lacau, R. G., 1987, "Prediction of Base Flows," in: *Special Course on Missile Aerodynamics*, AGARD Report 754, Chapter 11.
- [11] Ottens, H. B. A., Bannink, W. J., and Gerritsma, M. I., 2001, "Computational Study of Support Influence on Base Flow of a Model in Supersonic Flow," 15th AIAA Computational Fluid Dynamics Conference, Anaheim, 11–14 July 2001, AIAA Paper 2001–2638.
- [12] White, F. M., 1991, *Viscous Fluid Flow*, 2nd ed., McGraw-Hill, New York.
- [13] Schlichting, H., and Gersten, K., 2000, *Boundary Layer Theory*, 8th ed., Springer, New York.
- [14] Van Oudheusden, B. W., 1997, "A Complete Crocco Integral for Two-Dimensional Laminar Boundary Layer Flow over an Adiabatic Wall for Prandtl Numbers near Unity," *J. Fluid Mech.*, **353**, pp. 313–330.
- [15] Van Oudheusden, B. W., 2004, "Compressibility Effects on the Extended Crocco Relation and the Thermal Recovery Factor in Laminar Boundary Layer Flow," *J. Fluids Eng.*, **126**, pp. 32–41.
- [16] Scarano, F., and Van Oudheusden, B. W., 2003, "Quantitative Planar Velocimetry of a Turbulent Separated Wake Flow at Transonic and Supersonic Flow Regimes," 7th Int. Symp. on Fluid Control, Measurement and Visualization (FLUCOME'03), 25–28 Aug. 2003, Sorrento, Italy, Paper 118.

# Comparison of Exact and Sommerfeld Solution for the Pressure of a Journal Bearing

Yan Qu

e-mail: bill\_qu@mail.utexas.edu

Dohyung Kim

e-mail: dohkim@mail.utexas.edu

Ronald L. Panton<sup>1</sup>

e-mail: rpanton@mail.utexas.edu  
Mechanical Engineering Dept.,  
The University of Texas at Austin,  
Austin, TX 78712-0292

## Introduction

In this paper, we consider the flow in a journal bearing. The Sommerfeld approximate solution is well-known and is discussed in all lubrication texts [1–3]. Perhaps less well-known is that an exact solution exists in the applied mechanics literature. It is of interest to compare the two solutions and establish quantitatively the parameter region where the Sommerfeld solution is a good approximation of the exact results. Since micro-bearings have lower radius ratios than typical bearings, the Sommerfeld solution is sometimes not appropriate [4].

The geometry of a journal bearing is shown in Fig. 1. The displacement of the shaft center relative to the housing center is known as “eccentricity,” ( $e$ ), while the difference in radius ( $R_1 - R_2$ ) is known as “clearance,” ( $c$ ). The minimum film thickness around the bearing circumference is  $(c - e)$ , and the maximum film thickness is  $(c + e)$ . When  $R_2$  approaches  $R_1$ , the Sommerfeld method can be used and the film thickness is

$$h = (R_1 - R_2) + e \cos \theta = c + e \cos \theta = c(1 + \varepsilon \cos \theta)$$

where the eccentricity ratio  $\varepsilon$  is defined as  $e/c$ . When the shaft and bearing are concentric,  $\varepsilon = 1$ , and the bearing does not have any load-carrying capacity. When they touch,  $\varepsilon = 0$ , and the bearing has tremendous load support capacity.

In the exact solution [5] the geometry is described by introducing a bipolar coordinate system  $\xi, \eta$ , defined by

$$x = -b \frac{\sinh \xi}{\cosh \xi - \cos \eta}, \quad y = b \frac{\sin \eta}{\cosh \xi - \cos \eta},$$

where

$$b = \frac{1}{2e} [(R_1^2 + R_2^2 - e^2)^2 - 4R_1^2 R_2^2]^{1/2}.$$

This method is more generic and can be used for one or both cylinder rotations without any radius ratio restriction.

## Analytical Results

**Sommerfeld Solution.** The dimensionless form of the Sommerfeld solution for pressure distribution is

$$P^* = \frac{6\varepsilon \sin \theta (2 + \varepsilon \cos \theta)}{(2 + \varepsilon^2)(1 + \varepsilon \cos \theta)^2}$$

We know that positive pressures exist in the convergent film ( $0 \leq \theta \leq \pi$ ) and negative pressures in the divergent film ( $\pi \leq \theta \leq 2\pi$ ). The negative pressures are not realistic and are modified by using a half-Sommerfeld condition where the film diverges ( $\theta = \pi$ ) and the pressure is uniformly zero. For this reason we limit the analysis to the convergent film.

**Exact Solution.** The exact solution given in [4] is the Stokes solution for the stream function  $\nabla^4 \psi^{(0)} = 0$ . We obtain a relation for the pressure from these equations. The relation is

$$p^{(0)} = p_0 + \frac{2\mu}{b} [P_1(\xi) \sin \eta + P_2(\xi) \sin 2\eta],$$

where

$$P_1(\xi) = (D_0 - 2A_1) \sinh \xi - 2B_1 \cosh \xi,$$

and

$$P_2(\xi) = A_1 \sinh 2\xi + B_1 \cosh 2\xi.$$

$D_0, A_1, B_1$  are all constants and can be found in [5].

The nondimensional pressure is

$$p^* = \frac{p^{(0)} - p_0}{\mu \Omega_2} \left( \frac{c}{R_2} \right)^2 = \frac{2}{b \Omega_2} \left( \frac{c}{R_2} \right)^2 [P_1(\xi) \sin \eta + P_2(\xi) \sin 2\eta].$$

In order to compare the exact solution with the Sommerfeld solution, we transfer the center of the inner cylinder to the origin as follows:  $\theta = \tan^{-1}(y/(x - l + e))$ . Thus

$$p^*(\xi, \eta) = p^*(\xi, \theta).$$

The Sommerfeld solution is an approximate solution when radius ratio ( $R_2/R_1$ ) is close to unity. Figure 2 shows an extreme case when radius ratio is 0.3. Here, the Sommerfeld approximation gives a significant error for the maximum pressure. It also gives considerable error for the attitude angle at the maximum pressure. In order to investigate the error when using the Sommerfeld approximation to calculate maximum pressure, we have to examine the exact solution and determine which cylinder, the inner or the outer, has the greater pressure. The Sommerfeld approximation treats the radius ratio as unit, so the pressure on the outer cylinder is equal to the pressure on the inner cylinder, but as the radius ratio decreases, the pressure difference between the outer and inner cylinders becomes significant. Define  $\delta P_{12}$  as  $(P_{2 \max} - P_{1 \max})/P_{1 \max}$ .

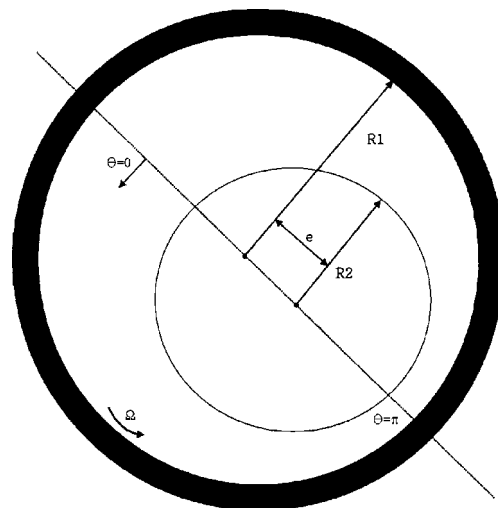


Fig. 1 Geometry of a journal bearing

Contributed by the Fluids Engineering Division for publication in the JOURNAL OF FLUIDS ENGINEERING. Manuscript received by the Fluids Engineering Division June 4, 2004; final revision received October 24, 2004. Associate Editor: S. Balachandar.

<sup>1</sup>Corresponding author.

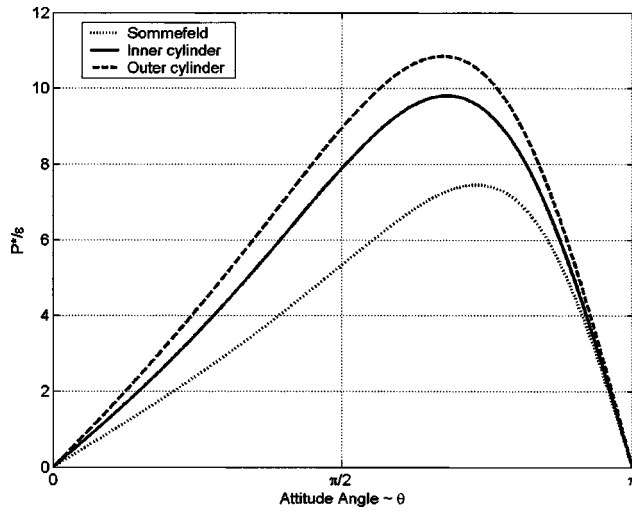


Fig. 2  $p^*/\epsilon$  vs attitude angle for radius ratio 0.3 and eccentricity ratio 0.5

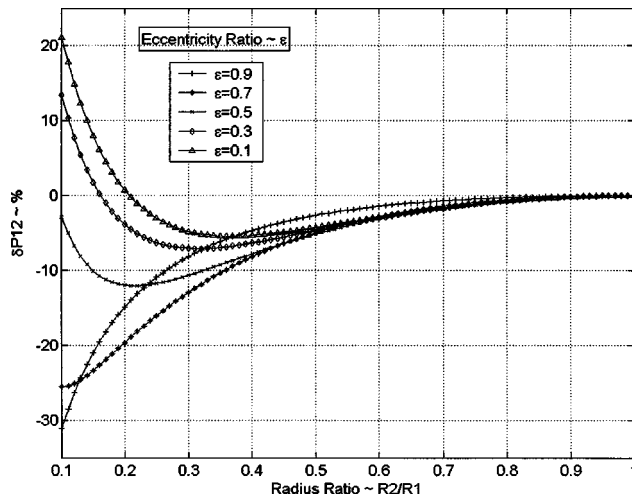


Fig. 3 Difference of maximum pressure between outer and inner cylinders

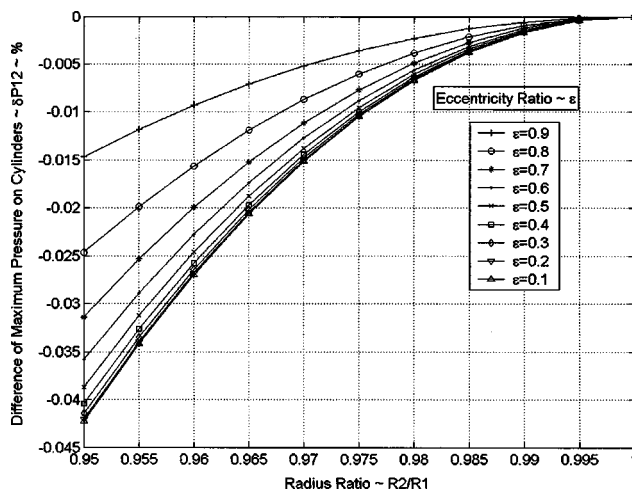


Fig. 4 Difference of maximum pressure between outer and inner cylinders for a high radius ratio

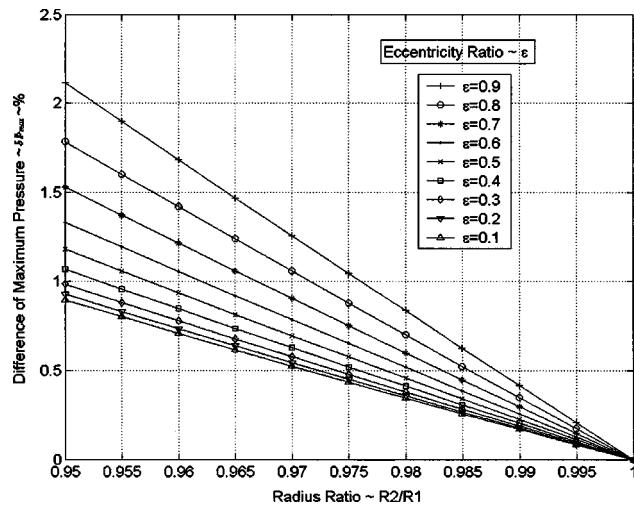


Fig. 5 Difference of maximum pressure for the two methods

$$-P_{1 \max} / P_{2 \max}$$

Figures 3 and 4 show that when the radius ratio is small,  $\delta P_{12}$  can be large, and the sign depends on eccentricity ratio  $\epsilon$ . However, when the radius ratio is greater than 0.95, which is the design range for most journal bearings,  $\delta P_{12}$  is always negative, indicating that the maximum pressure on the outer cylinder is always greater than the maximum pressure on inner cylinder. Then,  $\delta P_{\max}$  is defined as  $(P_{1 \max} - P_{\text{som}}) / P_{1 \max}$  to further benchmark the accuracy of the Sommerfeld approximation.

In Fig. 5, the Sommerfeld solution always gives smaller results than the exact solution and, as we can expect, when the radius ratio approaches unity, the error decreases to zero. Also, as the eccentricity ratio increases, the difference increases. For most journal bearing cases in which the radius ratio is greater than 0.98, the error within 1%. As we further investigate the attitude angle at maximum pressure,  $\Delta$  is defined as  $(\theta_{\max} - \theta_{\text{som}}) / \theta_{\max}$ . Figure 6 shows that the Sommerfeld solution always provides a greater attitude angle at maximum pressure, and as the radius ratio increases, the error rate increases as well. However, the difference remains within 0.20 deg when the radius ratio is larger than 0.95 for any eccentricity ratio.

### Conclusion

Both radius ratio and eccentricity ratio determine whether the pressure on the outer cylinder is greater than that on the inner cylinder. However, when the radius ratio is greater than 0.95, as in most journal bearings, the maximum pressure on the outer cylinder is always greater than the maximum pressure on inner cylinder.

The Sommerfeld solution always gives smaller pressures than the exact solution. The margin of error increases when the radius ratio decreases or when the eccentricity ratio increases. For most journal bearing cases where the radius ratio is greater than 0.95, the error rate remains within 0.5%. Also, the Sommerfeld solution always gives a greater attitude angle at the maximum pressure. This error increases as the radius ratio increases. Of course, micro-bearings with unusual radius ratios must be considered on a case-by-case basis.

### Nomenclature

- $c$  = radial clearance
- $e$  = eccentricity

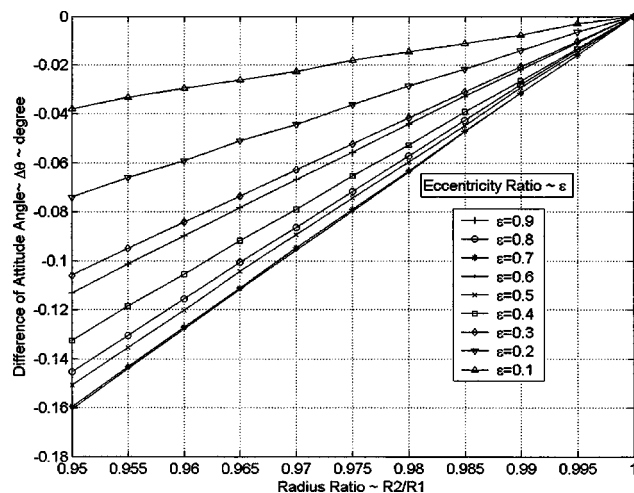


Fig. 6 Difference of angle at maximum pressure for the two methods

$h$  = film thickness  
 $P^*$  = dimensionless pressure  
 $\delta P_{\max}$  = difference of maximum pressure between exact solution and Sommerfeld solution  
 $P_{1 \max}$  = maximum pressure on outer cylinder  
 $P_{2 \max}$  = maximum pressure on inner cylinder  
 $P_{\text{som}}$  = Sommerfeld maximum pressure  
 $R_1$  = outer cylinder radius  
 $R_2$  = inner cylinder radius  
 $\delta P_{12}$  = maximum pressure difference  
 $\Delta$  = difference of the attitude angle at maximum pressure between exact solution and Sommerfeld solution  
 $\varepsilon$  = eccentricity ratio  
 $\theta$  = attitude angle  
 $\mu$  = dynamic viscosity

$\Omega$  = angular velocity

### Subscripts

1 = outer cylinder  
 2 = inner cylinder

### References

- [1] Cameron, A., 1981, *Basic Lubrication Theory, 3rd edition*, Ellis Horwood Ltd., England, Chap. 7.
- [2] Szeri, A. Z., 1980, *Tribology; Friction, Lubrication, and Wear*, Hemisphere Publishing Comp. McGraw-Hill, New York, Chap. 1.
- [3] Hamrock, B. J., 1994, *Fundamentals of Fluid Film Lubrication*, McGraw-Hill, New York, Chap. 10.
- [4] Gad-El-Hak, M., 2003, *The MEMS Handbook*, CRC Press, Boca Raton, FL.
- [5] Ballal, B. Y., and Rivlin, R. S., 1976, "Flow of a Newtonian Fluid Between Eccentric Rotating Cylinders: Inertial Effects," *Arch. Ration. Mech. Anal.*, **62**(3), pp. 237–294.



# Numerical Investigation of Baffle-Plate Effect on Hood-Capture Flow

Ming-Jyh Chern

Phone: +886-2-27376496

Fax: +886-2-27376460

e-mail: mjchern@mail.ntust.edu.tw

Jang-Xing Lee

Department of Mechanical Engineering, National Taiwan University of Science and Technology, Taipei 106, Taiwan

## 1 Introduction

To protect laborers in a working environment containing toxic vapor, particles and contaminants, an efficient ventilation facility is essential. A well-designed industrial ventilation facility should capture most of the pollutants. An exterior hood is one of the basic tools for local industrial ventilation. The aspiration of an exterior hood is able to extract pollutants into a certain space. A bell-like volume below an exterior hood is usually used to characterize its capture zone. Pollutants within this bell-like zone can be collected and released into the atmosphere. However, a cross draft may exist in the working site where an exterior hood operates due to, for example, flow induced by an air conditioner. Even a very slow cross draft at several centimeters per second could have a negative influence on the capture zone. As a result, a cross draft does not only change the shape of the capture zone, but also its capture efficiency. The bell-like capture volume becomes a Rankine body-of-revolution and the volume is contracted because of a cross draft. Avoidance of the detrimental influence of a cross draft on the capture zone becomes an important topic for the design and operation of an exterior hood. This study is to propose a passive control method which uses a flange and a baffle plate to overcome the negative effect and to enhance the capture efficiency. Numerical results are shown to investigate the effect of the proposed approaches and compared with available experimental data provided by Huang et al. [1–3]. Acceptable agreements are found between numerical and experimental results.

Local industrial ventilation has been used for a long time. The design principles for an exterior hood date back to Dalla Valle [4] and Silverman [5]. They provided the empirical formula to determine the axial velocity of an exterior hood according to the area of the hood opening and the suction speed. Subsequent researchers developed and modified the axial velocity formula for exterior hoods with various shapes (e.g., Garrison [6]). In 1990, the Environmental Protection Agency (EPA) of the USA provided the principle of the capture efficiency for the design of an exterior hood.

In academic research, Vincent [7] described the aspiration of an aerosol sampler in an air stream. The flow pattern in the flow field was very similar to the present study. The concepts of a stagnation point, a dividing streamline or streamsurface were provided. Ingham and Hildyard [8] utilized potential flow theory to study the flow pattern around an aerosol sampler in a free stream. They provided the solution to determine the location of the stagnation point. Sreenath et al. [9] conducted experiments to study the aspiration of an aerosol sampler in a wind tunnel. The stagnation point was located by flow visualization using the smoke-wire method. Kulmala [10] adopted a numerical model to study the

capture efficiency of an exterior hood operating in a cross draft. He mentioned that the main factors in the efficiency of the capture zone were the size of the exterior hood, its geometry and suction speed. Conroy et al. [11] studied the influence of a cross draft on an exterior hood using an analytical approach, numerical simulations, and experimental methods. He mentioned the concept of a dividing streamline which is highly relevant to the capture efficiency. Chen et al. [12] utilized the dividing streamline to define the capture zone for an exterior hood in a cross draft. The capture zone can be used as the indicator of the capture capability of an exterior hood. In terms of Chen et al.'s results, the capture zone looks like a Rankine body-of-revolution when the speed ratio of the suction to the cross draft is larger than 2. Huang et al. [1,2] studied the capture zones of hoods with circular and rectangular cross sections in a cross draft. Their experiments were performed in a wind tunnel. Flow fields were visualized using smoke and measured using a laser Doppler velocimetry (LDV). They found that the geometric shape of the capture zone was mainly affected by the ratio of the suction speed to the cross draft velocity and the aspect ratio of the rectangular cross section. They used the given semiempirical formula based on the potential flow theory and experimental data to determine the dividing streamline. Furthermore, they also found that a circular hood has the same capture zone and characteristic lengths as a rectangular hood when they have the same area. As a result, the formula for the rectangular hood can also be applied to a circular hood.

We employed a flange and a baffle plate to reduce the negative effect and proposed a 3D numerical model. Variations in flow structure obtained by the established numerical model are shown in detail and explained in this paper. The flow problems under consideration are shown in Fig. 1. The height and the width  $D$  of the exterior hood under consideration were 5 cm and 10 cm, respectively. The width  $W_f$  of the flange varied from  $1.2D$  to  $3D$ . The width  $b$  of the baffle plate was the same as  $D$ . The height of the vertical plate varied from  $1.5D$  to  $4.0D$ . Due to the baffle plate, the capture region was enlarged. The effect of the baffle plate is the main issue we are concerned with in this paper.

## 2 Mathematical Formulae and Numerical Model

We considered an incompressible fluid. The continuity and Navier–Stokes equations were adopted as the governing equations. Air was the working fluid in this problem, so the density and the dynamic viscosity of air were  $1.204 \text{ kg m}^{-3}$  and  $1.51 \times 10^{-5} \text{ m}^2 \text{ s}^{-1}$  ( $20^\circ\text{C}$ , 1 atm), respectively.  $U_c$  was the velocity component of a cross draft in the horizontal direction and was used as the initial condition. For the wall boundary and the solid boundaries of the hood, the flange and the baffle plate, we imposed a nonslip boundary condition at those boundaries. The established governing equations were solved numerically. We utilized the finite volume method to discretize the governing equations. The advective terms in Navier–Stokes equations were discretized using the QUICK scheme (Leonard [13]). The fourth order Adams–Bashforth scheme (Canuto et al. [14]) was employed for the temporal derivative. In addition, the SOLA scheme (Hirt et al. [15]) was used to predict and correct the pressure and velocity solutions.

The  $79 \times 43 \times 34$  mesh was employed in the following simulations. The minimum  $\Delta x/D$ ,  $\Delta y/D$ , and  $\Delta z/D$  were 0.1, 0.083, and 0.1, respectively in the adopted mesh. The 3D numerical simulations were performed by a PC cluster which consists of 17 nodes (AMD XP-2400). In the following numerical simulations, the total considered nondimensional physical time was about 150. The nondimensional time increment,  $\Delta t \cdot U_c/D$ , was  $4 \times 10^{-4}$  to  $1.6 \times 10^{-3}$ . At each time step, the maximum mass residual for all the cells was to be less than  $10^{-6}$  to satisfy the continuity equation. The whole nondimensional maximum velocity variation throughout the whole flow field between two time steps at the end of simulation were less than  $10^{-4}$ . This state was considered the steady state solution for all the simulations.

Contributed by the Fluids Engineering Division for publication in the JOURNAL OF FLUIDS ENGINEERING. Manuscript received by the Fluids Engineering Division August 4, 2004; Final manuscript received March 5, 2005. Associate Editor: Fernando Grinstein.

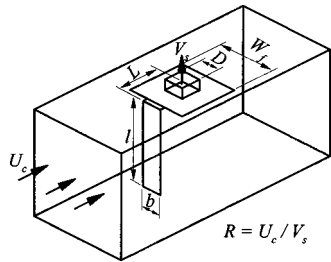


Fig. 1 Schematic diagram of the proposed hood with a flange and a baffle plate

### 3 Results and Discussion

To achieve the passive control of the capture flow, a flange and a vertical baffle plate were used. Various effects were considered in the capture flows. The capture envelope can be determined by a dividing stream surface (see Vincent [7]). At first, the effect of the flange installed at the hood opening was investigated. The geometric size of the flange affected the capture flow. The baffle plate was utilized to enlarge the capture zone. The plate caused a change in the capture flow. The affected capture flow was explored in the final subsection.

**3.1 Effect of Flange.** One of the methods to avoid the negative effect of a cross draft is to install a flange at the hood opening. The main idea is to avoid the influence of the wake behind the hood. A flange may achieve this purpose, because it separates the capture region and the wake behind the hood. Subsequently, another question is the determination of the flange size. Those points become the main topics in this subsection.

Various flanges of  $W_f/D=1.2-3.0$  were considered in this study.  $\zeta$ ,  $\eta$ , and  $\xi$  refer to the characteristic lengths of the capture zone.  $\zeta$  is the horizontal distance from the stagnation point of the dividing streamline to the center of the hood opening.  $\eta$  is the vertical distance from the center of the hood opening to the dividing streamline.  $\xi$  is the vertical distance from the horizontal level of the hood opening to the inlet location of the dividing streamline. They are relevant to the size of the capture volume. Figure 2 shows the variation of the characteristic lengths with respect to  $W_f/D$  and  $R$ .  $\eta$  and  $\xi$  did not change with  $W_f/D$  in Fig. 2.  $\zeta$ , relevant to the stagnation point, was affected by  $R$  and  $W_f/D$ . Let us investigate the variation of  $\zeta/D$  first for the case of  $W_f/D=3$ . It varied from 1.25 to 0.7 as  $R$  increased. The changed capture zone was larger than in the case without a flange ( $\eta/D=0.5$ ). Furthermore, a variety of flanges were considered to investigate their improvement on  $\zeta$ . It was found that all the considered flanges up to  $W_f/D=2.5$  improve  $\zeta$ . The improvement reduced as  $R$  increases. Meanwhile, large flanges caused better improvement. However, when  $W_f/D$  exceeded 2.5, the variation of  $\zeta$  with respect to  $R$  was the same. Hence, a flange of  $W_f/D$  larger than 2.5 is not necessary.

We also compared the results of characteristic lengths given by the established numerical model with the experimental results (Huang et al. [2]). Figure 3 demonstrates the comparison between those approaches. Numerical results of various  $W_f/D$  and  $R$  are close to the experimental ones. There are differences between them at  $R=0.113$ . However, the tendencies are the same. They both reveal that only  $\zeta$  is affected by a flange.  $\eta$  and  $\xi$  hardly change when a flange is used.

**3.2 Effect of Baffle Plate.** As illustrated in the above section, a flange may improve the capture zone in a cross draft, but it is very limited. An alternative is to utilize a baffle plate. Huang et al. [3] were the first to propose this idea to enhance the capability of the hood in a cross draft. They performed flow visualization experiments and LDV measurements to observe the flow variation

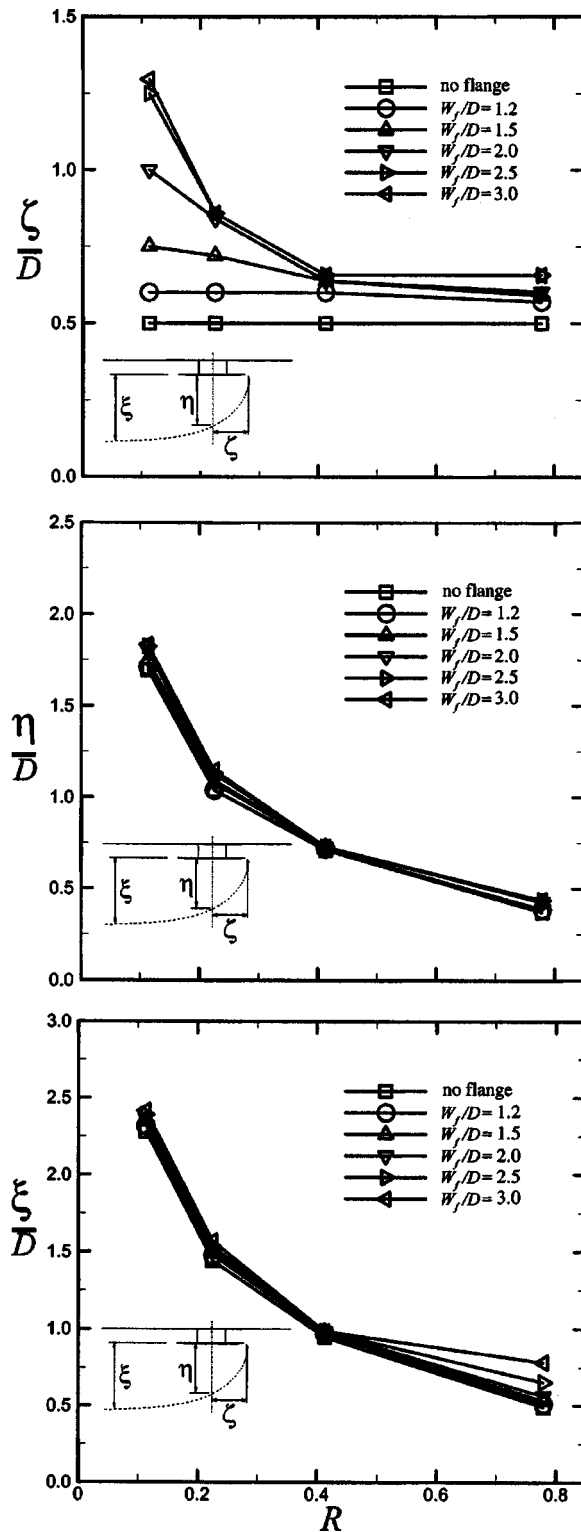


Fig. 2 Variation of characteristic lengths

due to a baffle plate. It is well-known that vortex shedding is expected to be found behind the plate (see Bradbury [16]). Consequently, a low pressure zone is formed behind the plate. Therefore, this may be helpful for capture of pollutants from other high pressure zones to the low pressure zone. Knowing this, the vertical plate may be installed between the hood and the inlet boundary of a cross draft. Figure 1 shows the location of the baffle plate with width  $b$  and length  $l$ . The distance between the plate and the

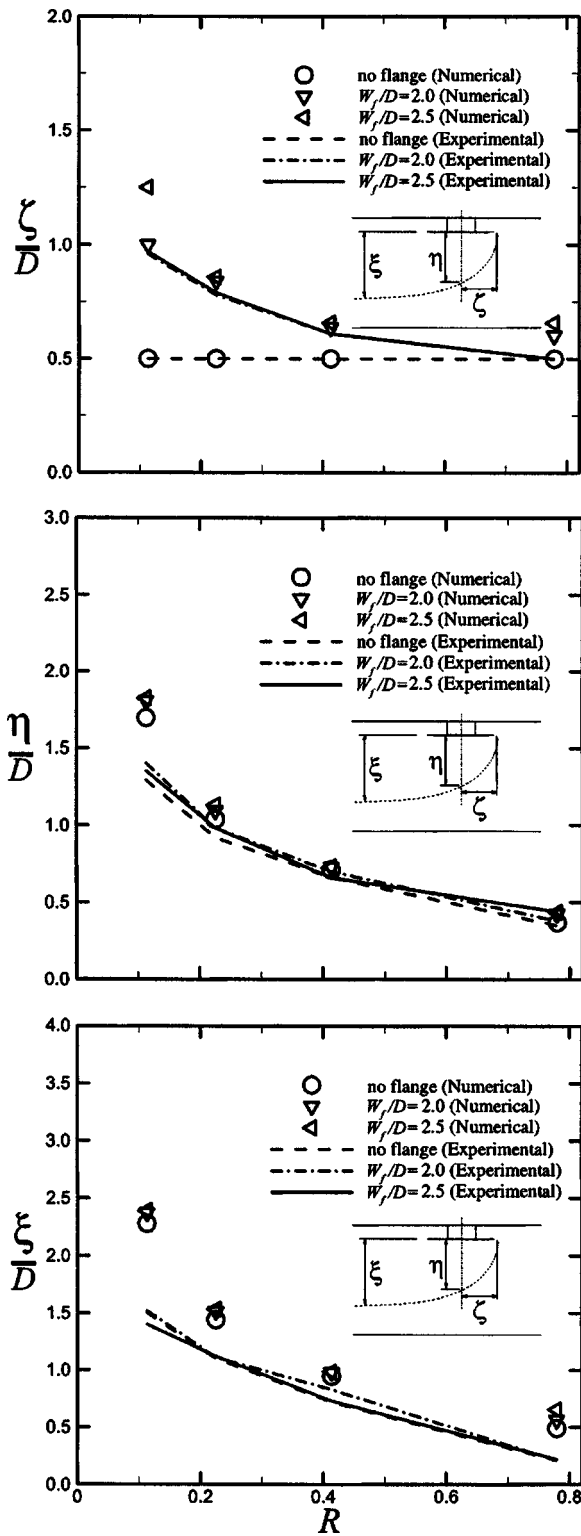


Fig. 3 Variation of characteristic lengths with respect to  $R$  and  $W_f/D$ . Experimental results can be found in Huang et al. [2].

center of the hood opening is  $L$ . There is a bridge to connect the vertical plate and the flange. How should we decide on  $L$  and  $b$ ? Since the width of the wake behind the plate is close to the width of the plate, the first idea is to let  $b$  be equal to the length of the hood,  $D=10$  cm. Hence the opening of the hood is within the

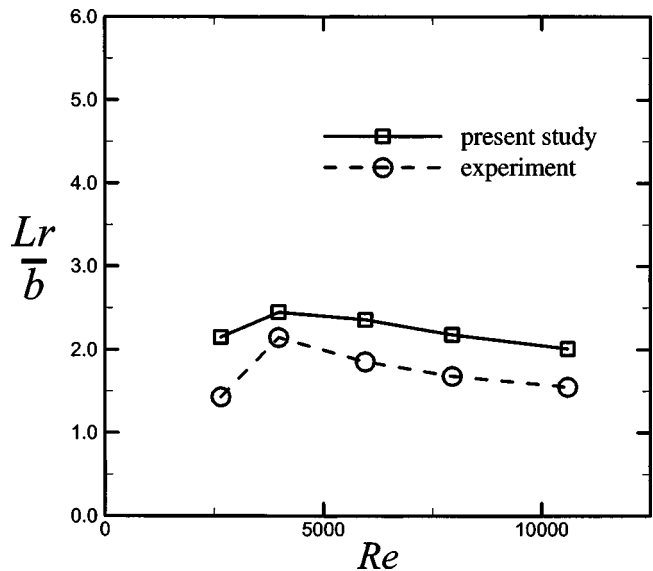


Fig. 4 Variation of the wake length with respect to  $U_c$ .  $U_c$  varies from  $0.4$  m  $s^{-1}$  to  $1.6$  m  $s^{-1}$ . Corresponding Reynolds numbers are 2 650 to 10 600. Experimental data are provided by Huang et al. [3].

recirculation zone.

**3.2.1 Determination of Recirculation Zone.** To make sure the hood opening was within the recirculation zone behind the plate, a uniform flow past a vertical plate with a height of 50 cm and width of 10 cm was simulated first. In order to get the time-averaged length of the recirculation zone, instantaneous velocity solutions were averaged to get a quasi-steady velocity field. We considered cross flows of  $U_c=0.4$  m  $s^{-1}$  to  $1.6$  m  $s^{-1}$ . The corresponding Reynolds number,  $Re=U_c b/\nu$ , varied from 2 650 to 10 600. Numerical simulations were performed to get instantaneous solutions for velocity and pressure. The total nondimensional physical time for the averaged solutions was about 1000. Figure 4 shows the variation of the average wake length,  $L_r$ , with respect to the Reynolds number.  $L_r$  is the horizontal distance from the plate to the saddle point of the recirculation zone. We compared the numerical results with the experimental results provided by Huang et al. [3]. Although the numerical results did not completely agree with the experimental results, their tendencies were very similar. We found the average length of the recirculation zone varies from  $1.5D$  to  $2.5D$ . The minimum difference between the numerical and experimental results is  $U_c=0.6$  m  $s^{-1}$  ( $Re=4000$ ). In terms of these results, the distance  $L$  between the plate and the end of the hood opening was  $2.2D$ , i.e., 22 cm. Meanwhile, the magnitude of  $U_c$  was fixed at  $0.6$  m  $s^{-1}$  to make the numerical results close to the real flow fields.

**3.2.2 Flow Variation Due to the Baffle Plate.** Another problem regarding the plate is its height,  $l$ . The main factor determining the height,  $l$ , is the suction speed,  $V_s$ . Hence, the following studies focus on the relationship among  $l$ ,  $V_s$  and the size of the capture zone.  $V_s$  ranged from  $2.35$  m  $s^{-1}$  to  $5.33$  m  $s^{-1}$ . The corresponding  $R$  ranged from 0.255 to 0.113. In addition,  $l/b$  ranged from 1.5 to 4. There was no vortex shedding behind the vertical plate due to the hood suction. The nondimensional physical time of the simulation was about 1200. At the end of the simulation, the nondimensional maximum variation of velocity through the whole flow field was less than  $10^{-4}$ . That meant the flow field was assumed to have reached a steady state at the end of the simulation.

First, let us observe the variation of the flow patterns with a vertical baffle plate. Figure 5 reveals the sketch of the controlled flow pattern. The capture zone enclosed by the dividing stream

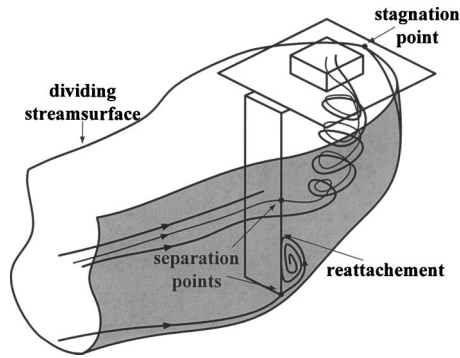


Fig. 5 Schematic diagram of the hood-capture flow pattern

surface was enlarged due to the vertical plate. We found that the capture zone stretched due to the plate. Meanwhile, a pair of vortices attracted into the opening of the hood just like a pair of cyclones. No vortex shedding was observed behind the baffle plate. The wake became stable and reached a steady state due to the interaction of the crossflow and the hood suction. Those vortices caused a low pressure region which made the capture zone larger than the one without a plate.

We investigated the effect of a baffle plate with respect to various  $V_s$  and  $l/b$ 's on the vertical central plane. The capture length  $\eta$  was the vertical distance from the center of the hood opening to the dividing stream surface. A long capture length  $\eta$  means a better capture efficiency.  $\eta$  was normalized by  $l$  first. Figure 6 demonstrates the variation of  $\eta/l$  with respect to  $l/b$  and  $R$ . When  $l/b$  was less than 3.5,  $\eta$  was inversely proportional to  $R$ . The capture zone contracted when  $R$  increased. Moreover, when  $l/b$  exceeded 3.5, it was found that  $\eta/l$  is mainly affected by  $l/b$ .  $\eta/l$  was proportional to  $l/b$  in this region.

Figure 7 shows the variation of  $\eta$  normalized by  $b$  with respect to  $R$ . We found the curves referring to  $l/b=4$  and 3.5 were almost horizontal. It meant that  $\eta/b$  was not affected by  $R$  in those cases. In addition,  $\eta/b$  was inversely proportional to  $R$  in the case of  $l/b=1.5$ . Cases between  $l/b=2$  and 3 were affected by  $R$  and  $l/b$ . Those results agree with Fig. 6.

The obtained numerical results were compared with experimental results given by Huang et al. [3]. Figure 8 demonstrates the comparisons. We found all the numerical results overestimated

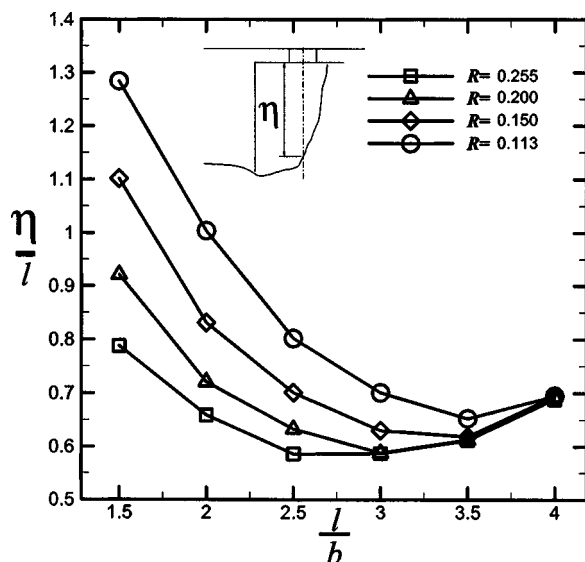


Fig. 6 Variation of  $\eta/l$  with respect to  $l/b$  and  $R$

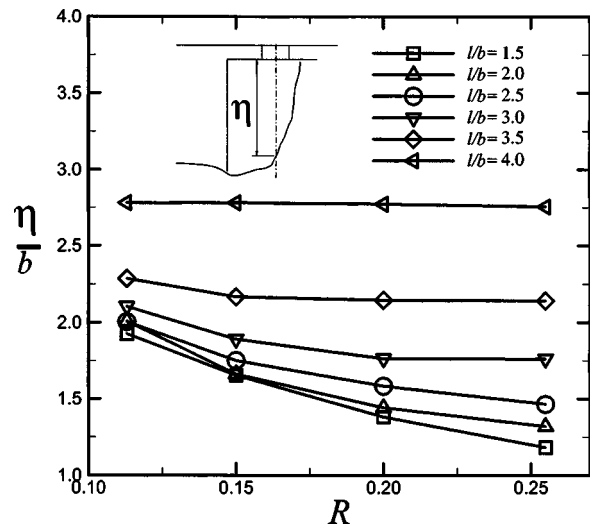


Fig. 7 Variation of  $\eta/b$  with respect to  $l/b$  and  $R$

$\eta/b$ . Good agreements could be found at large  $l/b$ 's and  $R$ 's. Although numerical results are not exactly the same as those of Huang et al. [3], the deviations are within an acceptable range.

#### 4 Conclusions

The effect of a passive control method on the hood-capture flow were studied numerically in this paper. In order to overcome the negative effect of cross draft on the hood performance, a flange and a baffle plate were used to improve the hood-capture flow. Numerical simulations were performed to study the changes of the hood flow induced by the flange and the baffle plate. The effect of a flange on the hood-capture flow was investigated. A large flange can enlarge  $\zeta$  effectively at a small  $R$  when  $W_f/D$  is not larger than 2.5. The baffle plate can improve the capture zone. The interaction of the cross draft and the hood-suction caused a stable recirculation behind the plate. The capture zone was stretched due to the existence of the low pressure zones caused by the stable recirculation behind the baffle plate. In practice, the width of the baffle plate can be equal to the length of the hood opening. When the velocity ratio of a crossflow to suction  $R$  is fixed, an increased aspect ratio  $l/b$  would enlarge the capture zone. The minimum

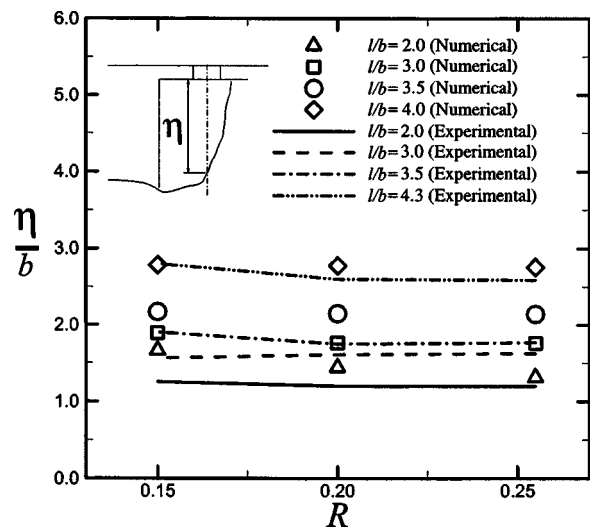


Fig. 8 Variation of  $\eta/b$  with respect to  $l/b$  and  $R$ . Experimental data are provided by Huang et al. [3].

$\eta/l$  is at least larger than 0.5. It is better than the one without a baffle plate. The negative effect of a crossflow decreases when plates of large  $l/b$  are utilized. When one uses a baffle plate,  $\eta$  improves. It means that a baffle plate can change the negative effect of crossflow successfully. It is a simple and passive method. Numerical results of  $\eta$  were compared with experimental results given by Huang et al. [3]. Acceptable agreements were found among present and experimental data. Figures 6 or 7 can be conveniently used to determine the proper size of a baffle plate. These results are very useful for design and operation of a hood in a crossflow.

### Acknowledgment

We are very grateful to Professor A.G.L. Borthwick for his comments on this paper.

### Nomenclature

- $b$  = width of baffle plate, cm  
 $D$  = length of square cross section of hood, cm  
 $L$  = horizontal distance between baffle plate and center of the hood opening, cm  
 $L_r$  = averaged length of steady wake behind a vertical plate normal to a cross draft, cm  
 $l$  = length of baffle plate, cm  
 $R$  = velocity ratio of crossflow to hood suction speed,  $U_c/V_s$   
 $Re$  = Reynolds number,  $U_c b/\nu$   
 $U_c$  = uniform velocity of cross flow,  $\text{m s}^{-1}$   
 $V_s$  = suction speed of hood,  $\text{m s}^{-1}$   
 $W_f$  = length of flange, cm  
 $\rho$  = density of air,  $1.204 \text{ kg m}^{-3}$  ( $20^\circ\text{C}$ , 1 atm)  
 $\nu$  = kinetic viscosity of air,  $1.51 \times 10^{-5} \text{ m}^2 \text{ s}^{-1}$  ( $20^\circ\text{C}$ , 1 atm)  
 $\eta$  = vertical distance from hood opening to dividing streamline along symmetry axis, cm  
 $\xi$  = vertical distance from hood opening to streamline at inlet boundary, cm

$\xi$  = horizontal distance from stagnation point on flange to central axis of hood, cm

### References

- [1] Huang, R. F., Sir, S. Y., Chen, Y. K., Yeh, W. Y., Chen, C. W., and Chen, C. C., 2001, "Capture Envelopes of Rectangular Hoods in Cross Drafts," *Am. Ind. Hyg. Assoc. J.*, **62**, pp. 563–572.
- [2] Huang, R. F., Chen, J. L., Chen, Y. K., Chen, C. C., Yeh, W. Y., and Chen, C. W., 2001, "The Capture Envelope of a Flanged Circular Hood in Cross Drafts," *Am. Ind. Hyg. Assoc. J.*, **62**, pp. 199–207.
- [3] Huang, R. F., Liu, G. S., Lin, S. Y., Chen, Y. K., Wang, S. C., Peng, C. Y., Yeh, W. Y., Chen, C. W., and Chang, C. P., 2004, "Development and Characterization of a Wake-controlled Exterior Hood," *J. Occup. Environ. Med.*, **1**, pp. 769–778.
- [4] Dalla Valle, J. M., 1945, *Exhaust Hoods*, Industrial Press, New York, pp. 21–48.
- [5] Silverman, L., 1943, "Fundamental Factors in the Design of Exhaust Hoods," Sc.D. thesis, Harvard University.
- [6] Garrison, R. P., 1981, "Centerline Velocity Gradients for Plain and Flanged Local Exhaust Inlets," *Am. Ind. Hyg. Assoc. J.*, **42**, pp. 739–746.
- [7] Vincent, J. H., 1989, *Aerosol Sampling—Science and Practice*, Wiley, New York.
- [8] Ingham, D. B., and Hildyard, M. L., 1991, "The Fluid Flow into a Blunt Aerosol Sampler Oriented at an Angle to the Oncoming Flow," *J. Aerosol Sci.*, **22**, pp. 235–252.
- [9] Sreenath, A., Ramachandran, G., and Vincent, J. H., 1997, "Experimental Investigation into the Nature of Airflows Near Bluff Bodies with Aspiration, with Implications to Aerosol Sampling," *Atmos. Environ.*, **31**, pp. 2349–2359.
- [10] Kulmala, I., 1995, "Numerical Simulation of the Capture Efficiency of an Unflanged Rectangular Exhaust Opening in a Coaxial Air Flow," *Ann. Occup. Hyg.*, **39**, pp. 21–33.
- [11] Conroy, L. M., Trevelyan, P. M., and Ingham, D. B., 2000, "An Analytical, Numerical, and Experimental Comparison of the Fluid Velocity in the Vicinity of an Open Tank with One and Two Lateral Exhaust Slot Hoods and a Uniform Crossdraft," *Ann. Occup. Hyg.*, **44**, pp. 407–419.
- [12] Chen, Y. K., Huang, R. F., and Chen, C. W., 2001, "Capture Envelope of a Hood Opening under Crosswind Condition—A Numerical Approach," *J. Inst. Occup. Safety Health*, **9**, pp. 225–239.
- [13] Leonard, B. P., 1979, "A Stable and Accurate Convective Modeling Procedure Based on Quadratic Upstream Interpolation," *Comput. Methods Appl. Mech. Eng.*, **19**, pp. 59–98.
- [14] Canuto, C., Yousuff, H. M., Quarteroni, A., and Zang, T. A., 1988, *Spectral Methods in Fluid Dynamics*, Springer-Verlag, Berlin, pp. 101–104.
- [15] Hirt, C. W., Nichols, B. D., and Romero, N. C., 1975, "SOLA—A Numerical Solution Algorithm for Transient Fluid Flow," LA-5852 technical report, Los Alamos Scientific Laboratory, New Mexico.
- [16] Bradbury, L. J. S., 1976, "Measurements with a Pulsed-wire and a Hot-wire Anemometer in the Highly Turbulent Wake of a Normal Flat Plate," *J. Fluid Mech.*, **77**, pp. 473–497.

# Analysis for Slip Flow Over a Single Free Disk With Heat Transfer

Aytac Arikoglu

Ibrahim Ozkol<sup>1</sup>

Faculty of Aeronautics and Astronautics, Istanbul Technical University, 34469 Maslak, Istanbul, Turkey

## 1 Introduction

In this study the equations of motion derived by von Karman [1], with Benton's transformations [2] for the flow over a single free disk is studied for the slip flow. The slip regime for the Knudsen number ( $Kn$ ) is valid in the range  $0.1 > Kn > 0.01$  [3]. For  $Kn < 0.01$  the no-slip condition is present and for  $Kn > 0.1$  the Navier–Stokes equations cannot be used since the flow field cannot be assumed to be continuum. In our study, the slip and the no-slip regimes that lie in the range  $0.1 > Kn > 0$  is considered.

The subject of the rarefied gas dynamics can be conveniently defined as the study of gas flows in which the average value of the distance between two subsequent collisions of a molecule, namely the mean free path, is not negligible in comparison with a characteristic length of the structure considered. This type of flow is commonly encountered in many engineering aspects such as, high-altitude flight, micro-machines, vacuum technology, aerosol reactors, etc.

Mainly, requirement of high temperatures in the turbine stage of a gas turbine engine to achieve high thermal efficiencies, cooling of the air is essential to ensure for extending the life of turbine disks and blades. It is vital to know how flow and thermal fields are at every stage for a safe and effective work life, in the operation of the rotary type machine systems. For an accurate determination of temperature distribution, firstly the flow field must be solved as precisely as possible. Since the governing equations, namely the momentum equations, are highly nonlinear and coupled, it is hard to obtain exact analytical solutions for the full problem.

In 1921, von Karman [1] discovered the self similar behavior of the flow over a single free disk and solved the resulting ordinary differential equation system by using an approximate integral method. Latter, Cochran [4] obtained more accurate results by matching a Taylor series expansion near the disk with a series solution involving exponentially decaying functions far from the disk at a suitable mid point. Benton [2] improved Cochran's solutions and solved the problem for the unsteady case. The problem of heat transfer was first considered by Millsaps and Polhausen [5] for the values of Prandtl number ( $Pr$ ) between 0.5 and 1.0. Then, Sparrow and Gregg [6] extended this work for a range of  $0.1 < Pr < 100$  by neglecting the dissipative terms in the energy equation.

In this study we used the differential transform method (DTM), which was introduced by Zhou [7] in a study about electrical circuits. It is semianalytical-numerical technique depending on Taylor series that is promising for various types of differential equations. With this technique, it is possible to obtain highly accurate results or exact solutions for the differential or integro-differential equation considered [8–10].

## 2 Theoretical Model for the Problem

Let  $(u, v, w)$  be the velocity components in the cylindrical coordinates  $(r, \theta, z)$ , respectively, and  $t$  be the temperature. Assuming that temperature is a function of the axial coordinate  $z$  only, the following similarity variables are introduced [1]:

$$u = \Omega r F(\zeta), \quad v = \Omega r G(\zeta), \quad w = \sqrt{\Omega \nu} H(\zeta),$$

$$p = -\rho \Omega \nu P(\zeta) \text{ and } T(\zeta) = (t - t_\infty)/(t_0 - t_\infty) \quad (1)$$

where,  $\zeta = z\sqrt{\Omega/\nu}$  is the dimensionless axial coordinate. To solve the problem in a bounded domain, we use the following dependent and independent variables introduced by Benton [2]:

$$\xi = e^{-c\zeta} \quad (2)$$

$$F(\zeta) = c^2 f(\xi), \quad G(\zeta) = c^2 g(\xi), \quad H(\zeta) = -c[1 - h(\xi)] \quad (3)$$

Then, the Navier–Stokes equations and the energy equation, by neglecting dissipation terms, read:

$$\xi^2 f''(\xi) = f^2(\xi) - g^2(\xi) - \xi f'(\xi) h \quad (4)$$

$$\xi^2 g''(\xi) = 2f(\xi)g(\xi) - \xi g'(\xi)h(\xi) \quad (5)$$

$$\xi h'(\xi) = 2f(\xi) \quad (6)$$

$$T''(\zeta) = Pr HT'(\zeta) \quad (7)$$

where,  $Pr$  is the Prandtl number. Since the assumption of continuum media fails, rarefied gases cannot be investigated with N.S. equations for a value of Knudsen number higher than 0.1 [11]. For the range  $0.1 > Kn > 0.01$  the no slip B.C. cannot be used and should be replaced with the following expression [3]:

$$U_t = \frac{2 - \sigma}{\sigma} \lambda \frac{\partial U_t}{\partial n} \quad (8)$$

where  $U_t$  is the tangent velocity,  $n$  is the normal direction to the wall,  $\sigma$  is the tangential momentum accommodation coefficient, and  $\lambda$  is the mean free path. For  $Kn < 0.01$  the viscous flow is recovered and the no slip condition is valid. In our considerations the slip and the no-slip regimes of the Knudsen number that lies in the range  $0.1 > Kn > 0$  will be taken into account. By using Eq. (8), the boundary conditions for the problem can be introduced as follows:

$$f(1) = \omega f'(1), \quad g(1) = c^{-2} - \omega c g'(1), \quad h(1) = 1 \quad (9)$$

$$f(0) = 0, \quad g(0) = 0, \quad h(0) = 0 \quad (10)$$

where,  $\omega = [(2 - \sigma)\lambda\Omega^{1/2}]/\sigma\nu^{1/2}$  is the slip factor. And the B.C.'s for the temperature are:

$$T(0) = 1, \quad T(\infty) = 0 \quad (11)$$

By integrating Eq. (7) with the first boundary condition in Eq. (11), the dimensionless temperature can be evaluated in terms of the axial part of the velocity field as follows:

$$T(\zeta) = T'(0) \int_0^\zeta e^{Pr \int_0^\eta H(\eta) d\eta} d\beta + 1 \quad (12)$$

where,  $\beta$  and  $\eta$  are dummy variables. The missing B.C.  $T'(0)$  is obtained from the far field B.C. given in Eq. (11) as follows:

$$T'(0) = -1 \int_0^\infty e^{Pr \int_0^\beta H(\eta) d\eta} d\beta \quad (13)$$

## 3 The Solution

In solving Eqs. (4)–(6) with the B.C.'s (9) and (10), we applied DTM at  $\xi=0$ . By using the theorems in [8], the differential transform of Eqs. (4)–(6) can be evaluated as follows:

<sup>1</sup>Corresponding author. E-mail: ozkol@itu.edu.tr

Contributed by the Fluids Engineering Division for publication in the JOURNAL OF FLUIDS ENGINEERING. Manuscript received June 10, 2004; revised January 8, 2005. Associate Editor: Malcolm Andrews.

$$\tilde{F}(k) = \frac{1}{k(k-1)} \sum_{l=0}^k [\tilde{F}(l)\tilde{F}(k-l) - \tilde{G}(l)\tilde{G}(k-l) - l\tilde{F}(l)\tilde{H}(k-l)] \quad (14)$$

$$\tilde{G}(k) = \frac{1}{k(k-1)} \sum_{l=0}^k [2\tilde{F}(l)\tilde{G}(k-l) - l\tilde{G}(l)\tilde{H}(k-l)] \quad (15)$$

$$\tilde{H}(k) = \frac{2}{k}\tilde{F}(k) \quad (16)$$

where,  $k \geq 2$  and  $\tilde{F}(k)$ ,  $\tilde{G}(k)$ , and  $\tilde{H}(k)$  denote to the differential transforms of  $f(\xi)$ ,  $g(\xi)$ , and  $h(\xi)$ , respectively. To evaluate the dependent variables, we need to know the missing B.C.'s  $f'(0)$  and  $g'(0)$ . In many studies, such as [12], the shooting method is used to determine unknown B.C.'s. Instead of using the shooting method, we obtained the values of  $\tilde{F}(k)$ ,  $\tilde{G}(k)$  and  $\tilde{H}(k)$  for  $k=2, 3, \dots, N$  in terms of  $f'(0)$  and  $g'(0)$ , which will be called as  $f_1$  and  $g_1$  respectively, then by using the B.C.'s given in Eq. (9) for  $\xi=1$ , we evaluated  $f_1$ ,  $g_1$ , and  $c$  numerically. This is much faster and cost efficient than the numerical techniques since it is not iterative. With the new defined ones, the B.C.'s given in Eq. (10) for  $\xi=0$  are transformed as follows:

$$\tilde{F}(0) = 0, \quad \tilde{G}(0) = 0, \quad \tilde{H}(0) = 0, \quad \tilde{F}(1) = f_1 \text{ and } \tilde{G}(1) = g_1 \quad (17)$$

By using the recurrence relations in Eqs. (14)–(16) and the transformed boundary conditions in Eq. (17),  $\tilde{F}(k)$ ,  $\tilde{G}(k)$ , and  $\tilde{H}(k)$  for  $k=2, 3, \dots, N$  are evaluated. Then, using the inverse transformation rule in [8], the series solutions are obtained from:

$$f(\xi) = \sum_{k=0}^N \tilde{F}(k)\xi^k, \quad g(\xi) = \sum_{k=0}^N \tilde{G}(k)\xi^k, \quad h(\xi) = \sum_{k=0}^N \tilde{H}(k)\xi^k \quad (18)$$

where,  $N$  is the number of terms to be calculated. By calculating up to  $N=6$ , we get:

$$f(\xi) = f_1\xi - \frac{1}{2}(f_1^2 + g_1^2)\xi^2 + \frac{1}{4}f_1(f_1^2 + g_1^2)\xi^3 - \frac{1}{144}(17f_1^4 + 18f_1^2g_1^2 + g_1^4)\xi^4 + \frac{1}{1152}f_1(61f_1^4 + 74f_1^2g_1^2 + 13g_1^4)\xi^5 - \frac{1}{86400}(1971f_1^6 + 2825f_1^4g_1^2 + 889f_1^2g_1^4 + 35g_1^6)\xi^6 + \dots \quad (19)$$

$$g(\xi) = g_1\xi - \frac{1}{12}g_1(f_1^2 + g_1^2)\xi^3 + \frac{1}{18}f_1g_1(f_1^2 + g_1^2)\xi^4 - \frac{1}{1920}g_1(53f_1^4 + 58f_1^2g_1^2 + 5g_1^4)\xi^5 + \frac{1}{5400}f_1g_1(65f_1^4 + 82f_1^2g_1^2 + 17g_1^4)\xi^6 + \dots \quad (20)$$

$$h(\xi) = 2f_1\xi - \frac{1}{2}(f_1^2 + g_1^2)\xi^2 + \frac{1}{6}f_1(f_1^2 + g_1^2)\xi^3 - \frac{1}{288}(17f_1^4 + 18f_1^2g_1^2 + g_1^4)\xi^4 + \frac{1}{2880}f_1(61f_1^4 + 74f_1^2g_1^2 + 13g_1^4)\xi^5 - \frac{1}{259200}(1971f_1^6 + 2825f_1^4g_1^2 + 889f_1^2g_1^4 + 35g_1^6)\xi^6 + \dots \quad (21)$$

**Table 2** Variation of  $T'(0)$ ,  $f_1$  and  $g_1$  with respect to  $\omega$  ( $N=60$ )

$\omega$	$T'(0)$	$f_1$	$g_1$
0.0	-0.32586039	1.182244779	1.536776526
0.1	-0.333496950	1.096913972	1.422174786
0.2	-0.336780900	1.038943086	1.339504645
0.5	-0.334652873	0.942790947	1.191324451
1.0	-0.320432993	0.875499819	1.076800290
2.0	-0.292997980	0.825074692	0.983003210
5.0	-0.244046155	0.783417800	0.898674732
10.0	-0.205049245	0.765039980	0.858998126
20.0	-0.168829630	0.753582150	0.833355187

The solutions are given here up to  $O(\xi^6)$ , however, one can easily obtain higher ordered terms. After evaluating  $f(\xi)$ ,  $g(\xi)$ , and  $h(\xi)$ , the original dependant variables  $F(\zeta)$ ,  $G(\zeta)$ , and  $H(\zeta)$  are obtained by using Eqs. (2) and (3). If necessary,  $P(\zeta)$  can be obtained from the following equation:

$$P(\zeta) - P_0 = H(\zeta)^2/2 - H'(\zeta) \quad (22)$$

## 4 Results and Discussion

The variation of the flow field parameters  $F'(0)$ ,  $G'(0)$ , and  $H(\infty)=-c$  with respect to the slip factor are given below in Table 1 with comparison to [13]. The other parameters, which are  $f_1$ ,  $g_1$ , and  $T'(0)$  are reported in Table 2.

We evaluated the results in Tables 1 and 2 and Figs. 1–10 by calculating  $N=60$  terms. One can see from Table 1 that the results obtained for  $F'(0)$ ,  $G'(0)$ , and  $H(\infty)$  are in good agreement with [13]. While evaluating the thermal field, we took  $Pr=0.71$ , which is the value of Prandtl number for air. By continuing the same procedure, the thermal field can be computed for other Prandtl numbers.

Figures 1 and 2 show that the magnitudes of the surface skin friction in radial and circumferential directions decrease with an increase in  $\omega$ . This is quite natural since  $\omega$ , the slip factor, is the ratio of slip to viscous effects. As a consequence and as it can be observed from Fig. 4, the inflow rate at infinity decreases since the radially outwards boundary layer loses its thickness and is fed by the fluid stream in axial direction.

As one can see from Fig. 3, the minimum value for  $T'(0)$  is not reached at  $\omega=0$ . We calculated this value as  $\omega=0.2836$  and the value corresponding to this point as  $T'(0)=-0.337462$ . This value of the slip factor is of great importance since the heat transfer from the rotating disk is directly related to the temperature gradient at  $\zeta=0$ . We can state that the maximum cooling of the rotating disk is reached at this value of the slip factor if the ambient fluid is colder than the rotating disk. The magnitudes of the radial and the circumferential velocities just above the rotating disk are given below in Figs. 5 and 6.

The highest value of the radial velocity on the surface is 0.128440 and this value is reached at  $\omega=1.1586$ . This value of the

**Table 1** Variation of the flow field parameters due to  $\omega$  with comparison to Ref. [13] ( $N=60$ )

$\omega$	$F'(0)$	$F'(0)$ [13]	$G'(0)$	$G'(0)$ [13]	$H(\infty)$	$H(\infty)$ [13]
0.0	0.510232619	0.51023262	-0.615922014	-0.61592201	0.88447411	0.8844742
0.1	0.421453639	0.42145364	-0.605835241	-0.60583524	0.88136423	0.8813642
0.2	0.352581007	0.35258101	-0.583676764	-0.58367676	0.87395729	0.8739572
0.5	0.223848209	0.22384821	-0.502809702	-0.50280970	0.84239263	0.8423926
1.0	0.127923645	0.12792364	-0.394927595	-0.39492760	0.78947720	0.7894772
2.0	0.061010098	0.06101010	-0.273370132	-0.27337013	0.71031331	0.7103134
5.0	0.018588527	0.01858853	-0.143388209	-0.14338821	0.58376463	0.5837646
10.0	0.006812558	0.00681256	-0.081030089	-0.08103009	0.48758465	0.4875846
20.0	0.002361594	0.00236159	-0.043788462	-0.04378846	0.39997581	0.3999758

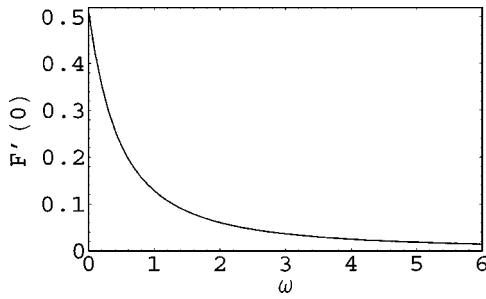


Fig. 1 Variation of  $F'(0)$  with  $\omega$

slip factor may be necessary and important practically, if the aim is to use the disk as a centrifugal fan. As one can see from Fig. 6, the maximum circumferential velocity on the surface is at  $\omega=0$ , where the no-slip condition is present. This is a result of the negative gradient of the circumferential velocity in  $z$  direction above the disk. Variations of  $F$ ,  $G$ ,  $H$ , and  $T$  for several values of  $\omega$  are given below in Figs. 7–10.

From Figs. 7–9, the decreasing effect of the slip factor  $\omega$  on velocity field can be easily seen. In the limit case  $\omega \rightarrow \infty$ , when the flow is entirely potential, the rotating disk has no effect on rotating the fluid particles, therefore, the velocity field is constant and equal to zero.

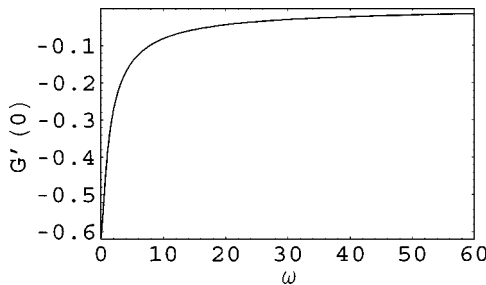


Fig. 2 Variation of  $G'(0)$  with  $\omega$

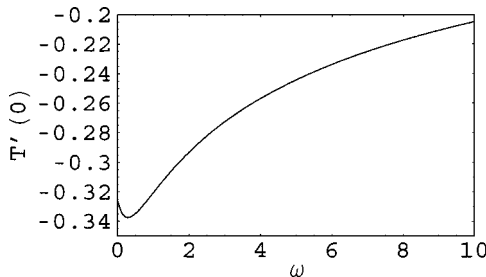


Fig. 3 Variation of  $T'(0)$  with  $\omega$

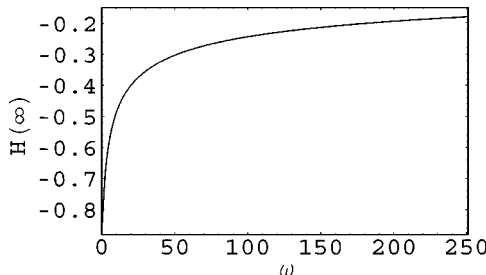


Fig. 4 Variation of  $H(\infty)$  with  $\omega$

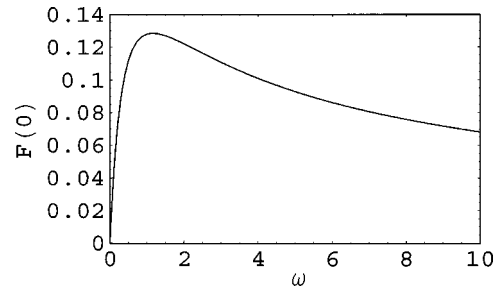


Fig. 5 Variation of the radial velocity with respect to  $\omega$  at  $\zeta=0$

This is natural, since the rotating disk acts like a centrifugal fan and owing to the centrifugal forces, throws the fluid that sticks on it. A fluid stream compensates this thrown fluid, which is in the axial direction. When  $\omega$  increases, less amount of fluid can stick and the rotating disk loses its efficiency to transfer its circumferential momentum to the fluid particles. The fluid loses circumferential velocity therefore the centrifugal forces that throw the fluid outwards decrease. Since the disk throws less fluid away, less amount of fluid stream in the axial direction exists.

From Fig. 10, one can conclude that as the slip factor  $\omega$  increases,  $T(\zeta)$  tends to vary linearly. This is a result of the fact that as  $\omega$  increases,  $H(\zeta)$  decrease and in the limit case of  $\omega \rightarrow \infty$ ,  $H=0$  can be taken. From Eq. (7), this leads to the following case:

$$\lim_{\omega \rightarrow \infty} T''(\zeta) = 0 \quad (23)$$

where, the solution is a line and for large values of  $\omega$ , it can be approximately taken as:  $T(\zeta) \cong T'(0)\zeta + 1$  to ease the computations, if necessary.

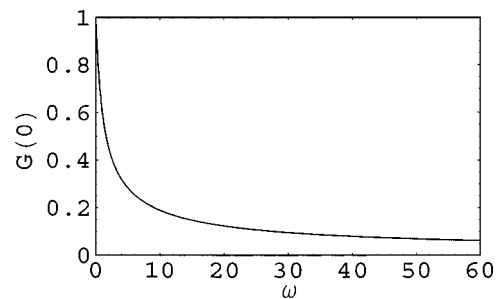


Fig. 6 Variation of circumferential velocity with respect to  $\omega$  at  $\zeta=0$

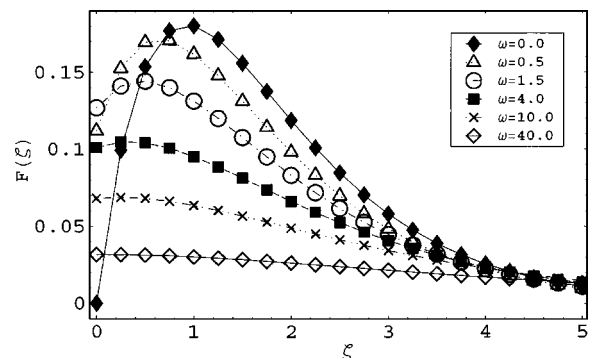


Fig. 7 Radial component of the velocity for several values of  $\omega$



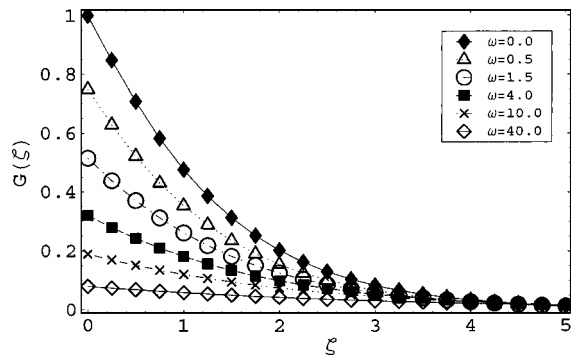


Fig. 8 Circumferential component of the velocity for several values of  $\omega$

## 5 Conclusion

In this study, the slip flow over a rotating infinite disk is considered. DTM is used as the solution technique after the domain is transformed to a bounded one. Velocity and thermal fields are evaluated accurately. Numerical and graphical results are given and the effect of slip to the flow field variables is discussed in detail. The point that is worth noticing in this paper is that robustness of the DTM since it solves nonlinear-coupled equations in a

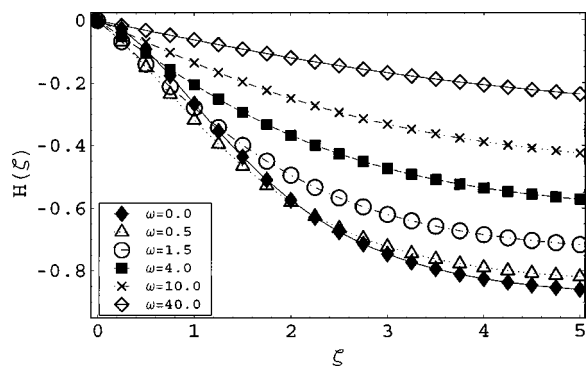


Fig. 9 Axial component of the velocity for several values of  $\omega$

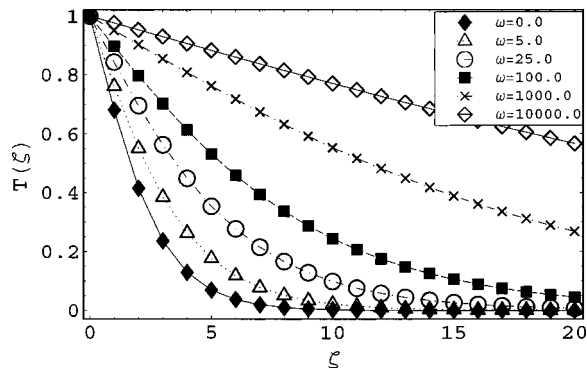


Fig. 10 Variation of temperature for several values of  $\omega$ ,  $Pr = 0.71$

simplified and tractable manner with high accuracy. This study also diverges from the similar studies in literature by solving temperature field for the slip flow over a rotating disk.

## References

- [1] Karman, T., 1921, "Über Laminare und Turbulente Reibung," *Z. Angew. Math. Mech.*, **1**, pp. 233–252.
- [2] Benton, E. R., 1966, "On the flow due to a rotating disc," *J. Fluid Mech.*, **24**, pp. 781–800.
- [3] Sharipov, F. and Seleznev, V., 1998, "Data on internal rarefied gas flows," *J. Phys. Chem. Ref. Data*, **27**, pp. 657–706.
- [4] Cochran, W. G., 1934, "The flow due to a rotating disc," *Proc. Cambridge Philos. Soc.*, **30**, pp. 365–375.
- [5] Millsaps, K., and Polhausen, K., 1952, "Heat transfer by laminar flow from a rotating plate," *J. Aeronaut. Sci.*, **19**, pp. 120–126.
- [6] Sparrow, E. M., and Gregg, J. L., 1959, "Heat transfer from a rotating disk to fluids of any Prandtl number," *ASME J. Heat Transfer*, **81**, pp. 249–251.
- [7] Zhou, J. K., 1986, *Differential Transformation and its Application for Electrical Circuits*, Huazhong University Press, Wuhan, China.
- [8] Arikoglu, A. and Ozkol, I., 2004, "Solution of boundary value problems for integro-differential equations by using Differential Transform Method," *Appl. Math. Comput.* (to be published).
- [9] Ayaz, F., 2003, "On the two-dimensional differential transform method," *Appl. Math. Comput.*, **143**, pp. 361–374.
- [10] Ayaz, F., 2004, "Solutions of the system of differential equations by differential transform method," *Appl. Math. Comput.*, **147**, pp. 547–567.
- [11] Kogan, M. N., 1969, *Rarefied Gas Dynamics*, Plenum, New York.
- [12] Owen, J. M. and Rogers, R. H., 1989, *Flow and heat transfer in rotating-disc systems, Vol. 1: Rotor-stator systems*, Research Studies Press, Taunton.
- [13] Miklavcic, M and Wang C. Y., 2004, "The flow due to a rough rotating disk," *Z. Angew. Math. Phys.*, **55**, pp. 235–246.